Classical Cepheids: High-precision Velocimetry, Cluster Membership, and the Effect of Rotation

Anderson, Richard Irving

UNIVERSITÉ DE GENÈVE
Département d'Astronomie

FACULTÉ DES SCIENCES
Docteur Laurent Eyer
Docteur Nami Mowlavi

Classical Cepheids: High-precision Velocimetry, Cluster Membership, and the Effect of Rotation

THÈSE

présentée à la Faculté des sciences de l'Université de Genève

pour obtenir le grade de

Docteur ès sciences, mention Astronomie et Astrophysique

par

Richard Irving ANDERSON

de

Aalen (Allemagne)

Thèse N° 4627

GENÈVE
2013

UNIVERSITÉ DE GENÈVE

FACULTÉ DES SCIENCES

Doctorat ès sciences
Mention astronomie et astrophysique

Thèse de *Monsieur Richard Irving ANDERSON*

intitulée :

" Classical Cepheids : High-precision Velocimetry, Cluster Membership, and the Effect of Rotation "

La Faculté des sciences, sur le préavis de Messieurs L. EYER, docteur et directeur de thèse (Département d'astronomie), N. MOWLAVI, docteur et codirecteur de thèse (Département d'astronomie), Madame C. CHARBONNEL, professeure associée (Département d'astronomie), Monsieur D. SCHAERER, professeur associé (Département d'astronomie), Monsieur F. BOUCHY, docteur (Laboratoire d'astrophysique de Marseille, France) et Monsieur M. GROENEWEGEN, docteur (Observatoire Royal de Belgique, Bruxelles, Belgique) autorise l'impression de la présente thèse, sans exprimer d'opinion sur les propositions qui y sont énoncées.

Genève, le 16 décembre 2013

Thèse - 4627 -

Le Doyen, Jean-Marc TRISCONE

N.B.- La thèse doit porter la déclaration précédente et remplir les conditions énumérées dans les "Informations relatives aux thèses de doctorat à l'Université de Genève".

Ce travail de thèse a donné lieu à des publications dont la liste se trouve à la page 203.

THE THESIS COMMITTEE WAS COMPOSED OF

LAURENT EYER
UNIVERSITÉ DE GENÈVE, SWITZERLAND

NAMI MOWLAVI
UNIVERSITÉ DE GENÈVE, SWITZERLAND

CORINNE CHARBONNEL
UNIVERSITÉ DE GENÈVE, SWITZERLAND

DANIEL SCHAERER
UNIVERSITÉ DE GENÈVE, SWITZERLAND

FRANÇOIS BOUCHY
LABORATOIRE D'ASTROPHYSIQUE DE MARSEILLE, FRANCE

MARTIN GROENEWEGEN
OBSERVATOIRE ROYALE DE BELGIQUE, BRUXELLES, BELGIUM

SUBMITTED: 8 NOVEMBER 2013
ACCEPTED: 16 DECEMBER 2013
FINAL VERSION: 4 MARCH 2014

UNIVERSITÉ
DE GENÈVE

Acknowledgments

The past four years have been very challenging, informative, intellectually stimulating and rewarding, exciting, and also a great deal of fun. During this time I had the opportunity to learn a lot, perform research that truly inspired and motivated me, meet remarkable people, and travel to extraordinary locations. The people I met and interacted with along the way have aided in shaping this thesis as well as myself. Hence, I would like to use these acknowledgments to express my gratitude and appreciation to all those who contributed to this endeavor in one way or another.

First and foremost, I would like to thank my thesis advisors Laurent Eyer and Nami Mowlavi who have earned my sincere gratitude for their strong continued personal and professional support. Their doors and minds were always open for brainstorming, advice, and feedback. I greatly enjoyed the friendly, honest, and outspoken contact with Laurent and Nami. I also greatly appreciated their enthusiasm towards my ideas, observational propositions or results, and their encouraging curiosity to explore them further. Merci infiniment!

To the members of the thesis committee, Martin Groenewegen, François Bouchy, Daniel Schaerer, and Corinne Charbonnel, I would like to express my gratitude for their interesting comments and questions about my work and manuscript, as well as for assisting in my defense.

I would also like to thank Prof. Burki for hiring me and for supporting my following a three weeks-long French course at the University from which I benefited greatly during the entire PhD. Many members of the stellar variability, Gaia-CU7, and stellar physics groups in Geneva have also contributed to this thesis through discussions. I wish to thank all past and present members of these groups for their assistance and the friendly atmosphere.

I feel deeply honored and very lucky to have had the opportunity to collaborate with the members of the Geneva stellar evolution group, in particular Sylvia Ekström, Cyril Georgy, and Georges Meynet. Working with them felt incredibly fast-paced and dynamic, was always upbeat and exciting, and an incredibly stimulating and satisfying experience. Thank you for everything.

Planning, organizing, carrying out, and analyzing observations were very time consuming. However, I was incredibly fortunate to have had assistance from many people as well as very flexible access to extremely well-operated telescopes and instruments. This help and support made the observational work exciting, efficient, and fun, and I am very grateful for the contributions from everyone who participated in one way or another. Thanks are due to Stéphane Udry and the planet group for agreeing to conduct flexible time exchanges which ensured that time-sensitive observations could be secured. On the observers' side, Lovro Palaversa's repeated availability to carry out entire observing runs was highly appreciated and deserves a special mention. Additionally, the plentiful observations acquired by Pierre Dubath, Berry Holl, Mihaly Váradi, Anne Thoul, Nicolas Cantale, Aurélien Wyttenbach, Maria Süveges, Janis Hagelberg, Monika Lendl, Dominique Naef, David Vance Martin, Amaury Triaud, Marion Neveu, and Bruno Chaselaz are also acknowledged. Behind the scenes, I would like to express my deep appreciation for the efficient and highly competent technical support teams in charge of Euler and Mercator, and in particular to Gregory Lambert whose good company at La Silla was much appreciated. Observing on these

two telescopes was a pleasure!

Data reduction and radial velocity pipelines require a tremendous amount of work, and I was fortunate to be able to benefit from infrastructure that remarkable and resourceful scientists and engineers have developed over decades. I am very grateful to have had access to the reduction pipelines of *CORALIE* and *HERMES*, which have made it possible for me to explore cross-correlation functions and radial velocity measurements without having to start from scratch. In particular, I would like to thank Maxime Marmier and Christophe Lovis for their help with the *CORALIE* pipeline and database.

For their contributions to this thesis, I would like to thank specifically: Amaury Triaud for many inspiring discussions, as well as his eager curiosity and real-time approach to investigating observational data that inspired my own observational strategy; Xavier Dumusque for the many interesting discussions, whether on a bike or a mountain, for brainstorming related to the development of the Doppler tomography masks, help with fitting Keplerians to radial velocity data, and for providing comments on parts of the thesis; François Bouchy for discussions related to estimating $v \sin i$ in Cepheids; Francesco Pepe for the idea to correct for radial velocity drifts via variations in measured ambient pressure; Laszlo Szabados for the fruitful collaboration and useful discussions.

The friendly and familiar atmosphere at the Observatory has really made these past years very special. Besides open doors that provided many opportunities for discussions or advice, I particularly enjoyed the lunches, coffees and laughter shared with everyone from EPFL's LASTRO group and Geneva University's astronomy department. Many thanks are due to the administrative staff for their efficient and competent assistance and to the IT specialists for working their digital magic that keeps everything operating smoothly.

My friends at the Observatory, you have made these past years extra special. Be it morning coffees, after work beers, hikes, laser tag, skiing, sailing, watching a movie, or else, you have given me many fond memories. Thank you for your friendship and support Monika, Xavier, Amaury, Anahí, Anaïs, Ati, Berry, David, Greg, Janis, Johannes, Lovro, Marion, Mihaly, Pedro, Roi and Sinziana! To my close friends near and far, in particular Lorenz, Valentin, Andreas, Marco, Dominik, Dylan, Michael, Fabian, and Ully, as well as all others: thank you for your friendship and support despite the often great distances and rare opportunities to spend time together.

Diese Dissertation ist meiner Familie gewidmet, die mich mit ihrer immerwährenden Unterstützung erst dazu befähigt hat, diese Doktorarbeit anzufertigen. Für meine Mutter Gisela, mein Zentralgestirn, die mir das Licht der Welt schenkte. Für meinen Vater Paul, dessen Vorbild mich sanft aber sicher zum Forscher werden ließ. Für meine Schwester Marlene, die immer für mich da war. And last, but not least, to my wife Miranda, for bringing out the best in me and making me the man I am today. Ich danke Euch von ganzem Herzen. Thank you all from the bottom of my heart.

Résumé

Dans le cadre de cette thèse, j'explore les propriétés observationnelles et théoriques de Céphéides classiques, ainsi que leur impact sur l'utilisation des Céphéides comme traceurs de distance par la relation période-luminosité (PLR).

L'un des principaux objectifs de cette thèse a été de créer un échantillon statistique de Céphéides dans les amas ouverts de notre Galaxie qui pourrait être utilisé pour tester les modèles d'évolution stellaire (par synthèse de population), et d'augmenter le nombre d'étalons pour la PLR des Céphéides Galactiques. Pour ce faire, j'ai été amené à développer une méthode astrostatistique pour déterminer l'appartenance des Céphéides connues aux amas connus.

Afin de pouvoir se fier à cette appartenance, de fortes contraintes observationnelles sont requises. Ainsi, j'ai lancé un grand programme d'observation dédié à la mesure à haute précision des vitesses radiales (VR) de Céphéides depuis les deux hémisphères en utilisant le télescope suisse 'Euler' et le télescope flamand 'Mercator', tous deux d'un diamètre de 1,2 mètre. Les observations effectuées pour ce programme ont abouti à un échantillon de données sans précédent comprenant plus de 5000 vitesses radiales à très haute précision. Pour assurer une précision maximale, j'ai développé une méthode pour corriger les dérives de vitesse dues aux variations de pression atmosphérique pendant les nuits. Cette correction se révèle être très précise ($\sim 10\,\mathrm{m\,s^{-1}}$) et améliore de manière significative la qualité des VRs déterminées à partir des spectres observés sans mesure de dérive simultanée.

En plus de l'utilisation de ces données comme contrainte d'appartenance, je les ai employées dans plusieurs études, dont beaucoup étaient liées à la forme et la variabilité des profils de corrélation croisée calculés. Il s'agit notamment de :

1. tests de la nature Céphéide de 153 étoiles classées comme telles par des programmes d'observation automatisés. Ces tests ont révélé un taux de contamination élevé (jusqu'à $\sim 70\%$ des objets mal classés) et ont confirmé 32 étoiles comme Céphéides. Cette étude peut trouver une application dans les futurs efforts consacrés à la classification automatisée d'étoiles variables.

2. l'estimation des vitesses de rotation projetées de 97 Céphéides observées avec *CORALIE*. Les valeurs typiques de $v \sin i$ sont de l'ordre de $10\,\mathrm{km\,s^{-1}}$, en accord avec l'ordre de grandeur prédit par les récents modèles évolutifs de Genève étudiés au cours de cette thèse.

3. la découverte d'une douzaine de binaires spectroscopiques parmi les Céphéides classiques. Deux de ces objets, pour lesquels des solutions orbitales ont été estimées, sont présentées dans la thèse, tandis que d'autres ont été publiés dans le cadre d'une collaboration.

4. la découverte de plusieures Céphéides pour lesquelles la forme de la courbe de VR change en fonction du cycle de pulsation. Cette variation est correlée au gradient des vitesses atmosphériques, observés par une méthode tomographique développée durant cette thèse.

5. la découverte d'une variabilité importante de la forme du dédoublement de raies dans la Céphéide X Sagittarii lors de deux cycles consécutifs.

Afin d'effectuer le recensement des Céphéides dans les amas ouverts Galactiques, j'ai compilé un vaste ensemble de données de la littérature pour les amas ouverts connus ainsi que les Céphéides connues, en y ajoutant également les nouvelles données et résultats observationnels. En utilisant des contraintes spatiales et cinématiques, ainsi que des paramètres liés aux populations, j'ai pu identifier 23 bons candidats Céphéides dans des amas ouverts, dont 5 ont été découverts pour la première fois. En utilisant cet échantillon fiable, j'ai pu revisiter l'étalonnage de la PLR des Céphéides Galactiques. J'ai ainsi obtenu: $M_V = -(2.88 \pm 0.18) \log P - (1.02 \pm 0.16)$.

Afin de bien contraindre les modèles, il faut les comprendre. Dans le cadre de cette thèse, j'ai eu l'occasion unique de présenter la première étude détaillée des effets de la rotation sur les populations de Céphéides prédits par les récents modèles d'évolution stellaire de Genève. En utilisant les prédictions des modèles de métallicité solaire, j'ai pu montrer que la rotation a des conséquences importantes pour les étoiles observées pendant le stade Céphéide et ne devrait plus être négligée. Les principales conséquences incluent que :

1. le vieux problème de la discrépance de masse des Céphéides peut être résolu en prenant en compte les effets de la rotation ainsi que le stade évolutif des Céphéides ($2^{\text{ème}}$ ou $3^{\text{ème}}$ traversée de la bande d'instabilité).

2. la rotation, ainsi que la métallicité, est à l'origine d'une dispersion intrinsèque de la PLR qui n'est actuellement pas pris en compte dans l'étalonnage de la PLR observationnelle.

Une étude encore plus approfondie dans ce sens est actuellement en cours, et plusieurs résultats préliminaires de cette recherche sont présentés ici.

Lors d'une prochaine étape, j'ai l'intention de poursuivre et de développer mes recherches liées au comportement observationnel des Céphéides comme on le voit dans les données vélocimétriques de haute précision et d'améliorer la compréhension théorique des Céphéides par l'exploration des modèles évolutifs, en les comparant aux observations. Par ailleurs, j'envisage d'étendre cette analyse à d'autres types d'étoiles pulsantes utilisées comme chandelles standards. Ce faisant, je vise à améliorer la compréhension des pulsations et de l'évolution stellaire, et à aider à assurer l'exactitude et la précision des relations période-luminosité qui sont fondamentales pour l'étalonnage de la constante de Hubble.

Abstract

In this thesis, I explore both observational and theoretical properties of classical Cepheids, as well as their impact on the application of Cepheids as distance tracers via the period-luminosity relation (PLR).

One of the primary objectives of this thesis was to establish a statistically significant sample of Cepheids in Galactic open clusters that could serve as a test-bed for stellar evolution models (via population synthesis) and increase the number of calibrators for the Galactic Cepheid PLR. This objective led me to develop an astro-statistical method for determining cluster membership of known Cepheids in known clusters.

In order to have confidence in membership, strong observational constraints are required. Thus, I launched a large observing program dedicated to measuring **high-precision radial velocities** (RVs) of Cepheids from both hemispheres using the 1m-class Swiss Euler and Flemish Mercator telescopes. The observations carried out for this program resulted in an unprecedented dataset of more than $5\,000$ high-precision RVs. To ensure maximal precision, I developed a method to correct for radial velocity drifts due to variations in ambient pressure. This correction is shown to be very precise ($\sim 10\,\mathrm{m\,s^{-1}}$) and significantly improves the precision of RVs derived from spectra observed without simultaneous drift measurements.

Besides using them as membership constraints, I employed these observational data for several auxiliary investigations, many of which are based on the shape and variability of computed cross-correlation profiles. These include:

1. a test of the Cepheid nature of 153 stars classified as Cepheid candidates by automated surveys, which exposed a high contamination rate (up to $\sim 70\%$ of misclassified objects) and confirmed the Cepheid nature of 32 stars. This investigation may find future application in efforts dedicated to automated variable star classification.

2. the estimation of projected rotational velocities for 97 Cepheids observed with *CORALIE*. Typical $v \sin i$ are in the order of $10\,\mathrm{km\,s^{-1}}$, consistent with the order of magnitude predicted by recent Geneva evolutionary models studied during this thesis.

3. the discovery of a dozen spectroscopic binaries among classical Cepheids. Two such objects for which orbital solutions could be estimated are presented in the thesis, while some others were published in a collaborative effort.

4. the discovery of a correlation between cycle-dependent radial velocity curves and cycle-dependent atmospheric velocity gradients observed via a Doppler tomographic technique developed during this thesis.

5. the discovery of the fast and significant variability of the line doubling pattern in X Sagittarii between subsequent cycles.

In order to carry out the intended census of **Cepheids in Galactic open clusters**, I compiled an extensive set of literature data for both known open clusters and known Cepheids, adding also the new observational data and results. Using kinematic, spatial, and population-specific membership criteria, I could identify 23 cluster Cepheid candidates, 5 of which were new discoveries. Using this sample of bona-fide cluster Cepheids, I then revisited the cluster Cepheid-based calibration of the PLR and obtained: $\langle M_V \rangle = -(2.88 \pm 0.18) \log P - (1.02 \pm 0.16)$.

Before one can effectively constrain models, one has to understand them. As part of this thesis, I had the unique opportunity to present the first detailed discussion of the **effect of rotation** on Cepheid populations as predicted by recent Geneva stellar evolutionary models. Using the predictions of Solar metallicity models, I could show that rotation has far-reaching consequences for stars observed during the Cepheid stage and should no longer be neglected. The main consequences include that:

1. the long-standing Cepheid mass discrepancy problem can be solved by taking into account rotation effects and the evolutionary phase of a Cepheid.

2. rotation, as well as metallicity, leads to intrinsic scatter in the PLR. Such effects are currently unaccounted for in observational PLR calibrations.

Further investigation along these lines is currently in progress, and several preliminary results of the ongoing research are presented here.

As a next step, I plan to continue and further develop my research related to both the pulsational behavior of Cepheids as seen in high-precision velocimetric data and to improve the theoretical understanding of Cepheids by exploring and testing evolutionary models. Furthermore, I plan to extend these efforts to other types of pulsating standard candles. In doing so, I aim to improve the understanding of stellar pulsations and evolution, and will help to ensure the accuracy of period-luminosity relations that are crucial for the calibration of the Hubble constant, and thus for cosmology.

Contents

List of Figures

List of Tables

Acronyms & Abbreviations

2MASS	Two Micron All Sky Survey . . . 101
AAVSO	American Association of Variable Star Observers . . . 102
ACVS	ASAS catalog of variable stars . . . 57
BAO	baryon acoustic oscillations . . . 2
BW	Baade-Wesselink . . . 22
CCF	cross-correlation function . . . 35
CDS	Centre de Données de Strasbourg . . . 43
CMB	cosmic microwave background . . . 2
CMD	color-magnitude diagram . . . 12
CRTS	Catalina Real Time Survey . . . 98
CU7	Coordination Unit 7 . . . 49
DASCH	Digital Access to a Sky Century @ Harvard . . . 98
DPAC	Data Processing and Analysis Consortium . . . 99
FWHM	full width at half maximum . . . 37
GCVS	General Catalog of Variable Stars . . . 52
HRD	Hertzsprung-Russell diagram . . . 4
IAU	International Astronomical Union . . . 103
IMF	initial mass function . . . 130
IRSB	infrared surface brightness . . . 11
IS	(classical) instability strip . . . 14
ISM	interstellar medium . . . 25
JWST	James Webb Space Telescope . . . 163
LMC	Large Magellanic Cloud . . . 4
LSST	Large Synoptic Survey Telescope . . . 163
MS	Main Sequence . . . 11
MW	Milky Way . . . 95
PIZ	partial ionization zone . . . 4
PLR	period-luminosity-relation . . . 1
PLCR	period-luminosity-color-relation . . . 25
PTF	Palomar Transient Factory . . . 98
RGB	red giant branch . . . 17

RV	radial velocity	6
RVS	Radial Velocity Spectrometer	61
SMC	Small Magellanic Cloud	1
S/N	signal to noise ratio	33
VO	Virtual Observatory	101
ZAMS	zero-age Main Sequence	14

Chapter 1

Introduction

> "I thought I could not do better than to address to you the following account of a periodical variation in the star δ Cephei, which I lately discovered. (...) They may probably lead to some better knowledge of the fixed stars, especially of their constitution and the cause of their remarkable changes."
>
> JOHN GOODRICKE, *28 June 1785*

Since their discovery more than two centuries ago, Cepheids have had an immense impact on astronomy and astrophysics. Cepheid-related investigations have contributed significantly to the understanding of stellar structure, evolution and pulsation, Galactic and extragalactic evolution and dynamics, the distance scale, and cosmology.

Cepheids, as well as other types of pulsating stars were vital in disproving contraction as the primary energy source of stars (Eddington 1918a, 1919a), in investigating the structure of the Milky Way (Hertzsprung 1913), and in demonstrating that the universe is larger than our Galaxy (Hubble 1925). A crucial element of all these studies, directly or indirectly, is the period-luminosity-relation (PLR) discovered by Henrietta Leavitt (Leavitt 1908) and Charles Pickering (Leavitt & Pickering 1912) among 25 Cepheids in the Small Magellanic Cloud (SMC). Much of our understanding of stars, galaxies, and even cosmology therefore rests to some extent on the study of Cepheids and other variable stars. Owing to the great historical significance of Cepheids for astronomy and astrophysics, a detailed, albeit concise, historical overview of these developments is indicated. This historical introduction is presented in Sec. 1.1.

Cepheids were discovered due to their remarkable light variations. For some of these, the variability is observable even with the naked eye. For instance, the prototype of Cepheids, δ Cephei, varies by about 1 magnitude, i.e., a factor of 2.5 in brightness, over a timescale of less than 6 days[1]. With an average visual magnitude of approximately 4 it is furthermore largely within the range of stars visible to the unaided eye. A more detailed overview of the observable properties of Cepheids is provided in Sec. 1.2.

Whenever people ask me "what do you do?" and I respond by telling them about Cepheids and their variability, the first follow-up question is a testimony to the inherent curiosity of humans: "Why do they do that?" The same question plagued scientists until the first quarter of the 20^{th} century and sparked great efforts to understand the nature of Cepheids. The result of so much scrutiny is that Cepheids now rank among the best-studied stars, and that the theoretical under-

[1] To be more precise, the period of δ Cephei was 5.366341 d in August 1957 (Samus et al. 2012)

standing of Cepheids is very far-advanced. Nevertheless, Cepheids remain crucial laboratories for testing stellar evolution theory. A basic description of the evolutionary status of Cepheids and their pulsations is therefore offered in Sec. 1.3.

The PLR is a consequence of the period-mean density and mass-luminosity relations and allows Cepheids to be used as standard candles for providing distance estimates. Distance determination is among the principal problems of astronomy and cosmology. In this regard, it is difficult to overestimate the importance of the PLR for astronomy, since Cepheids are standard candles[2] and are observable on Galactic as well as extragalactic scales. The latter part makes Cepheids crucial calibrators of the Hubble constant, H_0, since a "one-step" calibration can be achieved together with type-Ia supernovae (for a recent review, see Freedman 2013). Highly precise determinations of H_0 are of great value to cosmology, since they can serve as strong priors for the analysis of the cosmic microwave background (CMB) power spectrum, or baryon acoustic oscillations (BAO). Thus, precise values of H_0 can help to identify deviations from ΛCDM cosmology, constraining in particular the dark energy parameter Ω_Λ (Weinberg et al. 2013) and the effective number of neutrino species (Komatsu et al. 2009). Several aspects of my thesis work touch upon the PLR, and in particular on its intrinsic scatter. Sec. 1.4 therefore introduces the relevant concepts and the impact of Cepheids on the distance scale.

After introducing the current state of knowledge relevant for this thesis, this chapter's final Sec. 1.5 provides an overview of my thesis work and the structure of this document.

1.1 A brief historical perspective

The history of Cepheid-related studies is extremely rich, since it traces more than two centuries and is heavily intertwined with the key developments of astronomy and astrophysics in the first half of the 20th century, including the development of stellar evolution, stellar pulsation theory, and the distance scale. Therefore, this brief introduction is intended to give a taste, not a complete review, of this history. The interested reader is referred to the reviews of the development of stellar pulsation theory by Gautschy (1997), the monograph on classical Cepheids by Efremov (1975) and other literature in the same book (Kukarkin 1975) discussing other pulsating stars that were formerly referred to as Cepheids.

The term "Cepheid" has undergone significant changes over time. Cepheid variables are named after the archetype of periodic variable stars, δ Cephei[3], whose variability was discovered by Goodricke (1786), roughly at the same time as Edward Pigott discovered the same type of variability in η Aquilae. 10 months after announcing his discovery to Astronomer Royal Nevil Maskelyne, Goodricke died at the age of 21. More information on the discoverer of Cepheids and periodic variability in Algol can be found in the study by French (2012).

Following these initial discoveries, many variable stars were discovered and cataloged, although little was known about their nature until well into the 20th century. For a long time, Cepheids were thought to be binary stars. It should be noted, however, that this idea does not appear to have come from Goodricke, who did speculate about binarity or spots as possible explanations of the periodic variability of Algol (Goodricke 1783), but did not conjecture along the same lines for δ Cep. Perhaps it was in part Doppler (1842) who made the binary hypothesis plausible by explaining the red appearance and variability of the "periodic variables" as changing line-of-sight velocities due to eccentric orbits.

Until the early 20th century, several types of periodic variables that nowadays form distinct variability classes were jointly referred to as "Cepheids". At that time a distinction between classical Cepheids and "cluster variables" began to emerge. While investigating period distributions

[2] Astronomical standard candles are astronomical objects whose luminosity is well calibrated, enabling distance estimations via the observed flux which decreases as $1/r^2$, where r denotes distance

[3] Following the designation by Bayer (1603)

of known variable stars, Hertzsprung (1912) found three clear peaks at periods around 0.5, 7, and 300 days. These corresponded to RR Lyrae-type variable stars[4], δ Cephei-type stars, and the Miras (see also Chap. 3 of Campbell & Jacchia 1941). Using criteria on amplitude, period, and spectral type (where available), Hertzsprung (1912) could then demonstrate these sub-classes to be located in systematically different regions of the Galaxy by assigning the newly-communicated Galactic coordinates of Pickering (1912) to these variables.

Not even three months earlier, Leavitt & Pickering (1912) had announced the discovery of 25 periodic variable stars in the SMC among a total sample of 1777 variable stars published by Leavitt (1908). Their fundamental result that "[...] there is a simple relation between the brightness of the variables and their periods[...]" led to the conclusion that the "periods are apparently associated with their actual emission of light, as determined by their mass, density, and surface brightness" (Leavitt & Pickering 1912). Thus was discovered what is nowadays referred to as the Cepheid period-luminosity-relation (PLR), or (more recently) Leavitt-law. The first zero-point calibration of the PLR was attempted soon after by Hertzsprung (1913), who found a distance to the SMC of 2000 light years[5]. Following major improvements of the PLR calibration by Hertzsprung and Shapley, Hubble (1925) could eventually demonstrate the extragalactic nature of (the barred irregular galaxy) NGC 6822 using the periodic variables. This had profound implications for cosmology, fundamentally changing the accepted notion of the nature of galaxies and the size of the universe.

Even before the 20^{th} century, there had been evidence contradicting the binary hypothesis for Cepheids. Shapley (1914) studied these contradictions in detail and finally put forth a new hypothesis of the origin of the Cepheid phenomenon: stellar pulsation. In his seminal work, Shapley suggested the variability of Cepheids to be due to "intrinsic light fluctuations of a single star", concluding that "the explanation of their light-changes can [...] be found in a consideration of internal or surface pulsations". However, several key figures of the time did not readily accept the pulsation hypothesis, despite theoretical advances and observational evidence. This led, for instance, to the interpretation of Cepheids as rotating stars in the process of fissioning[6] by Jeans (1925), a claim which Eddington (1926b) refuted based on considerations of spectral line broadening. This debate continued to some extent for nearly three decades until observational evidence clearly favoring pulsation over binarity began to accumulate in the 1940s.

The observational method to test the pulsation hypothesis proposed by Baade (1926) marked a tipping point in this debate. The technique was improved by Becker (1940), van Hoof (1943), and Wesselink (1946), and provided the observational evidence needed for a broad acceptance of the pulsation hypothesis. Variations of this technique are still widely employed today and usually referred to as Baade-Wesselink-type techniques (for a very recent example, see Groenewegen 2013). In his book, Rosseland (1949, p. 13) noted that "the distribution of cepheids [sic] in the Hertzsprung-Russell diagram [...] indicates that cepheids are ordinary stars that happen to cross the danger line giving a combination of luminosity and density that makes pulsations inevitable." The notion of an intrinsic width of the instability strip was established observationally by Sandage (1958b), who studied Cepheids in different Galactic clusters. From his finding, Sandage then predicted that the finite width of the instability strip leads to an intrinsic scatter in the period-color and period-luminosity relations.

Gautschy (1997) argued that pulsation could have already been established more firmly by Shapley in 1914, if the investigations of Ritter (1879) had had a stronger impact on the community. However, this does not appear to have been the case. The possibility of pulsating stars acting as heat engines was first considered by Eddington (1917), laying the foundation for his future extensive contributions on Cepheid variables (Eddington 1918a,b, 1919b, among others) made during

[4]These were also referred to as cluster-types or Antalgol stars

[5]Newer estimates place the SMC at roughly 200 000 light years (e.g. 60.6 ± 3.0 kpc in Hilditch et al. 2005)

[6]Fissioning here refers to the breaking up of a star. Nuclear fission was discovered later by Meitner & Frisch (1939).

the development of the his seminal book *The Internal Constitution of the Stars* (Eddington 1926a). A key observation to be explained by any pulsational model is the lag between the phase points when the star is most contracted and brightest. This was one of the primary concerns in Eddington (1941), who speculated on a pulsation driving mechanism related to the build-up of a hydrogen partial ionization zone (PIZ). A driving mechanism via a helium PIZ was first proposed by Zhevakin (1953) and further explored by Cox & Whitney (1958), although the models were still computationally limited.

The breakthrough on the theoretical front was made by Baker & Kippenhahn (1962) who showed that "stars in the δ Cephei region [of the Hertzsprung-Russell diagram (HRD)] are pulsationally unstable due to the destabilizing effect of the He^+ ionization zone" using "linearized time-dependent equations representing radial pulsations" in models assuming hydrostatic equilibrium. This publication has had an important impact on the development of stellar pulsation theory and the acceptance of pulsation as the origin of the light variability of Cepheids.

By the late 1960s, computers had evolved sufficiently to compute increasingly complex models of stellar pulsation. This led to the discovery of the *Cepheid mass anomalies* by Christy (1968) and Stobie (1969a,b,c), which showed that Cepheid masses inferred from evolutionary models were systematically higher than those obtained from pulsational models, see also Cox (1980) and Sec. 1.3.4 for more information.

The distinction of classical Cepheids from other pulsating stars such as the type-II Cepheids (nowadays sub-classified into BL Herculis, W Virginis, and RV Tauri pulsators, sorted by increasing period) was achieved in the second half of the 20th century. Baade (1956) demonstrated that type I (classical) Cepheids are 1.5 mag brighter on average than type-II Cepheids of the same period. This finding had profound implications for the distance scale and led to an adjustment of Shapley's PLR zero-point as well as to a famous comment by Anonymous: "The Lord made the universe - but Baade doubled it" (comment found in Kippenhahn & Weigert 1994). Furthermore, the first classical Cepheids were found in open clusters around that time, see e.g. Irwin (1955); Kholopov (1956); Feast (1957); van den Bergh (1957); Sandage (1958a), and the references in Sec. 3.5. Since the distances of these Cepheids could be derived from the host clusters, this led to significant advances in the use of Cepheids as distance tracers.

More recent Cepheid-related developments will be discussed in the following sections that present the observational properties and the current theoretical understanding of Cepheids, as well as an introduction to the application of Cepheids as distance tracers. The scope of this thesis will then be outlined in Sec. 1.5 at the end of the chapter.

1.2 Observational properties of classical Cepheids

Cepheids were discovered via their variability, which is their defining observational property. Let us now have a look at how pulsations manifest themselves in these stars, before the theoretical paradigm of Cepheids is reviewed in the next section.

1.2.1 The photometric and spectroscopic variability of Cepheids

Observationally, classical Cepheids are subdivided into at least three sub-categories (GCVS abbreviations are given in parentheses): the δ Cephei (DCEP), *s*-Cepheids (DCEPS), and beat Cepheids (CEP(B)). Besides such an empirical sub-classification, it is also possible to determine the modes of pulsation via Fourier analysis. Figure 1.1 shows the Large Magellanic Cloud (LMC) Cepheids observed by the OGLE-III consortium Soszynski et al. (2008), ordered by pulsation mode.

The δ Cephei types are the most common and the most frequently-studied Cepheids and are fundamental mode pulsators. Their periods range from about 5 days up to about 50 days in the Galaxy (Samus et al. 2012) and up to a couple hundred days in the MCs (Soszynski et al. 2008,

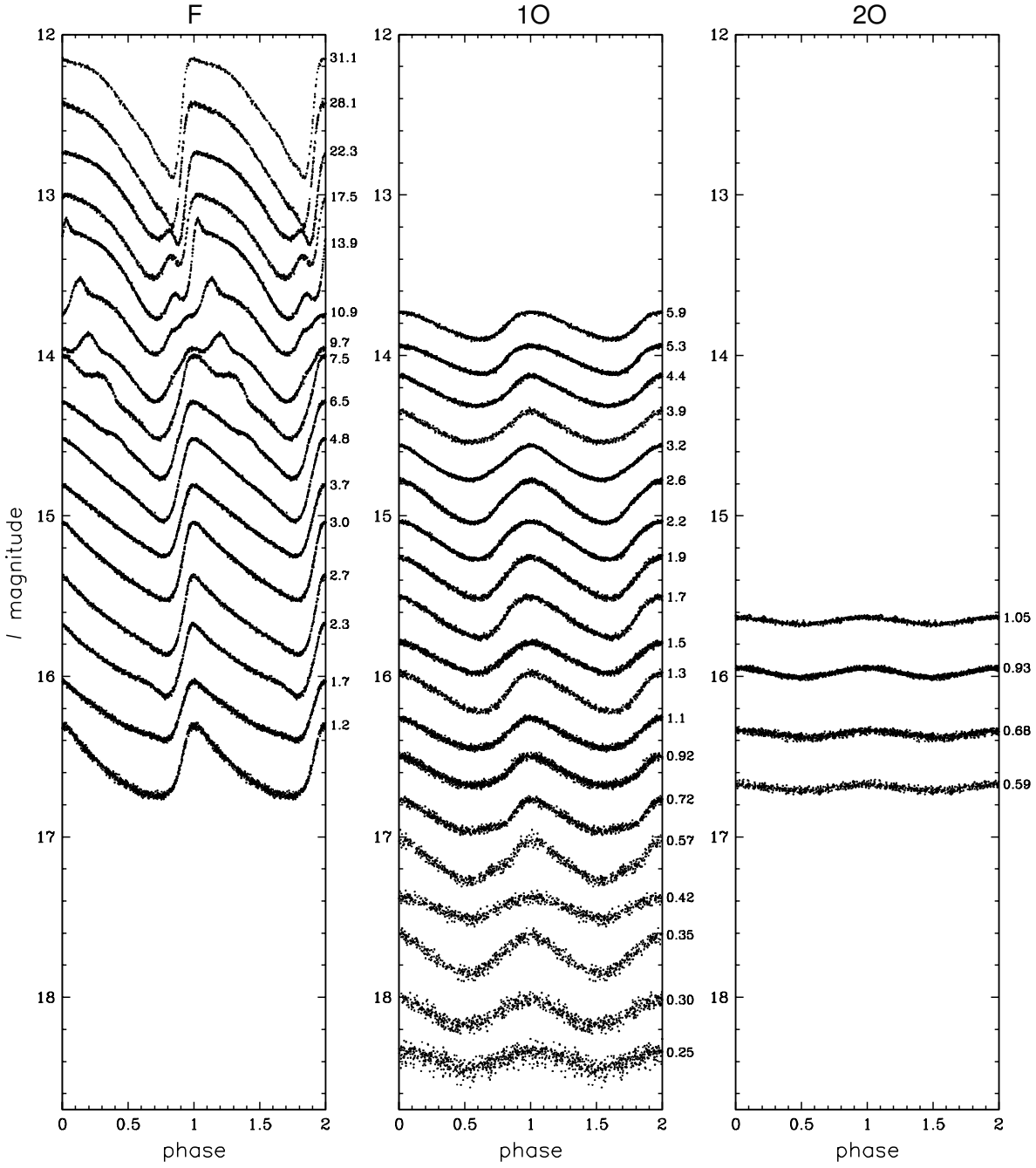

Figure 1.1: Cepheid light curve morphology as a function of period (indicated next to the light curve on the right) and pulsation mode. The panels from left to right show for fundamental mode (F), first overtone (1O), and second overtone (2O) Cepheids. The Hertzsprung progression is clearly seen among the fundamental mode Cepheids with periods between roughly $5 - 30$ days. Figure for OGLE-III Cepheids in the LMC by from Soszynski et al. (2008).

2010). In the MCs, shorter period Cepheids are found than in the Galaxy, pointing to a metallicity effect, see also Sec. 4.5. The light curve shapes of these stars are strongly correlated with pulsation period (Hertzsprung 1926). This fact is usually referred to as the Hertzsprung progression, describing the presence of a "bump" in the phased light curve whose location as a function of phase depends on the period. It is worth noting that the location of the bump at periods around 10 days is near the light curve's maximum, leading to systematically lower pulsation amplitudes at this period (e.g. Klagyivik & Szabados 2009). Figure 1.1 illustrates this progression as a function of pulsation period.

s-Cepheids are empirically defined by their sinusoidal light curve shapes whose amplitudes are typically smaller than those of ordinary δ Cep type. In the literature, the term s-Cepheid is frequently used as synonymous with overtone pulsation, although that is not necessarily correct. While the majority of s-Cepheids are indeed overtone pulsators (Klagyivik & Szabados 2009), it should be noted that this is not always the case, and pulsation modes should be identified using Fourier decomposition of the light curves.

Beat Cepheids exhibit beating due to the presence of at least two periods and are the least common among the different subclasses. The first signs of beating, and hence multiple periods in Cepheids, were discovered by Oosterhoff (1957) in the light curve of U Trianguli Australis. Beat Cepheids can be used to determine masses by comparing observed period ratios, luminosity, temperature, and metallicity with pulsational models (e.g. D'Cruz et al. 2000) in so-called Petersen diagrams (e.g. Petersen 1973) that show period ratios between higher and lower overtones as a function of the period of the lower mode. Thus, beat Cepheids played an important role for the mass discrepancy problem (Moskalik et al. 1992), see also Sec. 1.3.4, and aided in the improvement of opacities in stellar envelopes (see Petersen & Takeuti 2001, and references therein). It is worth noting that beat Cepheids are at the low-mass end of the Cepheid distribution, with masses in the range $3.8 - 4.5\,M_{\odot}$ (D'Cruz et al. 2000). Period ratios furthermore provide tight constraints on metallicity (e.g. Lee et al. 2013). Although the understanding has significantly improved, beat Cepheids still present considerable difficulties for detailed modeling (Smolec & Moskalik 2010).

It is well known that Cepheid variability is chromatic. Photometrically, temperature variations are observable as color variations, and Cepheids are brightest when they are bluest (hottest). The chromaticity of the variability is usually quite strong, depending on period, pulsation mode, and the photometric passbands used. For instance, the B-V variability is always stronger than the V-I variability. The high B-V variability is easily explained by Wien's displacement law and the varying location of the spectral energy distribution's (SED) peak due to temperature variations. The V-I variability is less sensitive to temperature variations, since it measures the red-ward decreasing slope of the SED. Figure 1.2 illustrates the observed chromaticity for the long-period Cepheid T Monocerotis (27 days) using data from Berdnikov (2008).

The spectroscopic variability of Cepheids was first noted by Belopolsky (1895) in δ Cephei, although variations in radial velocity had already been speculated on by Doppler (1842) in the context of the binary hypothesis. Belopolsky (1895) determined the elements of an assumed Keplerian orbit for a binary system using the velocities derived from his spectra, noticing that "the epoch of minimum brightness occurs a day earlier than the time of perihelion passage".

It is important to note that variability periods determined photometrically and spectroscopically agree to very high precision in Cepheids, thus pointing to a common origin of the two variable phenomena. This is further underlined by the fact that the Hertzsprung progression shown above for photometric data is also observed in radial velocity (RV) curves. Although the periods do agree, there are well-known phase lags between the phase points at which a Cepheid is most contracted and when it is brightest. Figure 1.3 illustrates this point schematically. These phase lags have played an important role in deciphering the Cepheid variability mechanism (Eddington 1941) and continue to provide challenges for theoretical modeling, see Szabó et al. (2007).

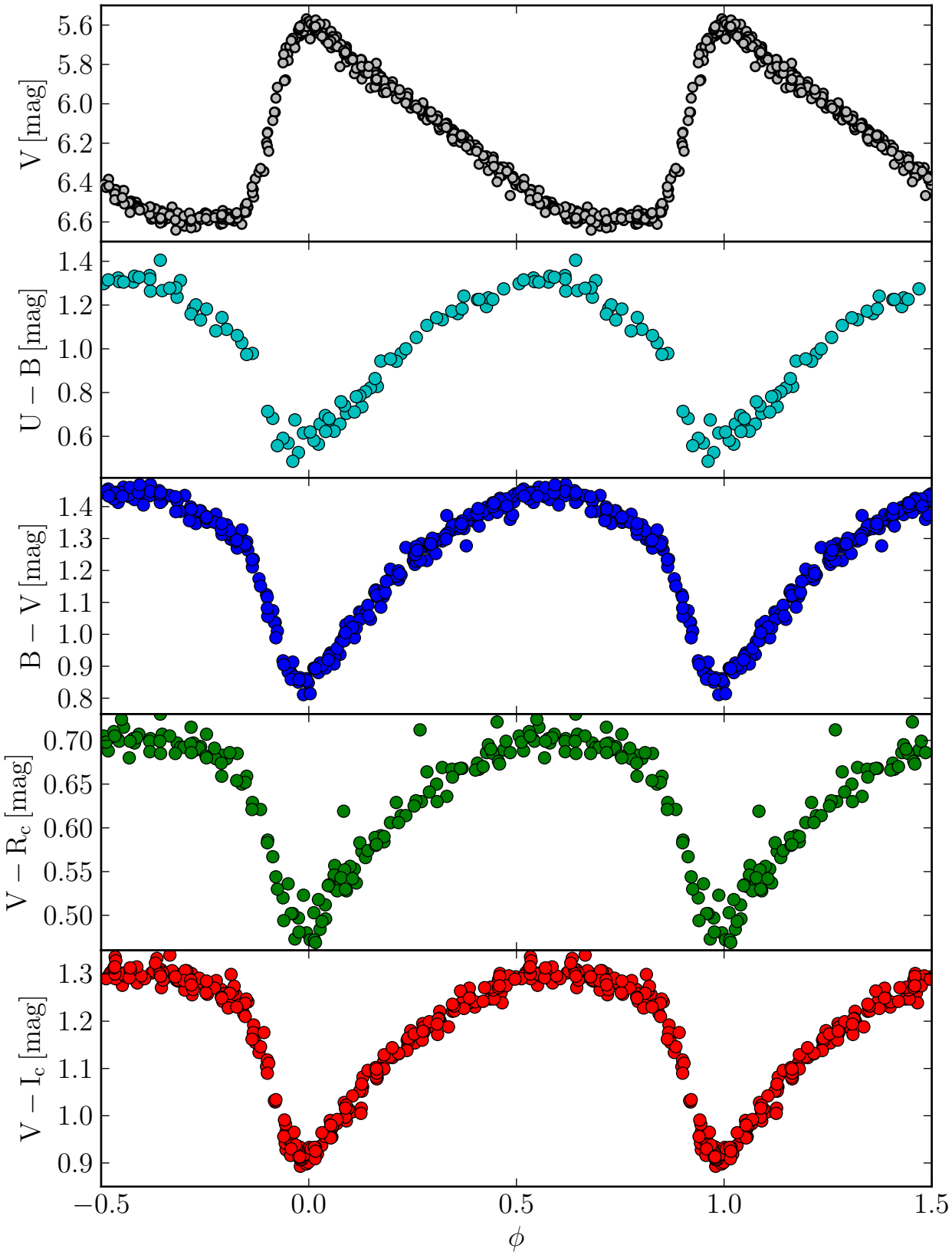

Figure 1.2: Multi-color photometry of long-period (27 day) Cepheid T Monocerotis from Berdnikov (2008).

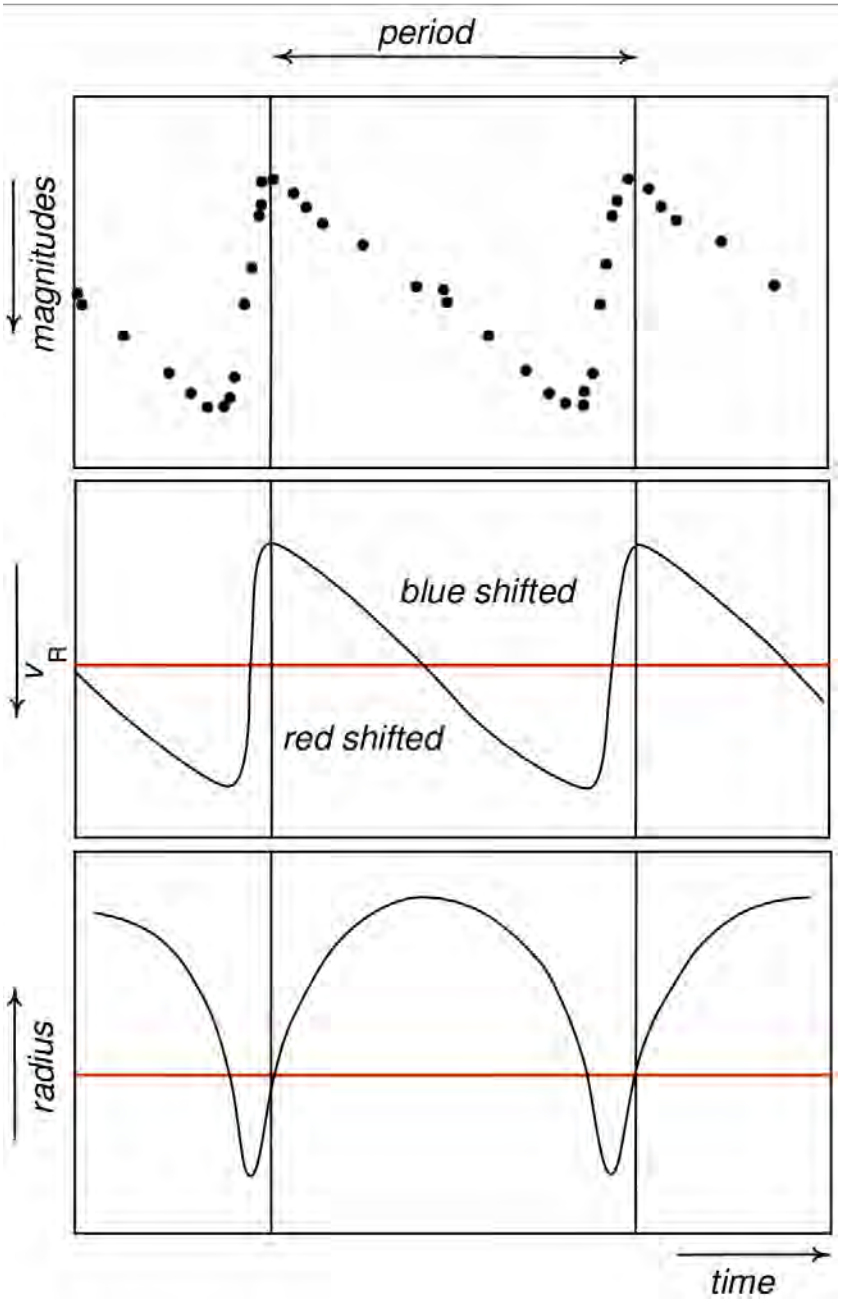

Figure 1.3: A schematic view of the variability in brightness (top panel), radial velocity (center panel), and radius (bottom panel). The ordinates of the magnitudes and the velocity curve increase from top to bottom. The ordinate of the radius increases from bottom to top. Vertical lines show the location of maximum flux. The horizontal red line in the center panel indicates the systemic velocity. The bottom panel clearly shows the phase lag between maximal brightness and minimal radius. Figure from Gautschy (2003).

Cepheid radius variations and distances

Cepheid variability is nowadays known to be due to radial pulsation. This pulsation has two important consequences: a variability of the temperature (color) and of the observed line-of-sight velocity of the stellar photosphere, i.e., the radial velocity. The observation of radial velocities provides a direct measurement of the radius variations $\Delta R(t)$ around the average radius R_0 of the star as a function of time, t, since

$$\Delta R(t) = R(t) - R_0 = -p \int_{t_0}^{t} (v_{\rm r}(t) - v_\gamma)\,{\rm dt}\,, \tag{1.1}$$

where p denotes the projection factor, and v_γ is the systemic velocity. A lot of work has been carried out to determine the most suitable values for p, including also investigations of period- and metallicity-dependencies (see e.g. Nardetto et al. 2004, 2007; Groenewegen 2007, 2013; Storm et al. 2011a).

Of course, Eq. 1.1 only provides the radius variation, not the average radius of the star. This information can, however, be obtained using the Baade-(Becker-)Wesselink technique (Baade 1926; Becker 1940; Wesselink 1946). In this technique, the ratio of radii, $R(t_1)/R(t_2)$ is determined from magnitude differences at phases of identical color (temperature). If radial velocity is measured simultaneously, then $\Delta R = \Delta R(t_1) - \Delta R(t_2)$ is known, and the average radius, R_0 can be obtained via:

$$R_0 \approx -\frac{5}{\ln 10}\frac{\Delta R}{\Delta m}\,, \tag{1.2}$$

where Δm denotes the difference in apparent magnitude, and both Δm as well as ΔR are measured at phases of identical temperature (color). Once radius and temperature are known, so is the mean luminosity, since

$$L = 4\pi\sigma R^2 T_{\rm eff}^4\,, \tag{1.3}$$

where $\sigma = 5.670373 \times 10^{-8}\,{\rm W\,m^{-2}\,K^{-4}}$ is the Stefan-Boltzmann constant. With the apparent average magnitude of the Cepheid measured, we thus obtain a direct distance estimate, since

$$d = \sqrt{\frac{L}{4\pi F}} \tag{1.4}$$

where F denotes the measured flux, which is related to apparent magnitude at wavelength λ compared to a standard star with index 0 (e.g. the Sun or Vega) via $m_\lambda - m_{\lambda,0} = -2.5\log\left(\frac{F_\lambda}{F_{\lambda,0}}\right)$.

Instead of using photometry, the interferometric BW method uses the direct observation of variations in apparent diameter, $\theta(t)$, to obtain an estimate of $R(t_1)/R(t_2)$, see Fig. 1.4. The geometric distance d can then be estimated by computing

$$\begin{aligned} d &= \frac{2\Delta R(t)}{\Delta\theta(t)} \\ &= 9.305\frac{\Delta R}{\Delta\theta}\frac{[{\rm R}_\odot]}{[{\rm mas}]} \end{aligned} \tag{1.5}$$

where $\Delta\theta(t)$ is the variation of the angular diameter derived interferometrically, and the second line corresponds to the quantities indicated in Fig. 1.4, in the typical units.

Interferometrically resolved angular diameters have another important application as calibrators for the so-called surface brightness, or Barnes-Evans, relations. These are of the form (Barnes & Evans 1976; Fouqué & Gieren 1997; Kervella et al. 2004b):

$$F_\lambda = 4.2207 - 0.1 m_{\lambda_0} - 0.5\log\theta_{\rm LD}\,, \tag{1.6}$$

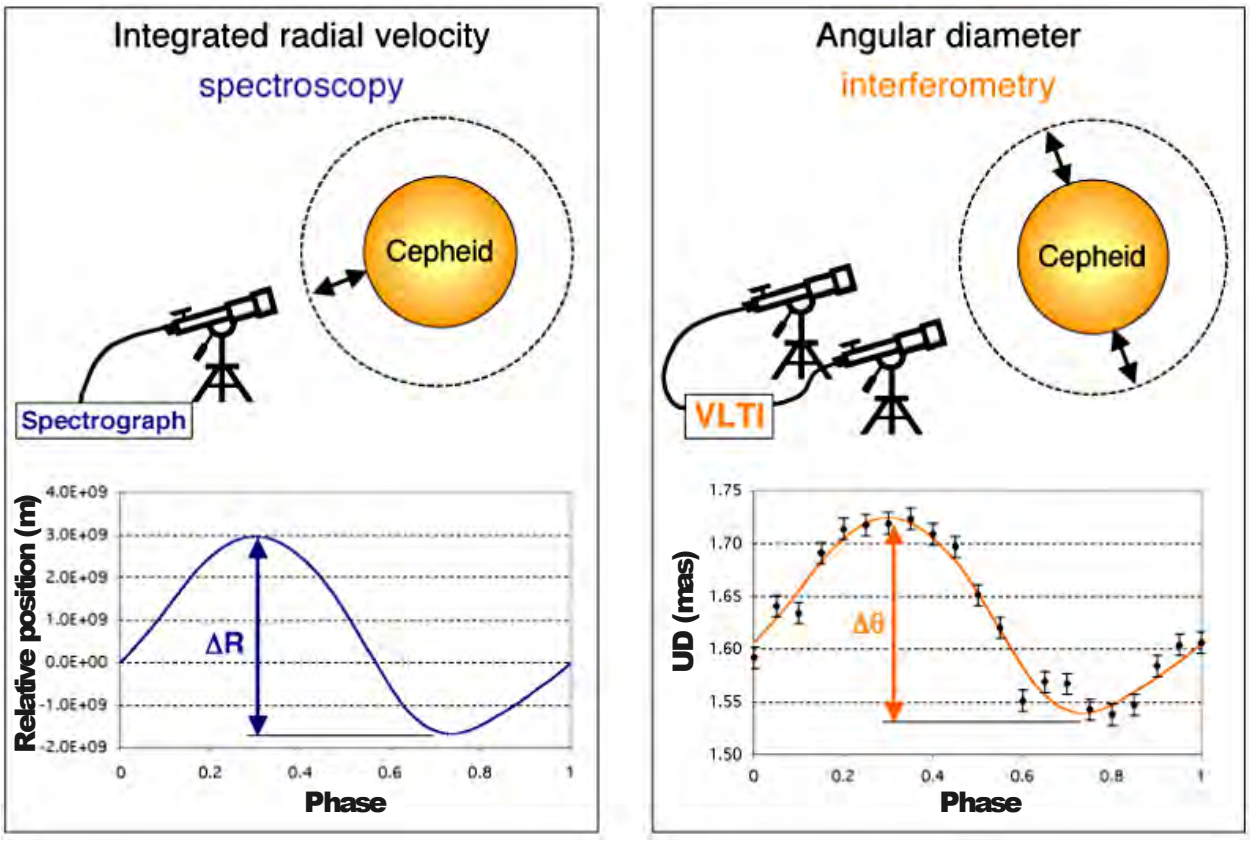

Figure 1.4: Illustration of the interferometric Baade-Wesselink technique. Radial velocities (left panel) measure the linear variation of the radius, whereas interferometric measurements determine variations of the angular diameter. The distance can be derived from the ratio of the two quantities, see Eq. 1.5. Original image credit: ESO (Kervella et al. 2004c).

where the factor 4.2207 depends on the bolometric absolute magnitude and the total integrated flux of the Sun, as well as on the Stefan-Boltzmann constant, i.e., it does not depend on the wavelength. m_{λ_0} refers to an apparent de-reddened magnitude, and $\theta_{\rm LD}$ to the limb-darkening corrected (via atmospheric models) angular diameter. For the determination of m_{λ_0}, fixed reddening laws (non line-of-sight dependent) are typically used. The interferometrically derived surface brightness, F_λ, can be compared to one based on linear radius variations (Thompson 1975; Fouqué & Gieren 1997):

$$S_\lambda = m_{\lambda_0} + 5 \log \left(\frac{r}{R_0} \right) . \tag{1.7}$$

Inserting Eq. 1.7 in Eq. 1.6, one obtains

$$F_\lambda = 4.2207 - 0.1 S_\lambda \, , \tag{1.8}$$

which enables calibration of surface brightness relations based on linear radius measurements, S_λ, using interferometrically calibrated surface brightness relations, F_λ.

For radially pulsating stars, apparent diameter and color index change as a function of pulsation phase. Since $F_\lambda \propto \log T_{\rm eff}$ (cf. Eqs. 1.3 and 1.4), variations in angular diameter can be directly linked with variations in temperature or color index. In their seminal work, Barnes & Evans (1976) already investigated the suitability of different colors for such a calibration and found $V-R$ colors to yield particularly precise results. More recently, Laney & Stobie (1995) have shown that the use of $V-K$ colors are least sensitive to variations in gravity and microturbulence. Furthermore, the

effect of reddening is reduced in the infrared, and pulsation amplitudes are small. Calibrating F_λ interferometrically for Cepheids yields impressive precision (Kervella et al. 2004b):

$$F_{V_K} = -(0.1336 \pm 0.0008) \cdot (V-K)_0 + (3.9530 \pm 0.0006)\ . \tag{1.9}$$

This is in excellent agreement with the calibration based on non-variable giants and supergiants derived by Fouqué & Gieren (1997). Inserting Eq. 1.9 into 1.6 finally allows to derive the angular diameter (see this example from Fouqué & Gieren 1997):

$$\log\theta = 0.5474 - 0.2V_0 + 0.262(V-K)_0\,. \tag{1.10}$$

Other variations of this technique exist and yield comparable results, see for instance Groenewegen (2013), who obtains $\log\theta = 0.5327 - 0.2V_0 + 0.2674(V-K)_0$. Using Eq. 1.10 in combination with color measurements covering the pulsation cycle and an according radial velocity curve, it thus becomes possible to derive distances according to Eq. 1.5. This infrared surface brightness (IRSB) technique is extremely useful to determine distances to far away Cepheids that are outside the range of currently feasible interferometric baselines, and have been applied to determine distances up to the SMC (Storm et al. 2004; Gieren et al. 2013).

Ultraviolet and X-ray spectroscopy of Cepheids

UV spectroscopy of Cepheids has mostly been used to search for the presence of companions, e.g. using the *International Ultraviolet Explorer* (IUE) data obtained between 1978 and 1996. Schmidt & Parsons (1982, 1984b,a) used IUE spectra to investigate the chromospheric variability of Cepheids, finding rather little variability that appeared to be increasing towards shorter wavelengths. More recently, Engle & Guinan (2012) have reported the detection of several Cepheids in X-rays using *XMM-Newton* and *Chandra* observations, finding the average X-ray surface flux of δ Cephei to be approximately 500 times lower than that of the Sun, and thereby confirming the faintness of Cepheids in the X-ray domain that was found via the absence of Cepheid detections of *ROSAT*.

The faintness of Cepheids at short wavelengths makes UV spectra ideal to search for Main Sequence (MS) companions to Cepheids. This can be achieved either by searching for flux excess (Böhm-Vitense & Proffitt 1985) or identifying spectral lines that are indicative of MS stars. Notably Evans (1991, 1992a,b, 1994), among others, consequently employed IUE spectra to search for MS companions, cf. Sec. 2.2 for more details on binaries among Cepheid. From spectral type estimates of the companions, Cepheid masses could thus be estimated. In this long-term effort, Evans was able to secure a complete set of time-resolved spectroscopy for the 76 Cepheids brighter than $8^{\rm th}$ magnitude in the visual (Evans et al. 2011). This dataset is vital for studying mass fractions among Cepheid binaries (Evans et al. 2013), and provides important constraints for the Cepheid mass discrepancy (cf. Sec. 1.3.4).

1.2.2 Interferometry and circumstellar environments

Interferometry of Cepheids is a fairly recent, though highly active and successful field of research enabled by technological advancements. The first angular diameters of Cepheids measured using interferometry were announced by Mourard et al. (1997), Kervella et al. (1999), Nordgren et al. (2000), Kervella et al. (2001), and Armstrong et al. (2001). These studies can resolve both angular diameters and their variation due to pulsation. Since then, more and more Cepheids have been studied interferometrically, notably by Kervella et al. (2004e, 2006) and Mérand et al. (2005, 2006). These studies have provided much-needed independent calibrations for the period-radius and period-luminosity relations (Kervella et al. 2004a), the surface brightness techniques (Kervella et al. 2004b,d), projection factors (Mérand et al. 2005), pulsation modes (Gallenne et al. 2012), and

detected extended envelopes around several Galactic Cepheids (Kervella et al. 2006; Mérand et al. 2006, 2007; Kervella et al. 2009; Gallenne et al. 2013a). This last point is crucial for the use of Cepheids as standard candles, since circumstellar extinction can be a bias for the PLR (Kervella et al. 2012).

One particularly interesting case of a Cepheid embedded in a large circumstellar environment (CSE) is the long-period Cepheid RS Puppis (the "nebulosity" was first discovered by Westerlund 1961). In fact, the CSE is so large that its projected angular diameter is in the order of a few minutes of arc, enabling the study of light echoes[7] passing through the CSE (Kervella et al. 2008). Unfortunately, however, these light echoes cannot be used straightforwardly to determine a distance to RS Puppis, since the nebulosity's distribution is not spherically symmetric around the Cepheid. In fact, it now appears that the nebulosity is a remnant of the star forming region (Feast 2008; Bond & Sparks 2009; Kervella et al. 2012), invalidating an initial distance estimate obtained from these light echoes.

1.3 The theoretical picture for Cepheids

Cepheids have played an important role in the development of the theory of stars, of their structure and evolution, and also of the theory of stellar pulsations. In this section, I aim to provide sufficient background information on the theoretical understanding of Cepheids as context for the research shown in the following chapters. However, more complete descriptions of stellar evolution and pulsations fill entire textbooks. Some excellent examples of such books are Eddington (1926a); Kippenhahn & Weigert (1994); Maeder (2009). The interested reader is referred to these and the references therein for further details.

1.3.1 The evolutionary path of Cepheid progenitors

"The nitrogen in our DNA, the calcium in our teeth, the iron in our blood, the carbon in our apple pies were made in the interiors of collapsing stars. We are made of starstuff." This quote by Carl Sagan (1980) neatly illustrates the importance of the study of stellar evolution for humankind by relating the essential things in life (including apple pie) directly to the processes occurring inside the stars.

Stars are essentially gigantic gas (plasma) balls that maintain thermonuclear fusion processes inside their cores in order to prevent gravitational collapse. The radiation created inside their cores interacts with the gas, exerting an outward force which is exactly[8] equal to the inward force due to gravity during most of their lifetimes. This fine balance is called hydrostatic equilibrium. Stars tend towards equilibrium states, favoring certain regions in the $\log L - \log T_{\rm eff}$ plane, since luminosity, L, and effective temperature, $T_{\rm eff}$, are related via the Stefan-Boltzmann equation (Eq. 1.3).

The $\log L - \log T_{\rm eff}$ plane is commonly referred to as the Hertzsprung-Russell diagram (HRD) and represents the theoretical version of a directly observable color-magnitude diagram (CMD). The CMD derived from the *Hipparcos* mission is presented in Fig. 1.5, courtesy of Laurent Eyer. The dominant sequence of stars running from top left to bottom right is called the Main Sequence (MS) on which stars spend the majority of their lifetimes fusing hydrogen into helium. Evolved stars are seen to clump to the top and right of the MS, forming the Red Clump, and some white dwarfs can be seen in the lower left corner at low absolute magnitude and high temperature.

The thermonuclear reaction processes inside stellar cores are nowadays well understood and may one day help to solve the world's future energy problems[9]. Several different reaction chains

[7] The video of these light echoes is a must-see: `http://www.eso.org/public/videos/eso0805a/`

[8] As always, the devil is in the details. This description neglects rotation and pulsations, for instance. These will be discussed later on.

[9] If projects like ITER prove to be successful, see `http://www.iter.org/`

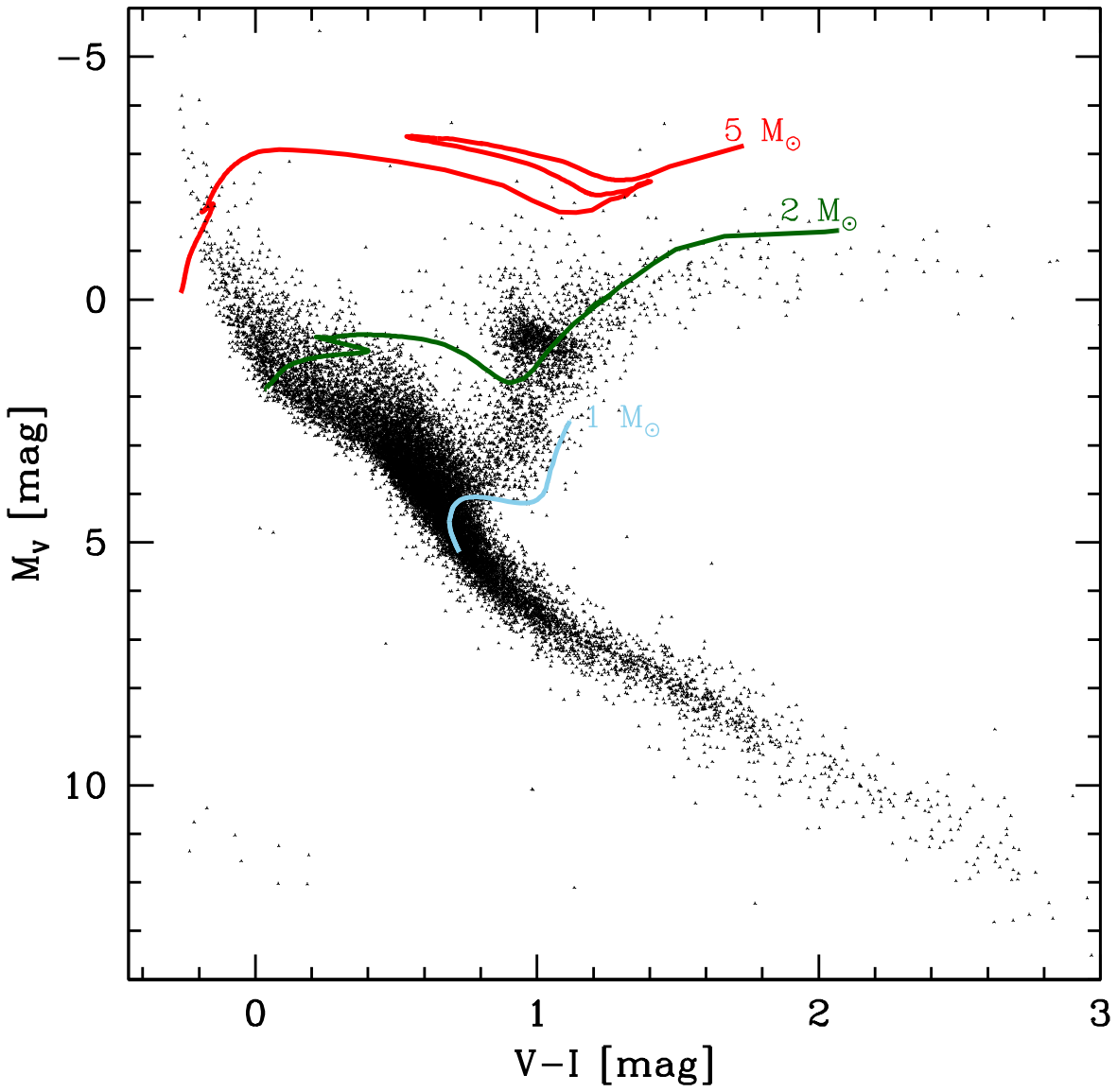

Figure 1.5: *Hipparcos* (Perryman & ESA 1997) color-magnitude diagram. M_V here denotes absolute magnitude, derived from *Hipparcos* parallaxes. Evolutionary tracks for 1, 2 and $5\,M_\odot$ shown in light blue, dark green, and red, respectively (Ekström et al. 2012). Figure credit: Laurent Eyer.

can occur in stars, depending on mass and evolutionary state, but the most important one for humans is certainly the pp-chain responsible for the stability of our Sun. The net reaction of the pp-chain is to transform four protons (hydrogen nuclei) into one helium nucleus, two positrons, two electron neutrinos[10], and two photons, thereby releasing the nuclear binding energy of $26.7\,\mathrm{MeV}$:

$$4\,{}^1_1H \rightarrow {}^4_2He + 2e^+ + 2\nu_e + 2\gamma\,. \tag{1.11}$$

Cepheid progenitors start out as B-type stars on the MS and lie in the mass range around $4-11\,M_\odot$. In this mass range, hydrogen burning[11] follows the CNO cycle on the MS. In the CNO cycle, the elements carbon, nitrogen, and oxygen have a role analogous to catalyzers, being used and reproduced such that the sum of CNO isotopes is conserved. However, the ratio of CNO isotopes changes with time (Maeder 1985), since the reaction ${}^{14}N + {}^1H \rightarrow {}^{15}O$ is significantly slower than all other reactions, acting as a bottleneck for the CNO cycle and dominating its rate of energy production (Kippenhahn & Weigert 1994, pp. 164). The net energy release of the CNO cycle is, however, the same as in the pp-chain, since four hydrogen nuclei are transformed into one helium nucleus plus several positrons, neutrinos, photons that share the binding energy of $26.7\,\mathrm{MeV}$.

Stars evolve gradually due to their changing chemical composition caused by the burning processes in the core. At a given point, virtually all hydrogen inside the core will have been converted into helium, causing the nuclear burning in the core to halt (H-burning then moves to a shell, see below) and the star's core to contract, since hydrostatic equilibrium is lost. The details of how this works depend strongly on stellar mass and cannot be described here. In the following I will therefore only consider the evolutionary path of a typical Cepheid progenitor of $5\,M_\odot$. This description is inspired by the one by Hofmeister et al. (1964); Kippenhahn et al. (1965) and Chap. 31 in Kippenhahn & Weigert (1994).

Three figures will form the basis of this discussion: the evolutionary track shown in Fig. 1.6, and the Kippenhahn diagrams in Figs. 1.7 and 1.8. Points annotated in the track can be followed in the Kippenhahn diagrams. Both types of figures were created using recent rotating Geneva tracks (Georgy et al. 2013b), cf. Chap. 4 for a more detailed view of the impact of rotation on Cepheids from an evolutionary perspective.

Figures 1.7 and 1.8 are so-called Kippenhahn diagrams that illustrate the location (in units of mass from the center) of convection zones and energy production zones of a $5\ M_\odot$ model as a function of time since the ZAMS and as a function of the logarithmic remaining time as calculated in the models, respectively. Convection zones are shown in shaded gray, and the total mass of the star is shown by a red solid line at the top of the figure. Towards the bottom of the figures, blue, green, and red lines indicate the locations of hydrogen, helium, and carbon burning, respectively. Dashed lines indicate the boundaries of these burning zones and solid lines show the location of maximal energy production.

Let us now turn to the annotated points in Fig. 1.6 to discuss the evolutionary path of a $5\,M_\odot$ star on the way to becoming a Cepheid. Note that theoretically, a star is considered to be a Cepheid each time it crosses the (classical) instability strip (IS). Point A indicates the zero-age Main Sequence (ZAMS), i.e., the point in time when the star has arrived on the MS in hydrostatic equilibrium, burning hydrogen in its core. In the latest Geneva models, this is adopted as the time when the core has burnt 0.3% of its available hydrogen (C. Georgy, priv. comm.). The evolution on the MS from point A to B is the longest phase of a star's life, governed by the slow burning of hydrogen until near depletion. According to Fig. 1.7, this takes about $78\,\mathrm{Myr}$ for the $5\,M_\odot$ model[12]. As the remaining hydrogen is burnt (point B to C in Fig. 1.6), the convective core shrinks rapidly and

[10] cf. also the *Solar neutrino problem* that led to the discovery of neutrino oscillations, thanks to experiments such as the Sudbury Neutrino Observatory (SNO)

[11] Although thermonuclear fusion is not a chemical reaction, it is often referred to as burning

[12] Note that this value depends strongly on rotation, cf. the submitted article in Chap. 4

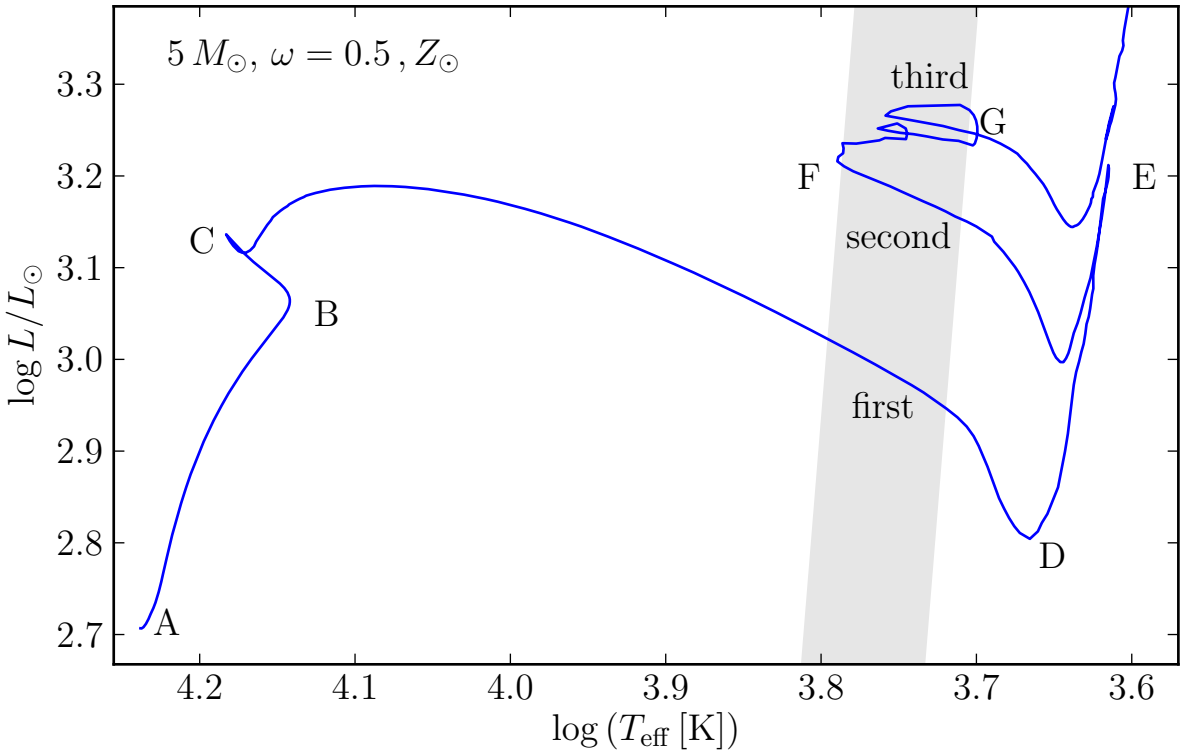

Figure 1.6: Annotated evolutionary track for $5\,M_\odot$ rotating model with Solar metallicity. Instability strip crossings during which the star is considered a Cepheids are labeled as first, second, and third. The points A-G are explained in the text. Evolutionary track from Georgy et al. (2013b), Solar metallicity IS according to Tammann et al. (2003) drawn in shaded gray.

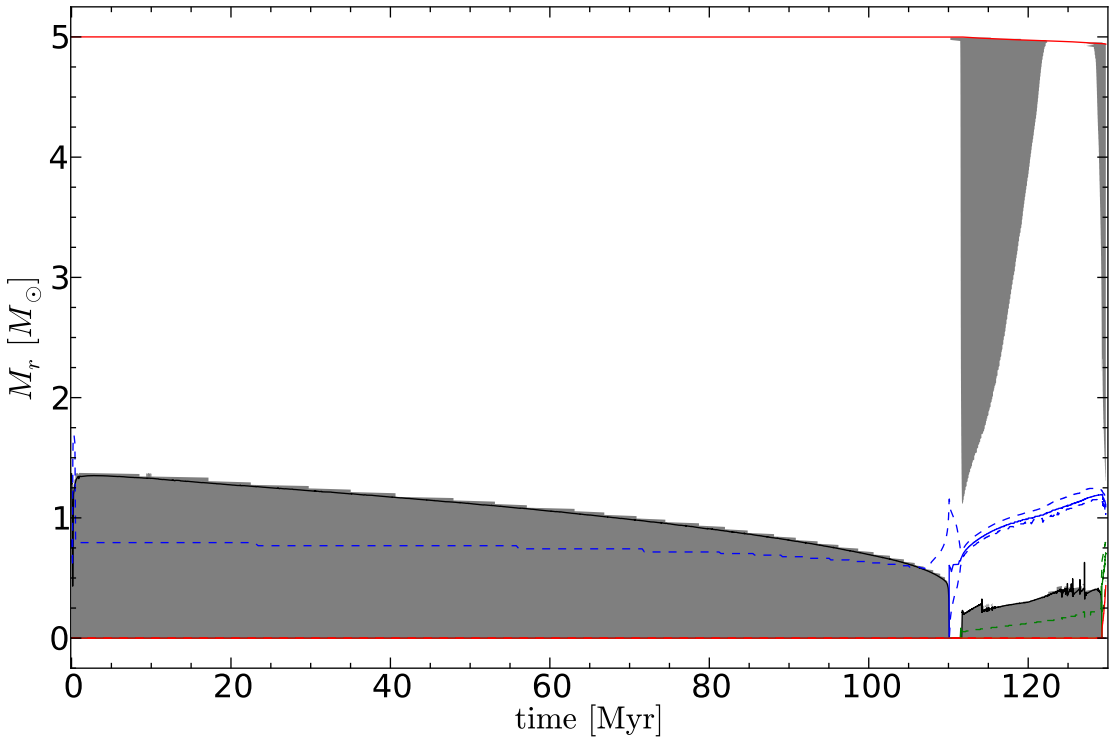

Figure 1.7: Kippenhahn diagram for $5\,M_\odot$ star of Solar metallicity and with initial rotation rate $\omega = 0.5$. Convection zones shown as gray shades. Fusion zones of hydrogen (blue), helium (green), and carbon (red) delimited by dashed lines; regions of maximal energy production shown as solid lines. Total mass shown by solid red line on top of figure. Figure credit: Cyril Georgy and Sylvia Ekström.

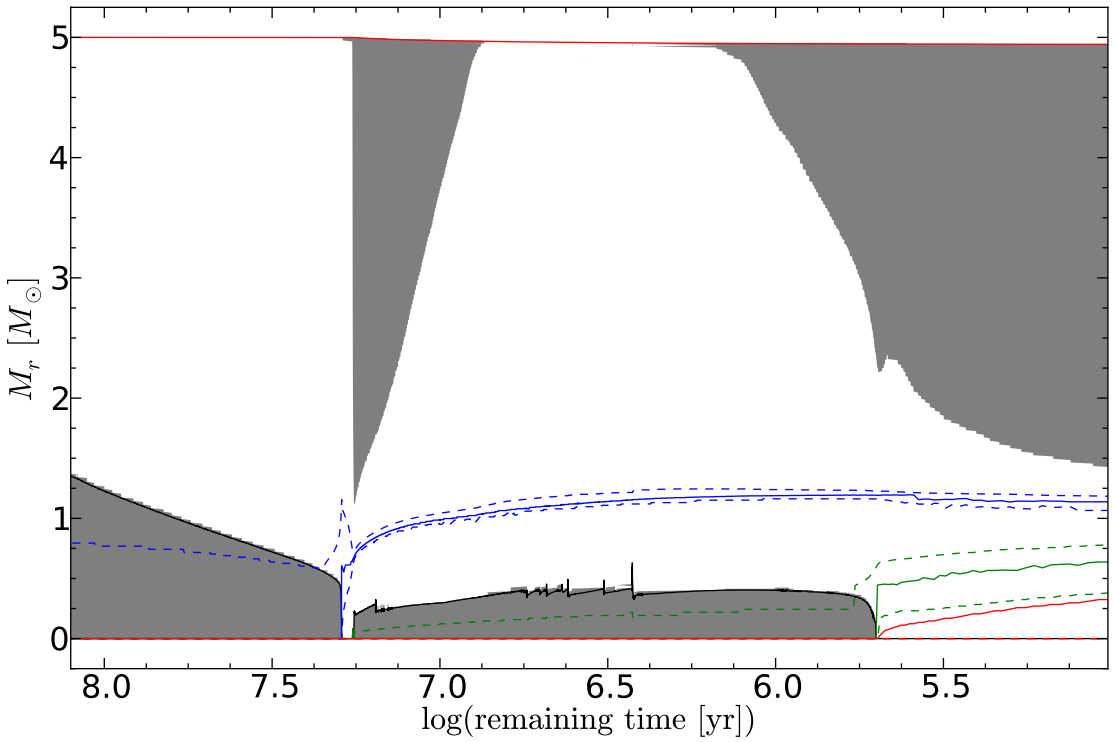

Figure 1.8: Same as Fig. 1.7 with logarithmic time axis counting down the early AGB phase, where the model calculations were stopped. Figure credit: Cyril Georgy and Sylvia Ekström.

eventually ceases fusioning. Around that time, according to Kippenhahn et al. (1965), a strong second maximum of energy production is starting to appear in the zone surrounding the core where more hydrogen is still available (cf. the solid blue line in Fig. 1.7), creating a thick non-convective shell within which hydrogen burning occurs. In Fig. 1.8, this is seen as a rapid outward shift of the solid blue line that indicates the location of maximum energy release due to hydrogen burning. At point C, the extent of the H-burning shell is maximal and then quickly becomes slimmer and is eventually confined to a narrow shell in which hydrogen burning continues.

On the path from C to D, the core contracts while the hydrogen burning shell moves outward, "mirroring" the behavior (expansion or contraction) of the core (see e.g. Kippenhahn & Weigert 1994). This mirroring effect causes the outer envelope of the star to expand and turns the hot MS star into a cool red giant on its way to the Hayashi line. This part of the evolution is quite fast (Kelvin-Helmholtz timescale, here $\sim 10^7$ years in total, accelerating towards the cool side of the HRD), leading to an absence of stars observed in this region of the HRD. For this reason, the path from C to D is often referred to as the Hertzsprung-gap. Note that a first crossing of the IS occurs during this part of the evolution. In principle, such stars are expected to be pulsationally unstable and to become Cepheids. However, due to the fast evolution in the Hertzsprung gap, few such objects are predicted and only a few candidates for first-crossing Cepheids are known (see e.g. Turner 2009, who argues that Polaris might be one such case).

After this first crossing, the outer convective envelope reaches very deep down into the interior of the star. This phenomenon is referred to as the first dredge-up, since convection can easily carry processed materials from the core to the surface, thereby modifying surface abundances. It is followed by the ascent onto the red giant branch (RGB).

At point E, the core has contracted sufficiently to ignite helium burning via the triple-α process ($3\alpha \rightarrow {}^{12}\mathrm{C}$). This occurs at a central temperature around $\log T_c = 8$. The conditions in the core of a $5\,M_\odot$ Solar metallicity models near the Cepheid stage shown in Fig. 1.9. Note that for Cepheid progenitors, helium burning ignites before the core becomes degenerate, and thus, no helium flash occurs. Also, the core mass (here $5 - 10\%$) is much lower during helium burning than during hydrogen burning.

Following helium ignition, the upwards trend in the HRD stops (when the core is nearly pure helium) and reverses. During this ensuing decrease in luminosity, about 46% of the helium in the core will be used up, making this a is very slow development ($\sim 8.0\,\mathrm{Myr}$). Then begins the blue loop, which will last just slightly longer ($\sim 8.4\,\mathrm{Myr}$) for this model. A detailed discussion of the effects leading to the creation or suppression of these loops is far too involved for this introduction. More details can be found in Kippenhahn & Weigert (1994, Chap. 31.4) and in the literature. It is interesting to note that the energy production in the core due to helium burning is smaller than the energy released due to shell H-burning during the entire core He-burning phase (between $\sim 6 - 48\%$ evolving along the loop). After helium ignition, the core slowly expands until a central temperature around $\log T_c \approx 8.2$ is reached. Here, the star remains in equilibrium, decreasing the helium fraction Y_c linearly with time. As can be seen in Fig. 1.8, the core is increasing in size, since the shell is becoming smaller. When Y_c is less than approximately 10%, the core starts to contract again.

Along the path from E to F, the star moves to hotter temperatures, and crosses the IS for the second time. The star as a whole is contracting during this phase, increasing in average density, $\bar{\rho}$. Since Cepheid pulsation periods $\propto \sqrt{1/\bar{\rho}}$ (cf. Eq. 1.12), Cepheid periods are decreasing along the way. Such considerations have been of historical importance in ruling out gravitational contraction as the primary energy source for stars (Eddington 1918a, 1919a), and are nowadays sometimes used to test predictions of evolutionary models using observed rates of period change from many stars in the Galaxy (Turner et al. 2006) or the Magellanic clouds (e.g. Pietrukowicz 2001). In the Kippenhahn diagrams, this phase is clearly seen to reduce the size of the convective envelope until it becomes essentially fully radiative.

Point F marks the tip of the blue loop, i.e., when the star is hottest. Since this describes a tempo-

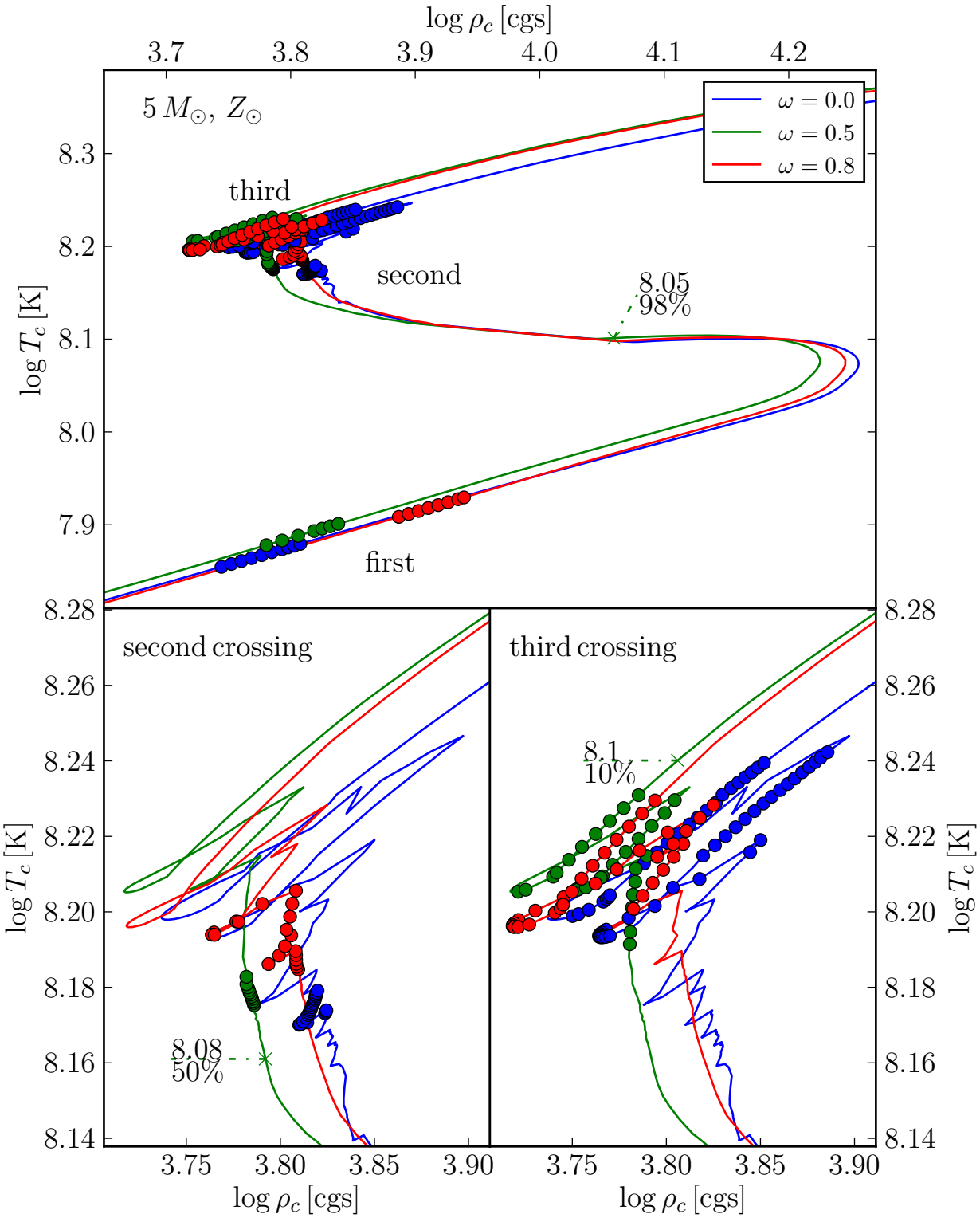

Figure 1.9: Core temperature vs. core density for 5 $M_\odot$ solar-metallicity models with three different initial rotation rates: $\omega = 0.0,\ 0.5,\ 0.8$ drawn in blue, green, and red, respectively. Grid points that lie inside the instability strip are highlighted by solid circles. *Bottom panels:* Zoom on the second (left) and third crossings (right). Key values for $\log$ age and helium mass fraction Y_c in per cent are annotated to the curve in the three panels for the $\omega = 0.5$ model.

rary equilibrium state for the star, evolution is slowest towards the tip of the blue loop. For a given crossing, the evolutionary timescale increases from the red to blue edge of the instability strip, i.e., is longer the greater the distance from the Hayashi line. Note, however, that the evolutionary timescale also depends on the crossing itself. The lifetimes of the crossings strongly depend on mass (and also on rotation). A detailed comparison of this can be found in Tab. 4 in the paper in Sec. 4.3. For reference, the relative lifetimes are approximately as follows (1st/2nd/3rd crossing): $0.5\%/15\%/85\%$ ($5\,M_\odot$); $6\%/39\%/55\%$ ($7\,M_\odot$); $10\%/40\%/50\%$ ($9\,M_\odot$). Thus, the third crossing is usually the longest-lasting, and the first crossing becomes more important with increasing mass. The chance of observing a first crossing Cepheid is therefore higher for longer periods (masses).

The strange additional loops at point G are caused by the increase in core size during He-burning and lead to so-called helium spikes in the models, cf. the oscillatory pattern in core size in Fig. 1.8 around $\log(\text{remaining time}) \approx 6.5$. Whether or not such spikes actually occur in stars is difficult to say. Following a test by Cyril Georgy for a $7\,M_\odot$ model, however, it was found that replacing Schwarzschild's criterion for convection with that by Ledoux appears to make these spikes disappear.

Once the helium fraction $\lesssim 10\%$, the core starts to contract once more, and the star moves back to the Hayashi line, crossing the IS a third time. This part of the blue loop is slowest, and Cepheid lifetimes predicted here are typically longer[13] than during the second crossing, cf. the article in Chap. 4. After the second crossing, as the star continues to cool, the outer convective envelope reaches deep into the inner layers of the star, causing a second dredge-up, and the ascent to the asymptotic giant branch (AGB) begins (e.g. Maeder & Meynet 1989). At this point, helium burning has moved to a shell source (green lines in Fig. 1.8).

The post-blue loop evolution along the AGB is a rich and complex topic. Since it is not immediately relevant to this thesis, its discussion is omitted here. Chap. 26 of Maeder (2009) provides an excellent overview of these stages. I shall, however, mention that intermediate mass post-AGB stars will pass through a planetary nebula phase during which they expel their envelopes, finally revealing hot white dwarfs.

Although rotating models have been used here to illustrate the evolutionary path of Cepheid progenitors, a discussion of the impact of rotation on stellar evolutionary models in general is out of scope for this introduction. The interested reader can find additional information on this topic in the review by Maeder & Meynet (2000) as well as in the textbook by André Maeder (2009). The impact of rotation specifically on the parameters predicted for Cepheids has thus far not been explored in detail in the literature. My thesis work on this subject is presented in Chap. 4 and in the paper recently submitted, which is found in Sec. 4.3.

1.3.2 The pulsation mechanism of Cepheids

Having seen the evolutionary scenario for a Cepheid in the preceding section, let us now consider the reason for the variability of Cepheids: radial pulsations. In order to be concise, I will present a qualitative overview of the most relevant basics. The interested reader is referred to the literature for more detailed descriptions, such as the review by Zhevakin (1963), or detailed textbooks. Brief descriptions of pulsations and Cepheids can be found in Kippenhahn & Weigert (1994) and Maeder (2009). More details specifically on asteroseismology can be found in Aerts et al. (2010) and the physics of pulsations are shown in great detail by Smeyers (2010).

Cepheid pulsations are driven by the so-called κ-mechanism. The name derives from the usual symbol of the opacity, κ, which acts as a valve in a heat engine. A key requirement for this mechanism to operate is the existence of a partial ionization zone (PIZ) located at the right depth inside the stellar envelope. A hydrogen PIZ was first proposed to be responsible for the pulsation (Eddington 1941), but nowadays it is known that helium PIZs are much more important for the

[13] In the case of a $5\,M_\odot$ Cepheid by up to an order of magnitude, cf. Sec. 4.3

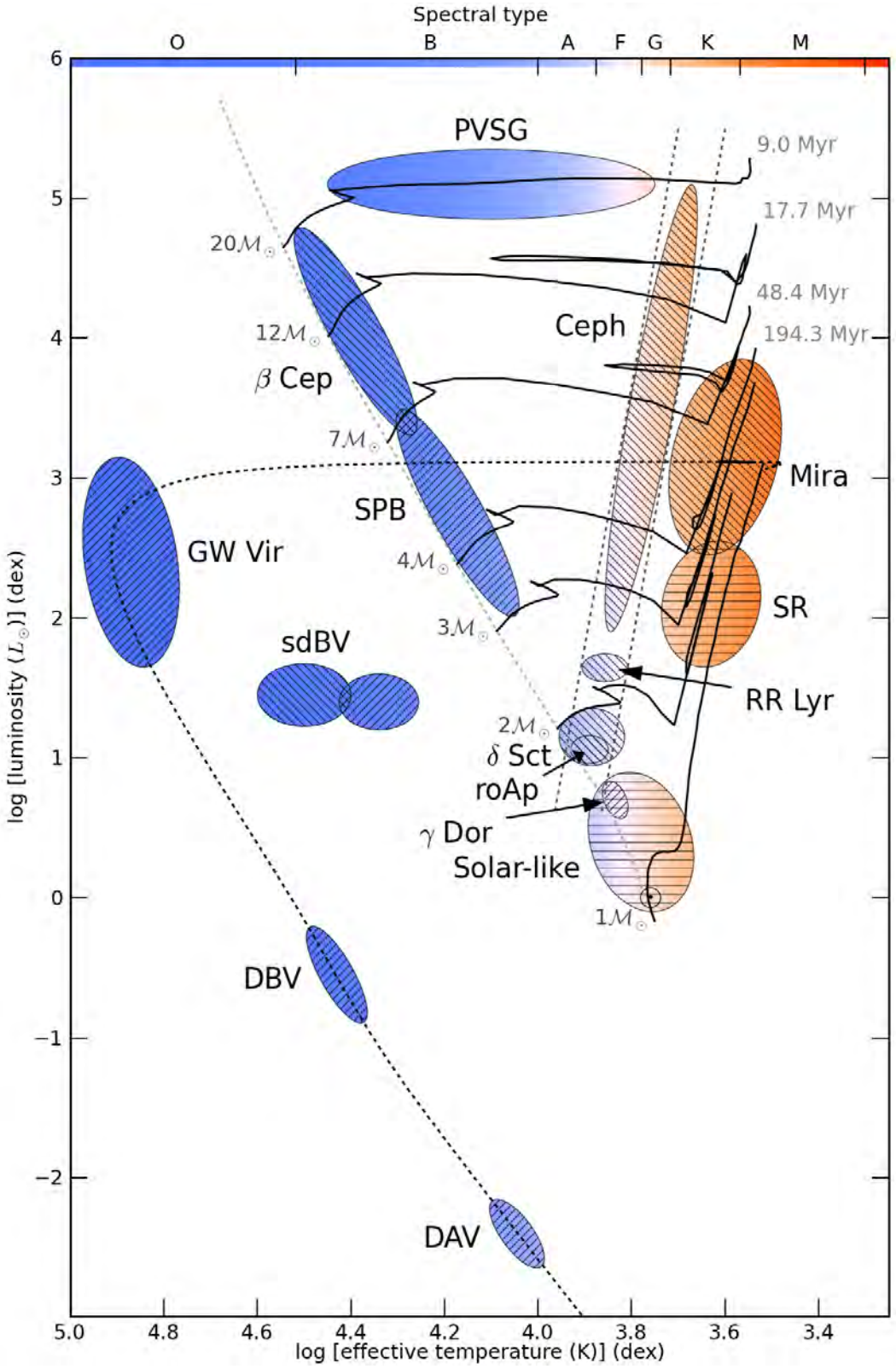

Figure 1.10: Hertzsprung-Russell diagram of pulsating stars. Figure from Papics (2013) with original image credit J. Christensen-Dalsgaard and P. Degroote. Evolutionary tracks by Schaller et al. (1992) are shown as solid lines with initial masses indicated at the ZAMS and final ages shown at the end of the evolutionary tracks. The dashed line indicating the evolutionary path from the Mira to the white dwarfs is taken from Driebe et al. (1998). Filling patterns distinguish between p-mode (\\), g-mode (//), and solar-like oscillations (=).

Cepheids (Baker & Kippenhahn 1962). However, the H I PIZ is required to explain the phase lag shown in Fig. 1.3. Other species can also cause pulsations via the same mechanism, see for instance the β Cephei stars where iron takes on this role (Aerts et al. 2010).

Let us consider how a PIZ drives the pulsation via the κ-mechanism, starting arbitrarily during the process of contracting due to a temporary loss of equilibrium. As radius decreases, temperature increases. According to the Saha-Boltzmann equation, this changes the ionization equilibrium among the different species. Due to the contraction, more and more He II is further ionized, i.e., $\mathrm{He}^{+} \rightarrow \mathrm{He}^{++} + \mathrm{e}^{-}$. In this way, the mechanical energy due to compression is used to increase the degree of ionization, and temperature rises only slowly (de Loore & Doom 1992, p. 230). This leads to an increase in opacity[14] and hence, pressure. At a given point, pressure exceeds gravity and pushes outwards the infalling layers, using the energy stored in the PIZ. As the envelope cools in this way, the gas can recombine with free electrons, leading to a drop in opacity. The radiation from the interior can now more easily diffuse through the outward layers, and pressure drops. Due to inertia, the outer layers are pushed outwards beyond the equilibrium location. From this expanded state with increased potential energy, the envelope starts to recontract, and the cycle repeats.

In Cepheids, the restoring force is pressure, i.e., Cepheids pulsate in p-modes and the oscillations are acoustic. The oscillation period of acoustic waves in a medium is related to the sound speed and the radius as well as the ratio of specific heats. Using the adiabatic exponent $\Gamma_1 \equiv (\mathrm{d} \ln P_{\mathrm{press}} / \mathrm{d} \ln \rho)_{\mathrm{ad}}$ with pressure P_{press} and density ρ, one can derive a period-mean density relation for adiabatic periods P (Maeder 2009):

$$P = \left(\frac{3\pi}{(3\Gamma_1 - 4) G \bar{\rho}} \right)^{1/2} , \tag{1.12}$$

where $\bar{\rho}$ denotes the mean density of the star and G is the gravitational constant. Therefore, the (acoustic) pulsation periods of stars are proportional to the inverse of their density.

The κ-mechanism is very sensitive to the (radial) location of the PIZs in the star's envelope, requiring temperatures of $\sim 10^4$ K for hydrogen and $\sim 4 \times 10^4$ K for the He II PIZ. For these zones to drive pulsations, there must be sufficient mass enclosed within them. Since ionization mainly depends on temperature and due to the inward-increasing temperature gradients of stars, the location of the PIZ is dominated by T_{eff}. This places structural constraints on the pulsating stars that rely on such mechanisms, resulting in well-defined regions of the HRD where pulsational instability occurs, cf. Fig. 1.10. The best-known example of these is, of course, the (classical) instability strip (IS) in which Cepheids are located. Since a star's position inside the HRD changes during its evolution, see Sec. 1.3, stars can become pulsationally unstable whenever they cross regions of instability such as the IS, cf. Fig. 1.6. Pulsation is therefore a transient evolutionary phenomenon that may have occurred or may occur in the future in stars currently observed as non-variable, and will cease in currently pulsating stars some time in the future. In this context it is worth noting that pulsation can be a very stable (long-term) phenomenon (Aerts et al. 2010). For instance, the star o Ceti (Mira) was discovered by Fabricius in 1596 and is still pulsating. There are, however, interesting examples such as the peculiar Cepheid HR 7308 (Burki et al. 1982) or Polaris (α Ursa Minoris) whose long-term amplitude variations have puzzled astrophysicists for a long time (e.g. Turner 2009, and references therein).

1.3.3 The theoretical interpretation of the period-luminosity-relation

As Eq. 1.12 shows, the pulsation periods of Cepheids are directly related to their mean density. Thus, it can be shown that pulsation periods are proportional to luminosity (the following line

[14] Note that the hydrogen and helium partial ionization zones have increasing opacity with increasing temperature, contrary to most other regions of a star, where opacity drops as temperature increases.

of argument is taken from Maeder 2009, Chap. 15.5). Note that in the following, P designates pulsation period.

The period-mean density relation is often written as

$$P = Q \left(\frac{\bar{\rho}}{\bar{\rho_{\odot}}} \right)^{-1/2} \sim Q \sqrt{\frac{R^3}{M}} \,, \tag{1.13}$$

assuming spherical symmetry. R denotes radius, M mass, and Q is the so-called pulsation 'constant', although it should be noted that Q depends on P, cf. Saio & Gautschy (1998). Typical values for Q in Cepheids (for fundamental mode pulsation) range from approximately $0.035 - 0.05$ days.

Using a mass-luminosity relation from stellar evolutionary models, one obtains

$$M \sim L^{1/\alpha} \tag{1.14}$$

and, from Eq. 1.3,

$$R^{3/2} \sim \left(\frac{L}{T_{\rm eff}^4} \right)^{3/4} \,, \tag{1.15}$$

which leads to

$$P \sim \frac{Q L^{-(1/2\alpha)} L^{3/4}}{T_{\rm eff}^3} \,. \tag{1.16}$$

If a slope of the mass-luminosity relation is inferred via the models, e.g. $\alpha = 3.3$ as in Maeder (2009, Eq. 15.91), then this leads to the period-luminosity-color relation

$$\log P \approx \log Q - 3 \log T_{\rm eff} + 0.60 \log \frac{L}{L_{\odot}} + \text{const} \,, \tag{1.17}$$

which can be re-arranged to yield:

$$\log \frac{L}{L_{\odot}} = 1.67 \log P + 5 \log T_{\rm eff} - 1.67 \log Q + \text{const}' \,. \tag{1.18}$$

However, the IS is nearly vertical and luminosity nearly constant during an IS crossing, which results in a weak dependence of luminosity on temperature inside the IS (Maeder 2009, $\log T_{\rm eff} = -0.05 \log \left(\frac{L}{L_{\odot}} \right) + const''$), so that Eq. 1.17 becomes:

$$\log \left(\frac{L}{L_{\odot}} \right) = 1.34 \log P - 1.34 \log Q + const''' \,. \tag{1.19}$$

Note, however, that the mass-luminosity relation used here takes into account neither the different crossings, nor the effect of rotation on Cepheid luminosity. These effects are described for the first time in the article presented in Chap. 4.

1.3.4 The Cepheid mass discrepancy

Once calibrated, the PLR can be used to infer Cepheid masses for an adopted $M - L$ relation. Non evolutionary model-based Cepheid masses can be obtained from Eq. 1.13, if independent estimates of R are available, e.g. via spectroscopic temperature estimates in Eq. 1.15, or via radius determinations based on the Baade-Wesselink (BW) technique, see Sec. 1.2.1.

Following the first pulsational model calculations by Christy (1968) and Stobie (1969a,b,c), it quickly became clear that there was a disaccord of about 40% in the masses determined via evolutionary models and other methods (Cox 1980, and references therein) in the sense that $M_{\rm evol} > M_{\rm other}$. Beat Cepheids played an important role in this problem, since their observed period ratios

could be compared to model predictions (Petersen 1973; Moskalik et al. 1992) and thus provided an important test for updated opacities in stellar envelopes (Petersen & Takeuti 2001, and references therein).

The current remaining Cepheid mass discrepancy figures at $10 - 20\%$, see e.g. Bono et al. (2006); Keller (2008). Other authors have claimed both that no mass discrepancy exists (Cassisi & Salaris 2011) and that the mass discrepancy can be solved by introducing enhanced mass loss Neilson et al. (2012). Prada Moroni et al. (2012) have furthermore shown that a combination of evolutionary parameters can be found that well matches the Cepheid with the most accurately-determined parameters, OGLE-LMC-CEP-0227 (Pietrzyński et al. 2010). So, what appears to be the problem?

The two main 'solutions' for the mass discrepancy proposed in the recent literature are:

1. to increase the size of the core via the overshooting parameter in order to increase luminosity (e.g. Cassisi & Salaris 2011), and

2. to decrease the mass of the star by enhanced mass-loss (Neilson et al. 2012, including also higher overshoot values).

However, there are two potential problems with both 'solutions.' Firstly, the physics underlying convective core overshooting are difficult to constrain, leading to different parametrizations of this parameter. In Ekström et al. (2012), the overshoot parameter was thus calibrated on observed main sequence stars, resulting in $d_{\rm over}/H_P = 0.10$, expressed in units of the pressure scale height, H_P. Other values ranging from $0.0 - 0.335$ can be found in the literature (e.g. Bono et al. 2000; Caputo et al. 2005; Pietrinferni et al. 2006; Keller 2008). While different evolutionary codes use different values for the overshoot parameter, it also appears that different observations that can potentially constrain overshooting require different amounts of it (Neilson & Langer 2012, and references therein). However, it is difficult to argue that overshooting should vary from star to star, casting doubt on the explanation of the mass discrepancy in terms of overshooting.

Secondly, pulsation-enhanced mass loss as proposed by Neilson & Lester (2008); Neilson et al. (2011) acts only during the lifetime of a Cepheid, thus depending strongly on the location and width of the IS. During the generally short[15] transient evolutionary stages when a star is actually pulsating (IS crossings), only a few percent of mass can be lost via this mechanism, which predicts pulsation-enhanced mass-loss rates in the order of $10^{-10} - 10^{-7}\ M_{\odot}$. Furthermore, removing the required amounts of mass from the envelopes yields significantly altered evolutionary paths (Prada Moroni et al. 2012). Note, however, that mass-loss in Cepheids has been observed (e.g. Matthews et al. 2012). In conclusion, it appears that no consensus has yet been established on how to resolve the mass discrepancy. However, in the paper included in Sec. 4.3, it is argued that rotation can resolve this old problem.

1.4 Cepheids and the distance scale

Ever since the discovery of the PLR by Henrietta Leavitt more than a century ago, Cepheids have played a fundamental role in establishing the astronomical distance scale. To this day, Cepheids are among the most important standard candles in the universe, and most research on Cepheids is somehow connected to the distance scale. This is obvious when looking at the recent IAU Symposium 289 dedicated to "advancing the physics of cosmic distances" (see de Grijs 2013a, for the conference proceedings), which contains many contributions related to Cepheids as well as other pulsating stars. During his conference summary, de Grijs (2013b) presented a figure from his book (de Grijs 2011) which nicely summarizes the current shift from a distance ladder to a "network of distance tracers". The figure is reproduced here as Fig. 1.11 to provide an overview for

[15] in the order of $10^4 - 10^6$ yr, depending on mass, rotation and assumed instability strip boundaries

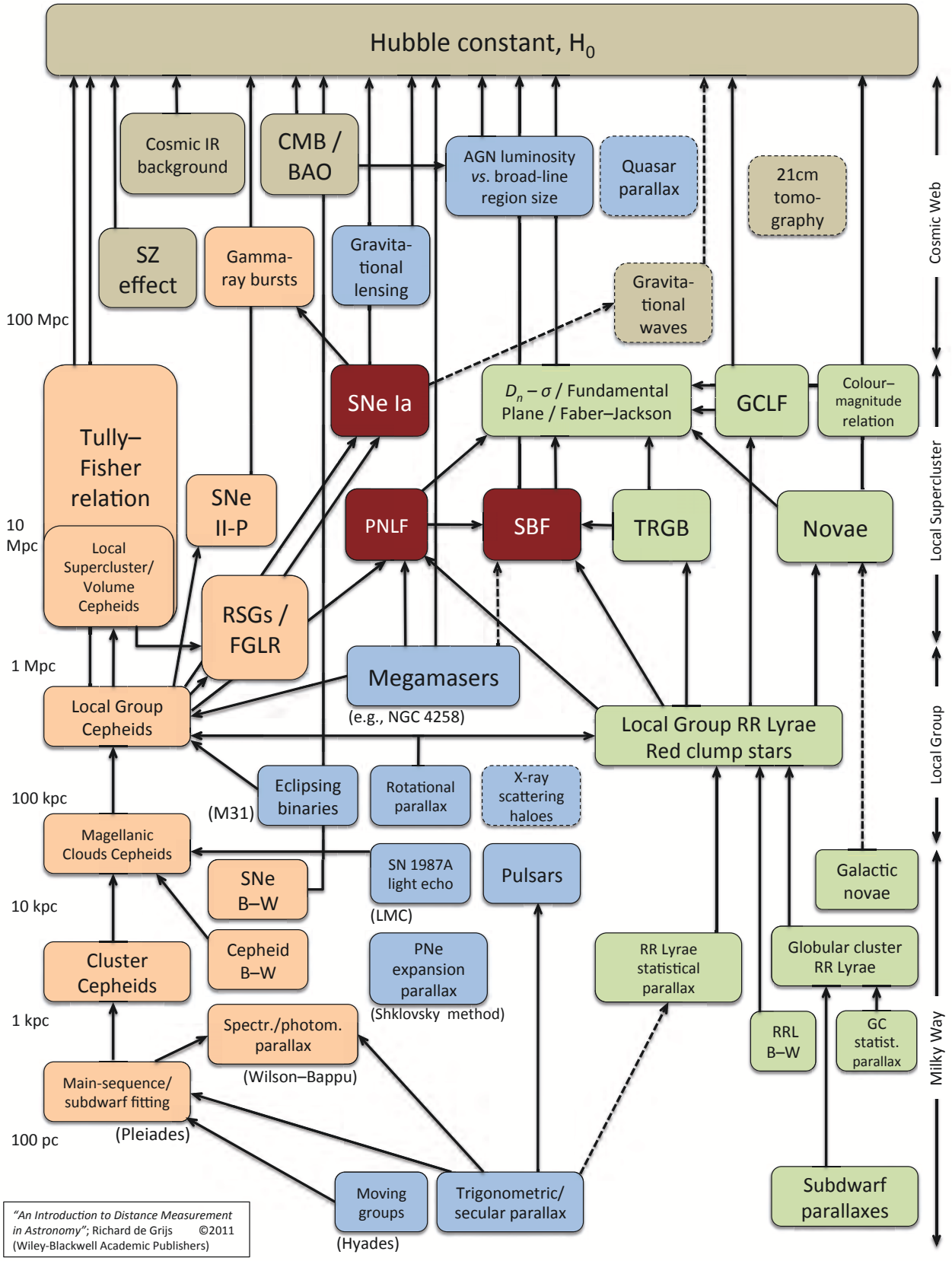

Figure 1.11: The *network of distance tracers*, originally from de Grijs (2011). Figure taken from arXiv preprint of de Grijs (2013b).

the initiated. As can be seen in the figure, Cepheid-based distance estimators (on the left branch), together with supernovae of type Ia allow for a one-step calibration of H_0 (using a parallax-based PLR calibration, see below). However, the main limitation for such an effort is the small statistics: only eight galaxies are currently known in which both Cepheids and type Ia SNe have been observed and thus allow for a cross-calibration (Freedman 2013). Furthermore, the Cepheids currently employed in this kind of cross-calibration often belong to the group of so-called ultra-long period Cepheids, which appear to be quite different beasts compared to the "ordinary" Cepheids known in the Galaxy and the MCs (de Grijs 2013b). These points will be discussed further in the future prospects at the end of this thesis in Sec. 5.2. Extensive details on the subject of the distance scale can be found in the book by de Grijs (2011). In the following, I provide a brief overview of the importance of Cepheid research for the distance scale focusing on methods applicable to the well-understood Cepheids in the MCs and the Galaxy. A nice review of the importance of Cepheids on the distance scale was contributed by Feast (1999), for instance.

The importance of Cepheids as distance indicators derives from the relation between period and luminosity discovered by Leavitt & Pickering (1912). Luminosity is the energy radiated by the source per unit time, which is related to the absolute magnitude via the bolometric correction. Most observational studies therefore derive absolute magnitude as a function of period. The result is a law of the form

$$M = \alpha \log P + \beta \,. \tag{1.20}$$

Once slope α and zero-point β are calibrated (see below), the absolute magnitude of Cepheids is easily estimated using only period P. Comparing Eq. 1.20 with Eq. 1.18, it is clear that the former ignores color effects due to the intrinsic width of the IS. The question of whether to use a PLR or a period-luminosity-color-relation (PLCR) has occupied researchers for decades (see e.g. Tammann et al. 2003; Sandage & Tammann 2006, and references therein). A historical overview of these and other developments of the Cepheid distance scale is provided online[16] by Nick Allen. The main problem was that the effects of reddening and a color-dependence on period are very difficult to separate (reddening and period-color slopes are very similar). In practice it seems, photometric methods were unable to reliably correct for reddening and color corrections simultaneously. Furthermore, the impact of reddening (e.g. due to variations among the field of view) is much larger than that due to color variations within the IS, so that most modern studies focus on diminishing the impact of reddening.

An elegant way of resolving the reddening problem observationally is to construct a reddening-free Wesenheit index (Madore 1982; Madore & Freedman 1991) via:

$$\begin{aligned} W &= m_V - R_V \cdot (B-V) \\ &= m_{V_0} + A_V - R_V \cdot (B-V)_0 - R_V \cdot E(B-V) \\ &= m_{V_0} - R_V \cdot (B-V)_0 \,, \end{aligned} \tag{1.21}$$

where m_V denotes the observed apparent magnitude (in this case in the visual filter V), and $A_V \equiv R_V \cdot E(B-V)$ is the total extinction in the line of sight due to the interstellar medium (ISM). Extinction is typically estimated from a calibrated reddening law R_V (the ratio of total to selective extinction, often assumed to be 3.1) and the color-excess $E(B-V)$. In principle, however, R_V is not a constant, since it depends on the properties of the ISM and is therefore line-of-sight dependent.

The power of the Wesenheit formulation is illustrated by Fig. 1.12 taken from Soszynski et al. (2008) for the OGLE-III LMC PLR. Clearly, the scatter is very significantly reduced in the lowest panel showing the Wesenheit index. Alternatively, Cepheids can be observed in the near infrared (e.g. Monson & Pierce 2011; Freedman et al. 2011) where reddening is much less important and where pulsation amplitudes are smaller, leading to smaller scatter.

[16] http://institute-of-brilliant-failures.com/

To derive the distance, the well-known formula of the distance modulus is required, i.e.,

$$\mu = m_V - M_V = 5 \log d - 5 + A_V \,, \tag{1.22}$$

where d is distance in parsec ($1\,\mathrm{pc} = 1/\mathrm{arcsec} = 3.26$ light years). In the reddening-free Wesenheit formulation, this simplifies to:

$$\mu = m_W - M_W = 5 \log d - 5 \,. \tag{1.23}$$

The high precision that can be achieved for PLR slope calibrations in the LMC make it an ideal "first rung" of a distance ladder, provided the zero-point can be established with similarly high confidence. While there does appear to be convergence on the horizon[17], Schaefer (2008) points out a worrying tendency regarding the agreement of various LMC distance indicators that could be interpreted as subjective bias. Since only few direct distance estimates to the LMC can be obtained (see Guinan et al. 1998; Pietrzyński et al. 2010, 2013, for some important successes), the zero-point calibration for the LMC PLR remains an important area of work. Furthermore, PLR slopes may be metallicity dependent (e.g. Storm et al. 2011b), making the LMC PLR calibration not directly applicable to galaxies of different metallicity. For more detail, see the recent comprehensive overview of the LMC and the distance scale by Walker (2012). An overview of pulsating variable stars in the MCs in general is given by Clementini (2009).

It should be noted here that the PLR in Fig. 1.12 is so nicely observed since all Cepheids are located at roughly the same distance (the depth of the LMC is negligible to first order compared to its distance). Inside our Galaxy, this is not at all the case, and significantly higher reddening inside the Galactic plane severely complicates the calibration closer to home. However, since many Cepheids in the Galaxy are much closer to Earth, there are some possible advantages of calibrating the Cepheid PLR in the Milky Way.

Certainly the most important method for calibrating the Galactic Cepheid PLR is based on trigonometric parallaxes. Until now, this method has suffered from small statistics, since trigonometric parallaxes cannot be measured to great distances, being essentially limited to a volume of approximately $500\,\mathrm{pc}$ (ℓ Carinae as determined by Benedict et al. 2007). In their seminal work, Feast & Catchpole (1997) employed the absolute trigonometric parallaxes derived by the ESA space mission *Hipparcos* for determining the Galactic PLR zero-point (assuming the LMC slope). van Leeuwen et al. (2007) later revisited the PLR calibration using the re-reduction of *Hipparcos* parallaxes by van Leeuwen (2007). Within the next decade, such a calibration will be carried out based on thousands of Cepheids whose parallaxes will be derived from *Hipparcos*' successor *Gaia*, which promises unprecedented accuracy and precision for its parallax-based PLR calibration.

The PLR most favored in the current literature is probably the *HST*-based calibration by Benedict et al. (2007) relying on astrometric measurements relative to a few reference stars whose parallaxes were derived using photometry and spectroscopy. This calibration is, however, based on only 10 Cepheids, and heavily relies on a single long-period calibrator in the sample, ℓ Carinae[18].

A very promising way to derive parallaxes for Galactic Cepheids is by variations of the BW technique. Several such studies have been published, providing the largest sample of Cepheids for calibrating the PLR (see notably Gieren et al. 1993; Fouqué et al. 2007; Storm et al. 2011a; Groenewegen 2008, 2013). While these determinations provide highly precise parallaxes, their accuracy appears to be currently limited by systematic uncertainties originating in the use of the p-factors employed (see Gieren et al. 2013, and the works by e.g. Parsons 1972; Nardetto et al. 2004, 2007, 2011). Further interferometric measurements are desirable to help resolve these issues. Potentially, I argue in Sec. 2.7, cycle-dependent radial velocity curves can also have a significant impact on BW distances.

[17] The latest figures appear to favor an LMC distance modulus just short of 18.50, e.g. $18.493 \pm 0.008(\mathrm{stat.}) \pm 0.027(\mathrm{syst.})$ in Pietrzyński et al. (2013)

[18] $\log P \sim 1.55$ for ℓ Carinae. The second longest period in the sample is $\log P \sim 1.02$, the shortest is $\log P \sim 0.56$.

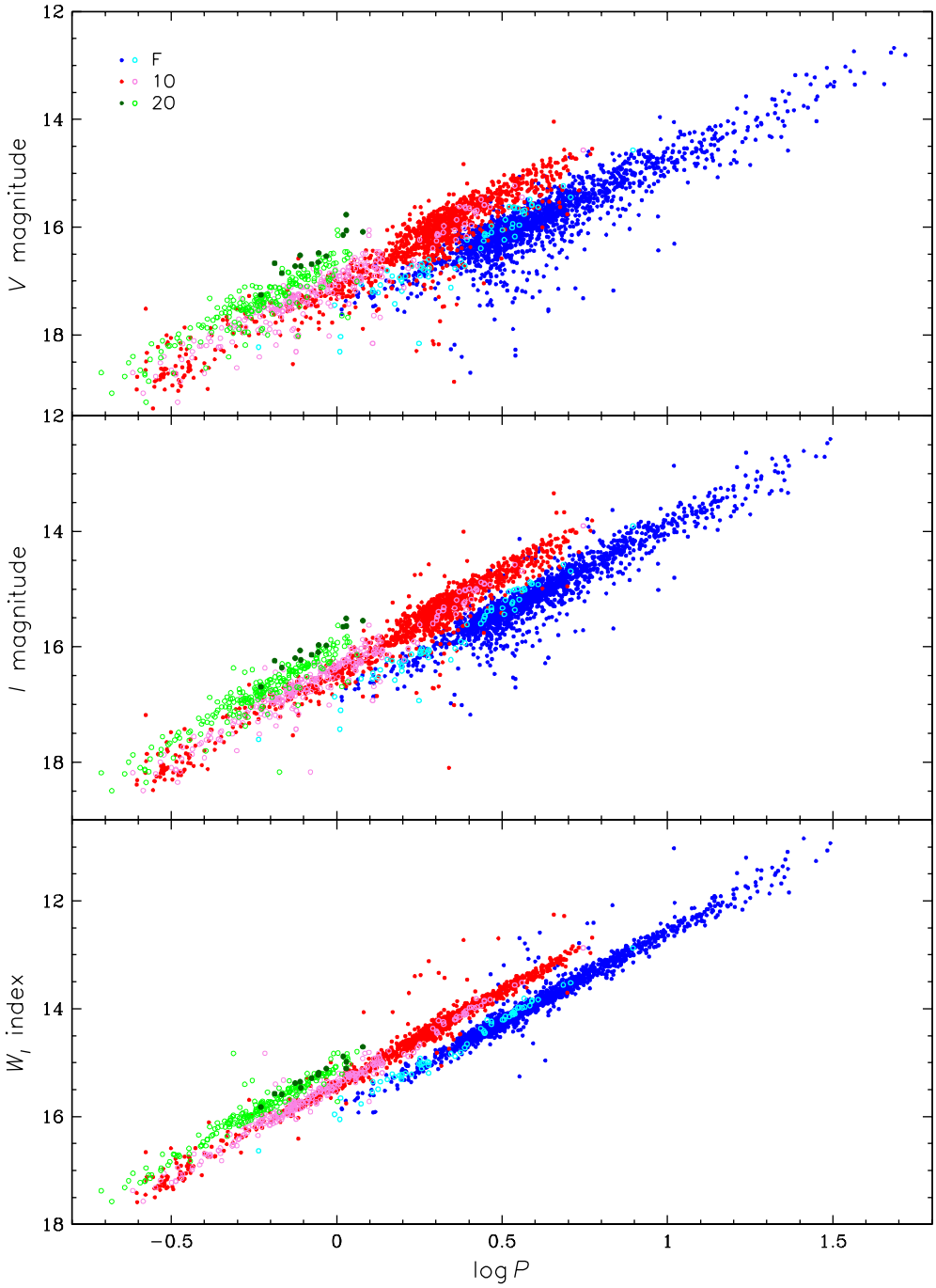

Figure 1.12: The OGLE-III PLR in the LMC by Soszynski et al. (2008). The panels show V and I-band magnitudes observed, and the W_I Wesenheit index computed as $W_I = I - 1.55(V - I)$. The legend in the top panel indicates the symbols used for fundamental mode (F), first overtone (1O), and second overtone (2O) Cepheids. Employing the Wesenheit index significantly reduces the observed scatter in the PLR.

Another historically important means of calibrating the PLR is related to Cepheids located in open clusters. Under the assumption that cluster membership holds for the Cepheid, the cluster distance estimated for instance via ZAMS-fitting can be used as the Cepheid's own (see Anderson et al. 2013a, and references therein). As a bonus, color excess can be very precisely determined in open clusters (e.g. An et al. 2007). There are, however, several issues involved in using cluster Cepheids to calibrate the PLR, see Chap. 3, and the publication included in Sec. 2.10.

1.5 Overview and scope of this thesis

When I arrived in Geneva in September 2009, I knew very little about variable stars. Accordingly, this thesis has been an exploratory journey that I found very interesting and challenging. At the start of the PhD, I was given a basic idea: to test stellar evolution models using populations of variable stars. Looking back at this task now, I would have probably chosen different paths to achieve this goal. But then again, this is how research works: there is a vague goal somewhere in the distance, and a complex space needs to be traversed in order to reach (somewhere close to) it. Neither the path nor the outcome is clear in the beginning, and that is exactly why it is interesting. Curiosity leads the way.

Before transitioning into my thesis topic, it was agreed upon with my advisers that I finish a project dedicated to magnetic field measurements in solar-like stars. This was an excellent experience for me and led to the publication of my first refereed article (Anderson et al. 2010) and a conference proceedings contribution (Anderson et al. 2011). Some remarks on this work and the publications are included in Appendix A.1.

My first steps taken in the direction of the thesis topic can be traced via a short contribution to the conference proceedings of JENAM[19] 2010 meeting in Lisbon (Anderson et al. 2012b). At the time I was familiarizing myself with the zoo of variable stars and several catalog tools. Notably among these is the excellent VO tool `TOPCAT` that greatly facilitates accessing and exploring catalog data and VO tables[20].

Initially, my thesis director Laurent Eyer had presented me with the idea of comparing the fraction of observed Cepheids to the fraction predicted by synthetic populations. In order to obtain such an estimate in the Galaxy, one would therefore have to know the number of Cepheids residing in open clusters. I therefore started to search the WeBDA database[21] for Cepheid cluster members and started to become increasingly interested in the (difficult) problem of determining cluster membership.

Having a relatively easy access to highly performing 1m-class telescopes on both hemispheres, I started to create an **observing program** aimed at providing barycentric line-of-sight velocities of Cepheids to be used as cluster membership constraints. As the first spectra started to come in from the telescope, I was captivated by the impressive line profile variations observed in these stars. Before long, I was exploring more and more interesting phenomena, including multiperiodicity, binarity, objects misclassified as Cepheids, cycle-dependent radial velocity curves and spectral line shapes, as well as the differential motion between atmospheric layers corresponding to different formation heights. Chap. 2 provides a concise overview of all of these and serves as a sneak preview of future publications. Some of the data observed during this program were critical for discovering the spectroscopic binary nature of 4 out of 9 Cepheids presented in collaboration with Laszlo Szabados et al. (2013b,a). These two publications are included at the end of Chap. 2 in Secs. 2.9 and 2.10.

What had initially started out as a compilation of data related to **Cepheids in Galactic open clusters** eventually turned into a quest to perform an all-sky census of cluster members among all

[19] Joint European and National Astronomy Meeting

[20] `http://www.star.bris.ac.uk/~mbt/topcat/`

[21] `http://webda.physics.muni.cz/`

known Cepheids (Anderson et al. 2013a, see Sec. 3.5). In the process, much had to be learned about the systematics of real data sets and the pitfalls of working with catalog data. However, in the end, a modern astro-statistical membership analysis was created that is suitable for and may find application in large data sets such as the one projected for the *Gaia* space mission. Furthermore, thanks to this census, 5 new cluster Cepheid candidates were discovered, increasing the number of such objects known in the Galaxy by approximately 20%. The resulting *bona fide* sample was then employed to revisit the cluster Cepheid-based calibration of the slope and zero-point of the Galactic PLR. The preliminary results of this study were presented as a contributed talk at IAU Symposium 289 in Beijing (Anderson et al. 2013b, see appendix B.2) and submitted to *MNRAS* a few months later. More details on the development and context of this project is provided in Chap. 3. The published article is included in Sec. 2.10.

As the Cepheids in open clusters project was nearing completion, I was asked by Georges Meynet, Sylvia Ekström, and Cyril Georgy of the Geneva stellar evolution group whether I was interested in studying **the effect of rotation on Cepheids** as predicted by their latest models. Of course, my answer was yes with an exclamation mark! The study of these models in the context of Cepheids is extremely rich, both because the models are so detailed and because so many observational constraints and literature are available for Cepheids. Thus, the submission of a first article on the subject (Sec. 4.3) just days before handing in this thesis marks only the beginning. At this point, it is already clear that rotation has far-reaching consequences for Cepheids, providing a plausible solution to the Cepheid *mass discrepancy* and predicting an intrinsic scatter of the PLR, among other nice results. A second publication that will present a detailed comparison of model predictions with observed features of Cepheids is currently in preparation for submission in early 2014, including also "the diagram I was hired for" that compares observed and predicted Cepheid frequencies, see Fig. 4.3. The current status of the research carried out thus far is presented in Chap. 4, and shall be continued and built upon in the near future.

A thesis is more than the sum of its chapters. Besides the research mentioned here, I was also involved in several other projects and have initiated or contributed to international collaborations. Not all of these explorations led to publications or converged to presentable results, and not all of these can be mentioned here. I have, however, decided to include in the appendix two noteworthy lines of research pursued. Appendix A.4 shows an investigation into possible effects of chromaticity on *Hipparcos* parallaxes of Cepheids. Appendix A.7 then presents observational contributions I made to the rapidly growing field of transient astronomy in the time-domain, including photometric follow-up of Blazar candidates, and high-resolution spectroscopy of the closest type Ia supernova observed within a generation[22], SN 2011fe.

In summary, the research performed for this thesis grew naturally from an initial goal to constrain stellar evolution models using populations of variable stars and the opportunities that presented themselves along the way. I am very grateful for the enthusiasm with which my advisers encouraged me to pursue my research ideas and for the opportunity to explore so many fascinating topics, be it through a telescope or numerical models. A summary of the methods explored, discoveries made, and results obtained, as well as their relevance for astronomy and astrophysics is presented in Sec. 5.1. Finally, an outlook towards future prospects for this work are presented in Sec. 5.2 of the same chapter.

[22]Since the famous SN 1987A

Chapter 2

Cepheid radial velocities and the versatile applications of cross-correlation functions

"(. . . dass die periodisch veränderlichen Sterne) von Farbe roth sind, nach ihrem grössten Glanze eine Kupferfarbe annehmen, und indem diese allmählig sich mehr und mehr verdunkelt, endlich völlig unsichtbar werden und verschwinden, bis sie nach einiger Zeit ihren periodischen Lichtwechsel wieder von vorne beginnen.(. . .)"

"(. . .) entweder sind sie an und für sich für uns unsichtbare Sterne (. . .) die nur durch ihre gegen uns gerichtete schnelle Bewegung die erste Stufe der Wahrnehmbarkeit erreichen, d. h. uns mit rothem Lichte erscheinen. Vielleicht aber sind sie in der That von röthlichem Lichte und verschwinden uns in Folge der von uns weggerichteten Bewegung."

CHRISTIAN A. DOPPLER, *1842*
Über das farbige Licht der Doppelsterne

Cepheids are late-type (super-)giants that maintain stable radial pulsation. Radial pulsation causes a Cepheid to expand and contract periodically, and this fact can be observed spectroscopically by variations in line-of-sight velocity. With average spectral types ranging from late F to early K, lines suitable for measuring radial velocity (RV) are plentiful in Cepheid spectra. Thus, Cepheid RVs can be derived using the cross-correlation technique (cf. Sec. 2.1.4) yielding high precision (cf. Sec. 2.1.6) RV estimates.

During my PhD, I had the opportunity to develop and lead an observing program on two telescopes equipped with high-resolution spectrographs. From many nights at the telescope, and even more days spent working with the data obtained, I was fortunate to learn a great deal of things and explore many facets of the observational properties of Cepheids. These included planning and carrying out observations (Sec. 2.1.1), determining radial velocities, and improving their calibration (Sec. 2.1.5), fitting observational data and discovering the spectroscopic binary nature of nearly a dozen Cepheids (Sec. 2.2), developing methods to test variability classification (Sec. 2.4) and deriving rotational surface velocities (Sec. 2.5), and finally to learn more about how pulsa-

tion affects the atmosphere by studying line doubling due to shock (Sec. 2.6), cycle-dependent RV curves (Sec. 2.7), and performing Doppler tomography of Cepheid spectra (Sec. 2.8).

This Chapter describes these endeavors, starting with the observing program dedicated to Cepheid RVs. Parts of this work have been used in publications. Notably, two publications resulted from a collaboration with Laszlo Szabados, that are included at the end of this chapter. The majority of the work presented here is of a preliminary nature and will be built upon in the future. Yet, these considerations and preliminary results are sufficiently far advanced and of sufficient interest to be presented here.

This work has greatly benefited from observations carried out by friends and colleagues. Without them, it would not have been possible for me to collect such a significant sample of spectra both hemispheres within the time frame of nearly three years. I would therefore like to express my gratitude and appreciation to (ordered by number of spectra for observers who contributed more than 10 spectra): Lovro Palaversa, Nami Mowlavi, Pierre Dubath, Berry Holl, Mihaly Váradi, Anne Thoul, Nicolas Cantale, Aurélien Wyttenbach, Maria Süveges, Janis Hagelberg, Monika Lendl, Dominique Naef, David Vance Martin, Amaury Triaud, Marion Neveu, and Bruno Chaselaz.

2.1 An all-sky observing program dedicated to Cepheid radial velocities

2.1.1 Observing program description

The observing program described here was originally born from the need for Cepheid RVs to be used as part of the Cepheids in open clusters project described in Chap. 3. The targets were selected according to several criteria, including notably on-sky proximity to Galactic open clusters. In addition, Cepheids with little to no available literature data were observed in order to search for binarity (cf. Sec. 2.2) and to provide a spectroscopic classification test for Cepheid candidates (cf. Sec. 2.4). Furthermore, several Cepheids with abundant literature RVs were selected in order to increase the baseline and the sensitivity to binarity, and to provide a reference sample, e.g. to search for zero-point offsets between RVs from *CORALIE*, *HERMES*, and the literature. When interesting features were noted, further observations were requested. Specifically, this led to observations dedicated to shock-related phenomena (line doubling, cf. Sec. 2.6) and to cycle-to-cycle RV variations (cf. Sec. 2.7).

The observations were carried out from both hemispheres using the Swiss Euler telescope located at ESO La Silla observatory (near La Serena in Chile, see Sec. 2.1.3) and the Flemish Mercator telescope located at Roque de los Muchachos observatory on La Palma (Canary Islands, Spain, see Sec. 2.1.3) starting in November 2010 and continued until the end of my thesis. Between November 2010 and December 2012, most observations carried out by the Stellar Variability group were part of this observing program. During this program, a total of 5156 spectra of 330 Cepheid candidates were collected, see Tab. 2.1 for some more details.

2.1.2 Observational strategy

The observational strategy employed depended on the reasons for observing a particular object.

To measure systemic velocities, v_γ, for *bona fide* Cepheids, the strategy was to obtain good phase coverage during at least one observing run and to search for signs of binarity using literature data, where available. Full phase coverage could not be achieved for long period Cepheids during single observing runs[1], while multiple pulsation cycles were sampled for short period Cepheids

[1]Our Stellar Variability group had access to Euler during 2 observing runs of 14 nights each per semester, and to Mercator during 3 observing runs of 10 nights each per year (later increased to 2 per semester following the installation

(depending, of course, also on the observing conditions). At Euler, scheduling limitations were efficiently mitigated by introducing time exchanges with the Geneva exoplanet group. This great flexibility in requesting observing time was a great advantage, and has significantly added to the quality of the final *CORALIE* data set.

In order to be sensitive to signs of spectroscopic binarity, most Cepheids were observed during more than one observing run, with minimal baselines ranging from months to a couple of years. This strategy was chosen since binary Cepheids have very long orbital periods (at least a year) due to their large radii ($30 - 200\,R_\odot$). Thus, if at least one pulsation cycle is well-covered during an observing run, binarity is easily discovered as a shift of the average velocity.

To test the classification status of Cepheid candidates, the strategy was as follows. First, a single observation was made. If the cross-correlation function returned by the pipeline was flat, i.e., no correlation peak was found (0 contrast) despite sufficient signal to noise ratio (S/N), no further observations were obtained and the target blacklisted on the observations list. If a correlation peak was found, two further observations, well-placed at different phase points, were obtained. The reasons for adopting this strategy are explained in Sec. 2.4.

Observations of Cepheids exhibiting line doubling and cycle-to-cycle variations were carried out following a similar strategy to that employed for spectroscopic binaries in order to be sensitive to long-term variations.

Thanks to the very flexible access to the telescope in the framework of time exchanges, time-critical and long-term follow-up observations were requested year-round whenever necessary. This allowed for several serendipitous insights and made running this observing program a great pleasure.

2.1.3 Instrumental setups and characteristics

Both *CORALIE* and *HERMES* are optical fiber-fed high-resolution cross-dispersed echelle spectrographs mounted to identically-built Ritchey-Chrétien reflector telescopes with a primary mirror diameter of $1.20\,\mathrm{m}$. The wavelength coverage of both instruments ranges across the most part of the optical spectrum ($377 - 900\,\mathrm{nm}$ for *HERMES*, and $381 - 681\,\mathrm{nm}$ for *CORALIE*). *HERMES* provides slightly higher resolution ($R \sim 85\,000$ vs. $R \sim 60\,000$ for *CORALIE*).

Efficient, fully automatic reduction pipelines are available for both instruments, greatly facilitating the job of the observer and the PI of the program. The pipelines perform bias correction via their detectors' overscan regions, flatfielding using tungsten lamps, order extraction, and cosmic removal. The wavelength calibration is performed using Thorium Argon (ThAr) lamps. Merged (1D) spectra are available for both instruments, although 2D (per-order) spectra are used

of the Geneva-built M3 at the telescope)

CORALIE

N_{spectra}	N_{Cepheids}	First observation	Last observation	HJD range
3382	220	2010-11-19	2013-08-07	55519.78 - 56511.55

HERMES

N_{spectra}	N_{Cepheids}	First observation	Last observation	HJD range
1774	143	2010-11-22	2013-09-18	55523.31 - 56554.75

Total

5156	330	33 Cepheids observed with both instruments

Table 2.1: A breakdown of the number of Cepheid (candidate) spectra observed using *CORALIE* and *HERMES*.

to calculate the cross-correlation. Instrument-specific information is provided in the following sections. Some fundamentals of how the pipelines compute radial velocities are briefly explained in Sec. 2.1.4.

The Southern hemisphere: *CORALIE* and the Euler telescope

An instrument description for *CORALIE* was published by Queloz et al. (2001b). Instrumental upgrades were implemented in 2007 and are described in Ségransan et al. (2010). All data in this observing program were obtained post 2007.

While *CORALIE* spectra are cross-correlated by the online reduction pipeline immediately following the observation, all spectra were re-correlated in Geneva. Depending on the star, full widths up to $200\,\mathrm{km\,s^{-1}}$ were employed. At such large widths, it is beneficial to correct for low-frequency trends induced by the blaze function of the spectrograph. A method of doing this is available in the *CORALIE* pipeline, where the normalized CCF of the spectrum is divided by the normalized CCF created from the same numerical mask and a blaze exposure obtained during nightly calibrations.

Two of the three observing modes available on the *CORALIE* spectrograph were used: i) the `OBJO` mode where only the stellar spectrum is dispersed onto the chip; ii) the `OBTH` mode which interlaces a ThAr calibration spectrum between the orders of the stellar spectrum in order to provide simultaneous wavelength-calibration allowing for instantaneous instrumental drift correction. RV drifts are primarily due to atmospheric pressure (and temperature) fluctuations. The `OBTH` mode was mostly used for bright objects with exposure times below approximately 1200 s. The `OBJO` observing mode was used when a possible contamination due to saturated ThAr lines had to be avoided. This was the case for fainter targets with long exposure times and when particularly clean spectra were desired, e.g. to study line profile variations.

Following a discussion with Francesco Pepe, I created a correction for atmospheric pressure variations that was applied to all `OBJO` measurements. This correction is derived and explained in Sec. 2.1.5.

The Northern hemisphere: *HERMES* and the Mercator telescope

An instrumental description of *HERMES* and its pipeline can be found in Raskin et al. (2011), as well as on the Mercator telescope website[2]. Another publication based on the experience of several years of *HERMES* observations was contributed by Raskin & Van Winckel (2013).

Virtually all observations carried out with *HERMES* were done using the `HRF` fiber intended for maximum throughput (efficiency), since this mode yields higher resolving power and allows to observe fainter targets than the other available mode (`LRF`).

RVs are not automatically calculated by the *HERMES* pipeline, although scripts capable of doing so are available as part of the pipeline package. Hence, I installed a version (DRS 3.0) of the pipeline locally and computed radial velocities using the script `hermesVR.py`.

Since *HERMES* is a much younger instrument than *CORALIE*, its long-term stability is not yet that well-known, although Raskin & Van Winckel (2013) figure it at $63\,\mathrm{m\,s^{-1}}$ for HD 164922 (in HRF mode, with wavelength calibrations carried out at the beginning and end of the night). In order to trace long-term variations of the instrument, observations of RV standard stars were requested during every observing run on *HERMES*. The four most stable object observed were HD 221354, HD 168009, HD 144579, and HD 10780. The RV data minus the median value obtained for these standards is shown in the top panel of Fig. 2.1. The lower panel of the same figure shows a histogram of the deviations from the median. Unfortunately, only two objects were observed during more than a single observing run, so the conclusions in terms of long-term stability to

[2] `http://www.mercator.iac.es/instruments/hermes/`

be drawn from this investigation are limited. However, it is worth pointing out that the highest precision achieved is $15\,\mathrm{m\,s^{-1}}$ for the most stable star, which is a factor 4 better than the value given by Raskin & Van Winckel (2013). Furthermore, the dispersion is $\lesssim 22\,\mathrm{m\,s^{-1}}$ for all four stars. The improved precision was enabled by corrections for ambient pressure changes that I applied to the data, cf. Sec. 2.1.5 below. It does appear, however, that there are some long-term trends in the data of the RV standards HD 168009 and HD 144579. More epochs of observations are required to investigate such long-term trends further.

2.1.4 Cross-correlation and radial velocity determination

CORALIE and *HERMES* both employ the cross-correlation technique to derive radial velocities (Baranne et al. 1996; Pepe et al. 2002), where the two-dimensional (per-order) wavelength-calibrated spectra are cross-correlated with a suitable numerical mask. In all applications besides Doppler tomography, a mask resembling a Solar spectral type (hereafter referred to as the G2 mask) was used. The implementation of this technique varies between *CORALIE* and *HERMES* and thus only the basic principles involved are presented here.

The cross-correlation function (CCF), $C(v)$, is computed as follows (this definition from Pepe et al. 2002):

$$\begin{aligned} C(v) &= \int S(\lambda) \cdot M(\lambda_{v_r})\,\mathrm{d}\lambda \\ &= \int S(\lambda) \cdot \sum_i M_i(\lambda_{v_r})\,\mathrm{d}\lambda \\ &= \sum_i \int S(\lambda) \cdot M_i(\lambda_{v_r})\,\mathrm{d}\lambda \\ &= \sum_i C_i(v_r)\,, \end{aligned} \tag{2.1}$$

where

$$\lambda_{v_r} = \lambda \sqrt{\frac{1-\frac{v_r}{c}}{1+\frac{v_r}{c}}}\,. \tag{2.2}$$

Here, $S(\lambda)$ represents the recorded spectrum, $M(\lambda_{v_r})$ the Doppler-shifted numerical mask that can be expressed as a sum of its individual components i, v_r is the radial velocity, and c the speed of light. In their paper, Pepe et al. (2002) introduced a weighting for each line, w_i, intended to utilize the greater RV information carried by spectral lines of higher contrast. This is done simply by computing

$$C^w(v_r) = \sum_i C_i(v_r) \cdot w_i\,. \tag{2.3}$$

All CCFs referred to in the following are such weighted CCFs, $C^w(v_r)$, which shall be abbreviated to read $C(v)$. The CCFs are furthermore constructed to have unity continuum intensity (by dividing the CCF by its maximum value) in order to better resemble their origin in absorption lines.

Since the CCFs of non-pulsating, slowly rotating stars are fairly Gaussian, radial velocity is usually determined by fitting a Gaussian to the CCF. Thus, the following function is fitted to the CCF:

$$f(v) = 1 - C\exp\left(-\frac{(v-v_\mathrm{r})^2}{2\sigma^2}\right), \tag{2.4}$$

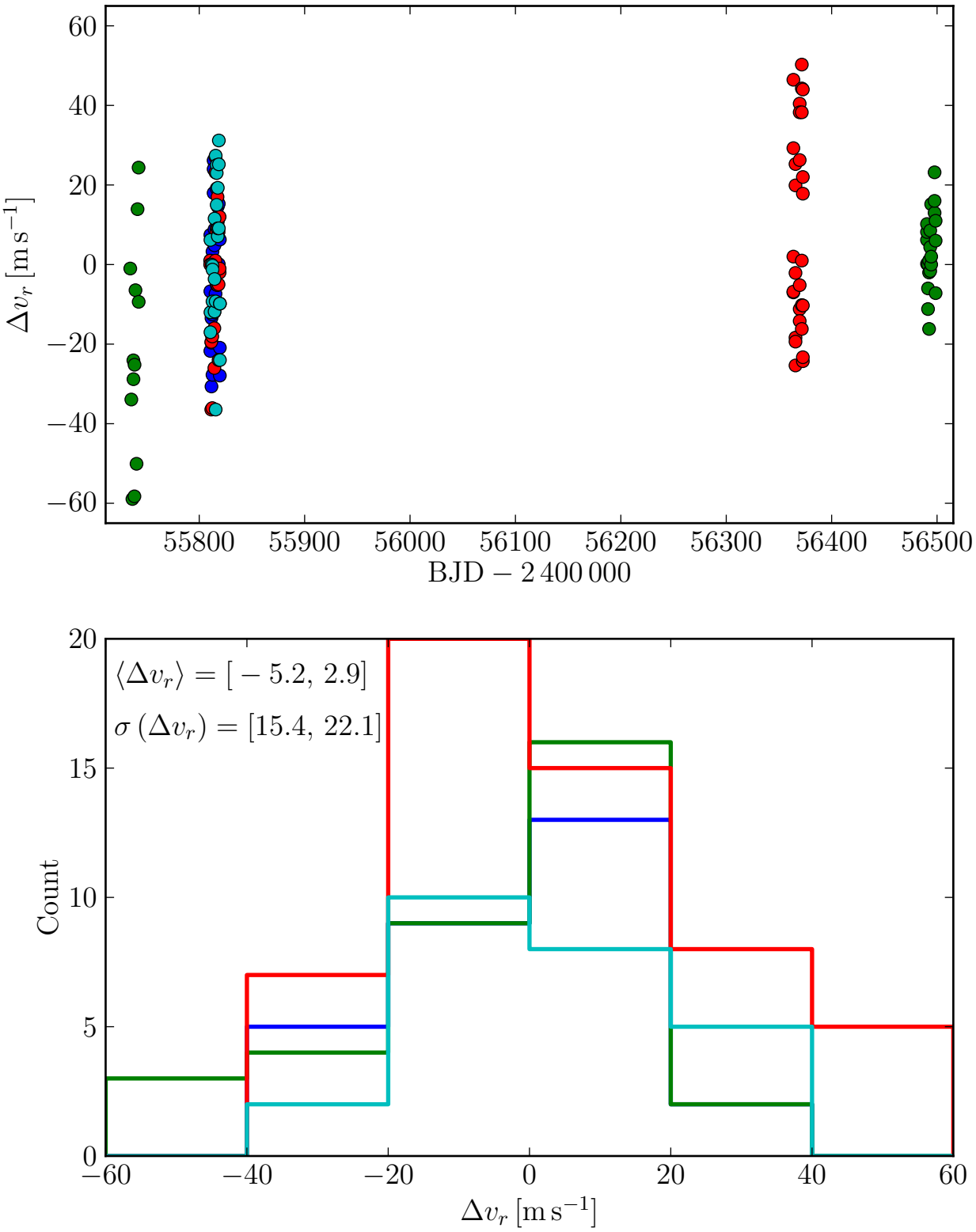

Figure 2.1: Investigating *HERMES* RV stability with standard stars. Standard stars used are HD 221354 (blue), HD 168009 (red), HD 144579 (green), and HD 10780 (cyan). Pressure corrections as described in Sec. 2.1.5 were applied. Each group of data in the top panel corresponds to one observing run of approximately 10 nights. In the lower panel, the ranges of mean and standard deviations for the four stars are given.

where C denotes contrast ($[0.0, 1.0)$), i.e., the amplitude of the Gaussian, and σ is related to the full width at half maximum (FWHM) via:

$$\sigma = \frac{\mathrm{FWHM}}{2\sqrt{2\ln 2}} \approx 0.42466 \cdot \mathrm{FWHM}\,. \tag{2.5}$$

Since the exact value of the correlation peak is more sensitive to noise than the value for C determined by the Gaussian fit, the latter shall be adopted as the measure of CCF contrast. Similarly, the FWHM values discussed in the following are based on the width of the Gaussian that best fits the CCF. Both quantities are readily supplied by the reduction pipelines.

It has to be noted that the shape of Cepheid CCFs can be quite far from Gaussian, since their shapes vary heavily as a function of phase, see Sec. 2.3. Using Gaussians to fit the CCFs may therefore lead to some errors. However, it also results in the highest RV precision, as is shown in Sec. 2.1.6. The strength of using Gaussians to estimate RV lies in the fact that only 3 parameters are fitted to all the points defining the CCF: center position (= RV), contrast, and width. These three parameters are well-constrained even at low S/N (< 20 around $550\,\mathrm{nm}$), since CCFs are calculated using thousands of spectral lines (in the case of the *CORALIE* G2 mask: 3625). This makes the Gaussian technique extremely efficient and allows the determination of very precise Cepheid RVs down to approximately 13^{th} magnitude (limited by the guiding system) on the 1 m class telescopes Euler and Mercator.

Alternatives to using Gaussians exist. For instance, the first moment of the CCF, also sometimes referred to as its centroid, is calculated as the weighted mean of the CCF Burki et al. (1982):

$$v_{\mathrm{centroid}} = \frac{\int C\,(v) \cdot v dv}{\int v dv}\,. \tag{2.6}$$

Other ways to derive RV are to simply take the point where correlation peak is maximal, or to fit a bi-Gaussian to the CCF (e.g. Nardetto et al. 2013; Figueira et al. 2013). Simple Gaussian RVs were used throughout this work following a comparison of several techniques presented in Sec. 2.1.6.

2.1.5 Correcting radial velocity drifts using atmospheric pressure measurements

In spectrographs such as *CORALIE* and *HERMES*, wavelength is calibrated to pixel position on the detector using ThAr lamps whose spectral lines are extremely precisely cataloged. During every night, several calibration exposures were obtained to correct for calibration offsets due to variations in experimental setup. During an ordinary observing night, such variations are the result of ambient pressure and temperature variations. Each intra-night calibration thus provides a new mapping of wavelength onto the detector, obtained for a set of experimental conditions. However, pressure and temperature fluctuate also in between calibration exposures. For the following development, it is my pleasure to acknowledge the help and advice of Francesco Pepe, who pointed out to me the possibility of using measured pressure variations to correct for RV drifts.

The group refractivity of visible and near infrared wavelengths in ambient moist air can be computed (Rüeger 2002, pp. 61) using the following formula[3]:

$$N = (n-1) \times 10^{-6} = \frac{273.15}{1013.25}\frac{N_g P}{T} - \frac{11.27 \times e}{T}\,, \tag{2.7}$$

where T denotes the temperature in Kelvin, $N_g \approx 287.6 \times 10^{-6}$ the group refractivity of standard air (cf. footnote 3), e partial water vapor pressure in [hPa], and P total pressure in [hPa].

[3] as recommended by the International Union of Geodesy and Geophysics during its 22nd General Assembly (IUGG 99), 18 to 30 July 1999, Birmingham, UK, `http://www.gfy.ku.dk/~iag/resolutions/res99.html`

From optics, it is known that wavelength in a medium, λ_n, is related to wavelength in vacuum, λ_0, via the refractive index, n:

$$\lambda_n = \frac{\lambda_0}{n} \propto \frac{1}{n}\,. \tag{2.8}$$

According to Eqs. 2.7 and 2.8, pressure and temperature variations can therefore lead to wavelength shifts on the detector. Let index 1 denote the experimental conditions during the calibration and index 2 those of the observation. Following the wavelength calibration, the wavelength λ_1 has been mapped onto a given set of pixel coordinates (X,Y). However, during exposure 2 a different wavelength λ_2 is observed at (X,Y) due to a change of experimental conditions. In other words, a wavelength shift $\Delta\lambda = \lambda_1 - \lambda_2$ has occurred at pixel coordinates (X,Y). $\Delta\lambda$ corresponds to a drift in radial velocity, since $\Delta\lambda/\lambda = \Delta v/c$ with $c = 299\,792\,458\,\mathrm{m\,s^{-1}}$ referring to the speed of light.

Ambient pressure changes by as much as 2 hPa during a typical observing night, and a rule-of-thumb says that a variation of 1 hPa in pressure corresponds to an RV variation of about $100\,\mathrm{m\,s^{-1}}$ (F. Pepe & S. Udry, priv. comm.). Thus, there is an obvious interest in taking into account pressure fluctuations to ensure maximal precision.

This pixel shift can be corrected to very high precision by feeding light from a ThAr lamp through a second fiber and interlacing its spectrum between the orders of the stellar spectrum. Such a simultaneous wavelength calibration hence provides a measure of $\Delta\lambda$, which is available e.g. in *CORALIE*'s `OBTH` observing mode and provides the extremely precise RVs required for exoplanet searches.

However, in certain cases it may not be desirable to interlace a ThAr spectrum between the orders of the observed target's spectrum. In this case, it is possible to correct for $\Delta\lambda$ approximately using the previous (or following) wavelength calibration and measuring the variation in ambient pressure between the calibration and the science exposures via the values stored in the file headers.

The drift computation is conceptually similar to the drift correction using an interlaced ThAr spectrum: a drift is computed and subtracted from the RV determined by the pipeline. This is done as follows. Since *CORALIE* and *HERMES* are both temperature stabilized, the dominant contribution to $\Delta\lambda$ originates in ambient pressure variations, and temperature is neglected in the following. The wavelength shift due to changes in air refractive index is

$$\Delta\lambda = \lambda_1 - \lambda_2 = \frac{\lambda_0}{n_1} - \frac{\lambda_0}{n_2} = \lambda_0\left(\frac{1}{n_1} - \frac{1}{n_2}\right) = \frac{\Delta v}{c}\cdot\lambda_0\,. \tag{2.9}$$

The resulting Doppler velocity shift can thus be computed by considering only the change in refractive index, since

$$\frac{\Delta\lambda}{\lambda_0} = \frac{\Delta v}{c} = \frac{1}{n_1} - \frac{1}{n_2} = \frac{n_2 - n_1}{n_1 n_2} = \frac{\Delta n}{n_1^2 + n_1\Delta n}\,,\ \text{where} \tag{2.10}$$

$$\begin{aligned}\Delta n &= n_2 - n_1 = N_2 + 1 - N_1 - 1 = N_2 - N_1\\ &= \frac{N_g}{1013.25}\frac{273.15}{T}\,(P_2 - P_1) - \mathcal{O}(10^{-2})\Delta e\,,\\ &\approx 2.7\times 10^{-7}\cdot\Delta P\,,\end{aligned} \tag{2.11}$$

with $\Delta P = P_2 - P_1$, and assuming the change in partial water vapor pressure, $\Delta e = e_2 - e_1$, to be small between the calibration and the observation.

With $n_1 = 1.00028$ (Eq. 2.7 under typical conditions), the radial velocity drift correction is obtained by inserting Eq. 2.11 in Eq. 2.10 and solving for Δv:

$$\begin{aligned}\Delta v &= \frac{\Delta n}{n_1^2 + n_1\Delta n}\cdot c\\ &\approx \frac{2.7\times 10^{-7}\cdot\Delta P}{1.0005 + \mathcal{O}(10^{-4})}\cdot c\\ &\approx 2.7\times 10^{-7}\cdot\Delta P\cdot c\,.\end{aligned} \tag{2.12}$$

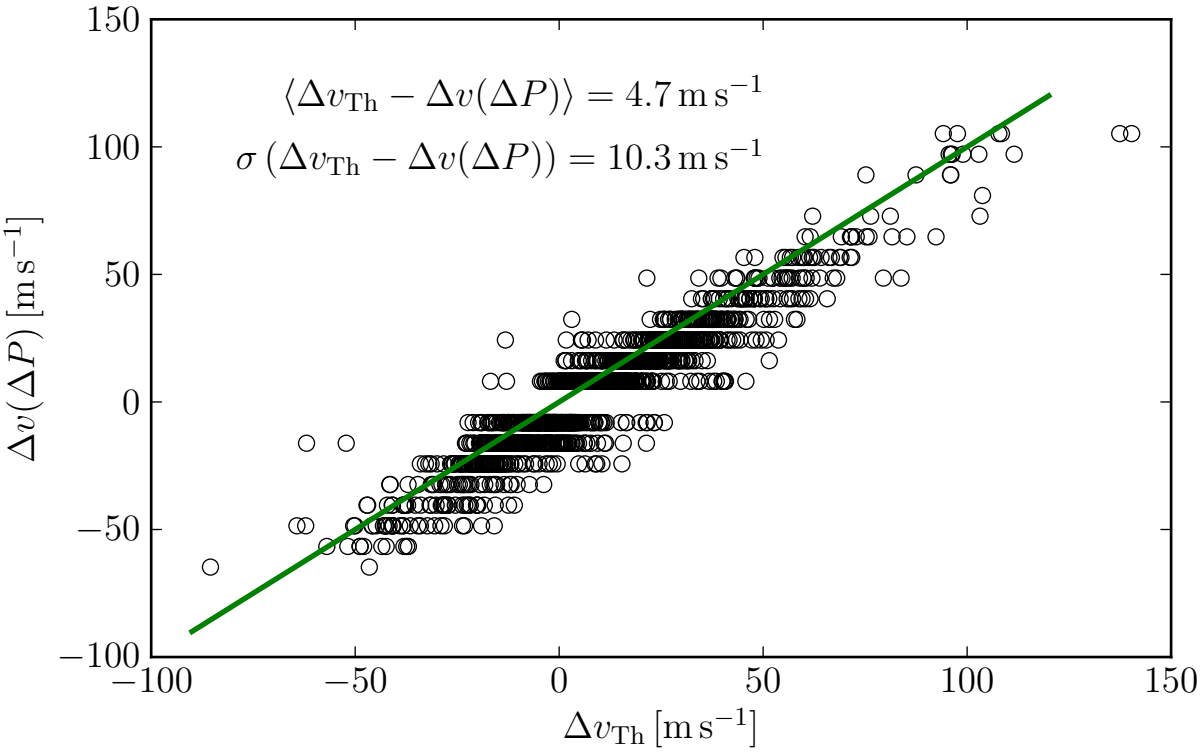

Figure 2.2: RV drift corrections derived from pressure variations (cf. Eq. 2.12), $\Delta v\,(\Delta P)$, against drift corrections determined via simultaneous Th exposures, Δv_{Th}. The discrete values of $\Delta v\,(\Delta P)$ originate from the single-decimal precision with which pressure is recorded in the FITS headers of the spectra. The green line indicates the diagonal where $\Delta v\,(\Delta P) = \Delta v_{\mathrm{Th}}$.

Thus, according to Eq. 2.12, the RV drift due to an increase of 1 hPa in atmospheric pressure corresponds to approximately $81\,\mathrm{m\,s^{-1}}$. These pressure measurement-based drift corrections were calculated for all observations made using *CORALIE* and *HERMES* using the wavelength calibration exposures obtained during the night and information on ambient pressure during the observations (stored in the FITS headers of the spectra). Due to the neglected dependence on temperature, these corrections are only suitable provided the temperature-stabilization worked well[4].

The *CORALIE* reduction pipeline computes the total uncertainty on radial velocity, σ_{RV}, as the squared sum of standard deviations, σ, of different origin:

$$\sigma_{\mathrm{RV}} = \sqrt{\sigma^2_{\mathrm{noise}} + \sigma^2_{\mathrm{Th}} + \sigma^2_{\mathrm{drift\_noise}}}\,, \tag{2.13}$$

Here, σ_{noise} represents photon noise (Bouchy et al. 2001), σ_{Th} the uncertainty on the wavelength calibration, and $\sigma_{\mathrm{drift\_noise}}$ the noise measured on the interlaced thorium spectrum. In the case of `OBJO` measurements, the *CORALIE* pipeline uses a fixed value of $100\,\mathrm{m\,s^{-1}}$ in order to attribute lower weight when these data are being fitted. σ_{noise}, σ_{Th}, and $\sigma_{\mathrm{drift\_noise}}$ are determined from the CCF according to the description by Boisse et al. (2010).

Using the set of measurements taken in `OBTH` mode, i.e., where the drift is corrected using the interlaced ThAr spectrum, it is possible to check how well the approximate pressure correc-

[4]The air conditioning system for *CORALIE* failed during an observing run in March 2012. As a result, large variations (hundreds of $\mathrm{m\,s^{-1}}$) occurred on a timescale of less than an hour. Since temperature variations are neglected here, this approximate formulation cannot fully correct for these issues. Although the extension to include temperature variations is straightforward, further complications such as the expansion of the optical bench due to heating, among others, introduce additional errors unrelated to the refractory index.

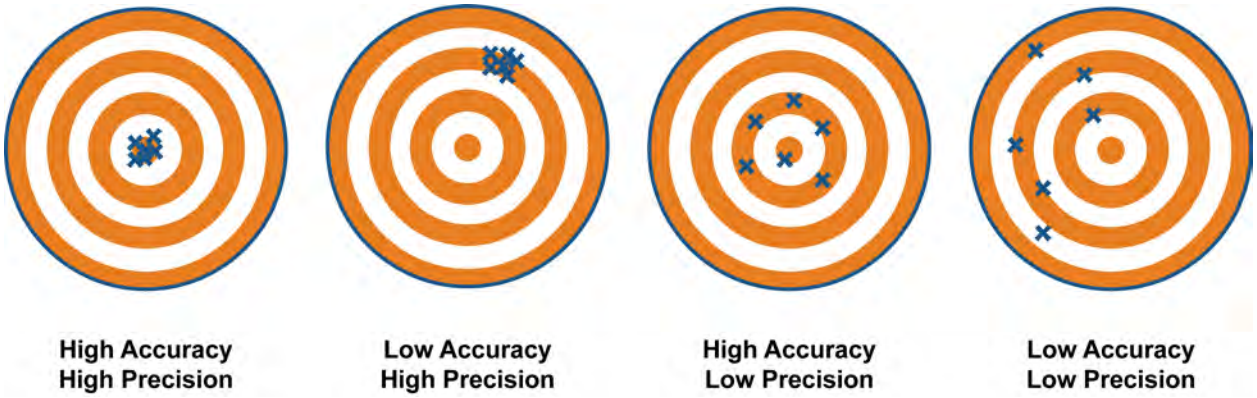

Figure 2.3: A graphical representation of the concepts of precision and accuracy. Image credit: Climatica

tion outlined above actually performs. This comparison is shown in Fig. 2.2, excluding the two observing nights[5] during which *CORALIE*'s air conditions malfunctioned. A total of 1125 measurements are shown in the figure, revealing very good agreement. However, it is evident that the `OBTH` drift correction is systematically larger than the correction predicted by Eq. 2.12 by approximately $4.7\,\mathrm{m\,s^{-1}}$. This difference may be due to a combination of effects, including neglected temperature variations. The root mean scatter of the difference between drifts determined by the two methods is $10.3\,\mathrm{m\,s^{-1}}$. Thus, the constant error budged of $100\,\mathrm{m\,s^{-1}}$ currently added for `OBJO` measurements could be reduced if the technique presented here were implemented in the pipeline. Given the huge number of `OBTH` observations in the *CORALIE* database, this relationship could be extremely well calibrated. Such a procedure would significantly improve the uncertainty estimate for faint targets with very long exposures where the `OBTH` mode cannot be used due to the danger of contamination by the interlaced Th spectrum.

The above formulation was also applied to *HERMES* spectra, since the two spectrographs are sufficiently similar in design and since the formulation of the drift computation using pressure differences is based on general optics and not directly related to the instrumental properties. As shown in Sec. 2.1.3 above, this correction enables an improvement in precision by a factor of four.

2.1.6 On precision and accuracy of Cepheid radial velocities

Precision and accuracy are two different concepts. Yet, they are often confounded. Precision refers to the spread or intrinsic closeness of measurements, while accuracy refers to how well measurements reproduce the 'true' value. A useful graphic comparison is shown in Fig. 2.3[6].

Precision is also often referred to as the internal error, and derived as the standard deviation of a series of measurements. Accuracy, also referred to as the external error, is much more difficult to determine. The field of radial velocities is no exception here. Instruments such as *HARPS* (Pepe et al. 2000) or *HIRES* (Vogt et al. 1994) are built to measure radial velocity at extreme precision (in the case of *HARPS* at the sub-$\mathrm{m\,s^{-1}}$ level), limited nowadays by stellar activity (see e.g. the discovery of an Earth-mass planetary companion to α Cen B by Dumusque et al. 2012). Accuracy, although high, is not particularly relevant to detect the orbital signature of a companion. Furthermore, accuracy is limited by other issues, such as gravitational redshifts or convection (Lindegren et al. 1999) as well as the calibration of the Solar spectral atlas (Gullberg & Lindegren 2002), which ultimately provides the zero-point of the absolute scale and thus defines its minimum accuracy ($\sim 100\,\mathrm{m\,s^{-1}}$).

[5] March 29 and 30 of 2012

[6] Figure taken from `http://climatica.org.uk/climate-science-information/uncertainty`

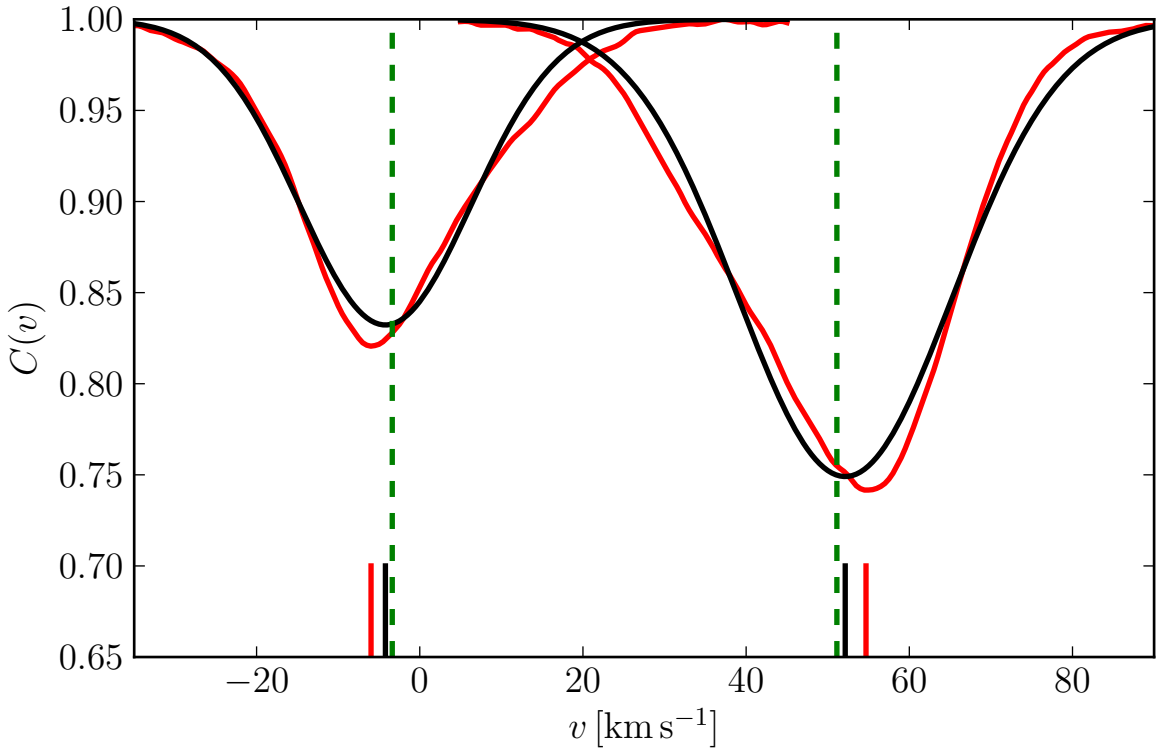

Figure 2.4: Dependence of RV amplitudes on the method employed to derive RV. Black solid curve: fitted Gaussian. Red solid curve: CCF. Ticks at bottom of the figure: point where CCF contrast is maximal (red), center position of Gaussian (black), CCF centroid (green dashed vertical line). The peak-to-peak amplitude of the CCF maximal-contrast RVs is 6.17 $\mathrm{km\,s^{-1}}$larger than that of the centroid RVs, i.e, $\sim 10\%$ larger.

In the case of the radially pulsating Cepheids, the situation is even more complex due to the dynamical structure (velocity gradients) in a Cepheid's atmosphere where the RV is measured. While convection causes signals in the order of ten $\mathrm{m\,s^{-1}}$ in late-type dwarfs, the difference between spectral lines formed at different heights in the atmosphere can vary by many $\mathrm{km\,s^{-1}}$ (e.g. Grenfell & Wallerstein 1969; Petterson et al. 2005) and see Sec. 2.8 on Doppler tomography below.

As mentioned briefly in Sec. 2.1.4, the systemic velocity, v_γ, derived for a (single, non-binary) Cepheid can be biased by the method applied to derive the individual RV points from CCFs. This bias can be avoided, if necessary (e.g. when studying the Galactic rotation curve), by deriving RVs based on the CCF centroid (Burki et al. 1982), or fitting bi-Gaussians Nardetto et al. (2013) to it. However, a small bias in the order of $1\,\mathrm{km\,s^{-1}}$ in v_γ was acceptable, and high precision was desired for low-S/N CCFs. Therefore, all radial velocities were derived using the Gaussian method, which shown below to yield highly precise velocities, even for relatively low-S/N data. The following thus presents a brief discourse on how the method of deriving RV for Cepheids is related to accuracy and precision.

Accuracy A well-known problem of Cepheid RVs is encountered when investigating the (axisymmetrical) Galactic rotation curve using Cepheids whose systemic velocities v_γ are determined using Gaussian RVs. This issue is known as the k-term problem (Joy 1939) and results in an apparent heliocentric motion of Cepheids in the Galaxy in the order of $\sim 1\,\mathrm{km\,s^{-1}}$ (Nardetto et al. 2008). The origin of the problem appears to lie in the fact that CCFs are intrinsically asymmetric, and that the degree of asymmetry is not identical on both sides of the systemic velocity v_γ. To be more

specific, CCFs become more asymmetric during expansion (RV $< v_\gamma$) than during contraction (RV $> v_\gamma$). Gaussians fitted to these asymmetric CCFs therefore lead to v_γ values that are systematically lower than they should be, resulting in a false apparent motion of Cepheids towards the Sun.

Figure 2.4 illustrates this problem (see also Nardetto et al. 2006). CCFs of RZ Vel during two phase points of maximum asymmetry (fastest expansion and contraction) are drawn as a red solid lines, and the Gaussians fitted to the CCFs are drawn as black smooth curves. Below the CCFs, Gaussian RVs and RVs derived using the CCF points of maximal contrast are indicated by black and red line segments, respectively. The CCF centroid RVs are shown by dashed green vertical lines. RZ Vel was chosen for this graph, since it exhibits particularly strong line asymmetry due to its high pulsational amplitude.

Figure 2.4 furthermore illustrates that pulsation amplitudes (in $\mathrm{km\,s^{-1}}$) also depend on the method applied, i.e., the method applied can bias the result. In fact, RV amplitudes based on CCF centroid RVs are systematically smaller than amplitudes determined using the Gaussian method. This effect is in the order of up to a few $\mathrm{km\,s^{-1}}$, and non-negligible when observed pulsation amplitudes are compared with the output of pulsation models.

Since the k-term problem seems to disappear when line asymmetry is accounted for in the determination of v_γ (Nardetto et al. 2008), it might be argued that non-Gaussian methods can provide more accurate RVs. However, this does not automatically make these RV estimates the most precise.

Precision Above, it is argued that Gaussian RVs may be biased, leading to inaccurate estimates of v_γ and overestimated pulsation amplitudes. However, as Fig. 2.5 illustrates, these biased (inaccurate) RV estimates can be very precise. Precision is more important than accuracy for certain applications, including e.g. the determination of orbital parameters (of exoplanets as well as for spectroscopic binary Cepheids).

On 22 June 2011 during an observing run at Euler I observed the bright long-period ($\langle m_\mathrm{V} \rangle = 7.16$ mag, $P \sim 20.4$ d) Cepheid RZ Vel to investigate the precision of Cepheid RV measurements. Within 45 min, 15 consecutive measurements were made around the phase point of maximum expansion velocity, i.e, where the overall acceleration is near zero. This phase point is particularly suitable to investigate precision, since the RV curve is flat and therefore no trend is expected during this short time. RZ Vel was a very good candidate for this due to its brightness (short exposures = many measurements) and long period (negligible RV variation during these 45 minutes).

Figure 2.5 shows the data obtained during these 45 minutes, with median RV subtracted. Red symbols indicate the velocity corresponding to the central dip of the CCF, black symbols the Gaussian method, and green symbols indicate the centroid RVs. The large errorbars represent the RMS of the central-dip and centroid velocities. Obviously, the Gaussian RVs are by far the most precise exhibiting minimal dispersion around the average. Centroid RVs are slightly less precise. Since the centroid technique weights every point along the CCF by its contrast, it is more sensitive to noise than the Gaussian method, leading to lower precision in these low S/N spectra ($\sim 25 - 30$). For the same reason, the mimimum-CCF-point method is easily discarded as very imprecise.

Figure 2.5 furthermore demonstrates the adequacy of the uncertainty estimates computed by the pipeline: the RMS for the Gaussian RVs is $38\,\mathrm{m\,s^{-1}}$ which is even slightly better than the average uncertainty estimated by the pipeline ($43\,\mathrm{m\,s^{-1}}$). For comparison, the RMS of centroid RVs in this case is $138\,\mathrm{m\,s^{-1}}$, and $544\,\mathrm{m\,s^{-1}}$ for the CCF-minimum RVs.

Hence, it can be concluded that the Gaussian method yields the highest precision and makes full use of *CORALIE*'s instrumental stability.

Precision vs. accuracy Depending on the aims of an investigation, one may want to choose between using Gaussian or centroids RVs, or other ways to derive the RV, e.g. using the bi-Gaussian

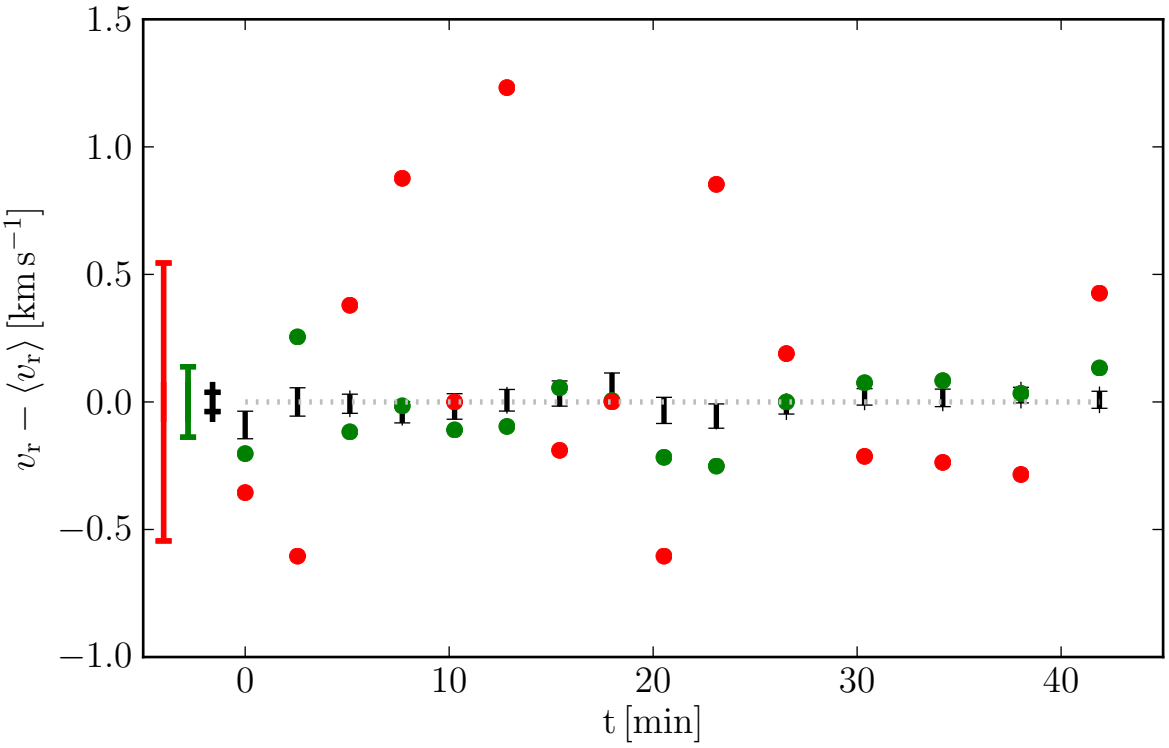

Figure 2.5: 15 observations of RZ Velorum obtained during 45 minutes around the phase corresponding to maximum expansion velocity. Errorbars at $t < 0$ indicate the RMS of the symbols of corresponding color. Black errorbars represent Gaussian RV estimates with errors from the pipeline. Green circles represent centroid RVs, and red points indicate the velocity of the central dip of the CCF. All values shown relative to their median. Gaussian RVs are clearly the most precise.

method. It is, however, very important to distinguish the methods from one another and clearly state how RVs were estimated in order to avoid a mixture of systematic effects in an observational sample.

During my thesis, I mainly focused on determining systemic velocities to an accuracy of approximately $1\,\mathrm{km\,s^{-1}}$ as membership constraints, and was furthermore interested in searching for binaries. Thus, I was mainly interested in having the utmost precision for low-S/N data, and could accept to incur small offsets in pulsation amplitudes or v_γ of Cepheids. Therefore, Gaussian RVs were used throughout my work. For maximal usability of the dataset, however, I plan to make the CCFs publicly available in conjunction with an article describing the data sets.

2.1.7 Comparison of this data set with literature data

There exists a long history of Cepheid RV measurements, opening up the possibility to study very long-term orbital periods for spectroscopic binaries among Cepheids, see for instance Groenewegen (2008) who could determine an orbital period of nearly 90 years for T Mon. A significant fraction of these measurements are included in the McMaster Cepheid database[7], and a multitude of catalogs can be obtained via the Centre de Données de Strasbourg (CDS). Probably the largest homogeneous sample of Cepheid radial velocities was published by Gorynya et al. (1992, 1996, 1998, 2002), spanning the years 1992-1998 and containing 5 905 measurements of 126 Cepheids.

[7] maintained by Doug Welch `http://crocus.physics.mcmaster.ca/Cepheid/`

These data are precise at the $\mathrm{km\,s^{-1}}$ level and are very useful to search for signs of binarity.

The probably most precise RVs published for Cepheids were obtained using *HARPS*, the famous Geneva-built planet hunting instrument which is fiber-fed by ESO's $3.6\,\mathrm{m}$ telescope at La Silla Observatory, Chile. Several studies have published data with *HARPS* among which are notably Nardetto et al. (2006, 2009); Pietrzyński et al. (2010). It should be noted, however, in the case of *CORALIE*, precision is limited by stellar features (such as asymmetry), not by the instrument. The precision of *HARPS*, although an order of magnitude better than *CORALIE*, will therefore probably not improve precision for Cepheids by the same amount, though the higher resolution should provide some benefits.

As part of the observing program described in this chapter, a total of 5156 Cepheid RVs were determined for 330 Cepheid candidates (cf. Sec. 2.4), making the combined *CORALIE* and *HERMES* sample one of the largest in the literature, cf. Tab. 2.1. These statistics render this dataset unprecedented in its combination of precision and size. Although the typical baseline is not very long compared to the timescale of orbital periods of classical Cepheids, these data were instrumental in discovering the spectroscopic binary nature among more than a dozen Cepheids. These data were used for several other projects as part of this thesis. Besides the ones mentioned in this chapter, they were used in the publication on Cepheids in open clusters (Sec. 3), and have been compared to model predictions of projected rotational velocities of Cepheids (Sec. 4). I plan to publish the *CORALIE* and *HERMES* Cepheid datasets in 2014.

2.2 Discovering the spectroscopic binary nature of classical Cepheids

Many Cepheids are part of star systems composed of multiple stars. According to L. Szabados' online database of Galactic binary Cepheids[8], 164 Cepheids are currently known in binary or triple (10) systems[9], and the binary fraction among Cepheids can be estimated to be $\sim 60\%$ (Szabados 2003). Of these 164, orbital solutions are listed for 28, i.e. for only 17% of known cases. 21 Cepheids are listed as part of visual binary systems. The orbital solutions listed clearly indicate the absence of short-period binaries among Cepheids, which is readily explained by their (super-)giant nature that places strong constraints on possible orbital configurations. In fact, the shortest orbital periods listed (ignoring the type II Cepheid TX Del) are approximately $382\,\mathrm{d}$ (Z Lac), $407\,\mathrm{d}$ (SU Cas), $440\,\mathrm{d}$ (MW Cyg), $505\,\mathrm{d}$ (S Mus), and $549\,\mathrm{d}$ (SU Cyg), and only 11 binary Cepheids have known orbital periods shorter than 2 years. T Mon wins the prize for longest known orbital period at $32449\,\mathrm{d}$ (Groenewegen 2008), i.e., nearly 90 years!

It is truly remarkable that nowadays such long orbital periods (for a limited number of objects) can be investigated using measurements dating back many decades. Determining orbital solutions for binary Cepheids is thus clearly an observationally expensive long-term endeavor, since most Cepheids with unknown orbital parameters are fainter than 10^{th} magnitude, requiring long exposure times in addition to a regular follow-up. Hence, Szabados et al. (2013a, see Sec. 2.10) point out that there is strong observational bias against not only the determination of orbital solutions, but also against the general detection of binarity among Cepheids. Within the past 20 years many new binaries among Cepheids have been identified, and it does appear that the binary fraction among them may be as high as 60% for Cepheids brighter than 8^{th} magnitude in V-band (57 binaries in this sample).

The vast majority of Cepheids known to belong to multiple star systems (from hereon for simplicity: binary Cepheids) are single-lined spectroscopic binaries (SB1) and their nature as binaries was discovered from RV measurements obtained over very long (years to decades) baselines. Owing to the high quality RV curves obtained as part of this Cepheid RV observing program, I was able to contribute to the effort of identifying spectroscopic binaries among Cepheids.

[8] `http://www.konkoly.hu/CEP/nagytab3.html`

[9] the two Cepheid components of the visual binary CE Cas A&B are counted twice herein

Following some context on the importance of Cepheid binarity in Sec. 2.2.1, this section presents two selected highlights of newly-discovered spectroscopic binaries with resolved (short) orbital periods within this program in Sec. 2.2.2, followed by a brief account of my contribution to a collaboration with L. Szabados and collaborators in Sec. 2.2.3. The two articles resulting from this collaboration (Szabados et al. 2013b,a) are included at the end of this chapter in Secs. 2.9 and 2.10.

2.2.1 Relevance of identifying binaries among Cepheids

There are at least three good reasons to study binary Cepheids.

For one, determining orbits of Cepheid binaries can provide mass estimates, which are badly needed in the context of the Cepheid mass discrepancy (cf. Sec. 1.3.4). Thus far, nearly all spectroscopic Cepheid binaries are SB1s[10]. Thus, the mass-related quantity obtained from an orbital solution to the primary's RV curve is the mass function, $f(m)$. Using eccentricity, e, semi-amplitude K of the primary (Cepheid) component, and orbital period, $P_{\rm orb}$, $f(m)$ is readily calculated. In the notation of Hilditch (2001, p. 46):

$$f(m) = \frac{m_2^2 \sin^3 i}{(m_1 + m_2)^2} = (1.0361 \times 10^{-7})(1 - e^2)^{3/2} K_1^3 P_{\rm orb} \quad [M_\odot] \,. \tag{2.14}$$

Two further elements are thus required in order to obtain the absolute mass of the Cepheid, m_1: an estimate of the secondary's mass, m_2, and the inclination of the orbital plane with respect to the observer, i.

Model-independent masses have been determined for only a handful of Cepheids (6 listed in Evans et al. 2011; Neilson et al. 2013). However, many different ways of determining Cepheid masses have been explored in the literature, owing to the importance of mass estimates for stellar evolution. A particularly interesting method is related to the determination of a Cepheid companion's spectral type using UV spectroscopy, exploiting the different spectral energy distributions of hot early-type MS stars and the cool evolved Cepheids. A companion mass estimate can be inferred using the spectral type estimate for the companion obtained in the UV, e.g. from International Ultraviolet Explorer (IUE) or Hubble Space Telescope (HST) observations (e.g. Evans & Bolton 1990). Recently, Evans et al. (2013) studied space-based UV spectra for the complete sample of 76 Cepheids brighter than $8^{\rm th}$ magnitude, in which they find companions with spectral types down to A2V, i.e., with $m_2 \gtrsim 2\,M_\odot$. The companion mass can then be inferred from evolutionary models using a mass-luminosity relationship for the ZAMS, leaving inclination unknown, unless orbital solutions for both components are known.

It may also be possible to detect an early-type companion in the blue part of the spectrum from ground-based observations, provided the S/N achieved is sufficiently high to compensate for the high contrast between Cepheid and companion. If companions can be detected in this way, then it is possible to determine the lower mass limits for both components (indices 1 and 2 for primary and secondary) via (Hilditch 2001, p. 46):

$$m_{1,2} \sin^3 i = (1.0361 \times 10^{-7})(1 - e^2)^{3/2} (K_1 + K_2)^2 K_{2,1} P_{\rm orb} \quad [M_\odot] \,, \tag{2.15}$$

since both semiamplitudes K_1 and K_2 can be measured in an SB2 (note the order of indices in Eq. 2.15). If the orbit can be resolved interferometrically, then absolute mass becomes accessible (Gallenne et al. 2013b).

Second, binarity has implications for stellar evolution. As mentioned above, orbital periods of Cepheids are very long, virtually never shorter than a year. However, the progenitors of Cepheids are B-type stars on the MS, and Huang et al. (2010) found that approximately 20% of MS B-type

[10] All of those known in the Galaxy are SB1s. However, there are two prominent examples of double-lined spectroscopic binary Cepheids in the LMC: OGLE-LMC-CEP-0227 (Pietrzyński et al. 2010) and OGLE-LMC-CEP-1812 (Pietrzyński et al. 2011).

stars are binaries with orbital periods $< 14\,\mathrm{d}$, and Sana & Evans (2011) find a binary fraction among OB stars of $\sim 44\%$ (which is similar to the estimate for solar-like stars by Duquennoy & Mayor 1991). Clearly, such short-period orbital configurations are not found among Cepheids. It is therefore very puzzling how the binary fraction among Cepheids can be so high ($\sim 60\%$). Possible ways of reconciling this problem may include Roche-lobe overflow during the crossing of the Hertzsprung gap which may modify the orbital configuration due to conservation of total angular momentum, or perhaps the destruction of the primary star due to a merger event. Given the high binary fraction among Cepheids, the first scenario seems more likely. Further investigations into binary fractions, distribution of orbital periods, and mass ratios of Cepheid such as that by Evans et al. (2013) are required to find answers to this apparent paradox.

Last, but not least, unseen companions contribute parasitic flux to the light interpreted as being emitted by the Cepheid alone. Thus, companions cause offset from (the single-Cepheid) and scatter in the (observed) PLR, complicating its calibration. Discovering binaries among Cepheids can help to mitigate this effect on the PLR by improving the understanding of the stars involved in its calibration. As an extreme case, one can mention here the eclipsing binary Cepheid OGLE-LMC-CEP-0227 for which the in- and out-of eclipse difference is almost 1 magnitude in I-band (Pietrzyński et al. 2010).

2.2.2 Newly-discovered binary Cepheids: highlights

Using the *CORALIE* and *HERMES* datasets, I was able to discover the spectroscopic binary nature of 7 classical Cepheids (6 with *CORALIE*, 1 with *HERMES*) in addition to co-enabling the same discovery for 4 out of 9 new SB1 Cepheids presented by Szabados et al. (2013b,a). The following shows two as-of-yet unpublished Cepheids for which the measurements can resolve (or at least constrain) the orbital period. In both cases, the data were fitted by the sum of a Fourier series (for the pulsation) and a Keplerian (for the orbital motion).

The RV curve due to pulsation can be described by a Fourier series, $F(\phi)_n$, as follows:

$$F(\phi)_n = v_\gamma + \sum_n a_n \sin(2n\pi\phi) + b_n \cos(2n\pi\phi) \tag{2.16}$$

where ϕ denotes pulsation phase (computed using ephemerides determined for Anderson et al. 2013a), n is the index of the harmonic, and a_n and b_n are constants to be determined. An F-test stop criterion was used to determine the optimal number of harmonics to be fitted: n is increased until the F-test probability for spurious improvement exceeds 0.0027, corresponding to a $3\,\sigma$ confidence level.

The Keplerian model fitted can be written as (Hilditch 2001):

$$u(t) = K\left[\cos(\omega + \theta) + e\cos\omega\right] + v_\gamma, \tag{2.17}$$

where v_γ denotes systemic velocity as in Eq. 2.16, ω argument of periastron, e eccentricity, and θ true anomaly. Semi-amplitude K is related to projected semimajor axis, $a\sin i$, and orbital period, P_{orb}, by

$$K = \frac{2\pi a \sin i}{P_{\mathrm{orb}}\sqrt{1-e^2}}\,. \tag{2.18}$$

The RV time series here describe the variation of $\theta = \theta(t)$ as a function of time.

Fitting the Keplerian model is a non-linear process and depends highly on the starting conditions. Since the orbital period for both cases presented here can be estimated from the RV data alone by eye, a good starting value can be provided in this case. A non-linear least squares fitting algorithm[11] is then used to find a satisfactory best fit solution.

[11] I used the `SciPy` implementation (`scipy.optimize.leastsq`) of the Levenberg-Marquardt algorithm

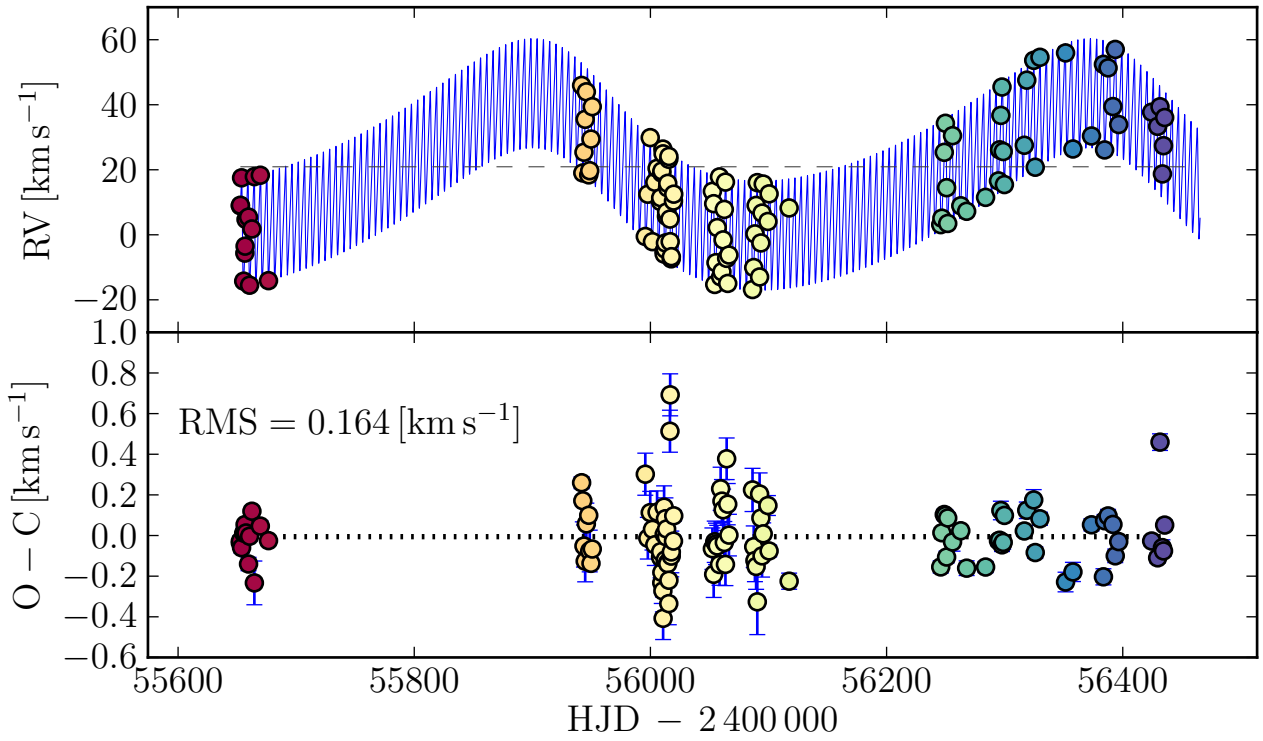

Figure 2.6: *CORALIE* RVs of FN Velorum as a function of observation date (top panel). The blue solid line represents the combined fit for pulsation and orbital motion. The lower panel shows the fit residuals. Note the larger error bars of *OBJO* measurements, and the two outliers (yellow, $O - C \sim 0.6\,\mathrm{km\,s^{-1}}$) that were observed during a night when the air conditioning system of *CORALIE* failed.

The publication of these and the other targets is currently in preparation, awaiting some more observational data to fully resolve the orbital period in some cases where this will soon be possible. Let us now have a look at the orbital solutions obtained for FN Velorum with *CORALIE* and MU Cephei with *HERMES* data.

A new Southern binary Cepheid: FN Velorum

FN Vel = HIP 48122 = 2MASS J09484148-5531104 = ASAS J094841-5531.2 was discovered to be a Cepheid by O'Connell (1951). It has been investigated (also spectroscopically) in several studies, albeit without being identified as a binary. Luck & Lambert (2011) report $T_{\mathrm{eff}} = 5809\,\mathrm{K}$, $\log g = 1.9$, and slightly super-solar iron abundance of $[\mathrm{Fe/H}] = 0.06$. FN Vel has an average magnitude of 10.3 in V-band, and a fixed exposure time of 16 min was chosen in order to yield good results regardless of pulsation phase, aiming for a typical S/N $\sim$ 30 with *CORALIE*. Observations were carried out in both observing modes according to the above description.

Figure 2.6 shows the *CORALIE* data obtained for FN Vel and immediately identifies this Cepheid as a spectroscopic binary. The baseline of our observations is 782.7 d. Both the pulsation and the orbit are very well-sampled.

Using a Fourier series with 8 harmonics and a Keplerian, 22 free parameters are fitted to 112 data points. The orbital solution is provided in Tab. 2.2. This solution places FN Vel 4^{th} among the shortest orbital periods known for Cepheids (471.6 d), and illustrates the high precision with which spectroscopic orbits of classical Cepheids can be determined using *CORALIE* data.

The top panel in Fig. 2.6 shows barycentric RV as filled circles plotted against heliocentric ob-

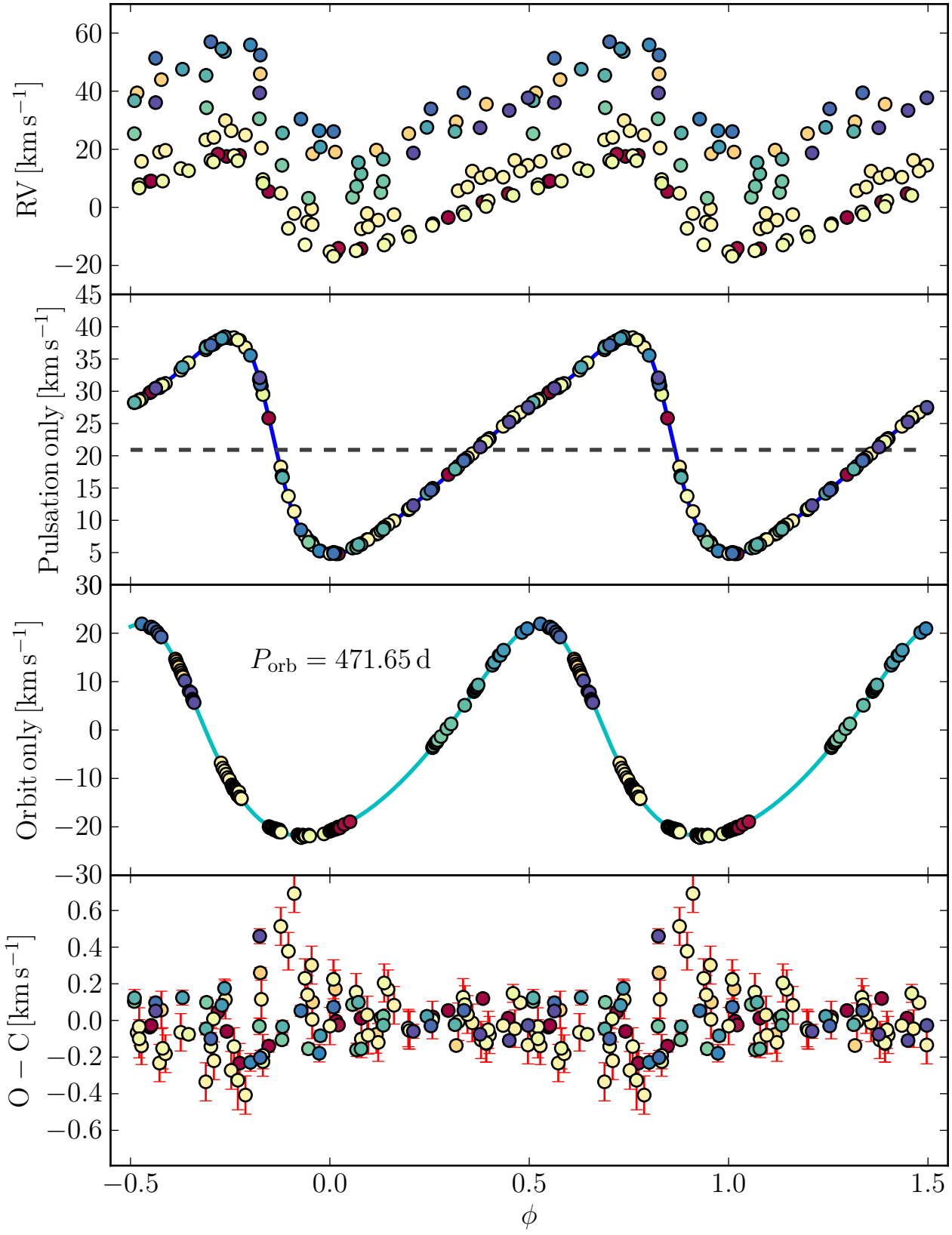

Figure 2.7: Phased *CORALIE* data for FN Velorum. The color coding corresponds to the one in Fig. 2.6. Panels from top to bottom: all RV data phased with the pulsation period of 5.32415 d; RV data phased with pulsation period, orbital solution subtracted; RV data as function of orbital phase ($P_{\rm orb} = 471.65$ d) with pulsation subtracted; residuals as function of pulsation phase.

Parameter	Value	units
Period	471.654 ± 0.130	[d]
e	0.2175 ± 0.0008	
v_γ	20.919 ± 0.026	[$\mathrm{km\,s^{-1}}$]
K	21.899 ± 0.081	[$\mathrm{km\,s^{-1}}$]
T_0	2455936.31 ± 1.746	[d]
ω	265.6 ± 1.33	[deg]
$a \sin i$	0.927 ± 0.53	[AU]
f_{mass}	0.477 ± 0.327	[$M_\odot$]

Table 2.2: Orbital parameters determined for FN Velorum

servation date, color-coded to indicate observation date and with the fit solution overplotted in solid blue. The bottom panel of the same figure shows the residuals of the fit against observation date, revealing impressive agreement. Note that observations of FN Vel were carried out in both observing modes. As mentioned in Sec. 2.1.5, the total uncertainty σ_{RV} computed by the pipeline is larger for the `OBJO` observing mode; hence the difference between large and small errorbars. The outliers around HJD $2\,456\,000$ were observed during nights when the air conditioning system of *CORALIE* failed.

Figure 2.7 uses the same color-coding to indicate data from different epochs. The panels from top to bottom show the following, each phase-folded with the appropriate period: barycentric RV as a function of pulsation phase ($P = 5.32415\,\mathrm{d}$); observed and fitted RV curves with orbital solution subtracted, i.e., the RV variation solely due to pulsation; the orbital motion with the pulsational RV signal removed; the fit residuals as a function of pulsation phase. The root mean square of $164\,\mathrm{ms^{-1}}$ underlines the remarkable agreement.

A new Northern binary Cepheid: MU Cephei

Cepheids in the Northern hemisphere have a much longer history of observations than those in the Southern hemisphere. As a result, one is nowadays much more likely to discover new binaries among Cepheids in the Southern hemisphere, rather than in the Northern. The situation is more favorable for fainter Cepheids, although these are observationally more expensive.

Using *HERMES* data, I was able to discover the spectroscopic binarity of MU Cep, i.e., 2MASS J22233861+5740508. Note that the comparatively faint Cepheid MU Cep ($\langle m_V \rangle = 12.3\,\mathrm{mag}$) is not to be confused with the very bright, bow shock-producing red supergiant μ Cep (Cox et al. 2012).

Figures 2.8 and 2.9 show the *HERMES* data observed and fit solution in the same was as presented above for FN Vel.

Using the approach outlined above, the combination of a Fourier series with 7 harmonics and a Keplerian were fitted to 57 data points. The observational baseline is shorter than the orbital period, which shows in the large uncertainties derived for the orbital solution presented in Tab. 2.3. Additional observations are required to improve this preliminary orbital estimate.

2.2.3 Binary Cepheid nature discovered in collaboration

As the above sections demonstrate, *CORALIE* and *HERMES* data are very well suited for discovering the spectroscopic binarity of Cepheids. Although this can be achieved from the present datasets alone in some cases, orbital periods for Cepheids tend to be very long and combining RVs from many different sources may be necessary to achieve this goal. During a meeting of the *Gaia* Coordination Unit 7 (CU7) in Geneva in December 2012, Laszlo Szabados and I started to collaborate on a number of Southern Cepheids he and his collaborators had been observing from Siding Springs observatory in Australia and using FEROS, the high-resolution spectrograph at the

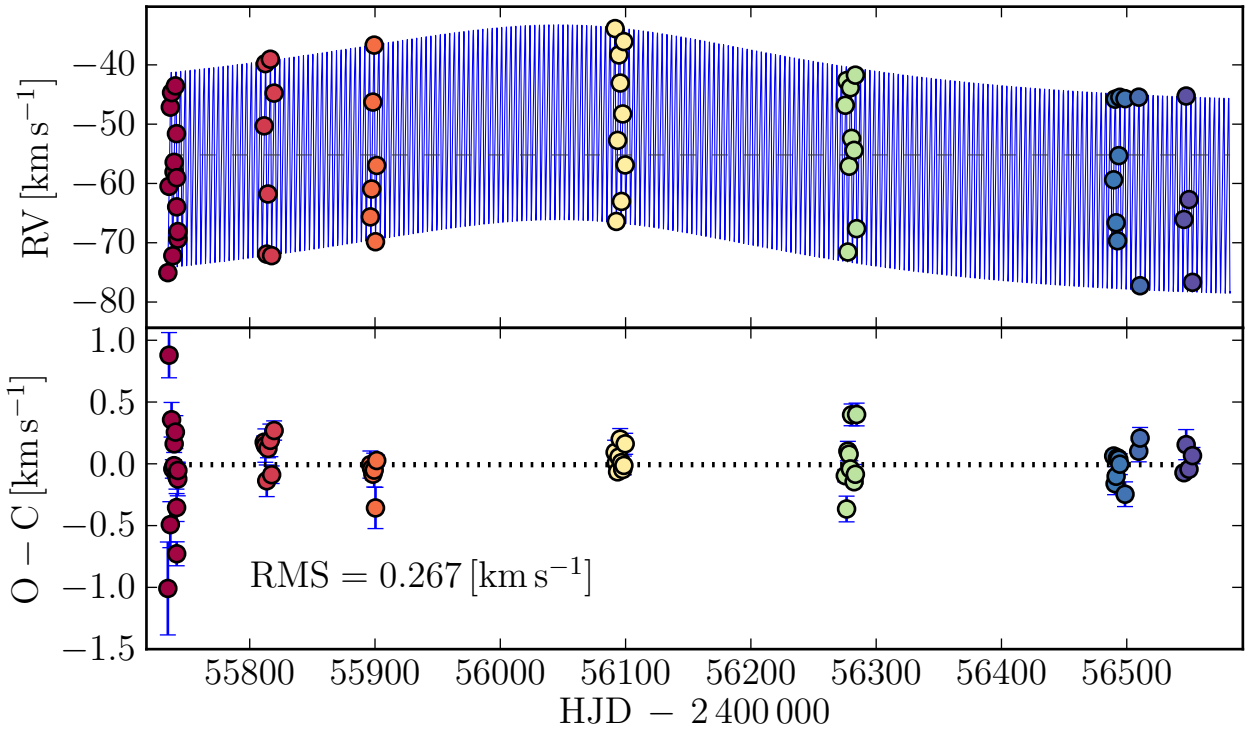

Figure 2.8: *HERMES* RVs of MU Cephei as a function of observation date (top panel). The blue solid line represents the combined fit for pulsation and orbital motion. The lower panel shows the fit residuals. Note the larger scatter of the earliest (red) measurements. The observational baseline is shorter than the orbital period.

Parameter	Value	units
Period	1522.1 ± 350.4	[d]
e	0.3245 ± 0.0889	
v_γ	-55.191 ± 0.359	[km s^{-1}]
K	6.443 ± 0.536	[km s^{-1}]
T_0	2457590.66 ± 121.77	[d]
ω	68.8 ± 24.05	[deg]
$a \sin i$	0.853 ± 0.935	[AU]
$f_{\rm mass}$	0.036 ± 0.040	[$M_\odot$]

Table 2.3: Orbital parameters determined for MU Cephei

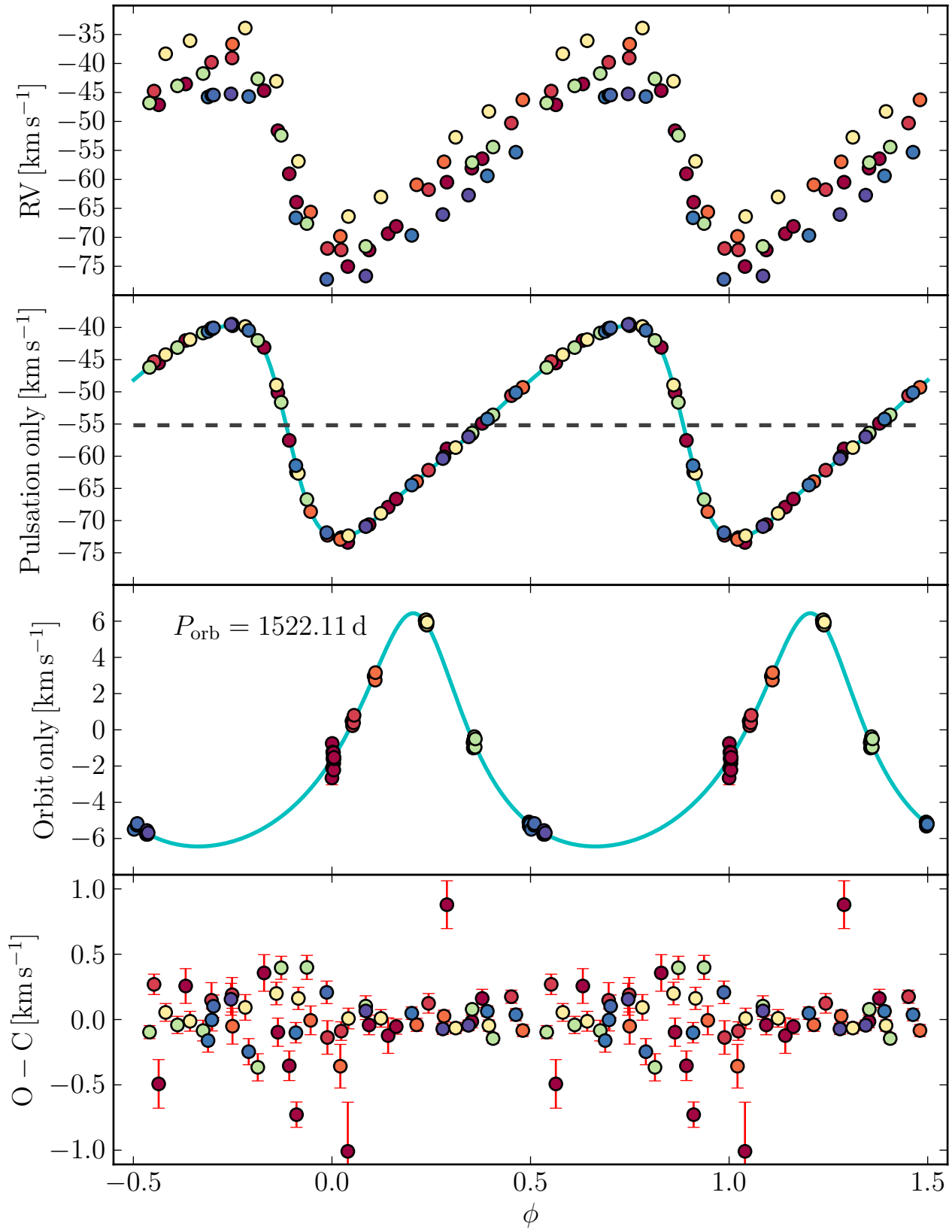

Figure 2.9: Phased *HERMES* data for MU Cephei. The color coding corresponds to the one in Fig. 2.8. Panels from top to bottom: all RV data phased with the pulsation period of 3.76787 d; RV data phased with pulsation period, orbital solution subtracted; RV data as function of orbital phase ($P_{\rm orb} = 1522.11$ d) with pulsation subtracted; residuals as function of pulsation phase.

ESO-MPG 2.2m telescope at La Silla. This was a great opportunity to share data and gain from his extensive experience. The ensuing collaboration resulted in two publications so far (Szabados et al. 2013b,a), enabling the discovery of spectroscopic binary nature for 9 Cepheids, for 4 of which *CORALIE* data were contributed from this observing program.

The *CORALIE* data were particularly helpful in determining the RV curve shape thanks to their excellent phase coverage and precision. In some cases it was necessary to determine accurate pulsation ephemerides as a function of time due to changing periods for several of the Cepheids in the sample and the long observational baseline covered. The O-C diagram (Sterken 2005) is an invaluable tool for doing this via the times of maximum light recorded from photometric observations in the literature over decades or even more than a century, see Turner et al. (2005) for more than 150 year of O-C data of Polaris, or Berdnikov & Turner (2004); Berdnikov et al. (2004, 2007) for some other examples spanning more than a century.

With accurate pulsation ephemerides and having determined the shape of the RV curve via a fitted Fourier series, it is then possible to compute v_γ as a function of epoch of observations and search for long-term signs of orbital motion.

2.3 On the variability of Cepheid cross-correlation functions

Besides providing a way to derive radial velocity, CCFs can also be useful to derive atmospheric parameters, since CCFs are created using thousands of spectral lines. In a sense, CCFs represent average spectral lines, although it must be kept in mind that the correlation according to Eq. 2.3 applies weights to lines according to their contrast in the numerical line mask. CCFs can thus be of interest to investigate atmospheric parameters of stars, since the S/N of a CCF is significantly higher than that of a single spectral line. Such applications have quite a bit of history. For instance, Benz & Mayor (1982) noted the variable width of CCFs in Cepheids, linking these to variable line broadening and interpreting the effect as due to phase-dependent turbulent velocities (see also Bersier & Burki 1996). Hindsley & Bell (1986) could demonstrate that the CCF varies as a function of pulsation velocity and atmospheric parameters. Furthermore, Fokin et al. (1996) provide an explanation of the FWHM variability in terms of compression- and/or shock wave-amplified turbulence for the archetype of Cepheids, δ Cephei. Kiss & Vinkó (2000) later showed characteristic FWHM curves for several Cepheids. RR Lyrae stars have also been investigated in terms of turbulence and rotation using CCFs, e.g. by Benz & Stellingwerf (1985); Chadid & Gillet (1996b); Peterson et al. (1996). It is also worth noting the possibility of determining certain stellar parameters such as iron abundance and projected equatorial velocities from CCFs of non-pulsating stars (Santos et al. 2002; Boisse et al. 2010).

This section provides an overview of Cepheid CCF properties as a function of pulsation phase using data obtained as part of the observing program described in this chapter. Following this purely phenomenological description, I will present two applications I developed that employ CCFs as tracers of atmospheric parameters. Section 2.4 presents a method to test the classification of Cepheid candidates using CCFs, and Sec. 2.5 employs CCFs to investigate surface rotation in Cepheids.

Figure 2.10 illustrates the variability of Cepheid CCFs for the long-period (35.5 d) Cepheid ℓ Carinae as an example. Pulsation phase is color-coded here going from purple to red via green and yellow (i.e., following the central dips counter-clockwise in the plot). This specific star was chosen here for several reasons: i) it is very bright ($\langle m_V \rangle \approx 3.75$ mag), yielding very high S/N spectra (typically $200 - 300$); ii) it exhibits large spectral type variations (between F6Ib and K0Ib according to the General Catalog of Variable Stars (GCVS)); iii) very good phase coverage was achieved for this Cepheid. While these CCFs are aesthetically pleasing and carry a great deal of information, it can be useful to reduce the information to a few numerical parameters that describe the CCF.

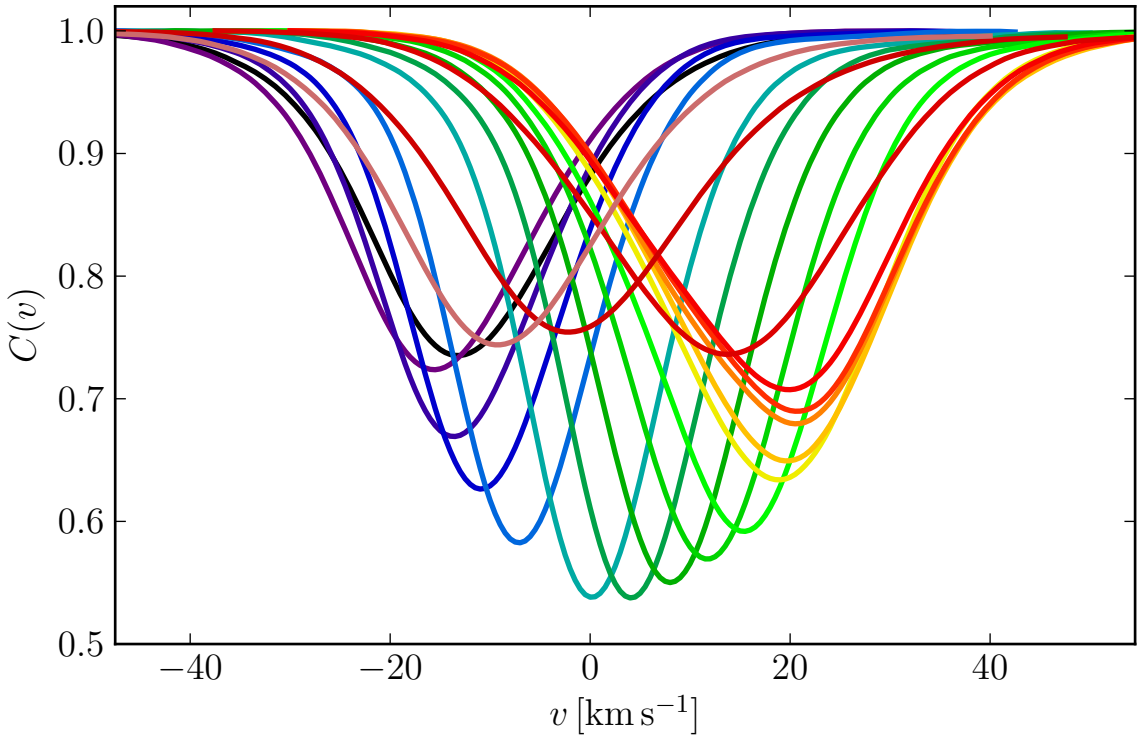

Figure 2.10: CCFs of the long-period (35.5 d) Cepheid ℓ Car. The color code traces pulsation phase from red via blue, green, and yellow to red, following the central dip of the CCF counter-clockwise.

Figure 2.11 shows CCF parameters derived by the *CORALIE* pipeline as a function of pulsation phase for the 6.64 d-Cepheid BB Sgr. From top to bottom, these are radial velocity, bisector inverse slope (BIS, see Queloz et al. 2001a), FWHM, contrast, and B-V color. BIS is a measure of the CCFs asymmetry, and is calculated as the difference of the bisector velocities near the top and bottom of the CCF, Contrast and FWHM refer the quantities derived via the Gaussian fitted to the CCFs, see Sec. 2.1.4, and the B-V color measurements are taken from Berdnikov (2008).

The BIS curve clearly shows that CCF asymmetry is largest when the pulsational velocity is extremal. In fact, the BIS curve very closely mirrors the RV curve. The reason for this close correspondence lies in the superposition of surface rotation and pulsational velocity which creates asymmetry (e.g. Sasselov & Lester 1990; Nardetto et al. 2006). Pulsation increases the Doppler shift due to rotation of those regions of the stellar surface that are seen to be moving in the same direction as the pulsation, whereas it diminishes the Doppler shift seen on the other side. Note that the BIS is near the mid-point of its variation (here $\sim -0.5\,\mathrm{km\,s^{-1}}$), but not zero, at the phase points corresponding to maximum and minimum radius.

The variability of the FWHM measured in spectral lines of Cepheids is typically interpreted in terms of variable turbulence (e.g. van Paradijs 1971; Fokin et al. 1996). Using a nonlinear non-adiabatic pulsation model and observations of δ Cep, Fokin et al. (1996) showed that the strong FWHM peak observed in the Fe I line at 5576.0883 around phase 0.77 is due to atmospheric compression possibly amplified by a shock wave. This phase point corresponds to the time when the Cepheid is nearing its maximum contraction, with inner layers being accelerated outwards, while outward layers are falling in ballistically, causing this strong compression (and possibly shock wave). Note that the CCF of BB Sgr appears to exhibit the same phenomenon. Interestingly, a small phase lag is seen between the minimum of the BIS curve and the peak of the FWHM, which is most likely related to the compression of the atmosphere due to the infalling moving layers.

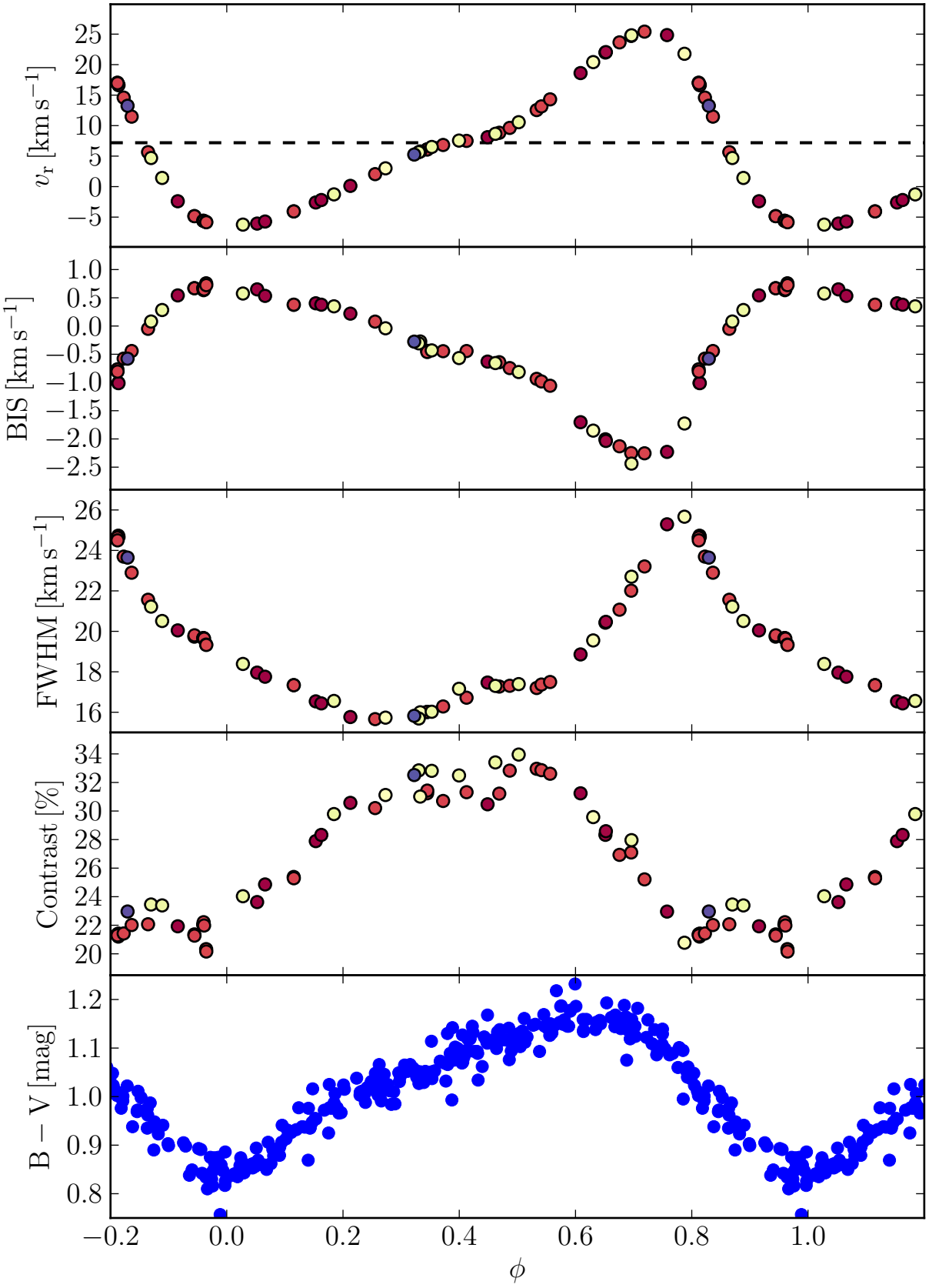

Figure 2.11: Upper four panels show radial velocity and CCF parameters derived from *CORALIE* data as function of pulsation phase for Cepheid BB Sagittarii ($P = 6.63716$ d). v_γ is indicated as dashed horizontal line in top panel. Bottom panel: B-V color from Berdnikov (2008).

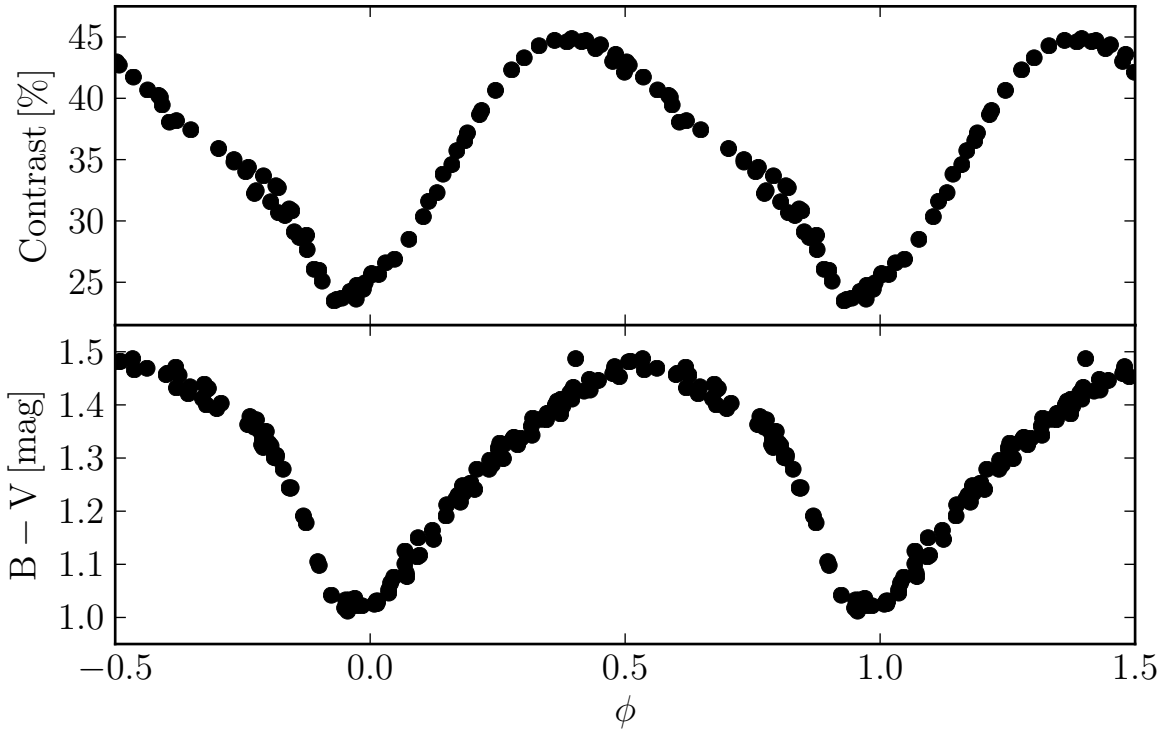

Figure 2.12: CCF contrast (*CORALIE*) and B-V color (Berdnikov 2008) for ℓ Carinae as a function of pulsation phase.

These questions are addressed in part in the section on Doppler tomography in Sec. 2.8.

B-V color is shown here to represent temperature, and it should be noted that Cepheids are brightest when they are hottest, i.e., when B-V is minimal, cf. Sec. 1.2.1. Note also the well-known lag between the phase when the Cepheid is brightest ($\phi = 0.0 = 1.0$ by definition), and where the star is smallest (as per the RV curve, $\phi \sim 0.83$). Thus, a Cepheid becomes brightest after it has recommenced expanding. In fact, the phases of greatest temperature and maximal expansion velocity indicate that the pulsation may be responsible for the final increase in temperature. Clearly, CCF contrast traces color variations quite well, indicating its suitability as a temperature indicator, although some limitations are apparent for instance at the coolest temperature (cf. Fig. 2.12) and around $\phi = 0.8 - 1.0$ (cf. Fig. 2.11). Hence, there may be a dependence on spectral type for the strictness of this correspondence, which is most likely due to differences among Cepheid average spectral types and the constant G2 "spectral type" of the mask.

In the case of BB Sgr, the CCF variations are well reproduced from one cycle to the next. However, this is not always the case, e.g. in Cepheids where line doubling (or splitting) due to shock is observed, see 2.6.

Figure 2.13 is analogous to Fig. 2.11 for the long-period (41.4 d) Cepheid RS Pup. It serves as an example for cases where differences are seen between two observational epochs (symbol color traces observation epoch: red is older, blue is newer). The peaks in FWHM (earlier) and BIS (later) exhibit a slight phase lag, similar to the case of BB Sgr, though this phenomenon shows less clearly due to the huge jumps in both curves. RS Pup exhibits cycle-dependent radial velocity curves, and exhibits clear signs of a velocity discontinuity using Doppler tomography. These points are explored in more detail in Secs. 2.7 and 2.8 below.

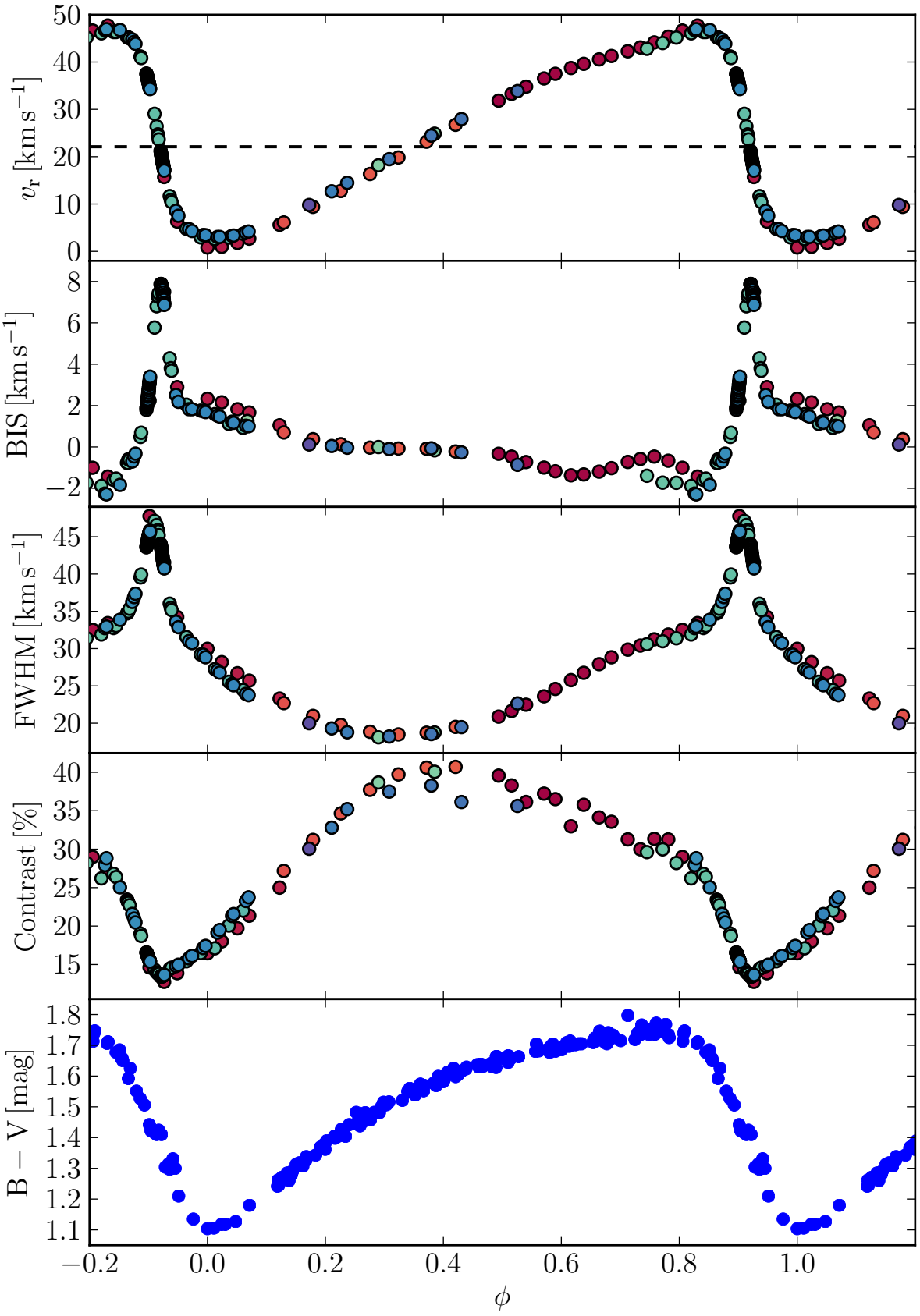

Figure 2.13: Upper four panels show radial velocity and CCF parameters derived from *CORALIE* data as function of pulsation phase for Cepheid RS Puppis ($P = 41.5134$ d). v_γ is indicated as dashed horizontal line in top panel. Bottom panel: B-V color from Berdnikov (2008). Note the intriguing peak in BIS and FWHM around the point of maximal contraction ($\phi \sim 0.9$) and the differences between observation epochs (color traces epoch).

2.4 Testing Cepheid classification using cross-correlation functions

Variable stars are commonly classified based purely on their monochromatic (single filter) light curves, since obtaining color information is significantly more expensive. This causes ample opportunity for misclassification among many eclipsing binaries and s-Cepheids, since both types of objects are virtually indistinguishable based on their monochromatic light curve alone, exhibiting sinusoidal light curves of similar period and amplitude. Among the short-period Cepheid candidates ($< 5\,\mathrm{d}$), it is also common to find RS CVn type variables, for instance. On the long-period end, it is common to find semi-regular variables that have been misclassified as Cepheids due to variable or falsely-determined periods of variability.

As a result of these plentiful opportunities for misclassification, the answer to the question "how many Cepheids are currently known in the Galaxy?" is not obvious. For the Cepheids in open clusters project (Sec. 3), I compiled an extensive list of Cepheid candidates from the Variable Star Index (Watson 2006, VSX) and the GCVS. This list included, among others, Cepheid candidates from the ASAS catalog of variable stars (ACVS), which at the time of writing this thesis contains $1\,594$ objects that are identified as Cepheid candidates, many of which have additional possible classifiers. Furthermore, it is known that the contamination of Cepheids in such surveys can be very high (e.g. Schmidt et al. 2011; Pigulski 2013). It thus became necessary to test the classification of Cepheid candidates that could not yet be considered bona fide Cepheids by virtue of having been studied for a long time, and this section describes my CCF-based approach to this problem.

First, it is helpful to review the principal characteristics identifying a star as a Cepheid. These are:

1. characteristic light curve shapes, ranging from sinusoidal to saw-tooth, exhibiting a "bump" in the light (and RV) curve whose phase location depends on period (the Hertzsprung progression, cf. Fig. 1.1)
2. chromatic variability due to temperature variations
3. characteristic location in the $\log P - \log A$ (period & amplitude) diagram (e.g. Eyer & Blake 2002)
4. variable radial velocity due to radial pulsation

Section 2.3 above shows that most of these aspects can also be studied using CCFs. Besides the measurement of varying radial velocity (from as little as two spectra), determination of period and amplitude (many data points required), the CCF also shows the chromaticity of the variability via changing contrast, and includes another characteristic of radial pulsation: (variable) CCF asymmetry. Certain aspects distinguishing stellar pulsation from other origins of variability such as rotation or eclipses are thus readily identifiable using CCFs.

When combined with photometrically-determined pulsation period, e.g. from ASAS, CCFs can be used to test Cepheid classification with only a few (between 1 and 3) well-placed (in phase) observations. Hence, an iterative observation scheme was implemented for Cepheid candidates listed in the VSX and Catalog of suspected variables (Kukarkin & Kholopov 1982). When the below conditions are all met, it is fairly certain that a star was correctly classified as a Cepheid:

1. The CCF computation with a G2 mask is successful at any phase point. This is a first test for excluding stars that are hotter than Cepheids, and can provide a rough estimate of spectral type. Any spectral types earlier than approximately early F will fail to produce clear cross-correlation peaks using this mask.
2. The RV varies between two phase points that are not identical. Exceptions to this rule are the two (different) phase points where the measured RV is equivalent to the systemic velocity and an unlikely coincidence due to orbital motion.

Type	Number
Cepheid candidates considered	153
Cepheids confirmed	32
Cepheids excluded	109
Inconclusive	12
Spectroscopic binaries (non-Cepheids)	44
SB1	17
SB2	26
SB3	1

Table 2.4: Statistics of Cepheid candidates tested for correct classification

3. CCF contrast changes significantly between two measurements indicating the variability's chromaticity. This is not necessary, however, as can be seen in Fig. 2.10.

4. CCFs observed sufficiently far from the phase of v_γ exhibit significant asymmetry. In the case of *CORALIE* this quantity is readily obtained from the RV pipeline.

In practice, many non-Cepheids could be ruled out after only a single observation. If the CCF was flat, the spectral type of the star is most likely much earlier than late F, indicating that the star is hotter than any of the known bona fide Cepheids, provided that the spectrum was of sufficient quality. Thanks to the high S/N on the CCF, this procedure could be applied to many Cepheid candidates brighter than approximately $\sim 13^{\rm th}$ magnitude, limited by the guiding systems of *CORALIE* and *HERMES*. When the CCF showed a clear peak during a first exposure, two further spectra were obtained at different phase points, yielding first estimates of v_γ and spectral type. If variable radial velocity, contrast, and CCF asymmetry are observed, non-Cepheid classifiers could be excluded at high confidence.

Using the above approach on Cepheid candidates, i.e., non-bona fide Cepheids, compiled for the Cepheids in open clusters project, I obtained the results summarized in Tab. 2.4. Less than one third of Cepheid candidates observed turned out to be bona fide Cepheids. Among the 110 ASAS (Pojmanski 1997, 2002; Pojmanski et al. 2005) Cepheid candidates observed, 78 are not classical Cepheids[12]. Among 11 UNSW (Christiansen et al. 2008) identifiers, none are considered bona-fide Cepheids, and the same is true for the 5 ROTSE (Akerlof et al. 2000) Cepheid candidates that were considered. These statistics reveal that the point made in the beginning of this section is correct: a majority (here: 71%) of automatically-classified newly-announced Cepheid candidates are likely misclassified. This points to a high contamination rate among stars classified as Cepheids in recent surveys, and underlines the necessity for observational follow-up.

It should, however, be noted that the sample investigated here focused on stars not already well-established as Cepheids. The contamination rate of the above-mentioned surveys should result in a much lower percentage, when the correctly-recovered bona fide Cepheids are counted as well.

For many of the SB2s identified here, ground-based photometry (e.g. from ASAS) is available. After all, these objects were identified as variables photometrically in the first place. Hence, this sample of SB2s could be of interest for further observationally follow-up aimed at deriving accurate distances and stellar parameters such as absolute mass, and so on. Figures 2.14 and 2.15 show some multi-lined binaries for which several spectra were obtained and clearly show the relative displacement due to orbital motion of the two spectral components. The top left panel of Fig. 2.15 furthermore reveals the nature of ASAS J020851-0721.5 as a triple-lined spectroscopic binary (SB3).

The imminent launch of the *Gaia* space mission[13] heralds an unprecedented all-sky census

[12]Note that this may include some type-II Cepheids which were not explicitly searched here

[13]currently planned for 19 December 2013 at 9:12:18 UTC, i.e., 2 3/4 days after the thesis defense

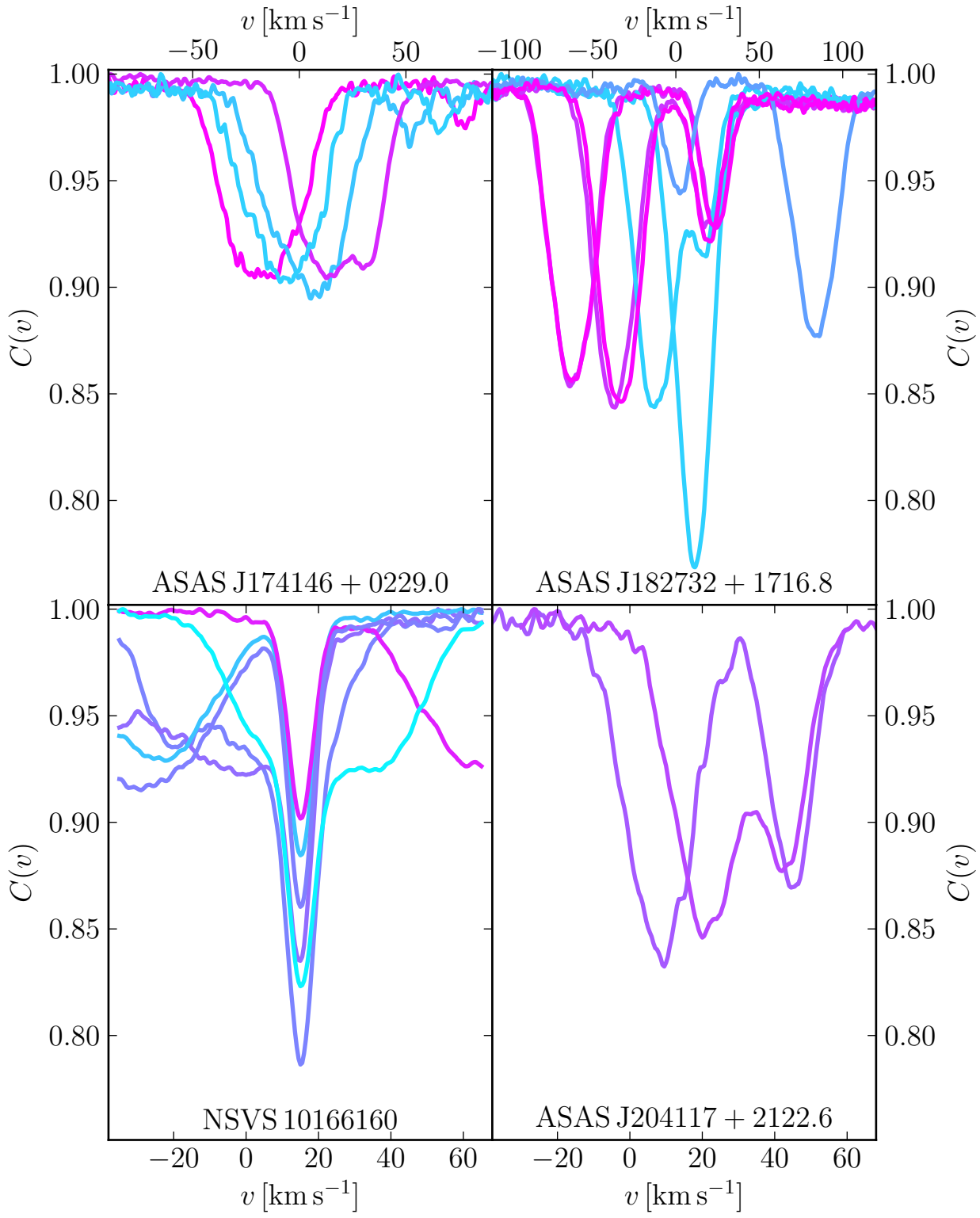

Figure 2.14: CCFs of some SB2s observed with *CORALIE*. Identifiers specified at the bottom of the panels. NSVS 10166160 has also been observed with *HERMES*, see Fig. 2.15.

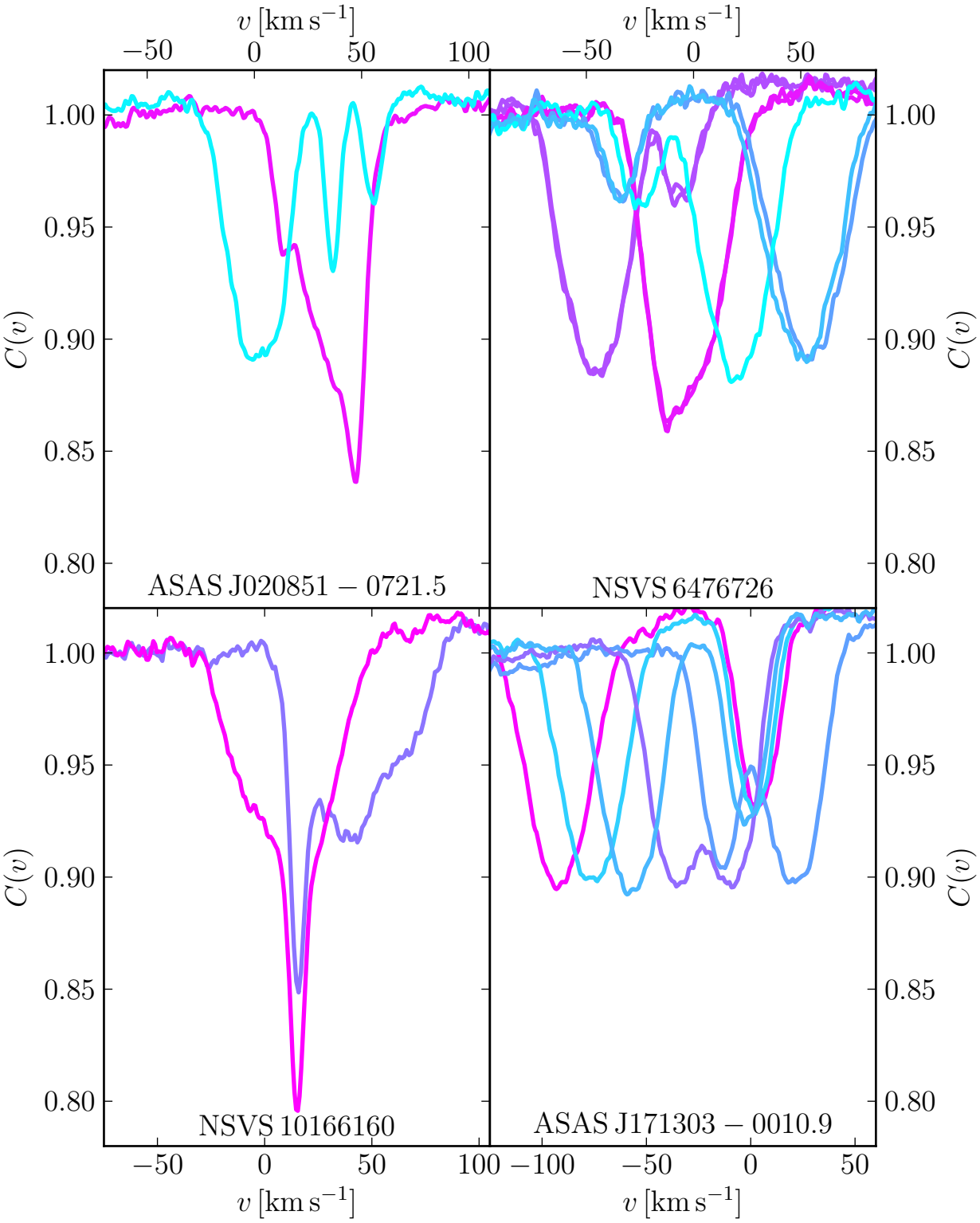

Figure 2.15: CCFs of some multi-lined spectroscopic binaries observed with *HERMES*. Identifiers are given at the bottom of the panels. ASAS J020851-0721.5 is an SB3. NSVS 10166160 has also been observed with *CORALIE*, see Fig. 2.14.

of the Milky Way. *Gaia* will measure astrometric parameters (position, parallax, proper motion) as well as time series photometry, low-resolution spectrophotometry for approximately 1 billion objects. For 150 million[14] of these, *Gaia*'s Radial Velocity Spectrometer (RVS) instrument will provide spectra of intermediate-to-high resolving power $R \sim 11\,000$, which can be used to construct CCFs during data processing. If the appropriate information will be available as part of *Gaia* data, then the above approach could find application in the automatic variable star classification, and should help to significantly reduce misclassification of Cepheids. Recently, François Bouchy has investigated the potential of CCFs for variable star classification using *CORAVEL* data for which *Hipparcos* photometry is available. An associated technical note is in preparation and will make a recommendation to store certain CCF parameters (such as FWHM and contrast) as part of the data available to CU7 for variable star classification and characterization. The above investigation illustrates how useful these parameters are for variable object classification. Based on my experience, I would advocate to furthermore include an asymmetry-related CCF parameter such as the BIS, which was not available for *CORAVEL* data.

2.5 Cepheid surface velocity estimates from cross-correlation functions

Spectral lines are broadened by several effects including (Gray 2008) temperature, pressure, rotation, turbulence, and magnetic fields (although this contribution is very small, see Anderson et al. 2010). Mathematically, a spectral line can be described as the result of the convolution of the intrinsic line shape with such broadening agents. Thus, spectral lines can be investigated in terms of different broadening agents by deconvolution. An interesting property of Gaussian curves is that convolution with another Gaussian yields also a Gaussian. As a result, the standard deviation of a Gaussian probability density function can be split up into the quadratic sum of two, i.e., $\sigma_{\rm tot} = \sqrt{\sigma_1^2 + \sigma_2^2}$.

CCFs, as argued above, correspond to average spectral lines. Furthermore, for non-pulsating stars, CCF shapes are approximately Gaussian. Thus, under the assumption of Gaussian CCF shape and for slowly-rotating non-pulsating stars, rotational broadening can be estimated by separating the width of CCFs into the contributions due to rotation and all other effects[15] (Santos et al. 2002). The standard deviation of the CCF, $\sigma_{\rm CCF}$, is thus separated into the contribution by rotation, $\sigma_{\rm rot}$, and an "intrinsic" width, σ_0, according to this formulation:

$$\sigma_{\rm CCF} = {\rm FWHM}/(2\sqrt{2\ln 2}) = \sqrt{\sigma_{\rm rot}^2 + \sigma_0^2}\,. \tag{2.19}$$

Statistically speaking, broadening due to turbulence, pressure, etc. can be approximated to be a function of spectral type, i.e., of a star's color. It is thus possible to calibrate statistically the minimal broadening as a function of color by fitting a polynomial to the lower envelope (these stars are assumed to show no signs of rotational broadening) of σ measured as a function of color. One thus obtains a relation of the form $\sigma_0 = a_0 + \sum_i a_i (B-V)^i$.

For a star of given color $B-V$, $\sigma_{\rm rot} = \sqrt{\sigma_{\rm CCF}^2 - \sigma_0^2}$ is translated into $v \sin i$ using a set of spectroscopically-determined (e.g. via spectral line fitting) projected rotational velocities which yield the conversion factor, A, see Benz & Mayor (1984). Once this calibration is performed for a given instrument, $v \sin i$ of slowly-rotating ($v \sin i < 20\,{\rm km\,s^{-1}}$) non-pulsating (Gaussian CCFs) MS dwarfs of late spectral types can be estimated using a B-V color and the FWHM of the CCF via:

$$v \sin i = A \cdot \sigma_{\rm rot} = A \cdot \sqrt{\sigma_{\rm CCF}^2 - \sigma_0^2} \quad [{\rm km\,s^{-1}}]\,. \tag{2.20}$$

For *CORALIE*, $A = 1.9$ (Santos et al. 2002), and $\sigma_{\rm CCF}$ is readily obtained from the Gaussian fitted to the CCF.

[14] `http://www.rssd.esa.int/index.php?page=Science_Performance&project=GAIA`

[15] I would like to acknowledge François Bouchy for pointing me in this direction.

In the case of Cepheids, the situation is rendered more complex due to the presence of pulsation which leads to time-dependent, intrinsically non-Gaussian CCF shapes with variable σ, and a severe lack of $v \sin i$ estimates from spectroscopic studies available for the calibration of A. It is hard to say why the latter is the case, but I conjecture that it must be related to a mixture of observational and theoretical considerations. Cepheids, being supergiant stars (luminosity classes I and II) may not be expected to rotate fast due to their large radii (angular momentum conservation). Furthermore, the evolutionary effects of rotation on Cepheids have thus far not been considered in detail although Maeder & Meynet (2000) have previously mentioned that surface velocities of Cepheids should be well within the observable range, cf. also the paper in Sec. 4.3. Finally, the observation of time-dependent turbulence may have resulted in the assumption that turbulent broadening should be the dominant line broadening effect in Cepheids.

However, as I show in Chap. 4, the latest rotating Geneva evolutionary models Ekström et al. (2012); Georgy et al. (2013b) predict that surface velocities in Cepheids should be clearly detectable, somewhere between $5-40\,\mathrm{km\,s^{-1}}$, depending on initial rotation rate, mass, crossing, and definition of the instability strip. The reason why Cepheids rotate faster than red giants is simple: spin-up due to contraction during the blue loop phase (angular momentum conservation). Furthermore, Cepheids should in principle have time-dependent equatorial velocity due to their periodic contraction and expansion driven by pulsation. Thus, rotation should not be negligible in Cepheid line shapes, and may be measurable via CCFs similar to the method by Santos et al. (2002), provided the requirement of Gaussian CCF shape is met sufficiently well.

As seen in Figs. 2.10 and 2.11 of Sec. 2.3 above, there does exist a phase point during which Cepheid CCFs show little asymmetry, are intrinsically rather narrow, and should be minimally affected by broadening effects acting on the CCF: the point of maximal expansion. Note, however, that $v \sin i$ is minimal at this phase point, since radius is largest. At any other phase point stronger rotational broadening may be present. This is consistent with the observed larger FWHM at other phase points, although other broadening effects, notably turbulence, dominate this increase in FWHM. Therefore, $v \sin i$ estimated at this phase point will yield lower limits on the average $\langle v \sin i \rangle$ predicted, e.g. by the Geneva evolutionary models.

To estimate $v \sin i$ for Cepheids statistically, I extracted the *CORALIE* observations[16] taken closest to the phase point of maximal radius as indicated by maximal contrast and an RV close to the systemic velocity. For a total of 97 Cepheids, such data are available in the *CORALIE* dataset.

As shown in Sec. 2.3 above, CCF contrast correlates well with color (cf. Fig. 2.12). It is thus possible to replace B-V color in the calibration of σ_0 with CCF contrast[17]. The top panel in Fig. 2.16 shows this comparison for the *CORALIE* Cepheids, analogous to Fig. A. 2 in Santos et al. (2002), with measurements taken particularly close to maximum radius drawn using gray filled circles, and the slightly less reliable ones drawn using open circles. There appears to be a steep increase in σ for hotter Cepheids (low contrast) reminiscent of the increase in σ for B-V < 0.6 in Santos et al. (2002, Fig. A. 2). In addition, there may also be a slight trend of increasing σ with increasing contrast (cooler objects). Both tendencies make it tempting to derive a contrast-dependent σ_0 for *CORALIE*. However, the lower envelope is rather flat and only few stars can be used to define an envelope, increasing the uncertainty on such a calibration. Hence, the overall minimum value of σ is used as a lower limit on σ_0 as a first estimate. The scaling factor A by Santos et al. (2002) was adopted, since it is i) calibrated for *CORALIE* and ii) no reliable literature $v \sin i$ estimates are available to calibrate A. $v \sin i$ estimates are then derived using Eq. 2.20.

The bottom panel in Fig. 2.16 shows the result obtained for these 97 Cepheids observed with *CORALIE*. Binned averages were estimated using variable bin width derived using the Bayesian Blocks method (Scargle 1998), indicating no significant dependency on period. The median of all

[16]This analysis is limited to *CORALIE* data, since a calibration of the scaling factor A (cf. Eq. 2.20) is available from the literature, whereas none is available for *HERMES*

[17]Note, that CCF contrast is also affected by metallicity, which is not yet taken into account here.

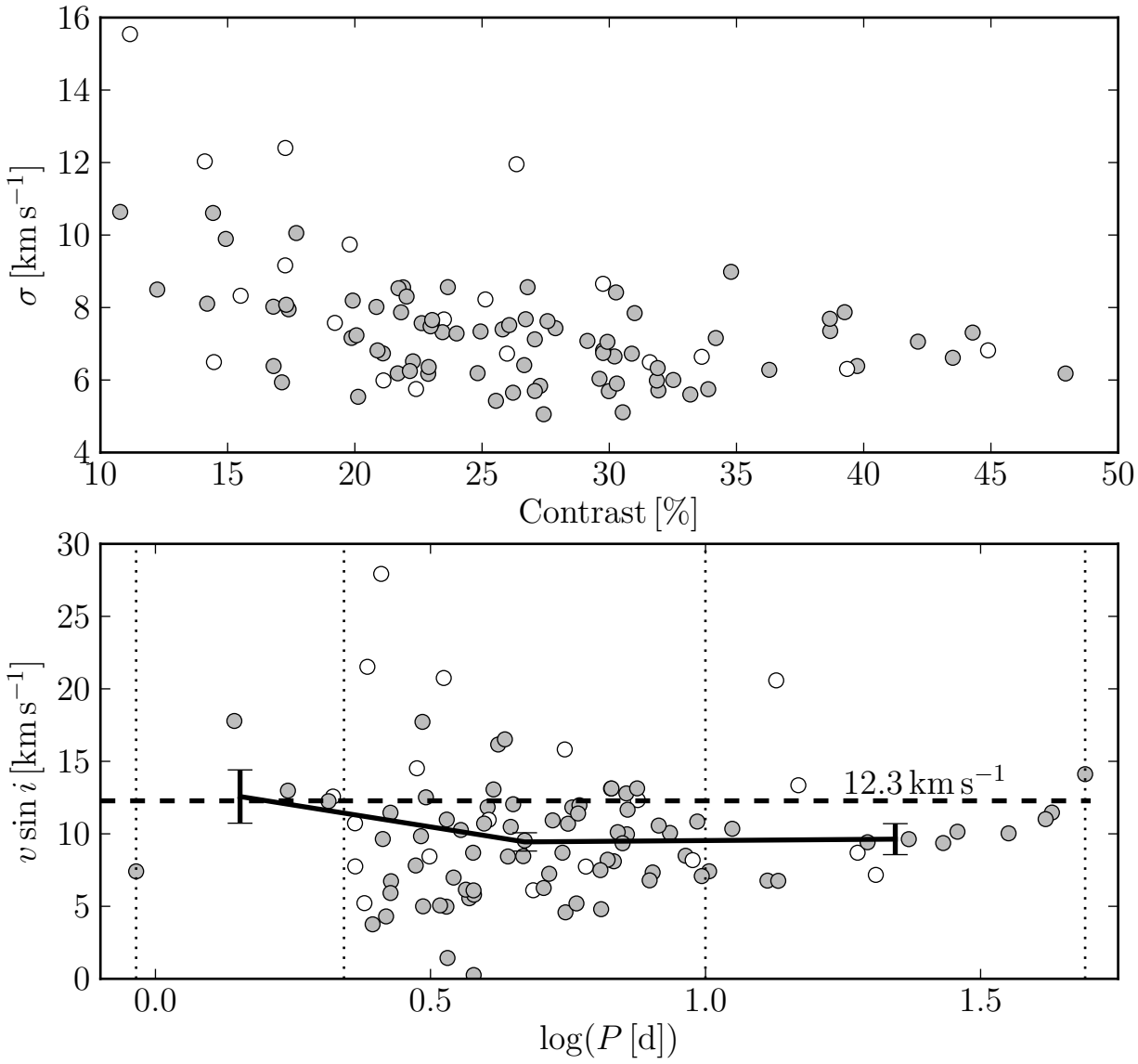

Figure 2.16: The typical equatorial velocity of Cepheids, $\langle v_{\rm eq} \rangle$, was estimated from CCF-based $v \sin i$ estimates of 97 Cepheids observed with *CORALIE*. Top panel: σ derived from CCF FWHM (cf. Eq. 2.5) as a function of CCF contrast. Circles with gray center indicate that the CCF measurement was taken particularly close to phase of maximal radius. Bottom panel: estimated projected rotational velocity as a function of logarithmic pulsation period. Per-bin averages (determined using Bayesian blocks technique by Scargle 1998) are shown as error bars and indicate no clear period-dependence. The dashed horizontal line corresponds to the average equatorial velocity $\langle v_{\rm eq} \rangle = (4/\pi) \langle v \sin i \rangle \approx 12.3\,{\rm km\,s^{-1}}$.

measurements, $\langle v \sin i \rangle$, is multiplied by $4/\pi$ to estimate a typical equatorial velocity assuming randomly oriented rotation axes (Gray 2008). This average $\langle v_{\rm eq} \rangle = (4/\pi)\langle v \sin i \rangle \approx 12.3\,{\rm km\,s^{-1}}$ is drawn as a dashed horizontal line.

Obviously, this estimation is a relatively crude approximation and can be improved. However, this marks the first time that projected rotational velocities for a large sample of Cepheids are estimated and clearly demonstrates that Cepheids do exhibit non-negligible surface rotation in the order of $10\,{\rm km\,s^{-1}}$ in their spectra. This result may have a significant impact on the estimation of surface abundances. Spectroscopic analyses currently often neglect rotational broadening, assuming micro- or macro-turbulent broadening instead (Luck & Lambert 2011; Takeda et al. 2013). However, line broadening profiles due to macro- or microturbulence differ from one another as well as from a rotational Doppler profile. Thus, the abundances derived may be systematically biased according to the particular combination of adopted broadening profiles.

2.6 Line splitting due to shock

Line splitting[18] due to shock is a known phenomenon in several types of pulsating stars, notably in RR Lyrae type stars (Fokin 1992; Chadid & Gillet 1996a; Fokin & Gillet 1997; Preston 2011), type-II Cepheids (Fokin & Gillet 1994, e.g. in BL Her stars), and long period variable stars (Alvarez et al. 2001b). However, the first discoveries of line doubling were probably made in the late 1950s by Kraft (1956); Merrill & Greenstein (1958). Line doubling can be explained by a shock wave passing through the atmosphere (Schwarzschild 1952). Figure 2.17, taken from Alvarez et al. (2000), illustrates this process. The basic idea is that a shock front acts as a kinematical separation in the line forming region for a given spectral line, shifting one part to the blue, and another to the red. As the shock wave traverses the atmosphere, it passes through zones of different temperature, i.e., different parts of the (extended) line forming regions. The result is a time-variable line doubling pattern as schematically shown in the Fig. 2.17.

In Cepheids, line splitting is rarely observed, at least in metallic lines. The first line-doubling Cepheid to be discovered was X Cyg (Kraft 1956). Dawe (1969) furthermore found line doubling in the Ca II lines of ℓ Carinae. Sasselov et al. (1989) and Sasselov & Lester (1990) presented line doubling detected in infrared spectra of η Aql and X Sgr, and discussed its origin in shock propagation and the dynamical structure of a Cepheid's atmosphere similar to Schwarzschild (1952). The sample of line-doubling Cepheids was significantly increased by Kovtyukh et al. (2003) who detected metallic line doubling in optical spectra in three additional Cepheids, EV Sct, BG Cru, and V1334 Cyg. Finally, Mathias et al. (2006) raised the question whether the presence of three components detected in high-resolution *HARPS* data provide evidence of multiple shock waves in X Sagittarii's atmosphere.

Originally, line doubling was mostly observed in Hα (Kraft 1967; Wallerstein 1983), since the weaker metallic lines are easily blended with other spectral lines. Incidentally, line doubling may also be easier to observe in Hα, given that Hα profiles of RS Pup and ℓ Car both show the phenomenon, while most other spectral lines in these stars do not.

The studies mentioned here typically investigate line doubling observed in individual spectral lines. However, if a CCF represents an average spectral line, then line doubling should also be observable in CCFs. That this is the case can be seen in Fig. 2.18, showing highly variable line splitting (not necessarily a doubling) in CCFs derived from *CORALIE* and *HERMES* observations of X Sagittarii. Interestingly, I did not find evidence for line doubling or splitting in the CCFs of all Cepheids for which this phenomenon has been previously reported. One such example is η Aql, indicating that detectability may depend on the line mask (choice of lines considered) as well as the properties of the star, e.g. spectral type. Note also that some stars such as RS Pup that do not exhibit line splitting in their CCFs do exhibit line doubling in individual lines such as Hα.

[18] line doubling refers to the special case of line splitting with two components

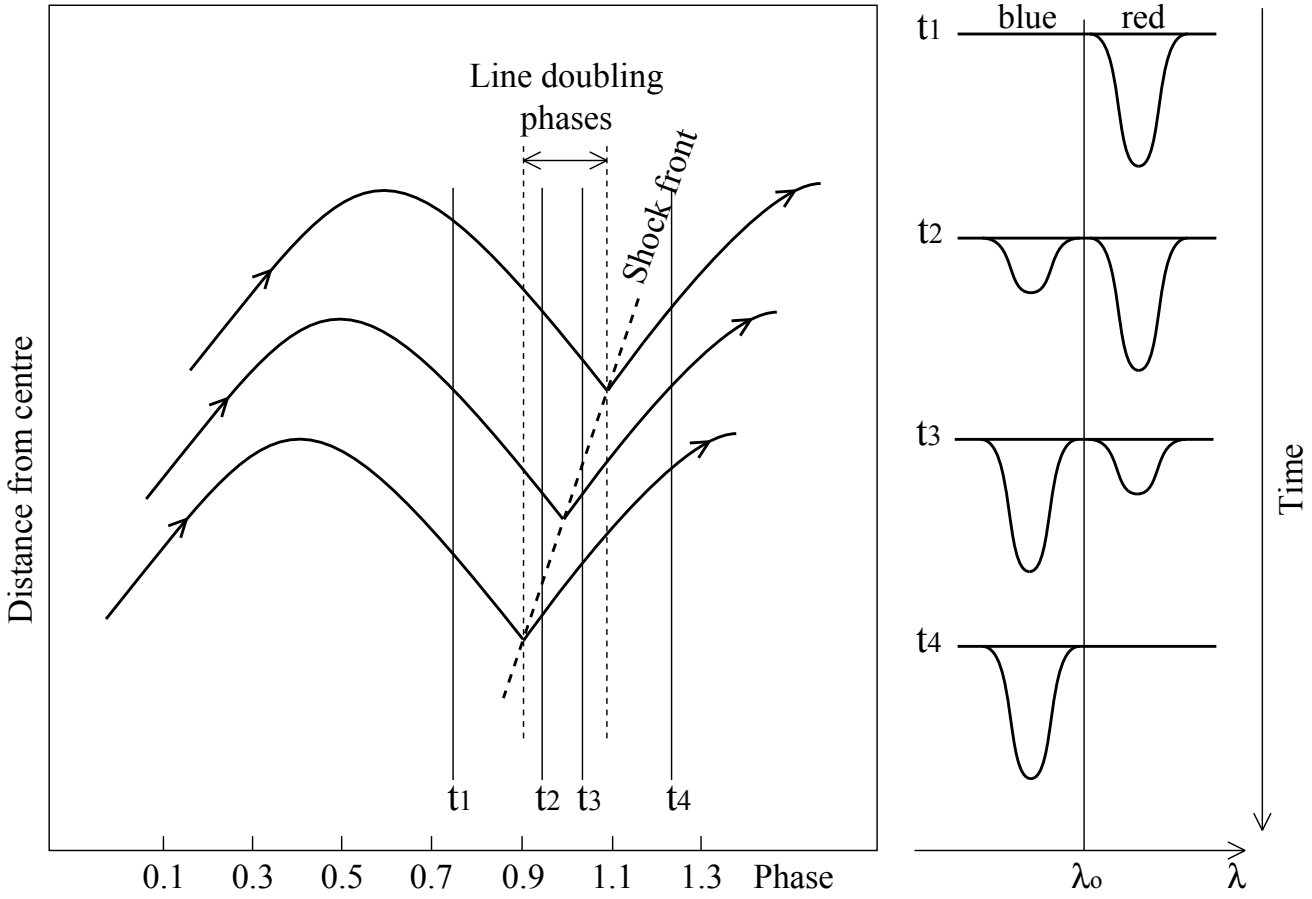

Figure 2.17: Schwarzschild (1952) mechanism of line doubling graphically explained. Figure from Alvarez et al. (2000).

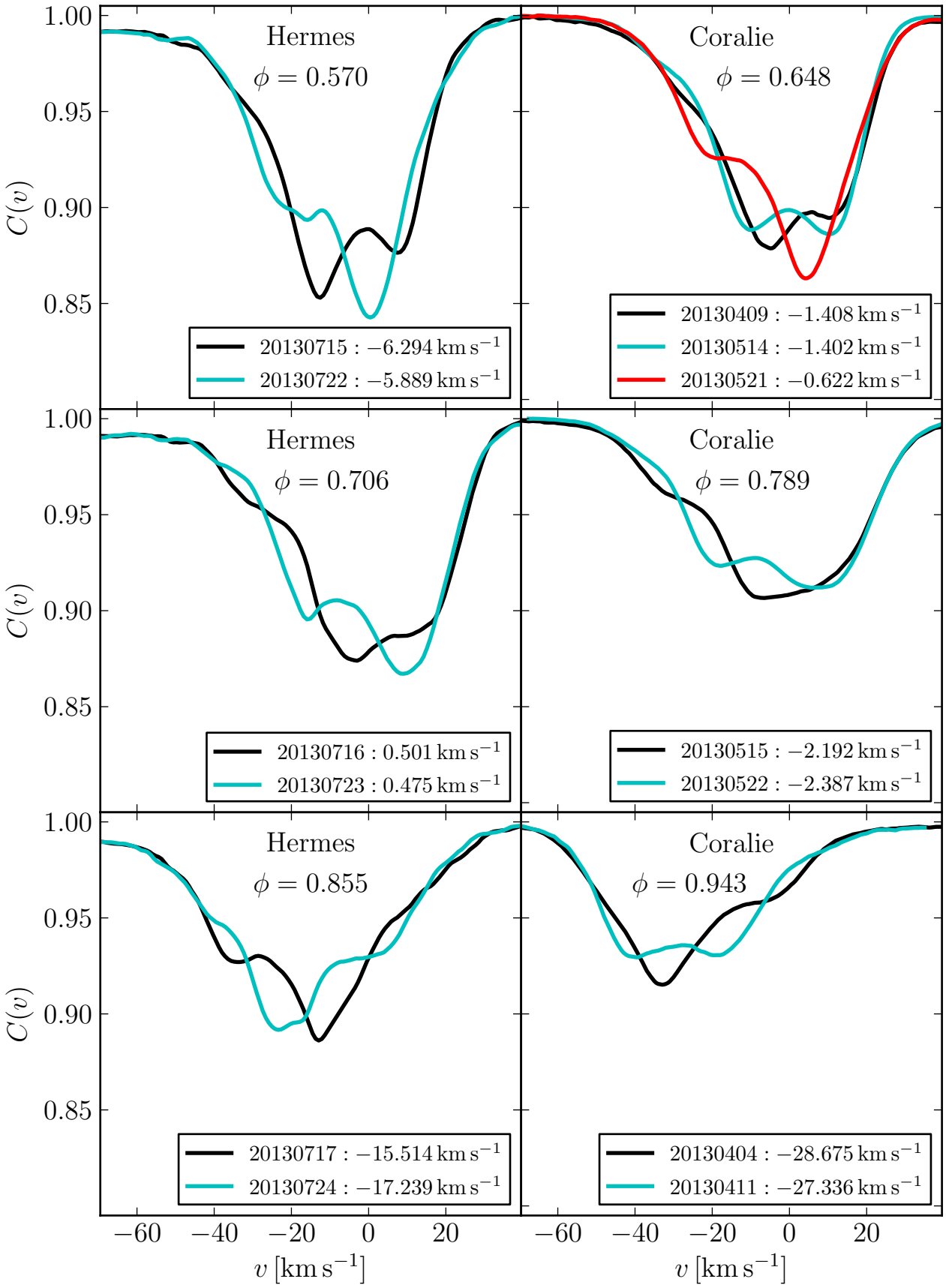

Figure 2.18: CCFs of X Sagittarii observed at virtually identical phases during different epochs using *HERMES* or *CORALIE*. Phase and instrument shown at the top in each panel. Legends indicate observation date and RV derived via fitting a Gaussian. Cycle-dependent line splitting patterns cause systematic error for RVs derived via fitting Gaussians.

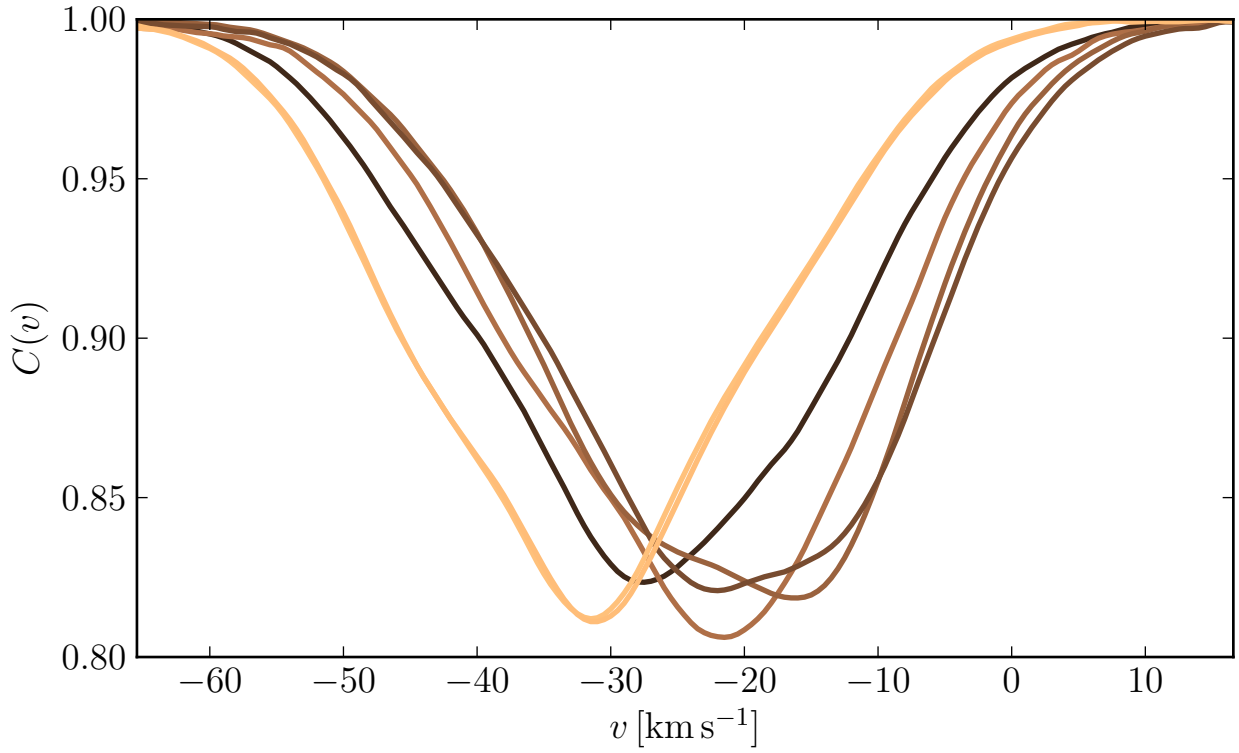

Figure 2.19: *CORALIE* CCFs of LR TrA showing deformation reminiscent of unresolved line splitting due to shock.

During my thesis, I serendipitously discovered line doubling in CCFs of one additional Cepheid, LR Trianguli Australis. Although subtle, line doubling is clearly detected, see Fig. 2.19.

Line splitting can significantly impact radial velocities derived using the Gaussian method, if the pattern is not constant over time. While Sasselov & Lester (1990) noted that line doubling in X Sgr was stable over a period of 11 months, Mathias et al. (2006) report the phenomenon to be variable on long timescales, noticing two components from data obtained in 1988 and three components in 1989 by inspecting Fig. 12 in Sasselov & Lester (1990). As Fig. 2.18 shows, however, the CCF line shape in X Sgr is not even stable from one pulsation cycle to the next (P $\sim$ 7 d). In fact, significantly different CCF patterns are derived from observations obtained at identical phase points of subsequent pulsation cycles, for three different epochs! As shown in the figure, observational data from *HERMES* obtained in July 2013 shows variability from one cycle to the next, and so do *CORALIE* data obtained in April and May of 2013. Interestingly, the *CORALIE* CCF obtained at phase 0.65 in April 2013 (top right panel) is more similar to the CCF obtained in May 2013 than the latter is to the CCF measured in the subsequent cycle one week later. The extent of the difference is largest in the *HERMES* data obtained in July 2013, resulting in systematic differences of the derived RVs as large as $1.7\,\mathrm{km\,s^{-1}}$. For the other phase points, the variability can range from a few tens to many hundreds of $\mathrm{m\,s^{-1}}$.

Cycle-dependent line splitting patterns can thus create systematic error for RVs derived using the Gaussian technique for such obviously non-Gaussian CCFs. A way to resolve such issues could be the use of bi-Gaussian (Nardetto et al. 2013, although sometimes more than two components are seen) or centroid RVs. However, due to the common use of the Gaussian technique and for the sake of the argument in the following section, I would like to point out here that line splitting can have a systematic effect on RV, making the RVs themselves cycle-dependent. As a result, the shape of an RV curve can depend on the epoch of observation and is directly influenced by the presence

of shock in a Cepheid's atmosphere. If this effect is small, cycle-dependent RV curves could be mistaken for binarity, especially if there is periodicity in the variability of the line doubling pattern.

Intriguingly, line doubling in RR Lyrae stars has been linked to the Blazhko effect, a century-old enigma of pulsating stars. Chadid & Gillet (1997) showed that line doubling is strongest in RR Lyrae stars with the strongest Blazhko effects. Furthermore, line doubling in metallic lines is detected in at least five Blazhko RR Lyraes, but not in a single stable, non-Blazhko RR Lyrae star (Preston 2011). Therefore, discovering and monitoring line doubling in Cepheids may provide an important link to the Blazhko effect and help to better understand shock propagation in Cepheid atmospheres. Since the line doubling pattern of X Sgr varies between each cycle, a very dense, long-term monitoring of this star is desirable.

2.7 Cycle-to-cycle variations

As mentioned in the previous section and shown by Fig. 2.18 above, line doubling can be cycle-dependent and significantly impact RV measurements, thereby introducing a cycle-dependence of RV curves. This was shown for X Sgr where line doubling is obviously strong and is also seen in the top panel in Fig. 2.20 that shows the RV curve against phase. However, no clear trend is seen given the incomplete sampling achieved during the different epochs[19].

Since resolved line splitting impacts the RV curve, one can wonder whether unresolved line splitting can do the same. Such an effect would make a strong case for photometric and spectroscopic observations intended for Baade-Wesselink analyses to be taken (nearly) simultaneously, depending on the time scale of the cycle-dependence. In the age of extreme precision on Baade-Wesselink type distances and radii, such effects are significant, and *CORALIE* data provide the stability and precision required to investigate these effects.

Serendipitously, I discovered that two short-period ($3-4$ d) s-Cepheids exhibit cycle-dependent RV curves, although no line doubling is detected in the CCFs. Figure 2.21 illustrates this for the 3.786 d overtone-pulsator Cepheid QZ Nor using *CORALIE* measurements obtained over an observational baseline of more than 2 years (783 d). In the top panel, RV is shown as a function of phase, with observation date color-coded, see the center panel for the color coding going from (very) dark blue to yellow. The phased RV curve clearly shows that the amplitude at the high RV values differs significantly at phases around 0.6, while the variations around phase 0.0 are much smaller and cannot be seen so clearly at this scale. The cycle-dependent difference at the high-RV end indicates an effect in the order of $600\,\mathrm{m\,s^{-1}}$. This is clearly non-negligible, since the median precision of the measurements is $20\,\mathrm{m\,s^{-1}}$, i.e., a factor 30 smaller. An instrumental origin of these variations can be excluded, thanks to the high long-term stability of *CORALIE* RVs, and since this effect is seen only in a few Cepheids. It is important to underline that the curve is changing shape, not simply amplitude, and the difference is not symmetric around the average RV. The variation observed is gradual and monotonous (increasing) over the entire baseline.

It was easy to mistake this phenomenon for signs of spectroscopic binarity at first. However, with more data and excellent phase coverage, it later became obvious that the RV curve itself was changing shape. With the data available at the time of writing, it is impossible to conclude on a periodicity of this phenomenon for QZ Nor; a longer observational baseline is required to address this question.

If periodicity is found, it will be interesting to compare the cycle-to-cycle variations observed for QZ Nor with those of Cepheids such as HR 7308 for which Burki et al. (1982) found amplitude variations in the order of $10\,\mathrm{km\,s^{-1}}$. Other Cepheids exhibiting amplitude variations are known, such as the famous North star Polaris. A few additional similar cases are mentioned in Turner

[19] At a period of 7.01 d, it is difficult to obtain good phase coverage for X Sgr in a short period of time. On the other hand, it is possible to obtain measurements at nearly identical phase points over several months, enabling the comparison of the line doubling phenomenon in subsequent cycles in Fig. 2.18.

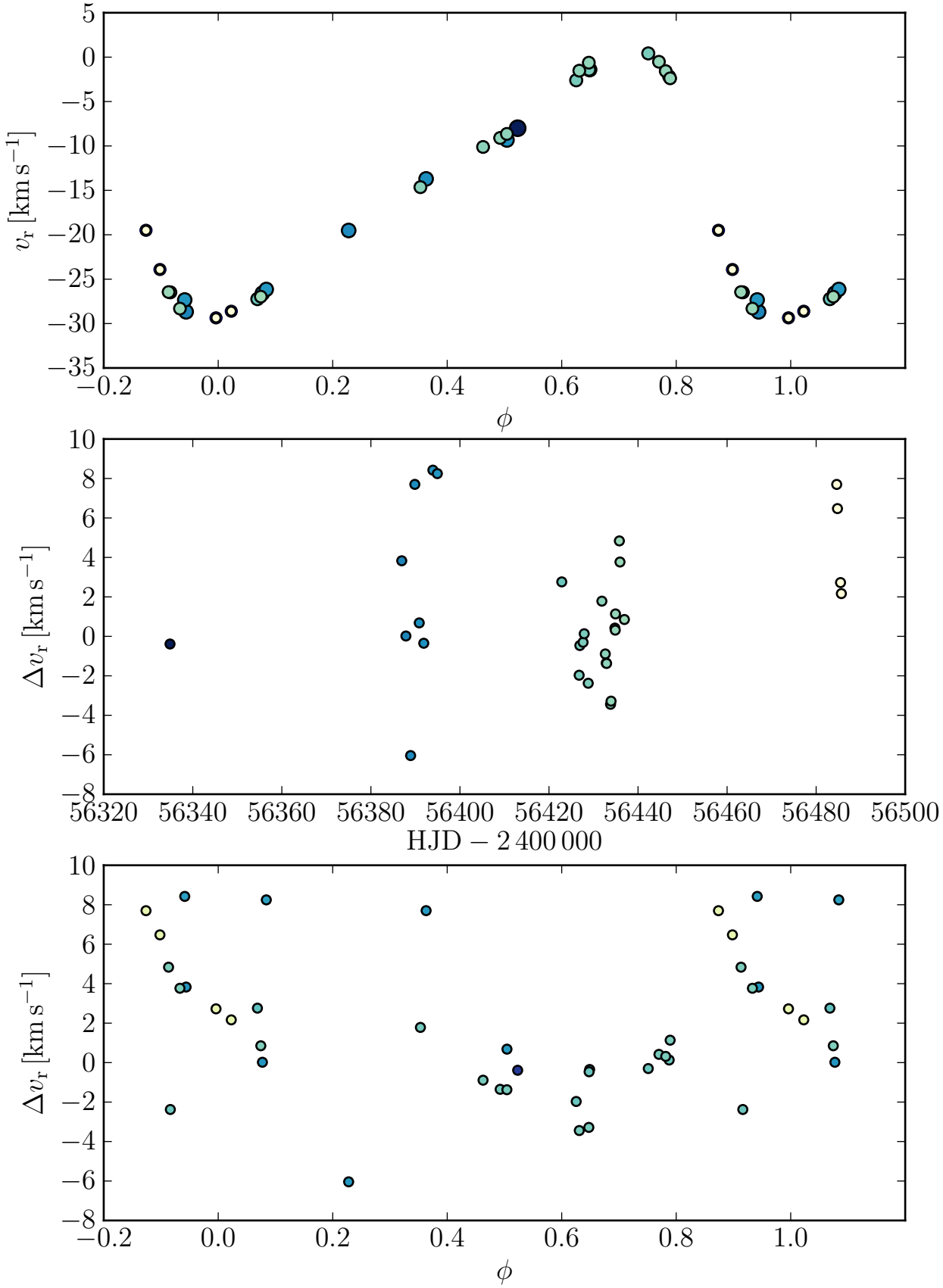

Figure 2.20: Cycle-to-cycle variations and Doppler tomography of X Sgr. Panels from top to bottom: (Gaussian) RV curve; differential velocity, Δv_r, as defined in Eq. 2.21 against observation date; Δv_r against pulsation phase. Color coding applied to distinguish between date of observation. Large variations in Δv_r are seen, although no clear trend is discernible.

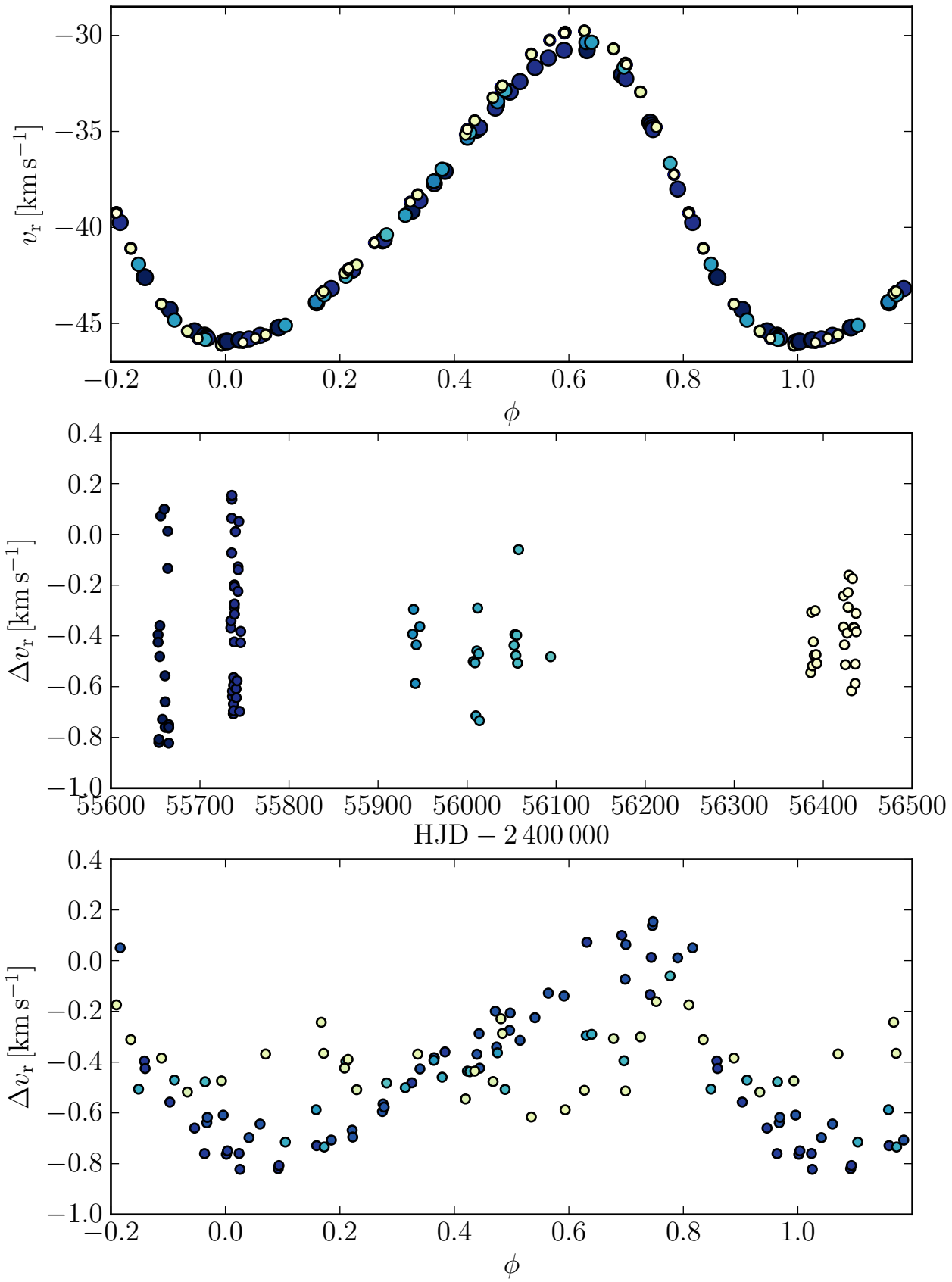

Figure 2.21: Cycle-to-cycle variations and Doppler tomography of QZ Normae. Panels from top to bottom: (Gaussian) RV curve; differential velocity, Δv_r, as defined in Eq. 2.21 against observation date; Δv_r against pulsation phase. Color coding applied to distinguish between date of observation. The variations in Δv_r are subtle, yet steady, and show a clear dependence on epoch. The cycle-dependent RV curve correlates with the cycle-dependence of Δv_r.

(2009, and references therein). However, at this point it is unclear whether QZ Nor changes amplitude secularly (due to its evolution), or whether the RV cycle-dependence is simply due to a variability of an unresolved line doubling pattern. If the latter is the case, a periodicity may suggest a link to the Blazhko phenomenon similarly to the finding of Chadid & Gillet (1997, line doubling stronger in Blazhko RR Lyrae stars) mentioned above.

A cycle-dependent RV curve was also detected for the long-period (41.5 d) Cepheid RS Puppis, see the top panel in Fig. 2.22. This star has much larger RV amplitude than QZ Nor, owing to its much longer period and fundamental-mode pulsation. The variations detected from one cycle to the next can reach up to $3\,\mathrm{km\,s^{-1}}$, which is highly significant. As was the case for QZ Nor, the RV curve changes shape, not simply amplitude, and does so gradually and monotonously over the entire baseline of *CORALIE* observations available. However, in RS Pup, this change is stronger at phase close to 0.0 than at the phase of fastest contraction (~ 0.8), i.e., the opposite direction as seen in QZ Nor.

Although RS Pup and QZ Nor are very different specimen among Cepheids, they share a common phenomenon: cycle-dependent RV curves. This suggests that this phenomenon may be common in Cepheids, leading to RV curves (and therefore radius variation cycles) that are more complex than previously thought. This would create a potentially systematic effect for Baade-Wesselink-type analyses that are of great relevance for the distance scale, see Sec. 1.2.1. Whether these cycle-to-cycle variations are secular or periodic is impossible to say at this point, and further observations shall be made to monitor these targets over longer baselines.

2.8 Doppler tomography

Doppler tomography in this section denotes the separation of a Cepheid's atmosphere in different regions (layers) whose velocities can be measured separately. The motivation for developing this work comes from a number of sources. First is the discovery made by van Hoof & Deurinck (1952) that there is a difference in radial velocities derived from Fe I and Fe II lines (also seen in ℓ Car by Dawe 1969), and the observed phase lag in the acceleration of metallic spectral lines and Hα in the long-period Cepheid T Monocerotis by Wallerstein (1972). Second, Mathias & Gillet (1993) showed that a single atmospheric layer model is not consistent with the observations of β Cephei stars (non-radial pulsators), and Albrow & Cottrell (1994) conclude that: "[...] discrepant line asymmetries cannot be due to geometric projection of a single pulsational velocity, an assumption inherent in calculations of radii and distances by the Baade-Wesselink method", cf. also Wallerstein et al. (1992). Petterson et al. (2005) presented species-by-species RVs for 14 Cepheids, showing that high velocity differences (up to $30\,\mathrm{km\,s^{-1}}$) exist between Hα or Ca II lines and metallic lines (at fixed phase). Among metallic lines, variations at the $1-2\,\mathrm{km\,s^{-1}}$ level were detected.

The observation of line doubling and cycle-dependent RV curves in Cepheids lead me to the question whether the two effects are related, especially since X Sgr exhibits both phenomena, cf. Sec. 2.6. However, cycle-dependent RV curves are discovered in stars that do not exhibit line doubling in their CCFs, namely QZ Nor and RS Pup, cf. Sec. 2.7. Since shock is responsible for line doubling, then perhaps shock is also (indirectly?) related to cycle-dependent RV curves. This is how I became interested to search for signs of shock in Cepheid atmospheres.

The observation of a remarkably strong BIS discontinuity in *CORALIE* data of RS Pup[20] (see Fig. 2.13) prompted me to request two sessions of continuous 6-hour long *CORALIE* observations on the nights of 18 and 19 March 2013. The goal of these observations was to trace the shock wave, if observable, as it passes through the line forming region during the phase when the star

[20]Nardetto et al. (2006) had also noted the exceptionally strong FWHM in a single exposure obtained at this phase and speculated about the presence of shock here

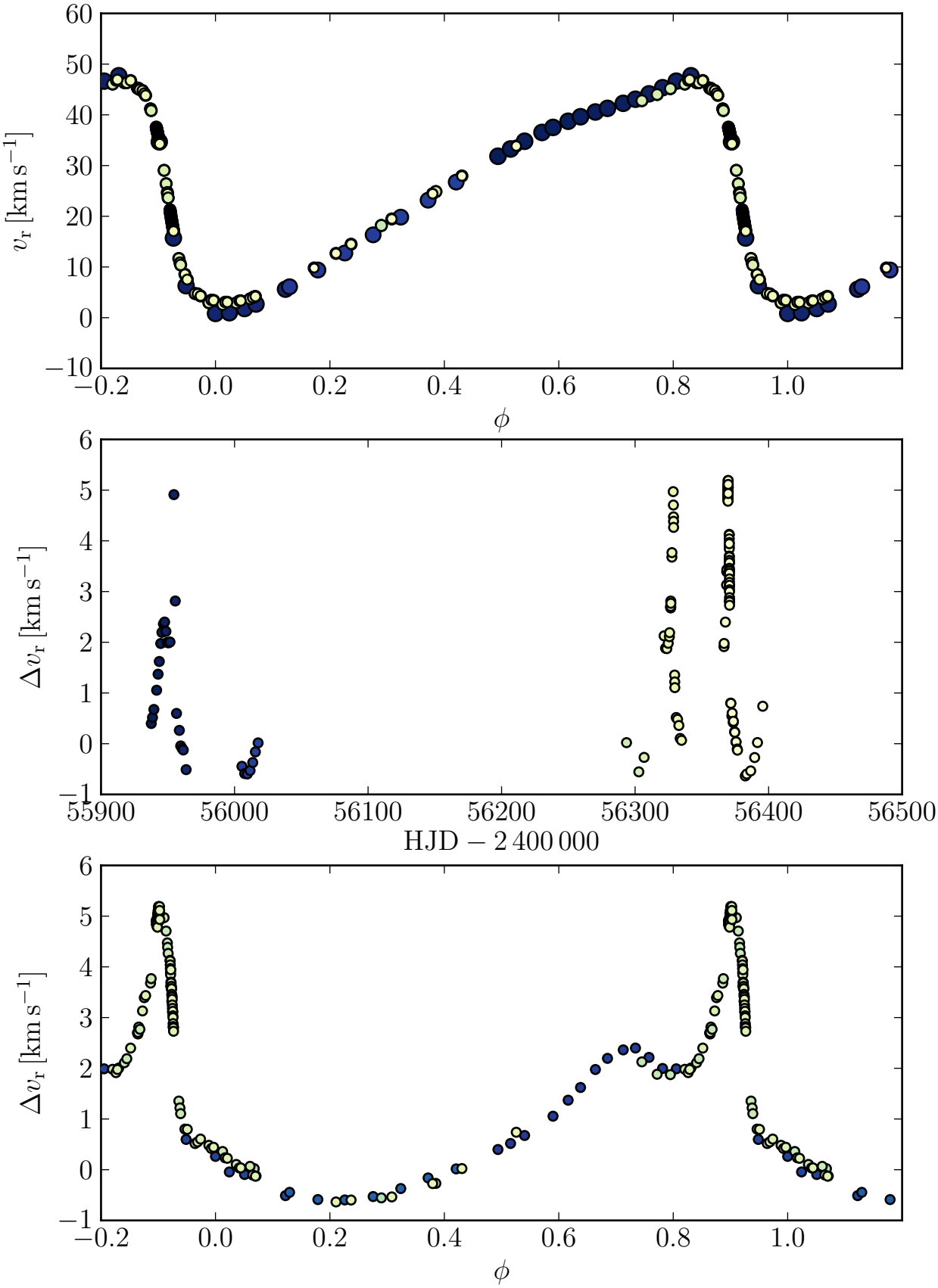

Figure 2.22: Cycle-to-cycle variations and Doppler tomography of RS Puppis. Panels from top to bottom: (Gaussian) RV curve; differential velocity, Δv_r, as defined in Eq. 2.21 against observation date; Δv_r against pulsation phase. Color coding applied to distinguish between date of observation. Δv_r correlates with phase. Variations in RV and Δv_r curves are seen between different epochs. Note the Δv_r discontinuity around $\phi \sim 0.9$, which correlates with the peak in BIS observed in Fig. 2.13).

is maximally contracted and driving its atmosphere outwards, providing a tomographic view of RS Pup's pulsating atmosphere.

Most of the lines in the G2 mask correspond to neutral iron lines. Lines of higher excitation potential require higher temperatures than low-excitation potential lines. This is related to the number of absorbers available and described by the Saha-Boltzmann equation (see e.g. Gray 2008). Since temperature increases towards the interior of the star, lines of higher excitation potential are formed deeper inside the star's atmosphere than low-excitation potential lines, thus tracing different layers inside it. At temperatures around $5500\,\mathrm{K}$, the vast majority of iron is singly ionized, resulting in a strong dependence of line contrast of Fe I on temperature (see also Sec. 2.3). Thus, it can be expected that line contrast of Fe I lines decreases with increasing excitation potential, and that shallower lines therefore tend to trace deeper atmospheric layers than high-contrast lines, see e.g. Grossmann-Doerth (1994) for a more detailed discussion. These facts were exploited previously for Cepheids by Butler (1993), who determined the velocity of lines with different excitation potentials.

Following this interpretation, two line masks were created from the original G2 mask, separating spectral lines formed in an "upper" and a "lower" region of a star's atmosphere. CCFs are then computed for each line mask, providing RV estimates for both layers separately[21]. While there are certain shortcomings of using CCFs for this purpose (such as the difficulty to quantify the geometrical depth of the layers probed by the masks, cf. Jorissen et al. 2003), CCFs have the great advantage of increased S/N compared to individual spectral lines. This fact enables much more precise estimates of RV for the CCF than to individual lines, and therefore allows to search for very small signals.

The line masks were created according to the following considerations: i) they should be equally weighted, i.e., the cumulative distributions of line contrasts are equal; ii) they should trace different line forming regions. Both constraints were satisfied by selecting lines shallower than 0.55 (55% contrast) for the low-contrast (deep) mask, and lines deeper than 0.65 (65% contrast) for the high-contrast mask[22]. Lines with contrasts between $55 - 65\%$ are thus currently excluded from the masks in order to achieve higher tomographic contrast, i.e., a larger velocity difference between the two layers.

By measuring RV using the mask corresponding to the upper (high contrast lines) and lower (low contrast lines) atmospheric layers, it is possible to investigate the differential velocity, Δv, which is defined here as:

$$\Delta v_\mathrm{r} = v_\mathrm{r,upper} - v_\mathrm{r,lower}\,. \tag{2.21}$$

Δv can then be studied as a function of pulsation phase to search for velocity discontinuities, i.e., shock fronts. Studying Δv_r over long baselines furthermore allows to investigate the regularity of the $\Delta v_\mathrm{r}(\phi)$ curve over many cycles, thereby providing a way to investigate the origin of cycle-dependent RV curves.

The results of determining Δv_r for RS Pup and QZ Nor are shown in the center and bottom panels of Figs. 2.22 and 2.21, respectively. The same figures were referred to earlier to illustrate the cycle-dependence of the RV curves of these stars. The center panel shows Δv_r as a function of observation date, the bottom panel as a function of pulsation phase. All are identically color-coded to trace the epoch of observation. To the best of my knowledge, these mark the first CCF-based Doppler tomographic observations of Cepheid atmospheres.

In RS Pup, strong differential motion at the order of several $\mathrm{km\,s^{-1}}$ is detected using these two masks. Δv_r varies significantly with phase, beautifully tracing the outward motion. A remarkable velocity discontinuity is tracked closely (thanks to the dense monitoring effort) around the phase

[21] It is worth noting here that this independently-derived approach constitutes a simpler version of the method applied to long-period variable stars by Alvarez et al. (2000, 2001a).

[22] It is a great please to acknowledge my friend Xavier Dumusque for his contributions to the development of these masks during a particularly cloudy night at La Silla observatory in late May 2013

of maximal contraction, around pulsation phase ~ 0.9. This marks the same phase when the BIS discontinuity is seen, cf. Fig. 2.13. Therefore, it appears evident that the fast reversal of the BIS is associated with the presence of shock in a Cepheid's atmosphere. While this phenomenon is particularly strong in RS Pup, most Cepheids show this behavior in BIS, cf. Fig. 2.11, which is directly related to the slope of the RV curve, i.e., its acceleration around the point of maximum contraction.

Figure 2.22 provides clear evidence for strong shock in RS Pup. This may provide a particularly useful constraint for recent models investigating pulsationally-driven mass loss in Cepheids that include momentum contributions due to pulsation and shock (Neilson & Lester 2008), especially since RS Pup is enshrouded in a very extended circumstellar environment (CSE, see Kervella et al. 2012). Although the currently accepted interpretation seems to be that RS Pup's nebulosity is a remnant of its birthplace, a possible contribution to the CSE due to shock-induced mass-loss is an exciting idea that is well worth following up.

Doppler tomography of QZ Nor (Fig. 2.21) also clearly shows the presence of differential motion between the two layers defined by the masks. However, $\Delta v_{\rm r}$ tends to be much smaller than in RS Pup, undoubtedly due to the lower pulsational amplitude of this overtone Cepheid. No velocity discontinuity resembling that of RS Pup is observed in QZ Nor. Its $\Delta v_{\rm r}(\phi)$ curve is nicely traced over multiple well-sampled pulsation cycles and enables the intriguing discovery that the shape of $\Delta v_{\rm r}(\phi)$ underwent a gradual significant change during the observational baseline of more than 2 years. Comparing points of identical color (same observational epoch) in the top and bottom panels in Fig. 2.21 reveals that the cycle-dependent RV curve is correlated with the shape of $\Delta v_{\rm r}(\phi)$. In fact, when $\Delta v_{\rm r}(\phi)$ is flat, the RV curve has higher amplitude. Furthermore, the average differential velocity of $\sim -0.4\,{\rm km\,s^{-1}}$ obtained during the later epochs is equivalent to the difference between cycle-to-cycle variations observed at the high and low extrema of the RV curve shown in the top panel. It is thus obvious that cycle-dependent RV curves and variations in differential velocity are linked. Further observations shall help to decide whether there is periodicity in this phenomenon.

Currently, $\Delta v_{\rm r}(\phi)$ is derived using Gaussians fitted to CCFs computed using the two different line masks. When (highly-variable) line doubling is resolved (such as in X Sgr), using Gaussians may present a serious limitation, as the center and bottom panels of Fig. 2.20 show.

For X Sgr, no clean temporal variation is yet discernible, although $\Delta v_{\rm r}(\phi)$ reaches values as high as $17\,{\rm km\,s^{-1}}$. Since the observed line splitting pattern changes from one pulsation cycle to the next (Fig. 2.18), it may be best to perform forward modeling of CCFs using simulations of pulsating atmospheres.

These preliminary Doppler tomographic results are very promising and provide a new insight into the pulsation properties of Cepheid atmospheres. They also demonstrate the high-quality results that can be obtained using small, 1m-class telescopes such as Euler, and the importance of a close monitoring of these fascinating stars over long and short baselines.

Comparing Doppler tomography of Cepheids with other radially pulsating stars may lead to additional insights. To this end, high-quality observations of the *Kepler* Cepheid V1154 Cygni and the archetypal star RR Lyrae were obtained using *HERMES* in July 2013. Extremely precise *Kepler* lightcurves are available for both stars, opening the window for comparing Doppler tomographic measurements with space-based photometry.

Monthly Notices of the ROYAL ASTRONOMICAL SOCIETY

MNRAS **430,** 2018–2028 (2013) doi:10.1093/mnras/stt027

Discovery of the spectroscopic binary nature of six southern Cepheids

L. Szabados,[1⋆] A. Derekas,[1,2] L. L. Kiss,[1,2,3] J. Kovács,[3] R. I. Anderson,[4] Cs. Kiss,[1] T. Szalai,[5] P. Székely[6] and J. L. Christiansen[7]

[1]*Konkoly Observatory, Research Centre for Astronomy and Earth Sciences, Hungarian Academy of Sciences, Konkoly Thege Miklós út 15-17, H-1121 Budapest, Hungary*
[2]*Sydney Institute for Astronomy, School of Physics, University of Sydney, NSW 2006, Australia*
[3]*ELTE Gothard-Lendület Research Group, Szent Imre herceg út 112, H-9700 Szombathely, Hungary*
[4]*Observatoire de Genève, Université de Genève, 51 Ch. des Maillettes, CH-1290 Versoix, Switzerland*
[5]*Department of Optics and Quantum Electronics, University of Szeged, Dóm tér 9, H-6720 Szeged, Hungary*
[6]*Department of Experimental Physics, University of Szeged, H-6720 Szeged, Hungary*
[7]*SETI Institute/NASA Ames Research Center, M/S 244-30, Moffett Field, CA 94035, USA*

Accepted 2013 January 3. Received 2013 January 3; in original form 2012 November 22

ABSTRACT

We present the analysis of photometric and spectroscopic data of six bright Galactic Cepheids: GH Carinae, V419 Centauri, V898 Centauri, AD Puppis, AY Sagittarii and ST Velorum. Based on new radial velocity data (in some cases supplemented with earlier data available in the literature), these Cepheids have been found to be members in spectroscopic binary systems. V898 Cen turned out to have one of the largest orbital radial velocity amplitude (>40 km s^{-1}) among the known binary Cepheids. The data are insufficient to determine the orbital periods nor other orbital elements for these new spectroscopic binaries.

These discoveries corroborate the statement on the high frequency of occurrence of binaries among the classical Cepheids, a fact to be taken into account when calibrating the period–luminosity relationship for Cepheids.

We have also compiled all available photometric data that revealed that the pulsation period of AD Pup, the longest period Cepheid in this sample, is continuously increasing with $\Delta P = 0.004567$d century^{-1}, likely to be caused by stellar evolution. The wave-like pattern superimposed on the parabolic $O - C$ graph of AD Pup may well be caused by the light-time effect in the binary system. ST Vel also pulsates with a continuously increasing period. The other four Cepheids are characterized with stable pulsation periods in the last half century.

Key words: binaries: spectroscopic – stars: variables: Cepheids.

1 INTRODUCTION

Classical Cepheid variable stars are primary distance indicators because owing to the famous period–luminosity (P–L) relationship they rank among standard candles in establishing the cosmic distance scale.

Companions to Cepheids, however, complicate the situation. The contribution of the secondary star to the observed brightness has to be taken into account when involving any particular Cepheid in the calibration of the P–L relationship. Binaries among Cepheids are not rare at all: their frequency exceeds 50 per cent for the brightest Cepheids, while among the fainter Cepheids an observational selection effect encumbers revealing binarity (Szabados 2003a).

It is essential to study Cepheids individually from the point of view of binarity before involving them in any calibration procedure (of e.g. P–L or period–radius relationship). This attitude is especially important if Cepheid-related relationships are calibrated using a small sample. However, a deep observational analysis of individual Cepheids can only be performed in the case of their Galactic representatives. When dealing with extragalactic Cepheids, unrevealed binarity is one of the factors that contributes to the dispersion of the P–L relationship. A detailed list of physical factors responsible for the finite width of the P–L relationship around the ridge line approximation is given by Szabados & Klagyivik (2012).

The orbital period of binaries involving a supergiant Cepheid component cannot be shorter than about a year. Spectroscopic binaries involving a Cepheid component with orbital periods longer than a decade are also known (see the online data base on binaries among Galactic Cepheids: http://www.konkoly.hu/CEP/orbit.html). Therefore, a first epoch radial velocity (RV) curve, especially based on data obtained in a single observational season, is usually insufficient for pointing out an orbital effect superimposed on the RV changes due to pulsation.

⋆ E-mail: szabados@konkoly.hu

Table 1. Basic data of the programme stars and the number of spectra.

Star	$\langle V \rangle$ (m)	P (d)	Mode of pulsation	No. of obs.
GH Car	9.18	5.725 532	First overtone	27+43
V419 Cen	8.19	5.507 123	First overtone	26
V898 Cen	8.00	3.527 310	First overtone	33+4
AD Pup	9.91	13.596 919	Fundamental	33
AY Sgr	10.55	6.569 667	Fundamental	22
ST Vel	9.73	5.858 316	Fundamental	27

In the case of pulsating variables, like Cepheids, spectroscopic binarity (SB) manifests itself in a periodic variation of the γ-velocity (i.e. the RV of the mass centre of the Cepheid). In practice, the orbital RV variation of the Cepheid component is superimposed on the RV variations of pulsational origin. To separate the orbital and pulsational effects, knowledge of the accurate pulsation period is essential, especially when comparing RV data obtained at widely differing epochs. Therefore, the pulsation period and its variations have been determined with the method of the $O - C$ diagram (Sterken 2005) for each target Cepheid. Use of the accurate pulsation period obtained from the photometric data is a guarantee for the correct phase matching of the (usually less precise) RV data.

In this paper, we point out SB of six bright Galactic Cepheids by analysing RV data. The structure of this paper is as follows. The new observations and the equipments utilized are described in Section 2. Section 3 is devoted to the results on the six new SB Cepheids: GH Carinae, V419 Centauri, V898 Centauri, AD Puppis, AY Sagittarii and ST Velorum, respectively. Basic information on these Cepheids is found in Table 1. Finally, Section 4 contains our conclusions.

2 NEW OBSERVATIONS

2.1 Spectra from Siding Spring Observatory

We performed a RV survey of Cepheids with the 2.3 m ANU telescope located at Siding Spring Observatory (SSO), Australia. The main aim of the project was to detect Cepheids in binary systems by measuring changes in the mean values of their RV curve which can be interpreted as the orbital motion of the Cepheid around the centre of mass in a binary system (change of γ-velocity). The target list was compiled to include Cepheids with single epoch RV phase curve or without any published RV data. Several Cepheids suspected members in spectroscopic binaries were also put on the target list. On 64 nights between 2004 October and 2006 March we monitored 40 Cepheids with pulsation periods between 2 and 30 d. (V898 Cen was observed in 2009 July too).

Medium-resolution spectra were taken with the Double Beam Spectrograph using the 1200 mm^{-1} gratings in both arms of the spectrograph. The projected slit width was 2 arcsec on the sky, which was about the median seeing during our observations. The spectra covered the wavelength ranges 4200–5200 Å in the blue arm and 5700–6700 Å in the red arm. The dispersion was 0.55 Åpx^{-1}, leading to a nominal resolution of about 1 Å.

All spectra were reduced with standard tasks in IRAF.[1] Reduction consisted of bias and flat-field corrections, aperture extraction, wavelength calibration and continuum normalization. We checked the consistency of wavelength calibrations via the constant positions of strong telluric features, which proved the stability of the system. RVs were determined only for the red arm data with the task *fxcor*, applying the cross-correlation method using a well-matching theoretical template spectrum from the extensive spectral library of Munari et al. (2005). Then, we made barycentric corrections to every single RV value. This method resulted in a 1–2 km s^{-1} uncertainty in the individual RVs, while further tests have shown that our absolute velocity frame was stable to within ±2–3 km s^{-1}. This level of precision is sufficient to detect a number of Cepheid companions, as they can often cause γ-velocity changes well above 10 km s^{-1}.

[1] IRAF is distributed by the National Optical Astronomy Observatories, which are operated by the Association of Universities for Research in Astronomy, Inc., under cooperative agreement with the National Science Foundation.

2.2 FEROS observations in ESO

V898 Centauri was observed on four consecutive nights in 2011 April, using the Fiber-fed Extended Range Optical Spectrograph (FEROS) instrument on the MPG/European Southern Observatory (ESO) 2.2 m telescope in La Silla Observatory, Chile (see Table 10). The FEROS has a total wavelength coverage of 356–920 nm with a resolving power of $R = 48\,000$ (Kaufer et al. 1999, 2000). Two fibres, with entrance aperture of 2.7 arcsec, simultaneously recorded star light and sky background. The detector is a back-illuminated CCD with 2948 × 4096 pixels of 15 μm size. Basic data reduction was performed using a pipeline package for reductions (DRS), in MIDAS environment. The pipeline performs the subtraction of bias and scattered light in the CCD, orders extraction, flat-fielding and wavelength calibration with a ThAr calibration frame (the calibration measurements were performed at the beginning of each night, using the ThAr lamp).

After the continuum normalization of the spectra using IRAF we determined the RVs with the task *fxcor*, as in the case of the SSO spectra (see Section 2.1). The velocities were determined in the region 500–600 nm, where a number of metallic lines are present and hydrogen lines are lacking. We made barycentric corrections to each RV value with the task *rvcorrect*. The estimated uncertainty of the RVs is 0.05 km s^{-1}.

2.3 CORALIE observations from La Silla

GH Car was among the targets during multiple observing campaigns between 2011 April and 2012 May using the fibre-fed high-resolution ($R \sim 60\,000$) echelle spectrograph CORALIE mounted at the Swiss 1.2 m Euler telescope at ESO La Silla Observatory, Chile. The instrument's design is described in Queloz et al. (2001); recent instrumental updates are found in Wilson et al. (2008).

The spectra are reduced by the efficient online reduction pipeline that performs bias correction, cosmics removal and flat-fielding using tungsten lamps. ThAr lamps are used for the wavelength calibration. The reduction pipeline directly determines the RV through cross-correlation (Baranne et al. 1996) using a mask that resembles a G2 spectral type. The RV stability of the instrument is excellent and for non-pulsating stars the RV precision is limited by photon noise, see e.g. Pepe et al. (2002). However, the precision achieved for Cepheids is lower due to line asymmetries. We estimate a typical precision of ∼0.1 km s^{-1} (including systematics due to pulsation) per data point for our data. The RV data are listed in Table 4.

3 RESULTS

3.1 GH Carinae

Accurate value of the pulsation period. The brightness variability of GH Car (HD 306077, $\langle V\rangle = 9.18$ mag) was revealed by Oosterhoff (Hertzsprung 1930). This Cepheid pulsates in the first overtone mode, therefore, it has a small pulsational amplitude and nearly sinusoidal light (and velocity) curve.

In the case of Cepheids pulsating with a low amplitude, the $O-C$ diagram constructed for the median brightness is more reliable than that based on the moments of photometric maxima (Derekas et al. 2012). Therefore, we determined the accurate value of the pulsation period by constructing an $O-C$ diagram for the moments of median brightness (the mid-point between the faintest and the brightest states) on the ascending branch of light curve since it is this phase when the brightness variations are steepest during the whole pulsational cycle.

All published observations of GH Car covering half a century were re-analysed in a homogeneous manner to determine seasonal moments of the chosen light curve feature. The relevant data listed in Table 2 are as follows.

Col. 1: Heliocentric moment of the median brightness on the ascending branch;

Col. 2: epoch number, E, as calculated from equation (1):

$$C = 2\,451\,266.2198 + 5.725\,532\times E \pm 0.0038 \pm 0.000\,004 \quad (1)$$

Table 2. $O-C$ values of GH Carinae (see the description in Section 3.1).

$JD_\odot$ 240 0000+	E	$O-C$	W	Data source
351 48.8988	−2815	+0.0516	2	Walraven, Muller & Oosterhoff (1958)
352 28.9336	−2801	−0.0711	2	Irwin (1961)
407 59.8900	−1835	+0.0214	3	Pel (1976)
441 32.1611	−1246	−0.0458	3	Berdnikov (2008)
481 68.7453	−541	+0.0383	2	*Hipparcos* (ESA 1997)
486 61.1326	−455	+0.0299	2	*Hipparcos* (ESA 1997)
495 42.9049	−301	+0.0702	2	Berdnikov (2008)
498 17.6922	−253	+0.0320	3	Berdnikov (2008)
503 90.1805	−153	−0.0329	3	Berdnikov (2008)
505 73.3930	−121	−0.0374	3	Berdnikov (2008)
508 94.0822	−65	+0.0220	3	Berdnikov (2008)
512 66.2270	0	+0.0072	3	Berdnikov (2008)
516 55.5715	68	+0.0155	3	Berdnikov (2008)
519 53.2783	120	−0.0053	2	ASAS (Pojmanski 2002)
519 58.9981	121	−0.0111	3	Berdnikov (2008)
523 48.3311	189	−0.0142	2	ASAS (Pojmanski 2002)
523 59.7765	191	−0.0199	3	Berdnikov (2008)
526 51.8321	242	+0.0336	3	Berdnikov (2008)
527 83.4687	265	−0.0171	3	ASAS (Pojmanski 2002)
529 72.4125	298	−0.0158	1	*INTEGRAL* OMC
530 12.4642	305	−0.0429	3	Berdnikov (2008)
531 09.8033	322	−0.0378	2	ASAS (Pojmanski 2002)
534 64.8631	384	+0.0390	3	ASAS (Pojmanski 2002)
537 96.9347	442	+0.0298	3	ASAS (Pojmanski 2002)
542 26.3353	517	+0.0155	3	ASAS (Pojmanski 2002)
545 18.3336	568	+0.0116	3	ASAS (Pojmanski 2002)
546 21.3538	586	−0.0278	3	ASAS (Pojmanski 2002)
548 50.4167	626	+0.0139	3	ASAS (Pojmanski 2002)
549 70.5964	647	−0.0426	3	ASAS (Pojmanski 2002)

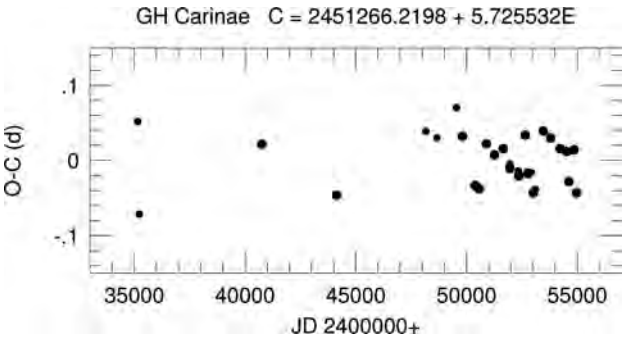

Figure 1. $O-C$ diagram of GH Car based on the values listed in Table 2. The pulsation period of GH Car is constant.

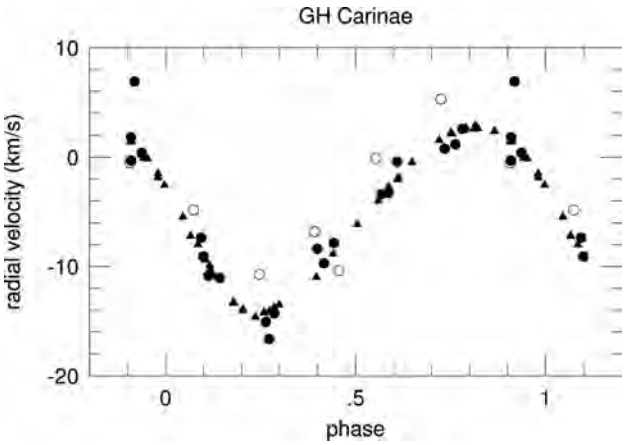

Figure 2. RV phase curve of GH Carinae. The filled circles represent data from 2004–2005, the open circles denote data from 2006, while the CORALIE data obtained in 2011–2012 are marked as triangles.

(this ephemeris has been obtained by the weighted least-squares fit to the tabulated $O-C$ differences);

Col. 3: the corresponding $O-C$ value as calculated from equation (1);

Col. 4: weight assigned to the $O-C$ value (1, 2 or 3 depending on the quality of the light curve leading to the given difference);

Col. 5: reference to the origin of data, preceded by the name of the observer if different from the author(s) cited.

The plot of $O-C$ values shown in Fig. 1 can be approximated with a constant period. The scatter of the points in the figure reflects the observational error and uncertainties in the analysis of the data.

Binarity of GH Car. There are no published RV data for this bright Cepheid. The phase diagram of our RV observations is plotted in Fig. 2. The observational data have been folded on the period given by the ephemeris in equation (1). The zero phase has been arbitrarily chosen at JD 240 0000 (similarly to all phase curves in this paper). Fig. 2 clearly shows a vertical shift between the mean values valid for 2004–2005 and 2006. For the first season, the γ-velocity (the mean RV averaged over a pulsational cycle) was -4.6 km s^{-1}, while one year later it became -3.5 km s^{-1}, while the CORALIE data result in the value of -5.3 km s^{-1} for the γ-velocity. Though the difference is small, homogeneity of the data and the identical treatment is a guarantee that the shift is not an artefact of the analysis. The individual data are listed in Tables 3 and 4.

SB of GH Car has to be verified by further observations.

Table 3. New RV values of GH Carinae from the SSO spectra. This is only a portion of the full version available online only.

$JD_\odot$ 240 0000+	v_{rad} (km s^{-1})
533 64.2431	−8.4
533 67.2163	6.9
533 68.2542	−9.1
533 69.2434	−16.6
534 51.0951	−3.4

Table 4. New CORALIE velocities of GH Carinae. This is only a portion of the full version available online only.

$JD_\odot$ 240 0000+	v_{rad} (km s^{-1})
556 52.8343	−9.9
556 53.8063	−13.7
556 54.6963	−8.9
556 55.6685	−2.0
556 56.6753	2.4

3.2 V419 Centauri

Accurate value of the pulsation period. The brightness variability of V419 Cen (HD 100148, $\langle V\rangle = 8.19$ mag) was revealed by O'Leary & O'Connell (1937). This Cepheid also pulsates in the first overtone mode, so the $O-C$ diagram was also constructed for the moments of the median brightness on the ascending branch, similar to the case of GH Car (see Section 3.1).

The $O-C$ diagram of V419 Cen based on the $O-C$ values listed in Table5 is shown in Fig. 3. The plot can be approximated by a constant period by the ephemeris for the moments of median brightness on the ascending branch:

$$C = 2\,452\,357.3949 + 5.507\,123\times E \pm 0.0053 \pm 0.000\,005. \quad (2)$$

However, a parabolic pattern indicating a continuously increasing period cannot be excluded. For the proper phasing of the RV data it is important that the $O-C$ differences are about zero for each epoch when RV data were obtained.

Binarity of V419 Cen. All RV data (including the new ones listed in Table 6) have been folded on the accurate pulsation period taken from the ephemeris given in equation (2), so the different data series have been correctly phased with respect to each other. The merged RV phase curve is plotted in Fig. 4. The individual data series are denoted with different symbols: filled squares – RVs from 1952 by Stibbs (1955); empty triangles – data by Lloyd Evans (1980) from 1969 to 1970; filled and empty circles – our 2004–2005 and 2006 data, respectively.

Variability in the γ-velocity is striking. Systematic errors can be excluded. Although our 2006 data are shifted to a larger value of the γ-velocity, similarly to the case of GH Car (see Section 3.1), other new spectroscopic binaries and dozens of Cepheids in our sample with non-varying γ-velocities indicate stability of the equipment and reliability of the data reduction. Another piece of evidence in favour of the intrinsic variability of the γ-velocity is that both Stibbs (1955) and Lloyd Evans (1980) used the same spectrograph during their observations.

To have a clearer picture, the γ-velocities (together with their uncertainties) are listed in Table 7 and also plotted in Fig. 5. The last two points (which are the most accurate ones), i.e. the shift between 2004–2005 and 2006 data implies an orbital period of several years instead of several decades suggested by the whole pattern of the plot.

Table 5. $O-C$ values of V419 Centauri (see the description in Section 3.1).

$JD_\odot$ 240 0000+	E	$O-C$	W	Data source
348 17.2512	−3185	+0.0431	2	Walraven et al. (1958)
352 19.2722	−3112	+0.0441	3	Irwin (1961)
402 85.8001	−2192	+0.0188	3	Stobie (1970)
407 37.4108	−2110	+0.0454	3	Pel (1976)
428 96.1636	−1718	+0.0060	3	Dean (1977)
443 00.3547	−1463	−0.1193	2	Berdnikov (2008)
446 30.7521	−1403	−0.1492	2	Eggen (1985)
481 66.4174	−761	−0.0569	3	*Hipparcos* (ESA 1997)
486 89.5720	−666	−0.0790	3	*Hipparcos* (ESA 1997)
495 43.1967	−511	−0.0583	2	Berdnikov (2008)
498 13.0946	−462	−0.0095	3	Berdnikov (2008)
503 85.8636	−358	+0.0187	2	Berdnikov (2008)
505 73.1155	−324	+0.0285	3	Berdnikov (2008)
509 03.5445	−264	+0.0301	3	Berdnikov (2008)
512 61.4846	−199	+0.0072	3	Berdnikov (2008)
516 47.0071	−129	+0.0311	3	Berdnikov (2008)
519 55.3943	−73	+0.0194	3	ASAS (Pojmanski 2002)
519 60.9164	−72	+0.0344	3	Berdnikov (2008)
521 26.0927	−42	+0.0030	3	ASAS (Pojmanski 2002)
523 57.3861	0	−0.0088	3	Berdnikov (2008)
524 67.5557	20	+0.0183	3	ASAS (Pojmanski 2002)
526 43.7458	52	−0.0195	3	Berdnikov (2008)
527 31.8585	68	−0.0208	3	ASAS (Pojmanski 2002)
530 12.7265	119	−0.0160	3	Berdnikov (2008)
530 62.2908	128	−0.0158	3	ASAS (Pojmanski 2002)
534 75.3737	203	+0.0328	3	ASAS (Pojmanski 2002)
535 24.8954	212	−0.0096	2	*INTEGRAL* OMC
537 89.2626	260	+0.0157	3	ASAS (Pojmanski 2002)
541 36.1005	323	−0.0951	1	*INTEGRAL* OMC
541 91.2873	333	+0.0204	3	ASAS (Pojmanski 2002)
545 87.8324	405	+0.0527	3	ASAS (Pojmanski 2002)
549 18.2426	465	+0.0355	3	ASAS (Pojmanski 2002)

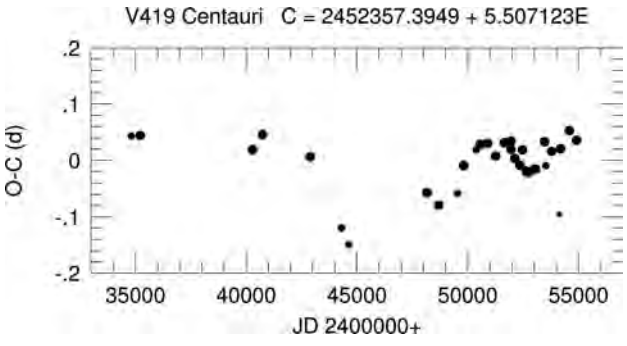

Figure 3. $O-C$ diagram of V419 Cen. The plot can be approximated by a constant period but a parabolic pattern indicating a continuously increasing period cannot be excluded.

Table 6. New RV values of V419 Centauri from the SSO spectra. This is only a portion of the full version available online only.

$JD_\odot$ 240 0000+	v_{rad} (km s^{-1})
533 69.2636	−1.8
534 51.1179	−4.8
534 52.0995	3.9
534 53.1895	−1.5
534 54.1215	−7.9

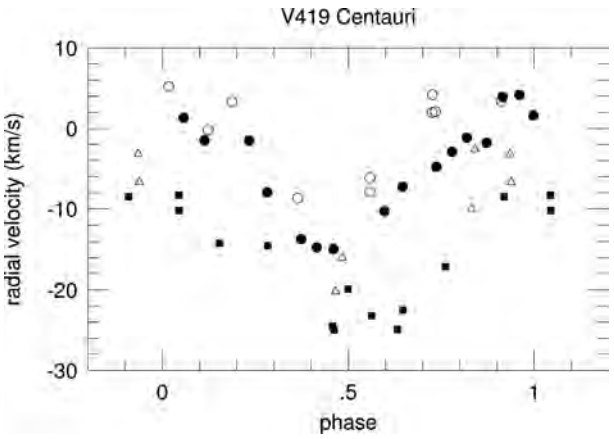

Figure 4. Merged RV phase curve of V419 Cen. There is a striking difference between the γ-velocities valid for the epoch of Stibbs' (1955) and Lloyd Evans' (1980) data (denoted as filled squares and empty triangles, respectively) and our recent data (denoted by circles, see the text).

Table 7. γ-velocities of V419 Centauri.

Mid-JD 240 0000+	v_γ (km s^{-1})	σ (km s^{-1})	Data source
341 29	−16.40	1.3	Stibbs (1955)
405 50	−11.70	1.5	Lloyd Evans (1980)
534 74	−5.53	0.3	This paper
538 00	−0.96	0.5	This paper

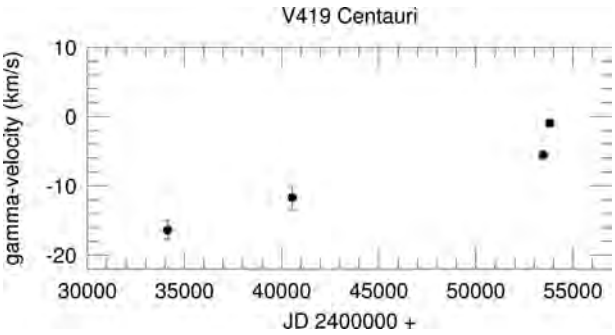

Figure 5. Temporal shift in the γ-velocity of V419 Cen.

3.3 V898 Centauri

Accurate value of the pulsation period. The brightness variability of V898 Cen (HD 97317, $\langle V\rangle = 8.00$ mag) was revealed by Strohmeier, Knigge & Ott (1964). This is also a low amplitude Cepheid pulsating in the first overtone mode. The first reliable photometric data were only obtained during the *Hipparcos* space astrometry mission (ESA 1997). Later on Berdnikov and his coworkers followed the photometric behaviour of V898 Cen (Berdnikov 2008).

Table 8. $O-C$ values of V898 Centauri (description of the columns is given in Section 3.1).

$JD_\odot$ 240 0000+	E	$O-C$	W	Data source
479 55.2823	−1247	+0.0023	3	*Hipparcos* (ESA 1997)
483 11.5410	−1146	+0.0027	3	*Hipparcos* (ESA 1997)
486 92.4782	−1038	−0.0096	3	*Hipparcos* (ESA 1997)
512 60.3772	−310	+0.0077	3	Berdnikov (2008)
516 48.3705	−200	−0.0031	3	Berdnikov (2008)
519 58.7588	−112	−0.0181	3	Berdnikov (2008)
523 53.8561	0	+0.0205	3	Berdnikov (2008)
526 50.1280	84	−0.0016	3	Berdnikov (2008)
530 06.4034	185	+0.0155	3	Berdnikov (2008)
531 40.4565	223	+0.0308	2	*INTEGRAL* OMC
537 18.7991	387	−0.1055	1	*INTEGRAL* OMC

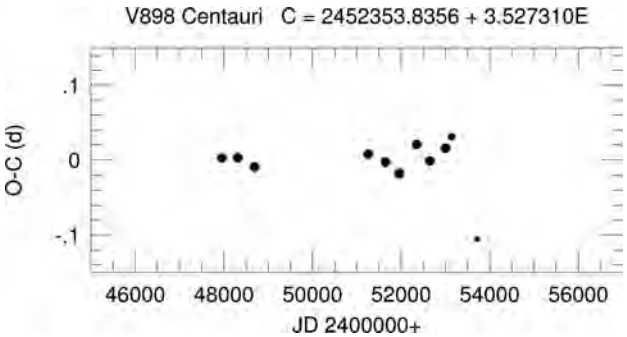

Figure 6. $O-C$ diagram of V898 Cen. The plot can be approximated by a constant period.

The $O-C$ diagram of V898 Cen was constructed for the moments of median brightness on the ascending branch (see Table 8). The weighted least-squares fit to the $O-C$ values resulted in the ephemeris:

$$C = 2\,452\,353.8356 + 3.527\,310\times E \pm 0.0052 \pm 0.000\,008. \quad (3)$$

The $O-C$ diagram of V898 Cen plotted in Fig. 6 indicates constancy of the pulsation period.

Binarity of V898 Cen. The Cepheid variable V898 Cen has been neglected from the point of view of spectroscopy, as well. A spectral type of F3III has been assigned to it in the SIMBAD data base which is atypical of a Cepheid (and probably erroneous). Cepheids are supergiants of Iab or Ib luminosity class and their short period representatives have a late F spectral type. Ironically, there is a single RV data, -2.4 ± 2.4 km s^{-1} (which is an average of two measurements) published by Nordström et al. (2004) in their catalogue of 14000 *dwarf* stars of F and G spectral types. However, the epoch of these particular observations has remained unknown. Therefore, our data provide a first epoch RV phase curve.

It became obvious already in the first observing season that an orbital effect is superimposed on the RV variations of pulsational origin (see the left-part of Fig. 7). Therefore, several spectra of V898

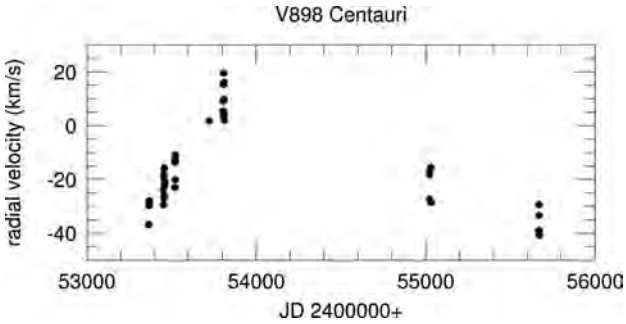

Figure 7. Merged RV curve of V898 Cen.

Table 9. New RV values of V898 Centauri from the SSO spectra. This is only a portion of the full version available online only.

$JD_\odot$ 240 0000+	v_{rad} (km s^{-1})
533 64.2485	−36.8
533 67.2225	−29.7
533 68.2618	−27.9
533 69.2529	−29.4
534 51.1003	−23.7

Table 10. New FEROS velocities of V898 Centauri.

$JD_\odot$ 240 0000+	v_{rad} (km s^{-1})
556 67.5948	−39.02
556 68.6044	−29.44
556 69.5644	−33.40
556 70.7789	−40.74

Cen have been taken in 2009 and 2011, as well. Our individual RV data are listed in Tables 9 and 10. Based on these data, the RV phase curve has been constructed using the 3.527 310 d pulsation period appearing in equation (3). The wide scatter in this phase curve plotted in Fig. 8 corresponds to a variable γ-velocity. The data series has been split into seven segments, denoted by different symbols in Fig. 8: empty circles – 2004 December; filled circles – 2005 March; empty squares – 2005 May–June; filled square – 2005 December; empty triangles – 2006 March; filled triangles – 2009 July and filled pentagons – 2011 April.

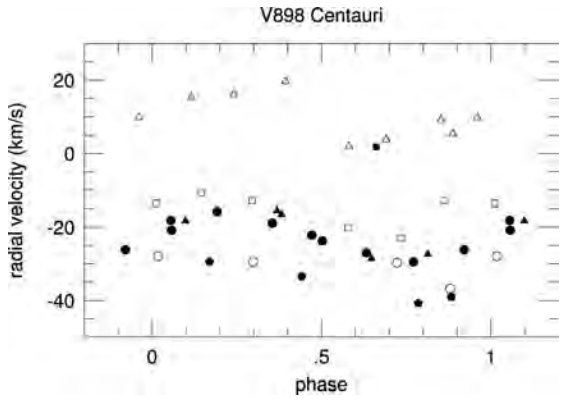

Figure 8. RV phase curve of V898 Cen. Various symbols refer to different observational runs (see the text).

Table 11. γ-velocities of V898 Centauri.

Mid-JD 240 0000+	v_γ (km s^{-1})	σ (km s^{-1})	Data source
533 67.7	−29.9	0.5	This paper
534 55.5	−22.8	0.4	This paper
535 21.4	−15.6	0.5	This paper
537 23.3	1.8	0.6	This paper
538 07.5	10.7	0.4	This paper
550 26.3	−21.8	0.5	This paper
556 69.2	−35.1	0.5	This paper

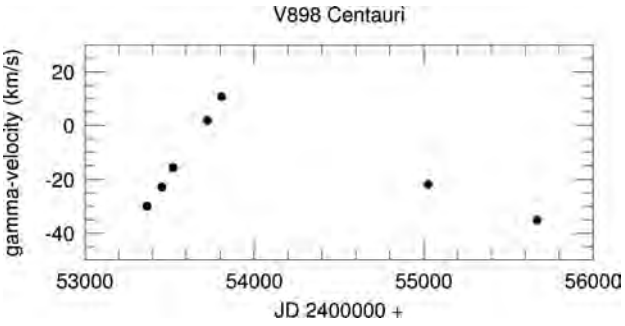

Figure 9. Temporal drift in the γ-velocity of V898 Centauri.

The γ-velocities determined from each data segment are listed in Table 11 and are plotted in Fig. 9. This latter plot implies that V898 Cen is a new spectroscopic binary and the orbital period is about 2000 or 3000 d, depending on whether the most negative value of the γ-velocity occurred before or after our measurements in 2011. The pattern of the points implies a non-sinusoidal shape of the orbital velocity phase curve, with much steeper ascending branch than descending one. This is a strong indication of an eccentric orbit; however, far more seasons of observations are needed before attempting to derive accurate orbital elements from the γ-velocity variations. The most important feature of Fig. 9 is the large amplitude of the orbital velocity variations: it exceeds 40 km s^{-1}. The 'recorder' among the known binary systems involving a Cepheid component has been the system of SU Cygni with a peak-to-peak orbital amplitude of 60 km s^{-1} (see the online data base of Cepheids in binary systems described by Szabados 2003a).

The orbital motion of the Cepheid component around the centre of mass in the binary system may cause a light-time effect in the $O - C$ diagram of the given variable star. In the case of V898 Cen the wave-like pattern characteristic of the light-time effect cannot be detected yet (see Fig. 6).

To provide reliable values for the physical properties of this bright Cepheid, our FEROS spectra were analysed in detail. The parameters $T_{\rm eff}$, $\log g$, [M/H] and $v \sin i$ were determined by searching for the best-fitting model in the synthetic spectrum library of Munari et al. (2005) using a standard χ^2 procedure. To derive the parameters and their errors we applied the following method. The model spectra were ordered according to their calculated χ^2 value, then we selected all with number less than 1.05 $\chi^2_{\rm min}$ and adopted the means and the standard deviations of this sample as values and errors of the parameters.

The best-fitting values are as follows:

$T_{\rm eff} = 5950 \pm 380$ K,
$\log g = 1.2 \pm 0.7$,
$[{\rm M/H}] = -0.4 \pm 0.2$
$v \sin i = 2 \pm 2$.

The effective temperature obtained by us corresponds to an F9 spectral type supergiant star, a typical value of a short-period Cepheid. Note, however, that these values are preliminary ones. The large number of SSO spectra of all 40 target Cepheids will be analysed for obtaining physical properties with smaller uncertainties.

3.4 AD Puppis

Accurate value of the pulsation period. The brightness variability of AD Pup (HD 63446, $\langle V \rangle = 9.91$ mag) was revealed by Hertzsprung (Wesselink 1935). This is the longest period Cepheid in this paper and it has been frequently observed from the 1950s. Long-period Cepheids are usually fundamental pulsators and they oscillate with a large amplitude. In their case, the $O-C$ analysis is based on the moments of brightness maxima.

The $O-C$ differences of AD Puppis are listed in Table 12. These values have been obtained by the following ephemeris:

$$C = 2\,451\,935.3031 + 13.596\,919 \times E \\ \pm 0.0065 \pm 0.000\,040 \qquad (4)$$

Table 12. $O-C$ values of AD Puppis (description of the columns is given in Section 3.1 but the first column contains the moments of brightness maxima).

$JD_\odot$ 240 0000+	E	$O-C$	W	Data source
346 14.2663	−1274	+1.4380	1	Walraven et al. (1958)
352 12.4702	−1230	+1.3775	2	Irwin (1961)
408 81.6304	−813	+0.6224	3	Pel (1976)
416 56.4884	−756	+0.4561	3	Madore (1975)
445 52.3367	−543	+0.1606	2	Eggen (1983)
456 94.4366	−459	+0.1193	2	Berdnikov (2008)
479 24.3692	−295	+0.1572	2	*Hipparcos* (ESA 1997)
484 00.1048	−260	+0.0006	3	*Hipparcos* (ESA 1997)
487 67.2244	−233	+0.0034	2	*Hipparcos* (ESA 1997)
498 14.2750	−156	+0.0913	3	Berdnikov (2008)
508 06.7186	−83	−0.0402	2	Berdnikov (2008)
512 69.0641	−49	+0.0100	3	Berdnikov (2008)
516 49.8321	−21	+0.0643	3	Berdnikov (2008)
519 35.3197	0	+0.0166	3	ASAS (Pojmanski 2002)
519 62.5484	2	+0.0515	3	Berdnikov (2008)
522 34.5236	22	+0.0883	3	ASAS (Pojmanski 2002)
523 43.2076	30	−0.0031	3	Berdnikov (2008)
524 11.1912	35	−0.0041	3	ASAS (Pojmanski 2002)
526 42.3572	52	+0.0143	3	Berdnikov (2008)
527 23.9484	58	+0.0240	3	ASAS (Pojmanski 2002)
529 95.8827	78	+0.0199	3	Berdnikov (2008)
530 50.3131	82	+0.0626	3	ASAS (Pojmanski 2002)
532 54.2231	97	+0.0189	3	*INTEGRAL* OMC
534 44.5663	111	+0.0052	3	ASAS (Pojmanski 2002)
537 70.8223	135	−0.0649	3	ASAS (Pojmanski 2002)
538 52.4136	141	−0.0551	3	ASAS (Pojmanski 2002)
541 78.8427	165	+0.0480	3	ASAS (Pojmanski 2002)
545 32.3418	191	+0.0272	3	ASAS (Pojmanski 2002)
548 31.3885	213	−0.0583	3	ASAS (Pojmanski 2002)

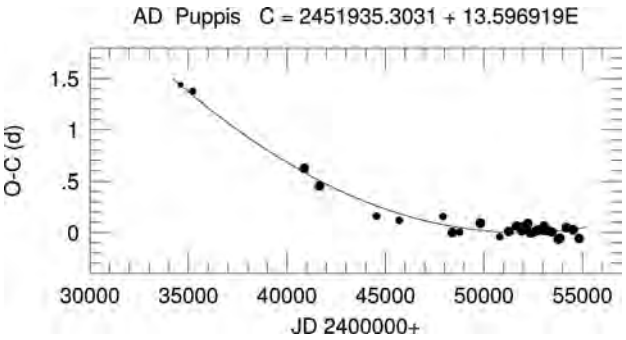

Figure 10. $O-C$ diagram of AD Pup. The plot can be approximated by a parabola indicating a continuously increasing pulsation period.

which contains the constant and linear terms of the weighted parabolic fit to the $O-C$ values. The parabolic nature of the $O-C$ diagram is clearly seen in Fig. 10.

This parabolic trend corresponds to a continuous period increase of $(1.7 \pm 0.09) \times 10^{-6}$ d cycle^{-1}, i.e. $\Delta P = 0.004567$ d century^{-1}. This tiny but non-negligible period increase has been caused by stellar evolution: while the Cepheid crosses the instability region towards lower temperatures in the Hertzsprung–Russell diagram, its pulsation period is increasing. Continuous period variations (of either sign) often occur in the pulsation of long-period Cepheids (Szabados 1983).

The pattern of fluctuations around the fitted parabola shows a wavy nature with a characteristic period of about 50 years as if it were a light-time effect.

Binarity of AD Pup. The earlier RV data by Joy (1937) imply a significantly different γ-velocity (66.5 km s^{-1}) than our recent ones (74.0 km s^{-1}) in spite of the uncertainty of his individual data as large as 4 km s^{-1}. Because the zero-point of Joy's system is reliable, as discussed by Szabados (1996), there is no systematic difference of instrumental or data treatment origin between Joy's and the more recent observational series. The only plausible explanation for the shift in the γ-velocity is the orbital motion in a binary system superimposed on the pulsational RV changes. The shift in the γ-velocity is obvious in the phase diagram of the RVs of AD Puppis plotted in Fig. 11 where Joy's data are denoted with empty squares, while our data are represented with filled circles. The γ-velocity of AD

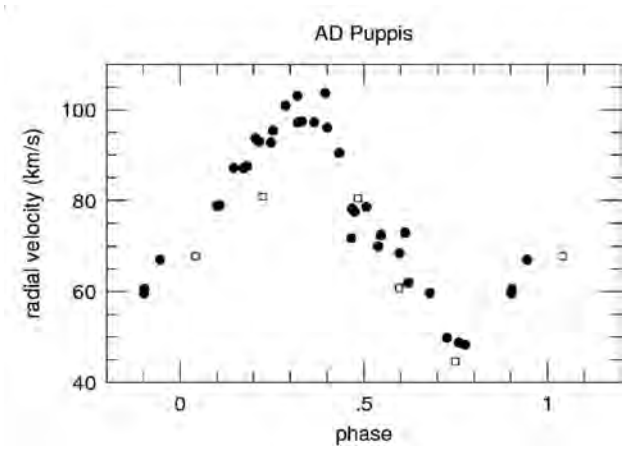

Figure 11. Merged RV phase curve of AD Pup. There is an obvious shift between the γ-velocities valid for the epoch of Joy's (1937) data (denoted by empty squares) and our data (filled circles).

Table 13. New RV values of AD Puppis from the SSO spectra. This is only a portion of the full version available online only.

$JD_\odot$ 2 400 000+	v_{rad} (km s^{-1})
533 04.2658	103.1
533 06.2580	71.8
533 07.2487	70.0
533 08.2504	72.9
533 09.1650	59.7

Pup did not change notably during the interval of our observations. Our RV data (listed in Table 13) have been folded with the period as given in the ephemeris in equation (4). Joy's data have been phased with the same period but a proper correction has been applied to correct for the phase shift due to the parabolic $O-C$ graph.

The smaller value of the γ-velocity determined from Joy's (1937) data is in a qualitative agreement with the wave-like pattern superimposed on the fitted parabola in Fig. 10. In this particular case, the light-time effect interpretation implies a 50 year-long orbital period.

3.5 AY Sagittarii

Accurate value of the pulsation period. The brightness variability of AY Sgr (HIP 90110, $\langle V\rangle = 10.55$ mag) was revealed by Henrietta Leavitt (Pickering 1904). Hoffmeister (1923) determined the pulsation period to be 6.744 26 d from his unpublished visual observations made in 1917–1918. Interestingly enough, this period is about 3 per cent longer than the value deduced from the $O-C$ diagram (see Table 14 and Fig. 12). Such a strong period change, if it really happened, is unprecedented among classical Cepheids.

Table 14. $O-C$ values of AY Sagittarii (description of the columns is given in Section 3.1 but the first column contains the moments of brightness maxima).

$JD_\odot$ 2400000+	E	$O-C$	W	Data source
214 25.45	−4722	−2.04	–	Hoffmeister (1923)
270 51.2394	−3866	0.1098	1	Florya & Kukarkina (1953)
349 60.9601	−2662	−0.0485	3	Walraven et al. (1958)
368 13.6830	−2380	+0.0283	3	Weaver, Steinmetz & Mitchell (1960)
407 81.6694	−1776	−0.0642	3	Pel (1976)
439 08.8993	−1300	+0.0042	2	Harris (1980)
483 30.3254	−627	+0.0444	2	*Hipparcos* (ESA 1997)
499 46.4248	−381	+0.0057	2	Berdnikov (2008)
509 05.5915	−235	+0.0010	3	Berdnikov (2008)
512 73.5280	−179	+0.0027	3	Berdnikov (2008)
516 47.9618	−122	−0.0010	3	Berdnikov (2008)
520 88.1177	−55	−0.0128	3	ASAS (Pojmanski 2002)
524 49.4780	0	+0.0158	3	ASAS (Pojmanski 2002)
528 43.6666	60	+0.0244	3	ASAS (Pojmanski 2002)
529 09.3756	70	+0.0367	3	*INTEGRAL* OMC
530 93.2519	98	−0.0377	3	Berdnikov (2008)
531 65.5436	109	−0.0123	3	ASAS (Pojmanski 2002)
535 59.7519	169	+0.0160	3	ASAS (Pojmanski 2002)
538 61.9333	215	−0.0073	3	ASAS (Pojmanski 2002)
543 41.5068	288	−0.0195	3	ASAS (Pojmanski 2002)
546 50.3169	335	+0.0163	2	*INTEGRAL* OMC
547 42.2598	349	−0.0162	3	ASAS (Pojmanski 2002)
549 85.3351	386	−0.0186	3	ASAS (Pojmanski 2002)

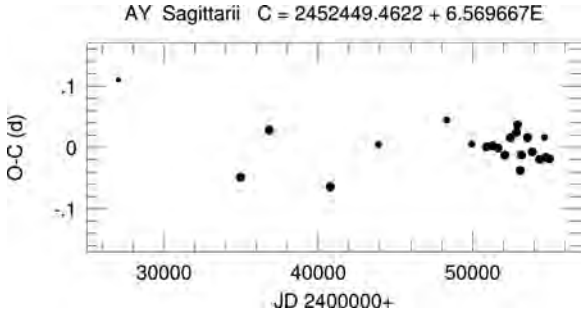

Figure 12. $O-C$ diagram of AY Sgr. The plot can be approximated by a constant period.

Table 15. New RV values of AY Sagittarii from the SSO spectra. This is only a portion of the full version available online only.

$JD_\odot$ 240 0000+	v_{rad} (km s^{-1})
534 51.2048	−12.9
534 52.2318	−6.1
534 53.2541	5.3
534 54.2702	−29.7
534 55.2032	−32.7

AY Sgr is a fundamental mode pulsator, so its $O-C$ diagram has been constructed based on the moments of brightness maxima. The tabulated $O-C$ values have been calculated by using the ephemeris:

$$C = 2\,452\,449.4622 + 6.569\,667\times E \\ \pm 0.0044 \pm 0.000\,004 \quad (5)$$

based on applying a weighted linear least-squares fit to the $O-C$ differences.

As is seen in Fig. 12, the pulsation period of AY Sgr has remained practically constant over decades.

Binarity of AY Sgr. Our new RV data are listed in Table 15. The first epoch RV phase curve of AY Sgr by Joy (1937) has been followed by our one 25 000 d later. The merged RV phase curve in Fig. 13 shows a significant increase in the γ-velocity during eight decades: at JD 242 7640 $v_\gamma = -22.4$ km s^{-1}, while at JD 245 3550 $v_\gamma = -15.5$ km s^{-1} indicating the membership of AY Sgr in a spectroscopic binary system. During the two observing seasons covered by our spectroscopic observations, no shift in the γ-velocity is apparent. Nevertheless, the larger amplitude of the phase curve based on Joy's data may be the consequence of the orbital motion in the binary system during his five-year-long observational interval.

3.6 ST Velorum

Accurate value of the pulsation period. The brightness variability of ST Vel (CD −50° 3533), $\langle V\rangle = 9.73$ mag) was suspected by Kapteyn (Gill & Innes 1903) and it was reported as a new variable by Cannon et al. (1909). Being a Cepheid that pulsates in the fundamental mode, the $O-C$ diagram in Fig. 14 has been constructed for the moments of brightness maxima listed in Table 16. The final ephemeris obtained by a weighted parabolic least-squares fit is

$$C = 2\,451\,939.5962 + 5.858\,316\times E \\ \pm 0.0025 \pm 0.000\,006. \quad (6)$$

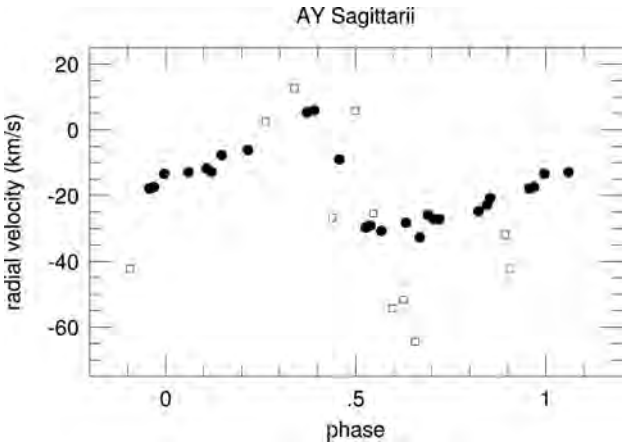

Figure 13. Merged RV phase curve of AY Sgr. There is a striking difference between the γ-velocities valid for the epoch of Joy's (1937) data (denoted as empty squares) and our recent data (filled circles).

The second-order term omitted from equation (6) results in a continuous increase in the pulsation period amounting to $(3.04 \pm 0.58) \times 10^{-8}$ d cycle^{-1}, i.e. 16.36 s century^{-1}.

Binarity of ST Vel. The available RV data – those by Pont et al. (1994) and our new ones listed in Table 17 – have been plotted in Fig. 15. When folding the data into a phase curve, the period of 5.858 316 d given in the equation (6) was used but due to the parabolic pattern of the $O-C$ graph, a tiny correction was applied when plotting the data by Pont et al. (1994). It is noteworthy that our own data show an excessive scatter that can be explained in terms of the variation in the γ-velocity. This effect is clearly seen in Fig. 16 where the annual γ-velocities listed in Table 18 have been plotted. The pattern of the points in this figure implies that the orbital period can be several hundred days, which is rather short among the spectroscopic binaries containing a Cepheid component.

4 CONCLUSIONS

We pointed out that six southern Galactic Cepheids, GH Carinae, V419 Centauri, V898 Centauri, AD Puppis, AY Sagittarii and ST Velorum have a variable γ-velocity which implies their membership in spectroscopic binary systems. The available RV data are insufficient to determine the orbital period and other elements of the orbit. We can only state that the orbital period of V419 Cen is several years, for V898 Cen it is 2000–3000 d, for AD Pup about 50 years, and for ST Vel several hundred days.

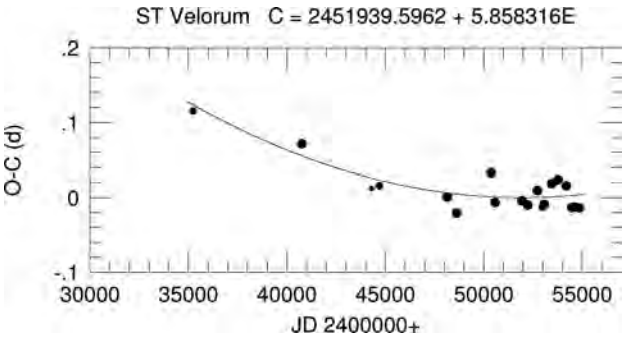

Figure 14. $O-C$ diagram of ST Vel. The plot can be approximated by a parabola indicating a continuous period increase.

Table 16. $O-C$ values of ST Velorum (description of the columns is given in Section 3.1 but the first column contains the moments of brightness maxima).

JD$_\odot$ 240 0000+	E	$O-C$	W	Data source
352 43.5109	−2850	+0.1153	2	Walraven et al. (1958)+ Irwin (1961)
407 62.0007	−1908	+0.0714	3	Pel (1976)
443 00.3645	−1304	+0.0124	1	Berdnikov (2008)
447 04.5918	−1235	+0.0159	2	Eggen (1985)
481 49.2664	−647	+0.0007	3	*Hipparcos* (ESA 1997)
486 29.6270	−565	−0.0207	3	*Hipparcos* (ESA 1997)
503 75.4585	−267	+0.0327	3	Berdnikov (2008)
505 74.6022	−233	−0.0064	3	Berdnikov (2008)
519 39.5921	0	−0.0041	3	ASAS (Pojmanski 2002)
522 38.3603	51	−0.0100	3	ASAS (Pojmanski 2002)
527 24.6201	134	+0.0096	3	ASAS (Pojmanski 2002)
529 76.5052	177	−0.0129	2	*INTEGRAL* OMC
530 70.2422	193	−0.0090	3	ASAS (Pojmanski 2002)
534 51.0604	258	+0.0187	3	ASAS (Pojmanski 2002)
537 67.4149	312	+0.0241	3	*INTEGRAL* OMC
537 79.1313	314	+0.0239	3	ASAS (Pojmanski 2002)
541 89.2053	384	+0.0158	3	ASAS (Pojmanski 2002)
544 70.3755	432	−0.0132	3	ASAS (Pojmanski 2002)
545 99.2593	454	−0.0124	3	ASAS (Pojmanski 2002)
548 62.8823	499	−0.0136	3	ASAS (Pojmanski 2002)

Table 17. New RV values of ST Velorum from the SSO spectra. This is only a portion of the full version available online only.

JD$_\odot$ 240 0000+	$v_{\rm rad}$ (km s^{-1})
533 10.2539	−12.9
533 12.2108	−1.9
533 64.2096	−9.1
533 67.1854	18.5
534 50.9950	−6.8

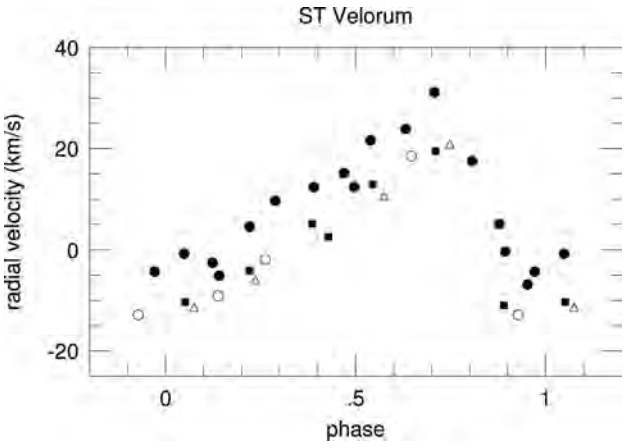

Figure 15. Merged RV phase curve of ST Vel. The triangles represent RVs obtained by Pont, Burki & Mayor (1994), our data are split into three parts: those from 2004 (empty circles), from 2005 (filled circles) and 2006 (filled squares).

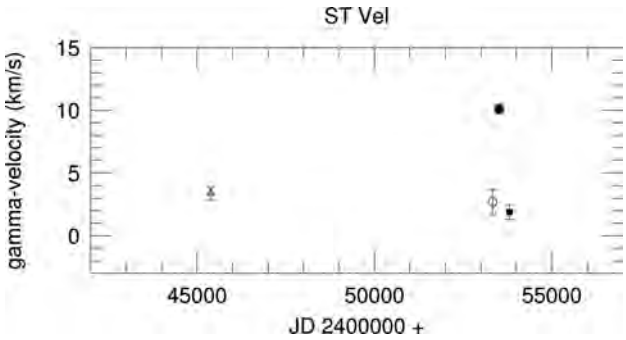

Figure 16. Temporal variations in the γ-velocity of ST Velorum. The symbols are consistent with those used in Fig. 15.

Table 18. γ-velocities of ST Velorum.

Mid-JD 2400000+	v_γ (km s^{-1})	σ (km s^{-1})	Data source
453 92	3.4	0.5	Pont et al. (1994)
533 35	2.7	1.0	This paper
535 20	10.1	0.4	This paper
538 08	1.9	0.6	This paper

The value of the orbital period for spectroscopic binary systems involving a Cepheid component is often unknown: according to the online data base (Szabados 2003a) the orbital period has been determined for about 20 per cent of the known SB Cepheids. Majority of the known orbital periods exceeds a thousand days.

Our finding confirms the previous statement by Szabados (2003a) about the high percentage of binaries among classical Cepheids and the observational selection effect hindering the discovery of new cases.

RV data obtained prior to ours were instrumental in discovering binarity of V419 Cen, AD Pup, AY Sgr and ST Vel, while the spectroscopic binary nature of GH Car and V898 Cen has been discovered from our observations alone.

A companion star may have various effects on the photometric properties of the Cepheid component. Various pieces of evidence of duplicity based on the photometric criteria are discussed by Szabados (2003b) and Klagyivik & Szabados (2009). As to our targets, there is no obvious sign of companion from photometry alone. This indicates that the companion star cannot be much hotter than the Cepheid component in either case. Nevertheless, weak evidence of anomalous photometric behaviour was reported for GH Car by Madore & Fernie (1980) (abnormal phase shift between the light curves in different photometric bands) and for V419 Cen by Onnembo et al. (1985) (anomalous behaviour when determining its physical parameters with the CORS method). The strange spectral type of F3III for V898 Cen appearing in the SIMBAD data base may be wrong because an F9 spectral type has been deduced from our spectra. Further spectroscopic observations are necessary to characterize these binary systems. In addition, accurate future photometric observations can be instrumental in confirming the interpretation of the wavy pattern superimposed on the parabolic $O - C$ graph of AD Pup in terms of a light-time effect.

Regular monitoring of the RVs of a large number of Cepheids will be instrumental in finding more long-period spectroscopic binaries among Cepheids. Quite recently, Evans et al. (2012) reported on their on-going survey for pointing out binarity of Cepheids from the existing RV data covering sufficiently long time interval. RV data to be obtained with the *Gaia* astrometric space probe (expected launch: October 2013) will certainly result in revealing new spectroscopic binaries among Cepheids brighter than 13 and 14 mag (Eyer et al. 2012).

When determining the physical properties (luminosity, temperature, radius, etc.) of individual Cepheids, the effects of the companion on the observed parameters (apparent brightness, colour indices, etc.) have to be corrected for. This type of analysis, however, should be preceded by revealing the binarity of the given Cepheid.

ACKNOWLEDGEMENTS

This project has been supported by the ESA PECS Project C98090, ESTEC Contract No. 4000106398/12/NL/KML, the Hungarian OTKA Grants K76816, K83790, K104607 and MB08C 81013, as well as the European Community's Seventh Framework Programme (FP7/2007-2013) under grant agreement no. 269194 and the 'Lendület-2009' Young Researchers Programme of the Hungarian Academy of Sciences. AD was supported by the Hungarian Eötvös fellowship. AD has been supported by the János Bolyai Research Scholarship of the Hungarian Academy of Sciences. AD is very thankful to the staff at The Lodge in Siding Spring Observatory for their hospitality and the very nice food, making the time spent there lovely and special. Part of the research leading to these results has received funding from the European Research Council under the European Community's Seventh Framework Programme (FP7/2007–2013)/ERC grant agreement no. 227224 (PROSPERITY). The *INTEGRAL* photometric data, pre-processed by ISDC, have been retrieved from the OMC Archive at CAB (INTA-CSIC). Critical remarks by Dr. Mária Kun and the referee's suggestions led to a considerable improvement in the presentation of the results.

REFERENCES

Baranne A. et al., 1996, A&AS, 119, 373
Berdnikov L. N., 2008, VizieR On-line Data Catalog: II/285
Cannon A., Wells L. D., Leland E. F., Pickering E. C., 1909, Harvard Coll. Obs. Circ., 15, 1
Dean J. F., 1977, Mon. Not. Astron. Soc. South. Afr., 36, 3
Derekas A. et al., 2012, MNRAS, 425, 1312
Eggen O. J., 1983, AJ, 88, 998
Eggen O. J., 1985, AJ, 90, 1297
ESA, 1997, The Hipparcos and Tycho Catalogues, ESA SP-1200. ESA, Noordwijk
Evans N. R. et al., 2012, AAS Meeting, 220, 329.07
Eyer L. et al., 2012, Ap&SS, 341, 207
Florya N. F., Kukarkina N. P., 1953, Sternberg Trudy, 23, 5
Gill D., Innes R. T. A., 1903, Cape Ann., 9, 9B
Harris H. C., 1980, PhD thesis, Washington University, Seattle
Hertzsprung E., 1930, Bull. Astron. Inst. Neth., 6, 6
Hoffmeister C., 1923, Astron. Nachr., 218, 325
Irwin J. B., 1961, ApJS, 6, 253
Joy A. H., 1937, ApJ, 86, 363
Kaufer A., Stahl O., Tubbesing S., Nørregaard P., Avila G., Francois P., Pasquini L., Pizzella A., 1999, Messenger, 95, 8
Kaufer A., Stahl O., Tubbesing S., Nørregaard P., Avila G., Francois P., Pasquini L., Pizzella A., 2000, in Iye M., Moorwood A. F., eds, Proc. SPIE Ser. Vol. 4008, Optical and IR Telescope Instrumentation and Detectors. SPIE, Bellingham, p. 459
Klagyivik P., Szabados L., 2009, A&A, 504, 959
Lloyd Evans T., 1980, South Afr. Astron. Obser. Circ., 1, 257
Madore B. F., 1975, ApJS, 29, 219
Madore B. F., Fernie J. D., 1980, PASP, 92, 315
Munari U., Sordo R., Castelli F., Zwitter T., 2005, A&A, 442, 1127

Nordström B. et al., 2004, A&A, 418, 989
O'Leary W., O'Connell D., 1937, Astron. Nachr., 264, 141
Onnembo A, Buonaura B., Caccin B., Russo G., Sollazzo C., 1985, A&A, 152, 349
Pel J. W., 1976, A&AS, 24, 413
Pepe F., Mayor M., Galland F., Naef D., Queloz D., Santos N. C., Udry S., Burnet M., 2002, A&A, 388, 632
Pickering E. C., 1904, Harvard Coll. Obs. Circ., 91, 1
Pojmanski G., 2002, Acta Astron., 52, 397
Pont F., Burki G., Mayor M., 1994, A&AS, 105, 165
Queloz D. et al., 2001, Messenger, 105, 1
Sterken C., 2005, in Sterken C., ed., ASP Conf. Ser. Vol. 335, The Light-Time Effect in Astrophysics. Astron. Soc. Pac., San Francisco, p. 3
Stibbs D. W. N., 1955, MNRAS, 115, 363
Stobie R. S., 1970, MNRAS, 148, 1
Strohmeier W., Knigge R., Ott H., 1964, Inf. Bull. Var. Stars, 66, 1
Szabados L., 1983, Ap&SS, 96, 185
Szabados L., 1996, A&A, 311, 189
Szabados L., 2003a, Inf. Bull. Var. Stars, 5394, 1
Szabados L., 2003b, Recent Res. Dev. Astron. & Astrophys., 1, 787
Szabados L., Klagyivik P., 2012, Ap&SS, 341, 99
Walraven Th., Muller A. B., Oosterhoff P. T., 1958, Bull. Astron. Inst. Neth., 14, 81
Weaver H. F., Steinmetz D., Mitchell R., 1960, Lowell Obser. Bull., 5, 30
Wesselink A. J., 1935, Bull. Astron. Inst. Neth., 7, 243
Wilson D. M. et al., 2008, ApJ, 675, L113

SUPPORTING INFORMATION

Additional Supporting Information may be found in the online version of this article:

Table 3. New RV values of GH Carinae from the SSO spectra.
Table 4. New CORALIE velocities of GH Carinae.
Table 6. New RV values of V419 Centauri from the SSO spectra.
Table 9. New RV values of V898 Centauri from the SSO spectra.
Table 13. New RV values of AD Puppis from the SSO spectra.
Table 15. New RV values of AY Sagittarii from the SSO spectra.
Table 17. New RV values of ST Velorum from the SSO spectra.
(http://www.mnras.oxfordjournals.org/lookup/suppl/doi:10.1093/mnras/stt027/-/DC1).

Please note: Oxford University Press are not responsible for the content or functionality of any supporting materials supplied by the authors. Any queries (other than missing material) should be directed to the corresponding author for the article.

This paper has been typeset from a TEX/LATEX file prepared by the author.

Monthly Notices of the ROYAL ASTRONOMICAL SOCIETY

MNRAS **434,** 870–877 (2013) doi:10.1093/mnras/stt1079
Advance Access publication 2013 July 5

Discovery of the spectroscopic binary nature of three bright southern Cepheids

L. Szabados,[1⋆] R. I. Anderson,[2] A. Derekas,[1,3] L. L. Kiss,[1,3,4] T. Szalai,[5] P. Székely[6] and J. L. Christiansen[7]

[1]*Konkoly Observatory, Research Centre for Astronomy and Earth Sciences, Hungarian Academy of Sciences, Konkoly Thege Miklós út 15-17, H-1121 Budapest, Hungary*
[2]*Observatoire de Genève, Université de Genève, 51 Ch. des Maillettes, CH-1290 Versoix, Switzerland*
[3]*Sydney Institute for Astronomy, School of Physics, University of Sydney, NSW 2006, Australia*
[4]*ELTE Gothard–Lendület Research Group, Szent Imre herceg út 112, H-9700 Szombathely, Hungary*
[5]*Department of Optics and Quantum Electronics, University of Szeged, Dóm tér 9, H-6720 Szeged, Hungary*
[6]*Department of Experimental Physics, University of Szeged, H-6720 Szeged, Hungary*
[7]*SETI Institute/NASA Ames Research Center, M/S 244-30, Moffett Field, CA 94035, USA*

Accepted 2013 June 13. Received 2013 June 13; in original form 2013 May 14

ABSTRACT

We present an analysis of spectroscopic radial velocity and photometric data of three bright Galactic Cepheids: LR Trianguli Australis (LR TrA), RZ Velorum (RZ Vel) and BG Velorum (BG Vel). Based on new radial velocity data, these Cepheids have been found to be members of spectroscopic binary systems. The ratio of the peak-to-peak radial velocity amplitude to photometric amplitude indicates the presence of a companion for LR TrA and BG Vel. *IUE* spectra indicate that the companions of RZ Vel and BG Vel cannot be hot stars. The analysis of all available photometric data revealed that the pulsation period of RZ Vel and BG Vel varies monotonically, due to stellar evolution. Moreover, the longest period Cepheid in this sample, RZ Vel, shows period fluctuations superimposed on the monotonic period increase. The light-time effect interpretation of the observed pattern needs long-term photometric monitoring of this Cepheid. The pulsation period of LR TrA has remained constant since the discovery of its brightness variation. Using statistical data, it is also shown that a large number of spectroscopic binaries still remain to be discovered among bright classical Cepheids.

Key words: binaries: spectroscopic – stars: variables: Cepheids.

1 INTRODUCTION

Classical Cepheid variable stars are primary distance indicators and rank among standard candles for establishing the cosmic distance scale, owing to the famous period–luminosity (*P–L*) relationship. Companions to Cepheids, however, complicate the situation. The contribution of the secondary star to the observed brightness has to be taken into account when involving any particular Cepheid in the calibration of the *P–L* relationship.

Binaries among Cepheids are not rare at all: their frequency exceeds 50 per cent for the brightest Cepheids, while among the fainter Cepheids an observational selection effect encumbers revealing binarity (Szabados 2003a).

Owing to some observational projects, aimed at obtaining new radial velocities (RVs) of numerous Cepheids, carried out during the last decades, a part of the selection effect has been removed. This progress is visualized in Fig. 1 where the current situation is compared with that 20 years ago. The data have been taken from the online data base of binaries among Galactic Cepheids (http://www.konkoly.hu/CEP/orbit.html). To get rid of the fluctuation at the left-hand part of the diagram, brightest Cepheids ($\langle V\rangle < 5$ mag) were merged in a single bin because such stars are extremely rare among Cepheids – see the histogram in Fig. 2.

In the case of pulsating variables, like Cepheids, spectroscopic binarity manifests itself in a periodic variation of the γ-velocity (i.e. the RV of the mass centre of the Cepheid). In practice, the orbital RV variation of the Cepheid component is superimposed on the RV variations of pulsational origin. To separate orbital and pulsational effects, knowledge of the accurate pulsation period is essential, especially when comparing RV data obtained at widely differing epochs. Therefore, the pulsation period and its variations have been determined with the method of the O−C diagram (Sterken 2005) for each target Cepheid. Use of the accurate pulsation period obtained from the photometric data is a guarantee for the correct phase matching of the (usually less precise) RV data.

⋆ E-mail: szabados@konkoly.hu

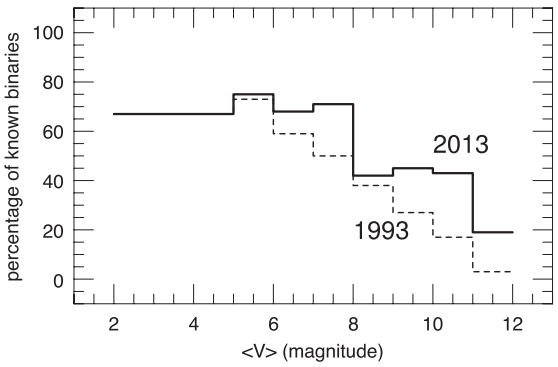

Figure 1. Percentage of known binaries among Galactic classical Cepheids as a function of the mean apparent visual brightness in 1993 and 2013. The decreasing influence of the observational selection effect is noticeable.

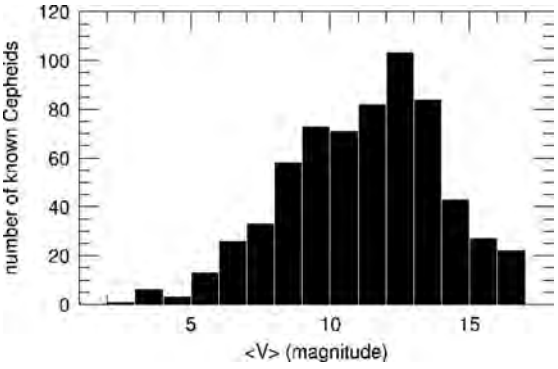

Figure 2. Histogram showing the number distribution of known Galactic classical Cepheids as a function of their mean apparent visual brightness.

In this paper, we point out spectroscopic binarity of three bright Galactic Cepheids by analysing RV data. The structure of this paper is as follows. The new observations and the equipment utilized are described in Section 2. Section 3 is devoted to the results on the three new spectroscopic binary (SB) Cepheids: LR Trianguli Australis (LR TrA), RZ Velorum (RZ Vel) and BG Velorum (BG Vel). Basic information on these Cepheids is given in Table 1. Finally, Section 4 contains our conclusions.

2 NEW OBSERVATIONS

2.1 Spectra from the Siding Spring Observatory

We performed an RV survey of Cepheids with the 2.3-m ANU telescope located at the Siding Spring Observatory (SSO), Australia. The main aim of the project was to detect Cepheids in binary systems by measuring changes in the mean values of their RV curve which can be interpreted as the orbital motion of the Cepheid around the centre-of-mass in a binary system (change of γ-velocity). The target list was compiled to include Cepheids with a single-epoch RV phase curve or without any published RV data. Several Cepheids suspected to be members of SB systems were also put on the target list. In 64 nights between 2004 October and 2006 March we monitored 40 Cepheids with pulsation periods between 2 and 30 d. Additional spectra of some targets were obtained in 2007 August.

Table 1. Basic data of the programme stars and the number of spectra.

Cepheid	$\langle V \rangle$ (mag)	P (d)	Mode of pulsation	Number of spectra SSO	CORALIE
LR TrA	7.80	2.428 289	First overtone	10	32
RZ Vel	7.13	20.398 532	Fundamental	30	67
BG Vel	7.69	6.923 843	Fundamental	27	33

Medium-resolution spectra were taken with the Double Beam Spectrograph using the 1200 mm^{-1} gratings in both arms of the spectrograph. The projected slit width was 2 arcsec on the sky, which was about the median seeing during our observations. The spectra covered the wavelength ranges 4200–5200 Å in the blue arm and 5700–6700 Å in the red arm. The dispersion was 0.55 Å $pixel^{-1}$, leading to a nominal resolution of about 1 Å.

All spectra were reduced with standard tasks in IRAF.[1] The reduction consisted of bias and flat-field corrections, aperture extraction, wavelength calibration and continuum normalization. We checked the consistency of wavelength calibrations via the constant positions of strong telluric features, which proved the stability of the system. RVs were determined only for the red arm data with the task `fxcor`, applying the cross-correlation method using a well-matching theoretical template spectrum from the extensive spectral library of Munari et al. (2005). Then, we made barycentric corrections to every single RV value. This method resulted in a 1–2 km s^{-1} uncertainty in the individual RVs, while further tests have shown that our absolute velocity frame was stable to within ±2–3 km s^{-1}. This level of precision is sufficient to detect a number of Cepheid companions, as they can often cause γ-velocity changes well above 10 km s^{-1}.

Discovery of six SBs among the 40 target Cepheids was already reported by Szabados et al. (2013). The binarity of the three Cepheids announced here could be revealed by involving independently obtained additional data (see Section 2.2). The individual RV data of the rest of the Cepheid targets will be published together with the results of the analysis of the spectra.

2.2 CORALIE observations from La Silla

All three Cepheids were among the targets during multiple observing campaigns between 2011 April and 2012 May using the fibre-fed high-resolution ($R \sim 60\,000$) echelle spectrograph CORALIE mounted on the Swiss 1.2-m Euler telescope at the ESO La Silla Observatory, Chile. The instrument's design is described in Queloz et al. (2001); recent instrumental updates can be found in Ségransan et al. (2010).

When it turned out that these three Cepheids have variable γ-velocities, several new spectra were obtained in 2012 December–2013 January and 2013 April.

The spectra are reduced by the efficient online reduction pipeline that performs bias correction, cosmics removal and flat-fielding using tungsten lamps. ThAr lamps are used for the wavelength calibration. The reduction pipeline directly determines the RV via cross-correlation (Baranne et al. 1996) using a mask that resembles a G2 spectral type. The RV stability of the instrument is excellent and for non-pulsating stars the RV precision is limited by photon noise (see e.g. Pepe et al. 2002). However, the precision achieved for Cepheids is lower due to line asymmetries. We estimate a typical precision of ∼0.1 km s^{-1} (including systematics due to pulsation) per data point for our data.

[1] IRAF is distributed by the National Optical Astronomy Observatories, which are operated by the Association of Universities for Research in Astronomy, Inc., under cooperative agreement with the National Science Foundation.

3 RESULTS FOR INDIVIDUAL CEPHEIDS

3.1 LR Trianguli Australis

Accurate value of the pulsation period. The brightness variability of LR TrA (HD 137626, $\langle V\rangle = 7.80$ mag) was revealed by Strohmeier, Fischer & Ott (1966) based on the Bamberg photographic patrol plates. The Cepheid nature of variability and the first values of the pulsation period were determined by Eggen (1983). This Cepheid pulsates in the first-overtone mode; therefore, it has a small pulsational amplitude and nearly-sinusoidal light and velocity curves.

In the case of Cepheids pulsating with a low amplitude, the O−C diagram constructed for the median brightness (the mid-point between the faintest and the brightest states) is more reliable than that based on the moments of photometric maxima (Derekas et al. 2012). Therefore, we determined the accurate value of the pulsation period by constructing an O−C diagram for the moments of median brightness on the ascending branch of the light curve since this is the phase when the brightness variations are steepest during the whole pulsational cycle.

All published photometric observations of LR TrA covering three decades were re-analysed in a homogeneous manner to determine seasonal moments of the chosen light-curve feature. The relevant data listed in Table 2 are as follows:
Column 1: heliocentric moment of the selected light-curve feature (median brightness on the ascending branch for LR TrA, maximum brightness for both RZ Vel and BG Vel, see Tables 6 and 10, respectively);
Column 2: epoch number, E, as calculated from equation (1):

$$C = 245\,3104.9265 + 2.428\,289 \times E \pm 0.0037 \pm 0.000\,003 \quad (1)$$

(this ephemeris has been obtained by the weighted least-squares parabolic fit to the O−C differences);

Table 2. O−C values of LR TrA (see the description in Section 3.1).

$JD_\odot$ 240 0000 +	E	O−C	W	Data source
450 18.7822	−3330	0.0581	3	Eggen (1983)
476 33.9607	−2253	−0.0307	3	Antonello, Poretti & Reduzzi (1990)
479 39.9568	−2127	0.0010	2	*Hipparcos* (ESA 1997)
481 39.0426	−2045	−0.0329	3	*Hipparcos* (ESA 1997)
484 40.1554	−1921	−0.0279	3	*Hipparcos* (ESA 1997)
487 50.9547	−1793	−0.0496	3	*Hipparcos* (ESA 1997)
498 14.6064	−1355	0.0115	3	Berdnikov (2008)
503 70.7115	−1126	0.0384	3	Berdnikov (2008)
505 74.6393	−1042	−0.0101	3	Berdnikov (2008)
509 09.7531	−904	−0.0001	3	Berdnikov (2008)
512 64.2883	−758	0.0049	3	Berdnikov (2008)
516 50.4058	−599	0.0244	3	Berdnikov (2008)
519 58.8010	−472	0.0269	2	Berdnikov (2008)
520 41.3435	−438	0.0076	2	ASAS (Pojmanski 2002)
523 66.7222	−304	−0.0044	3	Berdnikov (2008)
525 00.2709	−249	−0.0116	3	ASAS (Pojmanski 2002)
527 69.8038	−138	−0.0188	3	ASAS (Pojmanski 2002)
531 02.5159	−1	0.0177	3	Berdnikov (2008)
531 04.9151	0	−0.0114	3	ASAS (Pojmanski 2002)
535 20.1818	171	0.0179	3	ASAS (Pojmanski 2002)
538 40.7137	303	0.0156	3	ASAS (Pojmanski 2002)
542 51.0850	472	0.0061	3	ASAS (Pojmanski 2002)
546 15.3163	622	−0.0060	3	ASAS (Pojmanski 2002)
549 60.1214	764	−0.0179	3	ASAS (Pojmanski 2002)

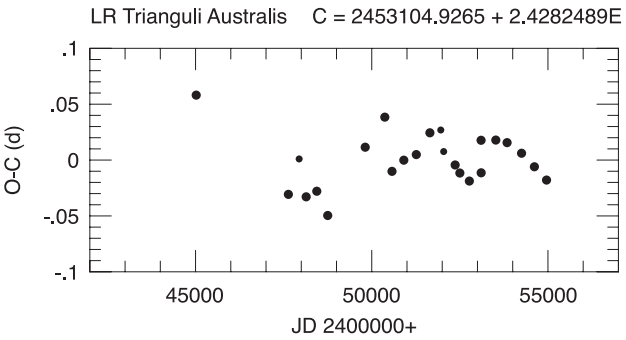

Figure 3. O−C diagram of LR TrA. The plot can be approximated by a constant period.

Column 3: the corresponding O−C value;
Column 4: weight assigned to the O−C value (1, 2 or 3 depending on the quality of the light curve leading to the given difference);
Column 5: reference to the origin of data.

The O−C diagram of LR TrA based on the O−C values listed in Table 2 is plotted in Fig. 3. The plot can be approximated by a constant period by the ephemeris (1) for the moments of median brightness on the ascending branch. The scatter of the points in Fig. 3 reflects the observational error and uncertainties in the analysis of the data.

Binarity of LR TrA. There are no earlier RV data on this bright Cepheid. Our new data listed in Tables 3 and 4 have been folded on the accurate pulsation period given in the ephemeris (see equation 1). The merged RV phase curve is plotted in Fig. 4. Both individual data series could be split into seasonal subsets.

Variability in the γ-velocity is obvious. The γ-velocities (together with their uncertainties) are listed in Table 5. The γ-velocity in 2007 is more uncertain than in other years because this value is based on a single spectrum. Systematic errors can be excluded. Dozens of Cepheids in our sample with non-varying γ-velocities

Table 3. RV values of LR TrA from the SSO spectra. (This is only a portion of the full version available online as Supporting Information.)

$JD_\odot$ 2 400 000 +	v_{rad} (km s^{-1})
535 99.9325	−21.2
536 00.9086	−32.0
536 03.9327	−27.6
536 05.9290	−31.0
538 05.1657	−29.3
...	...

Table 4. CORALIE velocities of LR TrA. (This is only a portion of the full version available online as Supporting Information.)

$JD_\odot$ 240 0000 +	v_{rad} (km s^{-1})	σ (km s^{-1})
559 38.8701	−27.97	0.05
559 38.8718	−28.10	0.05
559 39.8651	−29.85	0.02
559 40.8686	−22.40	0.03
559 41.8579	−33.14	0.04
...	...	...

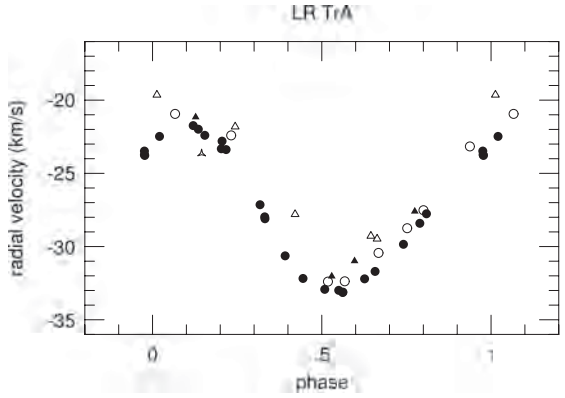

Figure 4. Merged RV phase curve of LR TrA. The different symbols mean data from different years: 2005: filled triangles; 2006: empty triangles; 2007: triangular star; 2012: filled circles; 2013: empty circles. The zero phase was arbitrarily chosen at JD 240 0000.0 (in all phase curves in this paper).

Table 5. γ-velocities of LR TrA.

Mid-JD 240 0000+	v_γ (km s^{-1})	σ (km s^{-1})	Data source
536 03	−25.5	0.5	Present paper
538 08	−24.8	0.5	Present paper
543 31	−29.0	1.0	Present paper
559 81	−27.5	0.1	Present paper
563 44	−26.4	0.1	Present paper

indicate the stability of the equipment and reliability of the data reduction. Fig. 5 is a better visualization of the temporal variation in the γ-velocity. The seasonal drift in the γ-velocity is compatible with both short and long orbital periods.

The photometric contribution of the companion star decreases the observable amplitude of the brightness variability as deduced from the enhanced value of the ratio of the RV to photometric amplitudes (Klagyivik & Szabados 2009). This is an additional (although slight) indication of the binarity of LR TrA.

3.2 RZ VELORUM

Accurate value of the pulsation period. The brightness variability of RZ Vel (HD 73502, $\langle V\rangle = 7.13$ mag) was revealed by Cannon (Pickering 1909). The Cepheid nature of variability and the pulsation period were established by Hertzsprung (1936) based on the Harvard and Johannesburg photographic plate collection which was further investigated by Oosterhoff (1936).

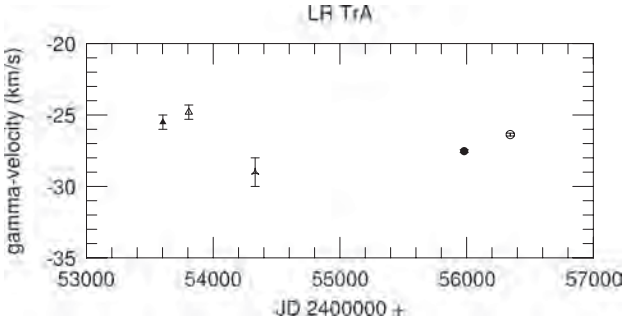

Figure 5. Temporal variation in the γ-velocity of LR TrA. The symbols for the different data sets are the same as in Fig. 4.

This is the longest period Cepheid announced in this paper and it has been frequently observed from the 1950s, first photoelectrically, then in the last decades by CCD photometry. The photometric coverage of RZ Vel was almost continuous in the last 20 years, thanks to observational campaigns by Berdnikov (2008) and his co-workers, as well as the ASAS photometry (Pojmanski 2002).

Long-period Cepheids are usually fundamental pulsators and they oscillate with a large amplitude, resulting in a light curve with sharp maximum.

The O−C diagram of RZ Vel was constructed for the moments of maximum brightness based on the photoelectric and CCD photometric data (see Table 6). The weighted least-squares parabolic fit to the O−C values resulted in the ephemeris:

$$C = 244\,2453.6630 + 20.398\,532 \times E + 1.397 \times 10^{-6} E^2 \pm 0.0263 \pm 0.000\,080 \pm 0.191 \times 10^{-6} \quad (2)$$

The O−C diagram of RZ Vel plotted in Fig. 6 indicates a continuously increasing pulsation period with a period jitter superimposed. This secular period increase has been caused by stellar evolution: while the Cepheid crosses the instability region towards lower temperatures in the Hertzsprung–Russell diagram, its pulsation period

Table 6. O−C values of RZ Vel (description of the columns is given in Section 3.1).

JD$_\odot$ 240 0000 +	E	O−C	W	Data source
337 84.5646	−425	0.2777	1	Eggen, Gascoigne & Burr (1957)
348 04.5174	−375	0.3039	1	Walraven, Muller & Oosterhoff (1958)
348 45.2119	−373	0.2013	3	Eggen et al. (1957)
351 92.0024	−356	0.2168	1	Irwin (1961)
407 60.8647	−83	0.2799	3	Pel (1976)
417 19.0924	−36	−0.2234	3	Madore (1975)
418 62.1249	−29	0.0193	3	Dean et al. (1977)
424 53.6330	0	−0.0030	3	Dean et al. (1977)
443 71.0472	94	−0.0778	3	Coulson & Caldwell (1985)
443 91.3842	95	−0.1393	2	Eggen (1982)
450 03.2906	125	−0.1889	3	Coulson & Caldwell (1985)
482 26.4369	283	−0.0107	3	*Hipparcos* (ESA 1997)
487 97.5877	311	−0.0188	3	*Hipparcos* (ESA 1997)
491 85.1653	330	−0.0133	1	Walker & Williams (unpublished)
498 17.8011	361	0.2680	3	Berdnikov (2008)
501 44.1979	377	0.2883	2	Bersier (2002)
503 89.0443	389	0.3524	3	Berdnikov (2008)
505 11.3662	395	0.2831	3	Bersier (2002)
505 72.4468	398	0.1681	3	Berdnikov (2008)
508 99.0581	414	0.4029	3	Berdnikov (2008)
512 66.1488	432	0.3200	3	Berdnikov (2008)
516 53.7650	451	0.3641	3	Berdnikov (2008)
519 39.2846	465	0.3042	2	ASAS (Pojmanski 2002)
519 59.7692	466	0.3903	3	Berdnikov (2008)
523 47.4262	485	0.4752	3	Berdnikov (2008)
526 53.3896	500	0.4606	3	ASAS (Pojmanski 2002)
526 53.4100	500	0.4810	3	Berdnikov (2008)
530 00.1794	517	0.4754	3	ASAS (Pojmanski 2002)
530 00.2610	517	0.5570	3	Berdnikov (2008)
534 28.4384	538	0.3652	3	ASAS (Pojmanski 2002)
537 54.8864	554	0.4367	3	ASAS (Pojmanski 2002)
541 83.1657	575	0.3468	3	ASAS (Pojmanski 2002)
545 09.5729	591	0.3775	3	ASAS (Pojmanski 2002)
548 15.4343	606	0.2609	3	ASAS (Pojmanski 2002)
551 21.3569	621	0.2055	2	ASAS (Pojmanski 2002)

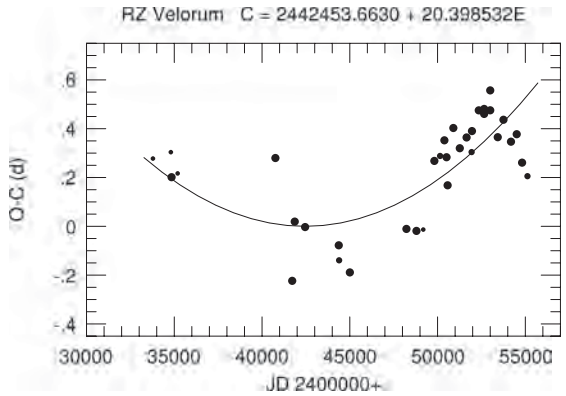

Figure 6. O−C diagram of RZ Vel. The plot can be approximated by a parabola indicating a continuously increasing period.

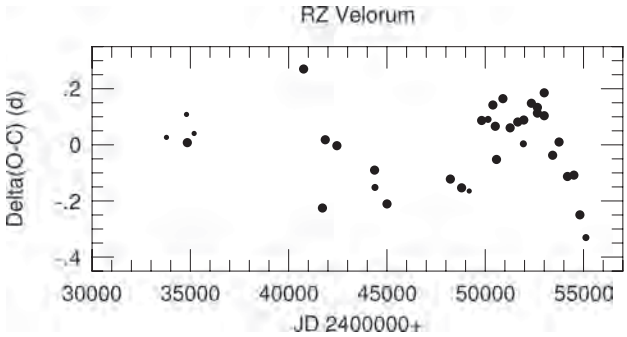

Figure 7. Δ(O−C) diagram of RZ Vel.

Table 7. RV values of RZ Vel from the SSO spectra. (This is only a portion of the full version available online as Supporting Information.)

$JD_\odot$ 240 0000 +	v_{rad} (km s^{-1})
533 07.2698	4.2
533 10.2504	1.4
533 12.2073	9.0
533 64.2062	49.6
533 67.1823	27.5
...	...

is increasing. Continuous period variations (of either sign) often occur in the pulsation of long-period Cepheids (Szabados 1983).

Fig. 7 shows the O−C residuals after subtracting the parabolic fit defined by equation (2). If the wave-like fluctuation seen in this Δ(O − C) diagram turns out to be periodic, it would correspond to a light-time effect in a binary system. In line with the recent shortening in the pulsation period, the current value of the pulsation period is 20.396 671 ± 0.000 200 d (after JD 245 2300).

Binarity of RZ Vel. There are several data sets of RV observations available in the literature for RZ Vel: those published by Stibbs (1955), Lloyd Evans (1968, 1980), Coulson & Caldwell (1985), Bersier (2002) and Nardetto et al. (2006). Our individual RV data are listed in Tables 7 and 8.

Based on these data, the RV phase curve has been constructed using the 20.398 532 d pulsation period appearing in equation (2). In view of the complicated pattern of the O−C diagram, the RV

Table 8. CORALIE velocities of RZ Vel. (This is only a portion of the full version available online as Supporting Information.)

$JD_\odot$ 240 0 000 +	v_{rad} (km s^{-1})	σ (km s^{-1})
556 54.5528	−3.08	0.02
556 56.6626	5.23	0.01
556 57.6721	9.86	0.02
556 59.6585	18.85	0.03
556 62.5137	31.50	0.01
...	...	...

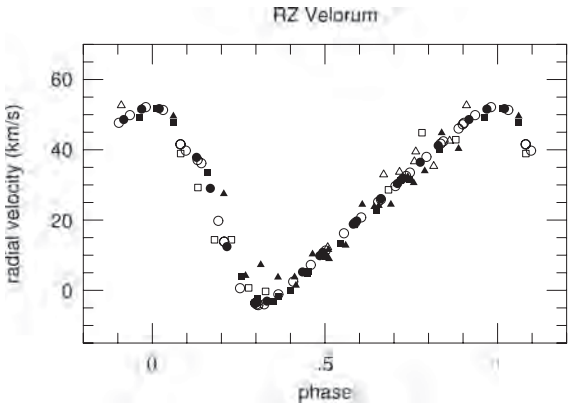

Figure 8. RV phase curve of RZ Vel. Data obtained between 1996 and 2013 are included in this plot. The meaning of various symbols is explained in the text.

data have been folded on by taking into account the proper phase correction for different data series. The merged RV phase curve is plotted in Fig. 8. For the sake of clarity, RV data obtained before JD 245 0000 have not been plotted here because of the wider scatter of these early RV data, but the γ-velocities were determined for each data set. The individual data series are denoted by different symbols: filled squares mean data by Bersier (2002), empty squares those by Nardetto et al. (2006), and our 2005, 2006, 2012 and 2013 data are denoted by filled triangles, empty triangles, filled circles and empty circles, respectively. The wide scatter in this merged RV phase curve plotted in Fig. 8 is due to a variable γ-velocity.

The γ-velocities determined from each data set (including the earlier ones) are listed in Table 9 and are plotted in Fig. 9. The plot implies that RZ Vel is really an SB as suspected by Bersier (2002) based on a much poorer observational material (before JD

Table 9. γ-velocities of RZ Vel.

Mid-JD 240 0000+	v_γ (km s^{-1})	σ (km s^{-1})	Data source
340 09	25.5	1.5	Stibbs (1955)
403 28	22.1	1.5	Lloyd Evans (1968, 1980)
421 86	29.2	1.0	Coulson & Caldwell (1985)
441 86	22.6	1.0	Coulson & Caldwell (1985)
447 36	24.4	1.0	Coulson & Caldwell (1985)
503 17	25.1	0.2	Bersier (2002)
531 84	24.0	0.5	Nardetto et al. (2006)
534 44	26.9	0.6	Present paper
537 83	28.8	1.0	Present paper
557 09	25.6	0.1	Present paper
560 38	25.3	0.1	Present paper

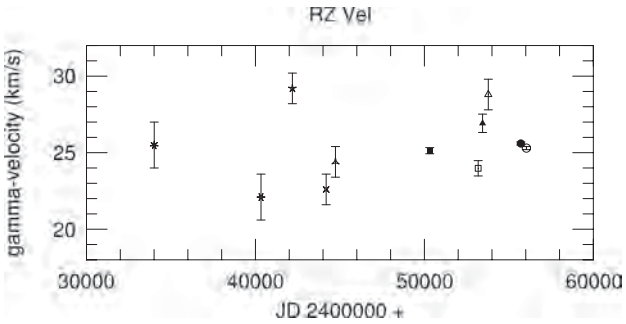

Figure 9. γ-velocities of RZ Vel. The symbols for the different data sets are the same as in Fig. 8.

245 0500). An orbital period of about 5600–5700 d is compatible with the data pattern in both Figs 7 and 9, but the phase relation between the light-time effect fit to the $\Delta(O-C)$ curve and the orbital RV variation phase curve obtained with this formal period is not satisfactory.

3.3 BG VELORUM

Accurate value of the pulsation period. The brightness variability of BG Vel (HD 78801, $\langle V\rangle = 7.69$ mag) was revealed by Cannon (Pickering 1909). Much later O'Leary (1937) independently discovered its light variations, but he also revealed the Cepheid nature and determined the pulsation period based on photographic plates obtained at the Riverview College Observatory. Van Houten (1950) also observed this Cepheid photographically in Johannesburg, but these early data are unavailable; therefore, we only mention their studies for historical reasons.

This Cepheid is a fundamental-mode pulsator. The O−C differences of BG Vel calculated for brightness maxima are listed in Table 10. These values have been obtained by taking into account the constant and linear terms of the following weighted parabolic fit:

$$C = 245\,3031.4706 + 6.923\,843 \times E + 2.58 \times 10^{-8} E^2$$
$$\pm\ 0.0020 \pm 0.000\,007 \pm 0.27 \times 10^{-8} \qquad (3)$$

The parabolic nature of the O−C diagram, i.e. the continuous increase in the pulsation period, is clearly seen in Fig. 10. This parabolic trend corresponds to a continuous period increase of $(5.16 \pm 0.54) \times 10^{-8}$ d cycle^{-1}, i.e. $\Delta P = 0.000\,272$ d century^{-1}. This tiny period increase has also been caused by stellar evolution as in the case of RZ Vel.

The fluctuations around the fitted parabola in Fig. 10 do not show any definite pattern: see the $\Delta(O-C)$ diagram in Fig. 11.

Binarity of BG Vel. There are earlier RV data of this Cepheid obtained by Stibbs (1955) and Lloyd Evans (1980). Variability in the γ-velocity is seen in the merged phase diagram of all RV data of BG Vel plotted in Fig. 12. In this diagram, our 2005–2006 data (listed in Table 11) are represented with the empty circles, while 2012–2013 data (listed in Table 12) are denoted by the filled circles, the triangles represent Stibbs' data, and the × symbols refer to Lloyd Evans' data. Our RV data have been folded with the period given in the ephemeris, equation (3), omitting the quadratic term. Data obtained by Stibbs and Lloyd Evans have been phased with the same period, but a proper correction has been applied to allow for the phase shift due to the parabolic O−C graph.

Table 10. O−C values of BG Vel (description of the columns is given in Section 3.1).

$JD_\odot$ 2 400 000 +	E	O−C	W	Data source
348 56.5526	−2625	0.1699	3	Walraven et al. (1958)
352 37.3813	−2570	0.1872	3	Irwin (1961)
407 48.6592	−1774	0.0861	3	Pel (1976)
428 53.4433	−1470	0.0219	3	Dean (1977)
443 00.5426	−1261	0.0380	3	Berdnikov (2008)
481 36.3167	−707	0.0031	3	*Hipparcos* (ESA 1997)
486 27.9239	−636	0.0174	3	*Hipparcos* (ESA 1997)
503 79.6329	−383	−0.0058	3	Berdnikov (2008)
505 73.4987	−355	−0.0076	3	Berdnikov (2008)
509 05.8549	−307	0.0041	3	Berdnikov (2008)
512 65.9127	−255	0.0221	3	Berdnikov (2008)
516 46.7345	−200	0.0325	3	Berdnikov (2008)
519 37.5210	−158	0.0176	3	ASAS (Pojmanski 2002)
519 58.2712	−155	−0.0038	3	Berdnikov (2008)
523 59.8640	−97	0.0062	3	ASAS (Pojmanski 2002)
523 59.8778	−97	0.0200	3	Berdnikov (2008)
526 50.6575	−55	−0.0017	3	Berdnikov (2008)
527 26.8212	−44	−0.0003	3	ASAS (Pojmanski 2002)
530 03.7916	−4	0.0164	3	Berdnikov (2008)
530 31.4758	0	0.0052	3	ASAS (Pojmanski 2002)
533 36.1201	44	0.0004	1	*INTEGRAL* OMC
534 60.7390	62	−0.0099	3	ASAS (Pojmanski 2002)
537 79.2202	108	−0.0254	3	ASAS (Pojmanski 2002)
541 80.8337	166	0.0052	3	ASAS (Pojmanski 2002)
545 40.8499	218	−0.0185	3	ASAS (Pojmanski 2002)
548 38.5810	261	−0.0126	3	ASAS (Pojmanski 2002)
551 43.2425	305	−0.0002	2	ASAS (Pojmanski 2002)

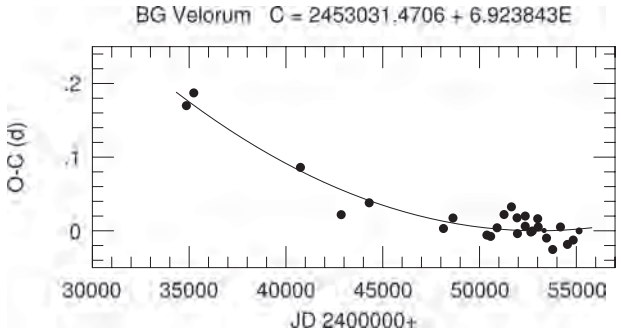

Figure 10. O−C diagram of BG Vel. The plot can be approximated by a parabola indicating a continuously increasing pulsation period.

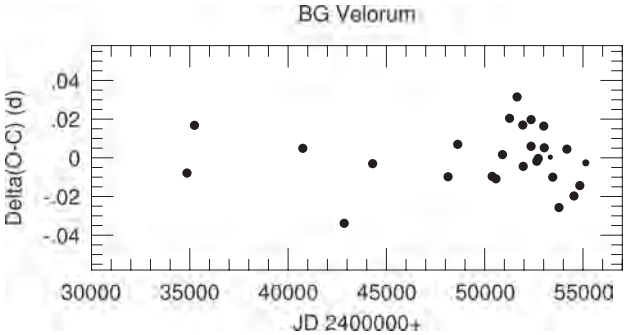

Figure 11. Δ(O−C) diagram of BG Vel.

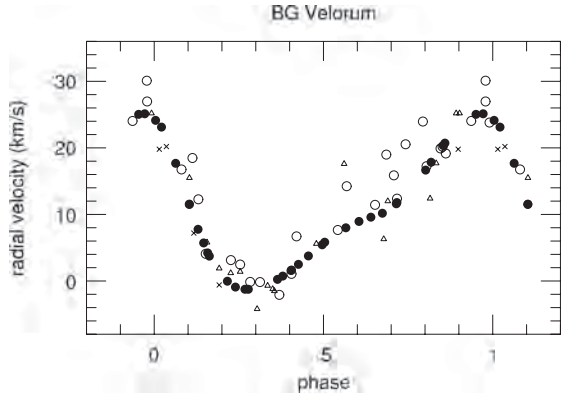

Figure 12. Merged RV phase curve of BG Vel. There is an obvious shift between the γ-velocities valid for the epoch of our data obtained in 2005–2006 and 2012–2013 (empty and filled circles, respectively). The other symbols are explained in the text.

Table 11. RV values of BG Vel from the SSO spectra. (This is only a portion of the full version available online as Supporting Information.)

$JD_\odot$ 2400 000 +	v_{rad} (km s^{-1})
533 12.2372	17.3
533 64.2219	−0.2
533 67.1992	20.5
534 51.0000	20.0
534 52.0021	23.8

Table 12. CORALIE velocities of BG Vel. (This is only a portion of the full version available online as Supporting Information.)

$JD_\odot$ 240 0000 +	v_{rad} (km s^{-1})	σ (km s^{-1})
559 37.7555	24.13	0.02
559 38.6241	7.77	0.02
559 39.6522	−1.25	0.01
559 41.6474	7.99	0.10
559 42.6917	11.78	0.03

The γ-velocities determined from the individual data sets are listed in Table 13 and plotted in Fig. 13. Since no annual shift is seen in the γ-velocities between two consecutive years (2005–2006 and 2012–2013), the orbital period cannot be short; probably, it exceeds a thousand days.

Similarly to the case of LR TrA, BG Vel is also characterized by an excessive value for the ratio of RV to photometric amplitudes, indicating the possible presence of a companion (see Fig. 14).

Table 13. γ-velocities of BG Vel.

Mid-JD 240 0000+	v_γ (km s^{-1})	σ (km s^{-1})	Data source
340 96	11.4	1.5	Stibbs (1955)
405 45	8.4	1.5	Lloyd Evans (1980)
535 72	12.6	0.6	Present paper
560 43	10.3	0.1	Present paper

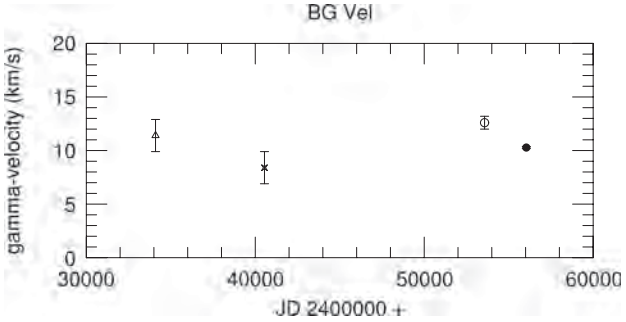

Figure 13. γ-velocities of BG Vel. The symbols for the different data sets are the same as in Fig. 12.

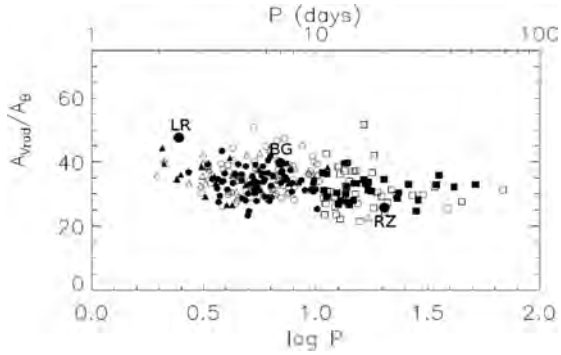

Figure 14. The slightly excessive value of the $A_{V_{RAD}}/A_B$ amplitude ratio of LR TrA and BG Vel (large circles) with respect to the average value characteristic at the given pulsation period is an independent indication of the presence of a companion star. This is a modified version of fig. 4(f) of Klagyivik & Szabados (2009). The open symbols in the original figure correspond to known binaries and the filled symbols to Cepheids without known binarity. For the meaning of various symbols, see Klagyivik & Szabados (2009).

4 CONCLUSIONS

We pointed out that three bright southern Galactic Cepheids, LR TrA, RZ Vel and BG Vel, have a variable γ-velocity, implying their membership in SB systems. RV values of other target Cepheids observed with the same equipment in 2005–2006 and 2012 testify that this variability in the γ-velocity is not of instrumental origin, nor an artefact caused by the analysis.

The available RV data are insufficient to determine the orbital period and other elements of the orbits. However, some inferences can be made from the temporal variations of the γ-velocity. An orbital period of 5600–5700 d of the RZ Vel system is compatible with the data pattern. In the case of BG Vel, short orbital periodicity can be ruled out. For LR TrA, even the range of the possible orbital periods remains uncertain.

The value of the orbital period for SB systems involving a Cepheid component is often unknown: according to the online data base (Szabados 2003a) the orbital period has been determined for about 20 per cent of the known SB Cepheids. The majority of known orbital periods exceed a thousand days.

A companion star may have various effects on the observable photometric properties of the Cepheid component. Various pieces of evidence of duplicity based on the photometric criteria are discussed by Szabados (2003b) and Klagyivik & Szabados (2009). As to our targets, there is no obvious sign of a companion from optical multicolour photometry. This indicates that the companion

star cannot be much hotter than any of the Cepheids discussed here. There is, however, a phenomenological parameter, viz. the ratio of RV to photometric amplitudes (Klagyivik & Szabados 2009) whose excessive value is a further hint at the probable existence of a companion for both LR TrA and BG Vel (see Fig. 14). Moreover, the *IUE* spectra of bright Cepheids analysed by Evans (1992) gave a constraint on the temperature of a companion to remain undetected in the ultraviolet spectra: in the case of RZ Vel, the spectral type of the companion cannot be earlier than A7, while for BG Vel this limiting spectral type is A0. Further spectroscopic observations are necessary to characterize these newly detected SB systems.

Our findings confirm the previous statement by Szabados (2003a) about the high percentage of binaries among classical Cepheids and the observational selection effect hindering the discovery of new cases (see also Fig. 1).

Regular monitoring of the RVs of a large number of Cepheids will be instrumental in finding more SBs among Cepheids. RV data to be obtained with the *Gaia* astrometric space probe (expected launch: 2013 September) will certainly result in revealing new SBs among Cepheids brighter than the 13–14th magnitude (Eyer et al. 2012). In this manner, the 'missing' SBs among Cepheids inferred from Fig. 1 can be successfully revealed within few years.

ACKNOWLEDGEMENTS

This project has been supported by ESTEC Contract No. 4000106398/12/NL/KML, Hungarian OTKA Grants K76816, K83790, K104607 and MB08C 81013, as well as the European Community's Seventh Framework Program (FP7/2007-2013) under grant agreement no. 269194, and the 'Lendület-2009' Young Researchers Program of the Hungarian Academy of Sciences. AD was supported by a Hungarian Eötvös Fellowship. AD has also been supported by a János Bolyai Research Scholarship of the Hungarian Academy of Sciences. AD is very thankful to the staff at The Lodge in the Siding Spring Observatory for their hospitality and very nice food, making the time spent there lovely and special. Part of the research leading to these results has received funding from the European Research Council under the European Community's Seventh Framework Program (FP7/2007–2013)/ERC grant agreement no. 227224 (PROSPERITY). The *INTEGRAL* photometric data, pre-processed by ISDC, have been retrieved from the OMC Archive at CAB (INTA-CSIC). We are indebted to Stanley Walker for sending us some unpublished photoelectric observational data. Our thanks are also due to the referee and Dr Mária Kun for their critical remarks leading to a considerable improvement in the presentation of the results.

REFERENCES

Antonello E., Poretti E., Reduzzi L., 1990, A&A, 236, 138
Baranne A. et al., 1996, A&AS, 119, 373
Berdnikov L. N., 2008, VizieR Online Data Catalog: II/285
Bersier D., 2002, ApJS, 140, 465
Coulson I. M., Caldwell J. A. R., 1985, SAAO Circ., 9, 5
Dean J. F., 1977, Mon. Notes Astron. Soc. South Afr., 36, 3
Dean J. F., Cousins A. W. J., Bywater R. A., Warren P. R., 1977, Mem. R. Astron. Soc., 83, 69
Derekas A. et al., 2012, MNRAS, 425, 1312
Eggen O. J., 1982, ApJS, 50, 199
Eggen O. J., 1983, AJ, 88, 361
Eggen O. J., 1985, AJ, 90, 1297
Eggen O. J., Gascoigne S. C. B., Burr E. J., 1957, MNRAS, 117, 406
ESA, 1997, The Hipparcos and Tycho Catalogues, ESA SP-1200
Evans N. R., 1992, ApJ, 384, 220
Eyer L. et al., 2012, Ap&SS, 341, 207
Hertzsprung E., 1936, Bull. Astron. Inst. Neth., 8, 25
Irwin J. B., 1961, ApJS, 6, 253
Klagyivik P., Szabados L., 2009, A&A, 504, 959
Lloyd Evans T., 1968, MNRAS, 141, 109
Lloyd Evans T., 1980, SAAO Circ., 1, 257
Madore B. F., 1975, ApJS, 29, 219
Munari U., Sordo R., Castelli F., Zwitter T., 2005, A&A, 442, 1127
Nardetto N., Mourard D., Kervella P., Mathias Ph., Mérand A., Bersier D., 2006, A&A, 453, 309
O'Leary W., 1937, Riverview Coll. Obs. Publ., 4, 49
Oosterhoff P. Th., 1936, Bull. Astron. Inst. Neth., 8, 29
Pel J. W., 1976, A&AS, 24, 413
Pepe F., Mayor M., Galland F., Naef D., Queloz D., Santos N. C., Udry S., Burnet M., 2002, A&A, 388, 632
Pickering E. C., 1909, Harvard Coll. Obs. Circ., 151, 1
Pojmanski G., 2002, Acta Astron., 52, 397
Queloz D. et al., 2001, The Messenger, 105, 1
Ségransan D. et al., 2010, A&A, 511, 45
Sterken C., 2005, in Sterken C., ed., ASP Conf. Ser. Vol. 335, The Light-Time Effect in Astrophysics. Astron. Soc. Pac., San Francisco, p. 3
Stibbs D. W. N., 1955, MNRAS, 115, 363
Strohmeier W., Fischer H., Ott H., 1966, Inf. Bull. Var. Stars, 120, 1
Szabados L., 1983, Ap&SS, 96, 185
Szabados L., 2003a, Inf. Bull. Var. Stars, 5394, 1
Szabados L., 2003b, Recent Res. Dev. Astron. Astrophys., 1, 787
Szabados L. et al., 2013, MNRAS, 430, 2018
van Houten C. J., 1950, Ann. Leiden, 20, 223
Walraven Th., Muller A. B., Oosterhoff P. T., 1958, Bull. Astron. Inst. Neth., 14, 81

SUPPORTING INFORMATION

Additional Supporting Information may be found in the online version of this article:

Table 3. RV values of LR TrA from the SSO spectra.
Table 4. CORALIE velocities of LR TrA.
Table 7. RV values of RZ Vel from the SSO spectra.
Table 8. CORALIE velocities of RZ Vel.
Table 11. RV values of BG Vel from the SSO spectra.
Table 12. CORALIE velocities of BG Vel. (http://mnras.oxfordjournals.org/lookup/suppl/doi:10.1093/mnras/stt1079/-/DC1).

Please note: Oxford University Press is not responsible for the content or functionality of any supporting materials supplied by the authors. Any queries (other than missing material) should be directed to the corresponding author for the paper.

This paper has been typeset from a TEX/LATEX file prepared by the author.

Chapter 3

Cepheids in Galactic Open Clusters

Far better an approximate answer
to the right question,
than an exact answer
to the wrong question

JOHN TUKEY
Statistician

3.1 Why search for Cepheids in open clusters?

3.1.1 The importance of cluster Cepheids for the distance scale

The calibration of the Cepheid period-luminosity-relation (PLR) is a corner stone of the astronomical distance scale. As was described in Sec. 1.4, Cepheids are standard candles that have had a significant impact on cosmology as calibrators of the Hubble constant, H_0, with recent publications based in part on Cepheids claiming precision down to a few percent. The role played by Cepheids is a crucial one, covering distances from hundreds of parsec up to tens of Megaparsecs and allowing a calibration of H_0 based purely on Cepheids and type Ia supernovae (e.g. Freedman 2013).

It is worthwhile to group calibrating efforts of the Cepheid PLR into two classes: Galactic calibrations, and extragalactic calibrations. A key difference between the two is the (heliocentric-) distance of the calibrating sample. Whereas this distance can be assumed to be nearly constant for extragalactic Cepheids within a given galaxy, this is not at all the case for Cepheids located in the Milky Way (MW). Cepheids are furthermore relatively easily identified via their high intrinsic brightness and characteristic light variations. As a result, calibrating the *slope* of the PLR in another galaxy is relatively straightforward. Even better, the application of reddening-free Wesenheit indices (Madore 1982, cf. Eq. 1.21) to such calibrations has effectively mitigated the issue of variable extinction across the field of view.

The Cepheids in the Magellanic Clouds have played a particularly important role in these developments, thanks to multi-band time series spanning several decades being available from multiple surveys such as MACHO (Alcock et al. 1999), EROS (Beaulieu et al. 1995), and OGLE (Udalski et al. 1999; Soszynski et al. 2008, 2010). In the approximately 40 square degrees (of the LMC) covered by the OGLE-III survey, for instance, 3361 classical Cepheids were discovered, of

which 1848 were identified as fundamental-mode pulsators (Soszynski et al. 2008). Very good precision is reached with such large statistics.

However, such a calibration does not yield a zero-point, since a distance to the galaxy in question has to be assumed to translate the apparent magnitude into an absolute magnitude. One way of resolving this issue is measuring radii using Baade-Wesselink techniques (cf. Sec. 1.2.1). However, the number of LMC Cepheids with determined BW distances is not (yet?) very large (Groenewegen 2013, lists 36 LMC and 6 SMC Cepheids) due to the faintness of LMC Cepheids (often $m_V > 15$ mag) and resulting long integration times for high-resolution spectroscopy, multiplied by the need for time series data. In this context it must be remembered that the PLR is a statistical calibration that is not technically valid for an individual object. A calibration on a relatively small sample is more sensitive to the intrinsic dispersion of the PLR due to binarity, rotation, metallicity, etc, cf. Sec. 5.2.3. In addition, a possible metallicity dependence of the slope of the PLR has been frequently discussed (e.g. Storm et al. 2011b; Majaess et al. 2011; Groenewegen 2013).

There are thus many good reasons to continue the effort of calibrating the PLR inside the Galaxy. Unfortunately, the Galactic calibration is severely complicated by at least two effects:

1. no common distance can be assumed for Galactic Cepheids
2. Cepheids are young, population I stars residing mainly in the thick disk of the Milky Way, and are subject to substantial reddening and extinction.

Point 1 represents a real difficulty, and requires distance estimates for individual Cepheids, e.g. via absolute trigonometric parallaxes (parallaxes were employed by Feast & Catchpole 1997, although the analysis was limited by small statistics and the adoption of the LMC's PLR slope). This issue is likely to be overcome once *Gaia* parallaxes become available, measuring Cepheid parallaxes to heliocentric distances in excess of 10 kpc within our Galaxy (extinction limited). Point 2, however, has seen significant improvement through the use of infrared photometry and reddening-free Wesenheit indices.

In the recent literature, impressive precision estimates are quoted for BW-distances (e.g. Fouqué et al. 2007; Storm et al. 2011a). Yet, BW-type methods are also (as any method) subject to certain shortcomings and systematic errors. For instance, the IRSB technique can be sensitive to parasitic flux from companion stars. Furthermore, such studies usually assume/adopt a fixed value for R, the ratio of total to selective extinction, which is a property of the scattering dust in the ISM and thus line-of-sight-dependent. When properly determined, it is obvious that the error bars on R alone are easily in the range of 10-15%. BW-type techniques also require so-called p-factors in order to translate the observed radial velocity into the pulsational velocity (cf. Sec. 1.4), on which different opinions exist in the community (e.g. Nardetto et al. 2007; Laney & Joner 2009; Groenewegen 2013). Despite some potential sources of error, very precise PLR calibrations have been achieved in the Galaxies, and there are signs that BW radii determinations are quite robust (Ngeow et al. 2012).

Judging from the recent literature, the Galactic calibration by Benedict et al. (2007) appears to be favored, even though it is based on *relative* trigonometric parallaxes, which rely on spectroscopic distances of only a few comparison stars. Furthermore, the calibration is obtained using merely 10 Cepheids, including only a single long-period Cepheid (ℓ Carinae) for which evidence of an attenuating circumstellar environment has been presented by Kervella et al. (2006, 2009). Furthermore, a controversial Lutz-Kelker-bias (Lutz & Kelker 1973) correction term was added in this calibration[1].

In light of the above discussion, it becomes clear that the most secure way of ensuring accuracy and avoiding bias is to pursue all possible routes. Cepheids belonging to open clusters offer an independent/complimentary method of calibrating the PLR, since cluster distances can be estimated independently of their member Cepheids. It is even possible to cross-calibrate distances

[1] A similar approach was chosen by van Leeuwen et al. (2007) using the re-reduced *Hipparcos* parallaxes

to individual Cepheids determined via BW-type methods and the cluster distance (Ngeow et al. 2012). There is furthermore the added benefit that reddening laws can be determined in clusters (e.g. Turner 1976) and color excess can be derived from the CMD of the cluster. My search for cluster Cepheids was thus aimed at improving the Galactic calibration by enlarging the sample of calibrators, as well as to provide a ranking of known cases according to membership probabilities.

Yet, even cluster-based PLR calibrations are not perfect. For one, cluster distances require a zero-point as well, the ZAMS, which can be fitted between a given cluster and the reference. In this respect it is worth noting that the ZAMS cluster distance to even the most commonly used reference cluster, the Pleiades, is (still) controversial (Robichon et al. 2000, and references therein, as well as Stello & Nissen (2001); Zwahlen et al. (2004); Pan et al. (2004); Soderblom et al. (2005); Miller et al. (2013), among others).

3.1.2 Cepheids as cluster members

Age and metallicity are key parameters for evolving stellar populations. Identifying variable stars belonging to open clusters may thus allow to improve the understanding of the evolutionary status of variable stars and can provide important constraints for stellar evolution. In this spirit, there are large ongoing efforts devoted to "ensemble asteroseismology" in which members of the Stellar Variability group at Geneva Observatory are heavily involved. For instance, the Geneva Open Cluster Survey has been monitoring photometrically 27 open clusters on both hemispheres using 1m-class telescopes for a duration of up to 8 years[2]. The first paper in this campaign's series has recently been published by Mowlavi et al. (2013). Their discovery of a new class of periodic variable star whose nature cannot currently be explained may present a real challenge to the theory of stellar pulsation. The open cluster in this case provided the evolutionary context for these stars and allowed to translate their position in the CMD into an HRD, unambiguously exposing this important discovery.

Besides searching for Galactic calibrators, a primary goal of this project was related to exactly this: better understanding the evolutionary status of Cepheids. As Kippenhahn & Weigert (1994) put it, Cepheids are "a sort of magnifying glass" for stellar evolution, since their location in the HRD depends very sensitively on the physics of their interiors and changes comparatively rapidly (more details on this subject are presented in Sec. 4) as a function of time. Hence, there are two ways in which cluster Cepheids could be employed for testing stellar evolution models. The first would be related to the study of individual clusters, whereas the second investigates the fraction of Cepheids in open clusters statistically. In both cases it is particularly important to be confident that cluster membership holds in order to avoid erroneous conclusions. In addition, when studying the fraction of cluster Cepheids, the question of completeness becomes very important due to the small number statistics (cluster Cepheids are rare, see below). Hence, in order to maximize the potential of using Galactic cluster Cepheids as test-beds for stellar evolution, a maximally[3] complete census of Cepheids in open clusters is required, cf. also Sec. 4.4.2.

3.1.3 Large surveys and big data

Large Surveys

A major development in astronomy during the second half of the 20^{th} century was the creation of an increasingly holistic observational perspective on astronomical objects accomplished by providing a suite of different data types and opening the time domain for ever-increasing portions of the sky. As a result, modern studies can take into account a diverse set of information available

[2]During my first observing run, I had the opportunity to contribute to this effort by observing at ESO La Silla Observatory in Chile while also encountering my first earthquake on 27 February 2010

[3]in the sense of "as complete as possible"

for the objects under investigation, and Virtual Observatory tools are available for finding and providing access to data stored in different online archives and catalogs.

Recent and ongoing surveys such as 2MASS[4], SDSS[5], LINEAR[6], PanSTARRS[7], and the surveys using the ESO VISTA survey telescope[8], among others, have already provided photometric data for hundreds of millions of objects. The future ESA space mission *Gaia*[9] and the planned LSST[10] will further increase this data avalanche, with expected numbers of sources being in the order of 1 billion (Gaia) and 10 billion stars plus 10 billion galaxies (LSST) (Eyer et al. 2012a).

On the spectroscopic side, the numbers tend to be lower, but are impressive nonetheless: RAVE[11] has already published precise ($\sim 2\,\mathrm{km\,s^{-1}}$) radial velocities for nearly $500\,000$ stars, and the ESO-Gaia public survey[12] also targets 10^5 stars, including also approximately 100 open clusters Gilmore et al. (2012).

It is clear from the above numbers of objects studied, the many different sources of information available, and the fact that time-resolved data are becoming the status quo, that astronomy is facing a problem of manpower[13]. This phenomenon is called the problem of "big data", a somewhat astronomy-biased background is presented below.

Big data

The digital revolution is exponentially increasing the capacity for long-term data storage. From Astronomy to Zoology, data volumes are increasing at phenomenal rates, resulting in datasets that are "too big to analyze" with conventional methods. Thanks to these developments, time series astronomy has made a quantum leap forward in the last two decades and greatly improved our understanding of the variable sky from Active Galactic Nuclei to ZZ Ceti short-period pulsating white dwarfs.

"New" data is pouring in from both the ends. Archival data stored in the form of hard copies is being digitized, see e.g. the Digital Access to a Sky Century @ Harvard (DASCH) project (Grindlay et al. 2012; Tang et al. 2013) that aims to digitize $500\,000$ astronomical glass plate images, or the electronic scans of old articles available through NASA's Astrophysics Data System[14]. However, the increase in new data is even more impressive. For instance, the final catalog of the *Gaia* space mission is expected to yield 1 petabyte of data of approximately one billion sources. Yet, it is only a matter of time before these data volumes will be dwarfed by future projects such as *LSST*, *LOFAR*, or *EUCLID*.

Whereas the (already large) data volumes created by surveys such as EROS, MACHO, or OGLE (Number of objects) are often still searched visually for variable objects, newer projects such as the Catalina Real Time Survey (CRTS) or the Palomar Transient Factory (PTF) rely on automated methods of data processing and object classification. Meanwhile, significant advancements are made in the automatic classification of transient and variable phenomena that explore supervised as well as autonomous methods, and are calibrated on training sets derived from well-known (visually classified) reference catalogs (e.g. Eyer & Blake 2005; Eyer et al. 2008; Dubath et al. 2011; Süveges et al. 2012; Rimoldini et al. 2012; Richards et al. 2012; Brink et al. 2013).

[4]Two Micron All Sky Survey, `http://www.lsst.org/lsst/`

[5]Sloan Digital Sky Survey, `http://www.sdss.org/`

[6]Lincoln Near-Earth Asteroid Research, `http://www.ll.mit.edu/mission/space/linear/`

[7]Panoramic Survey Telescope & Rapid Response System, `http://pan-starrs.ifa.hawaii.edu/`

[8]Visible and Infrared Survey Telescope for Astronomy, `http://www.eso.org/public/teles-instr/surveytelescopes/vista/surveys/`

[9]expected launch: 20 November 2013, `http://www.esa.int/Our_Activities/Space_Science/Gaia`

[10]Large Synoptic Survey Telescope, `http://www.lsst.org/lsst/`

[11]Radial Velocity Experiment, `http://www.rave-survey.aip.de/rave/`

[12]`http://www.gaia-eso.eu/`

[13]of course this includes women just as well!

[14]http://www.adsabs.harvard.edu/

In the *Gaia* era, it will no longer be feasible (considering the number of scientists) to visually inspect the light curves of all objects, and new challenges are posed to computer scientists for handling such large volumes of data. For instance, there are currently[15] more than 400 members of the *Gaia* Data Processing and Analysis Consortium (DPAC) working on the preparation for (all kinds of) *Gaia* data. Obviously, there is a strong interest in the development of automated reliable data analysis methods that are not prohibitively (time) expensive and thus applicable to large datasets.

An interesting way of dealing with the high abundance of data are so-called Citizen Science projects, e.g. as available through the Zooniverse website[16]. These projects essentially use the pattern recognition capacity of people worldwide to reduce the load on scientists, allowing them to focus on the data analysis. In this regard, space sciences were among the pioneers in this respect, launching the Galaxy Zoo project in July 2007. The public response to this initiative was so positive that there are now a range of citizen science projects including the categories space, climate, humanities, nature, and biology.

Big data-related developments are inherently interdisciplinary. For instance, during my thesis in the Geneva Stellar Variability group, I had the opportunity to observe the work of CU7 devoted to the analysis of variability, combining the expertise of astrophysicists, statisticians, and computer specialists. However, this topic is just as relevant for a plethora of other active fields outside of astronomy, from finance to intelligence & law enforcement. For instance, the recent scandal involving several spy agencies has offered a glimpse into the application of data mining methods on big data generated from mass-surveillance of world-wide telecommunications. The abstract goals are typically the same across the board: identifying trends and correlations, and exposing the most interesting objects in the sample, i.e., finding needle in the haystack.

Aimed at identifying Cepheid members of open clusters, the astro-statistical method described in the following follows a like-minded data mining approach and was created to be compatible with with large data sets such as those expected by *Gaia* and *LSST*.

3.2 Basis of membership analysis

3.2.1 Galactic open clusters as coeval populations

The simplest case of stellar populations are open clusters. In the canonical picture, open clusters are considered to be co-eval populations that formed nearly instantaneously from molecular clouds assumed to be chemically homogeneous. Consequently, all stars belonging to a given open cluster are considered to have the same age, a, and chemical composition, usually expressed using iron abundance relative to Solar, [Fe/H], as a proxy for metallicity, Z.

In this paradigm, the constituent stars of a cluster evolve in analogous fashion, every individual star's mass dictating its evolutionary path in the HRD. At a given time after the "birth" of the open cluster, the cluster stars therefore should all lie on a single curve that corresponds to stars of all possible masses for a given age, a so-called isochrone. However, this picture lacks an important ingredient: rotation, see Chap. 4. Suffice it here to mention that rotating models predict longer Main Sequence (MS) lifetimes than non-rotating models. As a results, stellar ages and therefore also open cluster ages should be approximately 20% higher than previously thought. Of course, this "increase" in age is also relevant for the Cepheid period-age relationship determined by Bono et al. (2005) and for the usage of Cepheids as tracers of star formation history (e.g. Matsunaga et al. 2011). More information on the effect of rotation on Cepheid populations is presented in Chap. 4.

[15] `http://www.rssd.esa.int/index.php?project=GAIA&page=DPAC_Introduction`
[16] `https://www.zooniverse.org/`

3.2.2 Cluster membership in 8D

As discussed above, clusters are co-eval populations, indicating that the member stars share common parameters or characteristics. Besides the already mentioned population-specific parameters metallicity and age, these are location and space motion, each of which can be expressed in 3-dimensional coordinates. Thus, using the 3 spatial and 3 kinematic membership constraints together with metallicity and age, a total of 8 membership constraints are considered in this approach. The details of the method are explained in Sec. 2 of the paper included below (Sec. 3.5). I here simply provide a quick overview before commenting on the available data used as membership constraints in the following Sec. 3.2.3.

Constraint type	Cluster	Cepheid
spatial: on-sky location (2D)	cluster center coordinates and radius	separation from cluster center
spatial: parallax [mas]	converted from distances [pc]	derived using various methods (depending on availability): trigonometric, BW distance, PLR
kinematic: on-sky motion (2D)	cluster mean proper motion	Cepheid proper motion
kinematic: radial velocity	cluster mean radial velocity	Cepheid systemic velocity
population: [Fe/H]	mean value for cluster stars	spectroscopic
population: $\log(age\,[\mathrm{yr}])$	based on isochrone fitting	period-age relation

Table 3.1: Membership constraints employed in the search for Cepheids in open clusters

Table 3.1 lists the parameters used as membership constraints and a quick statement about how they are derived. The on-sky constraints location and proper motion are inherently two-dimensional, since they are measured as projections on the sky.

Posterior membership probability, $P(A|B)$, denotes the probability of the hypothesis of membership, A, given the data, B, to be true. According to Bayes' Theorem, these are computed as follows (e.g. Jaynes 2003):

$$P(A|B) = \frac{P(A) \times P(B|A)}{P(B)}\,. \tag{3.1}$$

Here, $P(B|A)$ corresponds to the likelihood of observing the data given a certain hypothesis, allowing a computation via a simple hypothesis test. The implementation of the $P(B|A)$ computation was a simple extension of the method by Robichon et al. (1999) and Baumgardt et al. (2000) to higher dimensionality.

The real novelty in this approach was the use of $P(A)$, the prior probability assigned to quantify an initial belief in membership. This quantity was computed assuming a radial on-sky distribution of cluster members (consistent with the common practice of cluster radius determination in the literature, see King 1962) and using the on-sky separation (Cepheid from cluster center in minutes of arc) relative to the apparent cluster size on the sky as expressed by its core and limiting radii. It thus aims to perform a translation of the cluster's radial density profile into a prior probability of cluster membership for the Cepheid.

$P(B)$ is the probability of observing the data and is obviously very difficult to estimate. Accordingly, we set $P(B) = 1$ and computed $P(A|B) \equiv P(A) \cdot P(B|A)$. This should no longer be necessary once *Gaia* has mapped the extended Solar neighborhood. Hence, the method presented will benefit greatly by *Gaia*'s Galactic census.

For the time being, it was deemed best to investigate prior and likelihood separately due to the missing constraint on $P(B)$. Nevertheless, it was thus possible to rank cluster Cepheid candidates according to the likelihoods computed and identify potentially interesting cases by their priors.

3.2.3 On observational membership constraints

This study was based on samples of *known* open clusters and *known* Cepheid (candidates), and the analysis employed mostly published literature data, supplemented by a significant observational effort dedicated to Cepheid radial velocities, see Sec. 2. In the following subsections, I aim to provide some additional background and context related to the data employed for this study. More details can be found in the publication in Sec. 3.5.

Galactic Open Clusters

During the last decade, it has become possible to investigate cluster parameters automatically using public all-sky photometric data and other resources available through the Virtual Observatory (VO). For instance, Kharchenko et al. (2012) recently presented their method of searching the Galaxy for open clusters in a compilation of data based mainly on Two Micron All Sky Survey (2MASS) photometry (Cutri et al. 2003) and the PPMXL catalog (Roeser et al. 2010). Another large study of this kind to mention here is Bukowiecki et al. (2011), also based on 2MASS photometry.

Such self-consistent analyses are indispensable for obtaining parameters for larger cluster samples and must be developed in order to deal with the problem of big data, cf. Sec. 3.1.3. However, they are also currently limited in accuracy. For instance, such methods typically struggle when multiple clusters lie close to one another on the projected sky plane, since the usual underlying assumption is that only two stellar populations (field & cluster stars) are present in the field of view. Such is the case, for instance, for the cluster Trumpler 18. Another problem for automated cluster searches are false positives due to asterisms, fluctuations in field star density, and relatively extinction-free zones in otherwise heavily obscured directions of the sky. The cluster (candidate) Ruprecht 79 is a good (but not the only) example for this latter problem (McSwain & Gies 2005). However, promising developments have recently been made in this regard (Krone-Martins & Moitinho 2013) and await testing on real data. These problems are not unsolvable, and efforts are also being made in preparation for *Gaia*.

Galactic classical Cepheids

The problems encountered regarding available Cepheid data are in some ways similar to those of open clusters. First, the data available are highly inhomogeneous, since time-resolved observations of many faint individual stars is observationally expensive to obtain. Although the Cepheid database by Fernie et al. (1995) is sometimes criticized for containing hard-to-find errors and artifacts, it remains the most extensive compilation of a plethora of very useful parameters for more than 500 Galactic Cepheids and rightfully continues to be used in many studies dedicated to the subject. Klagyivik & Szabados (2009) have since made an effort to homogenize data for 369 Cepheids, notably iron abundances from the literature, and have made these publicly available.

For this work, however, data for an exhaustive list of known Galactic Cepheids was desired. Hence, a significant effort was dedicated to compiling data from the literature using the VO tool `TOPCAT` and the VizieR catalog tool offered by the CDS[17]. To make even better use of the available literature, tables published online were collected from journal websites, and in some cases, data tables were transformed from scanned documents into machine-readable form via freely-available web-based text-recognition tools. The effort of data homogenization is described in the final paper.

Using `TOPCAT`, data from general stellar catalogs such as PPMXL (Roeser et al. 2010), 2MASS (Cutri et al. 2003), and the Hipparcos catalog (Perryman & ESA 1997; van Leeuwen 2007) were cross-matched with the list of Cepheid candidates, and the quality of the cross-match was ensured

[17] `http://cds.u-strasbg.fr/`

by calculating coordinate offsets in the different catalogs as well as magnitudes listed. This cross-matching of literature data was done for more than $2\,000$ Cepheid candidates listed in the General Catalog of Variable Stars (GCVS, Samus et al. 2012) and the American Association of Variable Star Observers (AAVSO)'s Variable Star Index[18].

Most of the Cepheids present in this compilation were candidates discovered by surveys such as the All Sky Automated Survey (ASAS, Pojmanski 1997, 2002; Pojmanski et al. 2005), (ROTSE, Akerlof et al. 2000), and the Northern Sky Variability Survey (NSVS, Woźniak et al. 2004), to name but the most important ones. Furthermore, suspected variables were also included (Kukarkin & Kholopov 1982). In order to reduce contamination by misclassified objects, a visual inspection of light curves was carried out for the ASAS Cepheid candidates cross-matched with open clusters. 153 candidates from these surveys were furthermore observed as part of the observation program, cf. Sec. 2.4. The cleaned sample of Cepheid candidates contained $1\,821$ objects, of which $1\,021$ were cross-matched with open clusters. In this clean up effort, special attention was paid to Cepheid candidates located close to open clusters.

In the future, it would be beneficial for the community as a whole to have an updated and exhaustive list of known bona fide Cepheids including their observational properties and parameters. To this end, it would be beneficial to create an updated, open database of Cepheids which experts can contribute to, while ensuring internal consistency. The compilation created for this project would form a good starting point to this end, but the undertaking as a whole is too ambitious for a single person and will have to be a continued effort.

3.3 An astro-statistical approach to cluster membership

Previously, cluster membership of Cepheids was usually investigated on a case-by-case basis. Yet, in this era of large surveys and notably *Gaia*, new methods have to be created in order to discover these important calibrators. Such methods must be statistical due to the large data volume and great numbers considered, and their aim will be to "find the needle in the haystack". In this sense, searching for Cepheids in open clusters might be likened to finding terrorists through global monitoring of worldwide telecommunications.

During my thesis, I conceived and developed an astro-statistical method suitable for identifying cluster Cepheids using the data currently available via the Virtual Observatory and other published literature or catalogs. This study had four primary aims:

1. discovering cluster Cepheids that had escaped previous attention in order to enlarge the sample of calibrators
2. revisiting the calibration of the Cepheid PLR using the resulting *bona fide* cluster Cepheid sample
3. establishing a statistically significant sample of *bona fide* cluster Cepheids that can be used as a test-bed for stellar evolution, cf. Chap. 4
4. developing a membership determination technique suitable for large surveys such as *Gaia* and *LSST*.

In a nutshell, this study started with a positional cross-match of known Cepheids with known open clusters based on Cepheid and cluster coordinates as well as the clusters' radii. Then, membership probabilities were computed for all cross-matched cluster-Cepheid combinations (from hereon referred to as "Combos"). Confidence in membership could then be ranked according to the probabilities computed, thus exposing the sample particularly interesting objects.

[18] `http://www.aavso.org/vsx/`

The main difficulties encountered in the study were related to incompleteness, data inhomogeneity and a lack of suitable error estimates[19]. Therefore, one important aspect of this project was to understand the systematics involved in the determination of cluster or Cepheid parameters. In the case of cluster ages, for instance, I had to define suitable error budgets, based on an argument rooted in the evolution of stellar populations (age estimates for older populations are more precise than those of younger populations, cf. Sec. 3.1.6 in Anderson et al. (2013a) included below). In addition, the constraining power of proper motion was severely limited due to the typically very large (100s of pc to multiple kpc) distances of the objects considered.

Most of these systematic difficulties will disappear once *Gaia* data become public. Incompleteness will not pose major issues inside a considerable volume around the Sun, since *Gaia* will observe all objects between 2^{nd} and 20^{th} magnitude (L. Eyer, priv. comm.). Astrometry of unprecedented accuracy and precision will furthermore remove the model dependence of cluster distances originating in isochrone-fitting. And finally, even correlations between quantities, such as parallax and proper motion can be taken into account in the calculation; this has previously been done in determinations of membership in nearby ($< 300 - 500\,\mathrm{pc}$) open clusters using *Hipparcos* data (Robichon et al. 1999; van Leeuwen 2009).

3.4 Related results and publications

Preliminary results from this work were presented as poster contributions at two conferences and as a contributed talk at the International Astronomical Union (IAU) Symposium 289 "Advancing the Physics of Cosmic Distances" held during the 28^{th} IAU General Assembly in Beijing, China. Three proceedings articles were published in relation to this work, tracing its evolution and the preliminary results obtained (Anderson et al. 2012b,a, 2013b). The final results were published as an article entitled "Cepheids in open clusters: an 8D all-sky census" in the peer-reviewed journal *Monthly Notices of the Royal Astronomical Society*, Vol. **434**, pp. 2238 - 2261 (2013), attached below. Supplementary data were made public on the CDS at `http://cdsarc.u-strasbg.fr/cgi-bin/VizieR?-source=J/MNRAS/434/2238`.

This work's main contributions consist in the discovery of 5 new *bona fide* cluster Cepheids and a confirmation of 18 other, previously known, candidates. A ranking of confidence in membership for all Combos is provided, including most *bona fide* cluster Cepheid candidates known from the literature[20]. This being a statistical approach, all new bona fide cluster Cepheids presented should be considered candidates. Especially the cluster data used to determine membership may require validation and improvement. In this study, we also revisited the PLR calibration using the bona fide sample, and arrived at the conclusion that large discrepancies between open cluster data from different sources severely limits the precision attainable. A homogeneous, self-consistent analysis of all host clusters would be beneficial to improve this calibration. A homogeneous and detailed treatment of line-of-sight-dependent reddening laws and color excess would be particularly useful to this end.

[19] In the great majority of parameters found in the literature for open clusters or Cepheids, errors listed correspond to internal errors, or precision estimates. These error budgets do not, however, take into account systematic error, which limits the intercomparability of data from multiple, inhomogeneous sources.

[20] some combos could not be studied due to a lack of available data, see Sec. 4.1.1 in the paper

Monthly Notices of the ROYAL ASTRONOMICAL SOCIETY

MNRAS **434,** 2238–2261 (2013) doi:10.1093/mnras/stt1160
Advance Access publication 2013 July 22

Cepheids in open clusters: an 8D all-sky census★†

Richard I. Anderson,‡ Laurent Eyer and Nami Mowlavi
Observatoire de Genève, Université de Genève, 51 Ch. des Maillettes, CH-1290 Versoix, Switzerland

Accepted 2013 June 24. Received 2013 May 20; in original form 2012 December 20

ABSTRACT

Cepheids in Galactic open clusters (CCs) are of great importance as zero-point calibrators of the Galactic Cepheid period–luminosity relationship (PLR).

We perform an eight-dimensional all-sky census that aims to identify new bona fide CCs and provides a ranking of membership confidence for known CC candidates according to membership probabilities. The probabilities are computed for combinations of known Galactic open clusters and classical Cepheid candidates, based on spatial, kinematic and population-specific membership constraints. Data employed in this analysis are taken largely from published literature and supplemented by a year-round observing programme on both hemispheres dedicated to determining systemic radial velocities of Cepheids.

In total, we find 23 bona fide CCs, 5 of which are candidates identified for the first time, including an overtone-Cepheid member in NGC 129. We discuss a subset of CC candidates in detail, some of which have been previously mentioned in the literature. Our results indicate unlikely membership for seven Cepheids that have been previously discussed in terms of cluster membership.

We furthermore revisit the Galactic PLR using our bona fide CC sample and obtain a result consistent with the recent calibration by Turner. However, our calibration remains limited mainly by cluster uncertainties and the small number of long-period calibrators.

In the near future, *Gaia* will enable our study to be carried out in much greater detail and accuracy, thanks to data homogeneity and greater levels of completeness.

Key words: methods: data analysis – astronomical data bases: miscellaneous – catalogues – stars: variables: Cepheids – open clusters and associations: general – distance scale.

1 INTRODUCTION

The search for Cepheids in Galactic open clusters (CCs) has been a topic of interest in astronomy for the past 60 years, owing largely to their importance as calibrators of the Cepheid period–luminosity relation (PLR), discovered a century ago among 25 periodic variable stars in the Small Magellanic Cloud by Leavitt & Pickering (1912).

The proportionality between the logarithm of Cepheid pulsation periods and their absolute magnitudes, i.e. their (logarithmic) luminosities, gives access to distance determinations and has established PLRs as cornerstones of the astronomical distance scale (e.g. Freedman et al. 2001; Sandage et al. 2006). For reviews on Cepheids as distance indicators, see Feast (1999) and Sandage & Tammann (2006), for instance.

The existence of the Cepheid PLR is most obvious among Cepheids in the Magellanic Clouds (e.g. Udalski et al. 1999; Soszynski et al. 2008, 2010), due to common distances (small dispersion), large statistics (thousands) and relative proximity (detectability). However, knowledge of the zero-point(s) of such relations is also required; in this case, the distances to the Magellanic Clouds. For such zero-point calibrations, PLR-independent distance estimates are required, e.g. from trigonometric parallaxes (Feast & Catchpole 1997; Benedict et al. 2007), Baade–Wesselink-type methods (Gieren, Fouqué & Gomez 1997; Storm et al. 2011), or objects located at comparable distance, e.g. water masers (Macri et al. 2006) or open clusters (Turner et al. 2010).

For open clusters, distances can be determined via zero-age main sequence (ZAMS) or isochrone fitting. If membership can be

★Based on observations collected at the European Southern Observatory La Silla Observatory with the CORALIE echelle spectrograph mounted to the Swiss 1.2 m Euler telescope.

†Based on observations obtained with the HERMES spectrograph, which is supported by the Fund for Scientific Research of Flanders (FWO), Belgium, the Research Council of K.U. Leuven, Belgium, the Fonds National Recherches Scientific (FNRS), Belgium, the Royal Observatory of Belgium, the Observatoire de Genève, Switzerland and the Thüringer Landessternwarte Tautenburg, Germany. HERMES is mounted to the Mercator Telescope, operated on the island of La Palma by the Flemish Community, at the Spanish Observatorio del Roque de los Muchachos of the Instituto de Astrofísica de Canarias.

‡E-mail: richard.anderson@unige.ch

assumed at high confidence, the cluster provides the independent estimation of the Cepheid's distance. Confidence in cluster membership is thus critical for such calibrations.

Since the first discovery of CCs by Irwin (1955, identified S Nor in NGC 6087 and U Sgr in M 25) and Feast (1957, established membership via radial velocities, RVs), many researchers have contributed to this field (e.g. Kholopov 1956; van den Bergh 1957; Efremov 1964; Tsarevsky, Ureche & Efremov 1966; Turner 1986; Turner et al. 1993; Baumgardt, Dettbarn & Wielen 2000; Hoyle, Shanks & Tanvir 2003; An, Terndrup & Pinsonneault 2007; Majaess, Turner & Lane 2008; Turner 2010). Nevertheless, relatively few bona fide CCs (<30) have thus far been discovered.

We therefore carry out an all-sky census of classical Cepheids in Galactic open clusters that aims to increase the number of bona fide CCs and allows us to rank confidence in membership according to membership probabilities. Our approach is eight dimensional in the sense that three spatial, three kinematic and two population parameters (iron abundance and age) are used as membership constraints. Both data inhomogeneity and incompleteness are critical limitations to this work, and are acknowledged in the relevant sections. We describe our analysis in Section 2.

For the first time, we systematically search for cluster members among Cepheid candidates from surveys such as the All Sky Automated Survey (ASAS; e.g. Pojmanski et al. 2005), the Northern Sky Variability Survey (NSVS; Wozniak et al. 2004), the ROTSE All Sky Survey for Variable Stars (Akerlof et al. 2000), and also from the suspected variables in the General Catalogue of Variable Stars. Most data employed to do so are taken from published catalogues or other literature. However, we also perform RV observations of Cepheids on both hemispheres and determine systemic velocities, v_γ. To improve sensitivity to binarity, the literature RVs are added to the new observations. The data compilation is described in Section 3.1.

The results of our census are presented in Section 4, starting with cluster-Cepheid combinations (Combos) that were previously studied with respect to membership, see Table 1 in Section 4.1, and followed by Combos highlighted by our work, see Table 2 in Section 4.2. The full table containing all Combos investigated in this work is provided in digital form in the online appendix and via the CDS.[1] Combos that deserve observational follow-up are identified in the text. Particular attention is given to Combos previously discussed in the literature. Discussions of additional Combos can be found in the online appendix. In Section 4.3, we employ our bona fide CC sample in a calibration of the Galactic Cepheid PLR. The method and results are discussed in Section 5, which is followed by the conclusion in Section 6.

2 MEMBERSHIP ANALYSIS

Our all-sky census is structured as shown in Fig. 1. First, lists of known open clusters and known Cepheid candidates are compiled, see Section 3.1 for details. Secondly, the two lists are cross-matched positionally in a many-to-many relationship so that we investigate a given Cepheid's membership in multiple different open clusters, and a given open cluster can potentially host multiple Cepheids. The correct classification of cross-matched Cepheid candidates is verified by considering light curves and spectra. Misclassified objects are removed from the Cepheids sample. Thirdly, membership

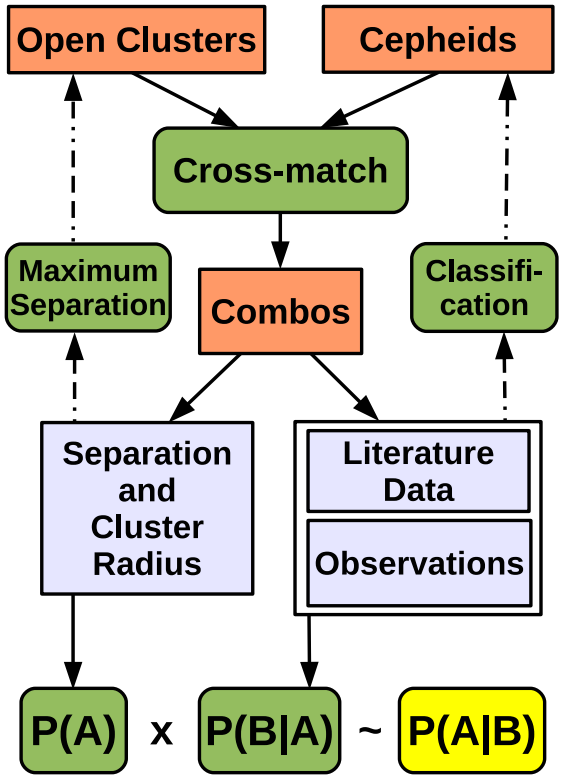

Figure 1. Schematic view of membership analysis. The rectangular boxes represent data sets used, the green rounded boxes indicate actions. Cepheids are cross-matched (within some maximum separation) with open clusters to form Combos. Data from the literature and new observations are combined for each Combo. Cepheid classification is verified based on the data compiled (light curves, spectra). Priors, $P(A)$, and likelihoods, $P(B|A)$, are calculated separately and joined as membership probabilities, $P(A|B)$.

probabilities are calculated based on all available membership constraints. These last two points are described in the present section.

Membership probabilities are calculated following Bayes' theorem that can be formulated as (Jaynes 2003, Section 4):

$$P(A|B) = \frac{P(B|A) \times P(A)}{P(B)} \propto P(B|A) \times P(A). \quad (1)$$

The posterior probability $P(A|B)$ (membership probability) is proportional to the product of likelihood, $P(B|A)$, and prior, $P(A)$. $P(B|A)$ represents the conditional probability of observing the data under the hypothesis of membership, and $P(A)$ quantifies the degree of initial belief in membership. The normalization term $P(B)$, of which we possess no knowledge, is the probability to observe the data. We define $P(A)$ in equations (3) and (4) and $P(B|A)$ in equation (7).

2.1 Prior estimation and positional cross-match

2.1.1 Positional cross-match

On-sky proximity is a necessary, but insufficient criterion for membership. Intuitively, if no other information is available, one might tentatively assume membership for a Cepheid that falls within the core radius of a potential host cluster.

Therefore, our census starts with a positional cross-match that aims to identify all combinations of cluster-Cepheid pairs that lie sufficiently close on the sky to warrant a membership probability

[1] http://cds.u-strasbg.fr

calculation (Combos). The cross-match itself is straightforward: if the separation between a cluster's centre coordinates and the Cepheid's coordinates is smaller than 2.°5 (to avoid unnecessary contamination), and less or equal to 5 limiting cluster radii,[2] we include the Combo in our analysis. Using this proximity criterion, we cross-match 990 different open clusters (of 2168 in Dias et al. 2002a) with 1021 Cepheids (of 1821 initially compiled) and obtain 3974 Combos that we investigate for membership.

The initial cross-match is purely positional, and the majority of Combos studied are non-members. Our analysis intends to weed out this majority and to indicate to us the good candidates through a high membership probability.

2.1.2 The prior

We define the prior, $P(A)$, using the on-sky separation[3] between cluster centre and Cepheid, weighted by the cluster radius, i.e. its apparent size on the sky.

The radius of an open cluster is typically determined by fitting an exponential radial density profile to a stellar overdensity on the sky, an approach originally developed for globular clusters by King (1962). The method relies on the assumption that two separate distributions are seen: a constant field distribution and one that is attributed to the cluster.

Various ways to define cluster radii can be found in the literature. Among these are the 'core radius' (most stars belong to cluster), r_c, and the 'limiting radius' for the cluster halo (strong field star contamination), $r_{\rm lim}$, see Kharchenko et al. (2005a,b) and Bukowiecki et al. (2011).

Intuitively, the probability of membership is related to separation and cluster radius (cf. Sánchez, Vicente & Alfaro 2010). Let us therefore define the quantity x as

$$x = \frac{r - r_c}{2r_{\rm lim} - r_c}, \tag{2}$$

where r denotes separation. x is negative, if the Cepheid lies within the cluster's (projected) core and becomes unity at a separation equal to twice the limiting radius. We define our prior, $P(A)$, so that (no other constraints considered) membership is assumed when the Cepheid lies within the cluster's core, i.e. $x < 0$. Outside r_c, inspired by radial density profiles of star clusters, we let the prior fall off exponentially and define it to reach 0.1 per cent $= 10^{-3}$ at $x = 1$. Hence,

$$P(A)(x < 0) \equiv 1 \tag{3}$$

$$P(A)(x \geq 0) \equiv 10^{-3x}. \tag{4}$$

Fig. 2 serves to illustrate this definition. The prior thus carries the two-dimensional information of separation and cluster radius, and thereby takes into account how concentrated a cluster is on the sky assuming circularly distributed member stars.

2.2 The likelihood $P(B|A)$

The likelihood, $P(B|A)$, is computed as a hypothesis test. It estimates the probability that the observed data is consistent with the null hypothesis of (true) membership. This approach was inspired by the *Hipparcos* astrometry-based studies by Robichon et al. (1999) and Baumgardt et al. (2000). We extend it here to take into account up to six dimensions using parallax, ϖ, RV, proper motion, μ_α^* and μ_δ, iron abundance, [Fe/H], and age (open clusters assumed to be co-eval), weighting all constraints equally.

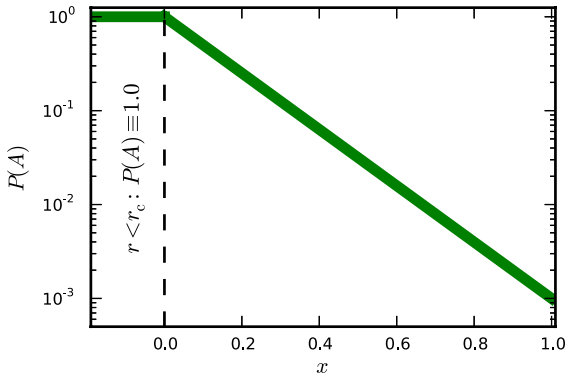

Figure 2. Illustration of the adopted prior, $P(A)$, as a function of separation normalized to a cluster's radii, expressed by the quantity x, cf. equation (2). If $x \leq 0$ (Cepheid within core radius, r_c): $P(A) \equiv 1$. Outside the core, $P(A)$ decreases exponentially, inspired by radial density profiles of stars clusters. We adopt $P(A) = 0.001$ at $r = 2\,r_{\rm lim}$.

Assuming that a given Cepheid was not used to determine a cluster's (mean) parameters, we can calculate the quantity

$$c = \boldsymbol{x}^T \boldsymbol{\Sigma}^{-1} \boldsymbol{x}, \tag{5}$$

where x denotes the vector containing as elements the differences between the (mean) cluster and Cepheid quantities:

$$\boldsymbol{x} = \left(\varpi_{\rm Cl} - \varpi_{\rm Cep}, \langle v_{r,{\rm Cl}}\rangle - v_{\gamma,{\rm Cep}}, \ldots\right). \tag{6}$$

Let $\mathbf{C}_{\rm Cl}$ be the covariance matrix of the cluster and $\mathbf{C}_{\rm Cep}$ that of the Cepheid. Let $\boldsymbol{\Sigma}$ then denote the sum of the two and $\boldsymbol{\Sigma}^{-1}$ its inverse. Since the data employed in this calculation come from many different sources, no knowledge of correlations between the different parameters is available. We thus make the assumption of independent measurements, which results in diagonal covariance matrices containing only parameter variances. Possible correlations between Cepheid and Cluster parameters are thus assumed to be negligible. We consider this justified, since we possess no knowledge of the extent of such correlations and assume that Cepheids were not used in the determination of cluster mean values. This formulation furthermore implicitly assumes normally (Gaussian) distributed errors.

Under these assumptions c is χ^2 distributed, i.e. $c \sim \chi^2_{N_{\rm dof}}$, where $N_{\rm dof}$ is the number of degrees of freedom equal to the length of vector x, ranging from 1 to 6. c thus depends on the number of membership constraints considered (the on-sky position is used in the prior). In cases where no membership constraints are available, i.e. $N_{\rm dof} = 0$, we set $P(B|A) \equiv 1$.

$P(B|A)$ is obtained by calculating unity minus the p-value of c, $p(c)$:

$$P(B|A) = 1 - p(c). \tag{7}$$

Since the χ^2 distribution (and therefore the p-value computed) is very sensitive to $N_{\rm dof}$ for small $N_{\rm dof}$, $P(B|A)$ naturally contains information on the number of membership constraints employed.

Of course, we cannot prove the null hypothesis, only exclude it. However, by including the greatest number of the most stringent membership constraints possible, this method very effectively

[2] This cut-off radius was adopted to include possible members of cluster haloes in the analysis, inspired by the well-known case of SZ Tau in NGC 1647.

[3] We avoid the term 'distance' when referring to the on-sky separation (in arcmin) in order to prevent confusion with radial distance (in pc).

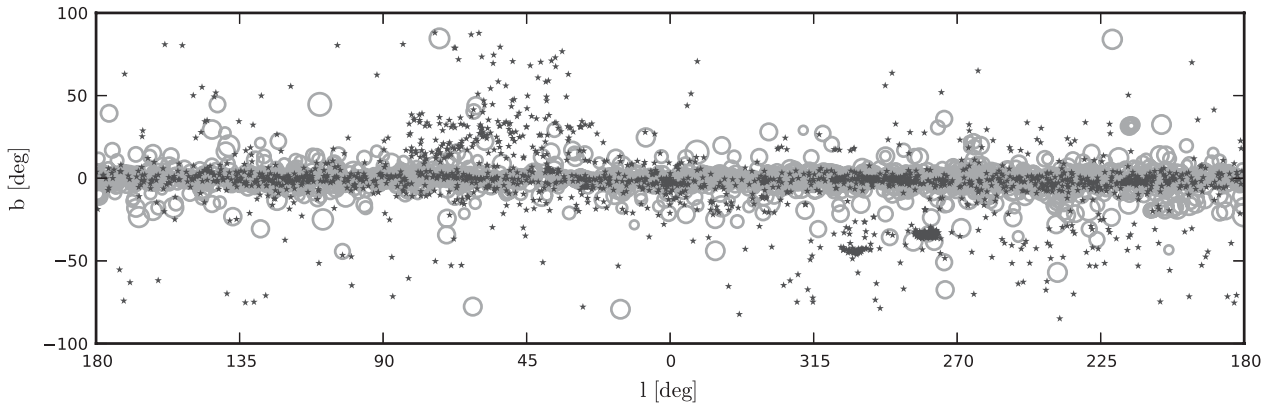

Figure 3. Distribution of open clusters and Cepheids compiled, shown in Galactic coordinates. Light grey open circles represent open clusters with markers logarithmically scaled for apparent size, darker grey star symbols Cepheids.

filters out non-members. The remaining candidates can therefore be considered bona fide members, provided the constraints taken into account are sufficiently strong.

The filtering effectiveness of the likelihood strongly depends on the uncertainties adopted for the constraining quantities: the larger the error, the weaker the constraint. Conversely, the smaller the error, the more important become systematic differences between quantities measured or inferred through different techniques. Obtaining reasonable estimates of the external uncertainties is of paramount importance to the success of this work, since the data considered are inhomogeneous and listed uncertainties typically provide formal errors or estimates of precision.

For certain quantities, we therefore adopt increased error budgets that we motivate and detail in the following sections. Care is taken to avoid too large or too small error budgets, and to ensure that likelihood remains an effective membership criterion.

3 DATA USED TO COMPUTE LIKELIHOODS

In this section, we describe how we compile the data used for our analysis. The constraints employed are: on-sky separation, parallax, proper motion, RV, and the population parameters iron abundance (as a proxy for metallicity) and age. Most data considered originate from published literature and catalogues. However, we also include RV data from an extensive, year-round observation programme carried out on both hemispheres. Some details on this programme are provided in Section 3.2.3.1. A full description, however, is out of scope for this work and will be published separately.

Very often, data on a given membership constraint can be found in different references. In such cases, a choice of which reference to prefer over the other ones has to be made. In each of the following subsections, the references mentioned first are the ones preferentially adopted. This section is divided into two parts: Section 3.1 is dedicated to open clusters and Section 3.2 to Cepheids. Stellar associations are not considered.

3.1 Open cluster data

For open cluster data used in this work, we largely rely on the Dias et al. (2002a, from hereon: D02) catalogue,[4] which builds partially on the WEBDA data base[5] originally developed by Mermilliod (1988, 1995), where additional useful information, e.g. on RVs, can be found. D02 is an extensive 'living' compilation of open cluster data that are regularly updated with the latest available information on open clusters. Thanks to this process, we can assume that the most accurate available information available for the open clusters is used in our analysis. D02 is furthermore the most complete compilation of open clusters available, so that only few potential Cepheid host clusters are missed (cf. Section 4.1.1).

The definition of $P(A)$ in equations (2) through (4) requires information for two types of radii, core and limiting. Since D02 list only a single quantity, apparent diameters, we adopt core and limiting radii from other sources, see Section 3.1.1. Further choices made regarding cluster data are presented in the subsections concerning parallax (Section 3.1.2), proper motion (Section 3.1.3), mean RV (Section 3.1.4), iron abundance (Section 3.1.5) and age (Section 3.1.6).

Fig. 3 shows the distribution of clusters (black open circles, scale with limiting radius) and Cepheids (light star symbols) in Galactic coordinates. Clusters closely trace the disc, and no obvious gaps are present in our all-sky census.

3.1.1 Cluster radii

In order to choose which literature radii to adopt, we start by investigating to what degree cluster radii are reliable quantities. To this end, we search the literature for extensive catalogues that provide both core and limiting radii. Three such studies are identified: Kharchenko et al. (2005a,b, from hereon, we refer to the combined catalogue from both studies as K05), Bukowiecki et al. (2011, from hereon: B11) and Kharchenko et al. (2012, from hereon: K12). We do not include Froebrich, Scholz & Raftery (2007) here, since we notice a suspicious correlation between r_c and r_{lim}. Note, however, that some clusters listed in K12 were originally identified by Froebrich et al. (2007).

Since many clusters in K12 were also studied by K05, we compare the three radii defined in K12 with the core and limiting radii in K05 and notice that the limiting radius in K05, R_{cl}, corresponds well to r_2 in K12 (though r_2 tends to be smaller), while r_1 in K12 is rather similar to the core radius in K05, R_{co}. Nevertheless, a fair amount

[4] Version V3.3, 2013 January 16.

[5] Maintained by E. Paunzen and C. Stütz in Vienna, cf. http://www.univie.ac.at/webda/

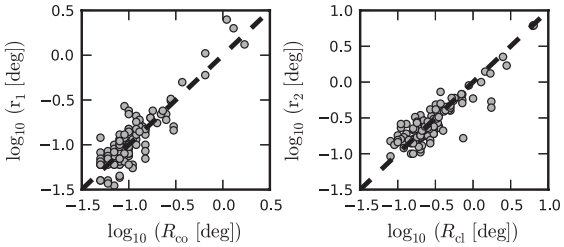

Figure 4. Left-hand panel: comparison between r_1 in K12 and the core radius, $R_{\rm co}$, in K05; right-hand panel: same for r_2 in K12 and the limiting radius, $R_{\rm cl}$, in K05. The radii are comparable.

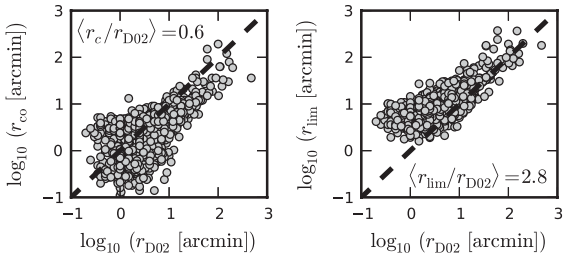

Figure 5. Radii based on apparent diameters from D02 compared to the core (left-hand panel) and limiting radii (right-hand panel) compiled from K12, K05 and B11, see the text. Median ratios printed on the graph.

of scatter exists between both studies, see Fig. 4. We consider K12 an update (and extension) of K05 and therefore prefer the newer cluster parameters over the older ones.

We previously compared radii given in K05 and B11 for the clusters common to both works in Anderson, Eyer & Mowlavi (2012). Rather large scatter is present (more than a factor of 2 for an appreciable fraction) and illustrates that cluster radii are subject to significant uncertainty. However, the radii from both studies follow the same trend and we therefore consider them comparable for our purpose, although K05 and K12 are based on optical and B11 on near-infrared (NIR) Two Micron All-Sky Survey (2MASS; Cutri et al. 2003) photometry.

Given the sometimes rather large difference between cluster radii mentioned in the literature, we adopt a 'permissive' scheme that gives preference to the study giving the largest limiting radius for the cluster and thereby bias ourselves towards higher $P(A)$. We therefore strongly rely on the remaining membership constraints that define the likelihood to filter out chance alignments.

For 478 clusters cross-matched, only an apparent diameter was available. For these, we thus approximate $r_{\rm c}$ and $r_{\rm lim}$ from the typical (here: median) ratios of D02 apparent radii, $r_{\rm D02}$, and the $r_{\rm c}$ and $r_{\rm lim}$ adopted as described above. Fig. 5 illustrates this: the median ratio of $\langle r_{\rm c}/r_{\rm D02}\rangle = 0.6$, and $\langle r_{\rm lim}/r_{\rm D02}\rangle = 2.8$. Priors estimated using this approach are identified in the online tables and marked with an asterisk in the tables presenting our results.

3.1.2 Cluster parallax

Distances in (pc), listed in D02, are converted to parallaxes in (mas) through equations (12) and (13), see Section 3.2.1. Since most cluster distances listed in D02 are based on isochrone fitting, i.e. are model dependent, we adopt an error budget of 20 per cent to account for uncertainties arising from rotation, binarity, metallicity and other modelling-related effects.

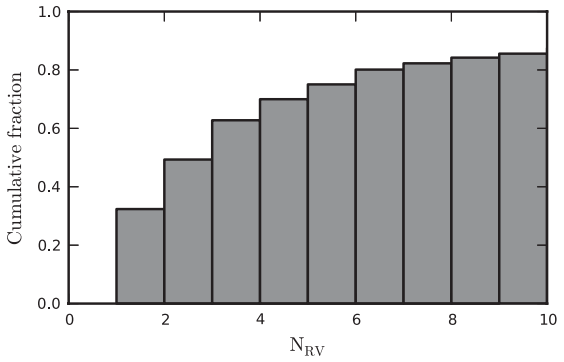

Figure 6. Cumulative fraction of clusters for which a given number of stars, $N_{\rm RV}$, were used to determine the average RV. About half of average cluster RVs are based on a couple of stars.

3.1.3 Mean proper motion

Mean cluster proper motions, $\bar{\mu}^*_{\alpha,Cl}$ and $\bar{\mu}_{\delta,Cl}$, are provided in D02.

The uncertainties on mean proper motion listed in these references are typically calculated either as intrinsic dispersions (e.g. for clusters closer than approximately 400 pc originally studied in K12), or as standard mean errors, i.e. the error decreases as $\sqrt{N_*-1}$, where N_* is the number of stars considered members, cf. D02.[6] The quoted uncertainties on the cluster mean are thus much smaller than the uncertainty on an individual cluster star's measurement. For example, in K12, the typical mean proper motion error is 0.4 mas yr^{-1}.

For the majority of Cepheids, however, the uncertainties on proper motion are much larger, and many have been obtained from different data sets, using different techniques. Therefore, to ensure comparability of inhomogeneous data and to reduce our sensitivity to offsets in zero-points due to data-related specificities such as reduction techniques, we adopt a more generous error budget for $\bar{\mu}^*_{\alpha,Cl}$ and $\bar{\mu}_{\delta,Cl}$ that resembles the uncertainty of an individual cluster star's proper motion. This is done by multiplying the uncertainty listed by the factor $\sqrt{N_*-1}$ and thus slightly reduces the weight of proper motion as a membership constraint. Empirically, we are confident that this is justified, since proper motions of Cepheids typically barely exceed their uncertainties, and care should be taken not to overinterpret their accuracy.

3.1.4 Mean radial velocity

Average cluster RVs and associated errors are listed in D02. However, qualitative differences can exist in the uncertainties listed. For some well-studied clusters, the uncertainty given is an estimate of the intrinsic RV dispersion. For the majority of cluster RVs, however, only a few stars were used to determine the mean cluster RV (about half on two stars or less, cf. Fig. 6). These cases are therefore subject to systematic uncertainties due to implicit membership assumptions, for instance. In addition, unseen binary companions and instrumental zero-point offsets can introduce systematic uncertainties at the level of a few km s^{-1}.

We therefore adopt 2 km s^{-1} as a minimum uncertainty of the mean cluster velocity. If no uncertainty estimate is given, we adopt $\sigma(RV_{\rm Cl}) = 10\,{\rm km\,s^{-1}}/\sqrt{N_{RV}}$ as a typical uncertainty on the mean cluster RV, where $N_{\rm RV}$ is the number of stars used to determine the mean cluster RV.

[6] See under 'version 2.3 (25/abr/2005)' in file: http://www.astro.iag.usp.br/~wilton/whatsnew.txt

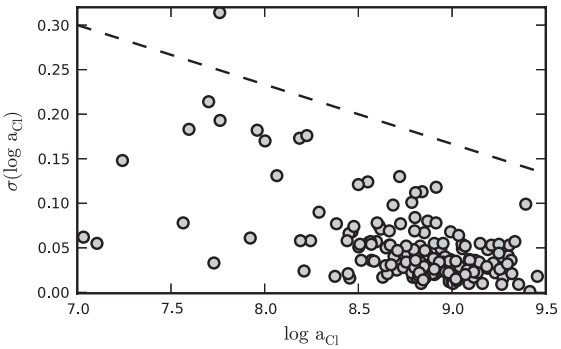

Figure 7. Age uncertainty, $\sigma(\log a_{Cl})$, as a function of cluster age, $\log a_{Cl}$, given by K12. Older clusters have more precisely estimated ages. We adopt as error budget for clusters without stated age uncertainties an upper limit to this proportionality indicated by the dashed line, cf. equation (8).

3.1.5 Iron abundance

We adopt iron abundances compiled in D02, including the uncertainties given. The mean uncertainty among the clusters compiled is 0.08 dex.

3.1.6 Cluster age

Ages were available for most clusters, since they are often determined simultaneously with the distance via isochrone fitting. Although for a model-dependent parameter, age does provide a valid constraint for membership, reflecting evolutionary considerations that are empirically validated. Quantifying an uncertainty for age as a parameter, however, is rather difficult.

Younger clusters exhibit a main-sequence turn-off at higher stellar masses than older clusters. As a consequence of the initial mass function (IMF), a younger cluster's turn-off point tends to be less populated than that of an older cluster. It therefore follows that age estimates tend to become more accurate with age, since the cluster's turn-off point tends to be defined more clearly against the field and therefore better constrains an isochrone fit.

Fig. 7 corroborates the above reasoning by showing cluster ages against their uncertainties as given in K12. We thus estimate an upper limit on the uncertainty of cluster age as the dashed line in Fig. 7, which is

$$\sigma(\log a_{Cl}) \leq 0.3 - 0.067\,(\log a_{Cl} - 7.0)\,. \qquad (8)$$

3.2 Cepheid data

Cepheid candidates were compiled from the 2012 January version of the General Catalogue of Variable Stars (from hereon: GCVS; Samus et al. 2012) and the 2012 May version of the AAVSO Variable Star Index (VSX).[7] From GCVS and VSX, we import the variability types CEP, CEP(B), DCEP, DCEPS; from VSX, we include the ASAS (Pojmanski 1997; Pojmanski 2002; Pojmanski, Pilecki & Szczygiel 2005) Cepheid candidates classified as DCEP-FU or DCEP-FO. This list also contains Cepheid candidates found by ROTSE (Akerlof et al. 2000) or NSVS (Woźniak et al. 2004), as well as the ones in the suspected variables catalogue (Kukarkin & Kholopov 1982).

This starting point contains an unknown, but probably high, fraction of non-Cepheids. Type-II Cepheids (halo objects) and Cepheids belonging to the Magellanic Clouds are mostly removed from the sample by cross-matching with the clusters (trace the disc, see Fig. 3). To further reduce contamination, we visually inspect all ASAS-3 *V*-band light curves of Cepheid candidates with ASAS identifiers.

Radial pulsation and colour variations during the pulsation are defining characteristics of Cepheids. We thus use the spectra obtained for RV observations described in Section 3.2.3.1 to verify classification. A total of 151 ASAS Cepheid candidates and 32 others are thus rejected from the Cepheid sample, resulting in a final list of 1821 Cepheid candidates, 1021 of which are cross-matched with open clusters.

The cleaned sample of Cepheids cross-matched with clusters was appended with literature data from many sources, and references are given in the text. Among the most relevant references are:

(i) The Fernie et al. (1995) DDO Cepheid data base.[8]
(ii) The Klagyivik & Szabados (2009, KS09) Cepheid data base.
(iii) The ASAS Catalogue of Variable Stars (Pojmanski et al. 2005, ACVS) and associated photometry.
(iv) The new *Hipparcos* reduction (van Leeuwen 2007).
(v) The extended *Hipparcos* compilation (Anderson & Francis 2012, XHIP).
(vi) The ASCC-2.5 catalogue (Kharchenko 2001) updated by Kharchenko et al. (2007).
(vii) The PPMXL catalogue (Roeser, Demleitner & Schilbach 2010).
(viii) The 2MASS catalogue (Cutri et al. 2003).
(ix) The Cepheid photometry obtained by Berdnikov, Dambis & Vozyakova (2000) and Berdnikov (2008).
(x) The McMaster Cepheid photometry and RV data archive maintained by Doug Welch.[9]
(xi) The RV data, see Section 3.2.3.

3.2.1 Cepheid parallaxes

Parallax, ϖ, is a key membership constraint, since cluster membership is virtually guaranteed if a Cepheid occupies the same space volume as a cluster. We combine parallax estimations from different sources, favouring *PLR-independent* determinations.

Parallax in (mas) is given preference over distance in (pc) here, since the uncertainty, σ_ϖ, is normally distributed, in contrast to the error in distance. This is important, since the computation of likelihoods by equation (7) assumes Gaussian uncertainties.

We compile parallaxes from Benedict et al. (2007, 8 Cepheids), Storm et al. (2011, 65 Cepheids), and the new *Hipparcos* reduction by van Leeuwen (2007, so long as $\sigma_\varpi/\varpi \leq 0.1$ and $\varpi > 0$, 5 Cepheids). We then calculate PLR-based parallaxes for 622 additional Cepheids, see below.

PLR-based parallaxes of fundamental-mode Cepheids are calculated from distances computed following Turner et al. (2010). Our choice of PLR was motivated mainly by the considerations that (i) *V*-band magnitudes can be obtained for the largest number of Cepheids; (ii) the above formulation is calibrated for the Galaxy using the most recent observational results, including the *Hubble*

[7] http://www.aavso.org/vsx/

[8] http://www.astro.utoronto.ca/DDO/research/Cepheids/
[9] http://crocus.physics.mcmaster.ca/Cepheid/

Space Telescope parallaxes by Benedict et al. (2007) and the cluster Cepheids from Turner (2010).

We thus calculate PLR distances as follows:

$$5 \log d = \langle m_V \rangle - \langle M_V \rangle - A_V + 5, \quad (9)$$

where $\langle m_V \rangle$ is the apparent mean *V*-band magnitude and the average absolute *V*-band magnitude, $\langle M_V \rangle$, is obtained from the pulsation period *P* via

$$\langle M_V \rangle = -(1.304 \pm 0.065) - (2.786 \pm 0.075) \log P. \quad (10)$$

Equation (10) is valid only for fundamental-mode pulsators, no distances were estimated for overtone pulsators. The total absorption, A_V, is defined as

$$A_V = R_V \cdot E(B-V), \quad (11)$$

with $R_V = 3.1$ being the canonical ratio of total-to-selective extinction (reddening law) and $E(B-V)$ the colour excess of the object, cf. Section 3.2.1.2. The parallax is simply

$$\varpi = \frac{1000}{d}\,(\mathrm{mas}), \quad (12)$$

with *d* in (pc). The parallax uncertainty, σ_ϖ, is obtained considering the error budget on the distance, σ_d:

$$\sigma_\varpi = \frac{1000}{d^2} \cdot \sigma_d\,(\mathrm{mas}). \quad (13)$$

Thus, to estimate a Cepheid's parallax, knowledge of the PLR, *P*, $\langle m_V \rangle$ and A_V is required. Periods are usually available in the GCVS or the VSX, whereas average magnitudes and colour excesses of many of the newer Cepheid candidates are not available in the literature. However, $E(B-V)$ can be estimated from combined NIR and optical data. The following sections describe in detail how these quantities are compiled.

3.2.1.1 Mean magnitude, $\langle m_V \rangle$. We compile mean *V*-band magnitudes, $\langle m_V \rangle$, from multiple references. Different methods of determining mean magnitudes exist, and the photometry employed is inhomogeneous, forcing us to adopt a zero-point for mean magnitudes compiled. In Fig. 8, we therefore compare mean magnitudes from KS09 with the Fernie et al. (1995) data base's magnitude-based means and the intensity means from Berdnikov et al. (2000). For the Cepheids common to both studies, KS09 and the Fernie magnitudes show excellent agreement. We therefore adopt the following order of preference for compiling mean magnitudes.

First, we adopt $\langle m_V \rangle$ values from KS09 with a fixed error budget of 0.03 mag, since the study carefully investigates amplitudes with a special focus on binarity.

Secondly, we adopt the magnitude-based means from the Fernie data base with uncertainties calculated as the difference between intensity and magnitude mean magnitudes, with a minimum error of 0.03 mag.

Thirdly, we include Berdnikov et al. (2000) mean magnitudes. As seen in Fig. 8, these $\langle m_V \rangle$ values are systematically smaller (brighter) by approximately 0.03 mag than KS09. This discrepancy is most likely due to different ways of determining the mean. We remove this offset from the Berdnikov et al. (2000) values for internal consistency and adopt 0.03 mag as error budget for these values, identical to KS09.

Fourthly, we employ median *V*-band magnitudes from the *Hipparcos* catalogue (Perryman & ESA 1997, obtained via XHIP) for eight Cepheids. The median *V*-band magnitudes derived from *Hipparcos* magnitudes can differ significantly from mean magnitudes listed in other references, cf. Fig. 9. Usually, this is due to contamination due to a nearby star within the instantaneous field of view. As error budget for the *Hipparcos* median *V* magnitudes, we adopt $\sigma(\Delta_{\mathrm{HIP,\,KS09}}) = 0.110$ mag, see Fig. 9. We note that we could find no dependence on period or number of transits for this dispersion.

Fifthly, we adopt average apparent *V*-band magnitudes that we determine from ASAS-3 light curves. To this end, we fit Fourier series (same procedure as described for RVs in Section 3.2.3.3) to the phased light curves and use the constant term as the average, $\langle m_V \rangle$. Fig. 10 shows a histogram of Δ_{ASAS}, the differences between the computed ASAS-based $\langle m_V \rangle$ and Fernie or KS09. We remove the offset of -0.01 mag from the ASAS mean magnitudes and adopt the dispersion of 0.10 mag computed as the error budget.

The large dispersion, $\sigma(\Delta_{\mathrm{ASAS}})$, in Fig. 10 probably originates from contamination due to nearby stars. To illustrate this, Fig. 11 shows phase-folded ASAS-3 *V*-band light curves of two Cepheids, CY Car (left) and BM Pup (right). Our mean magnitude agrees well with the literature value for CY Car. For BM Pup, however, a systematic difference of approximately 0.144 mag is evident, although the light curve appears to be clean otherwise. Inspection of a Digitized Sky Survey image, however, reveals that contamination from a nearby companion is likely. Out of 154 Cepheids for which the ASAS light *V*-band curves were inspected, 20 differed by more than 0.1 mag from the reference value and 28 agreed to within 0.01 mag.

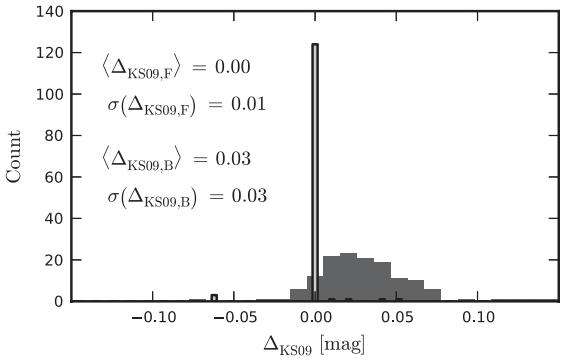

Figure 8. Histogram of differences in mean magnitudes relative to the KS09 values, Δ_{KS09}. Light slim bars show $\Delta_{\mathrm{KS09,\,F}}$ computed using Fernie values (123 Cepheids). The darker broad bars with no outline show $\Delta_{\mathrm{KS09,\,B}}$ computed using data from Berdnikov et al. (2000) (127 Cepheids). Mean differences, $\langle \Delta_{\mathrm{KS09}} \rangle$, and dispersions, $\sigma(\Delta_{\mathrm{KS09}})$, given in (mag).

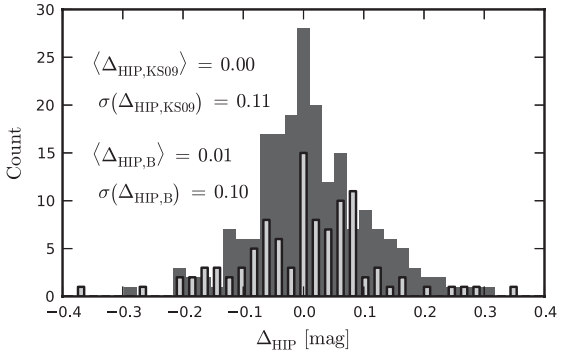

Figure 9. Histogram of differences in mean magnitudes relative to *Hipparcos* median *V* band, Δ_{HIP}. Light slim bars show $\Delta_{\mathrm{HIP,\,KS09}}$ computed using KS09 (104 Cepheids). The darker broad bars with no outline show $\Delta_{\mathrm{HIP,\,B}}$ computed using Berdnikov et al. (2000) (198 Cepheids). Mean differences, $\langle \Delta_{\mathrm{HIP}} \rangle$, and dispersions, $\sigma(\Delta_{\mathrm{HIP}})$, given in (mag).

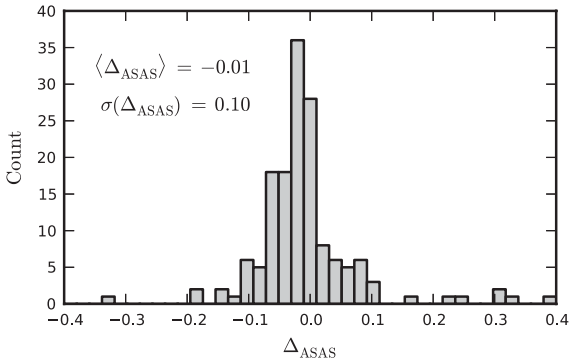

Figure 10. Histogram of differences in mean *V*-band magnitude computed from ASAS light curves for 154 Cepheids relative to reference values from Fernie and KS09, $\Delta_{\rm ASAS}$, cf. also Fig. 8. Mean difference, $\langle \Delta_{\rm ASAS} \rangle$, and dispersion, $\sigma(\Delta_{\rm ASAS})$, given in (mag).

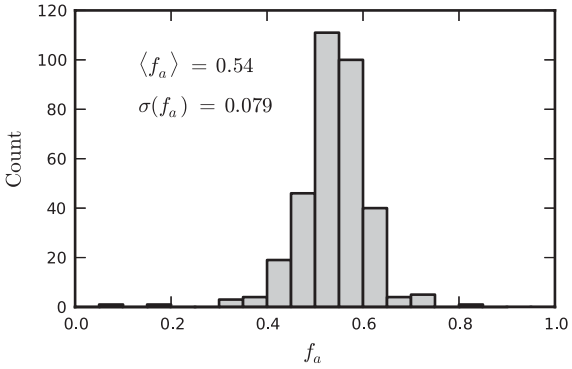

Figure 12. Fractional amplitudes, f_a, computed from Fernie mean, and GCVS maximum and minimum magnitudes, see equation (14).

If no mean magnitude is obtained from any of the above sources, we perform a (rough) estimate of $\langle m_V \rangle$ based on the information provided in the GCVS and the VSX, using the magnitude at maximum brightness, $\min_V$, and the amplitude, amp_V, of the *V*-band light curve. amp_V is either provided directly by the catalogues, or calculated as the difference between minimum and maximum brightness, $\mathrm{amp}_V = \max_V - \min_V$.

Since Cepheid light curves are skewed, their mean magnitudes do not necessarily lie at half the amplitude. We therefore estimate the typical fractional amplitude at mean brightness, $\langle f_a \rangle$, to compute $\langle m_V \rangle = \min_V + \langle f_a \rangle \, \mathrm{amp}_V$. Fig. 12 shows a histogram of f_a computed using mean magnitudes listed in the Fernie data base, $\langle m_{V,\mathrm{F}} \rangle$, and amplitudes, amp_V, from the catalogues. We find

$$\langle f_a \rangle \equiv \mathrm{median} \left(\frac{\langle m_{V,\mathrm{F}} \rangle - \max_V}{\min_V - \max_V} \right) = 0.54 \pm 0.079. \quad (14)$$

We derive an uncertainty on $\langle m_V \rangle$ thus obtained using the uncertainty on $\langle f_a \rangle$, an estimated error on the amplitude, and a prescribed error on the magnitude at maximum brightness (we adopt 0.1 mag for 12th magnitude and below and increase linearly to 0.5 mag at 20th magnitude). The resulting mean error on $\langle m_V \rangle$ is 0.27 mag.

This estimation works reasonably well, although there exist obvious limitations, such as inhomogeneity of passbands, accuracy of the upper and lower limits, the applicability of the above ratio for a given Cepheid. Nevertheless, it does provide access to rough estimates of $\langle m_V \rangle$ for Cepheids with little available information.

Given the many different ways in which average magnitudes were estimated, we keep track of the type of estimation to ensure traceability of any potential issues.

3.2.1.2 Colour excess, E(B − V). The principal references adopted for colour excess are Kovtyukh et al. (2008), Laney & Caldwell (2007), Sziládi et al. (2007) and Fouqué et al. (2007). Where available, we adopt stated uncertainties, $\sigma(E(B-V))$. If no $\sigma(E(B-V))$ are listed, we adopt an error budget of 0.05 mag for Kovtyukh et al. (2008) and Sziládi et al. (2007), and 0.03 mag for Laney & Caldwell (2007).

For other Cepheids, we adopt $E(B-V)$ from the Fernie data base and an error budget of 0.05 mag, unless the standard error from multiple reddening estimations was given.

Colour excesses for Cepheids with no literature $E(B-V)$ are estimated following Majaess et al. (2008) using mean *J*-band magnitudes by Monson & Pierce (2011), or single-epoch 2MASS (Cutri et al. 2003) *J*-band magnitudes, m_J(JD). The method requires knowledge of the pulsation period, *P*, and the average *J*-band magnitude, $\langle m_J \rangle$. If not known from the literature, the latter can be estimated by (Majaess et al. 2008, equation 5)

$$\langle m_J \rangle \simeq m_J(\mathrm{JD}) - \left[\frac{|m_{V(\phi_J)} - \max_V|}{\mathrm{amp}_V} - 0.5 \right] \cdot 0.37 \mathrm{amp}_V, \quad (15)$$

where ϕ_J denotes the pulsation phase of the *J*-band measurement and $m_{V(\phi_J)}$ is the *V*-band magnitude at that phase. $E(B-V)$ can then be estimated by

$$E(B-V) = -0.270 \log P + 0.415(\langle m_V \rangle - \langle m_J \rangle) - 0.255. \quad (16)$$

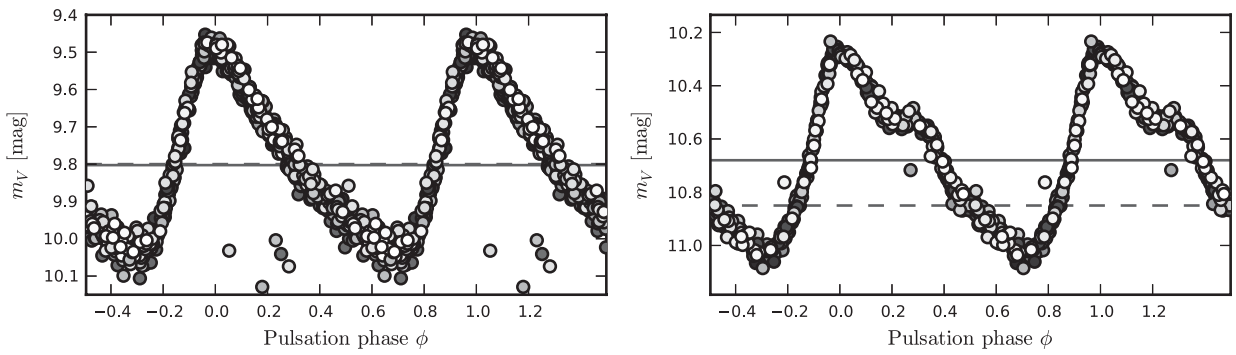

Figure 11. Phase-folded ASAS-3 *V*-band light curves of CY Car (left) and BM Pup (right). Julian date of observation indicated in grey-scale, increasing from black to white. The horizontal lines indicate reference average magnitude (dashed, KS09) and constant term of the fitted Fourier series (solid). For CY Car, the two are in excellent agreement. BM Pup has a bright neighbour that contaminates the aperture used to measure its flux, leading to an underestimated (too bright) mean magnitude.

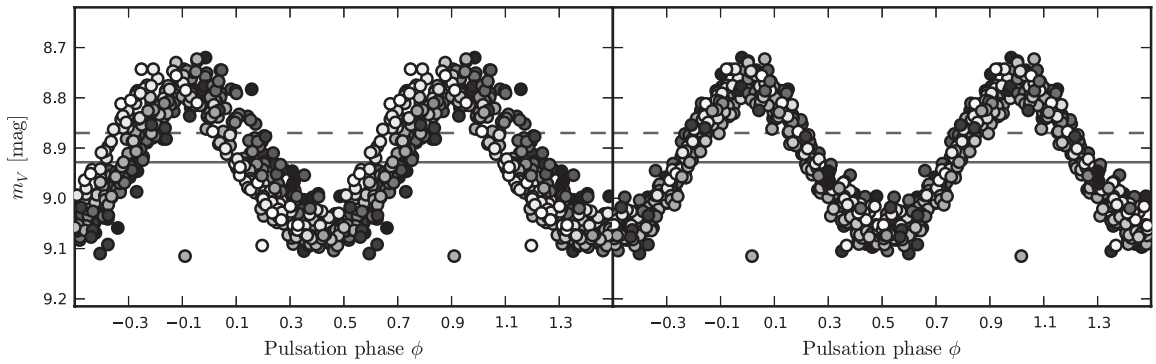

Figure 13. ASAS-3 *V*-band phase-folded light curve of QZ Nor. Grey-scaled symbols (from black to white) indicate increasing Julian date of observation. Left-hand panel: pulsation period and epoch of maximum light from the ACVS. Right-hand panel: optimized period and epoch used.

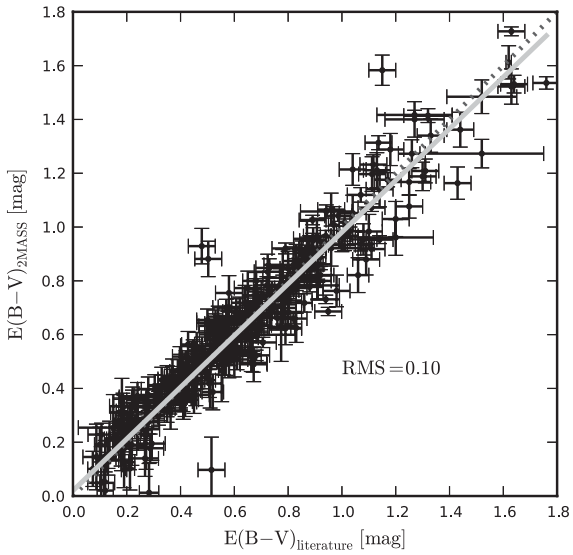

Figure 14. Colour excess from the literature against 2MASS-based estimate. The solid line represents a weighted least-squares fit, a dashed line indicates the diagonal. rms around either line: 0.10 mag.

Wherever possible, $m_{V(\phi_J)}$ was obtained from the ASAS light curve. If this is impossible, we assume a sinusoidal light curve with the given mean magnitude and (semi-)amplitude. Uncertainties or changes in pulsation period can significantly impact the phase calculated for the single-epoch 2MASS measurement, ϕ_J. We therefore optimize Cepheid ephemerides for which ASAS data were available. To do so, we compute a grid (at fixed periods) of Fourier series fits around the period provided in the ACVS and retain the solution with the minimum root mean square (rms). Epochs are optimized by simply shifting the phase-folded curve. Fig. 13 illustrates this step for the overtone Cepheid QZ Nor. We then take care to employ the most recently determined pulsation ephemerides available and estimate reddening uncertainties using error propagation for the quantities involved.

We note that this approach may be subject to multiple issues such as: (i) the unknown shape of the light curve; (ii) the applicability of equation (16); (iii) period changes that impact $m_{V(\phi_J)}$; and (iii) the approximate form of the relationship in equation (15). We therefore compare the 2MASS-based colour excesses to the reference values, see Fig. 14, where the result of a weighted least-squares fit is indicated by a straight line and does not differ much from the diagonal indicated by a dashed line. Despite considerable dispersion, the correspondence is clear and the results are promising (rms of 0.1 mag).

3.2.2 Proper motions

Cepheid proper motions are taken from the following sources in order of preference:

(i) *Hipparcos* proper motions from the new reduction by van Leeuwen (2007) and
(ii) The PPMXL catalogue by Roeser et al. (2010).

3.2.3 Systemic radial velocities

3.2.3.1 New observations. In order to extend the number of Cepheids with known systemic RVs, v_γ, we[10] carried out observations between 2010 November and 2012 July using the fibre-fed high-resolution echelle spectrographs CORALIE (Queloz et al. 2001, see also the instrumental upgrades described in Ségransan et al. 2010, $R \sim 60000$) at the 1.2 m Euler telescope at La Silla, Chile and HERMES (Raskin et al. 2011, $R \sim 80000$) at the identically built Mercator telescope on La Palma. In total, we observed 103 Cepheids with CORALIE and 63 with HERMES. 18 Cepheids were observed with both instruments, i.e. from both hemispheres. For 85 of these Cepheids, no RV data are available in the literature.

Efficient reduction pipelines exist for both instruments that include pre- and overscan bias correction, cosmic removal, as well as flat-fielding using Halogen lamps and background modelization. ThAr lamps are used for the wavelength calibration.

The RVs are computed via the cross-correlation technique described in Baranne et al. (1996). We use numerical masks designed for solar-like stars (optimized for spectral type G2) for all cross-correlations. Both instruments are very stable and yield very high precision RVs of $\sim$10 m s^{-1} (Queloz et al. 2000; Raskin et al. 2011). The measurement uncertainty is therefore not limited by the instrumental precision, but by line asymmetries due to pulsation. A detailed investigation of these effects is out of scope for this paper and will be presented in a future publication. The typical uncertainty on individual measurements is thus at the 100−300 m s^{-1} level, depending on the star and pulsation phase.

[10] The authors are grateful to the observers who contributed in this effort; names are given in the acknowledgments.

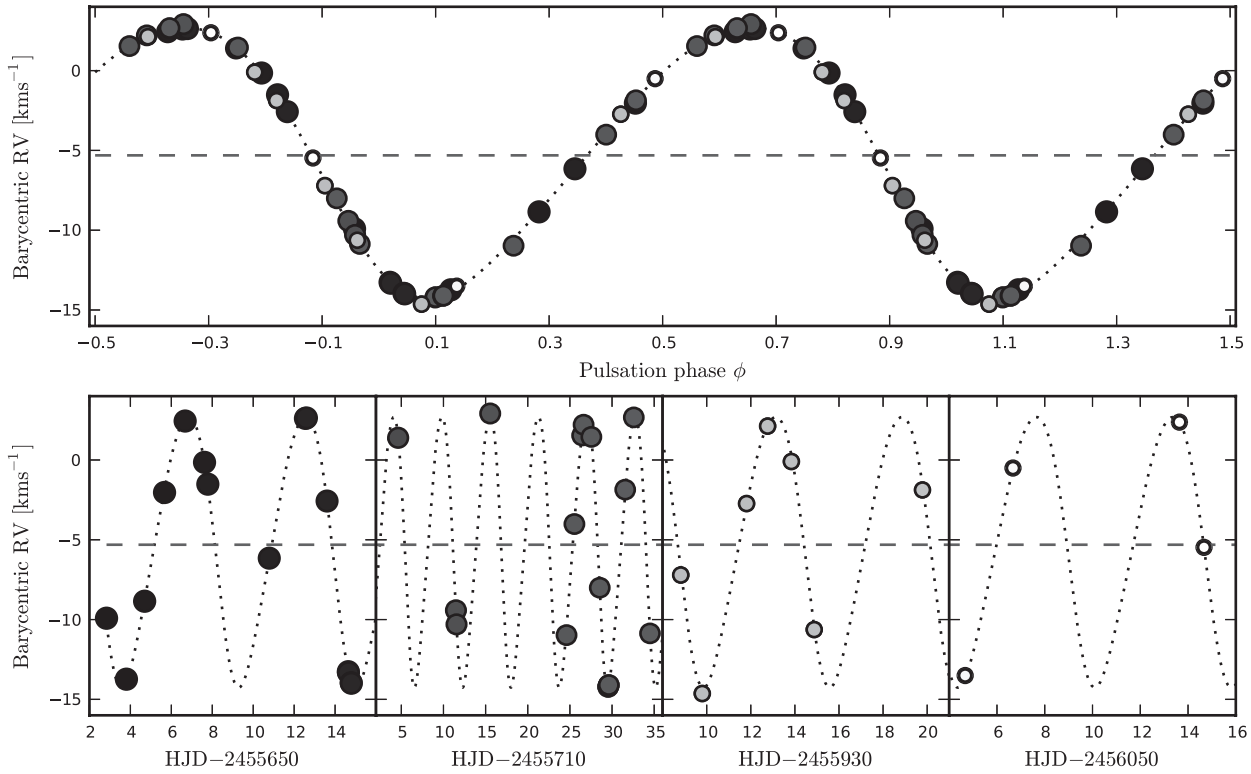

Figure 15. RV data recently published in Szabados et al. (2013) for first-overtone pulsator GH Car, obtained in Southern hemisphere with CORALIE as part of our programme. Grey-scale (black to white) and size-code (larger to smaller) indicate increasing Julian date of observation. Fit of triple-harmonic Fourier series indicated by a dotted line. v_γ indicated by a dashed horizontal line. Top panel: phase folded; bottom panel: non-folded, showing zooms of the four observing runs during which data were obtained.

3.2.3.2. Literature data. In addition to the previously unpublished RVs described in Section 3.2.3.1, we employ literature data from many references to determine systemic velocities, v_γ, see Section 3.2.3.3. The addition of the literature RVs extends the baseline of our otherwise relatively short (1.5 yr) observing programme, thereby enhancing our sensitivity to binarity. For binary Cepheids[11] with published orbital solutions, we adopt the literature v_γ.

Aside from the systemic RVs in the Fernie data base and KS09, we compile RV time series from the following sources: Lloyd Evans (1980), Gieren (1981), Gieren (1985), Evans (1983), Coulson, Caldwell & Gieren (1985), Coulson & Caldwell (1985), Barnes, Moffett & Slovak (1987, 1988), Gieren et al. (1989), Wilson et al. (1989), Metzger et al. (1991), Metzger, Caldwell & Schechter (1992), Metzger, Caldwell & Schechter (1998), Gorynya et al. (1992), Gorynya et al. (1996), Gorynya et al. (1998), Gorynya et al. (2002), Evans & Welch (1993), Pont, Burki & Mayor (1994), Pont et al. (1997), Bersier et al. (1994), Bersier (2002), Kiss (1998), Imbert (1999), Storm et al. (2004), Barnes et al. (2005), Petterson et al. (2005) and Baranowski et al. (2009). The data for most of these sources dated earlier than 1986 are extracted from the McMaster Cepheids data base. Newer data are obtained through VizieR.[12]

3.2.3.3 Systemic radial velocities, v_γ. The systemic RV, v_γ, is obtained by fitting a Fourier series to the RVs. We use pulsation period, P, as a fixed parameter, since it is known for all Cepheids we observed.

The basic analytical form applied was a Fourier series with n harmonics and phase ϕ is

$$FS_n = v_\gamma + \sum_{n=1,2,3,\ldots} a_n \sin(2n\pi\phi) + b_n \cos(2n\pi\phi). \qquad (17)$$

Since the number of data points available varies for each star, we do not fix the number of harmonics in this fit. Instead, we iteratively increase the degree of the Fourier series until an F-test indicates an overly complex representation, i.e. when spurious fit improvement is more likely than 0.27 per cent. For some stars, we therefore use only a simple sine function, whereas stars with many measurements are fitted using up to five harmonics. We show two examples of newly observed RV curves in Figs 15 and 16. A full description and publication of the new RV data will follow in the near future.

We adopt a fixed error budget of 3 km s^{-1} on v_γ. Although this may overestimate the uncertainties for some very good cases, it is intended to account for a range of systematic errors, such as unseen binarity, instrumental zero-point differences and insufficient phase coverage. We are confident that this error budget is sufficiently large to prevent the exclusion of good member candidates, while being sufficiently small to provide a stringent constraint. If insufficient data points render the Fourier fit unsatisfactory, we determine a rough estimate of v_γ and its error budget by eye.

[11] cf. Szabados' data base of binary Cepheids available at http://www.konkoly.hu/CEP/nagytab3.html
[12] http://vizier.u-strasbg.fr/viz-bin/VizieR

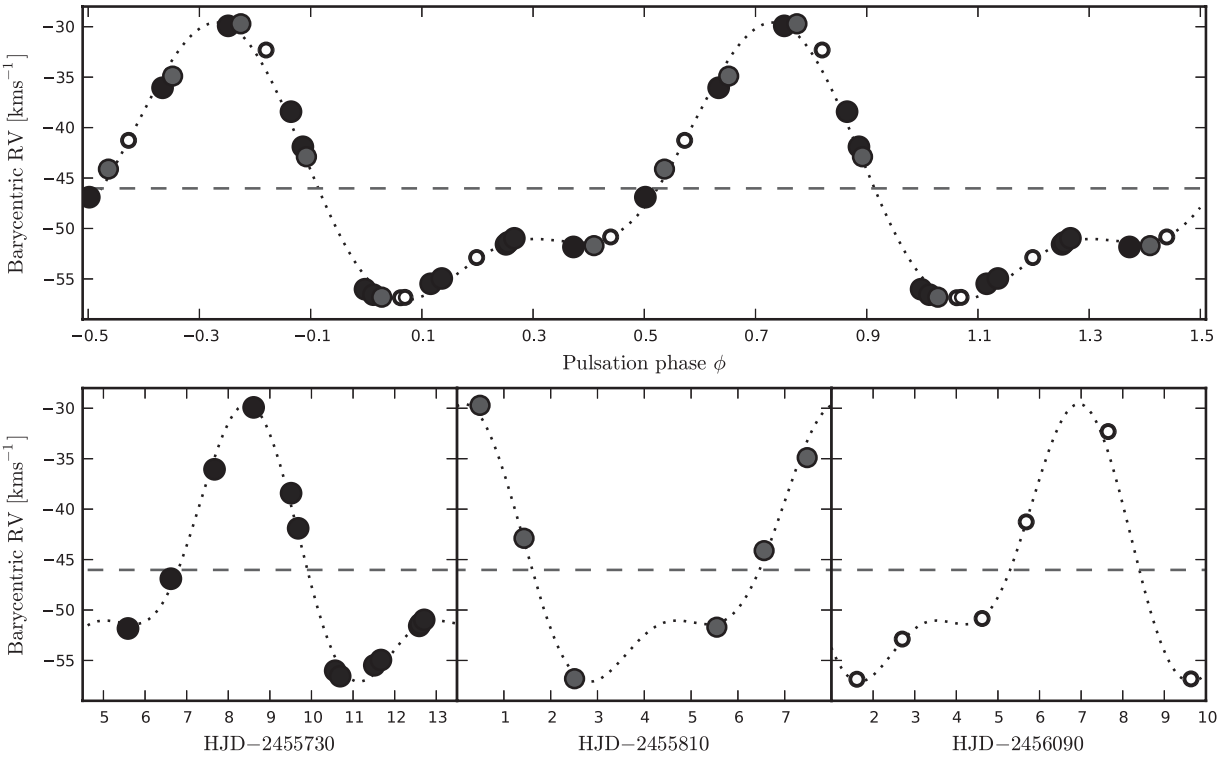

Figure 16. New RV data for fundamental-mode Cepheid V2340 Cyg, obtained in Northern hemisphere with HERMES. Grey-scale (black to white) and size-code (larger to smaller) indicate increasing Julian date of observation. Fit of triple-harmonic Fourier series indicated by dotted line. v_γ indicated by dashed horizontal line. Top panel: phase folded; bottom panel: non-folded, showing zooms of the three observing runs during which data were obtained.

3.2.4 Iron abundance

We rely mostly on iron abundances by Luck & Lambert (2011) and complement these with the compilation in KS09 that made the enormous effort of homogenizing iron abundances from the literature available, namely from Giridhar (1983), Fry & Carney (1997), Andrievsky et al. (2002a,b,c, 2004), Luck et al. (2003), Groenewegen et al. (2004), Andrievsky, Luck & Kovtyukh (2005), Kovtyukh, Wallerstein & Andrievsky (2005a), Kovtyukh et al. (2005b), Romaniello et al. (2005), Mottini (2006), Yong et al. (2006), Lemasle et al. (2007), as well as the work by Sziládi et al. (2007), Lemasle et al. (2008) and Romaniello et al. (2008).

Unfortunately, the adopted standard value of solar iron abundance can vary among references, possibly introducing systematic offsets between different authors' studies. Furthermore, an estimation of the iron abundance in a Cepheid is more complex than in a non-pulsating star, since the stellar parameters (e.g. temperature and turbulence) vary during the pulsation cycle, and since the atmosphere is not static. We therefore adopt generous error budgets of 0.1 dex for the values from Luck & Lambert (2011) and 0.15 dex in [Fe/H] for the others.

3.2.5 Age

Cepheid ages can be calculated for first overtone and fundamental-mode pulsators using the period–age (PA) relations given in Bono et al. (2005). For fundamental-mode Cepheids, we use $\log t = (8.31 \pm 0.08) - (0.67 \pm 0.01)\log P$. For overtone pulsators, the relation used is $\log t = (8.08 \pm 0.04) - (0.39 \pm 0.04)\log P$. Age error budgets are calculated from the uncertainties stated for slope and intercept.

4 RESULTS

This section presents the results from our census. As mentioned in Section 3.1, some host Cepheid clusters known in the literature (e.g. in Turner & Burke 2002, or Turner 2010) are not present in our cluster sample. Such cases are briefly mentioned in Section 4.1.1. We furthermore note that stellar associations are not considered here.

In addition to the membership probabilities computed, we consider the quality of the data employed to constrain membership, and compare our results to the published literature. We then flag Combos as bona fide, inconclusive, unlikely or non-members. These flags are attributed according to the following reasoning:

(i) *bona fide* is attributed to Combos with typically high priors and high likelihoods constrained by multiple parameters, in particular parallax. Closer inspection of the individual membership employed or the literature builds confidence in membership. Some Combos studied in detail in the literature prove to be strong candidates, despite low probabilities computed here, pointing to limitations of the data used as input in our analysis. We consider these Combos bona fide members.

(ii) *inconclusive* CCs are candidates for which the membership constraints available are insufficient to consider them bona fide, e.g. if $P(A) > 0.5$ with no additional membership constraints. We flag newly identified Combos as *inconclusive*, if the prior vanishes and $0.1 < P(B|A) < 0.8$ has been computed from at least three membership constraints that exceed the combined error budgets. These candidates warrant follow-up.

(iii) *unlikely* CCs have low likelihoods (<10 per cent) due to discrepant membership constraints (more than one constraint off by

approximately 2σ), although evidence supporting membership may exist in the literature. Membership cannot be ruled out altogether for these candidates that may benefit from additional follow-up.

(iv) *non-members* form the majority of Combos cross-matched. They are clearly inconsistent with membership.

It should be kept in mind that our analysis is of a statistical nature and may not provide the final answer for every Combo. While the benefit of our analysis is a consistent and transparent approach to determining membership, the correctness of our membership probabilities relies entirely on the accuracy of the input data; this is particularly true for reddening and distances, or pulsation modes. Therefore, we caution that CCs previously discussed in the literature that are found to be unlikely or non-members by our analysis should not be discarded fully without additional consideration or follow-up.

We start the presentation of our results with CCs known from the literature (Section 4.1). While we take care to include relevant references, it is almost inevitable that some works are overlooked in a field with this much history. The literature CCs are followed by new candidates and other newly identified Combos of interest (Section 4.2). For brevity of the main body, we defer presentation of inconclusive, unlikely and inconsistent Combos to Appendix A.

In Section 4.3, we then revisit the Galactic Cepheid PLR using our bona fide CC sample.

4.1 Literature Combos

The main references considered for CCs are Feast (1999), Turner & Burke 2002 and Turner (2010, from hereon: T10). Additional Cepheids whose cluster membership was considered in the literature are mentioned where appropriate, cf. also the references given in the caption of Table 1 and Section 4.1.1.

Table 1 lists the CCs previously discussed in the literature that are recovered by our analysis. A horizontal line divides cases that we find to be consistent with membership according to the data compiled (above), and those that tend to be inconsistent with membership in our analysis (below). Two essentially unconstrained

Table 1. Results of our membership analysis for combinations known in the literature. Constraints indicated are parallax, ϖ, RV, v_r, proper motion, μ_α^* and μ_δ, iron abundance [Fe/H] and age. The filled circles indicate constraints consistent between Cepheid and cluster, greater deviations are stated explicitly in units of the square-summed uncertainties. The open circles indicate unavailable membership constraints. $R_{\rm Cl}$ denotes the distance in parsecs of the Cepheid from cluster centre, assuming membership and the cluster's heliocentric distance. $P(A)$ is the prior used, asterisks mark $P(A)$ values based on D02 apparent diameters. Column $P(B|A)$ lists likelihoods and $P(A|B)$ the combined membership probability. The last column CC indicates qualitatively, how membership is judged for a particular Combo: 'y' denotes bona fide CCs; 'i' denotes that the data available yield an inconclusive result; 'u' denotes unlikely membership; 'n' denotes Combos that are clearly inconsistent with membership. Column Ref. lists some pertinent references: a: Irwin (1955), b: Kholopov (1956), c: Feast (1957), d: Sandage (1958), e: Eggen (1980), f: Turner (1982), g: Walker (1985b), h: Turner (1986), i: Turner, Forbes & Pedreros (1992), j: Matthews et al. (1995), k: Turner, Mandushev & Welch (1997), l: Hoyle et al. (2003), m: An et al. (2007), n: Turner (2010), o: Turner (1981), p: Flower (1978), q: Walker (1985a), r: Turner, Pedreros & Walker (1998), s: Turner & Pedreros (1985), t: Turner (1980), u: Yilmaz (1966), v: Turner (1998), w: Turner & Burke (2002), x: Turner (1976), y: Walker (1987), z: Turner, Mandushev & Forbes (1994), A: Turner et al. (1993), B: Turner (1992), C: Majaess et al. (2011), D: Vazquez & Feinstein (1990), E: Baumgardt et al. (2000), F: Turner et al. (2008), G: Balona & Laney (1995), H: Turner (1977).

Cluster	Cepheid	Constraints						$R_{\rm Cl}$	$P(A)$	$P(B\|A)$	$P(A\|B)$	CC	Ref.
		ϖ	v_r	μ_α^*	μ_δ	[Fe/H]	age	[pc]					
IC 4725	U Sgr	•	•	•	•	•	•	0.3	1.0	0.984	0.984	y	a, b, c, m
NGC 7790	CF Cas	•	•	•	•	○	•	0.9	0.955	0.975	0.931	y	d, j
NGC 129	DL Cas	•	•	•	•	○	•	0.2	1.0	0.857	0.857	y	b, i
Turner 9	SU Cyg	•	•	•	•	○	1.2σ	0.0	1.0	0.807	0.807	y	k, n
NGC 7790	CE Cas A	•	•	•	•	○	•	1.5	0.71	0.975	0.693	y	d, j
NGC 7790	CE Cas B	•	•	•	•	○	•	1.6	0.697	0.956	0.666	y	d, j
NGC 6649	V367 Sct	○	•	•	1.3σ	○	○	1.0	0.884*	0.65	0.574	y	o, p
NGC 6067	V340 Nor	•	•	•	•	•	1.9σ	0.6	1.0	0.573	0.573	y	g, m, n, l
Lyngå 6	TW Nor	1.2σ	•	•	1.3σ	○	•	0.6	1.0*	0.453	0.453	y	n, m, q, C
vdBergh 1	CV Mon	•	•	2.2σ	•	○	•	0.6	1.0	0.318	0.318	y	r
NGC 6087	S Nor	•	•	1.2σ	2.0σ	1.2σ	1.3σ	0.6	1.0	0.192	0.192	y	a, b, c, h
Trumpler 35	RU Sct	1.3σ	•	•	•	○	•	5.1	0.194*	0.840	0.163	y	n, l, t, u
Collinder 394	BB Sgr	1.0σ	•	•	1.2σ	○	•	3.7	0.208	0.637	0.133	y	n, s
Turner 2	WZ Sgr	•	○	•	2.2σ	○	•	5.3	0.337*	0.287	0.097	y	A
Trumpler 18	GH Car	○	1.4σ	•	•	○	2.0σ	2.9	0.194	0.143	0.028	u	D, E
NGC 6067	QZ Nor	•	•	•	•	•	•	7.4	0.029	0.963	0.027	y	e, g
Berkeley 58	CG Cas	•	○	•	3.3σ	○	•	5.0	0.308	0.027	0.008	y	F
NGC 5662	V Cen	•	•	•	•	•	•	5.8	0.006	0.958	0.006	y	f, m, n
NGC 6664	EV Sct	•	•	•	•	○	•	7.5	0.0	0.866	0.0	y	w, x
Ruprecht 173	X Cyg	○	○	○	○	○	○	–	0.878*	1.0	0.878	i	n, v, w
Dolidze 45	V1334 Cyg	○	○	○	○	○	○	–	0.017*	1.0	0.017	i	n
Ruprecht 79	CS Vel	1.8σ	1.5σ	1.2σ	1.9σ	○	2.3σ	1.5	1.0	0.007	0.007	i	n, y
Platais 1	V1726 Cyg	○	3.2σ	•	1.0σ	○	1.8σ	1.4	0.98	0.006	0.006	i	z
NGC 1647	SZ Tau	•	1.8σ	•	2.6σ	○	1.2σ	20.1	0.0	0.047	0.0	u	B
NGC 3496	V442 Car	○	○	1.1σ	2.3σ	○	○	1.0	0.625	0.039	0.024	n	G
King 4	UY Per	1.3σ	○	1.6σ	2.6σ	○	•	12.6	0.021	0.019	0.0	n	H
Turner 5	T Ant	4.3σ	•	3.3σ	4.5σ	○	3.2σ	0.0	1.0	0.0	0.0	n	w
NGC 4349	R Cru	6.8σ	•	2.1σ	1.1σ	2.1σ	2.3σ	9.5	0.048	0.0	0.0	n	w
NGC 4349	T Cru	6.7σ	•	2.1σ	•	2.2σ	2.5σ	19.9	0.0	0.0	0.0	n	w
NGC 2345	TV CMa	•	5.6σ	•	•	○	•	25.0	0.001	0.0	0.0	n	x, w

Combos known in the literature are included above the horizontal line. For each deviant membership constraint, i, we list the level of disagreement between cluster and Cepheid value, i.e. $|x_i|$ from equation (6), in units of the square-summed uncertainties $\sigma_i^2 = \sigma_{Cl,i}^2 + \sigma_{Cep,i}^2$.

4.1.1 Missed Combos

Our analysis is limited to open clusters listed in D02. The following CCs reside in nearby sparse clusters that are not included in D02 and could thus not be studied in our analysis: α UMi (Turner et al. 2013, but see also van Leeuwen 2013); δ Cep (e.g. Majaess, Turner & Gieren 2012b); ζ Gem (Majaess et al. 2012c); and SU Cas (Majaess, Turner & Gieren 2012a; Majaess et al. 2012d; Turner et al. 2012).

4.1.2 Bona fide CCs

Based on the available data and literature, we flag the following literature Combos as bona fide CCs, cf. Table 1: U Sgr in IC 4725; CF Cas, CE Cas A and B in NGC 7790; DL Cas in NGC 129; SU Cyg in Turner 9; V367 Sct in NGC 6649, V340 Nor and QZ Nor in NGC 6067; TW Nor in Lyngå 6; CV Mon in vdBergh 1; S Nor in NGC 6087; BB Sgr in Collinder 394; RU Sct in Collinder 394; CG Cas in Berkeley 58; V Cen in NGC 5662. For more information on those Combos with high priors and high likelihoods, i.e. the more or less obvious members, we refer to the original references listed in Table 1, as well as to the data table supplied in electronic form. As mentioned in Section 4, some Combos flagged as bona fide CCs require inspection of the available data and literature in addition to the membership probabilities in order to conclude on membership. We discuss these combos in the sections below.

4.1.2.1 V340 Nor and QZ Nor in NGC 6067. We find two Cepheids that appear to belong to NGC 6067, namely V340 Nor, which lies within its core radius, and QZ Nor, an overtone pulsator (KS09) that lies outside r_{lim}. Cluster membership for QZ Nor was first considered by Eggen (1983), and by Walker (1985b) for V340 Nor. All membership constraints were employed for both Cepheids, and both are consistent with membership for the open cluster data listed in D02. The only discrepant constraint is age for V340 Nor.

If both Cepheids belong to the same cluster, then their respective membership constraints should agree. Interestingly, the distance estimate of QZ Nor by Storm et al. (2011) is much closer to the cluster's, while there is nearly 400pc difference between the estimates for both Cepheids. In terms of parallax, QZ Nor [0.74 ± 0.07 (mas)] is consistent with NGC 6067 [0.71 ± 0.14 (mas)], but slightly off from V340 Nor [0.58 ± 0.09 (mas)]. However, the difference in v_γ between the two Cepheids is minimal ($0.73\,\mathrm{km\,s^{-1}}$). Given that V340 Nor is a visual binary, the small offset in proper motion between the two Cepheids is not alarming, and [Fe/H] is indistinguishable. In terms of age, QZ Nor seems to be slightly older than V340 Nor (7.85 ± 0.07 versus 7.60 ± 0.08), and better matches to the cluster's age (8.08 ± 0.23; D02).

In summary, the two Cepheids have differing parallax and age. The cluster values from D02 happen to lie between the two, oddly enough favouring QZ Nor, which lies at greater separation from the cluster's core. Therefore, the cluster parameters may require reconsideration. Since NGC 6067 is located in the Norma cloud (cf. atlas page in K05), the determination of cluster radii is rather difficult. Differential reddening may be important to resolve this conundrum (higher for V340 Nor which is closer to cluster centre). We therefore note that there are some issues with the membership constraints employed here, and detailed follow-up of the cluster is required. Until then, the constraints compiled are consistent with membership for both Cepheids, and we consider both to be bona fide cluster members.

4.1.2.2 CV Mon and van den Bergh 1. CV Mon lies right in the centre of cluster van den Bergh 1 and was studied in detail by Turner et al. (1998). The constraints employed are parallax, RV, proper motion and age, and yield a likelihood of 32 per cent, which is low due to the discrepant μ_α^*. The average cluster RV determined by Rastorguev et al. (1999) is identical to that of CV Mon and no information on the number of stars involved in its determination is given; it should thus be discarded as membership constraint (this would lower the likelihood to 20 per cent). Aside from this, the cluster data from D02 is largely consistent with the data for the Cepheid. Parallax (also reddening), μ_δ, and age agree well between cluster and Cepheid. Thus, the Cepheid likely lies inside the volume occupied by the Cluster, and therefore should be considered to be a bona fide CC. Observational follow-up of cluster proper motion and RV would be beneficial.

4.1.2.3 S Nor and NGC 6087. S Nor's membership in NGC 6087 was among the first to ever be suggested (Irwin 1955) and confirmed using RVs (Feast 1957), as well as the detailed study by Turner (1986) based on reddening and distance.

The values for the cluster's mean RV differ greatly among D02 ($6\,\mathrm{km\,s^{-1}}$), K05 ($-9\,\mathrm{km\,s^{-1}}$) and Feast (1957, $2.0\,\mathrm{km\,s^{-1}}$), which is important considering the Cepheid's $v_\gamma = 2.53\,\mathrm{km\,s^{-1}}$ (Groenewegen 2008). We note that the value adopted by D02 is measured on the Cepheid itself (Mermilliod, Mayor & Udry 2008), although without taking orbital motion into account, and is therefore not suitable as a membership constraint. Since Feast (1957) investigated the largest number of stars and specifically targeted this cluster, we trust that his $2.0\,\mathrm{km\,s^{-1}}$ is the best available estimate for the mean velocity of the cluster.

We note that proper motion, reddening, metallicity and age are slightly discrepant between cluster and Cepheid, resulting in a low likelihood. However, these differences barely exceed the combined uncertainties and may not be significant.

4.1.2.4 RU Sct and Trumpler 35. Based on age and distance from D02, this Combo would appear nearly inconsistent with membership. Unfortunately, the average cluster RV appears to have been measured on the Cepheid (Rastorguev et al. 1999) and can therefore not be considered a valid membership constraint. Membership of RU Sct in Trumpler 35 was studied in detail by Turner (1980), Hoyle et al. (2003) and T10. Closer inspection of these references reveals an underestimated cluster distance in D02 (compared also to Yilmaz 1966). The region around the Cepheid contains multiple associations, which may explain the confusion in D02. Using the cluster parallax and age from Turner (1980), we compute a likelihood of 84 per cent, and consider RU Sct a bona fide member of Trumpler 35.

4.1.2.5 BB Sgr and Collinder 394. BB Sgr lies at 21 arcmin separation from Collinder 394's centre, i.e. at a distance of 3.7 pc assuming membership. This Combo was first studied in detail by Turner & Pedreros (1985) after having been originally suggested by Tsarevsky et al. (1966). Most membership constraints could be employed and there are only small discrepancies in parallax and μ_δ. The low prior may be misleading in this case, since the high likelihood indicates membership. We thus consider BB Sgr a bona fide member of Collinder 394.

4.1.2.6 WZ Sgr and Turner 2. This Combo was first discussed by Turner et al. (1993) when the cluster was first discovered. Most membership constraints compiled from D02, i.e. parallax, μ_δ, and age, differ between Cepheid and cluster, which would result in a likelihood of <1 per cent. The cluster parameters listed in D02 were taken from the automated, 2MASS-based study by Tadross (2008). However, the much more detailed study by Turner et al. (1993) should be given higher weight, especially for its thorough treatment of reddening, and the more precise photometry used. Hence, we compute the likelihood using the cluster parameters for parallax and age from Turner et al. (1993) and find a combined membership probability of 10 per cent. The sole discrepant membership constraint remains proper motion. However, this discrepancy alone is not sufficiently strong to indicate non-membership.

4.1.2.7 CG Cas–Berkeley 58. CG Cas lies at a separation of 5.7 arcmin (outside r_c) from Berkeley 58's centre, at roughly half the limiting radius. While the Cepheid's PLR-based parallax is close to that of the cluster and reddening is in agreement, μ_δ is discrepant by 3.3σ and does not suggest a common point of origin. However, Turner et al. (2008) conclude in favour of membership based on a detailed study involving age, reddening, distance and RV. Since the cluster is located in the Perseus spiral arm, the proper motion estimate in K12 may well be dominated by Galactic motion. Hence, the likelihood computed here is likely underestimated, and we should trust the result by Turner et al. (2008).

4.1.2.8 V Cen and NGC 5662. Despite the low prior, all membership constraints indicate V Cen's membership in NGC 5662, yielding a very high likelihood of 92 per cent. At NGC 5662's distance of 666 pc, the Cepheid lies 5.8 pc from cluster centre. Hence, the prior may be misleading in this case, perhaps due to underestimated radii. We therefore consider V Cen a bona fide CC of NGC 5662.[13]

4.1.2.9 EV Sct and NGC 6664. This Combo, mentioned previously in Turner (1976) and Turner & Burke (2002), would be nearly inconsistent with membership if the cluster values listed in D02 are employed in the calculation: the highly discrepant age (2.5σ) and parallax (0.57 ± 0.09 versus 0.86 ± 0.17) would result in a likelihood of 13 per cent. However, a literature study reveals that the distance and age listed in D02 may be wrong. The distance by Arp (1958) and Schmidt (1982) are both much greater than the 1.1 kpc in D02. We thus adopt the distance and age by Schmidt (1982, 1.4 kpc) and obtain a very high likelihood of 87 per cent, using also proper motion and RV. As already noted by Laney & Caldwell (2007), a modern follow-up campaign is warranted for this cluster.

4.2 New Combos of interest

Our results suggest the following new bona fide CCs: SX Car in ASCC 61, ASAS J182714−1507.1 in Kharchenko 3, S Mus in ASCC 69, UW Car in Collinder 220 and V379 Cas in NGC 129, see Table 2. We discuss these Combos in some detail in the sections below, followed by the identification of some unconstrained high-prior Combos recovered by our work. Some Combos flagged as inconclusive or unlikely members are discussed in Appendix A.

[13] According to Turner (private communication), NGC 5662 is actually a double cluster and V Cen belongs to NGC 5662b.

4.2.1 New candidate CCs

4.2.1.1 SX Car and ASCC 61. The 4.86 d Cepheid SX Car is seen to be comoving with ASCC 61 in proper motion. Unfortunately, no average cluster RV is known. Parallax and age, however, agree very well between cluster and Cepheid, lending support to the hypothesis of membership with $P(B|A) = 92$ per cent. An in-depth analysis of the cluster, including its mean RV, is of the essence, since the cluster is located in a crowded field (K05). We tentatively consider SX Car as a member of ASCC 61.

4.2.1.2 ASAS J182714−1507.1 and Kharchenko 3. The 5.5 d fundamental-mode pulsator ASAS J182714−1507.1 = TYC 6266−797-1 lies at a large separation of 71 arcmin from cluster centre, which translates to approximately 44 pc at the cluster's estimated heliocentric distance of 2.1 kpc and casts some doubt on possible membership.

Reddening for cluster and Cepheid (estimated from 2MASS photometry, see Section 3.2.1.2) are in excellent agreement, while parallax and age are also consistent with membership. Proper motion does not exceed its error bars and is thus of limited constraining power in this case. Detailed observational follow-up is warranted for both Cepheid and cluster.

4.2.1.3 S Mus and ASCC 69. The membership constraints considered (all but [Fe/H]) for the binary Cepheid S Mus (e.g. Petterson et al. 2005) and ASCC 69 yield a very high likelihood of 88 per cent. ASCC 69 is a sparsely populated cluster for which K05 list merely 12 1σ members. Cluster radius and centre coordinates may therefore be rather imprecise. Furthermore, RVs are only of limited value as membership constraints, since the average cluster RV is based on only two stars. However, proper motion clearly indicates that cluster and Cepheid are comoving. We tentatively accept S Mus as a cluster member and stress the need for a detailed study of its candidate host cluster ASCC 69.

4.2.1.4 UW Car and Collinder 220. This new Combo yields a likelihood of 84 per cent from all membership constraints but [Fe/H]. The parallax of the Cepheid is estimated by the PLR, cf. Section 3.1.2. The most compelling evidence of membership comes from proper motion, while the large on-sky separation translates into a distance of 47 pc from cluster centre assuming the cluster's distance. A detailed review of the cluster's parameters, as well as a better parallax estimate of the Cepheid would help to conclude on this Combo.

4.2.1.5 V379 Cas and NGC 129. This high likelihood pair at large separation (44 arcmin or 20 pc at the estimated distance to NGC 129) has nearly vanishing proper motion, while the both RVs are in excellent agreement and the ages are consistent. We obtain a likelihood of 91 per cent. No parallax is computed, since V379 Cas is an overtone pulsator. Since NGC 129 has another known member, DL Cas, we can compare the pulsational ages of the two Cepheids and find both to be consistent within the uncertainties (7.70 ± 0.08 for DL Cas and 7.83 ± 0.07 for V379 Cas). Furthermore, the iron abundances of both Cepheids are close, as are their RVs (to within less than $1\,\mathrm{km\,s^{-1}}$). We further note that V379 Cas and DL Cas have similar reddening values, though $E(B-V)$ of V379 Cas is slightly (0.1 mag) higher (Kovtyukh et al. 2008, both). We therefore tentatively consider V379 Cas a member of NGC 129's halo, pending a better distance estimate and additional membership constraints. NGC 129

Table 2. New Combos of interest. Columns are described in Table 1. We visually separate (a) Combos with membership constraints that lie inside the core of a cluster, (b) Combos with high likelihood for which ϖ was available, (c) Combos without ϖ that yield high likelihoods, and (d) Combos for which no likelihoods could be computed, but that lie close to the core of their potential host clusters. Combos judged unlikely ('u') or bona fide ('y') are discussed separately in the text. Inconclusive Combos ('i') require additional data or stronger membership constraints.

Cluster	Cepheid	Constraints						$R_{\rm cl}$	$P(A)$	$P(B\|A)$	$P(A\|B)$	CC
		ϖ	v_r	μ^*_α	μ_δ	[Fe/H]	age	[pc]				
ASCC 60	Y Car	○	●	●	●	○	○	0.3	1.0	0.786	0.786	i
ASCC 61	SX Car	●	○	●	●	○	●	20.4	0.001	0.919	0.001	y
Kharchenko 3	ASAS J182714−1507.1	●	○	●	●	○	●	43.9	0.004*	0.905	0.004	y
ASCC 69	S Mus	●	●	●	●	○	1.0σ	11.4	0.004	0.879	0.004	y
Collinder 220	UW Car	●	●	●	●	○	1.1σ	47.2	0.001*	0.838	0.001	y
IC 4725	Y Sgr	1.2σ	●	●	●	●	●	26.8	0.0	0.781	0.0	u
NGC 6705	ASAS J184741−0654.4	●	●	1.3σ	●	○	○	34.6	0.0	0.778	0.0	i
King 4	GO Cas	●	○	●	●	○	1.3σ	21.7	0.0	0.684	0.0	i
Berkeley 60	BF Cas	●	○	●	●	○	1.1σ	33.9	0.0	0.672	0.0	i
Toepler 1	GI Cyg	1.0σ	○	○	○	○	●	18.7	0.0	0.568	0.0	i
Feinstein 1	U Car	●	1.6σ	●	●	○	●	20.8	0.0	0.52	0.0	i
ASCC 61	VY Car	●	○	●	●	○	2.0σ	21.9	0.0	0.385	0.0	i
NGC 129	V379 Cas	○	●	●	●	○	●	20.3	0.0	0.896	0.0	y
Ruprecht 18	VZ CMa	○	○	●	1.2σ	●	●	9.2	0.0	0.592	0.0	i
Berkeley 82	ASAS J190929+1232.8	○	○	●	●	○	1.3σ	10.9	0.0*	0.549	0.0	i
Ruprecht 118	ASAS J162811−5111.9	○	○	●	1.1σ	○	●	22.2	0.0*	0.536	0.0	i
Hogg 12	GH Car	○	○	●	1.1σ	○	1.1σ	9.8	0.0	0.503	0.0	i
NGC 6649	ASAS J183652−0907.1	○	●	●	1.1σ	○	1.3σ	36.7	0.0*	0.469	0.0	i
Trumpler 9	ASAS J075503−2614.3	○	○	1.1σ	1.1σ	○	●	15.2	0.0	0.463	0.0	i
NGC 2345	ASAS J070911−1217.2	○	○	●	1.8σ	○	●	36.6	0.0	0.317	0.0	i
Ruprecht 100	NSV 19202	○	○	○	○	○	○	–	0.837*	1.0	0.837	i
FSR 1595	NSV 18905	○	○	○	○	○	○	–	0.821*	1.0	0.821	i
Dolidze 53	V415 Vul	○	○	○	○	○	○	–	0.759*	1.0	0.759	i
Ruprecht 100	TY Cru	○	○	○	○	○	○	–	0.671*	1.0	0.671	i
SAI 116	NSV 18942	○	○	○	○	○	○	3.4	0.621*	1.0	0.621	i
Dolidze 34	TY Sct	○	○	○	○	○	○	–	0.547	1.0	0.547	i

is thus particularly interesting, containing both a fundamental-mode and an overtone pulsator, just as NGC 6067.

4.2.2 Unconstrained high-prior Combos

In Table 2, we highlight six Combos with $P(A) > 50$ per cent that have thus far not been studied for membership, and for which no membership constraints were available. Hence, no likelihoods could be computed for these cases. We therefore suggest the following Combos for observational follow-up: V415 Vul – Dolidze 53; TY Cru & NSV 19202 – Ruprecht 100; NSV 18942 – SAI 116; TY Sct – Dolidze 34; NSV 18905 – FSR 1595.

4.3 The Galactic Cepheid PLR revisited

Let us now employ our bona fide CC sample to revisit the calibration of the Galactic Cepheid PLR. It represents an ideal sample to this end, due to the high confidence we can have in cluster membership, though small statistics and a lack of long-period calibrators will limit the precision attainable.

A Cepheid's absolute V-band magnitude, M_V, is determined using the true distance modulus of the cluster, $(V_0 - M_V)_{\rm Cl}$, the Cepheid's mean magnitude, $\langle m_V \rangle$, the ratio of total-to-selective extinction towards the cluster, $R_{V,\,\rm Cl}$, and the Cepheid's colour excess, $E(B-V)$, as

$$M_V = \langle m_V \rangle - (V_0 - M_V)_{\rm Cl} - R_{V,\rm Cl} E(B-V), \quad (18)$$

where quantities refer to the Cepheid, unless subscripted by 'Cl'.

As described in Section 3.1, we compile cluster data from D02 for our membership analysis. These data, however, do not take into account line-of-sight dependences of reddening or non-canonical values of R_V. In the following, we refer to the set of data compiled for our membership analysis as the 'standard' set.

In an attempt to improve accuracy, we compile more accurate data from detailed studies of the host clusters. True distance moduli based on ZAMS fitting were taken from T10 and An et al. (2007), giving preference to the estimates with the smallest uncertainties. For the two ASCC clusters, we use the dereddened values by Kharchenko et al. (2005b), and for Collinder 220 we rely on the data in D02. For reddening, An et al. (2007) provide a convenient way to calculate R_V for some lines of sight in our sample as $R_V = R_{V,\,0} + 0.22(B-V)_0$, with $R_{V,\,0}$ tabulated for the cluster and taking into account the intrinsic colour of the Cepheids. For the two ASCC clusters and Collinder 220, we employ the canonical $R_V = 3.1 \pm 0.2$ since no other estimate is available. For Turner 9, Berkeley 58 and van den Bergh 1, we use the distance moduli and R_V values from Turner et al. (1997, 2008, 1998), respectively. For the long-period Cepheid hosts, Trumpler 35 and Turner 2, we employ the data published in Turner (1980) and Turner et al. (1993). Cepheid mean V magnitudes and $E(B-V)$ were compiled as described in Section 3.1. Note that ASAS J182714 − 1507.1 was not included in this calibration, since the data compiled were not of sufficient quality. The values thus compiled are listed in Table 3, and we refer to this data set as the 'optimal' one.

Fig. 17 shows the fits to both the 'standard' (left-hand panel) and the 'optimal' (right-hand panel) data sets. In both figures, four

Table 3. Parameters adopted for the 'optimal' set used in equation (18) and the right panel of Fig. 17. Newly-identified bona fide Combos employed in the fit are marked with an asterisk next to the Cepheids identifier. True distance moduli of clusters, $(V_0 - M_V)$, and absorption-relevant parameters were adopted according to the criteria specified in the text. We adopt 0.04 mag as the uncertainty on $\langle m_V \rangle$.

Cepheid	Cluster	$\langle m_V \rangle$	$E(B-V)$	$(V_0 - M_V)$	$R_{V,\,\mathrm{Cl}}$	$\log P$	M_V
SU Cyg	Turner 9	6.89	0.07 ± 0.02	9.33 ± 0.05	2.94 ± 0.38	0.585	-2.65 ± 0.08
CG Cas	Berkeley 58	11.37	0.69 ± 0.01	12.40 ± 0.12	2.95 ± 0.20	0.640	-3.07 ± 0.19
CE Cas B	NGC 7790	11.09	0.48 ± 0.05	12.46 ± 0.01	3.31 ± 0.26	0.651	-2.98 ± 0.21
SX Car*	ASCC 61	9.12	0.33 ± 0.03	11.14 ± 0.20	3.10 ± 0.51	0.687	-3.04 ± 0.28
CF Cas	NGC 7790	11.15	0.48 ± 0.03	12.46 ± 0.01	3.33 ± 0.26	0.688	-2.91 ± 0.16
CE Cas A	NGC 7790	10.94	0.48 ± 0.05	12.46 ± 0.01	3.33 ± 0.26	0.711	-3.12 ± 0.21
UW Car*	Collinder 220	9.46	0.46 ± 0.01	11.63 ± 0.20	3.10 ± 0.51	0.728	-3.60 ± 0.31
CV Mon	vdBergh 1	10.33	0.68 ± 0.05	11.08 ± 0.07	3.20 ± 0.04	0.731	-2.93 ± 0.18
V Cen	NGC 5662	6.87	0.25 ± 0.05	9.31 ± 0.02	3.47 ± 0.38	0.740	-3.32 ± 0.20
BB Sgr	Collinder 394	6.91	0.29 ± 0.05	9.38 ± 0.10	3.10 ± 0.51	0.822	-3.37 ± 0.24
U Sgr	IC 4725	6.72	0.39 ± 0.02	8.93 ± 0.02	3.32 ± 0.21	0.829	-3.52 ± 0.11
DL Cas	NGC 129	8.98	0.46 ± 0.02	11.11 ± 0.02	3.46 ± 0.22	0.903	-3.73 ± 0.13
S Mus*	ASCC 69	6.13	0.21 ± 0.02	10.0 ± 0.20	3.10 ± 0.51	0.985	-4.52 ± 0.24
S Nor	NGC 6087	6.41	0.12 ± 0.05	9.65 ± 0.03	3.74 ± 0.85	0.989	-3.70 ± 0.22
TW Nor	Lyngå 6	11.66	1.24 ± 0.03	11.51 ± 0.08	3.33 ± 0.10	1.033	-3.96 ± 0.18
V340 Nor	NGC 6067	8.41	0.32 ± 0.02	11.03 ± 0.01	3.36 ± 0.29	1.053	-3.68 ± 0.11
RU Sct	Trumpler 35	9.53	0.92 ± 0.03	11.58 ± 0.18	3.10 ± 0.20	1.295	-4.91 ± 0.27
WZ Sgr	Turner 2	8.09	0.62 ± 0.02	11.26 ± 0.10	3.00 ± 0.20	1.339	-5.02 ± 0.17

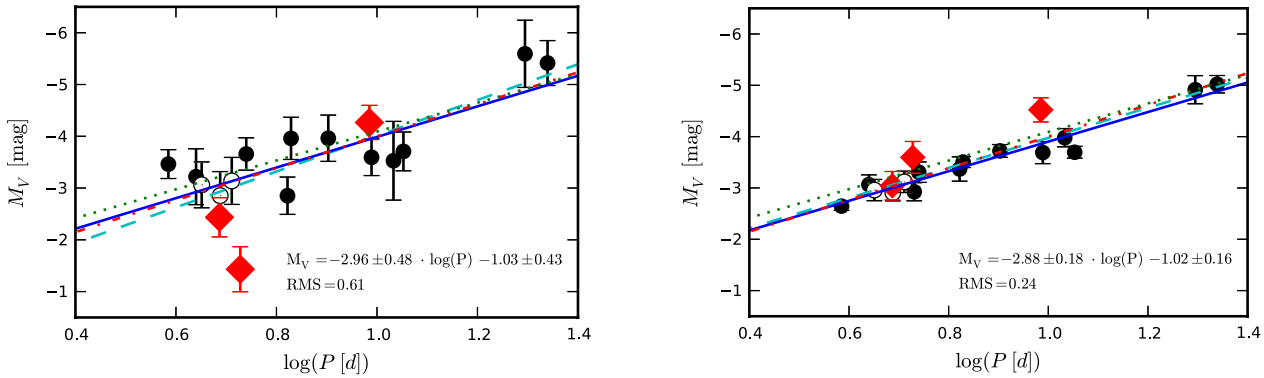

Figure 17. Cepheid PLRs fitted to the 'standard' (left-hand panel) and 'optimal' (right-hand panel) data sets. The solid circles indicate previously known CCs, the open circles highlight the three Cepheids in NGC 7790. The solid red large diamonds indicate the new bona fide fundamental-mode CCs S Mus, SX Car and UW Car included in the fit. The dotted line shows the PLR by Benedict et al. (2007), and the dash-dotted line represents Tammann, Sandage & Reindl (2003). The solid and dashed lines indicate weighted and non-weighted least-squares fits. An accurate PLR calibration critically depends on accurate distance estimates from detailed studies that include line-of-sight variations of extinction.

straight lines indicate the PLR calibrations by Tammann et al. (2003, red dash-dotted), Turner et al. (2010, green dotted, lower zero-point), as well as our non-weighted (dashed cyan) and weighted (solid blue) least-squares fits to the data. The large scatter (rms = 0.61) in the 'standard' data set is striking. Contrastingly, the 'optimal' set is much better indeed, with an rms of 0.24 mag. Hence, it is evident that the cluster data compiled for the membership analysis is rather limited in precision and sometimes also accuracy, a fact we already encountered when computing membership probabilities, see for instance the case of WZ Sgr in Section 4.1.2.6. Thus, there remains a need for detailed and deep photometric studies of open cluster parameters, and in particular reddening.

We determine the uncertainties on the 'optimal' set by linear regression and obtain

$$\langle M_V \rangle = -(2.88 \pm 0.18) \log P - (1.02 \pm 0.16)\,. \qquad (19)$$

Despite the reasonable formal uncertainties of our 'optimal' fit, our solution should not be considered definitive. The result of the fit is very sensitive to the absolute magnitude estimates of the extreme points at short and long periods, and the M_V estimates of the new candidates are clearly too crude at this point. Furthermore, despite our preference for cluster literature with the smallest uncertainties, there is no guarantee that the most accurate cluster data were employed; there appears to exist too little consensus on some clusters in the literature, e.g. for Lyngå 6, $(V_0 - M_V)_{\mathrm{Cl}}$ differs by 0.39 mag between T10 and An et al. (2007), exceeding the published combined uncertainties by a factor greater than 3. Binarity of the Cepheids was not accounted for, since the fit is dominated mainly by the cluster parameters. Yet, we note that our result is consistent with the calibration by T10 ($\langle M_V \rangle = -(2.78 \pm 0.12) \log P - (1.29 \pm 0.10)$), which is to be expected due to the significant overlap in the sample of CCs used for this calibration.

5 DISCUSSION

5.1 Constraining power and limitations of membership constraints

5.1.1 The prior P(A)

The form of the prior was motivated by radial density profiles of star clusters, see Section 2.1. However, the degree with which the distribution of stars in the cluster is known varies greatly between clusters, and deviations from circular cluster shapes were ignored for internal consistency. Furthermore, crowding, great distances ($\sim$ kpc) to host cluster candidates, differential reddening, sparsity, etc. all conspire to complicate the definition of cluster radii. It is thus not surprising that the prior does not perform extremely well as a membership constraint if taken at face value. Nevertheless, it does help to separate the interesting cases from the majority of null matches, since it reduces the question of proximity on the projected sky to a single number that contains information on the density of the cluster, since both cluster radii are used in its definition.

5.1.1.1 Chance alignment. Among our (bona fide or inconclusive) CCs, 7−9 are found to lie within r_c, and 8−17 at $r_c < R < r_{lim}$. Within the original cross-match, 25 Combos are matched within r_c and 520 within $r_c < R < r_{lim}$. Thus, we can estimate the rate of chance alignment within the core radius to be approximately 3:1. At separations inferior to r_{lim}, this ratio increases to between 20:1 and 35:1, depending on whether inconclusive cases are counted, or not.

Note that eight bona fide CCs lie outside r_{lim}, 6 of which are located within two r_{lim}; EV Scuti's separation from NGC 6664's centre is 2.6 r_{lim}, and that of V379 Cas from NGC 129 is 2.7 r_{lim}.

5.1.2 The likelihood P(B|A)

Intuitively, the greatest set of constraints used provides the tightest constraints on membership for any Combo. Fig. 18 illustrates this. It shows a logarithmic normalized histogram of likelihoods for two cases: more than three constraints used to calculate $P(B|A)$ (light grey distribution); all constraints used to calculate $P(B|A)$ (dark grey slim bars). However, the constraining power of a given set of constraints is not merely a function of its size. Here we discuss the membership constraining power of the different constraints used to calculate likelihoods.

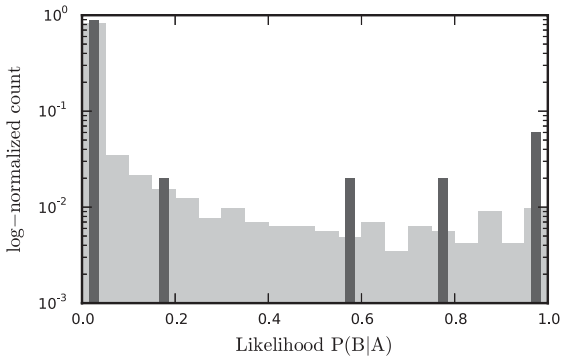

Figure 18. Log-normalized histogram of likelihoods. Light grey, broad bars: combinations with three or more parameters used for $P(B|A)$. The dark grey, slim bars: combinations with all membership constraints. The more membership constraints are employed, the more separated are high and low likelihoods, i.e. the better constraint is membership.

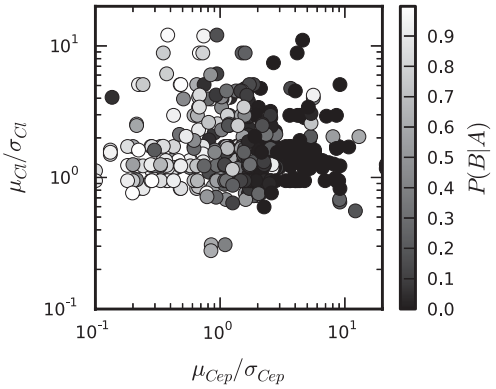

Figure 19. Likelihoods computed as a function of proper motion. Abscissa: proper motion of Cepheid divided by the squared-summed uncertainties, i.e. $\mu = \sqrt{(\mu^*_\alpha)^2 + \mu^2_\delta}; \sigma = \sqrt{\sigma\left(\mu^*_\alpha\right)^2 + \sigma\left(\mu_\delta\right)^2}$. Ordinate: same for cluster.

Proper motions can be very effective at ruling out membership if the motion clearly exceeds the uncertainties on the measurement. This is the case for a cluster cross-matched with a background Cepheid, for instance. However, for a significant fraction of Combos, the proper motion vector's magnitude was smaller than the uncertainty of the measurement, thus effectively not constraining membership, see Fig. 19. If the magnitude surpasses the uncertainties by at least a factor of 3, proper motion serves as a reliable constraint. For the majority of Combos that fulfil this criterion, membership tends to be excluded.

Distance is a potentially very strong membership constraint, since intuitively, a Cepheid that occupies the same space volume as a cluster should be a member. However, cluster distances can be subject to large systematic uncertainties due to parameter degeneracy (distance, age, reddening), model dependence (rotation, etc.), or previous distance estimates to, e.g., the Pleiades. Furthermore, implicit assumptions on cluster membership can significantly impact the distance determined, especially for relatively young clusters that harbour few stars around the main-sequence turn-off and few or no red giants. Very detailed studies of open clusters, and in particular of the line-of-sight extinction, are required for improvement in this domain, as is shown in Section 4.3, or demonstrated by the discussion of CV Mon's membership in van den Bergh 1 (cf. Section 4.1.2.2).

RVs have the potential to provide very tight membership constraints, since the RV dispersion within open clusters can be significantly below 1 km s^{-1} (Lovis & Mayor 2007), approaching the measurement precision on v_γ for non-binary Cepheids. However, estimates of average cluster RVs are usually based on only a few stars, see Fig. 6. In fact, approximately half of all clusters with 'known' average RVs are based on measurements of two stars or less, and strong selection effects (e.g. towards late-type stars) can severely impact the estimate. Since Cepheids are very bright and of late spectral type, it is rather likely that a cluster RV is in part based on measurements that include a Cepheid. We therefore highlight the need to observe more RVs of upper main-sequence stars in clusters in order to ensure the most accurate estimates of average cluster RV. Alternatively, larger telescopes may observe the much fainter lower main sequence. The *Gaia*-ESO public spectroscopic survey Gilmore et al. (2012) will soon provide precise RVs for a large number of clusters and thus can improve the reliability of a future study similar to the present one.

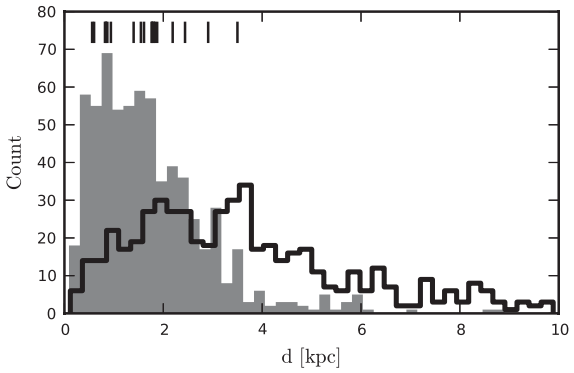

Figure 20. Distance distribution of known open clusters in log-age range [7.0, 8.5] (grey filled histogram, high peak at small d) and of Cepheids at low Galactic latitudes, $|b| \leq 10^{\circ}$ (black step histogram). Distances of bona fide CCs from this work indicated by short black lines at the top.

The iron abundances compiled here were, arguably, of limited use as membership constraints, since data inhomogeneity, the limited number of cluster stars used for determining the cluster average, and differences in the solar reference values used are at the same order of magnitude as the range of iron abundances found in the sample considered (that lies within the young metal-rich Galactic disc). For a few cases, however, the iron abundance did further strengthen the interpretation of excluded membership.

Age as a membership constraint quantifies valid evolutionary considerations that are established empirically. It is a particularly useful membership constraint, since it is readily available for clusters as well as for Cepheids (from PA relations), especially when few other constraints are available. However, ages for both kinds of objects are subject to model dependence, and the accuracy of the values inferred is difficult to quantify.

All of the above quantities have their own peculiarities, and thus no single one can be named the 'best' membership constraint. Instead, the greatest constraining power resides in the combination of all the data, as is seen in the bona fide CCs identified in this work, as well as in Fig. 18.

5.1.3 Membership probabilities P(A|B)

We computed $P(A|B)$ simply as the product of the prior and the likelihood, leaving out the normalization term $P(B)$ that would in principle be required, see equation (1). However, in order to make full use of the $P(A|B)$ values computed, $P(B)$ should not be neglected. Given that the incompleteness for open clusters is quite significant at heliocentric distances greater than, say, 1 kpc, we did not currently see this as feasible, cf. Fig. 20.

5.2 Incompleteness

Despite our aim to maximize the number of clusters and Cepheids considered, only 23 bona fide CCs were identified. This is a result of the apparent difference in sample completeness for clusters and Cepheids. Fig. 20 shows the histograms of heliocentric open cluster distances for clusters within the appropriate age range $\left(\log_{10}(\text{age(yr)}) = [7.0, 8.5]\right)$, taken from D02 as the grey filled distribution (peak at smaller d), and the Cepheid distances compiled (cf. Section 3.2.1, black step histogram). It is evident that the detection rate of open clusters stalls at distances greater than 1 kpc, probably since their identification against the field becomes increasingly difficult. Cepheids, on the other hand, are detectable at much greater distances, thanks to their high luminosity and characteristic brightness variations.

However, a cluster's probability of hosting a Cepheid is governed by stellar evolution and star formation. For a given distribution of stellar masses, only a small fraction will become seen as Cepheids during their lifetime (stars with masses between $\sim$4 and 11 $M_{\odot}$). Due to the nature of the IMF, these intermediate-mass stars constitute a small fraction of the total number of cluster stars, and few such intermediate-mass stars are present in typical (small) open clusters. Furthermore, only a fraction (perhaps 10–20 per cent) of a suitable star's lifetime during the core helium burning phase is spent on the blue loops, and even less within the instability strip. As a result, few CCs are known. The inverse problem of finding host clusters around known Cepheids (e.g. Turner et al. 1993; Turner 1998; Majaess et al. 2012a,c), however, can be interesting, e.g. to constrain the survival rate of open clusters. Such studies can be very successful, see e.g. the 'missing Combos' in Section 4.1.1 and the Cepheids belonging to OB associations listed in T10.

5.3 Implications for the distance scale

We are aware of the fact that our calibration, although performed on an 'optimal' set, remains inhomogeneous in the true distance moduli employed and the treatment of extinction. It is furthermore based on *V*-band data obtained in multiple different passbands with varying post-processing techniques. These are the main limitations of the data employed. Furthermore, the number of CCs employed in the fit (18) is not very large, and the distance to NGC 7790 enters the fit three times, since its three CCs are included in the fit. Finally, the fit obtained is very sensitive to outliers, due to the lack of long-period calibrators.

We advocate that the 'optimal' sample presented, although incomplete (missing host clusters), forms an ideal subset for PLR calibrations, since all cluster memberships were self-consistently evaluated. However, to improve upon the calibration of the cluster-based PLR, two things would be particularly useful: a detailed homogeneous deep photometric study of the host clusters that includes careful treatment of extinction, and observational follow-up of the inconclusive CC candidates identified. Given the large discrepancies that are found between recent Galactic PLR calibrations (and their zero-points), such an observational campaign would be very desirable.

6 CONCLUSION

Focusing on Cepheids, we have performed an all-sky cluster membership census. Our analysis considers an up to eight-dimensional membership space that includes spatial and kinematic information, as well as parent population parameters (age, iron abundance). Although in some ways limited by data inhomogeneity and incompleteness, we identify 23 bona fide cluster Cepheids, including most canonical CCs accessible within our sample, as well as five new ones, and multiple additional CC candidates of interest.

The newly identified CCs are: SX Car in ASCC 61, S Mus in ASCC 69, UW Car in Collinder 220, ASAS J182714−1507.1 in Kharchenko 3 (fundamental-mode pulsators) and V379 Cas in NGC 129 (overtone pulsator). The cluster membership of these candidates must have escaped previous discovery, since most of the host clusters are not very well studied, and the Cepheids are located outside the cluster cores, cf. Section 4.2.

Since we can rank candidates according to membership probabilities, we consider our bona fide CC sample ideal for calibrating the Galactic Cepheid PLR. However, data inhomogeneity, large uncertainties on cluster parameters, and a lack of long-period calibrators unfortunately limit the precision of the calibration we perform. We therefore highlight the need for observational campaigns dedicated to the host clusters of our bona fide CC sample, as well as other interesting CC candidates identified.

The limitations that our work suffers due to inhomogeneous and incomplete data will be significantly reduced in the near future, thanks to the *Gaia* space mission. Specifically, *Gaia* will improve our study in the following ways.

(i) Thousands of new Cepheids (Eyer & Cuypers 2000; Windmark, Lindegren & Hobbs 2011) will be discovered.

(ii) Accurate absolute trigonometric parallaxes of Cepheids will become available up to distances of 6–12 kpc, depending on extinction (Eyer et al. 2012), thereby enabling a direct calibration of the Galactic PLR similar to the one performed in the seminal paper by Feast & Catchpole (1997). This will remove our partial dependence on existing PLR calibrations when determining cluster membership. Accurate parallaxes to longer period Cepheids will also be obtained, thereby significantly improving the distance estimates to extragalactic Cepheids.

(iii) The accuracy of proper motions will be improved by orders of magnitude, moving from mas yr^{-1} to tens of μas yr^{-1}, see Lindegren (2010) and the *Gaia* Science Performance website.[14]

(iv) Homogeneous RVs (via the RVS instrument) and metallicity estimates (via the spectrophotometric instruments) will be available as membership constraints for a great number of Cepheids.

(v) Homogeneous metallicity estimates can be obtained through spectrophotometry and photometry (Liu et al. 2012).

(vi) Thousands of new open clusters (ESA 2000) will be discovered, forming a more or less complete census of open clusters to distances up to 5 kpc. As was shown in Fig. 20, the distribution of Cepheids is still increasing at these distances. Hence, one may expect to find many more CCs in these parts of the Galaxy.

(vii) Down to magnitude 20, all-sky homogeneous multi-epoch photometry and colours will be obtained that will include all the bona fide cluster Cepheids mentioned in this work.

(viii) Known clusters will be mapped in unprecedented detail, and intracluster dynamics will be accessible to determine membership.

Gaia's data homogeneity will significantly improve error budgets, since no offsets in instrumental zero-points (e.g. in RV) will have to be taken into account. The constraining power in terms of membership will thus be augmented considerably. Correlations between parameters, e.g. proper motion, parallax and RV, can be determined self-consistently and accounted for (cf. van Leeuwen 2007). Such factors will make the *Gaia* era particularly exciting for work such as this.

ACKNOWLEDGEMENTS

Many heartfelt thanks to the observers who contributed to the Cepheid RV campaigns, in particular to: Lovro Palaversa, Mihaly Váradi and Pierre Dubath. We gratefully acknowledge useful discussions with and comments received from Maria Süveges, Berry Holl, David G. Turner, Daniel Majaess, Laszlo Szabados, Imants Platais, Michael W. Feast, and the referee, C. David Laney; all of these helped to improve the manuscript.

This research has made use of: NASA's Astrophysics Data System Bibliographic Services; the SIMBAD data base and VizieR catalogue access tool (cf. A&AS 143, 23), operated at CDS, Strasbourg, France; the International Variable Star Index (VSX) data base, operated at AAVSO, Cambridge, Massachusetts, USA; the VO-tool TOPCAT,[15] see Taylor (2005); the WEBDA data base, operated at the Institute for Astronomy of the University of Vienna; other online data bases that provide Cepheid data, see the main text.

REFERENCES

Akerlof C. et al., 2000, AJ, 119, 1901
An D., Terndrup D. M., Pinsonneault M. H., 2007, ApJ, 671, 1640
Anderson E., Francis C., 2012, Astron. Lett., 38, 331 (XHIP)
Anderson R. I., Eyer L., Mowlavi N., 2012, in Griffin E., Hanisch R., Seaman R., eds, Proc. IAU Symp. 285, New Horizons in Time-Domain Astronomy. Cambridge Univ. Press, Cambridge, p. 275
Andrievsky S. M. et al., 2002a, A&A, 381, 32
Andrievsky S. M., Bersier D., Kovtyukh V. V., Luck R. E., Maciel W. J., Lépine J. R. D., Beletsky Y. V., 2002b, A&A, 384, 140
Andrievsky S. M., Kovtyukh V. V., Luck R. E., Lépine J. R. D., Maciel W. J., Beletsky Y. V., 2002c, A&A, 392, 491
Andrievsky S. M., Luck R. E., Martin P., Lépine J. R. D., 2004, A&A, 413, 159
Andrievsky S. M., Luck R. E., Kovtyukh V. V., 2005, AJ, 130, 1880
Arp H. C., 1958, ApJ, 128, 166
Bakos G. Á., Lázár J., Papp I., Sári P., Green E. M., 2002, PASP, 114, 974
Balona L. A., Laney C. D., 1995, MNRAS, 277, 250
Baranne A. et al., 1996, A&AS, 119, 373
Baranowski R. et al., 2009, MNRAS, 396, 2194
Barnes T. G., III, Moffett T. J., Slovak M. H., 1987, ApJS, 65, 307
Barnes T. G., III, Moffett T. J., Slovak M. H., 1988, ApJS, 66, 43
Barnes T. G., III, Jeffery E. J., Montemayor T. J., Skillen I., 2005, ApJS, 156, 227
Baumgardt H., Dettbarn C., Wielen R., 2000, A&AS, 146, 251
Benedict G. F. et al., 2007, AJ, 133, 1810
Berdnikov L. N., 2008, VizieR Online Catalog, II/285
Berdnikov L. N., Dambis A. K., Vozyakova O. V., 2000, A&AS, 143, 211
Bersier D., 2002, ApJS, 140, 465
Bersier D., Burki G., Mayor M., Duquennoy A., 1994, A&AS, 108, 25
Bono G., Marconi M., Cassisi S., Caputo F., Gieren W. P., Pietrzynski G., 2005, ApJ, 621, 966
Bukowiecki Ł., Maciejewski G., Konorski P., Strobel A., 2011, Acta Astron., 61, 231 (B11)
Coulson I. M., Caldwell J. A. R., 1985, South Afr. Astron. Obser. Circ., 9, 5
Coulson I. M., Caldwell J. A. R., Gieren W. P., 1985, ApJS, 57, 595
Cutri R. M. et al., 2003, 2MASS All Sky Catalog of Point Sources. NASA/IPAC Infrared Science Archive
Dias W. S., Lépine J. R. D., Alessi B. S., 2001, A&A, 376, 441
Dias W. S., Alessi B. S., Moitinho A., Lépine J. R. D., 2002a, A&A, 389, 871 (D02)
Dias W. S., Lépine J. R. D., Alessi B. S., 2002b, A&A, 388, 168
Efremov Y. N., 1964, Perem. Zvezdy, 15, 242
Eggen O. J., 1980, Inf. Bull. Var. Stars, 1853, 1
Eggen O. J., 1983, AJ, 88, 379
ESA, 2000, Gaia: Composition, Formation and Evolution of the Galaxy. Technical Report, ESA-SCI(2000)4
Evans N. R., 1983, ApJ, 272, 214
Evans N. R., 1992, ApJ, 385, 680
Evans N. R., Welch D. L., 1993, PASP, 105, 836

[14] http://www.rssd.esa.int/index.php?project=GAIA&page=Science_Performance#chapter1

[15] http://www.star.bris.ac.uk/∼mbt/topcat/

Eyer L., Cuypers J., 2000, in Szabados L., Kurtz D., eds, ASP Conf. Ser. Vol. 203, IAU Colloq. 176: The Impact of Large-Scale Surveys on Pulsating Star Research. Astron. Soc. Pac., San Francisco, p. 71
Eyer L. et al., 2012, Ap&SS, 341, 207
Feast M. W., 1957, MNRAS, 117, 193
Feast M., 1999, PASP, 111, 775
Feast M. W., Catchpole R. M., 1997, MNRAS, 286, L1
Fernie J. D., Evans N. R., Beattie B., Seager S., 1995, Inf. Bull. Var. Stars, 4148, 1
Flower P. J., 1978, ApJ, 224, 948
Fouqué P. et al., 2007, A&A, 476, 73
Francic S. P., 1989, AJ, 98, 888
Freedman W. L. et al., 2001, ApJ, 553, 47
Frinchaboy P. M., Majewski S. R., 2008, AJ, 136, 118
Froebrich D., Scholz A., Raftery C. L., 2007, MNRAS, 374, 399
Fry A. M., Carney B. W., 1997, AJ, 113, 1073
Geffert M., Bonnefond P., Maintz G., Guibert J., 1996, A&AS, 118, 277
Gieren W. P., 1981, ApJS, 46, 287
Gieren W. P., 1985, ApJ, 295, 507
Gieren W. P., Matthews J. M., Moffett T. J., Barnes T. G., III, Frueh M. L., Szabados L., 1989, AJ, 98, 1672
Gieren W. P., Fouqué P., Gomez M. I., 1997, ApJ, 488, 74
Gilmore G. et al., 2012, The Messenger, 147, 25
Giridhar S., 1983, JA&A, 4, 75
Gorynya N. A., Irsmambetova T. R., Rastorgouev A. S., Samus N. N., 1992, Sov. Astron. Lett., 18, 316
Gorynya N. A., Samus' N. N., Rastorguev A. S., Sachkov M. E., 1996, Astron. Lett., 22, 175
Gorynya N. A., Samus' N. N., Sachkov M. E., Rastorguev A. S., Glushkova E. V., Antipin S. V., 1998, Astron. Lett., 24, 815
Gorynya N. A., Samus N. N., Sachkov M. E., Rastorguev A. S., Glushkova E. V., Antipin S. V., 2002, VizieR Online Data Catalog III/229, 3229, 0
Groenewegen M. A. T., 2008, A&A, 488, 25
Groenewegen M. A. T., Romaniello M., Primas F., Mottini M., 2004, A&A, 420, 655
Harris G. L. H., van den Bergh S., 1976, ApJ, 209, 130
Hoyle F., Shanks T., Tanvir N. R., 2003, MNRAS, 345, 269
Imbert M., 1999, A&AS, 140, 79
Irwin J. B., 1955, Mon. Notes Astron. Soc. South Afr., 14, 38
Jaynes E. T., 2003, Probability Theory - The Logic of Science. Cambridge Univ. Press, Cambridge
Kharchenko N. V., 2001, Kinematika Fiz. Nebesnykh Tel, 17, 409
Kharchenko N. V., Piskunov A. E., Röser S., Schilbach E., Scholz R.-D., 2005a, A&A, 438, 1163
Kharchenko N. V., Piskunov A. E., Röser S., Schilbach E., Scholz R.-D., 2005b, A&A, 440, 403
Kharchenko N. V., Scholz R.-D., Piskunov A. E., Röser S., Schilbach E., 2007, Astron. Nachr., 328, 889
Kharchenko N. V., Piskunov A. E., Schilbach E., Röser S., Scholz R.-D., 2012, A&A, 543, A156 (K12)
Kholopov P. N., 1956, Perem. Zvezdy, 11, 325
King I., 1962, AJ, 67, 471
Kiss L. L., 1998, MNRAS, 297, 825
Klagyivik P., Szabados L., 2009, A&A, 504, 959 (KS09)
Kovtyukh V. V., Wallerstein G., Andrievsky S. M., 2005a, PASP, 117, 1173
Kovtyukh V. V., Andrievsky S. M., Belik S. I., Luck R. E., 2005b, AJ, 129, 433
Kovtyukh V. V., Soubiran C., Luck R. E., Turner D. G., Belik S. I., Andrievsky S. M., Chekhonadskikh F. A., 2008, MNRAS, 389, 1336
Kukarkin B. V., Kholopov P. N., 1982, New Catalogue of Suspected Variable Stars. Publication Office Nauka, Moscow
Laney C. D., Caldwell J. A. R., 2007, MNRAS, 377, 147
Lasker B. M. et al., 2008, AJ, 136, 735
Leavitt H. S., Pickering E. C., 1912, Harv. Coll. Obser. Circ., 173, 1
Lemasle B., François P., Bono G., Mottini M., Primas F., Romaniello M., 2007, A&A, 467, 283
Lemasle B., François P., Piersimoni A., Pedicelli S., Bono G., Laney C. D., Primas F., Romaniello M., 2008, A&A, 490, 613
Lindegren L., 2010, in Klioner S. A., Seidelmann P. K., Soffel M. H., eds, Proc. IAU Symp. 261, Relativity in Fundamental Astronomy: Dynamics, Reference Frames, and Data Analysis. Cambridge Univ. Press, Cambridge, p. 296
Liu C., Bailer-Jones C. A. L., Sordo R., Vallenari A., Borrachero R., Luri X., Sartoretti P., 2012, MNRAS, 426, 2463
Lloyd Evans T., 1980, South Afr. Astron. Obser. Circ., 1, 257
Lovis C., Mayor M., 2007, A&A, 472, 657
Luck R. E., Lambert D. L., 2011, AJ, 142, 136
Luck R. E., Gieren W. P., Andrievsky S. M., Kovtyukh V. V., Fouqué P., Pont F., Kienzle F., 2003, A&A, 401, 939
Macri L. M., Stanek K. Z., Bersier D., Greenhill L. J., Reid M. J., 2006, ApJ, 652, 1133
Majaess D. J., Turner D. G., Lane D. J., 2008, MNRAS, 390, 1539
Majaess D. et al., 2011, ApJ, 741, L27
Majaess D., Turner D. G., Gieren W., 2012a, MNRAS, 421, 1040
Majaess D., Turner D., Gieren W., 2012b, ApJ, 747, 145
Majaess D., Turner D., Gieren W., Balam D., Lane D., 2012c, ApJ, 748, L9
Majaess D., Turner D. G., Gallo L., Gieren W., Bonatto C., Lane D. J., Balam D., Berdnikov L., 2012d, ApJ, 753, 144
Matthews J. M., Gieren W. P., Mermilliod J.-C., Welch D. L., 1995, AJ, 110, 2280
McSwain M. V., Gies D. R., 2005, ApJS, 161, 118
Mermilliod J. C., 1988, Bull. Inf. Cent. Donnees Stellaires, 35, 77
Mermilliod J.-C., 1995, in Egret D., Albrecht M. A., eds, Astrophysics and Space Science Library, Vol. 203, Information & On-Line Data in Astronomy. p. 127
Mermilliod J. C., Mayor M., Udry S., 2008, A&A, 485, 303
Metzger M. R., Caldwell J. A. R., McCarthy J. K., Schechter P. J., 1991, ApJS, 76, 803
Metzger M. R., Caldwell J. A. R., Schechter P. L., 1992, AJ, 103, 529
Metzger M. R., Caldwell J. A. R., Schechter P. L., 1998, AJ, 115, 635
Monson A. J., Pierce M. J., 2011, ApJS, 193, 12
Mottini M., 2006, PhD thesis. Ludwig-Maximilians-Universität, München
Perryman M. A. C., ed., 1997, ESA Special Publication, Vol. 1200, The HIPPARCOS and TYCHO Catalogues. Astrometric and Photometric Star Catalogues derived from the ESA HIPPARCOS Space Astrometry Mission, ESA, Noordwijk
Petterson O. K. L., Cottrell P. L., Albrow M. D., Fokin A., 2005, MNRAS, 362, 1167
Platais I., 1979, Astron. Tsirkulyar, 1049, 4
Platais I., 1986, Nauchnye Inf., 61, 89
Pojmanski G., 1997, Acta Astron., 47, 467
Pojmanski G., 2002, Acta Astron., 52, 397
Pojmanski G., Pilecki B., Szczygiel D., 2005, Acta Astron., 55, 275
Pont F., Burki G., Mayor M., 1994, A&AS, 105, 165
Pont F., Queloz D., Bratschi P., Mayor M., 1997, A&A, 318, 416
Queloz D. et al., 2000, A&A, 354, 99
Queloz D. et al., 2001, The Messenger, 105, 1
Raskin G. et al., 2011, A&A, 526, A69
Rastorguev A. S., Glushkova E. V., Dambis A. K., Zabolotskikh M. V., 1999, Astron. Lett., 25, 595
Robichon N., Arenou F., Mermilliod J.-C., Turon C., 1999, A&A, 345, 471
Roeser S., Demleitner M., Schilbach E., 2010, AJ, 139, 2440
Romaniello M., Primas F., Mottini M., Groenewegen M., Bono G., François P., 2005, A&A, 429, L37
Romaniello M. et al., 2008, A&A, 488, 731
Samus N. et al., 2012, General Catalogue of Variable Stars (GCVS database, Version 2012 Jan, http://www.sai.msu.su/gcvs/gcvs/)
Sánchez N., Vicente B., Alfaro E. J., 2010, A&A, 510, A78
Sandage A., 1958, ApJ, 128, 150
Sandage A., Tammann G. A., 2006, ARA&A, 44, 93
Sandage A., Tammann G. A., Saha A., Reindl B., Macchetto F. D., Panagia N., 2006, ApJ, 653, 843
Schmidt E. G., 1982, AJ, 87, 1197
Ségransan D. et al., 2010, A&A, 511, A45
Soszynski I. et al., 2008, Acta Astron., 58, 163
Soszynski I. et al., 2010, Acta Astron., 60, 17

Storm J., Carney B. W., Gieren W. P., Fouqué P., Latham D. W., Fry A. M., 2004, A&A, 415, 531
Storm J. et al., 2011, A&A, 534, A94
Szabados L., 2003, Inf. Bull. Var. Stars, 5394, 1
Szabados L. et al., 2013, MNRAS, 430, 2018
Sziládi K., Vinkó J., Poretti E., Szabados L., Kun M., 2007, A&A, 473, 579
Tadross A. L., 2008, New Astron., 13, 370
Tammann G. A., Sandage A., Reindl B., 2003, A&A, 404, 423
Taylor M. B., 2005, in Shopbell P., Britton M., Ebert R., eds, ASP Conf. Ser. Vol. 347, Astronomical Data Analysis Software and Systems XIV. Astron. Soc. Pac., San Francisco, p. 29
Tsarevsky G. S., Ureche V., Efremov Y. N., 1966, Astron. Tsirkulyar, 367, 1
Turner D. G., 1976, AJ, 81, 1125
Turner D. G., 1977, PASP, 89, 277
Turner D. G., 1980, ApJ, 240, 137
Turner D. G., 1981, AJ, 86, 231
Turner D. G., 1982, PASP, 94, 1003
Turner D. G., 1986, AJ, 92, 111
Turner D. G., 1992, AJ, 104, 1865
Turner D. G., 1998, AJ, 116, 274
Turner D. G., 2010, Ap&SS, 326, 219
Turner D. G., Burke J. F., 2002, AJ, 124, 2931
Turner D. G., Pedreros M., 1985, AJ, 90, 1231
Turner D. G., Forbes D., Pedreros M., 1992, AJ, 104, 1132
Turner D. G., van den Bergh S., Younger P. F., Danks T. A., Forbes D., 1993, ApJS, 85, 119
Turner D. G., Mandushev G. I., Forbes D., 1994, AJ, 107, 1796
Turner D. G., Mandushev G. I., Welch G. A., 1997, AJ, 113, 2104
Turner D. G., Pedreros M. H., Walker A. R., 1998, AJ, 115, 1958
Turner D. G., Billings G. W., Berdnikov L. N., 2001, PASP, 113, 715
Turner D. G., Usenko I. A., Kovtyukh V. V., 2006, The Observatory, 126, 207
Turner D. G. et al., 2008, MNRAS, 388, 444
Turner D. G., Majaess D. J., Lane D. J., Rosvick J. M., Henden A. A. B. D. D., 2010, Odessa Astron. Publ., 23, 119
Turner D. G. et al., 2012, MNRAS, 422, 2501
Turner D. G., Kovtyukh V. V., Usenko I. A., Gorlova N. I., 2013, ApJ, 762, L8
Udalski A., Soszynski I., Szymanski M., Kubiak M., Pietrzynski G., Wozniak P., Zebrun K., 1999, Acta Astron., 49, 223
van den Bergh S., 1957, ApJ, 126, 323
van Leeuwen F., ed., 2007, Astrophysics and Space Science Library, Vol. 350, Hipparcos, the New Reduction of the Raw Data. Springer, Berlin
van Leeuwen F., 2013, A&A, 550, L3
Vazquez R. A., Feinstein A., 1990, A&AS, 86, 209
Walker A. R., 1985a, MNRAS, 213, 889
Walker A. R., 1985b, MNRAS, 214, 45
Walker A. R., 1987, MNRAS, 229, 31
Wilson T. D., Carter M. W., Barnes T. G., III, van Citters G. W., Jr, Moffett T. J., 1989, ApJS, 69, 951
Windmark F., Lindegren L., Hobbs D., 2011, A&A, 530, A76
Woźniak P. R. et al., 2004, AJ, 127, 2436
Yilmaz F., 1966, Z. Astrophys., 64, 54
Yong D., Carney B. W., Teixera de Almeida M. L., Pohl B. L., 2006, AJ, 131, 2256

APPENDIX A: DETAILS ON INDIVIDUAL CLUSTER CEPHEID COMBINATIONS

A1 Literature Combos

A1.1 Inconclusive Combos

A1.1.1 CS Vel and Ruprecht 79. Membership of CS Vel in Ruprecht 79 was thoroughly discussed by Harris & van den Bergh (1976) who credited Tsarevsky et al. (1966) with first suggesting this particular combination. It has since been studied multiple times, e.g. by Walker (1987) and T10. Due to the sparse nature of the cluster, its reality as such was doubted by McSwain & Gies (2005), who conclude that Ruprecht 79 rather be a hole in the dust of the Sagittarius–Carina spiral arm than a physical open cluster.

None of the data from D02 are fully consistent with cluster membership for CS Vel, see Table 1, and we calculate a likelihood of not even 1 per cent, which contrasts the Cepheid's location inside r_c. The Cepheid's colour excess from Laney & Caldwell (2007) agrees with the cluster value, however, and RV is not very far off. The cluster data from D02 and the uncertain existence of the cluster would suggest unlikely membership. However, the difficult parameter determination for this sparse cluster (candidate) means that only a very detailed study of this region can reliably conclude on membership.

A1.1.2 V1726 Cyg and Platais 1. V1726 Cyg's membership results for Platais1 are based on separation, proper motion, RV and age. The star was first considered for cluster membership by Platais (1979) and Turner et al. (1994), and is still often considered a bona fide member of Platais 1 (Turner, Billings & Berdnikov 2001; Turner, Usenko & Kovtyukh 2006). However, Platais (1986) concludes that the existence of this cluster is uncertain.

Of the membership constraints compiled, only proper motion does not significantly differ between cluster and Cepheid, although the magnitude of the Cepheid's motion is a bit larger than that of the cluster. RV differs significantly, with the cluster receding more than 10 km s^{-1} faster than the Cepheid (Frinchaboy & Majewski 2008). In addition, the cluster's age is significantly higher than the Cepheid's. We do not calculate a PLR-based parallax, since V1726 Cyg may or may not be an overtone pulsator; the Fernie data base places V1726 Cyg at approximately 2 kpc, while D02 list 1.3 kpc for Platais1.

Unfortunately, there are great differences in cluster parameters to be found in the literature. For instance, K12 list 3.5 kpc as the cluster's distance, which would exclude membership and be consistent with the higher proper motion of a foreground Cepheid. Interestingly, however, K12's average cluster RV (-15.4 km s^{-1}) would agree with the Cepheid's, although it is based on 21 stars in a poorly populated and supposedly distant (3.5 kpc in K12) cluster, rendering this estimate suspicious.

In summary, the constraints compiled here would tend to indicate non-membership. However, the significantly discrepant cluster distances and RVs from different references leave considerable doubt as to whether the cluster values adopted here are accurate. In light, these issues and the possible non-existence of the cluster, we cannot conclude on membership of this Combo.

A1.2 Unlikely literature Combos

A1.2.1 GH Car in Trumpler 18 or Hogg 12. Membership of the spectroscopic binary overtone pulsator GH Car (Szabados et al. 2013) in cluster Trumpler 18 was first proposed by Vazquez & Feinstein (1990) and then called into question by Baumgardt et al. (2000) who recommended RV follow-up to draw a firmer conclusion. We compute a low likelihood of 14 per cent based on proper motion, age and RV. No parallax was calculated, since GH Car is an overtone pulsator. However, the Cepheid's distance listed in the Fernie data base (2.2 kpc) is significantly larger than Trumpler 18's (1.4 kpc). Furthermore, the Cepheid is reddened by 0.1 mag more

than the cluster, which is consistent with a greater distance to the Cepheid. The average cluster RV is based on the measurements of a single star, and does not agree with that of the Cepheid. In short, membership of GH Car in Trumpler 18 is unlikely.

However, our analysis identifies Hogg 12 as an alternative host cluster for GH Car. Based on proper motion and age, we compute a likelihood of 50 per cent for this Combo. Proper motion is a very good match, and clearly detected. Finally, reddening for the cluster and the Cepheid are nearly identical, and the Cepheid's literature distance from the Fernie data base matches the cluster's distance very well. Follow-up is required to confirm this option.

A1.2.2 SZ Tau and NGC 1647. The membership of SZ Tau in the halo of NGC 1647 was first considered by Efremov (1964) and later studied in more detail by Turner (1992) who concluded that SZ Tau is a 'coronal' member, based on star counts, reddening, RV, proper motion from Francic (1989) and assuming overtone pulsation for SZ Tau.

From parallax (Storm et al. 2011), RV, proper motion and age, we compute a likelihood of membership of 5 per cent, the main discrepant constraints being RV and proper motion from Tycho2 and *Hipparcos* (Dias, Lépine & Alessi 2001; van Leeuwen 2007). The vanishing prior could, of course, be consistent with coronal membership. However, cluster membership based on proper motion was excluded by Geffert et al. (1996) using 2220 stars measured on photographic plates, and by Baumgardt et al. (2000) using *Hipparcos* proper motions. We therefore consider SZ Tau an unlikely member of NGC 1647, although an ejection cannot be excluded (Turner, private communication).

A1.3 Non-member Combos discussed in the literature

A1.3.1 V442 Car and NGC 3496. V442 Car was previously considered for membership in NGC3496 by Balona & Laney (1995) who concluded it to be a background star, based on age and reddening. From proper motion and separation, we come to the same conclusion. Furthermore, a rough distance estimate for a 14th magnitude 5.5 d Cepheid excludes membership in a cluster located approximately 1 kpc from the Sun.

A1.3.2 UY Per and Czernik 8 or King 4. Turner (1977) suggested that UY Per could be a member of Czernik 8 or King 4. Turner et al. (2010) again mention the latter combination. Our results, however, are inconsistent with membership in either cluster, based on the constraints parallax, proper motion and age.

The 'likelier' of the two Combos is King 4, for which parallax and age are in relatively good agreement; the Cepheid is slightly farther away and has larger reddening. Kinematically, however, the cluster's vanishing proper motion is inconsistent with membership of the rather fast moving Cepheid ($\mu^*_\alpha = -6.15 \pm 2.8$ mas yr^{-1}, $\mu_\delta = 12.89 \pm 2.9$ mas yr^{-1}, PPMXL).

A1.3.3 R Cru, T Cru and NGC 4349. The two Cepheids R Cru and T Cru have previously been considered as members of the open cluster NGC 4349 (Turner & Burke 2002), although they are no longer listed in Turner (2010). Our results are very clearly inconsistent with either Cepheid's membership in this cluster. However, both Cepheids have very similar parallaxes and proper motions, and lie close to the open cluster Loden 624. Little information is available for this cluster and observational follow-up is warranted.

A1.3.4 TV CMa and NGC 2345. The membership constraints parallax, proper motion (vanishes) and age agree within their respective uncertainties. The Cepheid's separation of 40 arcmin from cluster centre results in a very low prior. RV differs by $\sim$20 km s^{-1} between cluster and Cepheid, resulting in a low likelihood. RV is the prime excluding constraint for this combo, and appears to be robust.

A2 New Combos

In the following subsections, we discuss possible membership for selected Combos listed in Table 2. Observational follow-up is warranted for all the inconclusive Combos in the table, even if they are not discussed here in detail. Further information can be found in the data compiled that are available online, cf. Table A1. We furthermore remark that the ASAS targets in Table 2 are particularly worthy of follow-up, since they have not yet received much attention.

A2.1 Inconclusive Combos

A2.1.1 Y Car and ASCC 60. Y Car is a double-mode Cepheid in a triple system with a B9.0V companion (Evans 1992) on a known orbit (see the Szabados 2003 binary Cepheids data base[16]). The Cepheid lies well-inside ASCC 60's projected core. Since the RV of the cluster in K05 was measured on a single star and is identical to Y Car's v_γ, we cannot consider this a valid membership constraint. Proper motion, on the other hand, is clearly measurable and consistent with membership. Reddening is slightly larger (by 0.07 mag) for the Cepheid than for the cluster, and the absolute magnitude of Y Car estimated by Evans (1992) indicates a distance modulus incompatible with that of the cluster, though we note that due to the sparsity of this cluster, a revised distance estimate would be useful. A detailed photometric and RV study of ASCC60 is required to conclude on the possible membership of Y Car. We furthermore note the presence of another Cepheid, CR Car inside ASCC 60's core radius. This Combo, however, is clearly inconsistent with membership. CR Car lies in the background of the cluster.

A2.1.2 VZ CMa and Ruprecht 18. This combination yields a likelihood of 59 per cent, since metallicity and age are in excellent agreement between the cluster and the Cepheid. Proper motion is better discernible for the Cepheid than for the cluster, it seems, and colour excess is 0.14 mag less strong for the Cepheid than for the cluster. According to D02, the cluster (1.1 kpc) lies bit closer than the Cepheid (1.3 kpc, from the Fernie data base). In summary, both Cepheid and cluster require detailed follow-up for reddening and parallax, before we can conclude on the question of membership.

A2.1.3 WZ Car and ASCC 63. Likelihood and prior both tend to clearly exclude WZ Car's membership in ASCC 63; the large projected distance from ASCC 63's core (33 pc assuming membership) lends further support to this interpretation. However, the likelihood computed is completely dominated by the extreme mismatch in line-of-sight velocities ($\delta v_{\rm rad} = 120$ km s^{-1}). Looking at the other constraints, however, we find that age, reddening, parallax (Cepheid parallax from Storm et al. 2011) and proper motion strongly suggest membership. Suspiciously, the cluster RV is based on only two stars, and may therefore not be reliable, or point towards an ejection

[16] http://www.konkoly.hu/CEP/intro.html

Table A1. An excerpt of the data provided in the machine-readable online table. For each Combo we provide the parameters separation (R), prior, likelihood and combined membership probability, as well as the differences between the individual membership constraints used (defined as cluster value minus Cepheid value), the combined error budgets adopted and relevant references. For RefR, the cluster radius reference is provided. In column Refs_{ϖ}, references are listed in the following order: ϖ_{Cl}, ϖ_{Cep}, $E(B\text{-}V)_{\mathrm{Cl}}$, $E(B\text{-}V)_{\mathrm{Cep}}$, Cepheid $\langle m_{\mathrm{V}} \rangle$ and Cepheid period (the latter two are relevant if a PLR-based distance was used). For the remaining columns, two references are given; the first corresponds to the cluster, the second to the Cepheid. Due to spatial constraints, we abbreviate references in the following way: 'a' – values based on ASAS photometry, 'b' – values based on Berdnikov photometry, 'd' – Dias et al. (2002a) catalogue, 'f' – Fernie data base, 'fo' – Fouqué et al. (2007), 'g' – GCVS, 'h' – (van Leeuwen 2007), 'k' – Kovtyukh et al. (2008), 'ks' – Klagyivik & Szabados (2009), 'l' – Luck & Lambert (2011), 'p' – parallaxes computed from PLR-based distances, 'P' – PPMXL (Roeser et al. 2010), 's' – Storm et al. (2011), 't' – Dias et al. (2001), Dias, Lépine & Alessi (2002b), 'v' – VSX, '*' – newly determined v_γ used, '**' – period improved using RV data, 'B11' – Bukowiecki et al. (2011), 'FO' – first overtone ages from Bono et al. (2005), 'FU' – fundamental-mode ages from Bono et al. (2005), 'K05' – Kharchenko et al. (2005a,b), 'K07' – Kharchenko et al. (2007), 'K12' – Kharchenko et al. (2012), 'MMB, MMU, BDW, KHA' – see the references list in Dias et al. (2002a). The complete list of 3974 combinations can be retrieved from the online appendix to the paper.

Cluster	Cepheid	R	P(A)	$P(B\|A)$	$P(A\|B)$	$\Delta\varpi$	Δv_r	$\Delta\mu^*_\alpha$	$\Delta\mu_\delta$	Δ[Fe/H]	$\Delta \log a$
						σ_{ϖ}	σ_{v_r}	$\sigma_{\mu^*_\alpha}$	σ_{μ_δ}	$\sigma_{[\mathrm{Fe/H}]}$	$\sigma_{\log a}$
		RefR				Refs_{ϖ}	Refs_{v_r}	$\mathrm{Refs}_{\mu^*_\alpha}$	$\mathrm{Refs}_{\mu_\delta}$	$\mathrm{Refs}_{[\mathrm{Fe/H}]}$	$\mathrm{Refs}_{\log a}$
IC 4725	U Sgr	1.570	1.000 00	0.983 73	0.983 73	−0.114	−0.090	−0.850	0.780	0.040	0.210
						0.328	3.606	2.983	2.891	0.162	0.250
		K05				d, s, d, k, ks, V	MMB, *	t, h	d, ks		d, FU
NGC 7790	CF Cas	1.054	0.954 54	0.975 32	0.930 98	0.056	0.399	−0.430	−0.090		−0.100
						0.070	3.606	3.179	2.410		0.263
		B11				d, p, d, k, ks, G	MMU, *	BDW, h			d, FU
NGC 129	DL Cas	0.421	1.000 00	0.857 00	0.857 00	0.063	−0.880	1.360	2.810		0.181
						0.127	3.606	3.020	2.921		0.255
		K12				d, p, d, k, ks, G	MMU, *	t, h			d, FU
Turner 9	SU Cyg	0.067	1.000 00	0.807 43	0.807 43	0.074	5.791	0.370	0.260		0.282
						0.250	6.888	1.916	2.108		0.234
		K05				d, s, d, k, ks, G	K07, *	K05, h			d, FU
NGC 1647	SZ Tau	127.84	0.000 00	0.046 91	0.000 00	0.060	−6.499	0.200	3.910		0.272
						0.376	3.606	1.630	1.527		0.231
		K05				d, s, d, k, ks, G	MMU, *	t, h			d, FO
NGC 2345	TV CMa	38.208	0.000 69	0.000 01	0.000 00	0.043	20.190	−0.720	1.290		−0.009
						0.092	3.606	1.836	2.208		0.256
		B11				d, p, d, f, f, A	MMU, f	KHA, h			d, FU
NGC 4349	R Cru	14.985	0.047 71	0.000 00	0.000 00	−0.717	1.308	4.790	2.510	−0.250	0.518
						0.106	3.606	2.280	2.229	0.117	0.228
		K05				d, p, d, f, ks, b	MMU, *	BDW, h	d, l		d, FU
ASCC 61	SX Car	41.253	0.000 56	0.919 17	0.000 51	0.042		2.060	0.950		0.110
						0.122		2.985	2.480		0.250
		K05				d, p, d, f, ks, A		K05, h			d, FU
ASCC 69	S Mus	39.173	0.004 46	0.879 29	0.003 92	−0.166	3.723	0.270	−0.040		0.260
						0.215	12.266	1.414	1.807		0.253
		K05				d, s, d, fo, ks, **	K05, *	K05, h			d, FU
NGC 129	V379 Cas	42.900	0.000 00	0.895 94	0.000 00		0.440	2.960	1.320		0.053
							3.606	3.194	3.194		0.251
		K12					MMU, f	t, P			d, FO
ASCC 60	Y Car	1.228	1.000 00	0.786 42	0.786 42		−2.100	−1.520	−0.850		
							7.985	2.033	1.291		
		K05					K07, *	K05, h			

More data online

event. We therefore judge this Combo inconclusive and stress the need for follow-up of the cluster.

A2.2 Unlikely Combos

A2.2.1 Y Sgr and IC 4725 (M25). The parallaxes employed [Cepheid $\varpi_{\mathrm{Cep}} = 2.13 \pm 0.29$ from Benedict et al. (2007) and Cluster $\varpi_{\mathrm{Cl}} = 1.61 \pm 0.32$] in the calculation nearly agree within their respective error budgets. However, colour excess is 0.3 mag lower for the Cepheid, which indicates that Y Sgr lies in the foreground of M 25.

Using the well-established cluster member U Sgr as a point of reference, we remark that proper motion, age and metallicity are in excellent agreement between both Cepheids. v_γ differs slightly between the two, which could be explained by the known binarity of U Sgr and Y Sgr. The only significant discrepancy is in distance, which might be explained by uncertainties in extinction, since M 25 lies in the Orion arm (XHIP). However, we calculate a very low prior for this Combo, and if Y Sgr were a cluster member, it would lie at a large distance of 27 pc from cluster centre. From these considerations, it appears that Y Sgr is an unlikely cluster member candidate.

A2.2.2 BD+47 4225 (GSC 03642−02459) and Aveni-Hunter 1. The star was classified as a Cepheid by Bakos et al. (2002) with a light curve that suggests fundamental-mode pulsation. It lies barely outside r_{c} of cluster Aveni-Hunter 1. Unfortunately, proper motion

Table A2. New Combos inconsistent with membership, despite high priors. Columns are described in Table 1.

Cluster	Cepheid	Constraints						R_{cl} [pc]	$P(A)$	$P(B\|A)$	$P(A\|B)$
		ϖ	v_r	μ^*_α	μ_δ	[Fe/H]	age				
Alessi 5	EY Car	○	●	●	●	○	○	0.6	1.0	0.725	0.725
Koposov 12	CO Aur	○	○	2.0σ	1.9σ	○	○	3.5	1.0	0.023	0.023
Turner 1	S Vul	2.8σ	○	●	1.6σ	○	1.3σ	0.2	1.0*	0.015	0.015
NGC 5045	NSV 19655	○	○	2.2σ	2.2σ	○	○	1.8	1.0	0.008	0.008
Ruprecht 18	AO CMa	3.8σ	○	●	1.4σ	●	●	0.5	1.0	0.005	0.005
Collinder 173	AH Vel	○	○	○	○	1.1σ	2.3σ	11.8	1.0*	0.036	0.036
BH 34	ASAS J083130−4429.3	3.9σ	○	1.6σ	●	○	2.7σ	0.8	1.0*	0.0	0.0
ASCC 60	CR Car	4.4σ	5.0σ	1.3σ	●	○	3.2σ	0.7	1.0	0.0	0.0
Collinder 173	ASAS J080101−4543.6	○	○	○	○	○	3.1σ	5.3	1.0*	0.0	0.0
Collinder 65	V1256 Tau	4.7σ	○	●	1.3σ	○	4.7σ	3.4	1.0	0.0	0.0
Melotte 25	NSVS 9444700	○	○	○	○	○	7.7σ	1.2	1.0*	0.0	0.0
Stock 2	GL Cas	4.7σ	○	5.3σ	7.6σ	●	1.4σ	2.9	1.0	0.0	0.0
Turner 11	X Cyg	3.4σ	○	○	○	○	5.2σ	0.0	1.0*	0.0	0.0
Turner 7	V Cen	5.0σ	○	○	○	○	15.5σ	0.0	1.0*	0.0	0.0
King 7	V933 Per	○	○	●	2.0σ	○	5.1σ	3.4	1.0	0.0	0.0
NGC 6639	X Sct	2.9σ	1.5σ	●	1.7σ	○	5.0σ	1.2	0.853	0.0	0.0
Teutsch 14a	ASAS J180342−2211.0	1.8σ	○	○	○	○	3.1σ	2.2	0.814*	0.001	0.001
NGC 6873	ASAS J200829+2105.5	4.5σ	○	○	○	○	○	3.8	0.776*	0.0	0.0
SAI 94	SX Vel	3.8σ	○	○	○	○	8.0σ	4.2	0.761*	0.0	0.0
Collinder 240	FR Car	2.8σ	○	2.2σ	●	○	1.5σ	11.6	0.733*	0.005	0.004
NGC 6847	EZ Cyg	2.4σ	○	1.2σ	●	○	5.4σ	8.7	0.732*	0.0	0.0
BH 23	AT Pup	3.5σ	2.6σ	1.2σ	●	○	2.9σ	5.8	0.616*	0.0	0.0
Alessi-Teutsch 7	ASAS J082710−3825.9	3.9σ	○	2.6σ	●	○	●	17.8	0.59*	0.0	0.0
BH 164	AV Cir	1.3σ	1.3σ	2.6σ	5.0σ	○	●	9.1	0.572*	0.0	0.0
Czernik 43	PW Cas	2.8σ	○	●	●	○	1.1σ	2.4	0.565	0.044	0.025

and age are the only available membership constraints available in the literature compiled. Cluster and Cepheid appear to be comoving in proper motion. Furthermore, the pulsational age of the Cepheid is spot-on with the cluster. However, a very rough distance estimate using the *V*-band magnitude (10.47) found in the Guide Star Catalog V. 2.3.2 (Lasker et al. 2008) yields a distance of 2.5 kpc for the Cepheid, which is five times the cluster distance. Since both objects are thus far not very well studied, we highlight the need for follow-up of both cluster and Cepheid.

A2.3 Non-members of interest

Non-member Combos of interest are listed in Table A2. We here present Combos with $P(A) = 1$, as well as others with high priors and information on parallax. Some of the Cepheids listed here belong to other open clusters, e.g. V Cen or X Cyg or OB associations, e.g. S Vul (T10). Below, we discuss one of these cases, EY Car, since the membership probability computed is high.

A2.3.1 EY Car and Alessi 5. The beat Cepheid EY Car lies within the core radius of Alessi 5. The available (kinematic only) membership constraints are consistent with, but not very close to, each other. However, the literature distance from the Fernie data base places the Cepheid nearly 2 kpc farther than the cluster, and the larger magnitude of proper motion is consistent with a foreground cluster. EY Car is thus not a cluster member, mentioned here only due to the high membership probability computed.

SUPPORTING INFORMATION

Additional Supporting Information may be found in the online version of this article:

Table A1. For each Combo we provide the parameters separation (R), prior, likelihood, and combined membership probability, as well as the differences between the individual membership constraints used (defined as cluster value minus Cepheid value), the combined error budgets adopted and relevant references (http://mnras.oxfordjournals.org/ lookup/suppl/doi:10.1093/mnras/stt1160/-/DC1).

Please note: Oxford University Press are not responsible for the content or functionality of any supporting materials supplied by the authors. Any queries (other than missing material) should be directed to the corresponding author for the paper.

This paper has been typeset from a TEX/LATEX file prepared by the author.

Chapter 4

Towards a Cepheid paradigm including rotation

> Though the world does not change
> with a change of paradigm,
> the scientist afterward
> works in a different world.
>
> THOMAS S. KUHN, 1962
> *The Structure of Scientific Revolutions*

All stars rotate, at least a little. Although rotation has profound effects on the evolution of stars (see the review by Maeder & Meynet 2000), its impact on Cepheids has not yet been discussed in detail. However, in light of the importance of Cepheids as standard candles (rotation may influence the period-luminosity relation, see Maeder & Meynet 2001) and the mass discrepancy problem (cf. Sec. 1.3.4), it was high time to explore the effect of rotation on Cepheids. Fortunately, the recently published Geneva model grids (Ekström et al. 2012; Georgy et al. 2013b,a) provide a unique opportunity for such an investigation.

The long-term goal of the work described in this chapter is to establish rotation as a fixed element of the Cepheid paradigm and to quantify its impact on the PLR. To this end, I have thus far focused mainly on the predictions made by the Geneva models, which were recently submitted for peer review with *A&A*. A brief motivation for this work is provided in Sec. 4.2, and the submitted article is included in Sec. 4.3.

In order to test the accuracy of the predictions, a comparison with observed features is indispensable. Such a detailed comparison is currently being carried out and prepared for publication. Some preliminary results obtained from this comparison are presented in Sec. 4.4.

In order to separate the effect of rotation from metallicity effects, I have first focused on Solar metallicity models. However, a detailed investigation of rotating models at lower metallicities is currently in progress, since the Cepheids in the Magellanic Clouds are of particular importance for the distance scale. To show a first result from this extension to lower metallicities, I present a comparison of the mass-luminosity relationships of Cepheids at Solar and SMC metallicity in Sec. 4.5.

4.1 Geneva stellar evolution models

The recent Geneva evolutionary models by (Ekström et al. 2012; Georgy et al. 2013b,a) are ideally suited for the task of investigating the effect of rotation on Cepheid populations, since they cover the entire mass-range of Cepheid progenitors and consistently treat rotation throughout the evolution of the star, from the ZAMS to the end of core carbon burning. The most extensive grid presented (Ekström et al. 2012) consists of evolutionary tracks computed for a wide range in mass ($[0.8, 120]\,M_\odot$), computed for Solar metallicity ($Z = 0.014$), which was expanded by Georgy et al. (2013a) to low $Z = 0.002$. In these models, the initial rotation velocity is quantified in terms of $v_{\rm ini}/v_{\rm crit}$, where

$$v_{\rm crit} = \sqrt{\frac{2}{3}\frac{GM}{R_{\rm pb}}}\,, \tag{4.1}$$

G is the gravitational constant, M is stellar mass, $R_{\rm pb}$ is the polar radius at the critical limit, i.e., where the outward forces due to radiation pressure and rotation are stronger than gravity. A lower-mass model grid with less-than Solar metallicity was recently computed by Mowlavi et al. (2012) to enable dating of older stellar populations such as globular clusters. Furthermore, there are low-to-intermediate mass rotating models (Lagarde et al. 2012) available in Geneva for stars up to $6\,M_\odot$ covering a high range of metallicities. The model grid most suitable for the investigation of the effect of rotation on Cepheids was presented by Georgy et al. (2013b, "dense grid"). This dense grid was previously studied in terms of the impact of rotation on the formation of Be-stars by Granada et al. (2013). With 9 different initial rotation rates computed, the dense grid allows the detailed investigation of rotational effects on the evolution of intermediate-mass stars, and thus on Cepheids. Note that in this dense grid, initial rotation rates are quantified as $\omega_{\rm ini} = \Omega/\Omega_{\rm crit}$, with

$$\Omega_{\rm crit} = \sqrt{\frac{GM}{R_{e,\rm crit}}} \tag{4.2}$$

with $R_{e,\rm crit}$ denoting the equatorial radius when the star rotates at critical angular velocity $\Omega_{\rm crit}$, cf. Sec. 2.1 in Georgy et al. (2013b).

The models used in this work are static, one-dimensional models. Accordingly, they make no immediate predictions of pulsation periods or instability to pulsation. However, they can be used as a basis for investigating both (see Saio et al. 2013). Furthermore, the models predict the evolution of single stars, i.e., binary interactions are not accounted for, although they may well be significant for the post-MS evolution[1]. Finally, the models make only limited predictions on surface parameters and no radiation transport is computed to predict the emergent flux[2].

4.2 Predictions for rotating Cepheids and their implications

The evolutionary models consist of many stellar structures computed at many time steps for a range of stellar masses, initial rotation rates, and metallicities. Different interfaces with the models were created from these structures. Three interfaces with the models are thus easily accessible: i) evolutionary tracks tracing the evolution of a star with given mass, initial rotation rate, and metallicity as a function of time; ii) isochrones of co-eval populations predicting many parameters of stars of all masses for a given age, initial rotation rate, and metallicity; iii) synthetic populations that combine isochrones with the initial mass function (IMF), and are therefore more similar to observed populations than isochrones. Synthetic populations furthermore have the advantage

[1] see the note related to orbital periods in Sec. 3.1.2

[2] However, Geneva models have been used in conjunction with a radiative transfer code (Groh 2011) to investigate the emergent spectrum of supernova progenitors (Groh et al. 2013), resulting in the unexpected result that luminous blue variables (LBVs) may be progenitors of type IIb supernovae.

that a distribution of initial rotation rates can be assumed, rather than using a fixed value as in the case of isochrones.

The most important interface for the current study thus far have been the evolutionary tracks, providing predictions of stellar parameters as a function of time. Cepheid predictions can thus be obtained by defining the times when a star is considered to be a Cepheid. According to pulsation theory, there is a well-defined region in the HRD in which stars are pulsationally unstable, the (classical) instability strip (IS). By assuming a given definition of the IS, it is thus possible to investigate the model predictions for Cepheids by studying the portions of the evolutionary tracks that lie inside the IS boundaries.

Different IS definitions will, of course, yield different predictions for Cepheids, and several different definitions of IS boundaries can be found in the literature. Two different commonly-used sets of IS boundaries were considered in order to investigate how sensitive the predictions are to the adopted IS boundaries. The boundaries adopted are those published by Bono et al. (2000) and Tammann et al. (2003). The Bono IS boundaries were derived from a theoretical pulsational instability analysis based on non-rotating evolutionary models by Castellani et al. (1992), and the Tammann IS boundaries are based on an empirically-determined ridge-line using a fixed width. The times when an evolutionary track crosses the IS define the crossing times during which the model represents a Cepheid. This assumes the IS to be pure, i.e., all stars located inside it are pulsating. Other IS boundary definitions exist, see e.g. Turner (2001). The ones adopted here, however, have the advantage of clearly defining the IS boundaries for Solar metallicity, as well as the metallicities of the Magellanic clouds. It should be noted that the abundances adopted for Solar, LMC, and SMC mixtures differ between the Geneva models and the study by Bono et al. (2000), see Tab. 4.1. Note that metallicity Z is assumed lower in the Geneva models than in the study by Bono et al. A collaboration to determine IS boundaries consistently for the Geneva models has been started recently.

The details and results of this investigation of Solar-metallicity Cepheid predictions based on rotating Geneva models can be found in the publication included below (Anderson et al. 2013b, *submitted to A&A*). A quantitative comparison of the predictions with observed features is currently in preparation, see Sec. 4.4 below. An overview of the consolidated, most important findings of this work is presented in Sec. 4.6.

		Geneva	Bono et al.
Solar	$X_\odot$	0.720	0.700
	$Y_\odot$	0.266	0.280
	$Z_\odot$	0.014	0.020
LMC	X	0.738	0.742
	Y	0.256	0.250
	Z	0.006	0.008
SMC	X	0.747	0.746
	Y	0.251	0.250
	Z	0.002	0.004

Table 4.1: Comparison of Solar, LMC, and SMC abundances adopted for the Geneva models and by Bono et al. (2000). Hydrogen (X) and helium abundance (Y), as well as for metallicity (Z) mass fractions are listed.

Astronomy & Astrophysics manuscript no. RotatingCepheids
March 4, 2014

On the Effect of Rotation on Populations of Classical Cepheids I. Predictions at Solar Metallicity

Richard I. Anderson[1], Sylvia Ekström[1], Cyril Georgy[2], Georges Meynet[1], Nami Mowlavi[1], and Laurent Eyer[1]

[1]Observatoire de Genève, Université de Genève, 51 Chemin des Maillettes, CH-1290 Sauverny, Switzerland
[2]Astrophysics group, Lennard-Jones Laboratories, EPSAM, Keele University, Staffordshire, ST5 5BG, UK
e-mail: richard.anderson@unige.ch

Received 5 November 2013; accepted 6 February 2014

ABSTRACT

Context. Classical Cepheids are among the most important variable star types due to their nature as standard candles and have a long history of modeling in terms of stellar evolution. The effects of rotation on Cepheids have not yet been discussed in detail in the literature, although some qualitative trends have already been mentioned.
Aims. We aim to improve the understanding of Cepheids from an evolutionary perspective and establish the role of rotation in the Cepheid paradigm. In particular, we are interested in the contribution of rotation to the problem of Cepheid masses, and explore *testable* predictions of quantities that can be confronted with observations.
Methods. Recently developed evolutionary models including a homogeneous and self-consistent treatment of axial rotation are studied in detail during the crossings of the classical instability strip (IS). The dependence of a suite of parameters on initial rotation is studied. These parameters include mass, luminosity, temperature, lifetimes, equatorial velocity, surface abundances, and rates of period change.
Results. Several key results are obtained: i) mass-luminosity (M-L) relations depend on rotation, particularly during the blue loop phase; ii) luminosity increases between crossings of the IS. Hence, Cepheid M-L relations at fixed initial rotation rate depend on crossing number (the faster the rotation, the larger the luminosity difference between crossings); iii) *the Cepheid mass discrepancy problem vanishes* when rotation and crossing number are taken into account, without a need for high core overshooting values or enhanced mass loss; iv) rotation creates dispersion around average parameters predicted at fixed mass and metallicity. This is of particular importance for the period-luminosity-relation, for which rotation is a source of intrinsic dispersion; v) enhanced surface abundances do not unambiguously distinguish Cepheids occupying the Hertzsprung gap from ones on blue loops (after dredge-up), since rotational mixing can lead to significantly enhanced Main Sequence (MS) abundances; vi) rotating models predict greater Cepheid ages than non-rotating models due to longer MS lifetimes.
Conclusions. Rotation has a significant evolutionary impact on classical Cepheids and should no longer be neglected in their study.

Key words. Stars: variables: Cepheids – supergiants – Stars: evolution – Stars: rotation – Stars: abundances – distance scale

1. Introduction

Classical Cepheids are objects of interest for many areas of astrophysics. On the one hand, they are excellent standard candles allowing the determination of distances in the Milky Way and up to Virgo cluster distances. On the other hand, they are excellent objects for constraining stellar evolutionary models. Accordingly, Cepheids have played a special role among pulsating (variable) stars and have a long history of modeling efforts both in terms of their evolution and pulsations (see Bono et al. 2013, and references therein).

Following the development of pulsation models in the late 1960's (Stobie 1969a,b,c), systematic differences between pulsational and evolutionary masses of Cepheids became apparent. These differences were originally referred to as Cepheid mass anomalies (Cox 1980). Improved opacities (Iglesias & Rogers 1991; Seaton et al. 1994) could mitigate a good fraction of the disaccord in terms of masses. Nowadays, it is common to speak of *the mass discrepancy* as the systematic offset between evolutionary masses and those derived with other methods (e.g. Bono et al. 2006; Keller 2008), with a typical disagreement at the level of 10 – 20%.

Several mechanisms have been put forward to resolve the mass discrepancy problem. Among the most prominent in the recent literature are augmented convective core overshooting (Prada Moroni et al. 2012) and pulsation-enhanced mass-loss (Neilson & Lester 2008). However, the effect of rotation on evolutionary Cepheid masses has not been discussed in detail although the impact of rotation on the mass-luminosity and period-luminosity relations have already been mentioned previously in the literature (see Maeder & Meynet 2000, 2001).

The first large grid of models incorporating a homogeneous and consistent treatment of axial rotation was recently presented by Ekström et al. (2012, from hereon: paper I). Subsequently, Georgy et al. (2013, from hereon: paper II) extended the grid in terms of rotation for stars between 1.7 and 15 $M_{\odot}$. Using these state-of-the-art grids it is now possible, for the first time, to consider the effect of rotation on populations of classical Cepheids.

Cepheid progenitors are B-type stars on the Main Sequence (MS). Observationally, B-type stars are known for their fast rotation since the first homogeneous study of rotational velocities by Slettebak (1949). Thus, it is empirically known that fast rotation is common for the progenitors of Cepheids. Huang et al. (2010) have recently carried out a very detailed investigation of rotational velocities for B-stars of different masses and evolutionary states (on the MS), providing even an empirical distribution of rotation rates. Their distribution can serve as a guideline for our

A&A proofs: manuscript no. RotatingCepheids

study in the sense that the typical MS rotation rates of B-stars in the mass range appropriate for Cepheids ($\sim 5-9\,M_\odot$) is approximately $v/v_{\rm crit} = 0.3 - 0.4$, where $v_{\rm crit}$ denotes critical rotation velocity. As shown in papers I & II, such fast rotation can significantly alter the evolutionary path of stars by introducing additional mixing effects that impact MS lifetime, stellar core size, age, and MS surface abundances. Clearly, these effects will propagate into the advanced stages of evolution, such as the Cepheid stage.

The blue loop phase of intermediate-mass evolved stars during core helium burning is very sensitive to the input physics (see the "magnifying glass" metaphor in Kippenhahn & Weigert 1994, p. 305). Thus, there is a two-fold interest in studying the models presented in papers I & II in terms of their predictions for Cepheids: i) properties of Cepheids inferred using models (e.g. mass) can be updated to account for rotation; ii) certain predictions made by the models can be tested immediately using observational data (e.g. surface abundances).

This paper is the first in a series devoted to the endeavor of extending the evolutionary paradigm of Cepheids to include the effects of rotation. We here focus mainly on the detailed exploration of predictions made by the models as well as their interpretation. A detailed comparison of these predictions to observed features is in progress and will be presented in a future publication for the sake of brevity. Further projects will include the investigation of the combined effect of metallicity and rotation as well as a self-consistent determination of pulsation periods and instability strip boundaries.

The structure of this paper is as follows. In Sec. 2, we briefly state a few key aspects of the models presented in papers I & II relevant in the context of this work. Sec. 3 contains the predictions made by the rotating Cepheid models, focusing on the mass discrepancy and features that are accessible to observations. Sec. 4 discusses the reliability and implications of the predictions made, and Sec. 5 summarizes the key aspects.

2. Description and comparison of input physics

The input physics of the stellar models are explained in detail in paper I & II. We refer the reader to these publications for the detailed description of the models and summarize here only the most relevant features. The Solar composition adopted is that by Asplund et al. (2005), and the detailed abundances of all elements are listed in paper I.

Rotation is treated in the Roche model framework with the shellular hypothesis as presented in Zahn (1992) and Maeder & Zahn (1998). The shear diffusion coefficient is adopted from Maeder (1997) and the horizontal turbulence coefficient is from Zahn (1992). Both were calibrated (see paper I) so that models presenting an averaged equatorial velocity during the MS well in the observational range reproduce the mean surface enrichment of main sequence B-type stars at solar metallicity. Both were calibrated (see paper I) in order to reproduce the mean surface enrichment of main sequence B-type stars at solar metallicity.

At the border of the convective core, we apply an overshoot parameter $d_{\rm over}/H_P = 0.10$. This value was calibrated in the mass domain $1.35-9\,M_\odot$ at solar metallicity to ensure that the rotating models closely reproduce the observed width of the MS band. Overshooting at the base of the convective envelope is not explicitly included, although a particular choice of the mixing length

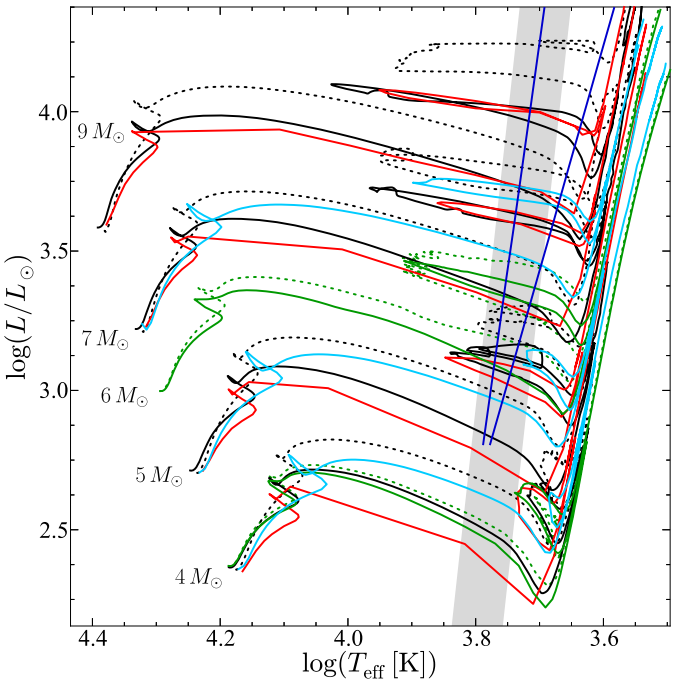

Fig. 1. Comparison of Geneva stellar evolutionary tracks (black solid lines : non-rotating; black dotted lines : $v/v_{\rm crit} = 0.4$) with Padova tracks (Bertelli et al. 2008, cyan solid lines), and tracks by Castellani et al. (1992, red solid lines) and Lagarde et al. (2012, green solid lines = non-rotating; green dotted lines = $v/v_{\rm crit} = 0.3$). The instability strips by Bono et al. (2000b, wedge-shaped dark blue solid lines) and Tammann et al. (2003, gray shaded area) are also included.

parameter[1] in the outer convective envelope may indirectly create a similar effect.

During the MS, intermediate-mass models ($M \leq 7\,M_\odot$) are evolved without mass loss, 9 to $12\,M_\odot$ models are evolved with the de Jager et al. (1988) mass-loss rates, and the more massive models with the mass-loss recipe from Vink et al. (2001). The radiative mass-loss rates used in the RSG and Cepheids phases are from Reimers (1975, 1977) with a factor $\eta = 0.5$ for $M_{\rm ini} \leq 5.0\,M_\odot$ and $\eta = 0.6$ for $M_{\rm ini} = 7.0\,M_\odot$. For $M_{\rm ini} \geq 9.0\,M_\odot$, we use the recipe from de Jager et al. (1988), and for the RSG with $T_{\rm eff} < 3.7$, we use a fit presented in Crowther (2001). No pulsation-enhanced mass-loss is included in these static models.

In the following initial rotation velocities v are stated relative to the critical velocity $v_{\rm crit}$, see paper I. Alternatively, initial rotation rates are defined as $\omega = \Omega/\Omega_{\rm crit}$, see paper II. For reference, the average initial rotation speed of most B-stars is $v/v_{\rm crit} = 0.4$ (Huang et al. 2010), which is equivalent to $\omega = 0.568$.

2.1. Geneva and other Cepheid models

The input physics and numerical implementation differ significantly between different groups developing evolutionary models. To benchmark and provide additional context for the Geneva models used here (paper I & II), we compare our evolutionary tracks with other references from the literature.

Figure 1 shows this comparison of non-rotating (black solid lines) and rotating ($v/v_{\rm crit} = 0.4$, black dotted lines) Geneva tracks with Padova tracks (Bertelli et al. 2008, cyan lines) and those used by Bono et al. (2000b) in their computation of in-

[1] Here, we employ $l/H_P = 1.6$, which reproduces the positions of both red giant branch and the red supergiant stars, see Fig. 2 in paper I.

stability strip boundaries used in the following (Castellani et al. 1992, red lines). Also shown are the non rotating (green solid lines) and rotating ($v/v_{\rm crit} = 0.3$, green dotted lines) models from Lagarde et al. (2012).

Generally speaking, all models in Fig. 1 have a lot in common and differ mainly in the details. For the non rotating models, the main sources of difference are the initial chemical composition (and thus the opacity), and the value adopted for the overshooting parameter. The difference in composition and opacity slightly shifts the tracks on the ZAMS, but in later phases, the main difference arises from the overshoot parameter. The tracks from Bertelli et al. (2008) show the high luminosity deriving from an overshoot parameter equivalent to 2.5 times the Geneva one, while the tracks from Castellani et al. (1992) do not have any overshoot during the main sequence.

The comparison of different evolutionary models in Fig. 1 clearly shows that the extent of the blue loops is sensitive to the value used for the overshoot parameter: the larger the overshooting parameter, the higher luminosity and the shorter the loop. The rotating Geneva tracks predict consistently higher luminosity than any of the other models in the figure, and should yield a lower mass limit for Cepheids than the Padova tracks by Bertelli et al. (2008), judging from a by-eye-interpolation.

3. Properties of rotating stellar evolution models in the Cepheid stage

In the following, the Cepheid stage refers simply to the portions of the evolutionary tracks that fall inside the classical instability strip (IS). A given evolutionary track can cross the IS three times, and thus may be considered as a Cepheid during three different crossing numbers. The first crossing occurs when the star evolves along the Hertzsprung gap towards the Red Giant phase during a core contraction phase. This crossing is expected to be very fast, and such Cepheids expected to be rare. Yet, some candidates have been reported in the literature (e.g. Turner 2009). The majority of Cepheids are expected to be on the second and third crossings. These stars are in the core helium burning phase and make up the majority of a Cepheid's lifetime and are therefore the most likely to be observed, see Sec. 3.4. We therefore focus our discussion mainly on Cepheids on second and third crossings, neglecting first crossing Cepheids for the sake of brevity when it is not essential.

Instability Strip (IS) boundaries have to be adopted in order to investigate the predictions made by the models specifically for Cepheids. Several IS boundary determinations can be found in the literature. We here adopt two such definitions, one theoretical (Bono et al. 2000b), and one observational (Tammann et al. 2003). We selected these references because they both provide analytical IS edge definitions for the range of metallicities covered by the models.

The IS boundaries by Bono et al. (2000b) are based on limiting amplitude, non-linear, convective pulsation models that use evolutionary models by Castellani et al. (1992) to predict luminosities for a given mass. We note that there are relevant differences between the models presented here and those underlying the pulsation analysis by Bono et al. (2000b), notably in the solar chemical composition, core overshooting, and, of course, the fact that our models include rotation. It must therefore be kept in mind that the present analysis uses IS boundaries that are not necessarily consistent with the present models. A self-consistent determination of IS boundaries and pulsation periods is foreseen for the near future. Obviously, the choice of IS boundaries affects the range of values predicted in the Cepheid stage such as

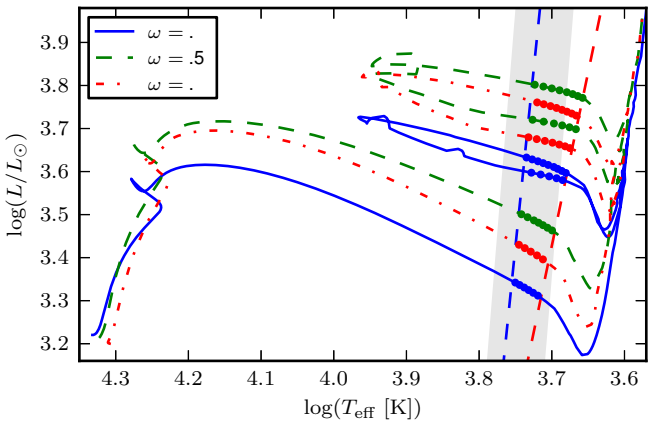

Fig. 2. Evolutionary tracks for 7 $M_\odot$ solar-metallicity models with different initial rotation rates: $\omega = 0.0, 0.5, 0.8$ are drawn as blue solid, green dashed and red dash-dotted lines, respectively. The red and blue edge of the instability strip (IS) according to Bono et al. (2000b) is indicated by dashed lines. Grid points inside the IS are marked as solid circles. The Tammann et al. (2003) IS is shown as a shaded gray area.

Cepheid lifetimes, or equatorial velocities. However, other parameters such as luminosity should not be very sensitive to it.

The typical rotation velocity of Cepheid progenitors is approximately $v/v_{\rm crit} = 0.3 - 0.4$ (Huang et al. 2010), which corresponds to a typical $\omega = 0.5$. We therefore occasionally refer to $\omega = 0.5$ as the 'average' rotation rate. The initial hydrogen abundance, $Z_{\rm ini}$, is solar ($Z_\odot = 0.014$) throughout this paper; a discussion of the combined effect of rotation and metallicity will be presented in a future publication.

3.1. Rotating Cepheids in the Hertzsprung-Russell Diagram

Figure 2 shows evolutionary tracks for 7 $M_\odot$ Solar metallicity models at three rotation rates $\omega = 0.0, 0.5, 0.8$.

As mentioned in paper II, rotation has two major effects on the evolutionary tracks.

Firstly, rotational mixing increases stellar core size and extends MS lifetimes, mixing hydrogen from outer layers into the core. It can be shown (Maeder 2009, p. 41, derived for the conditions close to the center) that luminosity depends on mass, mean molecular weight, μ, and opacity, κ. Due to the additional mixing, a star in rotation can continue burning hydrogen for longer and convert more hydrogen into helium, resulting in higher μ, which increases $L \propto \mu^4$. This furthermore reduces the (dominant) electron scattering opacity, since $\kappa = 0.2 \cdot (1 + X)$ is lowered when the hydrogen mass fraction X is reduced, and results in increased luminosity, since $L \propto 1/\kappa$.

Secondly, rotation causes the centrifugal force to modify hydrostatic equilibrium, leading to lower effective core mass, i.e., the star evolves as if it had lower mass, resulting in a decrease of luminosity. Hence, the ZAMS luminosity of a rotating model corresponds to a ZAMS luminosity of a non-rotating model of lower effective mass. Conversely, a non-rotating model requires higher mass to reach the same luminosity as a rotating model. Figure 2 serves to illustrate this: whereas little difference in ZAMS luminosity is seen between the non-rotating (blue solid line) and $\omega = 0.5$ models (green dashed line), the ZAMS luminosity of the $\omega = 0.8$ models (red dash-dotted) is significantly lower.

While the above is correct for a model at the ZAMS, the situation is very different at later evolutionary stages, e.g. when a star

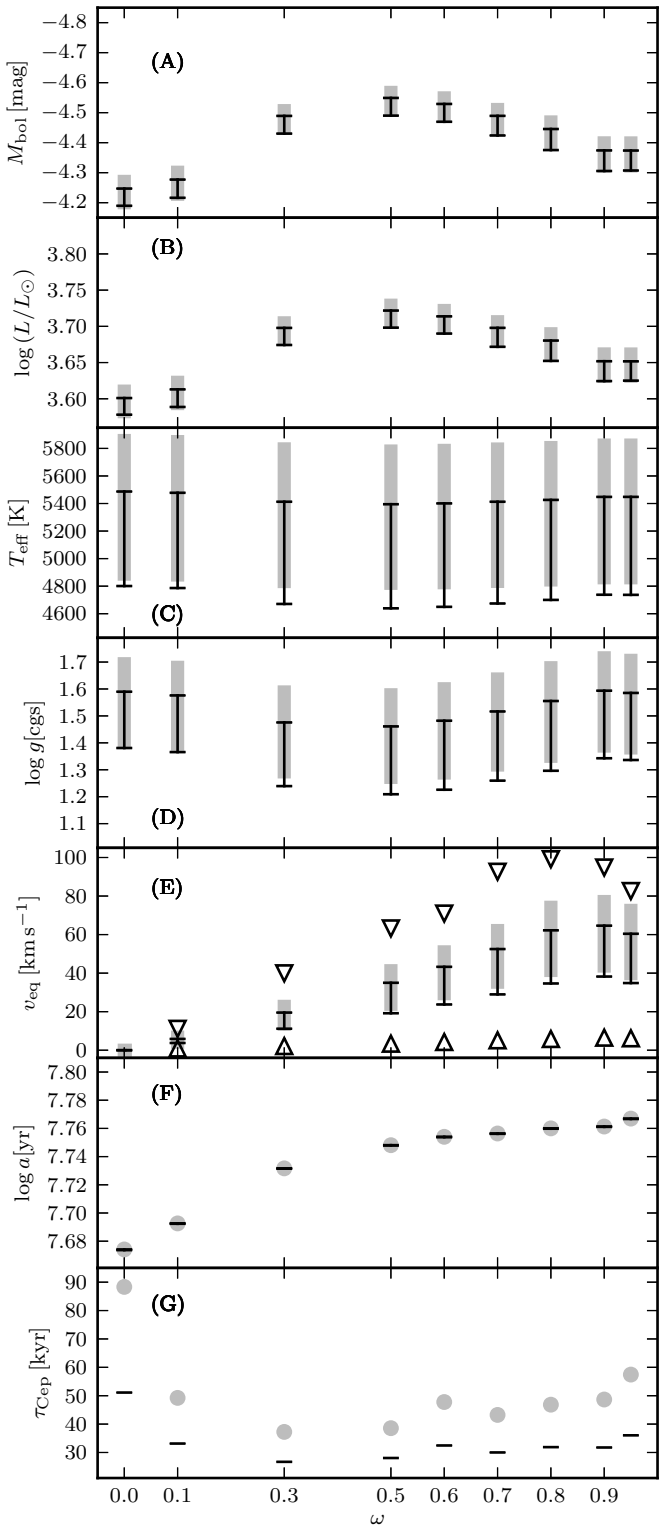

Fig. 3. Predictions for 7 $M_\odot$ Cepheids on the *second crossing* as function of ω. Panels A through G show bolometric magnitude, luminosity, effective Temperature, surface gravity, equatorial velocity, age, and lifetime. The range of values during the IS crossing is shown as black lines for the IS definition by Bono et al. (2000b), and as a light gray shade for the IS from Tammann et al. (2003). On the second crossing, all parameters increase during the evolution along the blue loop, except for $\tau_{\rm Cep}$ which shows the duration of the IS crossing. Triangles in panel E show the extreme values for surface velocity at the beginning of the blue loop near the Hayashi track (minimal) and at its greatest extension (maximal).

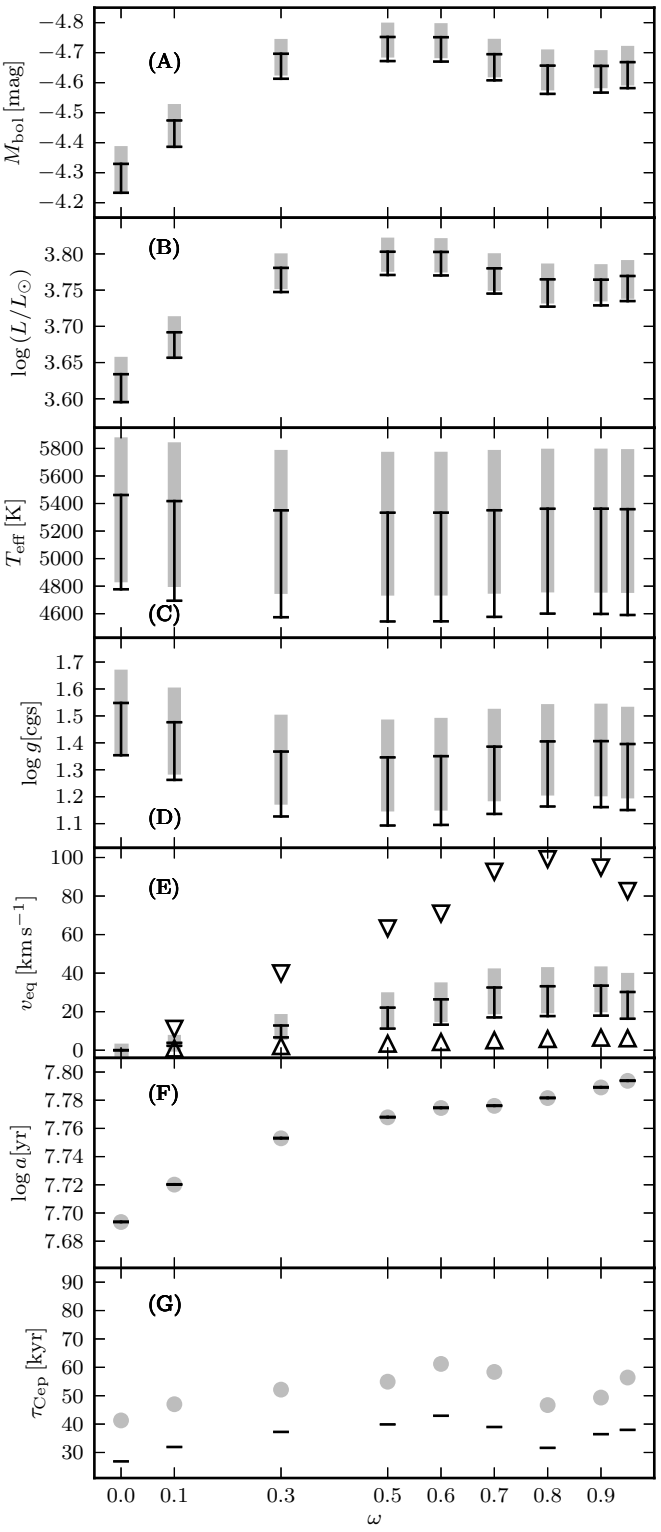

Fig. 4. Analogous to Fig. 3 for the *third crossing*. Note that the parameters in panels A through E are *decreasing* during the third IS crossing.

.

crosses the IS. Here, a rotating model has a luminosity that corresponds to a non-rotating model of higher initial mass. The increase in luminosity due to rotation is, however, not montonous, since the luminosity-increasing mixing effects are counteracted by the luminosity-decreasing centrifugal force.

lower mass limit		$v/v_{\rm crit}$	upper mass limit		$v/v_{\rm crit}$
$4.50\,M_\odot$	(4.25)	0.0	$11.50\,M_\odot$	(11.75)	0.0
$4.55\,M_\odot$	(4.50)	0.4	$10.00\,M_\odot$	(10.25)	0.4

Table 1. Mass limits for Cepheids without and with rotation. Lower limits (left) were explored using the web-based track interpolation tool. To investigate the upper limits, new evolutionary tracks were computed. The values in parentheses correspond to the next mass explored that no longer exhibits a blue loop.

The B panels in Figs. 3 and 4 show this balancing effect for the $7\,M_\odot$ models for the full range of initial rotation rates available from paper II. Luminosity reaches a maximum for $\omega \approx 0.5$ and decreases towards both extremes, with a relatively flat plateau for $0.3 < \omega < 0.7$. On the high ω end, the decrease in luminosity is greater during the second crossing than during the third, i.e. the blue loop becomes wider with greater rotation. Hence, the faster ω, the greater the difference in L between second and third crossing.

3.2. Cepheid masses

Let us now consider the effect of rotation on the mass predictions for Cepheids. We first inspect the upper and lower mass limits of (second and third crossing) Cepheids predicted by the models and then investigate the impact of rotation on the mass discrepancy problem.

3.2.1. Which progenitor masses become Cepheids?

As mentioned above, we assume that any model performing a blue loop becomes a Cepheid when it crosses the IS. Within this simplification, our models allow an investigation of the range of initial masses that evolve to become Cepheids, i.e., that develop blue loops crossing the IS, as a function of rotation. At the low mass end, this inspection can be done via interpolation, since the extent of the blue loops increases gradually with mass. At the upper mass end, however, the blue loop suddenly disappears, rendering interpolation inapplicable to this end. Depending on the desired resolution in mass, this endeavor becomes computationally expensive quickly. We therefore computed several new models to iteratively search for the point at which the blue loop disappears[2].

Table 1 presents the results of this search. Lower mass limits are shown on the left, upper mass limits on the right. The next model investigated is indicated in parenthesis.

On the low-mass end, we find that both rotating and non-rotating models yield a minimal Cepheid mass $\sim 4.5\,M_\odot$, independent of ω. Judging from Fig. 1, this is comparable to or lower than the mass limits predicted by other models.

Rotation does, however, significantly affect the upper mass limit, and yields $M \lesssim 11.5\,M_\odot$ for non-rotating, and $M \lesssim 10.0\,M_\odot$ for rotating models with $v/v_{\rm crit} = 0.4$. It is worth noting that the luminosity during the loop is $\log L/L_\odot \approx 4.3$ for either case. Hence, the upper mass limit for Cepheids to exhibit blue loops appears to be imposed by an upper limit on luminosity. Since rotation affects luminosity, this affects the predicted Cepheid mass ranges. *This leads to the interesting prediction that the longest-period Cepheids (the most massive ones) in sufficiently large stellar populations may preferentially have slowly rotating progenitors.*

3.2.2. Evolutionary masses of rotating Cepheids

A long-standing problem in Cepheid research is related to the Cepheid mass anomalies (see Cox 1980, and references therein), which are defined as disagreements between pulsational masses and those inferred from evolutionary models (Christy 1968; Stobie 1969a,b,c). The improvement of radiative opacities in stellar envelopes (Iglesias & Rogers 1991; Seaton et al. 1994; Iglesias & Rogers 1996) removed some of these anomalies, notably for the double-mode Cepheids (Moskalik et al. 1992). For single-mode Cepheids, however, the so-called mass discrepancy remains a topic of active research and discussion (e.g. Bono et al. 2006; Keller 2008; Cassisi & Salaris 2011; Prada Moroni et al. 2012). Evolutionary masses, i.e., those inferred from evolutionary models via a mass-luminosity relationship, are found to be systematically larger than mass estimates obtained by other means.

The most common strategies explored to resolve the mass discrepancy involve an increase in the size of the convective core via enhanced overshooting (e.g. Keller 2008), a decrease in envelope mass by enhanced mass loss (Neilson et al. 2011), or both. For instance, Prada Moroni et al. (2012) have recently found that the accurately determined mass of the Cepheid component in the eclipsing binary OGLE-LMC-CEP-0227 (Pietrzyński et al. 2010) located in the Large Magellanic Cloud can be satisfactorily reproduced by evolutionary models with a given set of parameters. Their best-fit solution favors increased core size over enhanced mass-loss, but requires a significantly higher amount of core overshooting than is implemented in the models presented here.

Another possibility for increasing core size is to introduce rotation. However, the evolutionary effect of rotation on Cepheids has not yet been discussed in detail in the literature. This is unfortunate, since rotation makes testable predictions for a range of parameters that can be confronted to observation, including enhanced surface abundances and (equatorial) rotational velocities, which make this effect distinguishable from enhanced core overshooting. It is therefore clear that rotation should not be neglected as a potential contributor to the solution of the mass discrepancy.

As mentioned in Sec. 3.1, the luminosity of rotating Cepheid models is generally larger than that of non-rotating Cepheids of the same mass. Judging from the tracks in Fig. 2, for instance, the increase in luminosity at fixed mass is approximately 50% (≈ 0.17 in $\log L/L_\odot$). A non-rotating Cepheid model must therefore have higher mass than a rotating one at a fixed luminosity.

Figure 5 serves to investigate the effect of rotation on the mass-luminosity (M-L) relationship. It was created using the regular models from paper II as well as interpolated models computed using the web-based interpolation tool[3]. As mentioned above, luminosity usually increases from the second to the third crossing, and this increase tends to be larger for higher ω, i.e., the loops become wider for higher ω. Hence, it seems obvious to distinguish not only between models with different ω, but also between Cepheids on different crossings, since M-L relations of Cepheids on different crossings and with different initial rotation rates have different zero-points and slopes.

[2] Rotating models calculated here as in paper I, where rotation is parametrized as $v/v_{\rm crit}$, with $v_{\rm crit}$ denoting critical rotation. $v/v_{\rm crit} = 0.4$ is equivalent to $\omega = 0.568$.

[3] `http://obswww.unige.ch/Recherche/evoldb/index/Interpolation/`

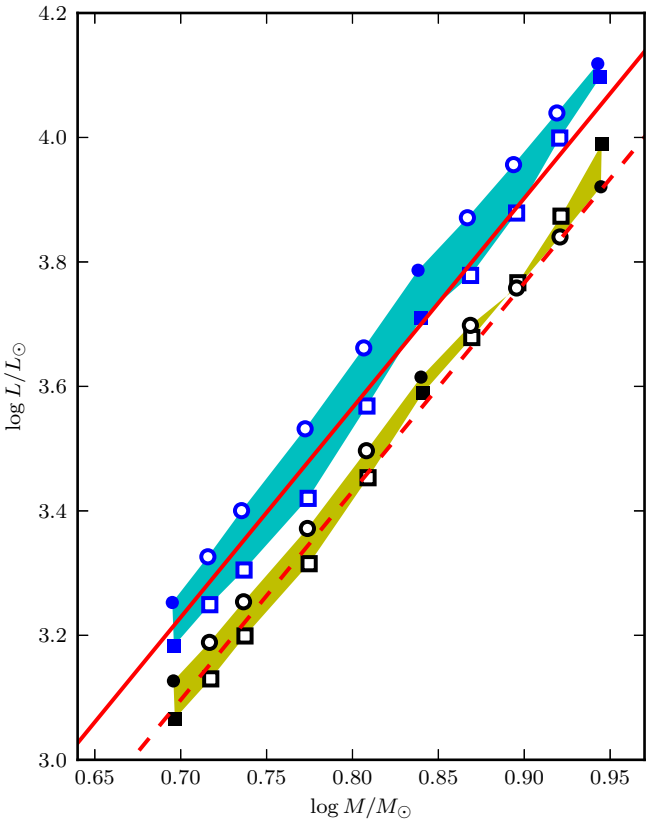

Fig. 5. The mass-luminosity relationship for rotating ($\omega = 0.5$, cyan, consistently higher luminosity) and non-rotating Cepheids (yellow, lower luminosity). Shaded areas show the range of values between the second (squares) and third (circles) crossings. Solid symbols are based on grid models, open symbols indicate models obtained via the web-based interpolation tool. The red dashed line that crosses the non-rotating area represents the M-L relation by Caputo et al. (2005, their Eq. 2 with $Z = 0.014$, $Y = 0.27$) whose investigation was based on the models by Bono et al. (2000a) and does not account for convective core overshooting. The solid red line crossing through the area delineated by rotating models is the M-L relationship used by Evans et al. (2013), which assumes a value of $d_{\rm over}/H_P = 0.2$ for convective core overshooting (based on models by Prada Moroni et al. 2012)

.

Figure 5 shows both rotating (cyan shaded area) and non-rotating M-L relations (yellow shaded area) based on the present models, as well as literature M-L relations with different assumptions regarding convective core overshooting: the Caputo et al. (2005) models (based on Bono et al. 2000a) assume no overshooting, whereas the relation given in Evans et al. (2013) assumes $d_{\rm over}/H_P = 0.2$ (based on models by Prada Moroni et al. 2012). Thus, Fig. 5 provides a means to compare the effects of increasing convective core overshooting via the literature relations, as well as of introducing rotation via the shaded areas (note, however, that the present models assume weak overshooting with $d_{\rm over}/H_P = 0.1$).

Figure 5 clearly exposes two important aspects to bear in mind with respect to the M-L relation. First, rotation increases Cepheid luminosities at a similar rate as high convective core overshooting values, thus pointing to the presence of a degeneracy between the two effects in terms of the M-L relation. Second, it is crucial to take into account the crossing number when inferring Cepheid masses, and the importance of doing so increases with ω (since the luminosity difference widens with ω). Hence, if rotation and crossing number are ignored, systematic errors will be made when inferring masses from a given M-L relation. As can be seen from Fig. 5, evolutionary masses will be overestimated, leading to a mass discrepancy.

Let us compare the systematic error on mass estimates incurred in four different situations:

1. both ω and the crossing number are unknown: using *non-rotating* models, masses are overestimated by 12 – 15 %.
2. ω is known, but not the crossing: assuming the star is on the second crossing while it is on the third, the masses are overestimated by 2-7 %.
3. The Cepheid is on the second crossing, ω is unknown: using *non-rotating* models, masses are overestimated by 8 %.
4. The Cepheid is on the third crossing, ω is unknown: using *non-rotating* models, masses are overestimated by 10–17, %.

Note that these systematic offsets approach the range of 10 – 20 % usually quoted for the Cepheid mass discrepancy (e.g. Bono et al. 2006; Keller 2008). The crucial point to remember is that two effects need to be taken into account simultaneously when inferring evolutionary masses: the rotational history of the star (ω), and the crossing number. Thankfully, both can in principle be constrained by observations, the former via estimates of $v \sin i$, Cepheid radii, and surface abundance enrichment, and the latter via rates of period changes (e.g. Turner et al. 2006).

Due to the balance between the mixing and hydrostatic effects, the majority of Cepheid models predict luminosities that deviate not too far from the $\omega = 0.5$ models, cf. Figs. 3 and 4. M-L relations for Cepheids based on rotating models with $\omega = 0.5$ therefore provide suitable estimates for a range of initial rotation rates observed in B-type stars on the MS.

The rotation-averaged M-L relation for the *second crossing* is thus:

$$\log(L/L_\odot) = (3.683 \pm 0.074)\log(M/M_\odot) + (0.598 \pm 0.006) \quad (1)$$

$$\log(M/M_\odot) = (0.271 \pm 0.006)\log(L/L_\odot) - (0.159 \pm 0.001)\,. \quad (2)$$

Analogously for the *third crossing*, we obtain:

$$\log(L/L_\odot) = (3.515 \pm 0.043)\log(M/M_\odot) + (0.818 \pm 0.004) \quad (3)$$

$$\log(M/M_\odot) = (0.284 \pm 0.003)\log(L/L_\odot) - (0.231 \pm 0.001)\,. \quad (4)$$

If the crossing number is also unknown, then an average relation in between these two should be used. We thus propose

$$\log(L/L_\odot) = (3.594 \pm 0.124)\log(M/M_\odot) + (0.712 \pm 0.011) \quad (5)$$

$$\log(M/M_\odot) = (0.272 \pm 0.009)\log(L/L_\odot) - (0.177 \pm 0.002) \quad (6)$$

to be used as an M-L relation in the absence of information on ω and the crossing number. We note that this average relation yields masses for low-luminosity ($\log L/L_\odot \approx 3.2$) Cepheids that agree to within less than 1% with the relationship by Prada Moroni et al. (2012, non-canonical overshooting) as given in Evans et al. (2013). Towards higher luminosity, the difference between the relationships increases, reaching nearly 5% at 9 $M_\odot$ (rotating models predict lower mass).

Figure 6 illustrates the importance of considering the crossing number when inferring the mass of a Cepheid. Cepheids with masses listed in Evans et al. (2013) are plotted as cyan open circles over the blue loop portions of evolutionary tracks in an HRD. Cepheid mass, luminosity and color are provided by Evans et al. (2013), and the temperature estimate is obtained by

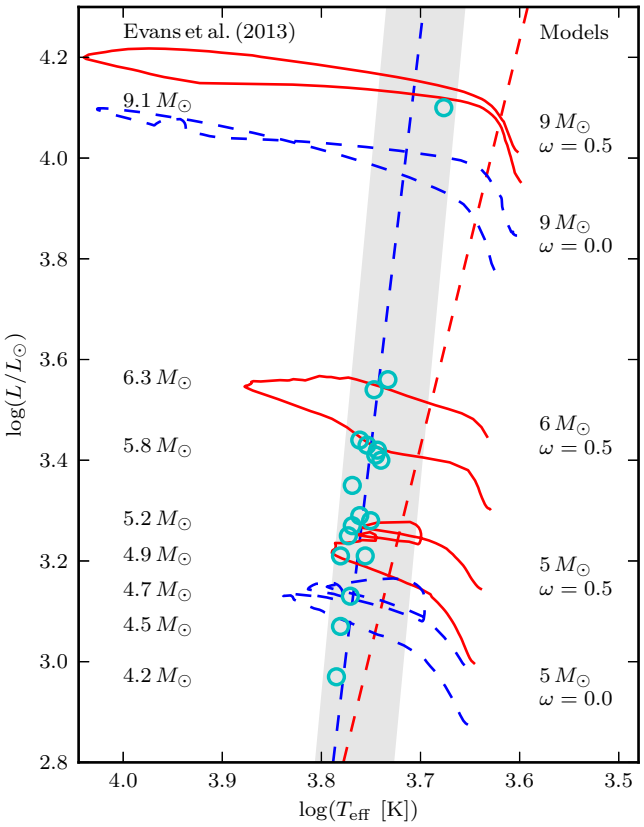

Fig. 6. Cepheid with masses determined by Evans et al. (2013) plotted as cyan open circles onto the blue loop portions of evolutionary tracks. Rotating tracks are drawn as red solid, non-rotating ones as blue dashed lines, the IS as in Fig. 2.

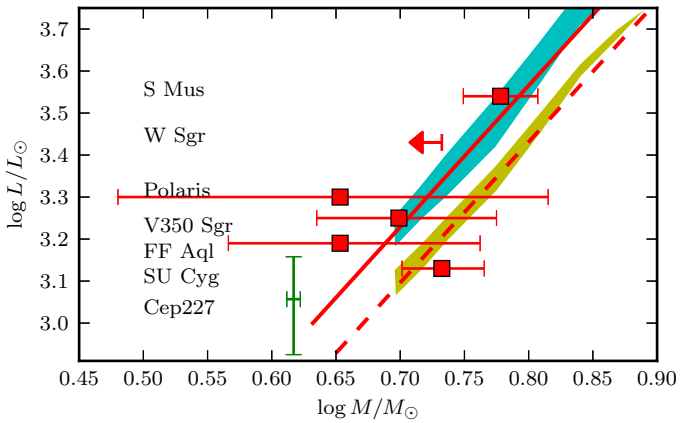

Fig. 7. Observed (non-model dependent) Cepheid masses (see Evans et al. 2011, and references therein) shown together with the M-L relations of Fig. 5. Luminosities were estimated by Evans et al. (2013) or Evans et al. (2011, Polaris & FF Aql) using the period-luminosity relationship by Benedict et al. (2007). The green errorbars labeled 'Cep227' show the highly accurate mass estimate for OGLE-CEP-LMC-0227 (Pietrzyński et al. 2010), where the luminosity was calculated from the published radius and temperature.

interpolating in the color grid by Worthey & Lee (2011) assuming solar metallicity and $\log g = 1.5$.

The figure clearly shows that there is overall very good agreement between the literature masses and the models. Furthermore, it underlines the penalty of ignoring the crossing number when inferring Cepheid masses. For instance, if the crossing is ignored, then Cepheids between 5.8 and 6.3 $M_\odot$ may both be interpreted as 6 $M_\odot$ Cepheids. Figure 6 also illustrates that the present models predict luminosities that are consistent with the period-luminosity relation (PLR) by Benedict et al. (2007), since the Cepheid luminosities in Evans et al. (2013) are based on this PLR relation together with an M-L relation which is analytically similar to Eq. 6.

Few model-independent Cepheid masses are known in the literature, and unfortunately, their associated uncertainties are rather large. In Fig. 7, we compare the model-independent masses shown in Evans et al. (2011) with the M-L relations presented in Fig. 5 above. This comparison is not very conclusive, unfortunately, though it does seem to favor the rotating M-L region shown. An interesting test to perform would be to investigate the Cepheid SU Cyg in terms of its observables related to rotation, since its location in the diagram is only consistent with virtually no rotation. Note that M-L relations are sensitive to metallicity in the sense that lower metallicity models yield higher luminosity. This is important to keep in mind when considering the LMC Cepheid OGLE-LMC-CEP-0227 (Pietrzyński et al. 2010) shown by green error bars.

While there does exist a degeneracy between the adopted value for the overshooting parameter and the rotation rate in terms of the M-L relation, rotation has implications on a star's evolution that may be observable in the late stages of its evolution. For instance, rotation leads to enhanced helium surface abundance and modified CNO element abundance ratios, see Sec. 3.5. For Cepheids of a fixed mass, enhanced helium abundance would increase pulsation amplitudes, since the total amount of helium in the partial ionization zone would be increased, see Sec. 3.5.1. Furthermore, rotating models predict surface velocities that are clearly within the detectable range, cf. Sec. 3.3. Hence, the present rotating models make several potentially observable predictions that can be used to constrain the value of ω for a given Cepheid, and help to distinguish between evolutionary effects due to rotation and those due to higher core overshooting.

To summarize the above, the current mass discrepancy (in the order of 10 – 20%) can be explained by a combination of increased luminosity due to rotation and luminosity differences between Cepheids on second and third IS crossings.

3.3. Surface gravity, radii, and equatorial velocity

As can be seen in the D panels of Figs. 3 and 4, rotation impacts surface gravity, $\log g$, during the IS crossings. Qualitatively similar in behavior to the increase in luminosity due to rotation, rotating models tend to have lower $\log g$, and the range of $\log g$ values between the two crossings increases with rotation. This is no surprise, since $\log g$ and L are intimately linked via the M-L relationship. Since $\log g$ is related to stellar radius, rotation also impacts a Cepheid's radius. These effects are particularly interesting to mention here, since $\log g$ and radius can be determined observationally and independently, providing constraints on a Cepheid's crossing number and on ω.

Due to the conservation of angular momentum, stars with greater rotation rates on the MS can be expected to have greater rotational velocities also during the red (super-) giant phase. Panels E of Figs. 3 and 4 show the dependence of the equatorial surface velocity for the 7 $M_\odot$ models, $v_{\rm eq}$ on initial rotation rate

Models		first		second		third	
$M/M_\odot$	ω	BE	RE	RE	BE	BE	RE
5.0	0.5	23.9	21.8	20.8	24.2	14.2	7.6
		26.1	17.6	18.5	25.4	21.2	5.8
7.0	0.5	14.6	11.0	19.2	35.0	22.1	11.2
		16.6	10.8	23.8	41.2	26.6	15.2
9.0	0.5	9.8	6.6	8.1	37.6	17.7	4.6
		11.6	7.7	22.7	52.0	23.8	11.5

Table 2. Range of equatorial velocities $v_{\rm eq}$ in km s^{-1} predicted by models with $\omega = 0.5$ for three different masses upon entering and exiting the blue (BE) and red (RE) edges of the IS. For each mass, values based on the Bono et al. (2000b) IS are presented first, followed by those for the Tammann et al. (2003) IS.

	log a [yr]					
	second crossing			third crossing		
ω	0.0	0.5	0.8	0.0	0.5	0.8
5 $M_\odot$	8.01	8.09	8.11	8.03	8.10	8.12
7 $M_\odot$	7.67	7.75	7.76	7.69	7.77	7.78
9 $M_\odot$	7.46	7.53	7.54*	7.48	7.55	7.56*

Table 3. Cepheid ages for three different masses and rotation rates. The typical difference between rotating and non-rotating models is approximately 20% across the board. *: for 9 $M_\odot$ models, this column actually shows $\omega = 0.7$.

during the second and third crossings: $v_{\rm eq}$ increases during the second crossing, decreases during the third. The minimum and maximum values during the entire blue loop are indicated by up- and downward facing triangles, respectively.

Equatorial velocities predicted for models with $\omega = 0.5$ for 5, 7, and 9 $M_\odot$ models between the red (RE) and blue (BE) edges of the IS are listed in Tab. 2. $v_{\rm eq}$ tends to be consistently larger on the second crossing than on the third due to larger radius (lower $\log g$). Given the predictions in Tab. 2, the presence of high $v \sin i$ would tend to be indicative of a Cepheid being on the second crossing.

At the velocities predicted here, rotation should be readily observed by spectral line broadening. A first estimate of the average $v_{\rm eq}$ based on a sample of 97 classical Cepheids observed with the high-resolution spectrograph *Coralie* as part of an observing program to search for Cepheids associated with open clusters (Anderson et al. 2013) yields $\langle v_{\rm eq} \rangle \approx 12.3$ km s^{-1} (R. I. Anderson 2013, PhD thesis). A detailed comparison with observed surface velocities is currently in preparation. Three published observational studies found $v_{\rm eq} \lesssim 10$ km s^{-1} (Bersier & Burki 1996, using CORAVEL), $v \sin i \leq 16$ km s^{-1} (Nardetto et al. 2006, estimates of $v \sin i$ in their Tab. 2), and $4.9 \leq v \sin i \leq 17.7$ km s^{-1} (De Medeiros et al. 2013, Cepheids identified via cross-match with the Variable Star Index, cf. Watson 2006).

At first sight, this comparison may appear to indicate overestimated predictions for $v_{\rm eq}$ for models with initial $\omega = 0.5$. Note, however, that the predicted values of $v_{\rm eq}$ vary significantly between the different crossings, within each crossing, as a function of mass (or period), and are moreover strongly dependent on the choice of instability strip (bluer boundary = more contracted = higher $v_{\rm eq}$). A detailed comparison must therefore take into account the crossings, temperature, masses (periods), and be based on a sufficiently large sample in order to deal with the randomly oriented rotation axes.

3.4. Cepheid ages & lifetimes

Rotating models yield older Cepheids than non-rotating ones (see panels F in Figs. 3 and 4), since rotation increases the MS lifetime of stars. For example, the difference in mean age during the second crossing between the non-rotating 7 $M_\odot$ model (49.4 Myr), and the $\omega = 0.5$ model of the same mass (58.6 Myr) is approximately 20%. Additional ages for Cepheid models of 5, 7, and 9 $M_\odot$ models for different initial rotation rates are listed in Tab. 3. It is evident from the table that moderate rotation ($\omega = 0.5$) causes a systematic increase in $\log a$ of approximately 0.08 dex, regardless of mass. Hence, the present models suggest that (rotating) real Cepheids may be systematically older by 20% than predicted by non-rotating models. Such considerations are relevant for calibrations of period-age relations (Bono et al. 2005) and their applications for constraining star formation histories, e.g. of the Galactic nuclear bulge (Matsunaga et al. 2011).

Besides age, rotation also impacts the duration of blue loops, and therefore Cepheid lifetimes (the time spent crossing the IS). Cepheid lifetimes and blue loop durations are listed in kyr in Tab. 4 covering three rotation rates with three initial masses for both the Bono et al. (2000b) and Tammann et al. (2003) instability strips. We note here that the 5 $M_\odot$ models are affected by helium spikes during the third crossing. These occasional sudden increases of available helium can extend the lifetime of the third crossing significantly, if they occur inside the IS. However, *Cepheid lifetime estimates depend much more strongly on the definition used for the IS boundaries* than on these He spikes. Hence, the reader is advised to consider the following discussion merely as an indicator of tendencies.

The overall trends predicted for Cepheid lifetimes in Tab. 4 are as follows:

- Lifetime estimates for the 5 and 7 $M_\odot$ models are much longer (by a factor 2-3 in the case of 5 $M_\odot$) when adopting the Tammann et al. (2003) IS rather than the Bono et al. (2000b) IS. The longer lifetimes can be explained by the greater width (in $T_{\rm eff}$) of the former IS definition and its bluer hot edge (evolution slower on the blue edge than the red). For 9 $M_\odot$ models, the Bono et al. (2000b) IS predicts longer lifetimes due to its wedge shape.
- First crossings are much faster than second or third crossings. The first crossing lifetime increases towards lower masses.
- The larger the mass, the longer the time spent on the first crossing, relative to the second or third. Hence, the larger the mass, the more probable it is for a Cepheid to be observed during the first crossing.
- Cepheid lifetimes for the 5 $M_\odot$ model are by far the longest. Compared to 7 $M_\odot$ models, 5 $M_\odot$ models predict lifetimes that are at least an order of magnitude longer, depending strongly on the IS boundaries adopted and on rotation. The reason is that evolution along the blue loop is slowest at the tip of the blue loop, which lies square inside the IS for these models.
- For the 5 $M_\odot$ model, the third crossing is always slower than the second. However, this is not always the case for the higher-mass models.
- The fractional time spent inside the IS, $\tau_{\rm Cep,total}/\tau_{\rm loop}$, decreases with increasing mass. This is related to the speed at which a star evolves along the IS. As a result, a 5 $M_\odot$ red giant is more likely to be caught (observed) during the Cepheid

	$\tau_{\rm Cep}$ [kyr]												$\tau_{\rm loop}$ [Myr]			$\tau_{\rm He}$ [Myr]		
	first			second			third			total								
ω	0.0	0.5	0.8	0.0	0.5	0.8	0.0	0.5	0.8	0.0	0.5	0.8	0.0	0.5	0.8	0.0	0.5	0.8
5 $M_\odot$	5.7	9.4	8.5	316	288	857	597	1553	1145	919	1851	2011	10.3	8.4	9.3	19.2	16.6	18.7
	38	35	35	879	930	2681	1977	3422	2804	2894	4387	5520						
7 $M_\odot$	4.0	4.5	4.1	51	28	32	27	40	31.6	82	72	68	3.0	3.4	3.9	6.8	6.7	7.3
	8.0	7.4	7.2	88	39	47	41	55	47	138	101	101						
9 $M_\odot$*	2.2	3.0	2.7	14	11	11	6	13	10	22	27	24	1.5	1.6	1.9	3.4	3.3	3.6
	2.7	2.7	2.6	9.4	6.7	8.9	6.9	12	9.2	19	21	21						

Table 4. Predicted timescales relevant for Cepheids of different initial mass and rotation rate. Cepheid lifetimes in the three crossings and their sum (total lifetime) are listed in [kyr]. The duration of the blue loop and the core helium burning timescale are given in [Myr]. The asterisk is a reminder that $\omega = 0.7$ was used instead of $\omega = 0.8$ for 9 $M_\odot$ models. The predicted values in the top rows for each mass are based on the Bono et al. (2000b) IS, the lower rows on Tammann et al. (2003).

stage than an ordinary red giant of 7 or 9 $M_\odot$. This is in addition to the effect of the IMF.
– The total lifetimes of intermediate and high mass Cepheids depend less on rotation than low-mass Cepheids do.

Better resolution in rotation rate regarding Cepheid lifetimes is provided for the 7 $M_\odot$ model in the G panels of Figs. 3 and 4, though no clear trend is discernible.

3.5. Surface abundance enrichment

Rotational mixing creates effects that can impact Cepheid surface abundances during two different evolutionary stages. First, during the MS, rotational shear creates turbulence that slowly mixes material processed in the core throughout the radiative envelope, leading to enhanced surface abundances of helium and of nitrogen relative to carbon and oxygen. When the star evolves to become a red giant or supergiant, the core material is carried to the stellar surface during the first dredge-up phase when the star develops a deep convective envelope during its approach of the Hayashi track after the first IS crossing. Hence, two kinds of surface abundance enhancement have to be distinguished: the rotational enhancement occurring towards the end of the Main Sequence, and the dredge-up related enhancement. As the predictions presented in the following clearly show, both kinds of surface abundance enhancement depend on mass and rotation.

Abundance enhancement of element $X_{\rm i}$ is defined as the post-dredge-up (index Cep) increase in mass fraction relative to the initial value (on the ZAMS, index 0), i.e.,

$$\Delta X_{\rm i} = \Delta X_{\rm i,DU} + \Delta X_{\rm i,MS} \equiv X_{\rm i,Cep} - X_{\rm i,0} \equiv X_{\rm i,Cep} - X_{\rm i,\odot}\,. \quad (7)$$

$\Delta X_{\rm i}$ has two contributions, one due to the dredge-up (index DU), and one related to rotational enhancement on the MS (index MS).

For CNO elements, we express the abundance enhancement in logarithmic units relative to hydrogen, where, in the case of nitrogen (N):

$$[{\rm N/H}] = \log\left(\frac{{\rm X_{N,Cep}}}{{\rm A_N}\cdot{\rm X_{H,Cep}}}\right) - \log\left(\frac{{\rm X_{N,\odot}}}{{\rm A_N}\cdot{\rm X_{H,\odot}}}\right) \equiv \Delta[{\rm N/H}]\,. \quad (8)$$

Here, $\rm A_N$ denotes the atomic mass number of nitrogen. Similarly, for ratio of nitrogen to carbon,

$$\Delta[{\rm N/C}] \equiv [{\rm N/C}] \equiv [{\rm N/H}] - [{\rm C/H}]\,. \quad (9)$$

Figure 8 shows predicted surface abundance enhancements for helium, $\Delta{\rm Y_S}$, as well as N relative to C and N relative to O as a function of initial rotation rate for 7 $M_\odot$ models. Similarly, Figs. 9, 10, and 11 show the same information as functions of both rotation (gray scaled, where darker represents higher ω) and mass. In all these figures, Terminal Age Main Sequence (TAMS) values are indicated as upward facing triangles. Post dredge-up values are shows as solid circles. As per their definition, initial (ZAMS) values are 0.

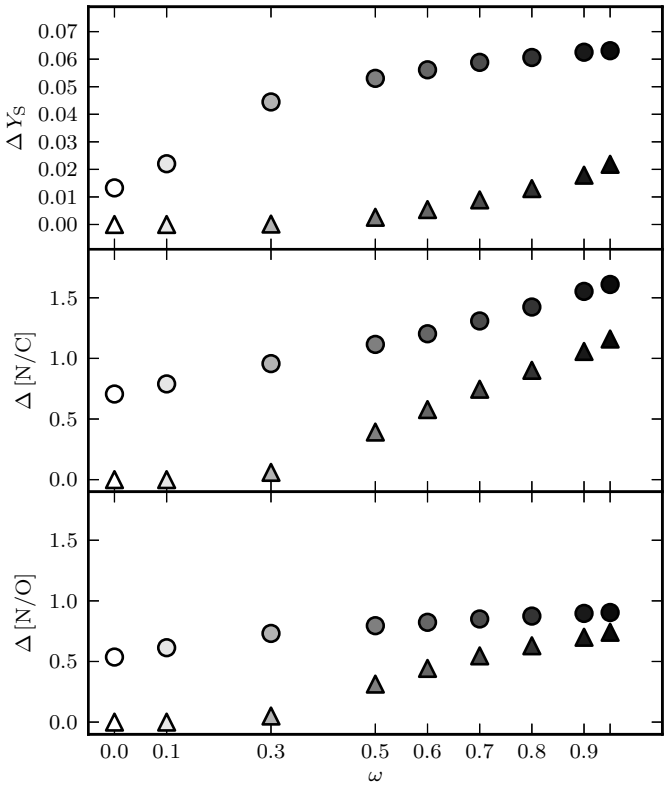

Fig. 8. Surface abundance enrichment for the 7 $M_\odot$ model as a function of initial rotation. Top panel shows surface helium mass fraction relative to starting value, center and bottom panels show [N/C] and [N/O] enhancement relative to starting (solar) value. Quantities before first dredge up is shown as upward triangles, post-dredge up as circles.

Since rotational mixing can enhance surface abundances towards the TAMS, the presence of enriched abundances is not an unambiguous argument for excluding a Cepheid's crossing the IS for the first time. As shown in the following subsections, the TAMS enhancement depends primarily on rotation, but also on

mass. Thus, especially high mass, i.e., long-period, Cepheids are expected to exhibit enhanced abundances even if they are on the first crossing. However, an absence of enhanced abundances may be indicative of small ω (rotational history of the Cepheid) and a first IS crossing.

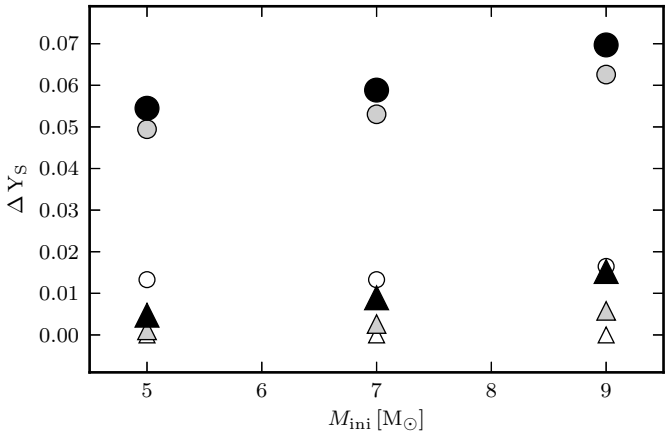

Fig. 9. Helium surface mass fraction enhancement as a function of mass and initial rotation. Open symbols represent non-rotating models, gray solid symbols $\omega = 0.5$, and black solid symbols $\omega = 0.8$. Pre-dredge-up enhancement is drawn as triangles, post-dredge-up values as circles.

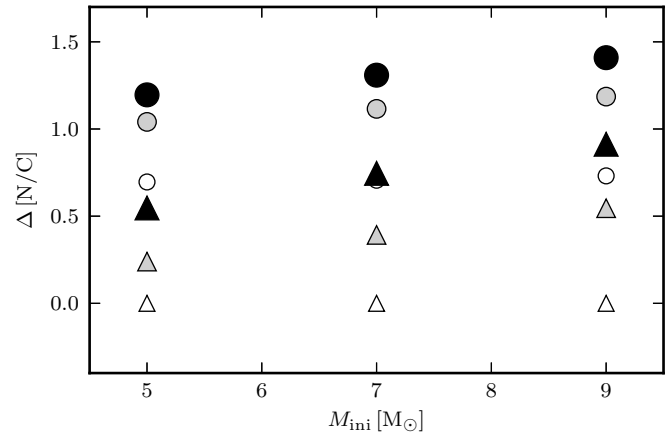

Fig. 10. Analogous to Fig. 9 for [N/C] surface abundance enhancement.

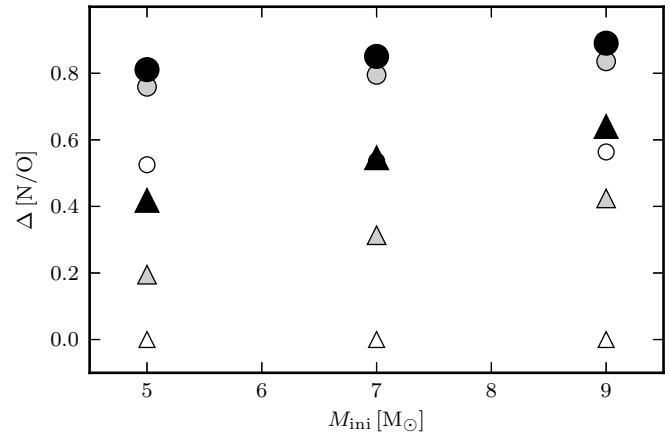

Fig. 11. Analogous to Fig. 9 for [N/O] surface abundance enhancement.

3.5.1. Helium

Figure 9 clearly shows that even small amounts of rotation considerably increase the post-dredge-up helium surface mass fraction Y_S drawn as circles whose recycle represents rotation rate (the darker, the faster). High rotation rates ($\omega > 0.5$) are required to cause significant enrichment on the MS (TAMS predictions drawn as upward triangles with same grayscale), although enhancement during the MS is a factor of 5-6 smaller than the post-dredge-up enhancement.

For a fixed mass, an increase in Y_S due to rotation also signifies an increase in the total mass of helium in the He partial ionization zone, ΔM_{He}. This should affect the pulsations, since the amplitude of light variation may depend on He abundance. For instance, Kovtyukh (1998) predicted an increase in amplitude ($\delta L \propto \Delta M_{He}/P$), where P denotes pulsation period. According to Cogan et al. (1980), an increase of He mass fraction by 0.1 would increase the light amplitude by 0.25 mag, and radial velocity amplitude by 15 m s^{-1}. However, in a recent investigation using nonlinear convective hydrodynamical models, Marconi et al. (2013) found only a weak dependence of pulsation amplitude to He abundance in the range of $Y_S = 0.26, 0.27, 0.28$ (note that the predicted enhancement, ΔY_S, due to rotation can reach up to 0.05, cf. Fig. 8). Furthermore, pulsation amplitudes might be expected to decrease with increased Y_S due to lowered opacity in the partial ionization zone (G. Bono, priv. comm.). In conclusion, pulsation amplitudes probably depend (in one way or another) on Y_S, which is affected by rotation. Hence, the observed spread in observed photometric and velocimetric amplitudes (e.g. Bono et al. 2000b) may partly be due to variations in rotation rate. However, the present static models cannot by themselves predict the behavior of pulsations.

3.5.2. CNO elements

In the intermediate-mass stars considered here, H-burning is dominated by the CNO cycle. Besides producing helium from hydrogen, the CNO cycle gradually transforms C and O into ^{14}N, since this element has the slowest rate of destruction (Maeder 1985). Hence, the ratios [N/C] and [N/O] are expected to be modified by rotation. We show the behavior of Δ[N/C] and Δ[N/O] as a function of rotation rate in the two lower panels of Fig. 8.

The TAMS enhancement is predicted to be much more noticeable for CNO elements than for helium, due to the fact that very early during the core H-burning phase, strong gradients of CNO elements appear between the convective core and the envelope triggering fast diffusion timescales. Clearly, the MS enhancement of nitrogen depends primarily on rotation, as seen by the upward facing triangles in Figs. 10 and 11 that are grayscaled for rotation rates (faster is darker). For fast rotating models of sufficiently high mass ($> 7\,M_\odot$) the rotational mixing during the MS leads to stronger abundance enhancement than dredge-up in non-rotating models of the same mass. It furthermore appears that the contribution of dredge-up to enhanced abundances is rather insensitive to rotation, though the MS enhancement is very sensitive to rotation. This is an interesting contrast with helium abundance enhancement, pointing out the large difference between the He and CNO abundance gradients between the convective core and the radiative envelope. In summary, the modification of CNO abundances due to rotational mixing during the MS and due to dredge up are of similar orders, with the rotational effect dominating for the highest-mass models. In contrast, helium enhancement occurs primarily after dredge-up.

We mention here that puzzling CNO abundance predictions made by rotating Geneva models of blue supergiant stars were previously pointed out by Saio et al. (2013). Although a detailed comparison with observed abundance enhancement will be presented in a publication to follow soon, we can already mention that the enhancement of CNO elements predicted by the present models appears systematically too high by up to 0.2 dex. However, measuring CNO abundances in the extended atmospheres of Cepheids is sufficiently complex to leave room for significant systematic errors associated with the measurement.

3.6. Tracing Cepheid evolution via period changes

Cepheids are among the rare objects whose evolution can be observed on human timescales thanks to variations in period that are interpreted as being due to contraction (period becomes shorter) or expansion (longer) as the Cepheid evolves along the IS crossing. The underlying idea is that in a radially pulsating star the pulsation period, P, is intimately linked with the mean density in solar units, $\bar{\rho}$, via the relation

$$P \cdot \sqrt{\bar{\rho}} = const \equiv Q\,. \tag{10}$$

This relation was first investigated in the context of stellar pulsations by Ritter (1879). Equation 10 was first applied to investigate the rate of progress of stellar evolution by Eddington (1918, 1919), demonstrating that the main energy source of stars could not be contraction. Thus, rates of period change have provided and continue to provide crucial tests of stellar evolution.

Estimates for predicted rates of period change can be obtained from evolutionary tracks such as the present ones, since variations in mean density are time resolved during the IS crossings. Starting from the time derivative of the period-density relation (Eq. 10), we obtain

$$\frac{\mathrm{d}P}{\mathrm{d}t} = \frac{\mathrm{d}}{\mathrm{d}t}\left(Q\cdot\sqrt{\frac{1}{\bar{\rho}}}\right) = \frac{\mathrm{d}Q}{\mathrm{d}P}\frac{\mathrm{d}P}{\mathrm{d}t}\sqrt{\frac{1}{\bar{\rho}}} - \frac{Q}{2}\sqrt{\frac{1}{\bar{\rho}^3}}\frac{\mathrm{d}\bar{\rho}}{\mathrm{d}t}\,,\ \text{and thus} \tag{11}$$

$$\frac{\mathrm{d}P}{\mathrm{d}t} = -\frac{1}{\left(1-\frac{\mathrm{d}Q}{\mathrm{d}P}\sqrt{\frac{1}{\bar{\rho}}}\right)}\cdot\frac{Q}{2}\sqrt{\frac{1}{\bar{\rho}^3}}\frac{\mathrm{d}\bar{\rho}}{\mathrm{d}t}\,. \tag{12}$$

Adopting the period-dependence of Q as investigated by Saio & Gautschy (1998), i.e.,

$$Q = 3.47\times10^{-2} + 5.2\times10^{-3}\log P + 2.8\times10^{-3}[\log P]^2\,, \tag{13}$$

with $0.035 \le Q \le 0.050$, we can estimate the importance of the first term in Eq. 12 using the average densities predicted by the models. We find this term to be close to unity and thus negligible for a first order estimate. A more detailed investigation would, however, involve a consistent determination of pulsation periods for these models. With $\frac{\mathrm{d}x/\mathrm{d}t}{x} = \frac{\mathrm{d}\ln x}{\mathrm{d}t}$ and dividing by P, we obtain a simple way to predict rates of period change to first order from the evolutionary tracks via

$$\frac{\dot{P}}{P} = \frac{\mathrm{d}\log P}{\mathrm{d}t} \approx -\frac{1}{2}\frac{\mathrm{d}\log\bar{\rho}}{\mathrm{d}t}\,. \tag{14}$$

Figure 12 shows the range of $|\dot{P}|/P$ estimated using Eq. 14 as a function of ω for second and third crossings. The absolute value is plotted here in order to have the direct comparison of the rates of period change for both crossings.

As expected from Cepheid lifetimes, higher mass stars are predicted to show faster rates of period change. No obvious dependence on ω emerges, although the values predicted for $\dot{P}/P$ do exhibit some fluctuations. The only slight tendency seen is that 7 $M_\odot$ models tend to show increasing in $|\dot{P}|/P$ with increasing ω on the second crossing, whereas the opposite is true on the third crossing. Furthermore, the ranges of $\dot{P}/P$ covered in a given crossing depend quite strongly on the IS boundaries adopted.

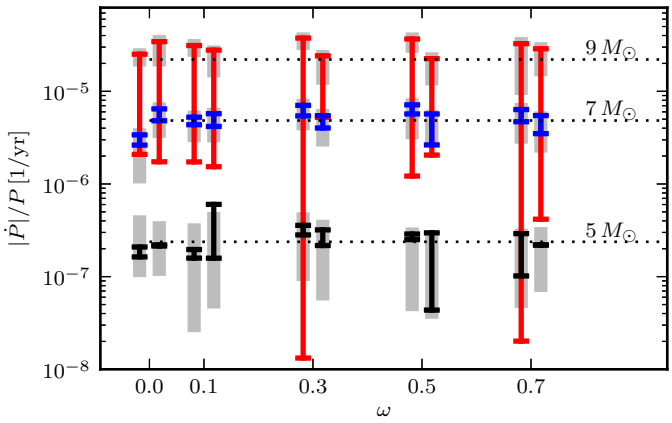

Fig. 12. Absolute values of predicted rates of period change for several Cepheid models are shown against initial rotation rate ω. Predictions for the Bono et al. (2000b) IS are drawn as black, blue, and red vertical lines for the 5, 7 and 9 $M_\odot$ models, respectively. Gray shaded bars represent the predictions assuming the Tammann et al. (2003) IS. Second crossing Cepheids are offset to slightly lower ω, third crossing Cepheids to higher ω for visibility. Period decreases along the second crossing, and increases along the third. Per-mass averages are shown as annotated horizontal dotted lines.

Period changes can be measured observationally using O-C diagrams, and are typically given in terms of the quantity $\dot{P}/P$. In the Galaxy, observational rates of period change have been determined for nearly 200 Cepheids (Turner et al. 2006), providing good statistics and long baselines that make this an exciting tool for comparisons with stellar models. Comparing the rates of period change predicted by the present models with the observed rates Turner et al. (2006, Fig. 3) yields very good agreement.

Several effects not considered here are likely to impact the predicted rates of period change, including for instance the distribution of helium inside the envelope, or the dependence of the neglected first term in Eq. 12 on density (which depends on ω). However, consistent determinations of the IS location and pulsation periods are out of scope for this paper. These and a detailed comparison with observed rates of period change are therefore postponed to a future publication.

3.7. Intrinsic dispersion of the Cepheid PLR

As was shown in the previous sections, rotation together with the crossing number lifts the uniqueness of the mass-luminosity relationship for Cepheids and affects their densities. One of the cornerstones of the universal distance scale is the empirically-calibrated period-luminosity-relation (PLR, Leavitt 1908; Leavitt & Pickering 1912) that attributes luminosities (or absolute magnitudes) to values of the pulsation period alone (e.g. Benedict et al. 2007; Freedman et al. 2012), or to period and color (e.g. Tammann et al. 2003; Sandage et al. 2004, leading to Period-luminosity-color relations). PLR calibrations are performed on real stellar populations (or at least samples of stars), whose constituents formed following an ω-distribution. The prediction that a Cepheid's luminosity depends on ω leads to the question how this may affect the PLR.

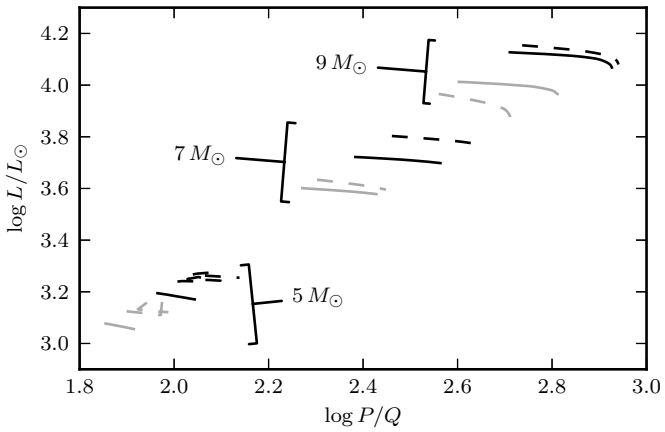

Fig. 13. Cepheid luminosity versus $\log P/Q$ for 5, 7 and 9 $M_\odot$ models in the second (solid lines) and third (dashed lines) crossings. Rotating models with $\omega = 0.5$ are shown in black, non-rotating models in gray. At a given value of $\log P/Q$, $\log L$ can easily vary by more than 0.1 dex (25%), depending on ω as well as the crossing number. Hence, rotation leads to an intrinsic dispersion of the period-luminosity-relationship.

Fig. 13 shows the relation between the (logarithmic) luminosity and the logarithm of the inverse average density ($1/\sqrt{\bar{\rho}} \equiv P/Q$, cf. Eq. 10) for the 5, 7, and 9 $M_\odot$ models with ($\omega = 0.5$) and without rotation. Second and third crossings are distinguished by line style (solid/dashed). It is clear from the figure that a range of luminosities is predicted for different ω values at a given $\log P/Q$. Models on different crossings can have the same effect. Hence, the present models predict an intrinsic scatter in luminosity at fixed $\log P/Q$ that is due to luminosity differences among crossings and initial rotation rates, enabled by the finite width (in temperature) of the IS. Naturally, if the boundaries of the IS should depend on rotation, then this may also affect the intrinsic dispersion of the Cepheid PLR. Note that color or effective temperature may likely be used to distinguish between the various luminosities associated with a given value of $\log P/Q$ (e.g. Tammann et al. 2003).

From Fig. 13 it appears that the maximal difference in $\log L$ (at fixed $\log P/Q$) due to rotation can be larger than the one due to confused crossing numbers. However, it should be remembered that luminosity is relatively stable over a range of ω for Cepheids of a given mass, cf. Figs. 3 and 4. Hence, the dispersion due to rotation alone is probably not very large, and the differences due to the increased luminosity on the third crossing (relative to the second crossing and at fixed $\log P/Q$) should be the dominant source of dispersion in the PLR.

4. Discussion

4.1. Rotation vs. overshoot and the mass discrepancy

In Sec. 3.2 we investigate Cepheid masses inferred using rotating models and find that neglecting the effect of rotation and crossing number on luminosity can lead to errors in the order of magnitude of the mass discrepancy. Furthermore, the 'average' M-L relationship of rotating models, i.e., neglecting the crossing number and using the average rotation rate $\omega = 0.5$, is consistent with an M-L relation assuming significantly stronger overshooting. This degeneracy can be easily explained, since both rotation and overshoot increase core size and therefore produce higher luminosities for lower masses.

However, besides increased luminosity, core-overshooting makes few other predictions, acting essentially like a fudge factor that is increased until evolutionary masses match pulsational ones. On the other hand, rotation is observed in most stars, and especially so in the progenitors of Cepheids. Furthermore, rotation makes several *testable* predictions of observable quantities. Accordingly, a detailed comparison of the predictions presented here with observational quantities is currently in preparation.

Another possibilty of diminishing the mass discrepancy, i.e., lowering the evolutionary mass at fixed luminosity, is to include pulsation-enhanced mass-loss (e.g. Neilson & Lester 2008; Neilson et al. 2011). This mechanism is not currently included in our models, and its total predicted mass loss depends strongly on Cepheid lifetimes, i.e., on the position and width of the IS. Observational constraints such as those by Matthews et al. (2012) are crucial to further investigate this issue.

4.2. Dependence on IS boundary definition

Clearly, adopting a given set of IS boundaries impacts the predictions obtained from our static evolutionary models, yielding IS boundary-dependent predictions for the range of luminosities, surface gravities, equatorial velocities, etc. This problem, however, is common in Cepheid research, complicated by model assumptions in the case of theoretical boundaries and by the correction for reddening and extinction in observational studies. In order to be sensitive to such systematic differences for the predicted values, two different IS boundary definitions were employed, one theoretically (Bono et al. 2000b) and one empirically-derived (Tammann et al. 2003).

The predictions obtained from the two different IS boundary definitions do generally vary quite a bit, although not by an order of magnitude. Generally speaking, the Tammann et al. (2003) IS is bluer, i.e., hotter, and therefore predicts more luminous Cepheids with higher surface gravity and surface rotation. As a result, the 'average' M-L relation for the Tammann et al. (2003) IS predicts even lower mass at a given luminosity than the (Bono et al. 2000b) IS, although the difference is generally $< 1\%$. As seen in Fig. 12, predicted rates of period change may also depend on the IS boundaries adopted. Other predicted quantities such as surface abundance enrichment, or Cepheid ages do not significantly depend on the IS definition.

For a given position in the HRD, rotation lowers stellar mean density hydrostatically, decreasing the temperature gradient. Thus, rotation is likely to affect the location of the IS boundaries in the HRD, since pulsational instability depends on the location of the partial He-ionization zone inside a star's envelope as well as the total mass of helium in that region. An ω-dependence of IS boundaries would require to replace the canonical notion of a single sharply-defined IS with a transition zone spanned by instability trips corresponding to different ω, with implications for the question of purity of the IS. Such questions shall be addressed in a future study focusing on the pulsational instability of the present models.

5. Conclusions

This paper presents the first detailed investigation of the effect of rotation on evolutionary models of classical Cepheids. The study is based on the latest state-of-the-art rotating Geneva models (cf. paper I) that incorporate a homogeneous and self-consistent treatment of rotation over the entire evolutionary cycle for a wide range of stellar masses. A dense grid of evolutionary tracks of

different rotation rates for intermediate-mass stars is available from paper II and enables a detailed investigation not only as a function of initial rotation rate, ω, but also as a function of time during the IS crossings.

Qualitative predictions are made as a function of initial rotation rate for an array of observable quantities, such as surface gravities, surface abundance enhancement, surface velocities, radii, and rates of period change. These will be quantified and compared to observational constraints in a subsequent publication.

The key results of this investigation are:

1. M-L relations depend on ω. This is true for all stars during all stages of evolution, although the difference is more obvious during the blue loop phase.
2. For Cepheids, an M-L relation at fixed ω furthermore depends on crossing number. The greater ω, the greater the difference between the crossings, since rotation broadens the blue loops.
3. The Cepheid mass discrepancy problem vanishes when rotation and crossing number are taken into account, without a need for high core overshooting values or enhanced mass loss.
4. Differences in initial rotation rate and crossing number between Cepheids of identical mass and metallicity create intrinsic scatter around the average values predicted. This is true for most parameters considered here, among them in particular the Cepheid period-luminosity-relation, i.e., rotation is a source of intrinsic dispersion for the PLR.
5. Rotational mixing can significantly enhance surface abundances during the MS phase. Consequently, enriched surface abundances do not unambiguously distinguish Cepheids on the first crossing from ones on second or third crossings.
6. Rotating models predict older Cepheids than currently assumed due to longer MS lifetimes.

Arguably the two most important results are result numbers 3 and 4, i.e., the solution of the mass discrepancy problem and the prediction of intrinsic scatter for Cepheid observables at fixed mass and metallicity. Since the mass discrepancy has been claimed to be solved by several other studies in the past, one may be reluctant to immediately adopt rotation as the best explanation. However, result 4 may provide the smoking gun for distinguishing between rotation and other effects such as core overshooting. While it would be difficult to explain why stars of identical mass and metallicity should present different overshooting values (leading to the observed scatter in, say, radius or luminosity), dispersion arises naturally when a dispersion in initial velocity is considered, which is an observational fact.

As this paper shows, the effects of rotation on Cepheid populations are highly significant, ranging from issues related to inferred masses to the prediction of systematic effects relevant for the distance scale. Further related research is currently in progress.

Acknowledgements. The authors would like to acknowledge Nancy Remage Evans for her communication regarding model-independent mass-estimates of classical Cepheids and the referee, Giuseppe Bono, for his valuable comments. This research has made use of NASA's Astrophysics Data System. CG acknowledges support from the European Research Council under the European Union's Seventh Framework Programme (FP/2007-2013) / ERC Grant Agreement n. 306901.

References

Anderson, R. I., Eyer, L., & Mowlavi, N. 2013, MNRAS, 434, 2238
Asplund, M., Grevesse, N., & Sauval, A. J. 2005, in Astronomical Society of the Pacific Conference Series, Vol. 336, Cosmic Abundances as Records of Stellar Evolution and Nucleosynthesis, ed. T. G. Barnes, III & F. N. Bash, 25
Benedict, G. F., McArthur, B. E., Feast, M. W., et al. 2007, AJ, 133, 1810
Bersier, D. & Burki, G. 1996, A&A, 306, 417
Bertelli, G., Girardi, L., Marigo, P., & Nasi, E. 2008, A&A, 484, 815
Bono, G., Caputo, F., Cassisi, S., et al. 2000a, ApJ, 543, 955
Bono, G., Caputo, F., & Castellani, V. 2006, Mem. Soc. Astron. Italiana, 77, 207
Bono, G., Castellani, V., & Marconi, M. 2000b, ApJ, 529, 293
Bono, G., Inno, L., Matsunaga, N., et al. 2013, in IAU Symposium, Vol. 289, IAU Symposium, ed. R. de Grijs, 116–125
Bono, G., Marconi, M., Cassisi, S., et al. 2005, ApJ, 621, 966
Caputo, F., Bono, G., Fiorentino, G., Marconi, M., & Musella, I. 2005, ApJ, 629, 1021
Cassisi, S. & Salaris, M. 2011, ApJ, 728, L43
Castellani, V., Chieffi, A., & Straniero, O. 1992, ApJS, 78, 517
Christy, R. F. 1968, QJRAS, 9, 13
Cogan, B. C., Cox, A. N., & King, D. S. 1980, Space Sci. Rev., 27, 419
Cox, A. N. 1980, ARA&A, 18, 15
Crowther, P. A. 2001, in Astrophysics and Space Science Library, Vol. 264, The Influence of Binaries on Stellar Population Studies, ed. D. Vanbeveren, 215
de Jager, C., Nieuwenhuijzen, H., & van der Hucht, K. A. 1988, A&AS, 72, 259
De Medeiros, J. R., Alves, S., Udry, S., et al. 2013, ArXiv e-prints
Eddington, A. S. 1918, The Observatory, 41, 379
Eddington, A. S. 1919, The Observatory, 42, 338
Ekström, S., Georgy, C., Eggenberger, P., et al. 2012, A&A, 537, A146, (paper I)
Evans, N. R., Berdnikov, L., Gorynya, N., Rastorguev, A., & Eaton, J. 2011, AJ, 142, 87
Evans, N. R., Bond, H. E., Schaefer, G. H., et al. 2013, AJ, 146, 93
Freedman, W. L., Madore, B. F., Scowcroft, V., et al. 2012, ApJ, 758, 24
Georgy, C., Ekström, S., Granada, A., et al. 2013, A&A, 553, A24, (paper II)
Huang, W., Gies, D. R., & McSwain, M. V. 2010, ApJ, 722, 605
Iglesias, C. A. & Rogers, F. J. 1991, ApJ, 371, 408
Iglesias, C. A. & Rogers, F. J. 1996, ApJ, 464, 943
Keller, S. C. 2008, ApJ, 677, 483
Kippenhahn, R. & Weigert, A. 1994, Stellar Structure and Evolution, Astronomy and Astrophysics Library (Springer)
Kovtyukh, V. V. 1998, Astronomical and Astrophysical Transactions, 17, 15
Lagarde, N., Decressin, T., Charbonnel, C., et al. 2012, A&A, 543, A108
Leavitt, H. S. 1908, Annals of Harvard College Observatory, 60, 87
Leavitt, H. S. & Pickering, E. C. 1912, Harvard College Observatory Circular, 173, 1
Maeder, A. 1985, in European Southern Observatory Conference and Workshop Proceedings, Vol. 21, European Southern Observatory Conference and Workshop Proceedings, ed. I. J. Danziger, F. Matteucci, & K. Kjar, 187–205
Maeder, A. 1997, A&A, 321, 134
Maeder, A. 2009, Physics, Formation and Evolution of Rotating Stars, Astronomy and Astrophysics Library (Springer)
Maeder, A. & Meynet, G. 2000, ARA&A, 38, 143
Maeder, A. & Meynet, G. 2001, A&A, 373, 555
Maeder, A. & Zahn, J.-P. 1998, A&A, 334, 1000
Marconi, M., Molinaro, R., Bono, G., et al. 2013, ApJ, 768, L6
Marengo, M., Evans, N. R., Barmby, P., et al. 2010, ApJ, 725, 2392
Matsunaga, N., Kawadu, T., Nishiyama, S., et al. 2011, Nature, 477, 188
Matthews, L. D., Marengo, M., Evans, N. R., & Bono, G. 2012, ApJ, 744, 53
Moskalik, P., Buchler, J. R., & Marom, A. 1992, ApJ, 385, 685
Nardetto, N., Mourard, D., Kervella, P., et al. 2006, A&A, 453, 309
Neilson, H. R., Cantiello, M., & Langer, N. 2011, A&A, 529, L9
Neilson, H. R. & Lester, J. B. 2008, ApJ, 684, 569
Pietrzyński, G., Thompson, I. B., Gieren, W., et al. 2010, Nature, 468, 542
Prada Moroni, P. G., Gennaro, M., Bono, G., et al. 2012, ApJ, 749, 108
Reimers, D. 1975, Memoires of the Societe Royale des Sciences de Liege, 8, 369
Reimers, D. 1977, A&A, 61, 217
Ritter, A. 1879, Wiedemanns Annalen, 173
Saio, H. & Gautschy, A. 1998, ApJ, 498, 360
Saio, H., Georgy, C., & Meynet, G. 2013, MNRAS, 433, 1246
Sandage, A., Tammann, G. A., & Reindl, B. 2004, A&A, 424, 43
Seaton, M. J., Yan, Y., Mihalas, D., & Pradhan, A. K. 1994, MNRAS, 266, 805
Slettebak, A. 1949, ApJ, 110, 498
Stobie, R. S. 1969a, MNRAS, 144, 461
Stobie, R. S. 1969b, MNRAS, 144, 485
Stobie, R. S. 1969c, MNRAS, 144, 511
Tammann, G. A., Sandage, A., & Reindl, B. 2003, A&A, 404, 423
Turner, D. G. 2009, in American Institute of Physics Conference Series, Vol. 1170, American Institute of Physics Conference Series, ed. J. A. Guzik & P. A. Bradley, 59–68
Turner, D. G., Abdel-Sabour Abdel-Latif, M., & Berdnikov, L. N. 2006, PASP, 118, 410
Vink, J. S., de Koter, A., & Lamers, H. J. G. L. M. 2001, A&A, 369, 574
Watson, C. L. 2006, Society for Astronomical Sciences Annual Symposium, 25, 47
Worthey, G. & Lee, H.-c. 2011, ApJS, 193, 1
Zahn, J.-P. 1992, A&A, 265, 115

4.4 Comparing rotating Cepheid predictions to observations

The best scientific theories make *testable* predictions (Popper 1935). In the same spirit, observational tests of predicted quantities are essential for the development of a theory. As argued in the above publication, rotating models can resolve the Cepheid mass discrepancy, without the need for extreme values of the convective core overshooting parameter. In addition, rotation leads to a suite of predictions of quantities that are accessible to observation, i.e., that are testable. A key consequence of rotation is that the rotation-sensitive, i.e., most, parameters of stellar (and also Cepheid) populations follow distributions, since the initial rotation rates of stars also follow distributions. By comparing the model predictions with observations, one can hope to achieve two things: i) investigate the role and impact of rotation on the Cepheid paradigm by demonstrating that predictions are consistent with observation; ii) improving the models by identifying and understanding contradictions between observations and predictions.

Predictions for the observable parameters and quantities are presented in the article in Sec. 4.3. All of these are being compared to actually observed values in a publication currently in preparation. Since this is unfinished work, only a preview can be presented here, focusing on two key comparisons. The first is related to surface abundance enhancement and the second to the frequency of Cepheids in stellar populations.

4.4.1 Predicted and observed Cepheid abundance enhancement

Abundance enhancement is not directly observed. However, young B-stars on the MS can be assumed to exhibit surface abundances representative of their initial values, $[\mathrm{X/H}]_{\mathrm{ini}}$. Thus, subtracting present-day B-star abundances from present-day Cepheid abundances, $[\mathrm{X/H}]_{\mathrm{Cep}}$, in a chemically similar sample can provide a lower limit estimate for the enhancement of surface abundances. Note that in the following, the standard notation for abundances relative to Solar values is employed, with N_{X} and N_{H} as the number of atoms of species X and hydrogen, respectively:

$$[\mathrm{X/H}] = \log\left(\frac{N_{\mathrm{X}}}{N_{\mathrm{H}}}\right) - \log\left(\frac{N_{\mathrm{X}}}{N_{\mathrm{H}}}\right)_{\odot} . \tag{4.3}$$

Nieva & Przybilla (2012) recently published high-quality 1D NLTE B-star abundances in the Solar neighborhood, and abundances of 12 Cepheids closer than 1 kpc were recently determined using the 1D NLTE analysis by Takeda et al. (2013). Using these two studies[3], observational Cepheid abundance enhancement, $\Delta[\mathrm{X/H}]_{\mathrm{obs}}$, can be estimated via:

$$\Delta[\mathrm{X/H}]_{\mathrm{obs}} = [\mathrm{X/H}]_{\mathrm{Cep}} - [\mathrm{X/H}]_{\mathrm{ini}} . \tag{4.4}$$

$\Delta[\mathrm{X/H}]_{\mathrm{obs}}$ can then be directly compared to the abundance enhancement predicted by the models, $\Delta[\mathrm{X/H}]_{\mathrm{model}}$, as defined in the article (Sec. 4.3):

$$\Delta[\mathrm{X/H}]_{\mathrm{model}} = [\mathrm{X/H}]_{\mathrm{Cep}} - [\mathrm{X/H}]_{\odot} = [\mathrm{X/H}]_{\mathrm{Cep}} , \tag{4.5}$$

since $[\mathrm{X/H}]_{\odot} \equiv 0$ by definition. With $[\mathrm{X_i/X_j}] \equiv [\mathrm{X_i/H}] - [\mathrm{X_j/H}]$, it is simple to compute:

$$\Delta[\mathrm{N/C}]_{\mathrm{model}} \equiv [\mathrm{N/C}]_{\mathrm{Cep}} - [\mathrm{N/C}]_{\odot} = [\mathrm{N/C}]_{\mathrm{Cep}} , \tag{4.6}$$

[3]Note that CNO abundance estimates are available for many more Galactic Cepheids, determined notably by Luck & Lambert (2011) and Andrievsky et al. (2002), assuming local thermodynamic equilibrium (LTE). However, CNO abundances are very sensitive to whether LTE is assumed, or not. Therefore, the estimation of abundance enhancements must be consistent in terms of LTE/NLTE abundances. The B-star abundances were determined by Nieva & Przybilla (2012) taking into account NLTE effects. Hence, only NLTE abundances (for both Cepheids and B-stars) in the Solar Neighborhood (to avoid differences due to the chemical gradient in the Galaxy) are used in this first comparison.

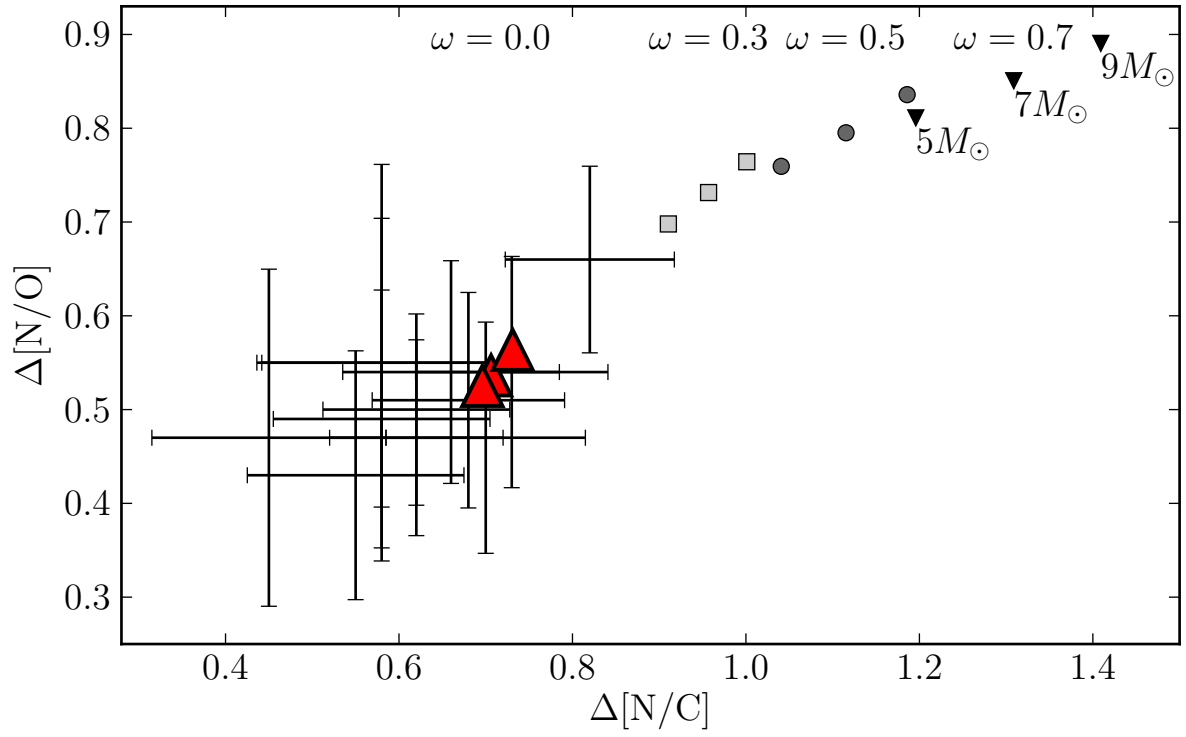

Figure 4.1: Comparison between observed and predicted relative surface abundance enhancement of nitrogen over oxygen and carbon. Observational values are shown as errorbars and are estimated using present-day Cepheid abundances from Takeda et al. (2013) and B-star abundances by Nieva & Przybilla (2012) as initial values. Models for different initial rotation rates and masses are represented by the following symbols: red large triangles (no rotation), light gray squares ($\omega = 0.3$), dark gray circles ($\omega = 0.5$), black downward triangles ($\omega = 0.7$) for models of 5, 7, and 9 $M_\odot$. Enrichment depends most strongly on rotation (indicated in the top), but also on mass (annotated for $\omega = 0.7$ models).

which yields for $\Delta[\mathrm{N/C}]_{\mathrm{obs}}$:

$$\Delta[\mathrm{N/C}]_{\mathrm{obs}} = [\mathrm{N/C}]_{\mathrm{obs}} - [\mathrm{N/C}]_{\mathrm{ini}} \,. \tag{4.7}$$

It is preferred to investigate the enrichment of nitrogen relative to carbon or oxygen (the sum of CNO elements stays constant during the CNO cycle), rather than that of nitrogen relative to hydrogen, since the exact mixture of initial abundances may vary between stars, and since this relative enrichment among CNO elements is well understood as part of the CNO cycle (e.g. Maeder 1985).

Figure 4.1 compares the theoretically predicted and empirically estimated enhancements of nitrogen over carbon an oxygen. Errorbar markers represent the empirical quantities derived using the phase-averaged Cepheid abundances. The uncertainties adopted here are the combined (added in quadrature) uncertainties of the Takeda et al. (2013) Cepheid abundances, the Nieva & Przybilla (2012) B-star abundances, and 0.05 dex for each of the two references' different Solar abundances. Models for different rotation rates and mass are represented by the following symbols: red large triangles (no rotation, highlighted for better visibility), light gray squares ($\omega = 0.3$), dark gray circles ($\omega = 0.5$), black downward triangles ($\omega = 0.7$) for models of 5, 7, and $9\,M_\odot$. The model masses are easily distinguished: the larger the mass, the higher the enhancement.

Judging from the figure, there either exists a systematic offset between the empirical and predicted relative abundance enhancements, or all Cepheids must have non-rotating progenitor stars

(although this would be difficult to explain). For more massive stars, Saio et al. (2013) already pointed out these puzzling CNO abundances, mentioning that the CNO surface abundances predicted by the same Geneva models appear too large compared to those observed in the blue supergiants Deneb and Rigel. If the empirical relative enhancement estimate is accurate, then this comparison may indicate that the effect predicted by the present models is overestimated. This possibility will be investigated further by the Geneva stellar evolution team. As a test, the criterion for convection by Schwarzschild was replaced with that by Ledoux. However, both criteria lead to nearly identical results in terms of surface abundances (Cyril Georgy, private communication). On the observational end, there are several effects that could lead to biased abundance estimates, including: i) the difficult determination of accurate abundances in only a handful absorption lines due to CNO elements (see e.g. Luck et al. 2013); ii) basic assumptions such as plane-parallel atmospheres that do not hold in the extended atmospheres of Cepheids, i.e., neglected 3D effects; iii) assumptions on line profiles and their analytic implementation, e.g. neglecting rotational broadening or choosing between cuspy macro-turbulence profiles and Gaussian microturbulence (see e.g. Gray 2008, for the definitions of analytic line profiles); iv) the appropriateness of estimating abundance enrichment using Cepheid and B-star abundances; v) neglected MS enhancement due to rotational mixing (B-star abundances).

At this point, it can be noted that the predicted relative abundance enhancement exceeds the empirical estimate by about 0.2 dex. However, it is not yet clear whether the predicted or the empirical estimates are responsible for this disagreement.

4.4.2 The frequency of Cepheids in stellar populations

Synthetic populations can be created using the Geneva population synthesis tool[4] that is currently being developed by the Geneva stellar evolution group. Such synthetic populations can be used to create artificial open clusters and the like, and the code currently assumes a single star forming event. Synthetic populations are drawn along an isochrone, or a set of isochrones in the case of a velocity distribution, following a probability distribution defined by the IMF.

To establish a Cepheid frequency, two things are needed: i) a sample of Cepheids; ii) a normalization sample. Theoretically, it is very simple to define both quantities, but observationally, this is more complex. From the theoretical point of view, the best way to define the normalization is to use MS stars within a given mass range that remains on the MS at ages less than 500 Myr (chosen as a conservative upper limit to Cepheid ages). For the models presented by Georgy et al. (2013b), this lower mass limit is $1.7\,M_{\odot}$. A suitable upper limit is $3\,M_{\odot}$, since $3\,M_{\odot}$ stars do not turn off from the MS before the lowest-mass Cepheids leave the third crossing. Thus, the ideal normalization sample is stars within the mass range $1.7-3\,M_{\odot}$. Using a very large synthetic population, it is then straightforward to count the Cepheids (all stars within the boundaries of the IS), $N_{\rm CC}$, and the normalization fiducial, $N_{[1.7,3.0]\,M_{\odot}}$.

Observationally, the main issue in determining the normalization sample is completeness. The simplest way to estimate the number $N_{[1.7,3.0]\,M_{\odot}}$ observationally is to count MS stars of approximately this mass in open clusters within a given volume around the Sun. As shown in Anderson et al. (2013a), completeness of open clusters is much more sensitive to heliocentric distance than that of Cepheids. Since the distribution of open clusters appears to be more or less complete within 1 kpc around the Sun, the final estimation is limited to open clusters and Cepheids in open clusters closer than ≤ 1 kpc from the Sun.

Center coordinates and apparent diameters of open clusters with ages between $\log \mathrm{age} = [7.4-8.5]$ were extracted from the Dias et al. (2002) catalog of open clusters, the most extensive compilation of open cluster data. Furthermore, cluster values for distance and color excess, $E(B-V)$, as well as cluster proper motion were extracted for later use. Using the bolometric magnitudes

[4] At the time of writing, no acronym had yet been decided on.

predicted by the Geneva models, the mass range $1.7 - 3\,M_\odot$ was translated into J-band absolute magnitude and J-K color ranges via interpolation inside the grid provided by Worthey & Lee (2011). Total extinction in J-band, A_J, was estimated for every cluster based on distance and color excess, assuming the ratio of total to selective color excess $R = 3.23$ as in Fouqué et al. (2007). The range of J-band magnitudes to extract for a given cluster was thus estimated using the well-known formula $\mu_J = 5 \log d - 5 + A_J$ and assuming $A_J/A_V = 0.292$ (Fouqué et al. 2007). The extinction in J-band is thus estimated using the optical color excess $E(B-V)$ via $A_J = A_J/A_V \cdot R \cdot E(B-V) = 0.94 \cdot E(B-V)$.

With these estimates, a massive query of the PPMXL catalog Roeser et al. (2010) was launched on the `GAVO Data Center` using a `TAP` shell[5]. The PPMXL catalog was chosen for two main reasons. First, it provides 2MASS photometry (Cutri et al. 2003) that is ideal for the purpose of counting stars, providing all-sky homogeneous data down to a nominal survey completeness limit of $J = 15.8$ mag and $K_S = 14.3$ mag. Second, re-reduced USNO-B1 proper motions (Monet et al. 2003) are available for hundreds of millions of objects, providing a non-photometric membership constraint for the star counting procedure. All stars matching the following criteria were extracted: i) located within the apparent diameter around the cluster coordinates; ii) within the magnitude range corresponding to the mass range $1.7-3\,M_\odot$ as defined by the models plus or minus 0.3 mag; iii) the stars' proper motion agrees to within 3σ with the cluster mean. At this point, no limits on heliocentric distance had yet been imposed. Following this procedure, PPMXL catalog entries for $372\,096$ stars nearby 332 clusters were extracted within the age range where Cepheids might be expected.

The cluster MS stars were traced automatically inside a color and magnitude range defined by the rotating models. Figure 4.2 illustrates this for a few clusters, showing all stars extracted in the field in black and the stars assumed to belong to the cluster in red. The procedure works reasonably well for most clusters, although some clusters appear to be heavily contaminated by field stars (e.g. NGC 7175 in the bottom left panel), and others may have inaccurate cluster parameters in the Dias et al. (2002) catalog (e.g. Kronberger 1 in the bottom right panel). Disregarding six clusters (including NGC 7175) for which more than 1000 stars were extracted in order to avoid excessive contamination by field stars, this procedure yields $N_{[1.7,3.0]\,M_{\odot,\mathrm{obs}}} = 2718$ in 117 open clusters.

Obviously, this star counting procedure is of an approximate nature and limited by several systematics as well as by the accuracy and availability of the catalog information. There are currently only very limited all-sky resources. With *Gaia* data, a much more accurate star count will be obtained.

The number of bona fide cluster Cepheids was taken from Anderson et al. (2013a), adding 3 bona fide cluster Cepheids known from the literature[6] that could not be studied in that publication due to limitations of available data. Hence, the number of cluster Cepheids within 1 kpc of the Sun is $N_{\mathrm{CC,obs}} = 9$.

Figure 4.3 shows the comparison of the predicted Cepheid fraction obtained via population synthesis with the empirical estimate as a function of age. It should be noted here that rotating stars are on average 20% older than non-rotating stars. Since the ages in the Dias et al. (2002) catalog are mostly based on non-rotating isochrones, a shift of $\Delta \log(\mathrm{age}) = 0.08$ was applied for consistency.

Smooth lines in Fig. 4.3 represent predictions obtained from population synthesis (at Solar metallicity), and histograms represent different binning methods applied to the empirical estimates. On the theoretical side, two different IS boundaries are explored. The predictions based on Bono et al. (2000) are drawn in magenta, those using the Tammann et al. (2003) IS are drawn in

[5]For more information on these tools, please see `http://dc.zah.uni-heidelberg.de/__system__/tap/run/info`

[6]These were δ Cephei, SU Cassiopeiae, and ζ Geminorum, see e.g. Majaess et al. (2012a,b,c) and references therein

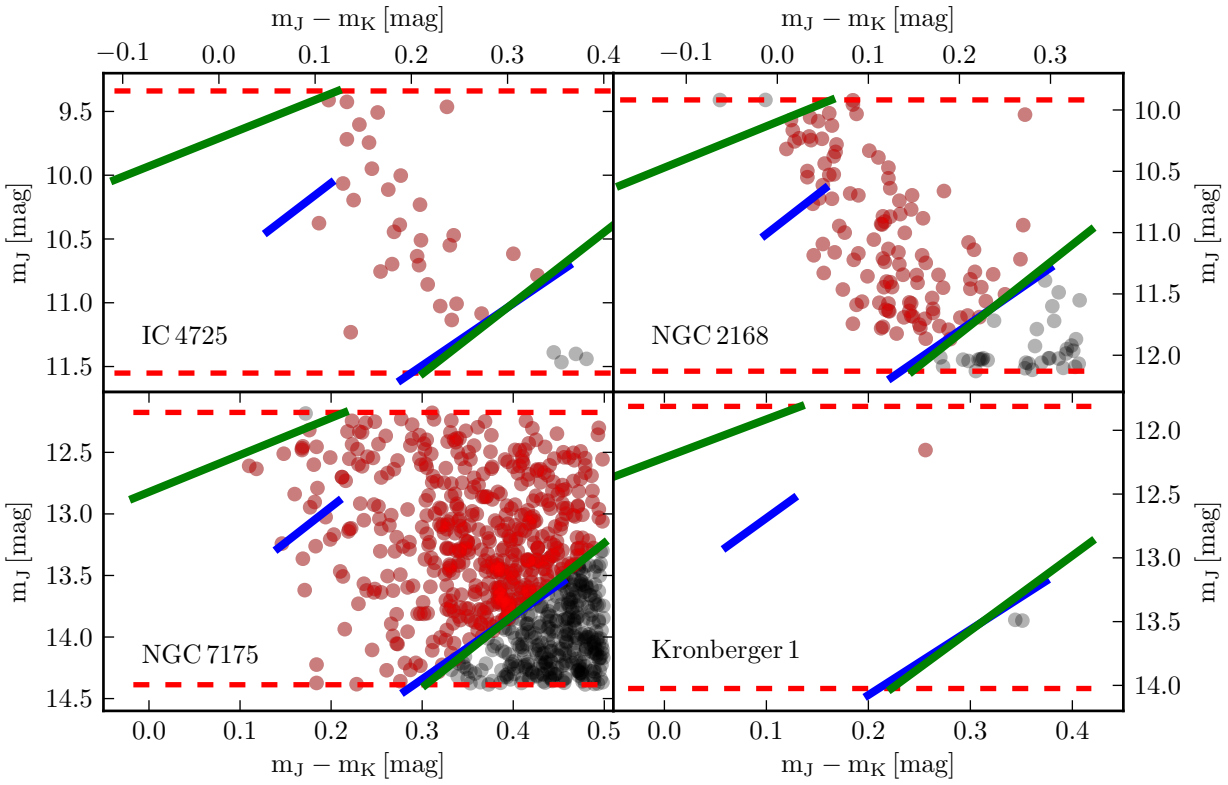

Figure 4.2: 2MASS photometry-based color-magnitude diagrams illustrating the counting procedure described in Sec. 4.4.2 for determining $N_{[1.7,3.0]\,M_{\odot},\mathrm{obs}}$. Grey circles show all stars extracted from the PPMXL catalog, red circles are counted as belonging to the cluster. Green and blue line segments show the rotating and non-rotating magnitude and color limits for the zero-age and terminal-age MS defined using cluster parameters and the models. NGC 7175 was excluded from the estimation due to significant field star contamination.

cyan. Non-rotating models are represented by dotted lines, $\omega = 0.5$ by a dashed line, and predictions employing the Huang et al. (2010) ω-distribution are drawn as solid lines. Since the statistics are very small here, a strong dependence of the predicted fraction on binning is to be expected. In order to prevent subjective bias in this respect, different methods of determining optimal bin sizes for the empirically-estimated Cepheid fraction were investigated[7]. The Bayesian blocks technique (Scargle 1998) based on the distribution of cluster Cepheid ages is shown as a green solid single-bin histogram. The Freedman & Diaconis (1981) rule is also applied, and shown in solid blue and dashed blue for the result based on the age distribution of cluster Cepheid ages and open cluster ages, respectively. Note the strong dependence of the peak around $\log(\mathrm{age}) = 8.1$ due to the small statistics.

A test such as the one presented in Fig. 4.3 can in principle test the predictions of Cepheid lifetimes, since the Cepheid frequency, defined here as $N_{\mathrm{CC}}/N_{\mathrm{MS}}$, is related to lifetimes via the following equation:

$$\frac{N_{\mathrm{CC}}}{N_{\mathrm{MS}}} \equiv \frac{\int_{M_{\mathrm{Cep,min}}(t)}^{M_{\mathrm{Cep,max}}(t)} \tau_{\mathrm{Cep}}(M)\phi(M)dM}{\int_{M_{\mathrm{MS,min}}(t)}^{M_{\mathrm{MS,max}}(t)} \tau_{\mathrm{MS}}(M)\phi(M)dM}\,, \tag{4.8}$$

where M denotes mass, $\phi(M)$ is the IMF, t is age, and τ stands for lifetime. This approach is valid for the case of open clusters, where a single star forming event is assumed.

[7]The python-based `astroML` distribution was very helpful for this, see Vanderplas et al. (2012); Ivezić et al. (2013) and `http://www.astroml.org/`

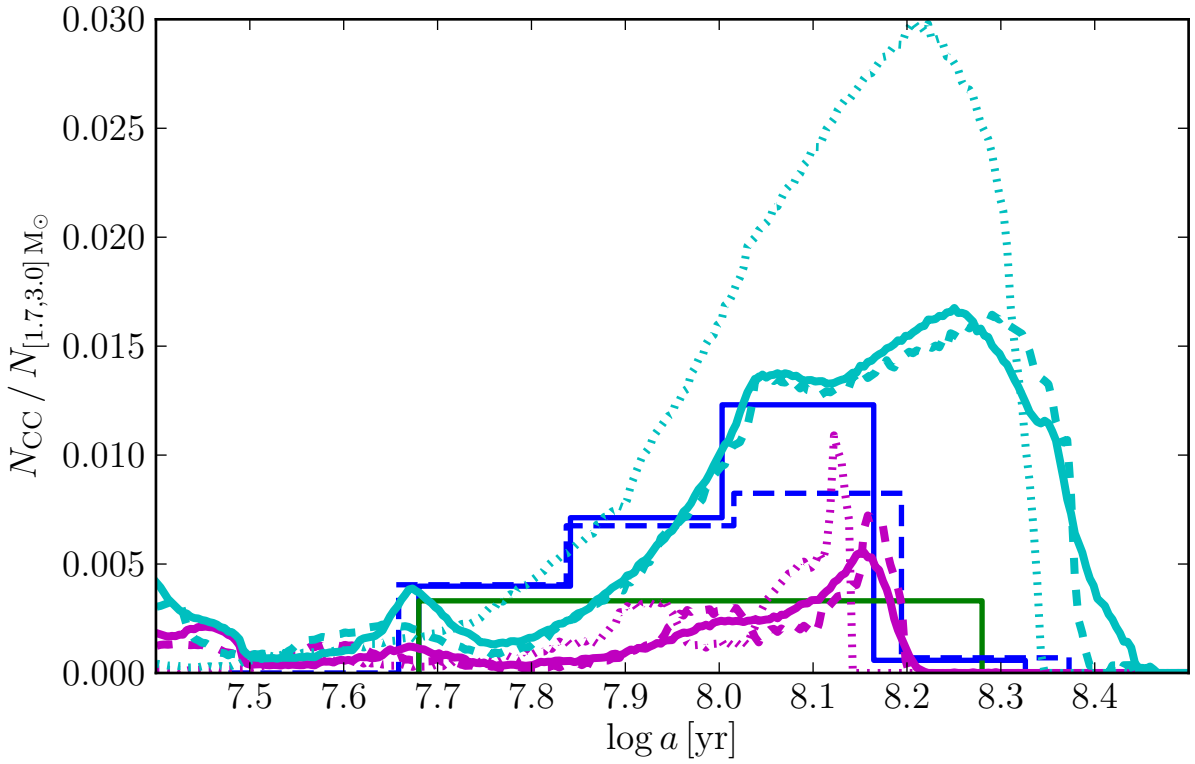

Figure 4.3: Comparison of predicted and empirical Cepheid fractions as a function of age at Solar metallicity, cf. Tab. 4.1. The predicted estimate was obtained via population synthesis, the empirical estimate is based on cluster Cepheids within 1 kpc from the Sun. The ordinate shows the number of cluster Cepheids divided by the number of Main Sequence stars with masses in the range $1.7 - 3\,M_\odot$. The relatively smooth lines are the results of population synthesis, in cyan (larger values) for the instability strip (IS) defined by Tammann et al. (2003), and in magenta (lower values) for the IS defined by Bono et al. (2000). Synthetic populations without rotation are plotted as dotted lines, rotating populations with $v/v_{\rm crit} = 0.4$ as dashed lines, and a distribution of initial rotation rates following Huang et al. (2010) is plotted as solid lines. Different "optimal" binning methods are applied to the observational cluster Cepheid sample, clearly showing the volatility due to small number statistics, see text.

While the present example shows an order-of-magnitude agreement between the empirical and predicted fractions for either the Bono or Tammann instability strips (at $Z_\odot$), no strong assertions can be made at this point due to the small number of cluster Cepheids and the large uncertainties related to counting MS stars in the observational sample. It is tempting to argue that the empirically-determined Cepheid fraction represents a lower limit, since a correction for contamination due to field stars would increase the fraction. However, the theoretically-determined fraction also likely represents an upper limit, since dynamical effects such as cluster expulsion and cluster disruption are not accounted for in the synthetic populations. Within these limitations and the uncertainties related to the adopted IS definitions, this comparison nevertheless shows that the fractions agree within an order of magnitude. A potentially more satisfying similar comparison is planned as part of the project described in Sec. 4.5 using Cepheid members of large star clusters in the MCs (e.g. Pietrzynski & Udalski 1999). For instance, in both NGC 1866 and NGC 2031 in the LMC are known to host more than a dozen Cepheids each (Testa et al. 2007).

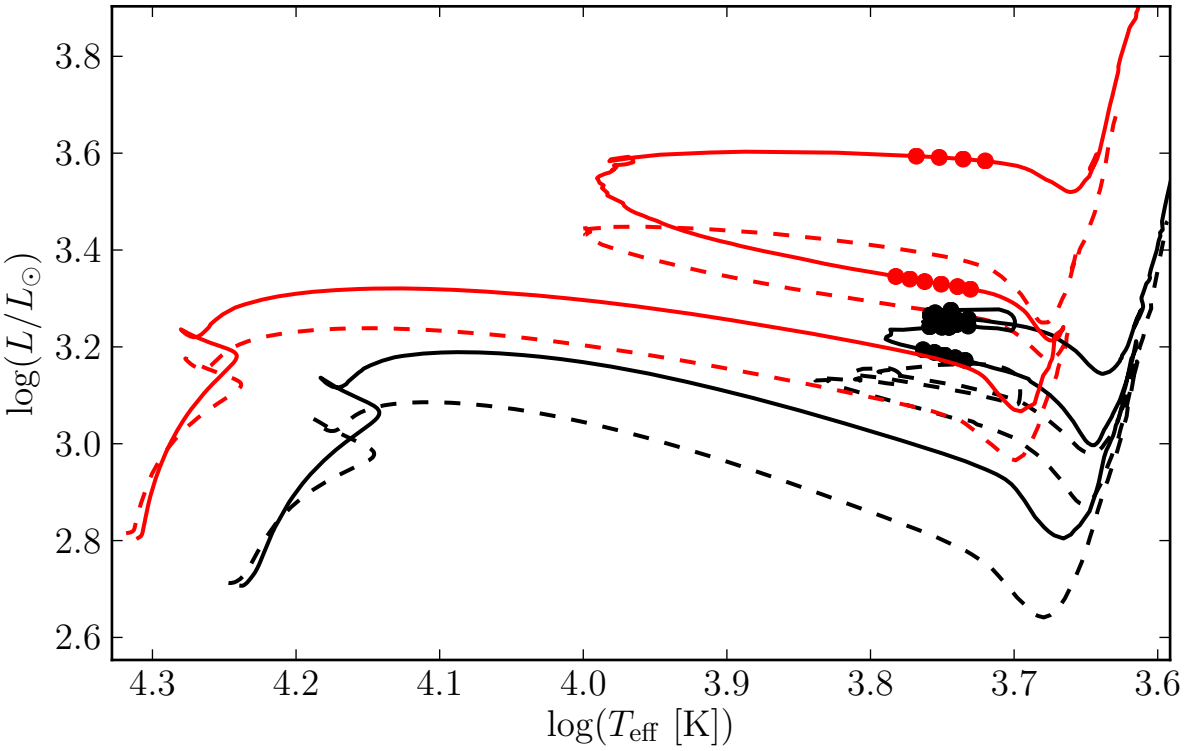

Figure 4.4: $5\,M_{\odot}$ evolutionary tracks of rotating (solid lines, $\omega = 0.5$) and non-rotating (dashed lines) models for Solar (black) and SMC (red) metallicity. IS crossings based on the Bono et al. (2000) IS boundaries for Solar and SMC metallicity are indicated by circles. For a given mass and IS crossing, both rotation and metallicity affect luminosity.

4.5 The combined effects of rotation and metallicity on Cepheid populations

The dense grid (Georgy et al. 2013b) of models was calculated for three different metallicities: Solar ($Z = 0.014$), LMC ($Z = 0.006$), and SMC ($Z = 0.002$). Hence, the work presented in Sec. 4.2 is straightforwardly extended to other metallicities, allowing to investigate the combined effects of rotation and metallicity on Cepheid populations. This investigation is planned for the near future, following the comparison of observations with the predictions at Solar metallicity. Here, I provide a short preview of how metallicity impacts mass-luminosity relations, focusing on the two extremes of Solar and SMC metallicity. Note that the IS boundaries vary with metallicity; for all metallicities, the IS boundaries by Bono et al. (2000) were adopted.

4.5.1 Comparison of Cepheid models at Solar and SMC metallicity

Figure 4.4 shows evolutionary tracks of $5\,M_{\odot}$. Solar metallicity non-rotating models are drawn in blue, $\omega = 0.5$ in green. SMC metallicity models ($Z = 0.002$) are drawn in magenta (non-rotating) and yellow ($\omega = 0.5$). The following immediate observations can be made:

1. SMC Cepheids of a given mass have higher luminosity than Solar metallicity Cepheids of the same mass and similar effective temperature.

2. Low-metallicity models lead to hotter stars, be it on the MS, the RGB, or during the Cepheid stage. The lower opacity (low metallicity = fewer absorbing species and less line blanketing)

allows the star to contract to smaller radii than Solar metallicity models, leading to higher effective temperature, cf. Eq. 1.3.

3. The SMC blue loops are much wider than the Solar ones and extend to higher temperatures. Stars spin up (increase $v_{\rm eq}$) along the blue loop towards greater temperature (contraction). Therefore, low-metallicity models can more easily reach critical velocities during the blue loop phase.

4.5.2 Mass-luminosity relationships at Solar and SMC metallicity

It was mentioned above that low-metallicity Cepheids are more luminous than high-metallicity Cepheids at a given mass and IS crossing. Figure 4.5 compares the mass-luminosity relations predicted for the SMC (red) and Solar (black) metallicity models for $\omega = 0.0$ (dotted lines) and $\omega = 0.5$ (solid lines). Since the appearance of blue loops is a little more chaotic for SMC metallicities than for Solar metallicities, some models with initial rotation rates other than $\omega = 0.5$ are included in the figure. These exceptions are: i) the $9\,M_{\odot}$ models, where $\omega = 0.3$ is used instead, since the $\omega = 0.5$ model no longer performs blue loops; ii) $\omega = 0.3$ is used for the $3\,M_{\odot}$ SMC track, since the $\omega = 0.5$ track's blue loop does not enter the IS. The figure allows the following immediate predictions for low metallicity Cepheid populations:

1. SMC metallicity models predict higher Cepheid luminosities than Solar models for all masses. The effect is in the order of $0.2 - 0.3$ dex for $5\,M_{\odot}$ Cepheids with similar rotation rates that lie on the same crossing.

2. Low-metallicity models predict a lower minimal mass for Cepheids than Solar models do. Since lower-mass stars are more frequent than high-mass stars (IMF effect), this leads to a higher fraction of Cepheids predicted in the SMC than in the LMC. This is consistent with the observed period distributions[8] in the SMC and LMC (particularly obvious in the OGLE-III Cepheid sample, see Soszynski et al. 2010).

3. The spread between second and third crossing (cf. Fig. 1.6) is much larger for SMC Cepheid models than for Solar metallicity models, irrespective of mass.

4. Metallicity leads to an additional (just as rotation does) source of intrinsic dispersion of the PLR of the MCs, since metallicity has an impact on luminosity and since stars in complex populations such as the SMC and LMC follow a distribution in metallicity.

In order to investigate further the question of dispersion in the PLR caused by rotation and metallicity, the population synthesis code could be adapted to include continuous star formation. Once this modification is made, the code could predict the Cepheid fraction in the MCs using the observationally constrained "recent" (up to ~ 500 Myr for Cepheids) star formation histories (Harris & Zaritsky 2004, 2009).

4.6 Results and implications

This section presents the preliminary results obtained from the first detailed investigation of the evolutionary effect of rotation on Cepheid populations. Recently, an investigation of the predictions for Solar metallicity has been submitted for peer-review. Further related work is already in preparation and will be carried out in the near future, including the detailed quantitative comparison of the predictions with observed quantities and the investigation of the combined effects

[8] The lower the metallicity, the shorter the shortest periods observed, and more Cepheids are observed in the SMC (4630, see Soszynski et al. 2010) than in the LMC (3361, see Soszynski et al. 2008)

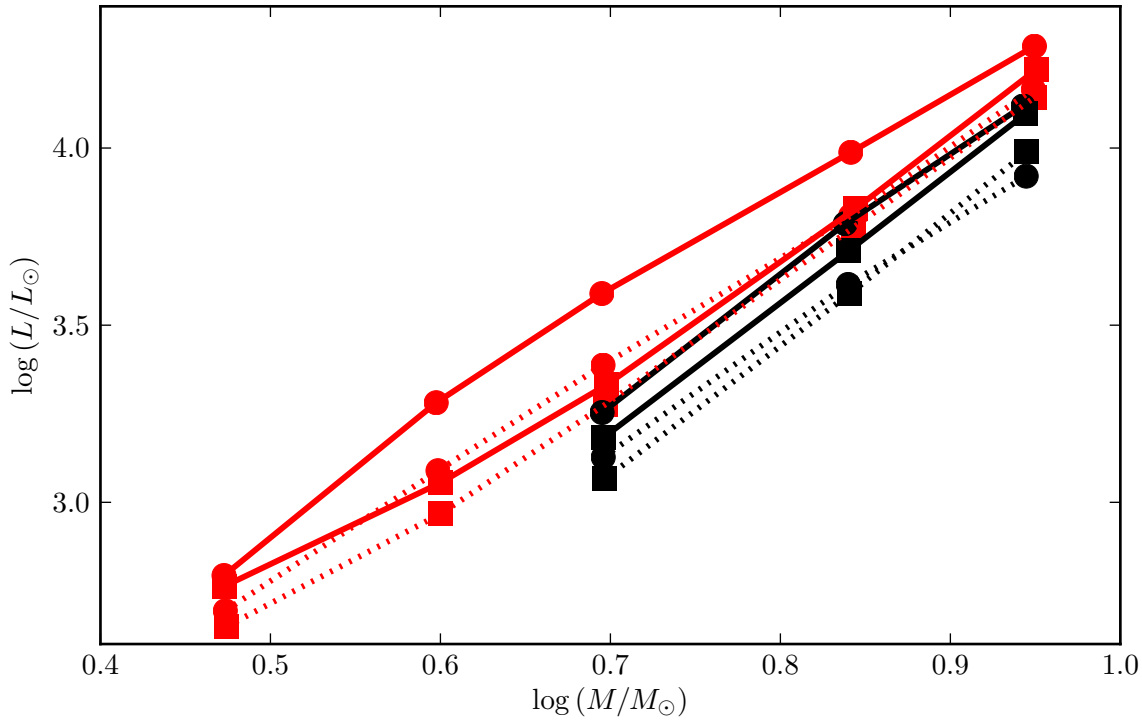

Figure 4.5: The mass-luminosity relation for non-rotating ($\omega \approx 0.0$) and rotating ($\omega \approx 0.5$) Cepheids for $Z = 0.014$ (black), and $Z = 0.002$ (red). Rotating models are connected with solid lines, non-rotating models are connected with dotted lines. Squares represent Cepheids on the second crossing, circles those on the third crossing (higher luminosity).

of metallicity and rotation. It is furthermore foreseen to investigate the pulsational stability of rotating Cepheid models with Prof. Hideyuki Saio in order to investigate in detail the intrinsic scatter of the PLR due to rotation.

The most important result obtained thus far is that rotation, together with accounting for the IS crossing number, impacts the M-L relationship in a way that can resolve the Cepheid mass-discrepancy, i.e., systematically higher Cepheid masses inferred from evolutionary models compared Cepheid masses derived with other methods, such as the pulsational masses (e.g. Caputo et al. 2005). Other solutions recently proposed to solve the mass discrepancy include pulsation-enhanced mass-loss and enhanced core overshooting (e.g. Neilson et al. 2011; Prada Moroni et al. 2012), although other authors have stated that the mass discrepancy problem is non-existent in modern evolutionary models (e.g. Cassisi & Salaris 2011). However, since rotation is clearly observed in stars and has profound evolutionary consequences, it should be difficult to ignore the impact of rotation on the mass discrepancy problem from now on.

Another result of the work so far is that rotation, contrary to higher convective core overshooting, makes specific predictions for several observable features, thereby enabling the models to be tested and constrained observationally. The key predictions are: i) intrinsic dispersion of the period-luminosity relation due to the distributed nature of initial rotation rates in any stellar population; ii) enhanced surface abundances for helium (affects pulsation amplitude) and nitrogen relative to oxygen or carbon (observable using spectroscopy); iii) non-negligible surface velocities, cf. also the determination of projected equatorial velocities in Sec. 2.5.

For the moment, the predicted enhancement of nitrogen is clearly larger than observed, cf. Sec. 4.4. However, no plausible explanation for a possible overestimation has been found yet, and

there are sufficient sources of uncorrected systematic observational offsets that may resolve this issue. Therefore, the cause of the discrepancy is unclear at this point.

Since rotation can also enhance surface abundances via mixing in the radiative outer envelope of early-type MS stars, it is not possible to exclude first-crossing Cepheids based solely on the observation of enhanced abundances. MS abundance enhancement increases with rotation rates and mass (in this order), and due to relative lifetimes, higher mass Cepheids (where higher MS enhancement is predicted) are more likely to be observed on the first crossing than their lower-mass counterparts.

Another potentially important result is that the rotating Geneva models predict post-MS stars to be consistently older than non-rotating post-MS stars (also Cepheids), since rotational mixing extends the MS lifetime. This effect is in the order of 20% and should be taken into account, e.g. when dating stellar populations or star formation histories using Cepheids as done e.g. in Matsunaga et al. (2011).

This investigation marks the first steps of establishing rotation as a key element in the Cepheid paradigm. Further investigations targeted at improving both the predictions and the observational tests will be carried out in the near future, focusing on features that can distinguish between rotational effects from those related to core overshooting.

Chapter 5

Conclusions

"The important thing is not to stop questioning.
Curiosity has its own reason for existing."

ALBERT EINSTEIN

This thesis started out with the basic idea to test stellar evolution models using populations of variable stars. How to achieve such a goal is, however, not immediately clear at the beginning of a thesis. Furthermore, the skills and tools required to carry out this research still have to be acquired and developed. In the process of developing my research, I was fortunate to have had a lot of freedom for defining my own research plans and developing my own ideas. This made researching an exciting adventure, sometimes to the point of feeling like a treasure hunt. Along the way, I was able to explore many different methods and techniques to perform astrophysical research, carrying out observations, analyzing data, and exploring theoretical models to satisfy my curiosity.

Now, however, is the time to review the fruit borne by the work invested during the past four years. Thus, this final chapter is intended to offer some concluding remarks on my thesis work, summarizing the key results and providing an outlook to future prospects. To this end, I have chosen a format intended to clearly show my contributions as a PhD student in Sec. 5.1.

At the end of this thesis, I have more questions than in the beginning. A key difference, however, is that I can now formulate my questions much better than before. This leads to new projects that I am eager to develop and explore as a post-doctoral researcher. A brief outlook to these and other future prospects is offered in Sec. 5.2.

5.1 Summary

During the past four years, I had the opportunity to research and learn about many different properties and characteristics of classical Cepheids. In this process, I have driven the creation of a sizable high-quality observational dataset, on which some concluding remarks are offered in Sec. 5.1.1.

Several methods were developed to analyze different kinds of observational or literature data. These techniques are summarized in Sec. 5.1.2, and the related discoveries are presented in Sec. 5.1.3.

Studying the predictions for Cepheids made by Geneva stellar evolution models has added an important theoretical component to this thesis and represents a first step to establish rotation as a

key element in the Cepheid paradigm. Results obtained from this chapter are summarized in Sec. 5.1.4.

The point of these conclusions is to be concise. Results are therefore stated briefly, and a reference is provided to the relevant chapters or sections of the thesis.

5.1.1 An unprecedented dataset of high-precision Cepheid radial velocities

In second year, I started an observing program that has grown from providing systemic radial velocities of Cepheids nearby open clusters to tracing shock propagation in Cepheid atmospheres. Chapter 2 describes the related details and applications, and the related discoveries made are summarized in Sec. 5.1.3 below.

5156 radial velocity (RV) measurements of 330 stars classified originally as Cepheid candidates were obtained over a duration of less than 3 years. A little more than 40% of these spectra were observed by myself, and the remaining nearly 60% by my friends and colleagues for whose contributions I am very grateful. Running this observing program was exciting and a great deal of fun, especially when time-critical observations provided results exceeding expectations. This was the case for instance for the two 6-hour continuous monitoring campaigns of RS Puppis, cf. Sec. 2.8, the discovery of cycle-dependent RV curves for QZ Normae, and the discovery that the line doubling pattern in X Sagittarii changes from one cycle to the next (Sec. 2.6).

The resulting observational dataset is unprecedented in its combination of size, precision, phase coverage achieved for certain objects, and the fact that Cepheids in both hemispheres were observed during all seasons. In a sense, this observing program was "all-sky", since Cepheids over the whole sky were observed, although as tracers of the Disk, Galactic Cepheids are mostly confined to a narrow region in the sky.

5.1.2 Methods developed and contributed to

A beautiful and challenging aspect of doing research is that it involves developing methods suited to resolve the problem(s) at hand. Developing a method can be regarded to be as important as obtaining a result, since the latter does not exist without the former. Hence, I summarize the principal methods developed and presented in this thesis. Although the methods presented here were developed primarily by myself, discussions, exchanging ideas, and brain storming sessions with friends and colleagues were essential for developing them. Unfortunately, it is virtually impossible to remember the contributions of everyone to each of these. Wherever this is possible, the people involved in these developments are acknowledged in the main sections.

Radial velocity drift corrections via ambient pressure measurements In Sec. 2.1.5, a novel technique for correcting pressure-induced RV drifts is presented. The technique is based on a simple model relating the variability of the air's refractive index to a drift in RV measured by the instrument. These drift corrections ensured maximum precision for observations obtained without simultaneous ThAr calibrations by removing systematic trends. Benchmarking this method on drift corrections determined using ThAr spectra reveals the technique to perform very well, provided other systematic variations (e.g. of temperature) are small. Drifts calculated via the model are systematically underestimated by approximately $4.7\,\mathrm{m\,s^{-1}}$, and show small ($10.3\,\mathrm{m\,s^{-1}}$) RMS scatter around the difference of the two methods. This method may be implemented in the *CORALIE* pipeline (and the *HERMES* RV scripts) in the future, improving precision especially of faint targets or for long exposures, where contamination of the science spectrum due to the interlaced ThAr spectrum must be avoided.

Testing Cepheid classification using cross-correlation functions In order to reduce contamination in the sample of Cepheids cross-matched with open clusters (cf. Chap. 3), I used cross-

correlation functions (CCFs) to test the classification status of 153 Cepheid candidates, see Sec. 2.4. Doing so demonstrated the potential of CCFs for variability classification and showed that most Cepheid candidates are well worth following up: 71% of (non-bona fide) Cepheid candidates observed turned out to be misclassified. 32 candidates were confirmed to be Cepheids and can now be considered bona-fide Cepheids. Both lists of objects will be made publicly available in the near future.

Estimating surface velocities of Cepheids using cross-correlation functions Rotation has been widely neglected in Cepheid studies, both observationally and theoretically. Using CCFs, projected rotational velocities, $v \sin i$ are estimated for 97 Cepheids in Sec. 2.5, demonstrating that rotational broadening is both present and detectable. The method developed here is based on Benz & Mayor (1984) and Santos et al. (2002), with two main modifications: i) a single point in phase is identified during which this estimate is expected to provide the most reliable result; ii) instead of color-index, CCF contrast is used to determine the non-rotational broadening in the Cepheids. The results imply that rotational broadening should not be neglected in spectroscopic studies of Cepheids, which is unfortunately common practice. Neglecting rotational broadening (which has a specific broadening profile different from macro-turbulence, for instance) may result in biased results of Cepheid atmospheric parameters such as temperatures, surface gravity, or surface abundances. The rotational velocities obtained will be used to test predictions of equatorial velocities during the Cepheid stage obtained from Geneva rotating evolutionary tracks (cf. Sec. 4.4) in a forthcoming publication that is currently in preparation.

Doppler tomography of Cepheids using cross-correlation functions Prompted by the observation of an apparent discontinuity in the BIS curve of RS Pup, a Doppler tomographic technique was developed to measure a velocity difference between two layers in a Cepheid's atmosphere, cf. Sec. 2.8. The method makes use of the high S/N afforded by cross-correlation functions and was developed independently, although it is conceptually similar to a method applied to long-period variable stars by Alvarez et al. (2001a). The high potential of this method is demonstrated by tracing shock wave propagation in the long-period Cepheid RS Puppis and discovering a cycle-dependence in the dynamical structure of QZ Normae's atmosphere. My plan is to further develop this method in the future and use it to study pulsational properties of pulsating stars across the instability strip.

Data mining for cluster Cepheids A modern data mining approach to determine membership of Cepheids in Galactic open clusters was created for the project presented in Chap. 3 and led to a first-author publication (Anderson et al. 2013a). The technique uses spatial, kinematic, and population-specific membership constraints (age & metallicity) to derive membership probabilities. Since the method used is identical for all cluster Cepheid combinations considered, confidence in membership can be ranked according to the probabilities computed. Currently, the method is limited by the input (catalog) data. In the *Gaia* era, methods compatible with large datasets will be vital in identifying objects of interest. The highly-precise, homogeneous, and diverse data gathered by *Gaia* will ensure that the full potential of the method can be exploited.

5.1.3 Observational discoveries made during this thesis

Several observational discoveries could be made using data from the observing program described in Sec. 2.1.1. Making these discoveries was one of my favorite things during the PhD, and felt a bit like hunting for treasure. Most of these are as-of-yet unpublished due to time restrictions, and this step is planned for the post-doctoral phase.

Spectroscopic binary nature of classical Cepheids In collaboration with Laszlo Szabados and his team, I was able to contribute to two publications, providing *CORALIE* data for GH Carinae for the first (Szabados et al. 2013b), and for all three Cepheids announced to be spectroscopic binaries in the second (Szabados et al. 2013a). These were cases where the observational baselines of *CORALIE* data alone were insufficient to make the discovery. For several other cases, however, *CORALIE* and *HERMES* data alone enabled such discoveries. In two of these, orbital solutions were derived, cf. Sec. 2.2. The orbital period of FN Velorum ranks $4^{\rm th}$ among the shortest for Cepheids. The orbital estimate of MU Cephei is still preliminary, since the orbital period is longer than the observational baseline. More data are required to achieve a good solution, although the binary nature of the star is obvious.

27 multi-lined spectroscopic binaries exhibiting photometric variability Among the sample of candidates found to be non-Cepheids in Sec. 2.4 are 27 multi-lined spectroscopic binaries, one of which is an SB3. These targets were classified photometrically as Cepheids and must therefore show photometric variability. This variability most likely originates in eclipses, although rotation or pulsation might also be noticeable in at least one of the components. Continued observational follow-up of this sample of stars using both photometry and spectroscopy would be useful with the potential to determine highly accurate stellar masses.

Evidence for shock-induced line splitting in LR Trianguli Australis *CORALIE* observations revealed that the short-period (2.4 d) Cepheid LR Trianguli Australis exhibits CCF profiles indicative of shock-related line splitting, see Sec. 2.6. This phenomenon has been observed in metallic lines (which are employed in the computation of CCFs) in only few (< 10) classical Cepheids. Notable known cases include X Sagittarii, V1334 Cygni, BG Crucis, η Aquilae, and X Cygni. CCFs obtained for the former three Cepheids resemble the CCF profiles of LR TrA.

Fast cycle-to-cycle variability of the CCF shape in X Sagittarii Figure 2.18 reveals that the shock-induced line splitting pattern responsible for the strange CCF shape observed in X Sagittarii ($P = 7.01$ d) changes significantly from one pulsation cycle to the next. This fact is observed during observations obtained in April, May, and July of this year with both instruments. Prior to this discovery, a variability of the line doubling pattern had been noted by Mathias et al. (2006), but no variability time scale was known, see Sec. 2.6. The variability of line doubling patterns is furthermore demonstrated to impact radial velocities derived using standard techniques.

Cycle-dependent radial velocity curves For RS Puppis and QZ Normae, two very different Cepheids, significant gradual and monotonous variations of RV curve shape are discovered over timescales exceeding 2 years using *CORALIE* data, see Sec. 2.7. In the case of QZ Nor, the cycle-dependent RV curve is later shown to correlate with systematic variations in the dynamical structure of the Cepheid's atmosphere using Doppler tomography, see Sec. 2.8.

Evidence of shock in RS Puppis A clear velocity discontinuity is discovered in the atmosphere of the long-period Cepheid RS Puppis using Doppler tomography, providing direct evidence for the presence of shock, cf. Sec. 2.8. RS Puppis is a particularly interesting object due to the presence of a very extended circumstellar environment. Following further development of the method, I plan to derive constraints and input for models of pulsation-driven mass loss (e.g. Neilson & Lester 2008) based on these observations.

Five new Galactic calibrators for the period-luminosity relation Using the astro-statistical method of membership determination for known Cepheids located nearby known Galactic open clusters described in Chap. 3, five new cluster Cepheid candidates were discovered (Anderson et al.

2013a). These are SX Carinae in ASCC 61, S Muscae in ASCC 69, UW Carinae in Collinder 220, ASAS J182714-1507.1 in Kharchenko 3, and V379 Cassiopeiae in NGC 129. For all of these, further observational follow-up will help to better constrain membership.

5.1.4 The Cepheid paradigm including rotation

The effect of rotation on populations of classical Cepheids is, for the first time, discussed in detail in Chap. 4. My work on this subject has thus far focused on Solar metallicity Geneva models, leading to an article that has been submitted to *A&A*, see Sec. 4.3. A preview of further investigations in progress is also provided, including a comparison of certain predictions to observations, and an investigation into predictions for lower metallicities representative of the Magellanic Clouds.

Predictions at Solar metallicity

The following quantitative predictions represent the key results from the investigation of the Solar models. A clear strength of the rotating models is that they make several testable predictions that can be uniquely linked to rotation, and therefore allow to distinguish the impact of rotation from other effects. This is crucial in order to argue in favor of rotation rather than (increased) convective core overshooting in the context of the Cepheid mass discrepancy problem. A crucial point to make here is that rotation leads to distributions of Cepheid parameters (luminosity, radii, surface abundances, pulsation periods and amplitudes, rotation rates, etc.) for a given mass, metallicity and age (crossing). When rotation is considered, such distributions arise naturally, since distributions of rotation rates are observed. Convective core overshooting, on the other hand, cannot be invoked to make the same prediction, since it is hardly plausible for core overshooting to vary from star to star.

There is no unique mass-luminosity relation for Cepheids at fixed Z Cepheid luminosity for a given mass depends on several factors. The most important ones are metallicity (see Sec. 4.5), rotation and the crossing number. The most accurate approach to derive mass-luminosity relations should consider the different crossings separately, as a function of initial rotation rate and metallicity. Neglecting the crossing (second or third) results in a systematic error that is in the order of 5% for Solar metallicity Cepheids, if ω is known. The combined effect of initial rotation rate and crossing number can impact inferred Cepheid masses by up to $\sim 17\%$, which is squarely in the range of the current mass discrepancy (e.g. Keller 2008). Thus, it appears that rotation can solve the Cepheid mass discrepancy problem without a need to invoke high values of convective core overshooting or enhanced mass loss.

Enhanced surface abundances do not unambiguously rule out first crossings for Cepheids Surface abundances (He, N) of early-type MS stars can be enhanced due to rotational mixing inside the radiative envelope, even before the first dredge-up occurs. For fast rotators in the higher mass-range ($\omega \geq 0.7$, $M \geq 7\,M_{\odot}$), abundances at the MS turn-off are predicted to be as high or higher than post-dredge-up abundances in non-rotating models.

Rotation increases MS lifetimes and leads to higher inferred Cepheid ages Rotation leads to longer MS lifetimes, since the core's hydrogen supply is replenished with material from outer layers. This effect propagates into the Cepheid stage, leading to $\sim 20\%$ older predicted Cepheid ages for models with $\omega = 0.5$ than for non-rotating models. This has implications for dating star formation events using Cepheids.

Surface rotation velocities are non-negligible The equatorial velocities predicted by the rotating models are in the order of $5 - 40\,\mathrm{km\,s^{-1}}$ and thus clearly detectable. The observability of rotational velocities was already pointed out by Maeder & Meynet (2000), although the dependence on crossing number, mass, and initial rotation rate is first explored in detail in this work. Statistically, hotter Cepheids should rotate faster than redder Cepheids of similar luminosity (fastest v_{eq} at the tip of the blue loop). This difference may be measurable, cf. also Sec. 2.5, although the unconstrained inclination angle presents a complication. Equatorial velocities predicted are generally higher on the second crossing than on the third, opening a new opportunity for constraining crossing numbers using surface velocities.

Rotation, metallicity, and crossing number create dispersion in the P-L relation Since initial rotation rates follow a distribution in real stellar populations, Cepheid progenitors present in any population are born with different values of ω. Since ω impacts luminosity, the distributed nature of initial rotation rates leads to a distribution in L. Analogously, additional dispersion will be present in populations with metallicity distributions, since luminosity is also metallicity-dependent. The luminosity spread of Cepheids on different crossings should also contribute significantly to the intrinsic scatter.

5.2 Outlook and perspectives

The above summary shows that I had the opportunity to investigate many interesting aspects and intriguing phenomena related to classical Cepheids during my thesis. Now, at the end of the thesis, some of these projects are nearly ready to be published, while others have just started. I am eager and excited to continue developing research ideas and methods, making new discoveries, and to continue working at the interface between observation and theory. This final section presents an outlook to the next steps I plan to take as a postdoctoral researcher and attempts to outline a guiding line for more research to come farther down the road.

5.2.1 Establishing rotation in the Cepheid paradigm

All stars rotate. Yet, rotation is a relatively new addition in the zoo of effects that are taken into account in the evolution of stars. In the case of Cepheids, rotation has not received much attention so far. this is probably because i) rotation is too slow to cause frequency splitting (and most Cepheids are mono-periodic); ii) as supergiants, Cepheids are expected to rotate slowly. However, as is shown in Chap. 4, rotation has profound implications for intermediate-mass MS stars that significantly affect evolutionary predictions in the Cepheid stage.

Rotation leads to testable predictions of observable parameters that provide opportunities to constrain and improve the models. Some of these predictions, specifically surface abundance enhancement and rotation velocities cannot be reproduced by increased convective core overshooting. This is important, since a new physical effect is likely to be widely accepted only if it performs significantly better than those already considered. This is one important goal that I would like to help achieve: anchoring rotation as a key element in the Cepheid paradigm.

Testing model predictions using observations

A crucial step towards the goal of establishing rotation as important for Cepheids is to carry out detailed observational tests of as many predicted quantities as possible. Particularly important to this end are quantities distinguishing rotation from core overshooting, i.e., ones that can provide a “smoking gun”.

Some first observational tests were shown in Sec. 4.4, and more have already been carried out as part of a publication in preparation. The comparison of observed and predicted abundance enhancement remains puzzling for the moment, and has already sparked discussions and an investigation of the related input physics of the models. The observational tests will first be completed for Solar metallicity Cepheids. Metallicity effects will be included later by studying Cepheids in the Magellanic Clouds.

An important quantity to consider are rates of period change for Cepheids. These probe essentially how fast a Cepheid evolves along the blue loops. Once pulsation periods can be estimated for rotating models, the predicted rates of period change can be compared to observed rates in the Galaxy and the MCs (e.g. Pietrukowicz 2001).

Baade-Wesselink radii (e.g. Groenewegen 2013) provide another excellent opportunity for testing model predictions.

Combined effects of rotation & metallicity on Cepheid populations

The study of the combined effects of rotation and metallicity will provide testable predictions in analogy to the investigation of Solar metallicity models. Section 4.5 presented a preview focusing on mass-luminosity relations. The tendency is clear, lower metallicity yields more luminous Cepheids, and inferred masses strongly depend on rotation, crossing number, and metallicity. A more detailed investigation of these combined effects is already in progress and will be compared to the plentiful observational data available for the MCs.

Pulsational instability analysis of rotating Cepheid models

As can be seen in Sec. 4.2, the predictions of the models currently strongly depend on boundaries of the adopted instability strip (IS). Since these boundaries have been derived using methods that are not necessarily consistent with the assumptions and input physics of rotating Geneva models, a self-consistent pulsational instability analysis for determining IS boundaries is indicated.

Rotation modifies stellar structure. Since pulsational instability depends on the location of the partial He ionization zone in the star's envelope, it is thus likely that the boundaries of the IS depend on rotation. Furthermore, predicted rates of period change appear to depend on initial rotation rate, see the submitted article in Chap. 4. However, the determination of these rates is currently too crude to make strong assertions, and it is therefore be very interesting to determine pulsation periods using the stellar structures computed for the grid of Georgy et al. (2013b).

Both IS boundaries and pulsation periods should be determined for all three metallicities covered by the models. An approach similar to that by Saio et al. (2013) would be ideal to this end, and a collaboration aimed at doing this has been started recently.

5.2.2 Doppler tomography of radially pulsating stars

Using Doppler tomography, I plan to study different types of radially pulsating stars comparatively. The goal of this project is to investigate how line doubling, cycle-dependent RV curves, and shock relate to each other for RR Lyrae stars, Miras, semi-regular variables, type-II and, of course, classical Cepheids. In doing so, I hope to improve the understanding of the envelope of stars and to provide observational constraints for models of pulsation-enhanced mass-loss (Neilson & Lester 2008). This possibility has become particularly interesting with the recent detections of circumstellar environments around Cepheids (Marengo et al. 2010; Matthews et al. 2012; Kervella et al. 2012).

As part of this project, better-suited line masks will have to be developed. In addition, specifically-targeted observations should be carried out, sampling different variability types, as well as different colors and periods for each variability type. Among the Cepheids, several promising candi-

dates have already been identified and will be observed extensively during upcoming observing runs at Euler in December 2013 and February 2014.

The cycle-dependent RV curves and dynamical structure of QZ Nor's atmosphere suggests a possible link with the Blazhko effect that is worth following-up. To this end, a first epoch of *HERMES* observations of RR Lyrae and V1154 Cygni has been obtained in July this year. These two objects are of particular interest, since extremely precise *Kepler* photometry is available[1], providing the opportunity to search for photometric signals associated with Doppler tomographic signs of cycle-dependent atmospheric velocity gradients observed in QZ Nor.

5.2.3 Sources of dispersion in the period-luminosity relation

Several results presented in this thesis have implications for the distance scale, although they were often obtained in studies carried out in different contexts. The most obviously distance-scale related result is the discovery of 5 new cluster Cepheids candidates that can be used to calibrate the period-luminosity relation in the Galaxy. Another important result seen in this thesis is that several effects can bias and create scatter in the PLR.

One well-known such effect is the contribution of parasitic flux by companions of binary Cepheids. To obtain the best distance estimates for individual Cepheids, binarity should be accounted for. In a statistical context it is furthermore important to constrain the binary fraction (which is an interesting topic in itself, see Sec. 2.2.1) and mass ratios in binary Cepheids, both in the Galaxy and elsewhere.

The newly-discovered cycle-dependent RV curves can cause a cycle-dependence of Baade-Wesselink distance estimates, which are among the most precise available. Continuing to study this effect will help to estimate its impact on the distance scale.

Shock may enhance mass-loss in Cepheids, potentially leading to extended light-attenuating circumstellar environments that lead to underestimated distances. Thus, detecting signs of shock among Cepheids and other stars obeying period-luminosity relations could perhaps be used to identify targets that are worth following up interferometrically.

Finally, crossing number, rotation, and metallicity are expected to create an intrinsic dispersion in the PLRs of real stellar populations, since both initial rotation rates and metallicity are distributed quantities in (complex) populations.

All of these effects increase the intrinsic scatter of the PLR, in addition to variable extinction across the field of view. In order to further improve the precision and accuracy of the PLR calibration, accounting for such effects will be necessary.

5.2.4 Cepheid research in the *Gaia* era

Soon after my thesis defense, the European Space Agency's cornerstone mission *Gaia* will be launched in a Soyuz-Fregat rocket from Kourou in French Guiana. *Gaia* has the enormous potential to revolutionize most fields of astrophysics by providing an astrometric census of one billion objects. According to recent estimates, up 9 000 Galactic classical Cepheids will be among the targets observed, and accurate absolute trigonometric parallaxes will be derived for most of them (Eyer et al. 2012b). These will enable a geometric calibration of the period-luminosity relations of Cepheids and other variable stars obeying such relations.

Thanks to extreme and unprecedented precision, the *Gaia* parallax-based PLR calibration will be very sensitive to the intrinsic scatter of the relation. Therefore, improving the understanding of these different effects will ensure the *Gaia*-based calibration to harvest its full potential. This is particularly important, since *Gaia* may partially rely on the PLR for self-calibration purposes at great distances (Windmark et al. 2011).

[1] For an overview of the most exciting *Kepler* results for RR Lyrae stars, see Kolenberg (2013)

Cepheids are primary calibrators of the distance scale, cf. Fig. 1.11, and the importance of the Cepheid PLR calibration can be expected to grow also in the extragalactic context thanks to future projects such as the Large Synoptic Survey Telescope (LSST) and the James Webb Space Telescope (JWST). For instance, thanks to LSST the number of Galaxies with observed Cepheids and supernovae will increase significantly. This will enable a much more solid tie-in of supernova type Ia and Cepheid distances via extremely precise space-based infrared photometry obtained with JWST. Therefore, improving the understanding and quantifying the impact of the various effects responsible for the intrinsic scatter of the PLR will ensure the most precise and accurate PLR calibration possible, leading to further improvements in the calibration of the Hubble constant, H_0.

A highly accurate ($< 1\%$) calibration of H_0 is required in order to significantly constrain cosmological parameters and detect deviations from standard ΛCDM cosmology (e.g. Suyu et al. 2012; Weinberg et al. 2013). As seen in Freedman (2013), three out of the five or six methods that are likely to yield this level of precision on H_0 depend on the calibration of the Cepheid PLR. However, as Fig. 5.1 (Planck Collaboration 2013) illustrates, several different methods to derive H_0 yield rather different results, despite impressive internal precision. Thus, it is particularly important to ensure not only the precision, but also the accuracy of the calibration of H_0 by investigating the origin of potential systematic effects that impact the Cepheid PLR.

The research presented in this thesis has touched upon several aspects related to the calibration of the PLR and its related sources of systematic observational error and theoretically expected intrinsic dispersion. Through the continued investigation and quantification of these effects and their impact on period-luminosity relations of pulsating stars, I will aim to improve the understanding of stellar pulsations and evolution, and to develop methods for mitigating systematic uncertainties involved in the calibration of H_0.

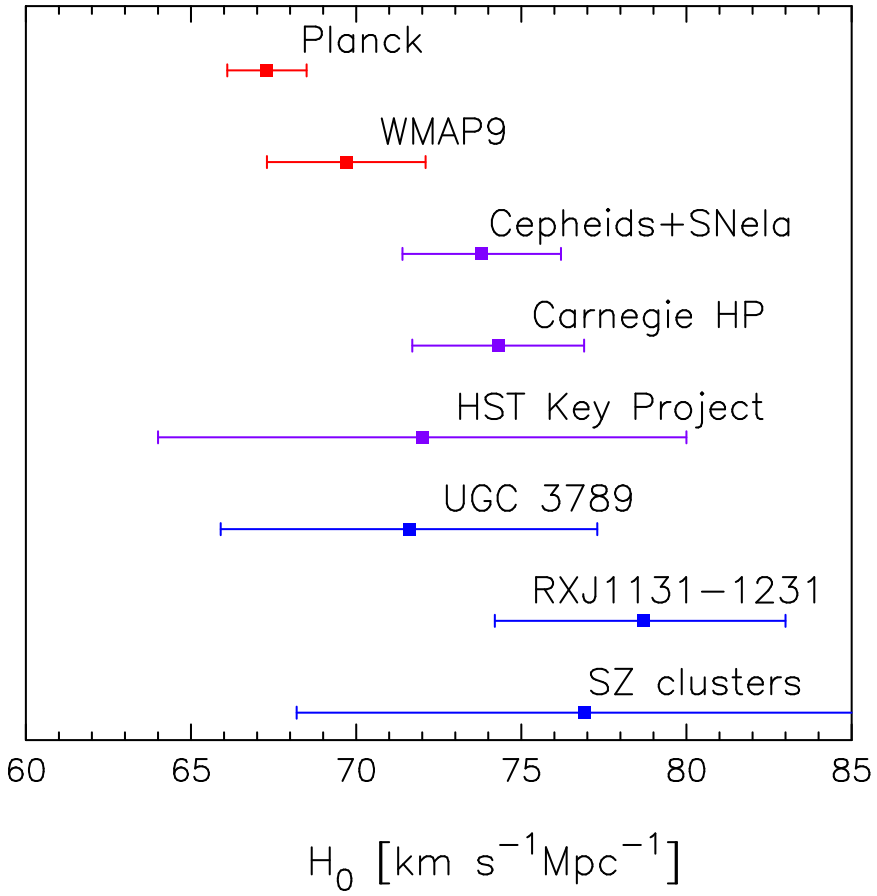

Figure 5.1: Different values for the Hubble constant H_0 as shown by the Planck Collaboration (2013).

Appendix A

Other activities and research performed during my PhD

During my PhD I had the opportunity to work on several very interesting subjects that were outside of the scope of this thesis, or that gave a result which represented a moot point. This appendix is dedicated to such work, and presents the results obtained in a very concise fashion. The topics discussed here are very varied and include spectroscopic, photometric, and astrometric projects dedicated to both Galactic and extragalactic objects.

A.1 Magnetic field measurements in solar-like stars

My first research endeavors in stellar astrophysics were dedicated to stellar magnetic fields, and in particular to the broadening of spectral lines due to the Zeeman effect. I started this work during my "Diplomarbeit" (Master's thesis) and finished it in the beginning of the PhD, before transitioning into my thesis topic. The results were published in a refereed article (Anderson et al. 2010) and presented at the conference "Cool Stars XVI" in Seattle, WA, USA (Anderson et al. 2011). Both documents produced are included below.

The goal of this work was to investigate detectability of Zeeman broadening in Stokes I using a state-of-the-art radiation transfer code (`STOPRO`, Rüedi et al. 1997; Frutiger et al. 2005) and very high-quality optical spectra obtained with the CES instrument at the ESO 3.6 m telescope located at ESO La Silla Observatory. A measurement of Zeeman broadening provides a direct measurement of the average magnetic field over the stellar surface, since the polarized σ-components of a spectral line are shifted in wavelength due to an applied magnetic field by

$$\Delta\lambda_B \propto g_{\rm eff} B \lambda^2 \,. \tag{A.1}$$

Here, B denotes magnetic field strength, $g_{\rm eff}$ is the effective Landé factor that describes the sensitivity of a spectral line to magnetic fields, and λ denotes wavelength. Using a set of lines spanning different Landé factors, one can therefore distinguish between magnetic and other line-broadening effects. Such estimates of the average magnetic field provide crucial constraints for stellar dynamo models used to explain the generation of stellar magnetic fields. However, Zeeman broadening in the optical is very small, complicating the measurement. One possible way out is to move to the infrared, since Eq. A.1 depends on λ^2, revealing Zeeman splitting in some cases (see e.g. Johns-Krull & Valenti 2000).

Many recent investigations of stellar magnetic fields have employed polarized light, which can pick up even very weak magnetic signatures, see the review by Donati & Landstreet (2009). Furthermore, such methods can recover the magnetic field *geometry* of the stars measured, e.g. in the

early type stars where dipole fields are frequent. However, a major shortcoming of techniques based on polarized Stokes V alone is that they are only sensitive to the longitudinal field component, B_ℓ, cf. Reiners (2011). This leads to two problems: i) the total magnetic flux and hence the energy stored in the field, is unconstrained; ii) on stars with complex surface fields, such as cool stars, randomly oriented field lines can cancel out each other's contribution to B_ℓ. Hence, methods including the unpolarized component of the light, Stokes I, remain crucial in order to provide constraints on the energy stored in the magnetic field.

The main result of this study was that Zeeman broadening is detectable in optical Stokes I, provided the average magnetic field is in the order of $500\,\mathrm{G}$ or higher. However, the results were found to be quite sensitive to the assumed surface temperature distribution (spots, plages). Hence, a concluding cautionary note was issued regarding previously announced detections of stellar magnetic fields based on line broadening techniques. For more details, please see the paper included below.

A&A 522, A81 (2010)
DOI: 10.1051/0004-6361/201014769

Astronomy & Astrophysics

On detectability of Zeeman broadening in optical spectra of F- and G-dwarfs⋆,⋆⋆

R. I. Anderson[1,2], A. Reiners[2], and S. K. Solanki[3,4]

[1] Observatoire de Genève, Université de Genève, 51 Ch. des Maillettes, 1290 Sauverny, Switzerland
[2] Institut für Astrophysik, Georg-August-Universität Göttingen, Friedrich-Hund-Platz 1, 37077 Göttingen, Germany
[3] Max-Planck-Institut für Sonnensystemforschung, Max-Planck-Straße 2, 37191 Katlenburg-Lindau, Germany
[4] School of Space Research, Kyung Hee University, Yongin, Gyeonggi 446-701, Korea
e-mail: richard.anderson@unige.ch

Received 12 April 2010 / Accepted 11 August 2010

ABSTRACT

We investigate the detectability of Zeeman broadening in optical Stokes I spectra of slowly rotating sun-like stars. To this end, we apply the LTE spectral line inversion package SPINOR to very-high quality CES data and explore how fit quality depends on the average magnetic field, Bf. One-component (OC) and two-component (TC) models are adopted. In OC models, the entire surface is assumed to be magnetic. Under this assumption, we determine formal 3σ upper limits on the average magnetic field of 200 G for the Sun, and 150 G for 61 Vir (G6V). Evidence for an average magnetic field of ∼500 G is found for 59 Vir (G0V), and of ∼1000 G for HD 68456 (F6V). A distinction between magnetic and non-magnetic regions is made in TC models, while assuming a homogeneous distribution of both components. In our TC inversions of 59 Vir, we investigate three cases: both components have equal temperatures; warm magnetic regions; cool magnetic regions. Our TC model with equal temperatures does not yield significant improvement over OC inversions for 59 Vir. The resulting Bf values are consistent for both. Fit quality is significantly improved, however, by using two components of different temperatures. The inversions for 59 Vir that assume different temperatures for the two components yield results consistent with 0−450 G at the formal 3σ confidence level. We thus find a model dependence of our analysis and demonstrate that the influence of an additional temperature component can dominate over the Zeeman broadening signature, at least in optical data. Previous comparable analyses that neglected effects due to multiple temperature components may be prone to the same ambiguities.

Key words. line: profiles – techniques: spectroscopic – Sun: surface magnetism – stars: late-type – stars: magnetic field

1. Introduction

Cool stars display a range of phenomena that are typical of magnetic activity, such as dark spots present at the stellar surface (see Berdyugina 2005, for a review), enhanced chromospheric emission in, e.g., the Ca II H and K lines (e.g., Wilson 1994; Pizzolato et al. 2003; Hall & Lockwood 2004), flares (e.g., Favata et al. 2000; Maggio et al. 2000) and coronae (Schmitt 2001). Although these manifestations of stellar activity and hence of the underlying magnetic field are well detected for large samples of stars, measuring the magnetic field itself turns out to be difficult on most cool stars. The reason is the complex small-scale geometry of the field, that is amply evident on the Sun. The mixture of nearly equal amounts of magnetic flux of opposite polarities on the stellar disk leads to cancellation of the circular polarization signal due to the longitudinal Zeeman effect, the most straightforward diagnostic of a stellar magnetic field.

Rapid stellar rotation partly removes the degeneracy between opposite magnetic polarities that lie sufficiently far apart on the stellar surface and thereby enables detection of a net (circular) polarization signal. Consequently, the magnetic field can be mapped on the stellar surface from the variation of the spectral shape and amplitude of this polarization signal over a stellar rotation, with the help of the Zeeman Doppler Imaging (ZDI) technique (Semel 1989), which has been successfully employed to reconstruct the large-scale distribution of the magnetic flux on the surfaces of a number of stars (Donati 2008; Donati & Landstreet 2009).

In spite of its success, ZDI does have some limitations. First, unless the field is homogeneously and unipolarly distributed on large scales, ZDI detects only some fraction of the true magnetic flux on the stellar surface. Second, the same is true for the measured field strength and hence the magnetic energy density. In general, the field strength is underestimated and consequently the magnetic energy density is even more strongly underestimated, since it is proportional to the square of the field strength (see Reiners & Basri 2009). Third, ZDI is limited to comparatively rapidly rotating stars. The slower a star rotates (or rather the smaller its $v \sin i$) the lower the spatial resolution of the stellar surface (and of the magnetic field) that can be achieved.

Therefore, the method proposed and applied to cool stars by Robinson (1980); Robinson et al. (1980), of looking for changes in the line profile shape of the intensity (Stokes I) due to Zeeman splitting, remains an interesting technique to complement ZDI. In particular, it allows an estimate of the total magnetic flux as well as of the field strength and filling factor to be obtained (and hence also of the magnetic energy density).

Zeeman broadening in stellar spectra (ZB) was first measured by Preston (1971) to determine the average surface magnetic fields of Ap stars. Robinson et al. (1980) then measured ZB in cool stars using his Fourier-based method which was taken

⋆ Based on observations collected at the European Southern Observatory, La Silla.
⋆⋆ Appendix A is only available in electronic form at http://www.aanda.org

A&A 522, A81 (2010)

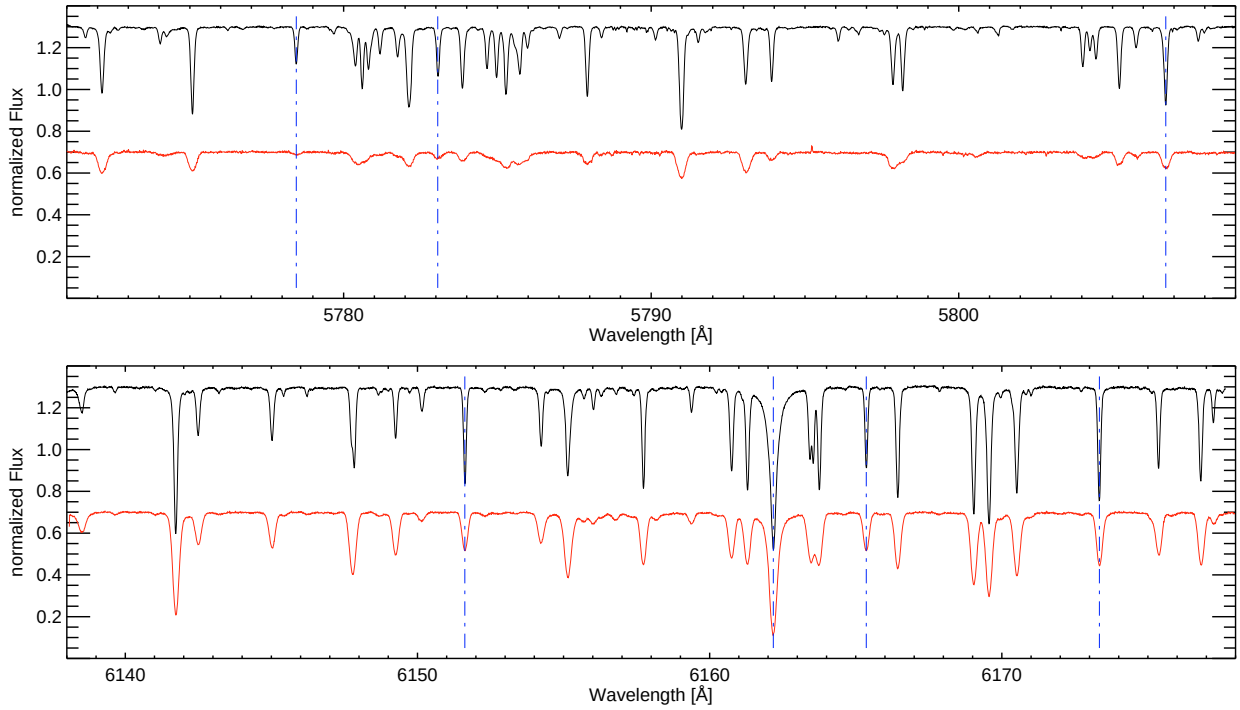

Fig. 1. Sample CES spectra illustrating data quality. Continua are shifted by ±0.3 from unity for visibility. Blue dash-dotted vertical lines indicate spectral lines used for analysis. *Upper panel*: data set A. Upper black spectrum: sunlight reflected from Jupiter's moon Ganymede; lower red spectrum: HD 68456 (F6V, $v \sin i \approx 10\,\mathrm{km\,s^{-1}}$). *Lower panel*: data set B. Upper black spectrum: inactive and slow rotator 61 Vir (G6V); lower red spectrum: active and faster rotator 59 Vir (G0V, $v \sin i \approx 6.5\,\mathrm{km\,s^{-1}}$).

up and extended by other authors (Gray 1984; Marcy 1982). It was soon realized, however, that the assumptions made in these Fourier techniques were too crude. Thus, a shift towards ever-improving forward radiative transfer calculations occurred. The development of these techniques was driven, among others, by Saar (1988, 1990b, 1996); Basri & Marcy (1988); Linsky et al. (1994); Rüedi et al. (1997); Johns-Krull & Valenti (2000).

The displacement of a circularly polarized σ-component from line center can be expressed by:

$$\Delta\lambda_B \approx 4.67 \times 10^{-13}\, g_{\mathrm{eff}}\, B\, \lambda^2 \quad [\text{Å}]. \tag{1}$$

For values typical of optical spectral lines, Eq. (1) demonstrates that even a comparatively strong field field along LOS is hard to detect. $Bf = 1\,\mathrm{kG}$ would produce a Zeeman splitting of merely $\lambda_B = 17\,\mathrm{mÅ}$ for the σ-components of a normal Zeeman triplet of a hypothetical line at 6000 Å with $g_{\mathrm{eff}} = 1.00$, or $\lambda_B = 42\,\mathrm{mÅ}$ in the case of a more sensitive $g_{\mathrm{eff}} = 2.50$ line. This should be compared to the line width of a typical stellar line profile broadened thermally and due to turbulence by $2\text{–}6\,\mathrm{km\,s^{-1}}$ (i.e. 30–60 mÅ), as well as by rotation between 0 and $5\,\mathrm{km\,s^{-1}}$ (i.e. up to 100 mÅ). In addition, the resolution element at even very high resolving power, R, is comparable in size, e.g. $\delta\lambda = 27\,\mathrm{mÅ}$ for $R = 220\,000$.

The present paper has a two-fold purpose. On the one hand, it is in the tradition of increasing the realism and accuracy of magnetic field measurements on cool stars. It applies state of the art inversion techniques to determine the magnetic field. Also, from observations of the Sun it is clear that magnetic fields are associated with significant brightenings or darkenings, which are generally neglected when measuring stellar magnetic fields. In the present paper we have carried out first simple computations looking at the effects that including such a diagnostic would have. We do not propose that this is an exhaustive or final study, but it can be considered as a first indicator. Finally, these techniques are also applied to spectral time series of an active star that has so far not been studied in this respect.

2. Data

2.1. Instruments and reduction

Spectra of the stars investigated were obtained with the Coudé Échelle Spectrometer (CES) at the 3.6 m ESO telescope at La Silla, Chile. This fiber-fed spectrometer achieved a spectral resolving power of approximately 220 000 using an image-slicer and projecting only part of an order onto the CCD, resulting in a small wavelength coverage of approx. 40 Å.

Spectra from two data sets were used in this work: data set A, with $5770 < \lambda < 5810$ Å, observed on 13 October 2000 (solar spectrum) and 2 October 2001 (HD 68456), and data set B, $6137 < \lambda < 6177$ Å, observed on 7 May 2005 (HD 68456, 59 Vir). Sample spectra from both sets are shown in Fig. 1. We refer to Reiners & Schmitt (2003, hereafter R&S03) for more details, as data set A was originally taken for the project described in that publication.

Where necessary, continuum normalization corrections were performed by division of linear slopes fitted to the original continuum. Spectra were shifted to laboratory rest-wavelengths, by cross-correlation using the FTS solar atlas (Kurucz et al. 1984).

2.2. Objects, spectral lines, and atomic line information

In this work, we present results for 4 objects ranging in spectral type from F6V to G6V, including sunlight reflected from

Ganymede (previously and hereafter referred to as the solar spectrum). These stars were especially suitable for our analysis for multiple reasons. First, identification of spectral line blends was facilitated in the effective temperature range covered by these stars and LTE atmospheres were readily available (Kurucz 1992). Second, the analysis of stars with relatively low projected rotational velocities, $v \sin i \lesssim 10$ km s^{-1}, allowed us to fully exploit the high resolving power of the data and minimizes effects due to differential rotation. Third, measured stellar parameters such as effective temperature, $T_{\rm eff}$, surface gravity, $\log g$ and elemental abundances, [Fe/H] in particular, were available as constraints and could be directly input into the inversion procedure. Last, but not least, measured X-ray luminosities, $L_{\rm X}$, and previously reported magnetic field detections could be considered as indicators for the presence of magnetic fields (Saar 1990b) and thus helped to constrain the sample.

Within the small wavelength coverage of the CES spectra, only few relatively blend-free lines could be identified. Among these, we searched for combinations of lines that provide strong constraints on atmospheric properties. For instance, lines of different excitation potentials, $\chi_{\rm e}$, have different temperature sensitivities and often probe different heights (depending also on their equivalent widths). Therefore they constrain temperature stratification. In order to exploit the differential effect of Zeeman broadening, we aimed to cover the largest possible range in $g_{\rm eff}$ as well as to use the line with the greatest possible $g_{\rm eff}$.

Most spectral lines could be identified in the postscript version of the FTS solar atlas available online. The remaining lines and blends were identified by searching the Vienna (Kupka et al. 2000, hereafter VALD) and Kurucz & Bell (1995) atomic line databases. These databases further provided the atomic line data, such as level configurations and $\log(g^* f^*)$ values required for the forward radiative transfer calculations, cf. Sect. 3. Effective Landé values, $g_{\rm eff}$, were calculated from the atomic level configurations following Beckers (1969). The calculated effective and empirical Landé factors determined by Solanki & Stenflo (1985) were found to agree for all but one line: Fe I at 6165.36 Å, for which $g_{\rm emp} = 0.69$ and $g_{\rm eff} = 1.00$. However, this line contains a blend at 6165.36 Å, for which $g_{\rm eff} = 0.67$, cf. Table 1.

For some lines, ranges of $\log(g^* f^*)$ values were found in VALD. We aimed to determine the best $\log(g^* f^*)$ value for our selected lines by means of a by-hand gauging procedure using the solar spectrum for data set A and that of 61 Vir for data set B, while taking care to stay as close to the literature values as possible. This approach was adopted in order to avoid multiple additional free fit parameters, since one $\log(g^* f^*)$ for each blend would have been required. An automated approach would have been dominated by degeneracy between oscillator strengths and stellar model parameters.

Table 1 lists all lines used and parameters adopted in our inversions. Horizontal spacings help distinguish between blends contributing to the shape of a given spectral line and different lines. Column 1 lists abbreviations used in this paper for the respective line sets. Column 2 contains wavelength in Å. Column 3 the corresponding ion in spectroscopic notation, i.e. Fe I is neutral iron. Column 4 lists $\log(g^* f^*)$ adopted after gauging with the closest literature value in brackets, if a value outside the VALD range was adopted. Columns 5 and 6 contain excitation potential of the lower level of the transition, $\chi_{\rm e}$, and effective Landé factor, $g_{\rm eff}$, respectively. The range in Landé factor covered by line set A3 is thus $\Delta g_{\rm eff} = 1.08$, and $\Delta g_{\rm eff} = 1.50$ for line sets B3 and B4, not counting blends. More importantly, the maximum $g_{\rm eff}$ is larger by 0.5 in line sets B3 and B4 than in line set A3.

Table 1. Spectral lines and their parameters used in inversions.

Line Set	λ [Å]	Ion	$\log(g^* f^*)$	$\chi_{\rm e}$ [eV]	$g_{\rm eff}$
A3:	5778.46	Fe I	−3.53	2.59	1.21
	5783.06	Cr I	−0.57 (−0.50)	3.32	2.00
	5783.11	Cr I	−1.32 (−1.82)	3.56	0.75
	5806.73	Fe I	−0.99	4.61	0.92
	5806.63	Fe I	−2.19 (−2.09)	4.91	1.50
	5806.73	Sc II	−3.02	1.36	1.67
B3:	6151.62	Fe I	−3.30	2.18	1.83
	6165.36	Fe I	−1.51	4.14	1.00
	6165.12	Fe I	−2.76	5.09	0.67
	6173.34	Fe I	−2.88	2.22	2.5
	6173.03	Eu II	−0.86	1.32	1.70
B4:	Same as B3 plus				
	6162.18	Ca I	−0.17	1.90	1.25

Notes. Horizontal lines group lines set. Spectral lines are separated by small spacings indicating which blends belong together. Dominant line components are listed first, blends follow by ascending wavelength. Brackets indicate the closest $\log(g^* f^*)$ (oscillator strength) literature value, if values outside the literature range were adopted.

Table 2. Logarithmic elemental abundances adopted on scale where hydrogen equals 12.

Name	HD	[Ca/H]	[Sc/H]	[Cr/H]	[Fe/H]	[Eu/H]
Sun	–	6.36	3.17	5.67	7.50	0.51
GJ 297.1	68456	6.10	2.90	5.37	7.19	0.35
59 Vir	115383	6.57	–	–	7.78	0.70
61 Vir	115617	6.36	–	–	7.55	0.50

Therefore, a stronger sensitivity to ZB in the latter two data sets can be expected.

Collisional damping parameters are derived internally by SPINOR from cross-sections published by Anstee & O'Mara (1995); Barklem & O'Mara (1997); Barklem et al. (1998) and are not listed in the table.

Table 2 lists the elemental abundances adopted. Solar abundances used were those determined by Grevesse & Sauval (1998) and served as the absolute scale for relative stellar literature values found in Valenti & Fischer (2005, from hereon V&F05) (59 Vir & 61 Vir) and Cayrel de Strobel et al. (1997) (HD 68456).

Lines that correspond to elements for which no abundance measurements were found were usually not included in the inversions. For the Cr I line in A3 as well as some blends, e.g. Eu II in B3, abundances were estimated from an iterative fitting procedure that took into account published average metallicities. This procedure is potentially flawed, since general abundances are not necessarily correlated with individual abundances. However, this flaw does not challenge the work presented here, since Fe I lines were the most important ones for our analysis and literature values for iron were available for all stars. The Cr I line was of great importance only for the solar case, for which measurements of

A&A 522, A81 (2010)

the chromium abundance (and also that of scandium) do exist. The blend due to Eu II was only of secondary significance, given its small impact on line shape. It was not discarded, however, since it provided continuum points for (at least the blue wing of) the Zeeman-sensitive 6173.3 Å line, for which the red wing was cut off due to the presence of unidentified blends.

One well known Zeeman sensitive line was omitted from the analysis, Fe II at 6149.24 Å. This line is very sensitive to magnetic fields due to its particular (doublet) Zeeman pattern, and displays clear Zeeman splitting in spectra of Ap stars (e.g. Mathys 1990; Mathys et al. 1997) and solar penumbrae (e.g. Lites et al. 1991). Unfortunately, this line is affected by blends in both line wings, as can be seen in Fig. 1 and we were not able to adequately reproduce these blended wings. While the blue wing blend is quite obvious, the red wing blend requires closer inspection. This blend is (at least in part) due to Ti I at 6149.73 Å and is hard to see due to rotational broadening, blending in with the smaller unidentified signatures seen in the slower rotator 61 Vir. This leads to the wing of the line just barely missing the continuum. Due to these two blended wings, the 6149.24 Å Fe II line profile used for inversion had either a badly defined continuum (the deviation from the continuum is around 1%), or lacked both line wings (if they were both cut off as was done for the red wing of the 6173 Å Fe II line) which meant not having any continuum points at all. Using either approach, we were not able to reach the same level of fit precision as presented for the other lines used in this analysis. Therefore, we chose to omit this line from our analysis.

Our results depend on the assumed Signal-to-Noise ratio (S/N), since $(S/N)^{-1} = \sigma_i$ and

$$\chi^2 = \sum_{i,j} \frac{\left(I_{ij} - I'_{ij}\right)^2}{\sigma_i^2}, \tag{2}$$

where σ_i is significance, i line index, j data point index for a given line, I_{ij} measured and I'_{ij} calculated intensity normalized to the continuum value. We determined σ_i from the mean continuum standard deviation of the spectra. The typical S/N ratio thus determined was 400−700, corresponding to σ between 0.0025−0.00143. Less statistical weight was assigned to the pressure-sensitive Ca I line at 6162.18 Å by lowering significance to $\sigma = 0.0040$, since the wings of the line are heavily blended and asymmetric. Furthermore, the core of this line is affected by non-LTE effects and was therefore removed from the measured line profile.

In every line, we aimed to take full account of line blends and included as many data points reaching as far as possible into the continuum, since ZB affects the far line wings most strongly. However, some line wings had to be severed farther from continuum than others, since unidentified blends were present; see, for instance, the far red wing of the Zeeman-sensitive line at 6173.34 Å Fe I. This line wing showed strong contributions from at least one blend that could not be identified in line databases. To circumvent this problem, Rüedi et al. (1997) included fake iron blends until the line shape was matched. We chose not to introduce additional fit parameters, and instead decided to sever the far red line wing.

3. Analysis

We use spectral line inversion as the tool to explore detectability of ZB in this paper. Spectral line inversion denotes a combination of two things: forward radiative transfer calculations and an iterative non-linear least squares fitting process. In other words, spectral line profiles are calculated using a given atmospheric model and model parameters are iteratively adjusted until the highest possible agreement between calculated and observed spectral lines is reached. The resulting best-fit model parameters thus characterize the adopted atmospheric model and, if the model is assumed to be correct, the actual stellar atmosphere. Hence, we investigate whether introducing a magnetic field significantly improves the agreement between observed and calculated line profiles. We explain the general approach of spectral line inversion in the following subsection.

We further investigate model-dependence and the influence of model assumptions. To this end, two different kinds of models are used. These fitting strategies are documented in Sect. 3.2.

3.1. Spectral line inversions

We employ the spectral line inversion package SPINOR developed and maintained at ETH Zürich and MPS Katlenburg-Lindau for this analysis. In short, SPINOR computes synthetic intensity profiles (SIPs), $L(\lambda)$, by solving the radiative transfer equation on a grid of optical depth points τ, accounting also for turbulence, rotation, magnetic fields, instrumental effects, etc. It then determines the model parameters used to compute $L(\lambda)$ that best fit the observed data using a non-linear least squares fitting algorithm. We now briefly discuss how the SIPs used for inversion are calculated and refer to Frutiger et al. (2000, 2005, from hereon Fru00 and Fru05, respectively) for further information regarding SPINOR.

First, annular SIPs, $I(\lambda, \theta)$, are computed as a sum of weighted Voigt profiles (cf. Gray 2008, from hereon Gr08) combining thermal and pressure broadening, microturbulence (mass motions on a scale that is much smaller than the optical depth lead to a Doppler broadening due to a Gaussian velocity dispersion), $v_{\rm mic}$, and the full Zeeman pattern as described below. "Annular" here denotes the θ-dependence, since synthetic profiles are calculated for each of 15 concentric annuli that taken together approximate a flux profile resulting from a much larger number of intensity profiles at different viewing angles (Rüedi et al. 1997; Fru05). By calculating annular SIPs at different angular distances from disk center, we can include limb darkening due to its dependence on $\mu = \cos\theta$.

To calculate the radiation transfer, we start with tabulated LTE atmospheres (Kurucz 1992). These atmospheres list the parameters temperature, pressure and electron pressure for a number of τ values and are calculated for given effective temperatures, $T_{\rm eff}$, and continuum opacity at 5000 Å. In general, the temperature values are allowed to vary in order to obtain an optimal fit to the spectral lines. Then, the whole temperature stratification $T(\tau)$ is shifted up or down. At each step in the inversion the atmosphere is always consistently maintained in hydrostatic equilibrium. Hence, from a prescribed temperature stratification, the gas and electronic pressures, the gas density and continuum opacity are computed assuming hydrostatic equilibrium. Note that temperature values returned by SPINOR correspond to unit optical depth calculated for continuum opacity at 5000 Å.

The Zeeman shifts and amplitudes of the polarized components are calculated as explained in, e.g. Wittmann (1974). A detailed description of the implementation of the Zeeman effect in SPINOR can be found in Frutiger (2000, and references therein).

In a next step, the individual annular $I(\lambda, \theta)$ are convolved with radial-tangential macroturbulence profiles, $\Theta(\lambda, \theta)$, that are intended to account for large-scale motion due to convection.

These profiles are described in Gray (1975) and Gr08. Thus, we obtain new annular SIPs, $I'(\lambda,\theta) = I(\lambda,\theta) * \Theta(\lambda,\theta)$, where "$*$" denotes convolution carried out as multiplication in Fourier space. In accordance with Fru05, we assume equal surface fractions covered by radial and tangential flows.

The radial velocities of individual surface elements vary across the stellar disk as a function of distance to the rotation axis, leading to rotational broadening in the integrated spectrum of a point source. This dependence is taken into account by introducing 15 new angles, ϕ, so that the radial velocity is constant at any given ϕ. Thus, the $I'(\lambda,\theta)$ are turned into $I'(\lambda,\theta,\phi)$ and each one is shifted for radial velocity. The disk-integrated line profiles are obtained by weighting the individual $I'(\lambda,\theta,\phi)$ for surface coverage, and summing up.

We obtain the final SIP, $L(\lambda)$, by computing $L(\lambda) = I'(\lambda) * I_{\rm inst}$, that is by convolution of $I'(\lambda)$ with an instrumental broadening function, $I_{\rm inst}$. $I_{\rm inst}$ is a Gaussian function with a FWHM defined as a velocity, $v_{\rm inst}$, in km s^{-1} that corresponds to the resolving power of CES. Hence, we have $R = 220\,000 = \lambda/\Delta\lambda = c/v_{\rm inst}$. Therefore, for CES, $v_{\rm inst} = 1.36$ km s^{-1}.

Summing up, our model parameters are: temperature T_1 (and T_2 for two-component inversions, cf. Sect. 3.2.2), in Kelvin at unit optical depth; surface gravity $\log g$ in cgs units; projected rotational ($v \sin i$), microturbulent ($v_{\rm mic}$) and macroturbulent ($v_{\rm mac}$) velocities, each in km s^{-1}. $\log g$ was kept fixed at literature values in most inversions, since narrow Fe I lines do not provide strong constraints on surface gravity. Inversions of line set B4, however, allowed $\log g$ to vary, since the pressure-sensitive Ca I line did provide this constraint. Finally, lines were allowed to be shifted in velocity space by ≤ 500 m s^{-1} (~0.01 Å at 6000 Å) to correct for slight differences in literature and data line center wavelengths, as well as possible shortcomings in the dispersion relation.

Our treatment is state-of-the-art for a line inversion technique and motivated by computational efficiency without departing from physical realism. However, it has to be kept in mind that the line profiles described here are approximations that rely on a particular implementation (e.g. of the radial-tangential macroturbulence, or the height-independence of other parameters). This will be a limiting factor for the achievable fit precision and we can expect to find some residual signatures of this treatment in our analysis. Thus, an important part of interpreting our results will be linked to distinguishing these effects from a ZB signature.

3.2. Fitting strategies and atmospheric models

Given the highly complex field topologies expected for sun-like stars, most past techniques to measure ZB assumed that coverage by magnetic regions was homogeneous and atmospheres identical in all but their magnetic properties. Usually, both magnetic field strength, B, and surface area covered by magnetic regions (filling factor), f, were then determined independently, while the effects of multi-modal surface temperature distributions were neglected. These models computed the total radiative flux from the star as the sum of flux from magnetic and non-magnetic (quiet) surface fractions with identical temperature stratification:

$$F_{\rm tot} = (1-f)F_{\rm quiet} + fF_{\rm magn}. \quad (3)$$

To investigate detectability, we chose two different strategies. First, models with a single homogeneous atmosphere were considered, so called one-component (OC) models, where only the product Bf was determined. Second, two-component (TC) models were used, where B and f are naturally segregated, since f defines the relative surface fractions covered by the respective components, cf. Eq. (3). A further refinement of this model takes into account the generally different temperature stratifications of magnetic and non-magnetic regions. This temperature difference is well-known from the Sun (see, e.g., Solanki 1993, for an overview). This dichotomy in fitting strategies is addressed in the following and results are presented in separate subsections.

For both strategies adopted, we allow all fit parameters aside from Bf (OC) or B and f (TC) to vary freely in the fit (see last paragraph of Sect. 3.1). However, as explained above, $\log g$ was frequently used at a fixed literature value. Thus, we calculate χ^2, cf. Eq. (2), for a range of values of Bf that we keep fixed in each inversion. In this way, we aim to avoid degeneracies that prevent the non-linear least-squares algorithm from finding the global minimum. This strategy implies that we do not aim to determine the other model parameters accurately. Our goal is to investigate whether introduction of magnetic flux (and how much) in the atmospheric model yields significantly better results.

To quantify our results, we determine the overall best-fit solution, i.e. where χ^2 reaches its global minimum, as well as formal errors on Bf following Press et al. (1999). The formal 1σ range is adopted as our standard error. To claim detection of magnetic fields, we require the non-magnetic best-fit solution to lie outside the 3σ confidence level (CL). Non-detections are characterized by 3σ upper limits.

The CLs on χ^2 are of a formal nature, since they depend on $\chi^2_{\rm min}$, cf. Sect. 2.2. Errors deduced from these CLs would therefore represent the true errors only in the case of a "perfect" fit. In addition, the choice of a specific (Kurucz) input atmosphere introduces a bias that affects χ^2 and thereby influences the formal error determination on Bf. However, spectral lines differ in their respective sensitivities to magnetic fields (usually expressed by their effective Landé factor, cf. Table 1). We employ both Zeeman sensitive and insensitive lines in simultaneous inversions. Each line's different reaction to a certain postulated magnetic flux directly impacts the obtained best-fit χ^2 for this Bf value. Therefore, provided the inversions are not dominated by systematic effects (see, however, Sect. 4.2.1), the CLs do allow us to evaluate whether evidence for a magnetic field is found, despite the above statements about their mostly formal nature. The CLs further provide an order-of-magnitude estimate on the uncertainty involved in the measurement.

3.2.1. One-component inversions

In the OC approach, we scan the dependence of χ^2 on the single parameter Bf. This is done by performing inversions for a set of fixed Bf values. Best-fit solutions for χ^2 and model parameters are obtained from each inversion.

In OC inversions we formally set $f = 1$ and investigate the line shaping effect due to the product Bf. Therefore, we assume a mean magnetic field covering the entire surface, aiming to avoid the degeneracy between B and f. The spacing of the Bf grid is usually 50 G, and is refined to 25 G close to the overall best-fit $\chi^2_{\rm min}$ for better sampling of χ^2 in this region.

3.2.2. Two-component inversions

Following the solar paradigm, magnetic fields in cool stars are expected to be concentrated in distinct elements that are usually described as flux tubes (Stenflo 1973; Spruit 1976; Solanki 1993). Our two-component (TC) inversions aim to take into account this physical fact by composing the atmospheric model of

A&A 522, A81 (2010)

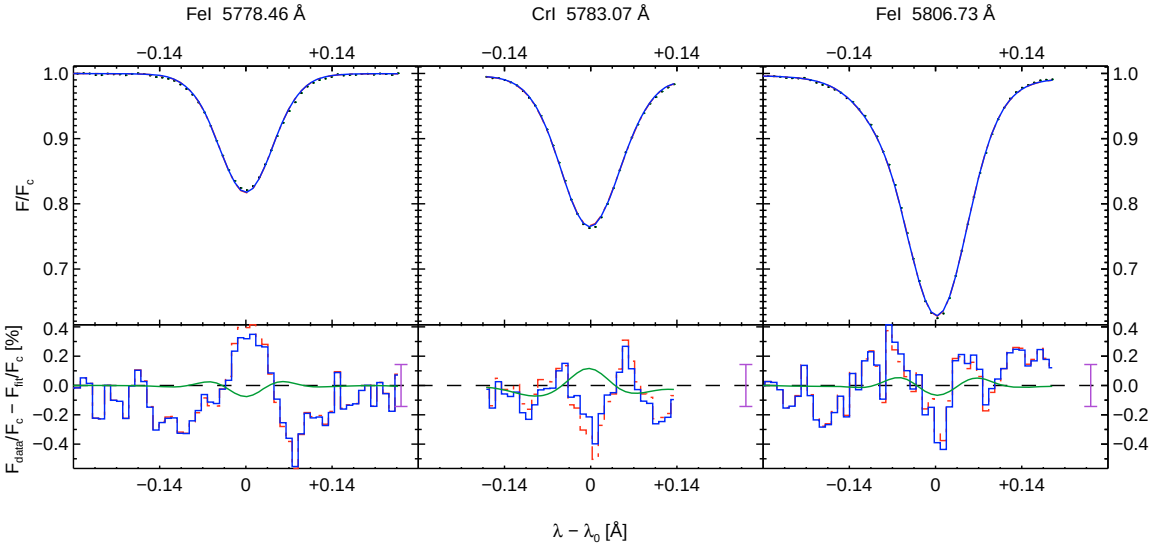

Fig. 2. Sun, line set A3, one-component model: Data and best-fits with $Bf = 0$ G (solid blue) and $Bf = 225$ G (dash-dotted red).

a magnetic and a field-free component. Thereby, we can investigate the impact of the $f = 1$ assumption made for OC models as well as the effect of a bimodal surface temperature distribution.

Hence, we perform three cases of TC inversions: those where both components have identical temperature, as well as those where magnetic regions are either cool, or warm with respect to the non-magnetic component. The equal temperature case was frequently used in the literature and allows for a more direct comparison of our results than OC inversions. Our incremental approach of increasing model complexity aims to distinguish between geometrical and temperature-related effects.

We compute the best-fit χ^2 for each point of the B-f-plane defined by a grid of fixed B and f values. As a result, this approach is computationally much more expensive.

In the TC inversions, the model contains surface filling factor, f, as an additional fixed parameter, since we scan the B-f-plane. In addition to f, we introduce the additional fit parameter T_2 for temperature at unit optical depth for the second component. For the equal temperature case, T_2 and T_1 are fitted, but kept equal. Both parameters can vary freely and independently in the cool and warm cases. To quantify our results, we construct formal CLs on the two-dimensional χ^2-maps in analogy to the OC inversions.

In this paper, we perform TC inversions for the Sun and 59 Vir. For 59 Vir, for which a magnetic field is detected with a high CL, we investigate and compare the three different TC cases discussed above.

4. Results

We present our results in two kinds of figures, namely line fit plots and χ^2-plots or -maps. Figure 2 is an example of line fit plots that help to assess the qualitative difference between magnetic and non-magnetic best-fit models. The upper panels contain the measured line profiles as ticks of length σ_i overplotted by best-fit solutions. Solid blue represents the overall best-fit solution, and dash-dotted red lines are used to draw either the non-magnetic, i.e. 0 G (if evidence for magnetic fields is found), or formal 3σ upper limit on Bf. Residuals are drawn in histogram style in the lower panels using the identical color and line style theme and visualize the difference between measured and calculated line profiles, scaled by factor 100. The purple error bar at the right end in each of the residual panels indicates σ_i.

The residuals contain smooth solid green lines that indicate the difference in line shape between the overall best-fit and the other best-fit model plotted, i.e. the change in line shape due to introduction of magnetic flux. The other fit parameters such as $v \sin i$, etc., adapt to each fixed Bf value, since they are allowed to vary freely. Hence, the green line does not represent the Zeeman pattern alone. It illustrates the combined effect due to ZB and different best-fit parameters for the two cases plotted.

Our inversions converged after relatively few iterations and although a given choice of starting values for the fit parameters (especially temperature) introduces a bias (if the χ^2 surface has multiple minima), no dependence on these was found for the best-fit parameters.

Table 3 lists our results for Bf and overall best-fit parameters, i.e. those at $\chi^2_{\rm min}$, for both OC and TC inversions. The overall best-fit values for B and f from TC inversions are found in the text in the respective subsections. Columns 1–3 contain the star's name, HD number and spectral type. Spanning these columns, we indicate if and for what kind of TC model results were obtained. The line sets used, as introduced in Table 1, are listed in Col. 4. Columns 5–7 list the overall best-fit $\chi^2_{\rm min}$, number of degrees of freedom ($N_{\rm DOF}$), and continuum signal-to-noise (S/N) measured in the data. Columns 8–10 provide literature values for effective temperature, $T_{\rm eff}$, as well as overall best-fit temperature at unit optical depth computed for continuum opacity at 5000 Å, T_1, and, in the case of TC inversions, T_2, in Kelvin, cf. Sect. 3.2. Column 11 contains literature values for logarithmic gravitational acceleration in cgs units, unless marked by an asterisk (*). In this case, $\log g$ was used as a free fit parameter, constrained by the pressure-sensitive Ca I line, and the overall best-fit value is presented. Columns 12–14 list the overall best-fit parameters obtained for macroturbulence, $v_{\rm mac}$, microturbulence, $v_{\rm mic}$, and projected rotational velocity, $v \sin i$, each in km s^{-1}. Column 15 contains literature values for Bf, where available. Column 16 lists our results for average magnetic field with formal 1σ errors obtained from interpolation of the χ^2-plots

R. I. Anderson et al.: On detectability of Zeeman broadening in optical spectra of F- and G-dwarfs

Table 3. Objects investigated sorted by increasing HD number.

Name	HD	Sp. Type	line set	$\chi^2_{\rm min}$	$N_{\rm DOF}$	S/N	$T_{\rm eff}$	T_1 [K]	T_2	$\log g$ [cgs]	$v_{\rm mac}$	$v_{\rm mic}$ [km s^{-1}]	$v \sin i$	$Bf_{\rm lit}$	Bf [G]	$Bf(3\sigma)$
Sun	–	G2V	A3	237.6	132	700	5780	6565		4.44	3.29	0.65	1.34	$\lesssim$130[a]	0^{+90}	0–200
		TC, cool	A3	169.5	130	700		6571	4876	4.44	2.80	0.61	1.93		245^{+5}_{-10}	150–1400
GJ 297.1	68456	F6V	A3	245.6	227	400	6396	7178		4.14	1.52	3.30	9.48	–	1100^{+350}_{-550}	0–1950
			B3	318.6	248	420		7249		4.14	2.33	3.05	9.39	–	1050^{+100}_{-110}	750–1300
			B4	384.5	309	420		7209		4.40*	4.63	1.84	9.35	–	950^{+110}_{-80}	600–1200
59 Vir	115383	G0V	B3	262.5	223	420	6234	7075		4.60	4.89	1.21	6.67		500^{+40}_{-60}	300–600
			B4	401.9	332	420		7077		4.50*	4.76	1.23	6.70		525^{+30}_{-60}	350–650
		TC, equal	B3	262.5	222	420		7075	7075	4.60	4.88	1.21	6.68	190[b]	420^{+30}_{-265}	100–550
		TC, cool	B3	216.2	221	420		7517	5978	4.60	4.29	1.42	6.72		120^{+70}_{-120}	0–300
		TC, warm	B3	226.1	221	420		6047	7440	4.60	4.39	1.33	6.70		270^{+60}_{-60}	0–450
61 Vir	115617	G6V	B3	198.1	175	400	5571	6284		4.47	3.09	<0.10	0.46	600[c]	0^{+80}	0–150

Notes. Values for $T_{\rm eff}$ and $\log g$ from literature, unless otherwise indicated. Note that T_1 and T_2 are SPINOR best-fit temperatures corresponding to unit optical depth calculated for continuum opacity at 5000 Å. Overall best-fit results as well as 1σ and 3σ ranges determined for Bf, see text. 3σ Bf range rounded to 50 G. [a] Trujillo Bueno et al. (2004); [b] Linsky et al. (1994) ; [c] Gray (1984); * $\log g$ used as free fit parameter.

or -maps. The last Column 17 quotes the 3σ range of Bf rounded to 50 G.

Additional figures for OC results obtained can be found in the appendix. These include behavior of best-fit parameters with Bf as well as line profile plots for all OC results listed in Table 3 that are not included in the main article body.

4.1. One-component inversions

OC inversions were carried out for 4 stars in different line sets, see Table 1. Figure 3 shows the χ^2-plots determined for (from top left to bottom right) the Sun (A3), HD 68456 (A3), 61 Vir (B3), HD 68456 (B4), 59 Vir (B3), and 59 Vir (B4), where brackets indicate line sets used. The dashed red horizontal lines indicate the formal 3σ CL defined by $\chi^2_{\rm min} + 9$, cf. Sect. 3.2.1.

4.1.1. The Sun

The spectrum of sunlight reflected from Ganymede's surface is the highest-quality spectrum used in this work with $S/N \sim 700$. We adopted solar abundances as determined by Grevesse & Sauval (1998) and Kurucz (1992) input atmosphere `asun.dat13`. Surface gravity was fixed at $\log g = 4.44$.

The upper left panel of Fig. 3 clearly shows that the non-magnetic model yields our overall best-fit result for the Sun. We determine $Bf = 0^{+90}$ G and a formal 3σ upper limit: $Bf \leq 200$ G. χ^2 increases smoothly and steeply above 200 G, indicating a robust non-detection. The overall best-fit parameters are listed in Table 3 and are consistent with the literature values published by V&F05: $v \sin i = 1.63$ km s^{-1}, $v_{\rm mac} = 3.98$ km s^{-1}, $v_{\rm mic} = 0.85$ km s^{-1}.

Figure 2 shows the measured line profiles (black tick marks) of line set A3 overplotted by non-magnetic (blue) and magnetic (red, $Bf = 225$ G) best-fit calculated profiles. The agreement between either model and the measured line profiles is so close that amplified residuals have to be considered to view the difference. The most Zeeman-sensitive line, Cr I with $g_{\rm eff} = 2.00$ (center), exhibits the strongest reaction to magnetic flux. This is indicated by the smooth green line. However, the amplitude of this reaction is of the same order of magnitude as σ_i.

A clear systematic signature is seen in the residuals, notably in the 5778.46 Å Fe I line. This W-shaped signature is not removed by ZB in this OC inversion and is roughly twice as large as the solid green line that indicates the difference between the non-magnetic and magnetic models. This indicates a systematic shortcoming in our ability to reproduce line shape and may indicate that, for instance, our approximate treatment of convection (as a macroturbulence) may be inadequate at this level of precision.

From this analysis, which is consistent with the upper limit of 140 G set by Stenflo & Lindegren (1977), also using broadening of intensity profiles, we can neither confirm nor rule out the result by Trujillo Bueno et al. (2004) of $Bf \sim 130$ G, since this value is consistent with our formal 3σ CL. The same is true for other, generally smaller, literature values of average (turbulent) magnetic fields determined for the quiet Sun (Solanki 2009). We conclude that magnetism averaged over the solar surface is too weak to be detected using this line set and method. Note that the above literature values refer to the quiet Sun, whereas the Sun was rather active at the time the analyzed data were recorded (13 October 2000). However, adding the active-region magnetic flux would raise the Bf value by a couple of 10 G only and thus would not affect our conclusions.

4.1.2. 61 Vir – HD 115617

The spectrum of the G6V field dwarf 61 Vir in data set B was an ideal candidate for a robust magnetic field measurement due to its slow rotation (R&S03: $v \sin i < 2.2$ km s^{-1}), close-to solar metallicity ([Fe/H] = 0.05), $T_{\rm eff} = 5571$ K (latter two in V&F05), and low X-ray activity (NEXXUS2 database (Schmitt & Liefke 2004): $\log L_{\rm X} = 26.65$). We used an input atmosphere calculated for $T_{\rm eff} = 5500$ K. $\log g = 4.47$ (V&F05) was used as a fixed parameter.

The χ^2-plot in the center left panel of Fig. 3 confirms the robust non-detection for 61 Vir. This is in agreement with

A&A 522, A81 (2010)

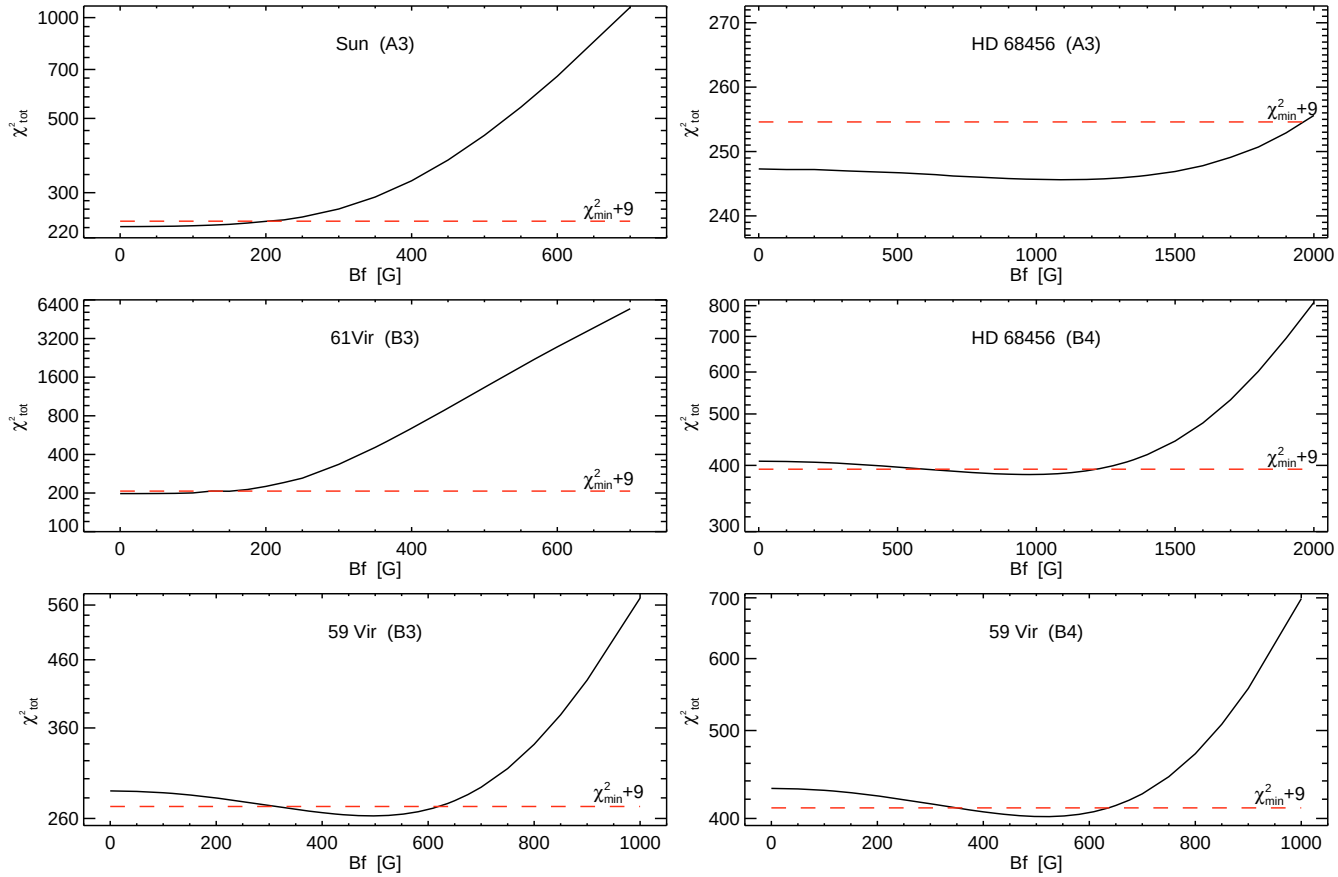

Fig. 3. χ^2-plots obtained from one-component inversions. Object names are given inside the respective panels, and line sets used are mentioned in parentheses. 3σ confidence level on Bf indicated by dashed red horizontal lines.

expectations motivated by findings that link X-ray luminosity with magnetic flux (Pevtsov et al. 2003). The overall best-fit is reached for $Bf = 0$ G and formal 1σ and 3σ upper limits are established at $Bf = 80$ and 150 G, respectively. See Table 3 for details on other best-fit parameters. The lower 3σ upper limit obtained for 61 Vir than for the Sun can be explained by the higher Zeeman sensitivity of the line set B3 (61 Vir) relative to A3 (Sun).

We found one previous measurement of magnetic flux for 61 Vir in the literature. Gray (1984) determined $B\sqrt{A_0} = 600\,\mathrm{G} \pm 10\%$, where A_0 is related to f by average viewing angle. This result is inconsistent with our null detection. We speculate that the difference between the two measurements is due to our higher data quality and different, possibly more sophisticated analysis technique.

4.1.3. 59 Vir – HD 115383

59 Vir is a G0V field dwarf known for its activity and has been extensively studied by many authors. V&F05 measured its $v \sin i = 7.4$ km s^{-1}, $T_{\rm eff} = 6234$ K, $\log g = 4.60$ and [Fe/H] = 0.28 (relative to solar). $\log L_{\rm X} = 29.41$ (NEXXUS2), approximately 2.8 dex higher than that of 61 Vir. Given its spectral type and observed rotation period $P_{\rm rot} = 3.3$ d measured by Donahue et al. (1996), 59 Vir would be classified as a young star. However, using multiple age-indicators, Lachaume et al. (1999) favor an age of 3.8 Gyr. Thus, 59 Vir is an interesting object to study regarding the age-activity relationship.

Inversions for 59 Vir were performed using line sets B3 and B4, cf. Table 1. In the latter case, surface gravity was well-constrained, despite the less-than-ideal fit to the Ca I line, and $\log g = 4.49$ was obtained, consistent with the literature value. The other best-fit parameters are also consistent with the literature (Takeda et al. 2005; Sousa et al. 2008).

We determine $Bf = 500^{+40}_{-60}$ G for 59 Vir from line set B3 and $Bf = 525^{+30}_{-60}$ G from B4, cf. the bottom left and right panels in Fig. 3. The 3σ CLs determined from both data sets are roughly the same with approximately $300 \leq Bf \leq 650$ G. χ^2 varies smoothly over the entire Bf range, and a steep incline is seen above $Bf \sim 800$ G. Furthermore, the best-fit solution for $Bf = 0$ G lies nearly 5σ from $\chi^2_{\rm min}$.

The 6173 Å line was assigned a slightly higher statistical weight, since it is the most Zeeman-sensitive line in the set with $g_{\rm eff} = 2.5$. The blue wing of this line contains a blend due to Eu II that was not fully reproduced, despite our effort to include all available atomic line information in the inversions. Due to the presence of unidentified blends, the red wing had to be severed before reaching continuum. Line blends as well as the systematic signature seen also in the results for the Sun are clearly visible.

The residuals in Fig. 4 indicate improvement in fit quality due to introduction of magnetic flux for all lines. However, the largest differences between the magnetic ($Bf = 500$ G) and non-magnetic best-fit results are of the same magnitude as the S/N of the data. This result thus illustrates how difficult it is to detect ZB in optical Stokes I, even for relatively high values of Bf. The presence of systematic residual signatures similar to those found

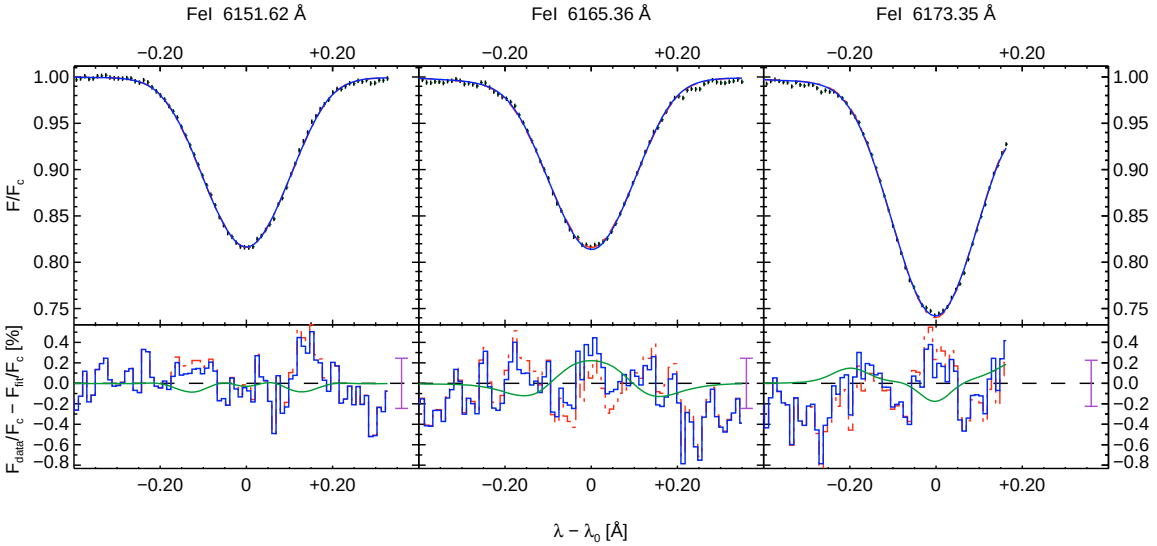

Fig. 4. 59 Vir, line set B3, one-component model: data and best-fit with $Bf = 500$ G (solid blue) and $Bf = 0$ G (dash-dotted red).

for the Sun and 61 Vir underline the need for rigorous and accurate implementation of radiative transfer and line broadening functions.

4.1.4. HD 68456

The F6 dwarf HD 68456 was of particular interest in our analysis, since data were available in both data sets and thus allowed our results to be tested for consistency. Since the dates of observation were nearly 4 years apart, we did not simultaneously invert lines from both sets. After all, changes in atmospheric parameters, for instance due to activity cycles, within this time span cannot be excluded. Fundamental parameters of this object are given by Hauck & Mermilliod (1998) ($T_{\rm eff} = 6396$ K, $\log g = 4.14$, [Fe/H] $= -0.29$) and R&S03 ($v \sin i = 9.8$ km s^{-1}). NEXXUS2 indicates a high level of activity of this star ($\log L_{\rm X} = 29.05$). Furthermore, HD 68456 is a particularly interesting object to study in this context, since we are not aware of any previous ZB measurement in a late F-type star[1].

Relatively fast rotation and high effective temperature combine to produce very shallow absorption lines in this star's spectra. This fact complicated the analysis of line set A3 where lines are generally shallower than in data set B. Furthermore, data set A for this star was of lower quality than the other spectra analyzed in this work, containing individual data points that deviate significantly from the general line shape, while continuum S/N was approximately 400 in both data sets. The deviations seen are not consistent with the signature expected from a starspot.

The top and center right panels in Fig. 3 show our results obtained for line sets A3 and B4, respectively. For line set A3, the overall best-fit $Bf = 1100$ G, but no detection can be claimed. This is underlined by an F-test probability $P_{\rm f} = 0.21$ for this result indicating spurious fit improvement. Using line set B4, however, we do find evidence for a magnetic field and obtain $Bf \sim 1$ kG, with the formal 3σ CL being $600 \leq Bf \leq 1200$ G.

[1] But note the work of Donati et al. (2008) on the changing magnetic field topology on τ Boo (F7 IV-V, Gray et al. 2001).

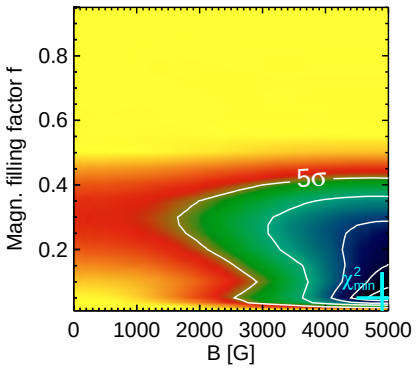

Fig. 5. χ^2-map for the Sun, line set A3, TC model with cool magnetic regions.

4.2. Two-component inversions

The concept of two-component (TC) inversions was introduced in Sect. 3.2.2. We carried out these more complex inversions for the Sun and 59 Vir. For the Sun, for which no one-component detection of a magnetic field was made, we did not expect reliable 2-component results. These inversions were carried out purely as a test. In the illustrative case discussed in the first subsection below we made the starting assumption for magnetic flux to be concentrated in cool regions, such as spots. The results are quite instructive regarding systematic effects. For 59 Vir, where the probability of attaining additional information from a two-component inversion is higher, we investigated the three cases mentioned above: equal temperatures for both components; warm magnetic component (warm case); cool magnetic component (cool case).

4.2.1. The Sun

Figure 5 shows the χ^2-map calculated from TC inversions of solar line set A3. The input atmospheres used were `asun.dat13` (cf. Sect. 4.1.1) for the warm and a $T_{\rm eff} = 4750$ K Kurucz atmosphere for the cool component. We obtain $\chi^2_{\rm min} = 170$, a value considerably lower than that obtained for the OC model,

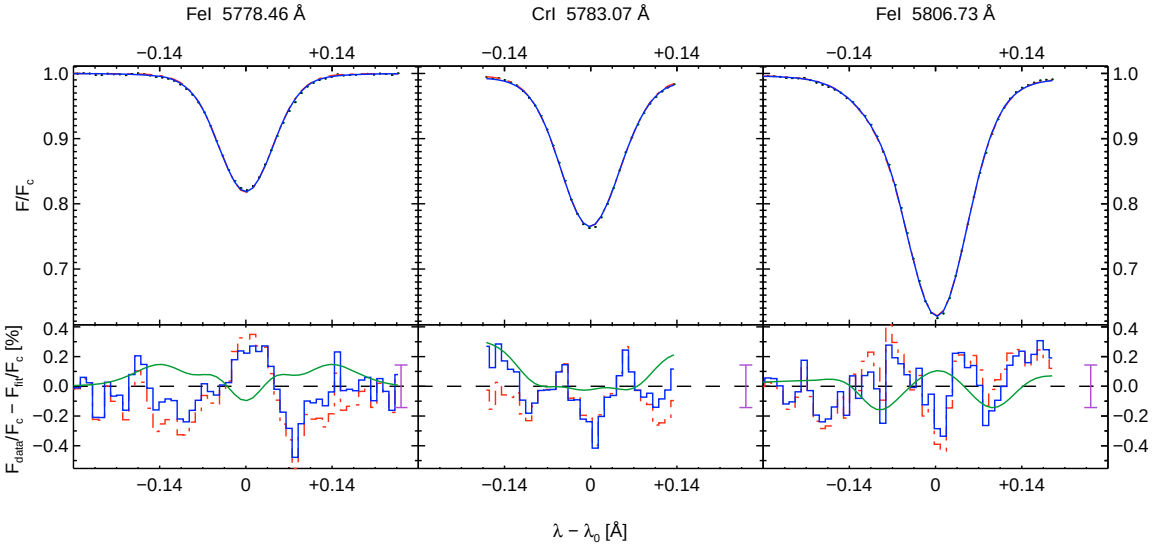

Fig. 6. Sun, line set A3, comparison of overall best-fit TC ($B = 4900$ G, $f = 0.05$, blue solid) and OC ($Bf = 0$ G, red dash-dotted) results.

for $B = 4950$ G and $f = 0.05$. The Bf grid was calculated for field strengths of up to 5000 G, with filling factors up to 0.95 for $B \leq 2000$ G and $f \leq 0.5$ for $B > 2000$ G. The CLs are $235 \leq Bf \leq 250$ G (1σ) and $150 \leq Bf \leq 1400$ G (3σ), and thus would suggest evidence for very strong surface fields in the Sun. However, there are a number of problems with these results. For instance, magnetic fields in sunspots do not usually exceed ~3 kG while the average field strength of sunspots is roughly 1000−1300 G (Solanki & Schmidt 1993) and the field strength averaged over sunspot umbrae usually does not exceed 2500 G. In contrast, our 3σ confidence level suggests that B is well above 4 kG with f between 1–~30% in disagreement with the observed sunspot coverage which is (always) below 1%. Furthermore, a multitude of measurements places the average Bf of the (quiet) Sun considerably lower (Solanki 2009). Last, the 3σ range for Bf is vastly larger than that found for the OC result. Therefore, we conclude that our fit was not well-constrained and that in this case the more complex TC model yielded less significant results than the simpler OC model.

Figure 6 helps to understand what happened here. The greatest decrease in χ^2 was achieved by decreasing the systematic signature in the 5778 Å Fe I line. This apparent improvement in fit quality has stronger influence on χ^2 than the deteriorating agreement between the measured and calculated profiles of the Cr I line at 5783 Å, since the former line contributes more degrees of freedom. Therefore, the magnetic field (or rather the lower temperature associated with the magnetic component) improves the fit of the Zeeman-insensitive ($g_{\rm eff} = 1.2$) line, while the Zeeman-sensitive ($g_{\rm eff} = 2.0$) line is less well matched. The worse fit in the blue Cr line wing is compensated in part by a small unidentified blend in the red wing that is falsely removed by the magnetic model. Thus, our conclusion is that this TC inversion is driven by systematic difficulties and yields a result that is less representative of the physical processes, albeit superior in terms of pure χ^2. It therefore serves as an example of how line blends and other systematic effects on line shape affect our results.

4.2.2. 59 Vir – HD 115383

The results obtained for 59 Vir using OC models indicated formal 3σ detections of significant magnetic flux. To assess, if this detection is actually robust and significant, we performed TC inversions for this strongest candidate. The following results were obtained from our physically motivated TC inversions that distinguish between magnetic and non-magnetic components.

We investigated three different cases of TC inversions: equal temperatures, cool magnetic, and warm magnetic components. Thus, in the latter two cases, we investigate the effect of having different temperatures for the two components.

For the equal temperature case, we used the $T_{\rm eff} = 6250$ K Kurucz atmosphere for both components and coupled the two parameters T_1 and T_2, forcing them to be equal. In the cool case, we used tabulated atmospheres calculated for $T_{\rm eff} = 6250$ K and 5000 K for the non-magnetic and the magnetic component, respectively. The warm case was motivated by the warmer plage or network regions on the Sun. The Kurucz atmospheres were those with $T_{\rm eff} = 6250$ K for the magnetic and $T_{\rm eff} = 6000$ K for the non-magnetic regions. The temperature parameters T_1 and T_2 could vary freely and independently in both the warm and cool cases. The fitting ranges for T_1 and T_2 were large enough to allow turning the cool component into the hotter one and vice versa. The starting values of the fit parameters were identical in both cases, apart from the inverted values of T_1 and T_2 (the second temperature component was magnetic). All other starting values were identical to the OC inversions of 59 Vir.

Equal temperatures: Figure 7a shows the χ^2-map obtained from our inversions of a model with equal temperatures for both components. As can be seen in Table 3, our overall best-fit parameters are virtually identical with our OC results. Even the two Bf values lie within their 1σ CLs. $\chi^2_{\rm min}$ is reached for $B = 700$ G and $f = 0.6$. However, even the 1σ CL spans a large range in f-values, and the 3σ CL is consistent with almost any f value. The reason for this lies in the χ^2 surface, which has the well-known banana-shape, with a minimum running from the combination of high f and small B to the opposite extreme of small f and large B, while maintaining roughly equal magnetic flux (i.e. Bf). This is the signature of degeneracy between these two parameters. Of particular importance is the fact that in spite of the additional parameter f, the $\chi^2_{\rm min}$ is identical to the OC case, which also indicates that there is not sufficient information in the

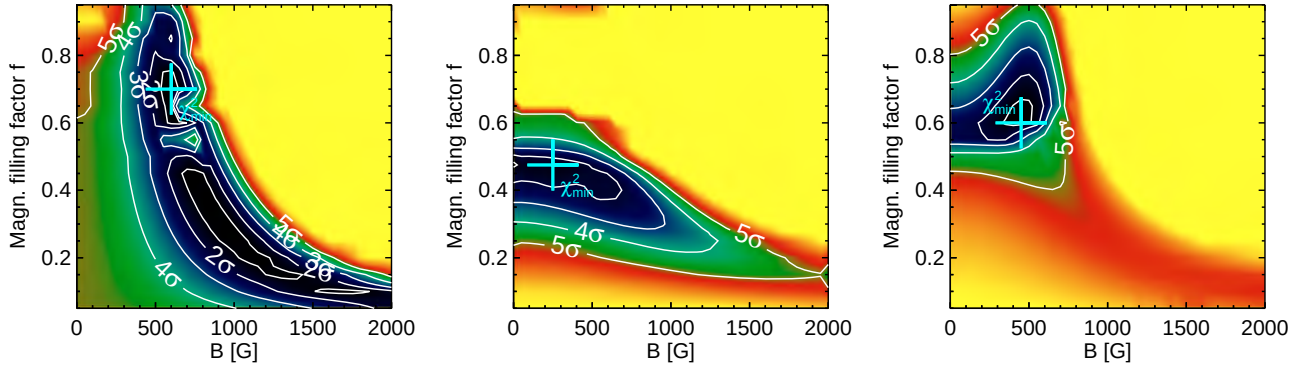

(a) χ^2-map, same atmospheres for magnetic and non-magnetic regions

(b) χ^2-map, cool magnetic regions

(c) χ^2-map, warm magnetic regions

Fig. 7. Results obtained from TC inversions of 59 Vir, line set B3. χ^2_{min} indicated by large cyan pluses. CLs indicated by solid white lines.

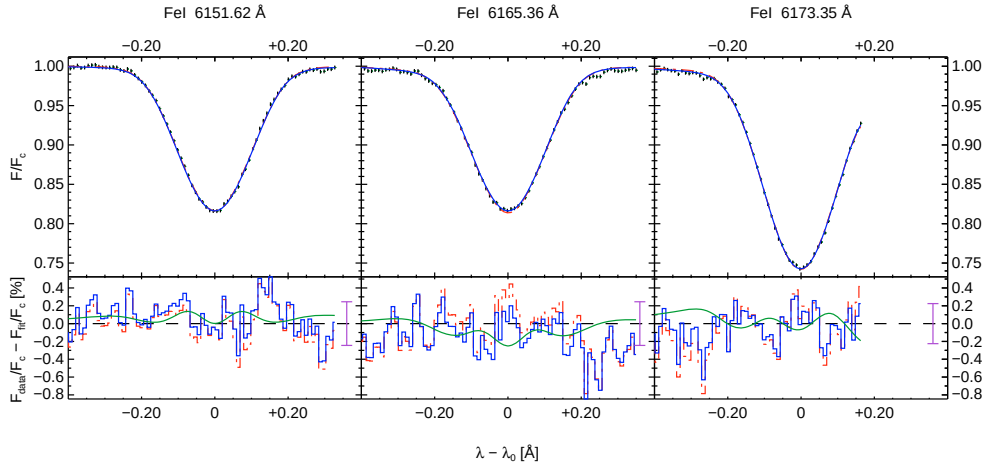

Fig. 8. 59 Vir, line set B3: Comparing $Bf = 120$ G TC (blue solid) to $Bf = 500$ G OC (red dash-dotted) best-fit results.

data to distinguish between B and f. Furthermore, the formal Bf error margins for this case are larger than for the OC inversions and the other best-fit parameters nearly identical. Therefore, we conclude that a distinction made between magnetic and non-magnetic regions is insignificant.

Linsky et al. (1994, hereafter Li94) determined $Bf = 190$ G for 59 Vir (number published in Saar 1996) using an equal temperature TC model. Their Bf value is lower than, yet consistent with, our 3σ Bf range obtained from the TC inversions in the equal temperature case. It is, however, inconsistent with our 3σ Bf range determined from the OC inversions that favor higher Bf. At present it is not possible to say whether the difference to our results is due to differences in technique or due to the evolution of the stellar magnetic field.

Cool magnetic regions: As in the above example for the Sun, we assume the majority of the magnetic flux to originate in starspots, i.e. in cool regions on the stellar surface. Figure 7b shows the χ^2-map corresponding to this case. The overall best-fit $\chi^2_{min} = 216$ is reached for $B = 250$–300 G with $f = 0.475$ for both, i.e. $Bf = 120$–140 G. χ^2_{min} is lowered by 46.3 relative to the OC and TC equal temperature models and the formal 3σ confidence level is $0 \leq Bf \leq 320$ G. The formal 3σ range in Bf is smaller than in the equal temperature TC case. The improvement in fit quality over the OC model is most clearly seen in the better matching central depth of the Zeeman-insensitive 6151 Å and of the Eu II blend to the Zeeman-sensitive line at 6173 Å, cf. Fig. 8. Both improvements are likely due to changes in level populations. The presence of a cool component enables a better matched line depth of Fe I, whereas the warm component contributes additional ionized europium thereby better matching the Eu II blend. In fact, the other two iron lines are also better matched by the TC inversion.

Figure 9 clearly shows that the difference in best-fit T_1 and T_2 within the 3σ CL lies between 1400–1600 K. This is roughly in agreement with the difference in temperatures chosen for the input atmospheres and the temperature differences between the quiet solar photosphere and sunspot umbrae.

Warm magnetic regions: For this case, we employed a model containing slightly warmer magnetic than non-magnetic regions, i.e. assumed a model representative of plage or network-regions. This case is particularly interesting, since a warm second component contributes more flux than a cool one. Thus, the effect due to a certain Bf on line shape can be expected to be stronger.

Figure 7c illustrates our results. $\chi^2_{min} = 226$ is slightly higher than in the above cool case and yields $B = 450$ G and $f = 0.6$.

A&A 522, A81 (2010)

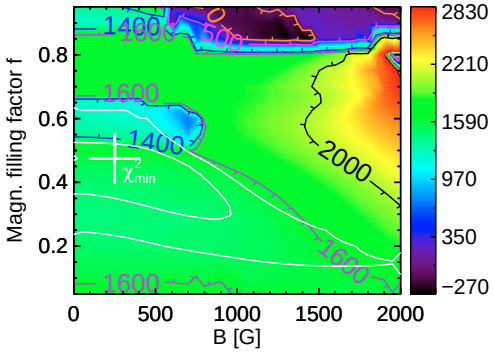

Fig. 9. ΔT-map for 59 Vir, cool case. Difference in K between T_1 and T_2 indicated by colors indicated in legend on right. Contours drawn for $\Delta T = T_1 - T_2 = 0$ K (orange), 500 K (magenta), 1400 K (blue), 1600 K (purple), and 2000 K (black). White contours indicate 3 and 5σ CLs. The large white plus indicates the point of overall best fit.

Bf ranges from 210−325 G in the formal 1σ interval, while we find it consistent with 0−450 G at 3σ.

The 3σ range in B values is roughly the same as in the cool case, whereas the 5σ level is limited to lower B values. Opposite to the cool case, high-f solutions are favored. Thus, both cases favor a slight majority of the surface covered by warm elements. Despite the small (250 K) difference in $T_{\rm eff}$ of the input atmospheres, the difference in best-fit parameters T_2 and T_1 within the 3σ CL ranges 1300−1400 K ($\Delta T = T_2 - T_1$ in the warm case, since $T_2 > T_1$). This temperature difference is very similar to that found in the case of cool magnetic regions (for the 3σ CL).

Comparison of TC cases (equal, cool and warm): The equal temperature TC case yields results in agreement with OC inversions, but wider CLs on Bf. Significantly lower $\chi^2_{\rm min}$ is found in the two different temperature cases, also for the non-magnetic best-fit solutions (lowest χ^2 for $Bf = 0$ G in equal, cool & warm cases: 287, 217, 231). Interestingly, the warm and cool TC cases tend towards virtually identical atmospheric configurations with nearly the same overall best-fit parameters for T_1, T_2 (though T_1 and T_2 are switched among the cool and warm cases), $v \sin i$, $v_{\rm mac}$, and $v_{\rm mic}$, cf. Table 3.

This suggests that the true reason for the improved fit to the observations is the presence of two temperature components. These simulate the inhomogeneity of the stellar atmosphere produced by starspots, granulation, oscillations, etc. and possibly also non-LTE effects in the line formation, which are not taken into account in the LTE modeling we have carried out.

A key difference between the different TC cases is the flux contribution from the respective magnetic component. Due to this difference in contrast, different Bf values may be expected. Our inversions yield comparable Bf for the OC and TC equal temperature model, while Bf is lower for the cases with different temperatures. Among these latter two, the warm case (brighter magnetic component) yields a slightly larger Bf. However, both are consistent with no magnetic field at the 3σ CL (though the warm case is not consistent with $Bf = 0$ G at 2σ).

5. Discussion

To assess detectability of ZB for this kind of analysis, we first discuss the general uncertainties and sources of error before examining the impact of model assumptions.

Our analysis is prone to uncertainties from various sources, such as degeneracies among various line broadening agents and uncertainties in information used as input (atmospheres, line data, lines used, etc.). We attempted to avoid degeneracy among line broadening agents by allowing all fit parameters to vary freely for given average magnetic fields. This approach helped to nudge the non-linear χ^2-minimization routine towards the global minimum. In addition, it provided a clear visualization (see Fig. 3) of the range of acceptable Bf values, thereby providing very solid upper limits on Bf of, say, a few hundred to 1.5 kG depending on the star.

More spectral lines could have provided more stringent constraints on model parameters. Unfortunately, our choice of lines was severely limited by the small wavelength coverage of the CES spectra. Temperature stratification would have been even better constrained by using lines from multiple ionization stages. In order to achieve the fit quality presented in this paper, however, we relied on lines from different excitation potentials. We had found that some combinations of lines yielded better fit agreement than others. The reasons for this empirical fact are likely related to blends; specifically, to blend abundances (often unconstrained), lack of literature on transition parameters needed for SPINOR, uncertainties in oscillator strengths or rest-wavelengths, and unidentified line blends or even relative displacements of blend wavelengths due to convection. For a literature comparison of the fit quality presented here, see Frutiger et al. (2005) who applied SPINOR in simultaneous inversions of 14 lines for α Cen A and B, including lines from different ionization stages. Their Figs. 2 and 3 clearly illustrate the larger discrepancy between model and data when a large number of lines is used.

Small systematic effects (best visible in the spectral difference between observed and computed lines profiles) complicated our analysis. The high quality of the data revealed these systematic shortcomings in reproducing real line profiles. The data for the Sun was both the highest quality spectrum (in terms of S/N) and one of the least rotationally broadened. The fact that the TC inversions for the Sun produced such implausible results may indicate that a limit was surpassed for an adequate representation of line profiles by simple broadening functions such as the radial-tangential macroturbulence profile. However, some of the difficulties in the solar TC inversion were also related to the lower Zeeman sensitivity of line set A3, in addition to the low level of solar magnetism and the data-related problems of line blends, etc. Further candidates for the origin of the systematic signatures at this level may be related to any of a number of sources, such as the implementation of limb-darkening and disk-integration, temperature stratification, neglect of stellar convection (granulation) and oscillations, differential rotation, neglect of non-LTE effects, depth-dependent magnetic field strength, scattered light in CES data, etc. In addition, the temperature gradients of active stars may differ significantly from those of inactive stars. Thus, the representation of magnetic regions by "quiet" atmospheres may also be too crude an approximation, since it neglects inhibition of convection and the influence of magnetic fields on temperature stratification. Thus, applicability of LTE Kurucz input atmospheres could be questioned. Non-LTE effects might also be seen, since the systematic residual signature appears to be enhanced in hotter stars. The analysis thus suffers from a multitude of highly degenerate effects originating in approximations. Most of these flaws cannot be easily resolved, however, and there are valid reasons for adopting at least some of these approximations.

Two kinds of fitting strategies were explored: one-component (OC) and two-component (TC) models, cf. Sect. 3.2 for details. OC models assume a homogeneous atmosphere with a single temperature stratification and an average magnetic field, Bf, covering the entire stellar surface. For the Sun and 61 Vir, both stars with low X-ray activity, our OC results excluded Bf exceeding a few hundred Gauss. OC inversions further yielded evidence of 500 G to 1 kG fields for two faster rotators with higher X-ray luminosity, namely 59 Vir and HD 68456. As could be expected from its larger maximum $g_{\rm eff}$ value and $g_{\rm eff}$ coverage, line set B3 was more sensitive to ZB than A3.

Two-component (TC, cf. Sect. 3.2.2) inversions were performed to distinguish between magnetic and non-magnetic surface regions. For our solar spectrum in line set A3, we present a case study that assumed the magnetic fields to be concentrated in spots, i.e. in significantly cooler regions. However, the solar TC model was driven by systematic effects (partly due to weak blends in the line wings) and yielded a result inconsistent with the OC result and the literature.

For 59 Vir, we explored three different cases of TC inversions: a) equal temperatures for both components; b) a cool magnetic; and c) a warm magnetic component. We find that the equal temperature TC case is consistent with the results from the OC inversions. Furthermore, the Bf determined is consistent with the only available literature value. However, no improvement in χ^2 is seen over the OC model, while an additional fit parameter, f, was introduced. This is consistent with the well known result that the product Bf is much better constrained than B and f individually (Saar 1990a).

The picture changes, however, when the model takes into account two different temperatures in the two components, as was done for the cool (spots) and warm (plage and network regions) TC cases. In fact, a significant improvement of χ^2 was seen for both of these more complex inversions. Independent of the input atmospheres used for the two components, these inversions converged towards a very similar photospheric model featuring similar coverage ($f \approx 50\%$) by hot and cool features with $\Delta T \approx 1300$ K. The difference in $\Delta\chi^2_{\rm min} \approx 10$ between the warm and cool case is probably the result of the a priori choice of input atmospheres. Magnetic flux did not play a deciding role in the inversions' ability to converge towards this common overall best-fit model. Note, however, that the improvement of the fit comes at the expense of additional free parameters (2 new parameters are introduced compared to the OC case).

For both the warm and the cool TC case, Bf was lower than in the OC or TC equal temperature case and consistent with no magnetic field at the 3σ CL (however, not at 2σ in the warm case). Thus, while some evidence for ZB was found in these cases, no detection can be claimed when allowing for two different temperature components, one magnetic, the other field free.

Given the significant improvement of $\chi^2_{\rm min}$, we find that model assumptions impact our ability to reproduce the observed line shape more strongly than the presence or absence of ZB in optical Stokes I, even for relatively high Landé factors. At the same time, the presence of ZB is not excluded, either.

As a next step, even more complex models might be invoked. However, this does not appear to be expedient at this point, given the limited number of lines used for analysis, the approximative treatment of line profiles (e.g. the radial-tangential macroturbulence and the height-independent microturbulence), the smallness of the Zeeman signature, and the fact that the TC inversions of 59 Vir already reached the noise limit.

A more prudent approach would be to increase sensitivity to ZB. This could be done by using high-resolution infrared spectra. In this way, the λ^2 dependence of Eq. (1) could be exploited to provide stringent constraints that are in addition to the differential Bf-response that was at the base for this investigation. Furthermore, the IR contrast between cool and warm regions would be lower, thereby enhancing Zeeman signatures (e.g. Johns-Krull 2007). In M-dwarfs, successful measurements of strong magnetic fields have been reported using molecular lines, e.g. using FeH lines in the Wing-Ford bands (Reiners & Basri 2006, 2007). With the majority of their flux in the infrared and strong fields, these stars constitute prime candidates for direct Bf measurements using spectral line inversion as outlined in this work.

6. Summary

In this paper, we investigated detectability of ZB in optical Stokes I spectra of the Sun and three slowly rotating sun-like stars by performing spectral line inversion with SPINOR.

Thanks to the ability of SPINOR to perform spectral line inversion, different scenarios could be compared and model assumptions evaluated by scanning the χ^2 plane for fixed Bf, or combinations of B and f, values. This approach enabled us to investigate the form of χ^2 as a function of Bf as shown in Fig. 3 and therefrom determine formal errors on Bf.

Systematic uncertainties in our analysis are in part related to literature used as input, such as atomic line data and elemental abundances. Due to the small magnitude of the Zeeman broadening even weak line blends complicated the analysis. Approximations, such as the representation of turbulence in the stellar atmosphere by radial-tangential macroturbulence and height-independent microturbulence, also influenced our results.

OC inversions excluded the presence of significant magnetic flux ($Bf < 150$ G at the 3σ CL) for the Sun and 61 Vir. Our results for HD 68456 may be interpreted as first evidence for a magnetic field in a late F-type dwarf obtained by the ZB technique, with $Bf \approx 1$ kG and formal 3σ errors of approximately 350 G. The OC result for 59 Vir is $Bf = 500^{+40}_{-60}$ G.

The TC equal temperature case yielded $Bf = 420$ G for 59 Vir, a higher value than that reported by Li94, but consistent within the (large) formal 1σ error. TC inversions with components of different temperatures were consistent with Bf between 0 G and 450 G at the 3σ CL. The case of a warm magnetic component was inconsistent with an absence of magnetic field at 2σ. Previous investigations of this kind frequently used models similar to our equal temperature TC case. Our investigation of the different TC inversion cases demonstrates the strong influence of model assumptions. In fact, the freedom to freely and independently vary both atmospheric temperatures in TC models was shown to influence line shape more strongly than ZB for the lines used in this work, cf. Sect. 4.2.2. The improvement of χ^2 due to a second component of different temperature was significantly larger than that due to a magnetic field, irrespective of whether the magnetic component was defined as warm, or cool. The present data quality exceeds that of previous studies, while our sensitivity to Zeeman broadening as expressed by the $g_{\rm eff}$ values in our line sets is comparable to that in the literature with the exception of studies in the infrared.

We conclude that measurements of ZB in optical Stokes I data of slowly rotating sun-like stars are subject to large uncertainties. These are mostly due to data related uncertainties, assumptions on atmospheric models, approximations in line broadening agents, and degeneracy between line broadening agents. However, the Zeeman sensitivity of every individual line (as expressed by its $g_{\rm eff}$ value) differs from line to line by a factor

of up to 2.5. This provides a powerful discriminant for our analysis, since the other relevant broadening effects depend mostly on temperature or wavelength and are thus essentially the same for all lines used. It is this differential reaction of each spectral line to a given magnetic field that ensured the significance of the measurements presented in this work, despite the small magnitude of the ZB signature.

The most promising way to improve the present approach is to further exploit the λ^2-dependence of ZB and use longer wavelength data. In the (near) infrared, Zeeman broadening clearly dominates over Doppler effects and Zeeman splitting can be seen directly, see e.g. Saar (1994); Johns-Krull & Valenti (1996); Valenti & Johns-Krull (2001). New high-resolution near infrared spectrographs have become available for these tasks.

Acknowledgements. We thank the referee John D. Landstreet for his detailed report that resulted in a much clearer explanation of our analysis and a significantly better manuscript.
Thanks are due to the following people: Christian Schröder for observing data set B; A. Lagg at MPS for SPINOR related support; S. H. Saar for very fruitful advice and discussion.
R.I.A. and A.R. acknowledge research funding from the DFG under an Emmy Noether Fellowship (RE 1664/4-1). R.I.A. further acknowledges funding by the Fonds National Suisse de la Recherche Scientifique (FNRS). The work of S.K.S. has been partially supported by the WCU grant No. R31-10016 funded by the Korean Ministry of Education, Science and Technology.
This research has made use of NASA's Astrophysics Data System Bibliographic Services and the SIMBAD database, operated at CDS, Strasbourg, France.

References

Anstee, S. D., & O'Mara, B. J. 1995, MNRAS, 276, 859
Barklem, P. S., & O'Mara, B. J. 1997, MNRAS, 290, 102
Barklem, P. S., O'Mara, B. J., & Ross, J. E. 1998, MNRAS, 296, 1057
Basri, G., & Marcy, G. W. 1988, ApJ, 330, 274
Beckers, J. M. 1969, A table of Zeeman Multiplets, AFCRL-69-0115, No. 371
Berdyugina, S. V. 2005, Liv. Rev. Sol. Phys., 2, 8
Cayrel de Strobel, G., Soubiran, C., Friel, E. D., Ralite, N., & Francois, P. 1997, A&AS, 124, 299
Donahue, R. A., Saar, S. H., & Baliunas, S. L. 1996, ApJ, 466, 384
Donati, J. 2008, in 14th Cambridge Workshop on Cool Stars, Stellar Systems, and the Sun, ed. G. van Belle, ASP Conf. Ser., 384, 156
Donati, J., & Landstreet, J. D. 2009, ARA&A, 47, 333
Donati, J., Moutou, C., Farès, R., et al. 2008, MNRAS, 385, 1179
Favata, F., Reale, F., Micela, G., et al. 2000, A&A, 353, 987
Frutiger, C. 2000, Ph.D. Thesis, Institute of Astronomy, ETH Zürich
Frutiger, C., Solanki, S. K., Fligge, M., & Bruls, J. H. M. J. 2000, A&A, 358, 1109 (Fru00)
Frutiger, C., Solanki, S. K., & Mathys, G. 2005, A&A, 444, 549 (Fru05)
Gray, D. F. 1975, ApJ, 202, 148
Gray, D. F. 1984, ApJ, 277, 640
Gray, D. F. 2008, The Observation and Analysis of Stellar Photospheres (Cambridge University Press) (Gr08)
Gray, R. O., Napier, M. G., & Winkler, L. I. 2001, AJ, 121, 2148
Grevesse, N., & Sauval, A. J. 1998, Space Sci. Rev., 85, 161
Hall, J. C., & Lockwood, G. W. 2004, ApJ, 614, 942
Hauck, B., & Mermilliod, M. 1998, A&AS, 129, 431
Johns-Krull, C. M. 2007, ApJ, 664, 975
Johns-Krull, C. M., & Valenti, J. A. 1996, ApJ, 459, L95
Johns-Krull, C. M., & Valenti, J. A. 2000, in Stellar Clusters and Associations: Convection, Rotation, and Dynamos, ed. R. Pallavicini, G. Micela, & S. Sciortino, ASP Conf. Ser., 198, 371
Kupka, F., Ryabchikova, T. A., Piskunov, N. E., Stempels, H. C., & Weiss, W. W. 2000, Vienna Atomic Line Database [Online], Baltic Astronomy, 9, 590, http://vald.astro.univie.ac.at
Kurucz, R. L. 1992, in The Stellar Populations of Galaxies, ed. B. Barbuy, & A. Renzini, IAU Symp., 149, 225
Kurucz, R. L., & Bell, B. 1995, Atomic Line Data Kurucz CD-ROM No. 23, Smithsonian Astrophysical Observatory, http://cfa-www.harvard.edu/amp/ampdata/kurucz23/sekur.html
Kurucz, R. L., Furenlid, I., Brault, J., & Testerman, L. 1984, National Solar Observatory Atlas No. 1 – Solar Flux Atlas From 296 to 1300 nm (University Publisher, Harvard University)
Lachaume, R., Dominik, C., Lanz, T., & Habing, H. J. 1999, A&A, 348, 897
Linsky, J. L., Andrulis, C., Saar, S. H., Ayres, T. R., & Giampapa, M. S. 1994, in Cool Stars, Stellar Systems, and the Sun, ed. J.-P. Caillault, ASP Conf. Ser., 64, 438
Lites, B. W., Bida, T. A., Johannesson, A., & Scharmer, G. B. 1991, ApJ, 373, 683
Maggio, A., Pallavicini, R., Reale, F., & Tagliaferri, G. 2000, A&A, 356, 627
Marcy, G. W. 1982, PASP, 94, 989
Mathys, G. 1990, A&A, 232, 151
Mathys, G., Hubrig, S., Landstreet, J. D., Lanz, T., & Manfroid, J. 1997, A&AS, 123, 353
Pevtsov, A. A., Fisher, G. H., Acton, L. W., et al. 2003, ApJ, 598, 1387
Pizzolato, N., Maggio, A., Micela, G., Sciortino, S., & Ventura, P. 2003, A&A, 397, 147
Press, W. H., Teukolsky, S. A., Vetterling, W. T., & Flannery, B. P. 1999, Numerical recipes in C., The art of scientific computing (Cambridge: University Press), 2nd edn. reprinted with corrections
Preston, G. W. 1971, ApJ, 164, 309
Reiners, A., & Basri, G. 2006, ApJ, 644, 497
Reiners, A., & Basri, G. 2007, ApJ, 656, 1121
Reiners, A., & Basri, G. 2009, A&A, 496, 787
Reiners, A., & Schmitt, J. H. M. M. 2003, A&A, 398, 647 (R&S03)
Robinson, R. D., Worden, S. P., & Harvey, J. W. 1980, ApJ, 236, L155
Robinson, Jr., R. D. 1980, ApJ, 239, 961
Rüedi, I., Solanki, S. K., Mathys, G., & Saar, S. H. 1997, A&A, 318, 429
Saar, S. H. 1988, ApJ, 324, 441
Saar, S. H. 1990a, in Solar Photosphere: Structure, Convection, and Magnetic Fields, ed. J. O. Stenflo, IAU Symp., 138, 427
Saar, S. H. 1990b, Mem. Soc. Astron. Ital., 61, 559
Saar, S. H. 1994, in Infrared Solar Physics, ed. D. M. Rabin, J. T. Jefferies, & C. Lindsey, IAU Symp., 154, 437
Saar, S. H. 1996, in Magnetodynamic Phenomena in the Solar Atmosphere – Prototypes of Stellar Magnetic Activity, ed. Y. Uchida, T. Kosugi, & H. S. Hudson, IAU Colloq., 153, 367
Schmitt, J. H. M. M. 2001, in Recent Insights into the Physics of the Sun and Heliosphere: Highlights from SOHO and Other Space Missions, ed. P. Brekke, B. Fleck, & J. B. Gurman, IAU Symp., 203, 475
Schmitt, J. H. M. M., & Liefke, C. 2004, A&A, 417, 651
Semel, M. 1989, A&A, 225, 456
Solanki, S. K. 1993, Space Sci. Rev., 63, 1
Solanki, S. K. 2009, in ASP Conf. Ser., ed. S. V. Berdyugina, K. N. Nagendra, & R. Ramelli, 405, 135
Solanki, S. K., & Schmidt, H. U. 1993, A&A, 267, 287
Solanki, S. K., & Stenflo, J. O. 1985, A&A, 148, 123
Sousa, S. G., Santos, N. C., Mayor, M., et al. 2008, A&A, 487, 373
Spruit, H. C. 1976, Sol. Phys., 50, 269
Stenflo, J. O. 1973, Sol. Phys., 32, 41
Stenflo, J. O., & Lindegren, L. 1977, A&A, 59, 367
Takeda, Y., Ohkubo, M., Sato, B., Kambe, E., & Sadakane, K. 2005, PASJ, 57, 27
Trujillo Bueno, J., Shchukina, N., & Asensio Ramos, A. 2004, Nature, 430, 326
Valenti, J. A., & Fischer, D. A. 2005, ApJS, 159, 141 (V&F05)
Valenti, J. A., & Johns-Krull, C. 2001, in Magnetic Fields Across the Hertzsprung-Russell Diagram, ed. G. Mathys, S. K. Solanki, & D. T. Wickramasinghe, ASP Conf. Ser., 248, 179
Wilson, P. R. 1994, Solar and stellar activity cycles, Cambridge Astrophysics Series (Cambridge, MA: Cambridge University Press)
Wittmann, A. 1974, Sol. Phys., 35, 11

Pages 15 to 17 are available in the electronic edition of the journal at http://www.aanda.org

Appendix A: Online figures

We present additional figures illustrating our OC results in this appendix.

A.1. Additional one-component fit results

Figure A.1 shows the OC fit results not presented in the main article body whose corresponding χ^2-plots were included in Fig. 3. The best-fit models drawn are mentioned in the respective captions of the sub-figures.

A.2. Free fit parameters

Figure A.2 shows the behavior of the free fit parameters with Bf in the OC inversions. Red error bars indicate formal singular value decomposition (SVD) errors obtained from `SPINOR`. They also indicate the spacing of the Bf grid scanned, thereby illustrating the higher sampling close to $\chi^2_{\rm min}$. Generally, fit parameters behave smoothly, apart from regions where small numerical jumps are visible, such as for $v \sin i$ in Fig. A.2a. The center panel in each sub-figure labeled $v_{\rm turb}$ contains both macro- and microturbulent velocities, with macroturbulence generally stronger than microturbulence. Degeneracy of fit parameters is evident from the combined reaction of the parameter set caused by the fixed values of Bf.

A&A 522, A81 (2010)

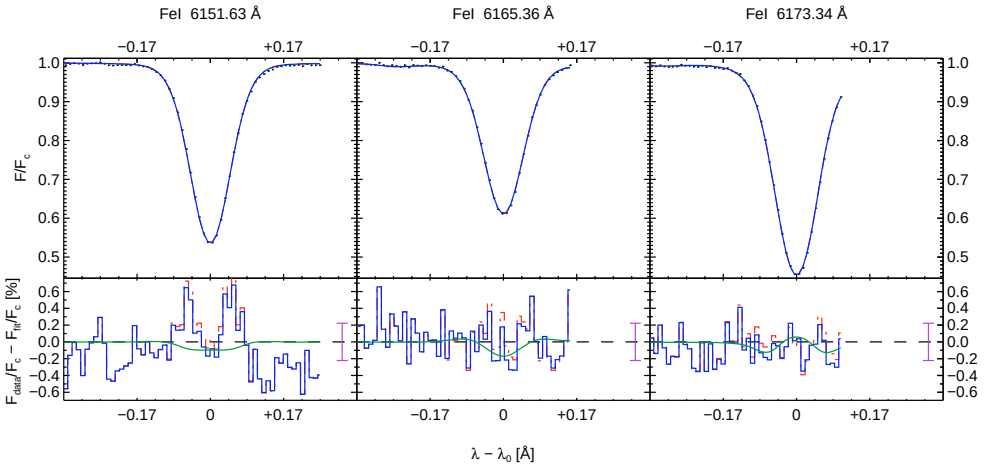

(a) 61 Vir, line set B3. Blue solid: 0 G. Red dash-dotted: 175 G

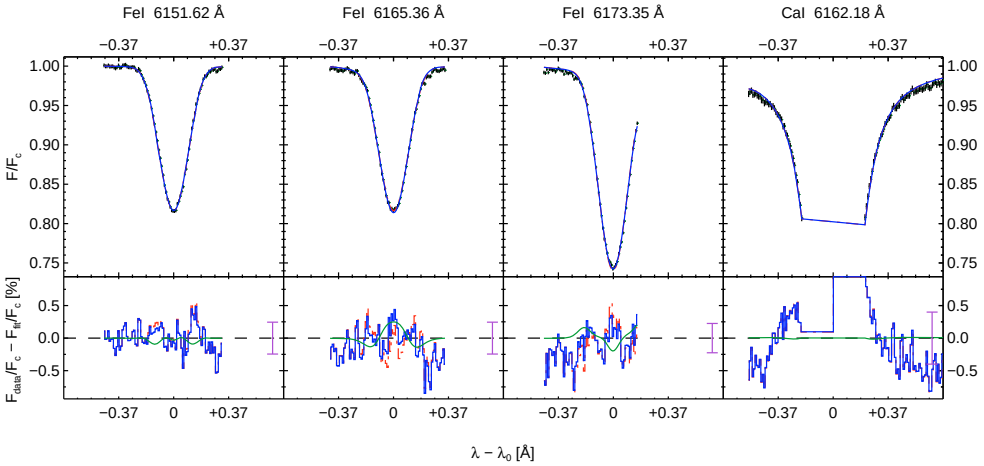

(b) 59 Vir, line set B4. Blue solid: 500 G. Red dash-dotted: 0 G

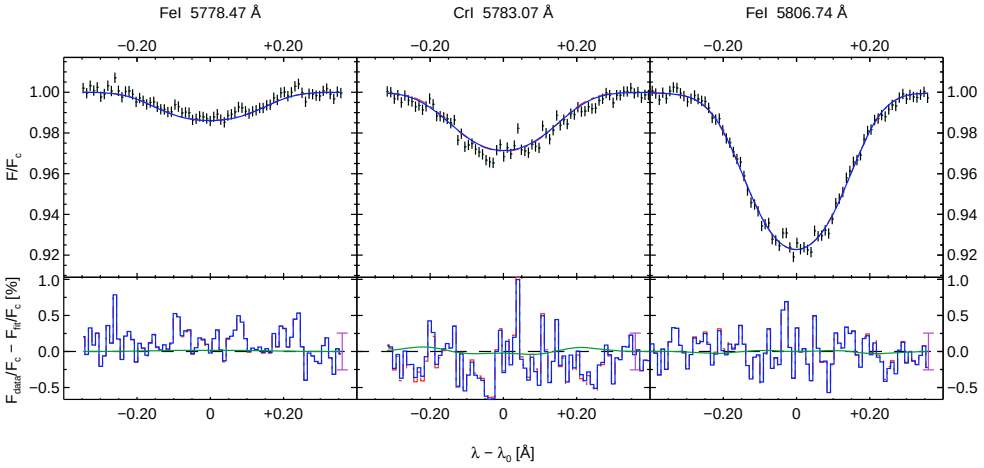

(c) HD 68456, line set A3. Blue solid: 1100 G. Red dash-dotted: 0 G

Fig. A.1. Additional comparison of overall best-fit results from one-component inversions with non-magnetic models and 3σ upper limits, respectively.

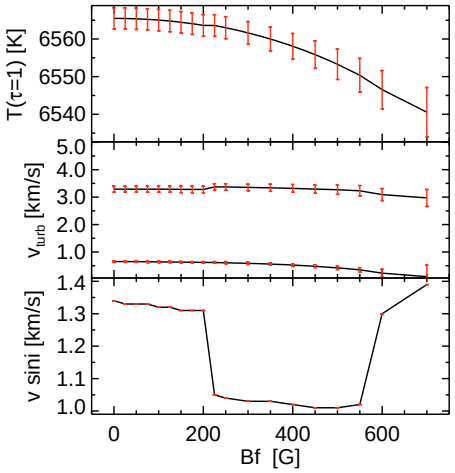

(a) Sun, line set A3

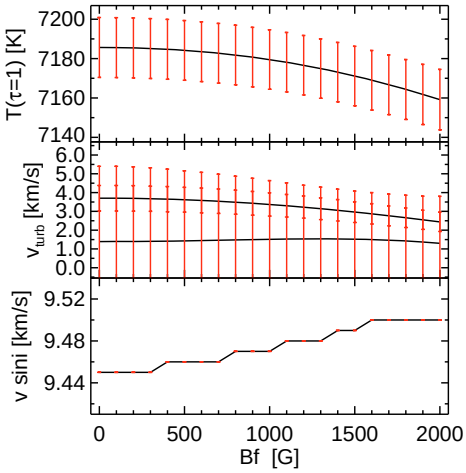

(b) HD 68456, line set A3

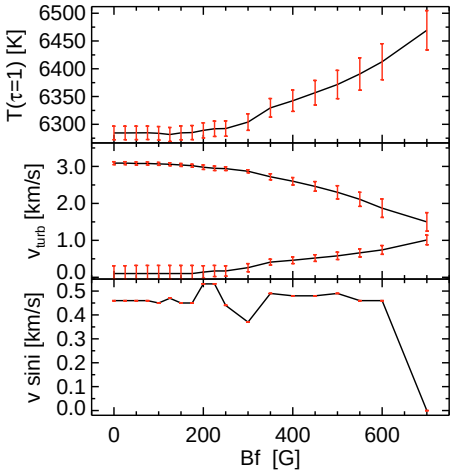

(c) 61 Vir, line set B3

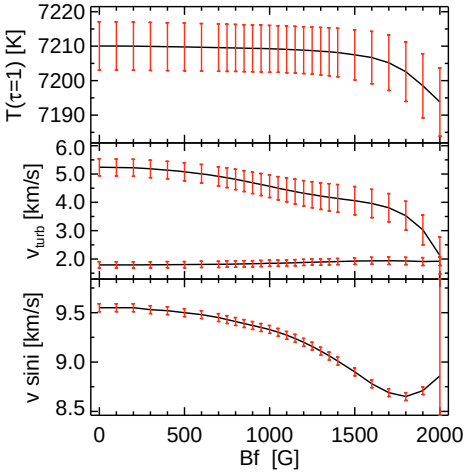

(d) HD 68456, line set B4

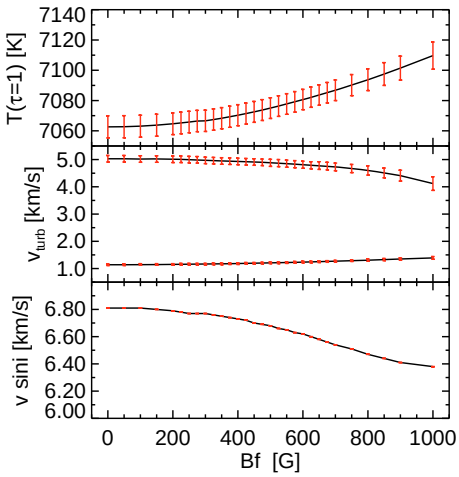

(e) 59 Vir, line set B3

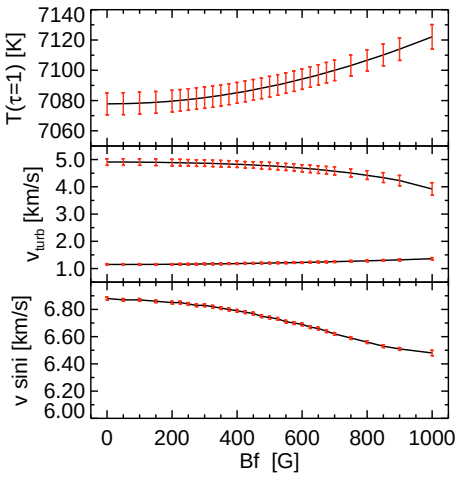

(f) 59 Vir, line set B4

Fig. A.2. Behavior of best-fit parameters with Bf using one-component models. Plot organized the same way as Fig. 3. $v_{\rm turb}$ indicates micro- and macroturbulent velocities, with macroturbulence usually larger than microturbulence.

The 16th Cambridge Workshop on Cool Stars, Stellar Systems and the Sun
ASP Conference Series, Vol. 448, Electronic Edition
Christopher M. Johns-Krull, Matthew K. Browning, and Andrew A. West, eds.

Zeeman Broadening in Optical Stokes I of Solar-like Stars

Richard I. Anderson,[1,2] Ansgar Reiners,[2] and Sami K. Solanki[3,4]

[1]*Observatoire de Genève, Université de Genève, 51 Ch. des Maillettes, CH-1290 Sauverny, Switzerland*

[2]*Institut für Astrophysik, Georg-August-Universität Göttingen, Friedrich-Hund-Platz 1, D-37077 Göttingen, Germany*

[3]*Max-Planck-Institut für Sonnensystemforschung, Max-Planck-Straße 2, D-37191 Katlenburg-Lindau, Germany*

[4]*School of Space Research, Kyung Hee University, Yongin, Gyeonggi 446-701, Korea*

Abstract. We present our analysis aimed at inferring average magnetic fields in slowly-rotating solar-like stars. Using the spectral line inversion code SPINOR, we perform high-accuracy line profile fitting and investigate whether Zeeman broadening can be reliably detected in optical data of unprecedented quality. We argue that our usage of both high- and low-$g_{\rm eff}$ lines does provide a certain sensitivity to magnetic fields that may, indeed, be detected. However, the measurement is subject to a model dependence and prone to ambiguities, e.g. due to spectral blends. Hence, while a field may be successfully recovered, the quantification of this field is subject to large uncertainties, even for the highest-quality optical data.

1. Introduction

Direct detections of magnetic fields in slowly-rotating ($v \sin i < 10\,\mathrm{km\,s^{-1}}$) solar-like stars (SRSLS) are somewhat rare. Since the first application of the Zeeman broadening technique to cool stars by Robinson (1980), much effort was made to infer their field strengths, e.g. in order to constrain stellar dynamo theory. The more recent advances, however, come from different directions, such as direct detections for very late-type stars, e.g. Reiners & Basri (2007), and detections of magnetic field geometry reversals for faster rotators (Fares et al. 2009). The rotation-activity relationship and the absence of accurate and recent measurements of SRSLS magnetic fields thus suggest that the corresponding field strengths may be too low to enable clear and robust detections.

We aim to shed some light on the question of Zeeman broadening detectability in optical Stokes I of SRSLS, and quantify the fields found. To this end, we apply the state-of-the-art line inversion code SPINOR (Frutiger et al. 2005) to data of unprecedented quality and search for signs of Zeeman broadening, see Anderson et al. (2010)[from hereon PaperI].

E-1061

2. Observations and Analysis

The spectra used in this work were taken with the Coudé-Échelle Spectrometer, formerly fiber-fed from the ESO 3.6m at La Silla, Chile. The resolving power $R = 220\,000$ and S/N between 400 and 700 render these the best data considered in this kind of analysis as of yet. This high resolution, however, comes at the expense of a very short wavelength coverage of only 40 Å, severely limiting the number of spectral lines suitable for analysis. The main criterion for suitability is the absence of blends (or at least that the blends present can be well enough reproduced), a utopia as becomes clear with increasing data quality.

Zeeman splitting is a second-order line broadening effect (the splitting of the circularly polarized σ components is not resolved) in the optical range and is easily outweighed by thermal, rotational, or turbulent broadening. However, contrary to the latter, Zeeman splitting depends on λ^2. Additionally, there exists a linear dependence on the Landé factor of the transition, usually expressed in terms of the effective Landé factor, $g_{\rm eff}$. These dependences have two important consequences:

1. Zeeman splitting can become stronger than e.g. rotational line broadening in slowly rotating stars in the infrared

2. the extent of magnetic broadening varies between lines of different $g_{\rm eff}$ and thereby provides a way of distinguishing between Zeeman broadening and other broadening agents.

As we use optical spectra, we do not benefit from point 1. However, due to the very high precision of CES, we can attempt to exploit point 2 by using both high- and low-$g_{\rm eff}$ lines (cf. Tab. 1) in simultaneous inversions. Thereby, we have a strong magnetic field discriminant at our disposal whose detectability limit we can explore.

We investigate two kinds of models, one-component (OC) and two-component (TC) models. The two differ in surface field coverage; OC models assume a surface covered entirely by an average magnetic field, while TC models distinguish between the magnetic and non-magnetic surface fractions. The filling factor f represents the magnetic surface fraction. In TC models, we investigate the impact of different assumptions on the temperatures of both components.

A grid of fixed values for B and f (in OC models, f is effectively 1) is provided. Best-fit values for the merit function and the free parameters (temperature,

Table 1. Lines used in inversions. Oscillator strengths, abundances adopted, and blends included in calculation of line profiles presented in PaperI. $g_{\rm eff}$ is the effective Landé factor, χ_e the lower excitation potential.

Data set A: 5770 Å				Data set B: 6137 Å			
λ [Å]	Ion	$g_{\rm eff}$	χ_e [eV]	λ [Å]	Ion	$g_{\rm eff}$	χ_e [eV]
5778.46	Fe I	1.21	2.59	6151.62	Fe I	1.83	2.18
5783.06	Cr I	2.00	3.32	6165.36	Fe I	1.00	4.14
5806.73	Fe I	0.92	4.61	6173.34	Fe I	2.50	2.22

$v \sin i$, and turbulent velocities) are computed using a non-linear χ^2 minimization algorithm (Frutiger 2000). To claim detection of Zeeman broadening, we require that the $3\,\sigma$ confidence level ($3\,\sigma$ CL, defined by $\chi^2_{\rm min} + 9$, see Press et al. 1999) be inconsistent with $Bf = 0\,G$. More detail on the analysis and the inversion code `SPINOR`, can be found in PaperI and references therein.

3. Results

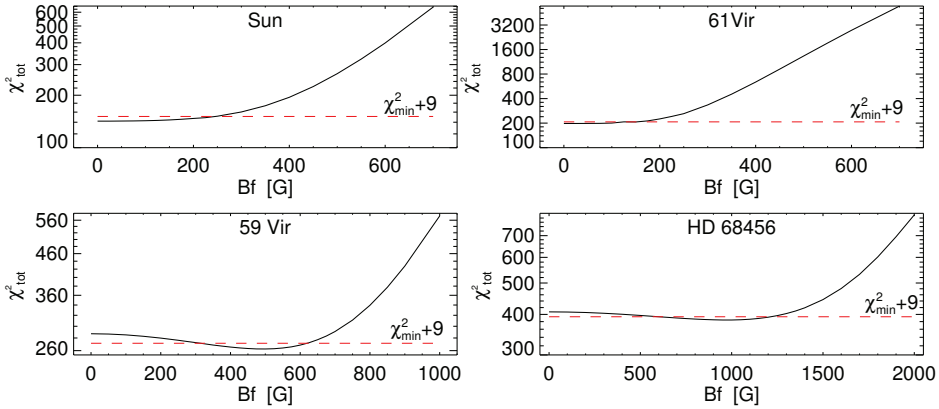

Figure 1. Some OC results shown in PaperI, Fig. 3: logarithmically-drawn best-fit χ^2 against fixed Bf for the Sun, 61 Vir, 59 Vir, and HD 68456. $3\,\sigma$ CLs indicated by dashed lines.

Figure 1 shows the behavior of χ^2 as a function of fixed Bf values in OC inversions of (top left to bottom right) an integrated solar spectrum (sunlight reflected by Ganymede, close to maximum activity in October 2000), the inactive G6 dwarf 61 Vir, the active G0 dwarf 59 Vir, and the active F6 dwarf HD 68456; spectral types taken from `SIMBAD`, active denotes high X-ray luminosity as found in the NEXXUS2 database (Schmitt & Liefke 2004, `www.hs.uni-hamburg.de/DE/For/Gal/Xgroup/nexxus/nexxus.html`) .

In Tab. 2, we list the results for the stars from Fig. 1 together with their logarithmic X-ray luminosities, projected rotational velocities, and the results obtained for our OC inversions of data set A for the Sun and data set B for 61 Vir, 59 Vir, and HD 68456.

OC inversions clearly exclude significant magnetic flux ($> 200\,G$) on the (active) Sun and 61 Vir. Under the OC assumption, we find significant magnetic flux for 59 Vir and HD 68456. For 59 Vir, TC inversions yielded results consistent with both the OC result and $Bf = 0$ G at the $3\,\sigma$ CL, since Bf was $0-300$ G (cool magnetic regions case). Comparing the three cases of equal temperature, warm, and cool magnetic regions, we find that the influence on χ^2 of a second temperature component is considerably larger than that of even a rather strong magnetic field. Hence, the numerical value of the OC detection is challenged. However, the TC results for 59 Vir are inconsistent with $Bf = 0\,G$ at the $2\,\sigma$ CL.

Table 2. Stars investigated with their activity-relevant parameters. $\log L_X$ from Judge et al. (2003) (Sun) and NEXXUS2 (stars), $v \sin i$ from inversions (consistent with literature), the $3\,\sigma$ CLs on Bf are from OC inversions.

HD Number	alt. ID	Sp.Type	$\log L_X$ [ergs s^{-1}]	$v \sin i$ [km s^{-1}]	Bf $3\,\sigma$-range [G]
	Sun (active)	G2V	27.1 – 27.75	1.3	0 – 200
68456	GJ 297.1	F6V	29.05	9.5	600 – 1200
115383	59 Vir	G0V	29.41	6.7	300 – 600
115617	61 Vir	G6V	26.65	0.5	0 – 150

4. Conclusion

Our analysis to infer average magnetic fields in optical spectra takes us close to the detectability limit of Zeeman broadening for SRSLS. Overall, we find that even the highest quality data do not yield clear and robust detections. The analysis is subject to a model dependence related to the inital choice of temperature configuration for the stellar surface, and may further be influenced by the approximative treatment of convection by analytical macroturbulence profiles (see PaperI). Also, blends (and their reproducability) gain in importance at the present level of accuracy and therefore constitute a limiting factor. However, there does remain a sensitivity to the Zeeman broadening signature, cf. the case of 59 Vir, thanks to the simultaneous use of both high- and low-$g_{\rm eff}$ lines. It is therefore the numerical amount of magnetic flux detected that is questioned by the OC-TC-related model dependence, not the presence of a magnetic field on the star.

Acknowledgments. RIA and AR acknowledge research funding from the DFG under an Emmy Noether Fellowship (RE 1664/4-1). RIA further acknowledges funding by the Fonds National Suisse de la Recherche Scientifique (FNRS). The work of SKS has been partially supported by the WCU grant No. R31-10016 funded by the Korean Ministry of Education, Science and Technology. This research has made use of NASA's Astrophysics Data System Bibliographic Services and the SIMBAD database, operated at CDS, Strasbourg, France.

References

Anderson, R. I., Reiners, A., & Solanki, S. K. 2010, A&A, 522, A81. PaperI, 1008.2213
Fares, R., Donati, J., Moutou, C., Bohlender, D., Catala, C., Deleuil, M., Shkolnik, E., Cameron, A. C., Jardine, M. M., & Walker, G. A. H. 2009, MNRAS, 398, 1383. 0906.4515
Frutiger, C. 2000, Ph.D. thesis, Institute of Astronomy, ETH Zürich
Frutiger, C., Solanki, S. K., & Mathys, G. 2005, A&A, 444, 549. (Fru05)
Judge, P. G., Solomon, S. C., & Ayres, T. R. 2003, ApJ, 593, 534
Press, W. H., Teukolsky, S. A., Vetterling, W. T., & Flannery, B. P. 1999, Numerical recipes in C. The art of scientific computing (CUP, —c1999, 2nd ed. reprinted with corrections)
Reiners, A., & Basri, G. 2007, ApJ, 656, 1121. arXiv:astro-ph/0610365
Robinson, R. D., Jr. 1980, Ap. J., 239, 961
Schmitt, J. H. M. M., & Liefke, C. 2004, A&A, 417, 651. arXiv:astro-ph/0308510

A.4 Searching for chromaticity effects in *Hipparcos* Cepheid parallaxes

In 2012, I stumbled over an article by Pourbaix et al. (2003) investigating chromaticity effects of *Hipparcos* stars classified as Variability-Induced Movers (VIMs). These VIMs were originally thought to be candidates for binaries whose variability causes time variations of the photocenter, resulting in scattered parallax measurements. However, as Pourbaix et al. (2003) could demonstrate, the majority (79%) of these candidates were not true VIMs, but long-period variable stars. The cause of the error? The neglected chromaticity of the variability of long-period variable stars (LPV).

The required chromaticity correction determined by Pourbaix et al. (2003) has been applied to *Mira* stars in the re-reduction of the *Hipparcos* catalog by van Leeuwen (2007, p. 175). However, no mention is made by neither van Leeuwen (2007) nor van Leeuwen et al. (2007) that a similar correction has been applied for the Cepheids.

As shown in Sec. 1.2, the variability of Cepheids is strongly chromatic. Hence, there was a good reason to investigate whether there might be a simple way to significantly improve parallaxes for Cepheids in order to obtain a new parallax-based PLR calibration similar to the one by Feast & Catchpole (1997).

To this end, I asked my friend Johannes Sahlmann who had worked extensively on *Hipparcos* parallaxes (e.g. Sahlmann et al. 2011; Sahlmann & Fekel 2013) to re-reduce the *Hipparcos* intermediate astrometric data from the DVD supplied by van Leeuwen (2007) for the 26 Cepheids for which good precision was quoted in the catalog. Johannes then reconstructed the abscissae as described in Sahlmann et al. (2011), and fitted them using the standard 5-parameter model without outlier elimination, cf. Eq. 8 in his paper. I then gathered the near-simultaneous Tycho-2 photometry from *VizieR* and searched for a correlation between the residuals of the astrometric solution and the color at that phase point.

Figure A.1 shows the results obtained for three Cepheids. From top to bottom, the stars shown are Polaris, δ Cephei, and ℓ Carinae (the only long-period Cepheid in the Benedict et al. 2007 sample). The upper panels for each star (red circles) show the astrometric residuals as a function of simultaneous B-V color obtained from Tycho-2, and the lower panels (green circles) show the residuals as a function of pulsation phase. For all 26 objects investigated, the same null result was obtained. We then repeated the test for some LPVs mentioned in Pourbaix et al. (2003) and found that they, too, showed no dependence on color. It is therefore evident that this effect has already been corrected in the new *Hipparcos* reduction by van Leeuwen (2007).

A.5 Spectroscopic observations of supernovae

In an announcement made on 4 October 2011, the Nobel Prize in Physics was awarded to Saul Perlmutter, Brian P. Schmidt, and Adam G. Riess "for the discovery of the accelerating expansion of the Universe through observations of distant supernovae". Just a few months before, the Palomar Transient Factory (PTF), discovered one very notable such type-Ia supernova in galaxy Messier 101 on 24 August 2011. Originally designated as PTF 11kly, the SN was later renamed to SN 2011fe, and turned out to become the brightest type Ia SN since the famous SN 1987A in the LMC.

Incidentally, Lovro Palaversa and I were observing at the Mercator telescope at the time when the SN became brightest in early to mid September 2011. I was contacted by Nick Cox, Martin Cordiner, and Ferdinando Patat with a request to observe the SN as part of a larger effort using several telescopes and, of course, did not hesitate to place the optical fiber of *HERMES* onto the object.

Two spectra were secured and used in a publication (Patat et al. 2013) which studied the circumstellar material of the SN progenitor as well as other absorption features along the line of sight. The investigation found a very "clean" environment of the SN, consistent with a progenitor

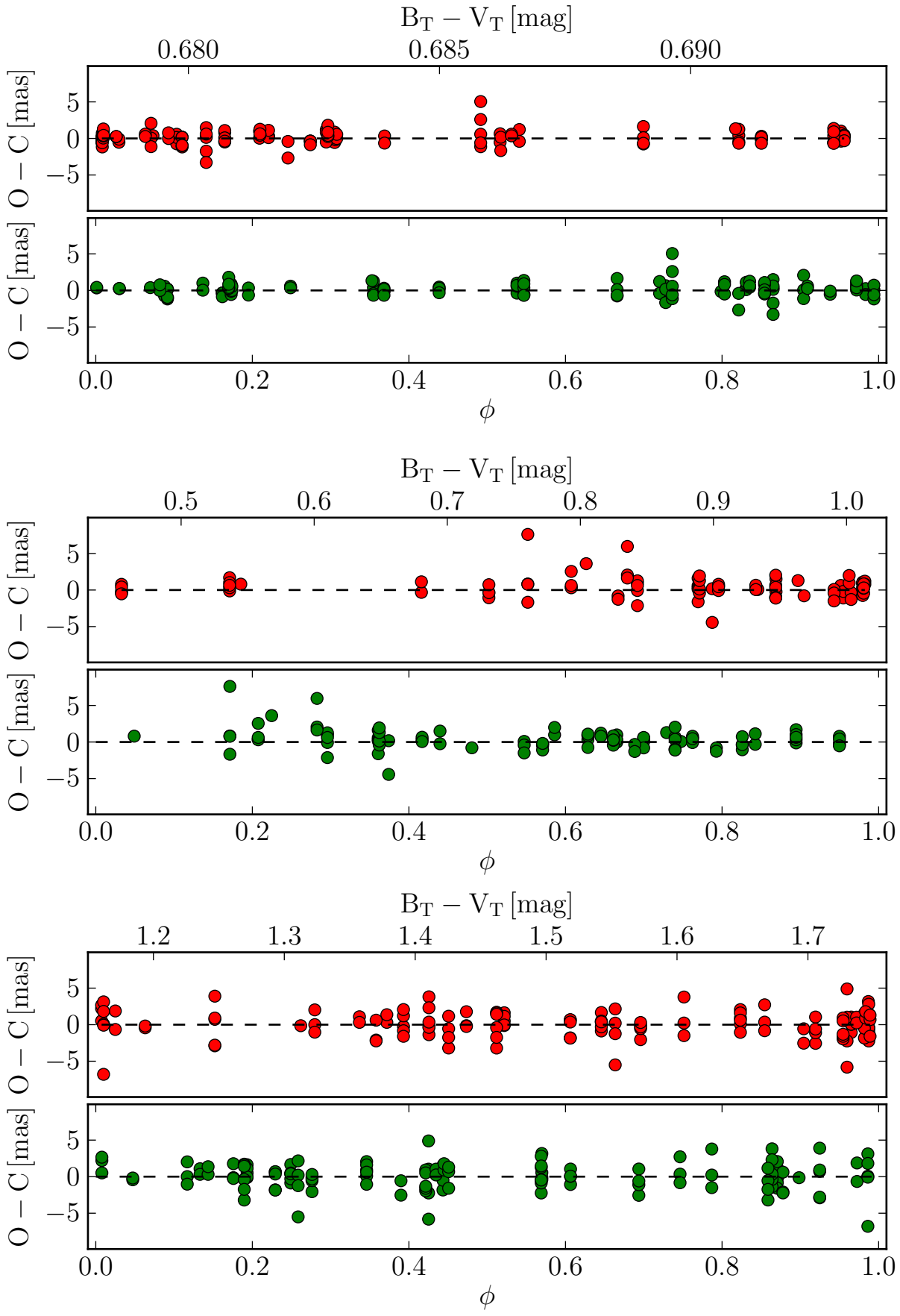

Figure A.1: Re-analyzed Hipparcos parallax residuals (abscissa - fit) as a function of near-instantaneous Tycho-2 color (red, upper panels) and pulsation phase (green, lower panels). Stars shown, from top to bottom: Polaris, δ Cepheid, and ℓ Carinae. No systematic trends are seen in the residuals.

scenario involving a MS or degenerate companion star.

More recently, I was again contacted to observe a relatively bright supernova during a Geneva observing run with *HERMES*, SN 2013dy. Berry Holl carried out these observations. However, this time the object was just barely within the observable range of the small telescope, and at the time of writing, no conclusive results had been obtained.

A&A 549, A62 (2013)
DOI: 10.1051/0004-6361/201118556

Astronomy & Astrophysics

Multi-epoch high-resolution spectroscopy of SN 2011fe

Linking the progenitor to its environment⋆

F. Patat[1], M. A. Cordiner[2], N. L. J. Cox[3], R. I. Anderson[4], A. Harutyunyan[5], R. Kotak[6], L. Palaversa[4], V. Stanishev[7], L. Tomasella[8], S. Benetti[9], A. Goobar[10], A. Pastorello[9], and J. Sollerman[10]

[1] European Organization for Astronomical Research in the Southern Hemisphere (ESO), Karl-Schwarzschild-Str. 2, 85748, Garching b. München, Germany
e-mail: fpatat@eso.org
[2] Astrochemistry Laboratory and the Goddard Center for Astrobiology, Mailstop 691, NASA Goddard Space Flight Center, 8800 Greenbelt Road, Greenbelt, MD 20770, USA
[3] Instituut voor Sterrenkunde, KU Leuven, Celestijnenlaan 200 D, 3001 Leuven, Belgium
[4] Observatoire de Genève, Université de Genève, 51 Ch. des Maillettes, 1290 Sauverny, Switzerland
[5] Fundación Galileo Galilei - Telescopio Nazionale Galileo, Rambla José Ana Fernández Pérez 7, 38712 Breña Baja, TF, Spain
[6] Astrophysics Research Center, School of Mathematics and Physics, Queens University Belfast, Belfast, BT7 1NN, UK
[7] CENTRA – Centro Multidisciplinar de Astrofísica, Instituto Superior Técnico, Av. Rovisco Pais 1, 1049-001 Lisbon, Portugal
[8] INAF, Osservatorio Astronomico di Padova, via dell'Osservatorio 8, 36012 Asiago (VI), Italy
[9] INAF, Osservatorio Astronomico di Padova, v. Osservatorio n. 5, 35122 Padua, Italy
[10] Albanova University Center, Department of Physics, Stockholm University Roslagstullsbacken 21, 106 91 Stockholm, Sweden

Received 1 December 2011 / Accepted 12 July 2012

ABSTRACT

Aims. The nearby Type Ia supernova (SN) 2011fe has provided an unprecedented opportunity for deriving some of the properties of its progenitor. This work provides additional and independent information on the circumstellar environment in which the explosion took place.
Methods. We obtained high-resolution spectroscopy of SN 2011fe for 12 epochs, from 8 to 86 days after the estimated date of explosion, testing in particular the time evolution of Ca II and Na I.
Results. Three main absorption systems are identified from Ca II and Na I, one associated to the Milky Way, one probably arising within a high-velocity cloud, and one most likely associated to the halo of M101. The total (Galactic and host galaxy) reddening, deduced from the integrated equivalent widths (EW) of the Na I lines, is $E_{B-V} \lesssim 0.05$ mag. The host galaxy absorption is dominated by a component detected at the same velocity measured from the 21-cm H I line at the projected SN position (~180 km s^{-1}). During the ~3 months covered by our observations its EW peak-to-peak variation is 15.6 ± 6.5 mÅ. This small and marginally significant change is shown to be compatible with the geometric effects produced by the rapid SN photosphere expansion coupled to the patchy fractal structure of the interstellar medium (ISM). The observed behavior is fully consistent with ISM properties similar to those derived for our own Galaxy, with evidences for structures on scales ≲100 AU.
Conclusions. SN 2011fe appears to be surrounded by a "clean" environment. The lack of blueshifted, time-variable absorption features is fully consistent with the progenitor being a binary system with a main-sequence, or even another degenerate star.

Key words. supernovae: general – supernovae: individual: SN2011fe – ISM: general – dust, extinction – ISM: clouds

1. Introduction

Since the introduction of the accreting white dwarf (WD) scenario (Wheelan & Iben 1973), the question about the nature of the progenitor systems of Type Ia supernovae (hereafter SN Ia) has become more and more pressing (see Patat 2011, for a general review on the subject). One of the most well beaten tracks for obtaining information on the progenitor system has been the search for imprints of circumstellar material (CSM) lost by the system prior to the explosion. Notwithstanding the extensive attempts undertaken to detect such material, as of today no signs of it have been found in Branch-normal events in the form of optical (Lundqvist 2003, 2005; Mattila et al. 2005), radio (Panagia et al. 2006, Chomiuk et al. 2011) and UV/X-ray emission (Immler et al. 2006). Similarly, no evidence for the explosion effects on the companion (e.g. collision and/or envelope stripping) was found so far (Hayden et al. 2010; Bianco et al. 2011; Leonard 2007).

These non-detections were generally interpreted as favoring progenitor systems where the donor is either a main sequence (MS) star, or another degenerate object. However, it is only with the advent of SN 2011fe that very stringent constraints could be placed on the exploding star and its companion. This SN Ia was discovered by the Palomar Transient Factory in the nearby, face-on galaxy M101, less than one day after the explosion (Nugent et al. 2011a,b). The detailed optical and UV studies made possible by the very early detection and the relatively small distance led to two important conclusions: i) the exploding star

⋆ Based on observations collected at the Mercator telescope, Telescopio Nazionale Galileo, Nordic Optical Telescope at Roque de los Muchachos, La Palma (Spain), and at the 1.82 m Copernico telescope on Mt. Ekar (Asiago, Italy).

A&A 549, A62 (2013)

Table 1. Log of the observations.

Date	UT (start)	JD (start)	Phase (days)*	Epoch (days)**	Airmass (start)	Exposure (s)	Instrument	Hel. correction (km s^{-1})
2011-08-31	20:39	24 55 805.357	−10	8.2	1.64	1800	FIES	−4.19
2011-09-03	20:20	24 55 808.344	−7	11.2	1.52	3600	SARG	−3.46
2011-09-07	20:20	24 55 812.340	−3	15.1	1.58	1800	HERMES	−2.47
2011-09-13	19:23	24 55 818.308	+3	21.1	1.60	4200	AES	−0.94
2011-09-13	20:16	24 55 818.342	+3	21.1	1.72	1350	HERMES	−0.96
2011-09-14	18:57	24 55 819.290	+4	22.1	1.50	3600	AES	−0.69
2011-09-21	18:59	24 55 826.291	+11	29.1	1.63	5400	AES	+1.09
2011-09-22	18:40	24 55 827.278	+12	30.1	1.56	9000	AES	+1.35
2011-09-29	20:47	24 55 834.363	+19	37.2	2.63	2700	FIES	+3.10
2011-10-18	17:54	24 55 853.246	+38	56.1	1.84	7200	AES	+7.68
2011-11-15	16:52	24 55 881.203	+66	84.0	2.80	4800	AES	+12.86
2011-11-18	01:28	24 55 883.561	+68	86.4	2.65	12600	AES	+13.52
2011-11-18	05:05	24 55 883.710	+68	86.5	2.92	4800	SARG	+13.55

Notes. * Phases from *B* maximum were computed assuming a rise time of 18.3 days (Röpke et al. 2012). ** Epochs were computed from the estimated explosion time (JD = 2 455 797.196; Nugent et al. 2011c).

must be a compact body (a C-O WD is most favored); and ii) systems with Roche-lobe overflowing giants and MS stars as companions are excluded (Li et al. 2011; Nugent et al. 2011c; Brown et al. 2012; Liu et al. 2012; Bloom et al. 2011). The very stringent limits on the mass loss rate set by radio and X-ray observations point in the same direction (Horesh et al. 2012; Chomiuk et al. 2012; Margutti et al. 2012).

After studying an object whose progenitor system is reasonably well known, we can now ask ourselves a new question. Would we recognize similar systems in other SN Ia, whose distance and discovery time do not allow the close, multi-wavelength scrutiny that was possible for SN 2011fe? The key problem here is that one needs to consider the largest possible number of observables, because SN Ia coming from different channels may display similar spectra and light curves.

In this article we focus on the properties of the circumstellar environment. For this purpose, and following previous studies (e.g. Patat et al. 2007a; Simon et al. 2009), we obtained multi-epoch, high-resolution, optical spectroscopy of SN 2011fe covering the first three months of its evolution. The paper, reporting the results of this campaign, is structured as follows. In Sect. 2 we give an account of the observations and data reduction. Section 3 describes the detection of narrow absorption features, whereas Sect. 4 discusses the implications on the extinction suffered by the SN. In Sect. 5 we illustrate the properties of the intervening gas as derived from Voigt profile fittings, and we study their behavior as a function of time. The results of this study in connection to the progenitor's nature are finally discussed in Sect. 6, which also summarizes our conclusions.

2. Observations and data reduction

We obtained high-resolution spectroscopy of SN 2011fe for 12 epochs, ranging from 8 to 86 days after the estimated date of explosion (JD = 2 455 797.2; Nugent et al. 2011c). The observing log is presented in Table 1, which includes exposure times, phase from maximum light, epoch from explosion, airmass, and heliocentric correction. Phases were computed by adopting a rise time of 18.3 days (Röpke et al. 2012). The observations were carried out with four different instrumental setups. These are summarized in Table 2 and are detailed in the next subsections.

Table 2. Instrumental setups.

ID	Site	Telescope	Res. power	Disp. (Å/pixel)	Range (Å)
AES	Asiago	1.8-m	18 000	0.126	3800–7500
FIES	La Palma	2.6-m	48 000	0.036	3650–7350
HERMES	La Palma	1.2-m	82 000	0.016	3770–9000
SARG	La Palma	3.5-m	66 000	0.021	4600–6150

2.1. Asiago Echelle Spectrograph

Seven spectra of SN 2011fe were obtained with the REOSC Asiago Echelle Spectrograph (hereafter AES) that is attached to the 1.82 m telescope on Mt. Ekar (Asiago, Italy). The spectrograph is equipped with an an E2V CCD42-40 AIMO, back-illuminated detector (2048 × 2048 pixel, 13.5 μm in size). A 2″ slit was used, with a fixed east-west orientation, yielding a resolving power $R = \lambda/\Delta\lambda \sim 18\,000$. The wavelength range covered by the spectra is 3780–7620 Å. The data reduction was performed with tasks within the IRAF[1] `ECHELLE` package following the standard procedures. All images were first overscan-corrected and trimmed. A normalized flat-field image was then derived from observations of a halogen lamp and was used to flat field the science exposures. Next, each spectral order was traced and the spectra were extracted with the optimum extraction algorithm of Horne (1986), which simultaneously subtracts the scattered light. The transformation from pixels to wavelength was derived from observations of a thorium-argon arc-lamp.

2.2. FIES

Two spectra (Aug. 31 and Sep. 29, 2011) were obtained with the fiber-fed (1.3″) echelle spectrograph (FIES[2]) mounted at the Nordic Optical Telescope (NOT) on La Palma (Spain). We used the medium-resolution fiber, which provides a resolving power $R \sim 48\,000$ and a continuous spectral coverage from 3700 to

[1] IRAF is distributed by the National Optical Astronomy Observatories, which are operated by the Association of Universities for Research in Astronomy, under contract with the National Science Foundation.

[2] http://www.not.iac.es/instruments/fies/

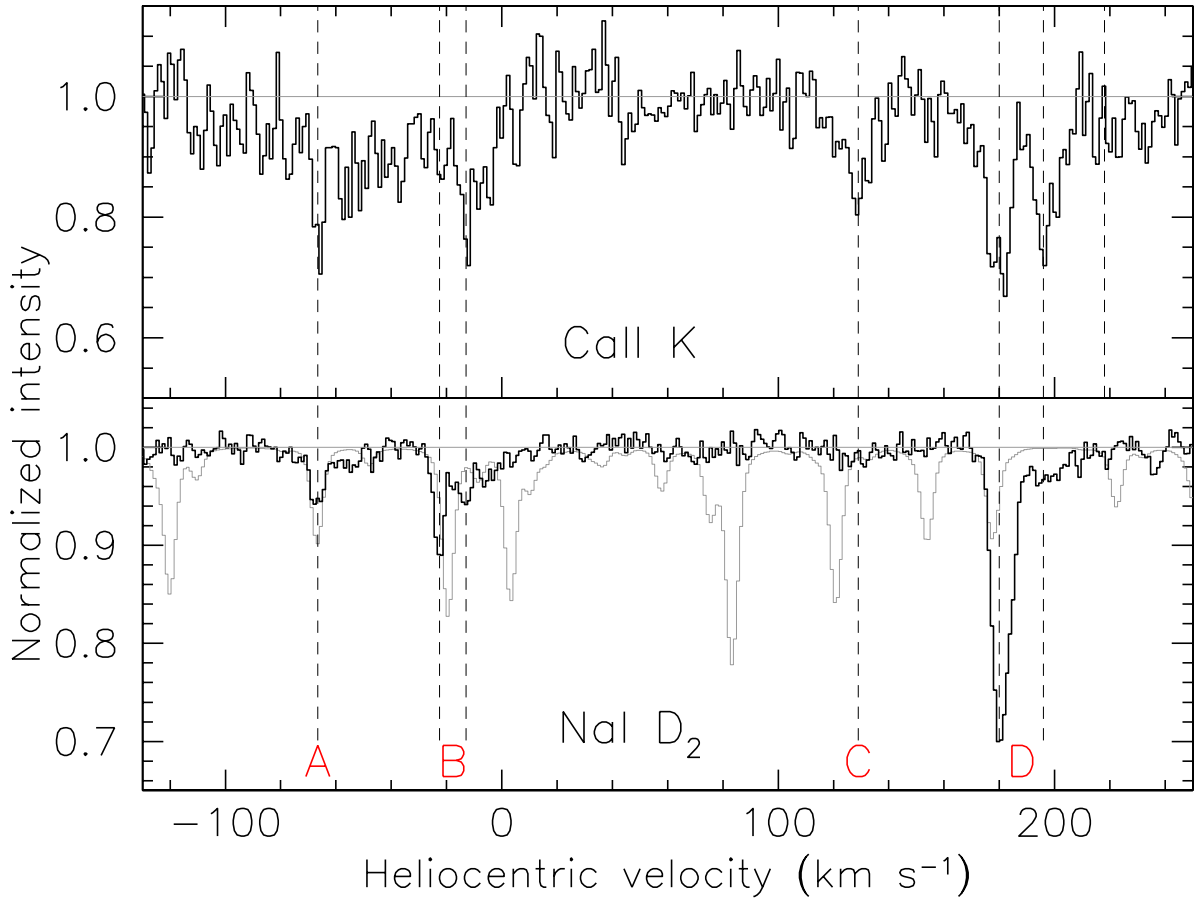

Fig. 1. Narrow absorption components toward SN 2011fe for Ca II K (*upper panel*; day 21) and Na I D_2 (*lower panel*; day 11.2). Main absorption features are marked by vertical dashed lines.

7300 Å in a single exposure. Data were reduced using standard IRAF tasks, as outlined in the previous section.

2.3. HERMES

Two spectra (Sep. 7 and 13, 2011) were obtained with the High Efficiency and Resolution Mercator Echelle Spectrograph (HERMES; Raskin et al. 2011), mounted on the Mercator 1.2 m telescope in La Palma. HERMES is a high-resolution fiber-fed (2.5″) echelle spectrograph offering spectral resolution of $R \sim 80\,000$, and full spectral coverage from 3770 to 9000 Å in a single exposure. Data were processed with an automated data reduction pipeline that includes bias correction from the pres-can region on the CCD, flat-field correction via halogen lamps, wavelength calibration through Th-Ar reference spectra, cosmic clipping, and background modelization.

2.4. SARG

Two spectra (Sep. 3, and Nov. 18, 2011) were obtained with the Spettrografo Alta Risoluzione Galileo (SARG; Gratton et al. 2001), mounted at the 3.5 m Telescopio Nazionale Galileo (TNG) in La Palma. SARG is a cross-dispersed echelle spectrograph that provides spectral resolution ranging from $R = 29\,000$ up to $R = 164\,000$. For our observations we used the cross-disperser #3 grism, a GG455 order-sorting filter, and slit #2 (0.8″ × 5.3″). This setup yields $R \sim 66\,000$ and a wavelength range 4600–6150 Å. The data reduction was performed using standard IRAF tasks, as outlined in Sect. 2.1. The removal of telluric absorption features was performed by means of synthetic atmospheric models. The procedure is discussed in Appendix A.

For the sky background subtraction, we note that in some spectra the terrestrial Na I D emission components (both natural and artificial) are not completely removed. Because of the wavelength shift of most features, this problem affects only a Galactic absorption close to null restframe velocity (see Sect. 3), whose profile (and thus equivalent width) is most likely affected by the incomplete sky subtraction.

Equivalent widths (EW) were estimated by integrating the line profiles in the telluric-corrected spectra. The local pseudo-continuum was derived by means of a straight line least-squares fit to two symmetric, equally extended regions on either side of the absorption. The EW uncertainty was derived using the formulation by Chalabaev & Maillard (1983), which includes the uncertainty on the continuum determination.

3. Narrow absorption features in SN 2011fe

3.1. Ca II *H&K and* Na I *D*

Several Ca II H, K and Na I D components are detected at different velocities, as shown in Fig. 1, which presents the highest resolution spectra available for the two wavelength ranges

A&A 549, A62 (2013)

(obtained with HERMES and SARG, respectively; see Tables 1 and 2).

Two main Galactic absorption systems are detected around −70 and −20 km s^{-1} (marked as A and B in Fig. 1), with weaker and diffuse absorptions possibly present at intermediate velocities (see the Ca II profile). A third system is clearly detected at about +130 km s^{-1} (C). The recession velocity of M101 is 241 ± 2 km s^{-1} (de Vaucouleurs et al. 1991), and therefore this component may be generated within a high-velocity cloud (HVC) that belongs either to the Milky Way or to the host galaxy. The radial velocity derived from 21-cm line observations at the projected SN site is about 180 km s^{-1} (Bosma et al. 1981; their Fig. 1). This makes the association to M101 more plausible, although not certain (see also Sect. 5). Finally, we detect an absorption system with two main components at about 180 and 195 km s^{-1} (D). These velocities are fully consistent with the radial velocity field at the projected SN location (Bosma et al. 1981). This strongly suggests that the corresponding absorptions arise in M101. All features are detected in both H and K lines, while system C is not detected in Na I. The component close to 195 km s^{-1} is clearly detected in Na I only in the highest signal-to-noise (S/N) spectrum (SARG, day 11) with a total equivalent width EW = 7 ± 2 mÅ, while it is only marginally detected in all other spectra.

Nugent et al. (2011c) reported the detection of one single absorption feature (EW = 45 ± 9 mÅ), which they identified as Na I D_2 at v = 194 ± 1 km s^{-1}. Although the weighted average EW we derive from our data (EW(Na I D_2) = 47 ± 1 mÅ, EW(Na I D_1) = 27 ± 1 mÅ; see Sect. 5.1) is consistent with that reported by Nugent et al., the velocity discrepancy is statistically very significant (∼14 km s^{-1}), and cannot be explained in terms of the quoted errors. Once applying the heliocentric corrections listed in Table 1 to the different spectra, the velocities deduced for the Na I D components all agree to within a few 0.1 km s^{-1}. The average heliocentric velocity deduced from the best-fit profile of the most intense host galaxy component (see Sect. 5) is 179.6 ± 0.2 km s^{-1}. Given the very consistent results we obtain from different setups and epochs, we consider our result to be correct to within the reported errors.

3.2. Other absorptions

A careful inspection of the telluric-corrected spectra that cover relevant wavelength range shows no trace of the two typical K I lines at 7665 and 7699 Åfor the Galaxy or for M101 (at the velocities derived for the Ca II and Na I features. See previous section). For the host galaxy the 5-σ detection limit derived from the HERMES spectrum taken on day 15 is EW(K I λ7699) < 5 mÅ. The K I λ7665 is severely affected by a telluric absorption, and so the upper limit estimate for this line is more problematic. However, the two lines have very similar strengths, and so the limit derived above applies to both of them. Similar considerations apply to the non-detection of Ti II, Ca I, CH and CH+. Finally, none of the known strong Diffuse Interstellar Bands (DIBs; 5780, 5797, 6284, 6379, 6613; Herbig 1995) are detected.

4. Reddening

The galactic Na I D components are very weak (see Fig. 1), indicating that SN 2011fe suffers a very low Galactic reddening. The integrated EW(Na I D_1) derived from our highest S/N spectrum (SARG, day 11) for the Galactic components (systems A and B in Fig. 1) is 38 ± 5 mÅ. Applying the relation inferred by Munari & Zwitter (1997) for Galactic reddening, we derive E_{B-V} = 0.01, which is consistent with the expected Galactic extinction along the line of sight to M 101 (E_{B-V} = 0.009 mag; Schlegel et al. 1998). According to the Munari & Zwitter relation, the expected EW for the K I λ7699 is ∼4 mÅ, which is fully consistent with the lack of K I detection in our spectra.

As shown in the previous section, we detect two features most probably associated to the host galaxy, at ∼180 and ∼200 km s^{-1}, with the latter contributing only marginally to the total Na I column density. The integrated D_2 EW measured on the SARG spectrum (day 11) is 47 ± 2 mÅ (EW(Na I D_1) = 25 ± 1 mÅ). Applying the Munari & Zwitter relation, this turns into E_{B-V} = 0.014 (A_V = 0.04 mag), in agreement with the value derived by Nugent et al. (2011c) using the same method. Because the total EW(Na I D_2) is 85 ± 6 mÅ, we conclude that the reddening along the line of sight to SN 2011fe is most probably lower than 0.05 (Munari & Zwitter 1997).

5. Narrow absorption line modeling

To derive interstellar cloud velocities, Doppler widths, and column densities we modeled the best resolution and S/N ratio spectra using the VAPID routine (Howarth et al. 2002). Saturation effects were implicitly taken into account by fitting simultaneously lines of the same species (Na I D_1 and D_2; Ca II H and K). The results for the FIES, HERMES and SARG (first epoch only) spectra are shown in Figs. 2 and 3 for Na I and Ca II. The Na I spectra require five components for a good fit, while nine components were required for Ca II. Error estimates were derived using Monte Carlo noise replication. The models were re-fitted to 1000 replicated data-sets, each with Gaussian noise of rms equal to that of the continuum added. The ±68% ranges in the resulting data give rigorous 1-sigma errors on each parameter. Table 3 shows the results for each epoch, as well as the results of a weighted-average fit to all epochs, in which the fitted data points were weighted by the continuum S/N ratio of the respective spectra. The data show no evidence for statistically significant variations in cloud component velocities or Doppler b parameters between epochs (see below), therefore the v and b values were held fixed at the weighted-average fit values and only the N values were allowed to vary for each epoch. Column densities (cm^{-2}) are given as base-ten logarithms. The units of v and b are km s^{-1}.

The analysis of Milky Way interstellar gas is beyond the scope of this paper. Here we mention that for the most pronounced Galactic feature (−23 km s^{-1}), the N(Na I)/N(Ca II) ratio is ∼0.50, which is typical of galactic halos (Hobbs 1978; Crawford 1992; Bertin et al. 1993). Sembach & Danks (1994) measured a mean Galactic halo N(Na I)/N(Ca II) ∼ 0.5.

Interestingly, the N(Na I)/N(Ca II) ratio for the main feature in M101 (+180 km s^{-1}) is ∼0.43, indicating that it may also originate in the halo of the host galaxy (see also King et al. 1995, for the case of SN 1994D). The really deviating case is that of the component at ∼128 km s^{-1}, which is clearly detected in Ca II, but not in Na I. The upper limit to the Na I column density deduced from the high S/N ratio SARG spectrum (day 11) is 1.5 × 10^{10} cm^{-2}, which yields N(Na I)/N(Ca II) ≤ 0.04. Such low values are rarely observed and indicate a mild depletion of calcium onto dust grains. A similar case was observed for one high-velocity component along the line of sight to SN 2000cx, where Ca II was detected, while Na I was not (Patat et al. 2007b). The corresponding ratio was N(Na I)/N(Ca II) ≤ 0.1.

Table 3. Na I and Ca II interstellar cloud model parameters.

Weighted average			Day 8	Day 11	Day 15	Day 21	Day 37
v	b	N	N	N	N	N	N
				Na I			
−67.2	2.1	$10.52^{+0.08}_{-0.11}$	$10.52^{+0.18}_{-0.26}$	$10.53^{+0.06}_{-0.07}$	$10.36^{+0.16}_{-0.19}$	$10.62^{+0.08}_{-0.10}$	$10.50^{+0.18}_{-0.25}$
−23.3	3.0	$10.74^{+0.07}_{-0.08}$	$10.70^{+0.13}_{-0.16}$	$10.80^{+0.04}_{-0.04}$	$10.80^{+0.07}_{-0.08}$	$10.73^{+0.06}_{-0.08}$	$10.60^{+0.16}_{-0.20}$
−12.6	3.4	$10.55^{+0.11}_{-0.11}$	$10.18^{+0.35}_{-0.79}$	$10.64^{+0.06}_{-0.06}$	$10.27^{+0.20}_{-0.29}$	$10.66^{+0.08}_{-0.09}$	$10.80^{+0.11}_{-0.14}$
179.6	3.8	$11.44^{+0.02}_{-0.02}$	$11.43^{+0.03}_{-0.04}$	$11.43^{+0.01}_{-0.01}$	$11.43^{+0.02}_{-0.02}$	$11.44^{+0.02}_{-0.02}$	$11.51^{+0.03}_{-0.03}$
193.6	6.4	$10.57^{+0.12}_{-0.16}$	$10.56^{+0.20}_{-0.29}$	$10.46^{+0.09}_{-0.13}$	$10.50^{+0.16}_{-0.18}$	$10.64^{+0.11}_{-0.11}$	$10.42^{+0.26}_{-0.46}$
				Ca II			
−66.4	0.7	$11.10^{+0.17}_{-0.20}$	$11.05^{+0.34}_{-0.69}$		$11.15^{+0.16}_{-0.21}$	$11.07^{+0.18}_{-0.24}$	
−65.7	32.0	$11.90^{+0.07}_{-0.07}$	$12.00^{+0.08}_{-0.07}$		$11.85^{+0.10}_{-0.10}$	$11.89^{+0.09}_{-0.10}$	
−37.5	1.0	$10.91^{+0.20}_{-0.24}$	<11.10		$10.91^{+0.20}_{-0.30}$	$10.97^{+0.18}_{-0.25}$	
−23.5	3.1	$11.04^{+0.17}_{-0.24}$	$11.00^{+0.23}_{-0.35}$		$11.03^{+0.19}_{-0.26}$	$11.03^{+0.17}_{-0.26}$	
−9.4	7.3	$11.63^{+0.06}_{-0.06}$	$11.72^{+0.07}_{-0.09}$		$11.61^{+0.08}_{-0.08}$	$11.58^{+0.08}_{-0.10}$	
127.8	6.2	$11.54^{+0.07}_{-0.07}$	$11.61^{+0.09}_{-0.10}$		$11.55^{+0.07}_{-0.10}$	$11.46^{+0.09}_{-0.13}$	
179.2	5.5	$11.82^{+0.04}_{-0.04}$	$11.89^{+0.05}_{-0.07}$		$11.80^{+0.05}_{-0.06}$	$11.78^{+0.05}_{-0.05}$	
197.0	6.7	$11.58^{+0.07}_{-0.08}$	$11.64^{+0.08}_{-0.09}$		$11.50^{+0.09}_{-0.11}$	$11.60^{+0.09}_{-0.09}$	
218.5	3.5	$10.89^{+0.21}_{-0.31}$	<11.10		$10.99^{+0.18}_{-0.31}$	$10.82^{+0.26}_{-0.50}$	

Finally, King et al. (1995) found N(Na I)/N(Ca II) = 0.1–0.3 for the high-velocity clouds observed along the line of sight to SN 1994D. Low ratios are, in general, typical of high velocity gas (Siluk & Silk 1974). The low value we derived for the component at ∼180 km s^{-1} is similar to those observed in intermediate- and high-velocity clouds by Molaro et al. (1993), who concluded that these clouds may contain very little dust, with calcium and sodium mainly in gaseous form (see also the properties measured by Cox et al. 2007, toward the LMC sight-lines). For these reasons it is reasonable to conclude that absorption system C (see Fig. 1) arises in an HVC.

5.1. Time evolution

The derived cloud parameters show some marginal evidence for time variability. The only possibly significant variation is seen for the host galaxy Na I component at ∼180 km s^{-1}. While the logarithmic column density derived for this absorption is 11.44 ± 0.02 on days 8, 11, 15 and 21, on day 37 this grows to 11.52 ± 0.03, which indicates a variation at the 3-sigma level. One may be tempted to attribute this fluctuation to the different instrumental setups. However, a direct comparison of the two spectra taken on days 8 and 37 (both obtained with FIES and the same setup) clearly shows that both components D_1 and D_2 had consistently deepened by about 16% on the second epoch, while their FWHM remained unchanged. The integrated EWs directly measured on the two spectra are 23.6 ± 1.9, 46.1 ± 2.0 mÅ, and 30.4 ± 2.4, 53.0 ± 2.5 mÅ for D_1 and D_2 on the two epochs, respectively, implying a variation ΔEW(Na I D_2) = 6.9 ± 3.2 mÅ. This strengthens the conclusion that whatever the reason for the change it cannot be attributed to a variation of instrumental resolution[3].

Although AES spectra have a significantly lower resolution (16.7 km s^{-1}, see Table 2), given the simple structure of the component at ∼180 km s^{-1}, they can be used together with the higher resolution data to study the variability on the whole time range spanned by the available observations (the relevant spectral regions are presented in Fig. A.2). To increase the S/N ratio we stacked the last two AES epochs (days 84 and 86).

In Table 4 we report the EWs of Na I D_2 and D_1 directly measured on all our spectra, together with their associated rms uncertainties, the S/N ratio achieved at 5900 Å, and the FWHM resolution. The weighted average EWs computed over all epochs for the two lines are 47.1 ± 0.8 mÅ and 27.4 ± 1.1 mÅ, respectively (the standard deviation of the EW measurements is 2.6 and 3.4 mÅ, respectively). The EWs are plotted as a function of time in Fig. 4 (empty symbols indicate the lower resolution AES data). Although all measurements are within less than 3-sigma from the weighted average (and are therefore formally consistent with a null variation), there is a systematic increase in both components. This becomes more evident if one considers only the higher resolution data (filled symbols in Fig. 4). However, the overall trend is mainly dominated by the last SARG measurement, which is characterized by a low S/N ratio, and may therefore be affected by larger systematic errors (e.g. continuum determination and telluric correction). For this reason, we do not attach too much confidence to it.

Because of the measured standard deviation (see above), the expected ±3-σ peak-to-peak range is $2 \times 3 \times 2.6$ mÅ = 15.6 mÅ. Considering the two extreme values (days 15.1 and 86.4), the observed peak-to-peak Na I D_2 EW variation amounts to 15.6 ± 6.5 mÅ. This is fully consistent with the expected value, and we therefore regard it as an upper limit on the observed EW variation. This is very small compared to the changes seen in SN 2006X (Patat et al. 2007a), and SN 2007le (Simon et al. 2009) during the first three months of their evolution, which exceeded 100 mÅ[4].

The fast SN expansion, coupled to the patchy nature of the ISM, can produce short time-scale changes in the IS absorption

[3] Because it is a fiber-fed spectrograph, FIES is not subject to changes of resolution caused by seeing variations. Moreover, a check on the comparison lamp emission lines on the two epochs shows that the resolution indeed remained constant.

[4] Even stronger variations were reported for SN 1999cl (Blondin et al. 2009) and SN 2006dd (Stritzinger et al. 2010), but no high-resolution spectroscopy was available in those cases.

A&A 549, A62 (2013)

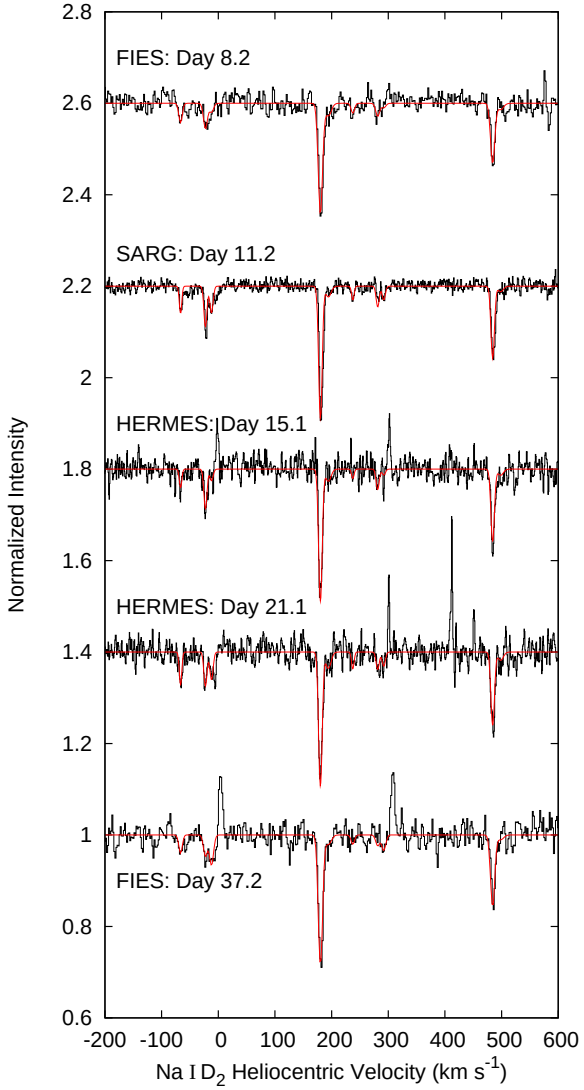

Fig. 2. Na I D spectra for each epoch (black histograms), with best-fit models overlaid (red curves). Spectra were normalized and offset vertically for display. Heliocentric velocity scale is given with respect to the Na D_2 line rest wavelength. The spurious emissions observed in some spectra around 0 and 300 km s^{-1} are residuals of the sky subtraction (see Sect. 2).

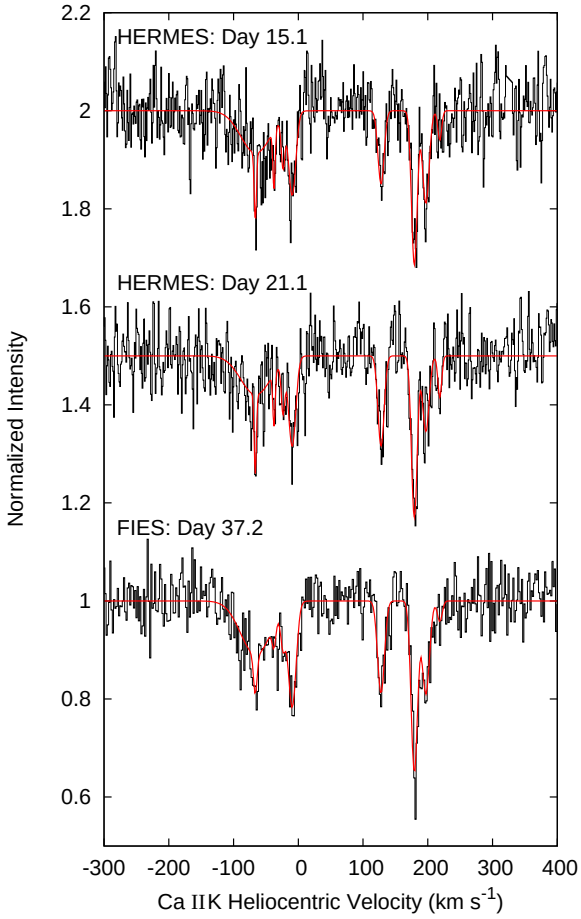

Fig. 3. Ca II K spectra for each epoch for which these data were obtained (black histograms), with best-fit models overlaid (red curves). Spectra were normalized and offset vertically for display. Heliocentric velocity scale is given with respect to the Ca II K line rest wavelength.

features. The analysis of their variations can be used to study the ISM small scale structure down to a few tens of AUs (Patat et al. 2010). The data currently available for SN 2011fe allow us to apply this method for the first three months of the SN evolution, when the photospheric radius increased from ∼10 AU to ∼350 AU. The simulations, run along the lines described in Patat et al. (2010), show that peak-to-peak variations $\Delta EW \lesssim 15$ mÅ imply $\Delta N \lesssim 4 \times 10^{11}$ cm^{-2} ($\Delta N/N \lesssim 1.4$). The maximum deviation measured in our simulations between any pair of epochs in the simulated data-set is ∼16 mÅ. The rms EW variation from the weighted average is 2.6 mÅ, matching the value derived from the data (see previous section).

The derived density contrast is compatible with the values measured in the Milky Way (Frail et al. 1994) and, therefore, the upper limit on the column density variation is fully in line with what is expected for a diffuse ISM with the same properties as in our own Galaxy. In other words, even if the observed fluctuations were real (including the apparent steady growth), these are consistent with the geometrical effect described in Patat et al. (2010). Therefore, we conclude that the absorption feature observed at ∼180 km s^{-1} is most likely associated to the ISM, and is placed at distances larger than $\sim 10^{19}$ cm (∼10 light years) from the explosion site, where the effects of the SN radiation field on the Na I ionization balance are negligible (Patat et al. 2007a; Simon et al. 2009). Unfortunately, the S/N ratio at ∼3900 Å in our data is not sufficient to study with the required accuracy the evolution of the Ca II H&K features, which in SNe 2006X and 2007le showed a distinct behavior (Patat et al. 2007a; Simon et al. 2009).

6. Discussion and conclusions

SN 2011fe is a slightly subluminous, Branch-normal explosion, very similar to the well studied SN 1994D (Nugent et al. 2011c). However, it is by no means clear whether all "normal" events, which share very similar spectroscopic and photometric properties, do also share a common progenitor channel. For this reason it is important to tie the reasonably well known progenitor nature of this particular event to other properties, which may allow us to identify similar events in less favorable cases, i.e. at

Table 4. Na I D equivalent widths.

Setup	Epoch (days)	$EW(D_2)$ (mÅ)	$EW(D_1)$ (mÅ)	S/N (5900 Å)	Resolution (km s^{-1})
*	1.5	45.0 ± 9.0	–	–	6.0
FIES#1	8.2	46.1 ± 2.0	23.6 ± 1.9	60	6.3
SARG#1	11.2	46.6 ± 1.5	26.3 ± 1.0	115	4.5
HERMES#1	15.1	44.3 ± 1.8	27.6 ± 1.8	50	3.7
AES#1	21.1	49.2 ± 2.2	34.2 ± 1.9	130	16.7
HERMES#2	21.1	44.3 ± 1.8	27.6 ± 1.8	50	3.7
AES#2	22.1	53.8 ± 4.2	28.5 ± 4.0	105	16.7
AES#3	29.1	51.9 ± 2.7	31.0 ± 2.2	190	16.7
AES#4	30.1	44.5 ± 2.3	33.7 ± 2.5	155	16.7
FIES#2	37.2	53.0 ± 2.5	30.4 ± 2.4	55	6.3
AES#5	56.1	48.7 ± 7.1	34.4 ± 7.3	50	16.7
AES#6+#7	85.2	58.7 ± 3.7	33.5 ± 3.0	115	16.7
SARG#2	86.4	59.9 ± 6.2	23.7 ± 7.3	16	4.5
Weighted average		47.1 ± 0.8	27.4 ± 1.1		

Notes. (*) The first epoch is from Nugent et al. (2011c).

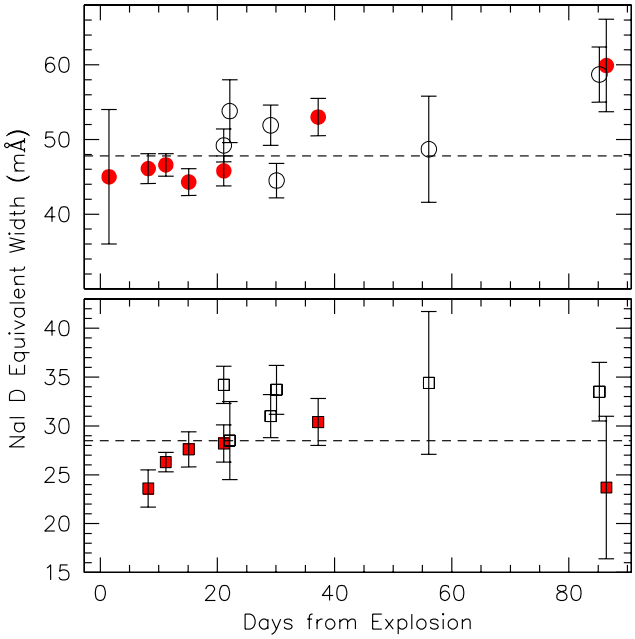

Fig. 4. EW time evolution of Na I D_2 (*upper panel*) and D_1 (*lower panel*). Values are from Table 4. The short-dashed horizontal lines mark the weighted average values. AES data are identified by empty symbols.

larger distances and without such exceptionally early discoveries. Among these is the circumstellar environment.

The method proposed by Patat et al. (2007a) that was subsequently expanded by Simon et al. (2009) has been applied to study the CSM of number of SNe Ia. In two cases it led to the detection of time-variant Na I features, which were interpreted as arising in the material lost by the progenitor system before the explosion (Patat et al. 2007a; Simon et al. 2009). The velocities of this material are consistent with those of a red giant, hence favoring a symbiotic system. The complex velocity structure shown by SN 2006X was explained as being the possible outcome of recurrent-novae episodes (Patat et al. 2007a). This suggestion is supported by the results of a similar analysis carried out on the known recurrent nova RS Oph, which shows strikingly similar CSM properties (Patat et al. 2011).

A study conducted on a large number of SN Ia has shown a statistically significant excess of blueshifted Na I features, which were interpreted as arising in material lost by the progenitor system (Sternberg et al. 2011). In addition, Foley et al. (2012) found that SN Ia displaying blue-shifted absorption features are characterized by higher ejecta velocities and redder colors with respect to the rest of the SN Ia sample. This gives support to the conclusions reached for SNe 2006X and 2007le. If this interpretation is correct, the measured fraction of SN Ia that display blueshifted features indicates that this channel is not a significant contributor to the global rate of thermonuclear events.

This result has to be reconciled with opposing evidence provided by the lack of CSM signatures in radio, UV, and X-ray domains. The two apparently contradicting results may be reconciled by a complex CSM structure (Patat 2011, Chomiuk et al. 2011), a delay between mass loss and SN explosion (Chomiuk et al. 2012; Margutti et al. 2012), or stellar evolution effects (Justham 2011). In this context we emphasize that, although it showed a marked Na I variation, SN 2006X was not detected by the VLA (Stockdale et al. 2006; Chandra, et al. 2006). Therefore, if the interpretation of the blueshifted absorption features is correct, the absence of a radio detection does not necessarily imply that the CS environment is "clean".

What makes SN 2011fe special is that its progenitor system was constrained with a significant confidence through a number of very stringent constraints (Li et al. 2011; Brown et al. 2012; Nugent et al. 2011c; Bloom et al. 2011; Liu et al. 2012). The absence of time-variable, blueshifted features and the "clean" environment reported in this paper fully agrees with the progenitor nature derived from the very early observations. The key question is whether the argument can be reversed, and the absence of such features in any SN Ia can be interpreted in terms of a similar progenitor, at least in a statistical sense. The answer to this question is awaiting detailed hydrodynamical modeling, which would tell us how frequently the physical conditions for producing observable narrow features are met, and what the viewing angle effects are (Mohamed et al., in prep.). Before this is accomplished, we can only speculate based on very small numbers.

As pointed out by Nugent et al. (2011c), SN 2011fe is spectroscopically very similar to the somewhat subluminous events SN 1992A (Kirshner et al. 1993) and SN 1994D (Patat et al. 1996). Although the link between these objects needs to be assessed considering a number of observables, we notice that all three objects present a very "clean" circum/interstellar environment (Kirshner et al. 1993; King et al. 1995; Patat et al. 1996). In the schema devised by Sternberg et al. (2011), SNe 1994D and 2011fe would be classified in the single/symmetric group (SS-type, 14.3%), while SN 1992A would fall in the group with no absorption detection (N-type, 37.1%). An inspection of the SS group shows that three SS-type events (out of five) have a single component, similar to SN 2011fe. If we assume that in all these cases the absorption is attributable to the host galaxy (and not to the CSM environment), and we add them to the N-type events, then the fraction of "clean" events in the Sternberg et al. sample is ~46%. One can imagine cases where the CSM environment is "clean", but the line of sight intercepts ISM clouds that are totally unrelated to the progenitor. Therefore, while the lack of conspicuous absorption features can be confidently interpreted in terms of a gas-free environment, the reverse argument does not hold.

The projected position of SN 2011fe falls close to a peripheral spiral arm (see for instance Nugent et al. 2011c). However,

A&A 549, A62 (2013)

the very low reddening and the absence of complex absorption structures strongly suggest that the explosion took place on the front side of the face-on host, most probably well above its galactic plane. Had the SN been placed on the rear side of the galaxy, the IS imprints would have been much more complex, irrespective of the progenitor's nature deduced from the early data. Therefore the above fraction can only represent a lower limit. On the other hand, because of the viewing angle effects, the fraction of events allegedly produced by systems that host a giant estimated by Sternberg et al. (2011) is also a lower limit (20–25%).

The sample of SN Ia with sufficient spectral resolution and time coverage is still relatively small, and therefore it may be premature to draw conclusions. The fraction of events showing time-variant features is ~17% (Patat 2011). Probing only the line of sight, this indicator also suffers from viewing-angle effects. In addition, the method only reveals material placed in the suitable range of distances from the SN that has the required densities (Patat et al. 2007a; Simon et al. 2009). Therefore, again, it gives only a lower limit to the fraction of events generated through this channel. Interestingly, this limit is reasonably similar to that derived from the excess of blue-shifted features (20%; Sternberg et al. 2011), and it supports the conclusion that this channel contributes in a significant way to the global SN Ia rate.

Acknowledgements. This work has been conducted in the framework of the European collaboration SN Variety and Nucleosynthesis Yields. This work is partially based on observations made with the Mercator Telescope, operated on the island of La Palma by the Flemish Community, at the Spanish Observatorio del Roque de los Muchachos of the Instituto de Astrofísica de Canarias. This work is partially based on observations obtained with the HERMES spectrograph, which is supported by the Fund for Scientific Research of Flanders (FWO), Belgium, the Research Council of K. U. Leuven, Belgium, the Fonds National Recherches Scientific (FNRS), Belgium, the Royal Observatory of Belgium, the Observatoire de Geneve, Switzerland and the Thüringer Landessternwarte Tautenburg, Germany. This work is partially based on observations made with the Nordic Optical Telescope, operated on the island of La Palma jointly by Denmark, Finland, Iceland, Norway, and Sweden, in the Spanish Observatorio del Roque de los Muchachos of the Instituto de Astrofisica de Canarias. This work is partially based on observations made with the SARG spectrograph at the Italian Telescopio Nazionale Galileo (TNG), operated on the island of La Palma by the Fundaciòn Galileo Galilei of the INAF (Istituto Nazionale di Astrofisica) at the Spanish Observatorio del Roque de los Muchachos of the Instituto de Astrofisica de Canarias. This work is partially based on data collected at the 1.82 m Copernico telescope on Mt. Ekar (Asiago, Italy). M.C. thanks the NASA Astrobiology Institute via the Goddard Center for Astrobiology. V.S. acknowledges financial support from Fundação para a Ciência e a Tecnologia under program Ciência 2008 and a research grant PTDC/CTE-AST/112582/2009.

Appendix A: Removal of telluric features

Although the spectral region of Ca II H&K is free of telluric absorption features, this is not the case for Na I D, and especially K I λ7665 and λ7699. Because the observations were conducted mostly at relatively high airmasses (see Table 1), these are quite severely disturbed by water bands.

The removal of telluric absorption features is usually performed using spectra of bright stars obtained with the same instrumental setup and similar airmass as for the scientific target. In this paper we adopted a different approach, using an atmospheric transmission model (see for instance Stevenson 1994; Seifahrt et al. 2010). The advantages over a direct observation are a) the absence of intrinsic photospheric features; b) the absence of interstellar features (chiefly Na I D lines); c) the infinite S/N ratio, and d) the exact wavelength scale. The latter provides an absolute reference to which the observed spectra can be corrected via cross-correlation techniques (see below).

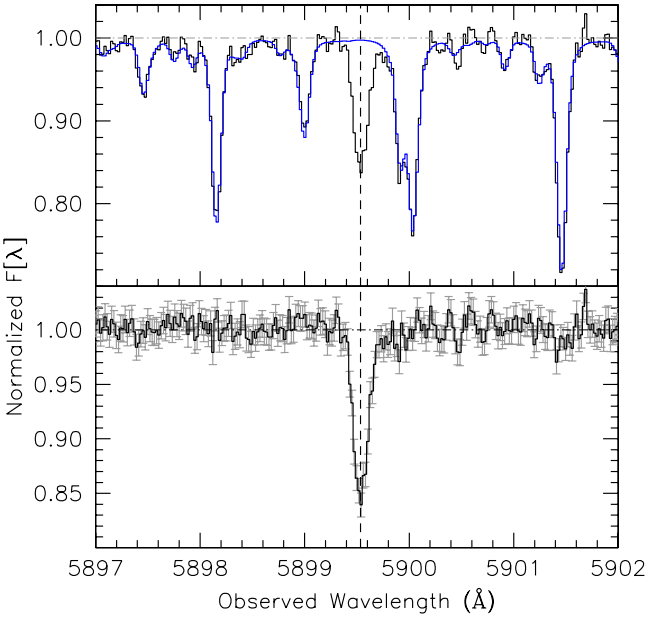

Fig. A.1. Example of telluric features removal for the SARG spectrum in the region of Na I D_1. *Upper panel*: observed data (black line) and best fit LBLRTM model (blue line). *Lower panel*: telluric-corrected spectrum. The dashed vertical line marks the position of Na I D_1 (v_{hel} ~180 km s^{-1}). The S/N ratio on the continuum is about 100 (the error-bars indicate the estimated rms noise).

In this work we adopted the Line By Line Radiation Transfer Model (LBLRTM; Clough et al. 2005). This code is based on the HITRAN database (Rothman et al. 2009). It has been validated against real spectra from the UV to the sub-millimeter, and is widely used for the retrieval of atmospheric constituents[5]. LBLRTM solves the radiative transfer using an input atmospheric profile, which contains the height profiles for temperature, pressure, and chemical composition. For our purposes we adopted the standard LBLRTM equatorial profile.

After computing the synthetic model in the regions of interest and for the given airmass, this is convolved with the instrumental profile and the wavelength correction is computed via cross-correlation. The absence of intrinsic narrow absorptions in the SN spectrum and the weakness of the interstellar features in the Na I and K I regions (see below) make the correlation function peak very well defined. The wavelength solutions for FIES, HERMES and SARG spectra were all found to match the model wavelength with a maximum deviation of 130 m s^{-1}, that is more than five times smaller than the pixel size. Therefore, no wavelength correction was applied to these data. For the AES spectra, maximum deviations of 6.6 km s^{-1} (about one pixel) were found, and the spectra were corrected accordingly. The final wavelength accuracy is ~0.1 km s^{-1} for the FIES, HERMES and SARG data, while it is ~0.3 km s^{-1} for the AES spectra.

An example of telluric correction is presented in Fig. A.1 for the SARG spectrum. All telluric features are removed at the level of a few percent, which is comparable to (or better than) the continuum rms noise of all spectra presented in this paper.

[5] See http://rtweb.aer.com/lblrtm.html

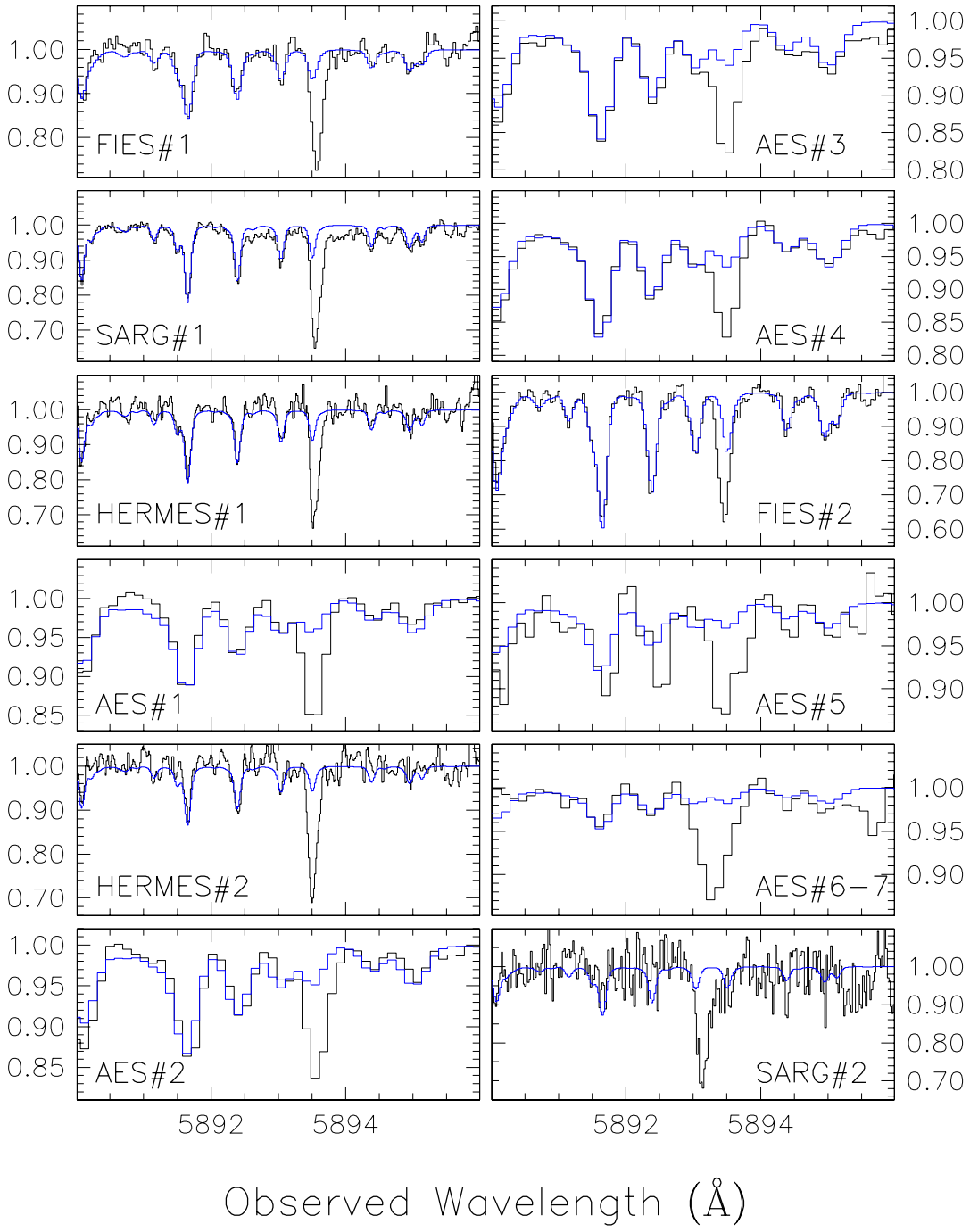

Fig. A.2. Region of the Na I D_2 at the host galaxy restframe velocity for the twelve epochs presented in this paper. The blue curves trace the best-fit telluric synthetic spectrum.

The best-fit telluric spectra for all epochs are presented in Fig. A.2 for the Na I region at the host galaxy restframe velocity.

References

Bertin, P., Lallement, R., Ferlet, R., & Vidal-Madjar, A. 1993, A&A, 278, 549
Bianco, F. B., Howell, D. A., Sullivan, M., et al. 2011, ApJ, 741, 20
Blondin, S., Prieto, J. L., Patat, F., et al. 2009, ApJ, 693, 207
Bloom, J. S., Kasen, D., Shen, K. J., et al., 2012, ApJ, 744, L17
Bosma, A., Goss, W. M., & Allen, R. J. 1981, A&A, 93, 106
Brown, P. J., Dawson, K. S., de Pasquale, M., et al. 2012, ApJ, 753, 22
Chalabaev, A., & Millard, J. P. 1983, A&A, 127, 279
Chandra, P., Chevalier, R., & Patat, F. 2006, ATel, 954
Chomiuk, L., Soderberg, A. M., Chevalier, R., Badenes, C., & Fransson, C. 2011, A&AS, 21730405C
Chomiuk, L., Soderberg, A. M., & Moe, M. 2012, ApJ, 750, 164
Clough, S. A., Shephard, M. W., Mlawer, E. K., et al. 2005, J. Quant. Spectrosc. Radiat. Transfer, 91, 233
Cox, N. L. J., & Patat, F. 2008, A&A, 485, L9
Cox, N. L. J., Cordiner, M. A., Ehrenfreund, P., et al. 2007, A&A, 470, 941
Crawford, I. A. 1992, MNRAS, 254, 264
de Vaucouleurs, G., de Vaucouleurs, A., Corwin, H. G., et al. 1991, Third Reference Catalogue of Bright Galaxies, Ver. 3.9
Deshpande, A. A. 2000, MNRAS, 317, 199

Foley, R. J., Simon, J. D., Burns, C. R., et al. 2012, ApJ, 752, 101
Frail, D. A., Weisberg, J. M., Cordes, H. M., & Mathers, A. 1994, ApJ, 436, 144
Gratton, R. G., Bonanno, G., Bruno, P., et al. 2001, Exp. Astron., 12, 107
Hayden, B. T.,Garnavich, P. M., & Kasen, D. 2010, ApJ, 722, 1691
Heiles, C. 1997, ApJ, 481, 193
Herbig, G. H. 1995, ARA&A, 33, 19
Hobbs, L. M. 1978, ApJS, 38, 129
Horesh, A., Kulkarni, S. R., Fox, D. B., et al. 2012, ApJ, 746, 21
Horne, K. 1986, PASP, 98, 609
Howarth, I. D., Price, R. J., Crawford, I. A., & Hawkins, I. 2002, MNRAS, 335, 267
Immler, S. I., Brown, P. J., Milne, P., et al. 2006, ApJ, 648, L119
Justham, S. 2011, ApJ, 730, L34
King, D. L., Vladilo, G., Lipman, K., et al. 1995, A&A, 300, 881
Kirshner, R. P., Jeffery, D. J., Leibundgut, B., et al. 1993, ApJ, 415, 589
Leonard, D. C. 2007, ApJ, 670, 1275
Li, W., Bloom, J. S., Podsiadlowski, Ph., et al. 2011, Nature, 480, 348
Liu, J., Di Stefano, R., Wang, T., & Moe, M. 2012, ApJ, 749, L141
Lundqvist, P., Sollerman, J., Leibundgut, B., et al. 2003, in From twilight to highlight: the physics of Supernovae, eds. W. Hillebrandt, & B. Leibundgut (Berlin: Springer), 309
Lundqvist, P., Matheson, T., Sollerman, J., et al. 2005, in Cosmic Explosions, eds. J. M. Marcaide, & K. W. Weiler, CD-ROM version, IAU Coll., 192, 81
Margutti, R., Soderberg, A. M., Chomiuk, L., et al. 2012, ApJ, 751, 734
Mattila, S., Lundqvist, P., Sollerman, J., et al. 2005, A&A, 443, 649
Molaro, P., Vladilo, G., Monai, S., et al. 1993, A&A, 274, 505
Munari, U., & Zwitter, U. 1997, A&A, 318, 269
Nugent, P., Sullivan, M., Bersier, D., et al. 2011a, ATel #3581
Nugent, P., Magill, L., Kotak, R., et al. 2011b, CBET, 2791, 1
Nugent, P. E., Sullivan, M., Cenko, S. B., et al. 2011c, Nature, 480, 344
Panagia, N., Romaniello, M., Gilmozzi, R., et al. 2006, ApJ, 469, 396
Patat, F., 2011, in Binary paths to Type Ia Supernova explosions, IAUS. 281, AIPC, eds. R. Di Stefano, & M. Orio, in press [arXiv:1109.5799]
Patat, F., Benetti, S., Cappellaro, E., et al. 1996, MNRAS, 278, 111
Patat, F., Kumar, R., Barley, M. E., et al. 2007a, Science, 30, 490
Patat, F., Jeffery, D. J., Leibundgut, B., et al. 2007b, A&A, 474, 931
Patat, F., Cox, N. L. J., Parrent, J., & Branch, D. 2010, A&A, 514, A78
Patat, F., Chugai, N. N., Podsiadlowski, Ph., et al. 2011, A&A, 530, A63
Raskin, G., van Winckel, H., Hensberge, H., et al. 2011, A&A, 526A, A69
Schlegel, D. J., Finkbeiner, D. P., & Davis, M. 1998, ApJ, 500, 525
Röpke, F. K., Kromer, M., Seitenzahl, I. R., et al. 2012, ApJ, 750, 19
Rothman, L. S., Gordon, I. E., Barbe, A., et al. 2009, J. Quant. Spectrosc. Radiat. Transfer, 110, 533
Seifahrt, A., Käufl, H. U., Zängl, G., et al. 2010, A&A, 524A, 11
Sembach, K. R., & Danks, A. C. 1994, A&A, 289, 539
Siluk, R. S., & Silk, J. 1974, ApJ, 192, 51
Simon, J., Gal-Yam, A., Gnat, O., et al. 2009, ApJ, 702, 1157
Sternberg, A., Gal-Yam, A., Simon, J. D., et al. 2011, Science, 333, 856
Stevenson, C. C. 1994, MNRAS, 267, 904
Stockdale, C. J., Kelley, M., Sramek, R. A., et al. 2006, CBET 396
Stritzinger, M., Burns, C. R., Phillips, M. M., et al. 2010, AJ, 140, 2036
Whelan, J., & Iben, I. 1973, ApJ, 186, 1007

A.7 Observations of transient astronomical objects

As part of some preparations for the *Gaia* space mission, I planned, carried out, and supported observations of Blazar candidates discovered by the Catalina Real Time Survey (CRTS). These observations had two primary goals, namely i) to provide real-life tests for the pipeline being developed as part of the *Gaia* science alerts[1] system (e.g. Wyrzykowski et al. 2012); ii) to observationally verify the classification of the candidates by investigating the location of the Balmer discontinuity using the multiple filters.

To this end, multi-band photometry (typically in filters B, R, and I) were obtained using ECAM mounted to the 1.2 m Swiss Euler telescope at ESO La Silla observatory. Using the basic calibration procedures developed by my friend Monika Lendl, I then performed basic calibration of the data, i.e., flatfielding using master flat fields and bias subtraction (dark current corrections are not required due to the low noise level of ECAM). With help from Ashish Mahabal, astrometric calibrations were performed using the excellent tool `astrometry.net` before uploading the data to the Cambridge photometric calibration server. These efforts, besides the difficult-to-quantify gain in experience and value of providing feedback for the *Gaia* science alerts system, resulted in the discovery of a Galactic Cataclysmic Variable, see Mahabal et al. (2012).

[1] `http://www.ast.cam.ac.uk/ioa/wikis/gsawgwiki/index.php/Main_Page`

Appendix B

Publications prepared during this thesis

B.1 List of publications

B.1.1 Refereed articles

On the Effect of Rotation on Populations of Classical Cepheids I. Predictions at Solar Metallicity
R. I. Anderson, S. Ekström, C. Georgy, G. Meynet, N. Mowlavi, and L. Eyer
A&A 2014, in press

Cepheids in open clusters: an 8D all-sky census
R. I. Anderson, L. Eyer, and N. Mowlavi
MNRAS, **434**, pp. 2238-2261, 2013

Discovery of the spectroscopic binary nature of three bright southern Cepheids
L. Szabados, **R. I. Anderson**, A. Derekas, L. L. Kiss, T. Szalai, P. Székely, and J. L. Christiansen
MNRAS, **434**, pp. 870-877, 2013

Discovery of the spectroscopic binary nature of six southern Cepheids
L. Szabados, A. Derekas, L. L. Kiss, J. Kovács, **R. I. Anderson**, C. Kiss, T. Szalai, P. Székely, and J. L. Christiansen
MNRAS, **430**, pp. 2018-2028, 2013

Multi-epoch high-resolution spectroscopy of SN 2011fe. Linking the progenitor to its environment
F. Patat, M. A. Cordiner, N. L. J. Cox, **R. I. Anderson**, A. Harutyunyan, R. Kotak, L. Palaversa, V. Stanishev, L. Tomasella, S. Benetti, A. Goobar, A. Pastorello, and J. Sollerman
A&A, **549**, A62, 2013

Standard candles from the Gaia perspective
L. Eyer, L. Palaversa, N. Mowlavi, P. Dubath, **R. I. Anderson**, D. W. Evans, T. Lebzelter, V. Ripepi, L. Szabados, S. Leccia, and G. Clementini
Ap&SS, **341**, pp. 207-214, 2012

On detectability of Zeeman broadening in optical spectra of F- and G-dwarfs
R. I. Anderson, A. Reiners, and S. K. Solanki
A&A, **522**, A81, 2010

B.1.2 Conference proceedings

THE GALACTIC CEPHEID PERIOD-LUMINOSITY RELATION REVISITED USING BONA FIDE CLUSTER CEPHEIDS
R. I. Anderson, N. Mowlavi, and L. Eyer
In Advancing the Physics of Cosmic Distances, ed. R. de Grijs
IAU Symposium (CUP), **289**, pp. 153-156, 2013

CEPHEIDS IN GALACTIC OPEN CLUSTERS: AN ALL-SKY CENSUS
R. I. Anderson, L. Eyer, N. and Mowlavi
In New Horizons In Time-Domain Astronomy, eds. E. Griffin, R. Hanisch, R. Seaman
IAU Symposium (CUP), **285**, pp. 275-277, 2012

POPULATIONS OF VARIABLE STARS IN OPEN CLUSTERS
R. I. Anderson, N. Mowlavi, and L. Eyer
In Star Clusters in the Era of Large Surveys, eds. A. Moitinho J. Alves
Astrophysics and Space Science Proceedings (Springer), pp. 255-256, 2012

TIME-RESOLVED SURVEYS OF STELLAR CLUSTERS
Eyer, L., Eggenberger, P., Greco, C., Saesen, S., **Anderson, R. I.**, and Mowlavi, N.
In Star Clusters in the Era of Large Surveys, eds. A. Moitinho J. Alves
Astrophysics and Space Science Proceedings (Springer), pp. 21-29, 2012

ZEEMAN BROADENING IN OPTICAL STOKES I OF SOLAR-LIKE STARS
R. I. Anderson, A. Reiners, S. K. Solanki
16th Cambridge Workshop on Cool Stars, Stellar Systems, and the Sun, eds. C. Johns-Krull, M. K. Browning, A. A. West
ASP Conf. Series, **448**, pp. 1061-1064, 2011

B.1.3 Online catalogs

CEPHEIDS IN OPEN CLUSTERS
R. I. Anderson, L. Eyer, N. Mowlavi
VizieR Online Data Catalog, J/MNRAS/434/2238, 2013

B.1.4 Other publications

A SEARCH FOR ROCKY PLANETS TRANSITING BROWN DWARFS
A. H. M. J. Triaud, M. Gillon, F. Selsis, J. N. Winn, B.-O. Demory, E. Artigau, G. P. Laughlin, S. Seager, C. Helling, M. Mayor, L. Albert, **R. I. Anderson**, E. Bolmont, R. Doyon, T. Forveille, J. Hagelberg, J. Leconte, M. Lendl, S. Littlefair, S. Raymond, J. Sahlmann
ArXiv e-prints, **1304.7248**, 2013

CSS120113:040822+141516 = MASTER040821.91+141515.0 IS A CV
A. A. Mahabal, A. J. Drake, S. G. Djorgovski, R. Williams, M. J. Graham, C. Donalek, **R. Anderson**, L. Eyer, E. C. Beshore, S. M. Larson, J. Prieto, M. Catelan, E. Christensen
The Astronomer's Telegram, **3872**, 2012

Advancing the Physics of Cosmic Distances
Proceedings IAU Symposium No. 289, 2012
Richard de Grijs & Giuseppe Bono, eds.

DOI: 00.0000/X000000000000000X

The Galactic Cepheid period–luminosity relation revisited using *bona fide* cluster Cepheids

Richard I. Anderson, Nami Mowlavi, and Laurent Eyer

Observatoire de Genève, Université de Genève, 51 Ch. des Maillettes, CH-1290 Versoix, Switzerland

email: richard.anderson@unige.ch

Abstract. Classical Cepheids in Galactic open clusters (cluster Cepheids: CCs) have been studied extensively for multiple decades, thanks to their importance as calibrators of the Galactic Cepheid period–luminosity relation (PLR). Here we revisit the calibration of the Galactic PLR using a new sample of CCs, since even recent calibrations show significant discrepancies. The CC sample employed for the calibration is based on the preliminary results of a self-consistent, eight-dimensional all-sky census. This census is based mostly on literature data, supplemented with high-precision radial-velocity observations from both hemispheres. New CCs are identified from our census and the degree of confidence in membership is quantified for known candidates. Using only *bona fide* CCs, we obtain $M_V = (-3.08 \pm 0.50) \log P + (-0.94 \pm 0.42)$ mag, which is in perfect agreement with the results by Sandage, Tammann, and Reindl, albeit with larger error bars and an rms of 0.21 mag. The key to obtaining a meaningful calibration is to employ accurate cluster distance moduli and space reddening values. A homogeneous study of all *bona fide* host clusters would be desirable to increase precision and confidence in the calibration.

Keywords. Cepheids, open clusters and associations: general, stars: distances, distance scale

1. Introduction

This year marks the centennial anniversary of the discovery of period–luminosity (density) relationships by Leavitt & Pickering (1912), who identified this important proportionality in a sample of 25 periodic variable stars identified among 1777 stars in the Small Magellanic Cloud. A century later, Cepheids and other pulsating stars are corner stones of the distance scale and commonly used to determine distances of up to tens of Mpc, and this Symposium had many excellent examples that this can be done at impressive precision. Nevertheless, there exist significant differences between PLRs found in the (recent) literature, possibly indicating less consensus on the accuracy of these measurements than sometimes acknowledged. We illustrate this fact in Fig. 1, which shows PLRs based on different methods, including absolute and relative trigonometric parallaxes, Baade–Becker–Wesselink-type methods, as well as the calibration by Sandage et al. (2004) which is partially based on Cepheids in Galactic open clusters. In light of such discrepancies, we deem that a self-consistent analysis of membership for CCs is warranted, and here we present a calibration obtained from the preliminary results of our mostly literature-based, eight-dimensional, self-consistent all-sky census of classical Cepheids in Galactic open clusters.

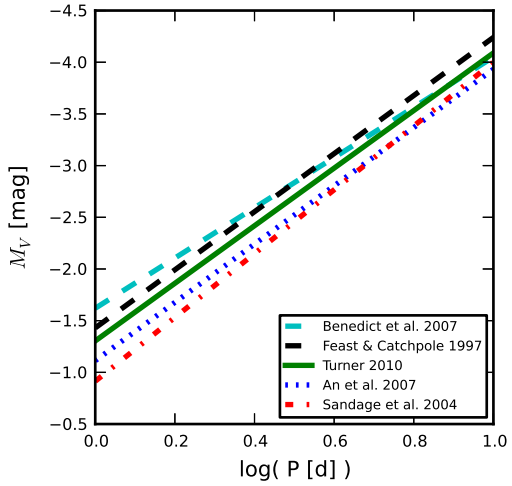

Figure 1. Literature PLRs, see legend

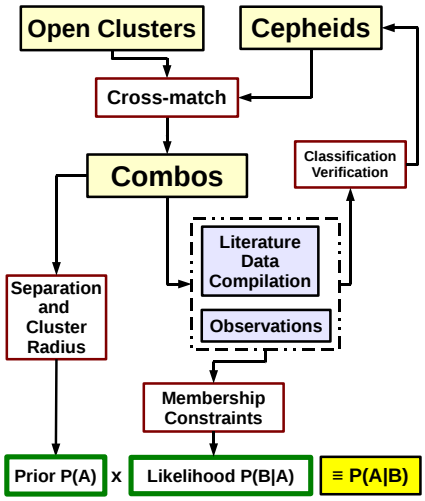

Figure 2. Membership analysis overview

2. The Cluster Cepheid Sample

Fig. 2 schematically shows how the all-sky membership census for CCs is set up. Starting from a cross-match of known open clusters and Cepheids, a prior (from the position on the sky and the cluster radius) and a likelihood (using all other available data) are used to calculate membership probabilities. The data used to calculate the likelihoods is mostly from published literature, and supplemented by observations taken at the Swiss Euler telescope at ESO La Silla, Chile, and at the Mercator telescope at the Roque de los Muchachos Observatory on La Palma, Spain.

The membership census is eight-dimensional, employing the three spatial dimensions, proper motion, radial velocity, iron abundance as proxy for metallicity, and the age as constraints. A total of 2570 cluster–Cepheid combinations were investigated with the aim of identifying new CCs and quantifying the degree of confidence one can have in the membership of CC candidates previously discussed in the literature. We identify 13 *bona fide* members of open clusters, three of which are pulsating in their first overtones. Unfortunately, our analysis is somewhat limited by the open cluster data available, so that another 12 CCs known in Turner (2010) could not be revisited. We ignore these cases here, and stick to the highest-confidence CCs for the calibration.

Another important part of the process is classification verification through photometry and spectroscopy, since we systematically include Cepheid candidates from automated surveys such as ASAS, NSVS, and ROTSE that are not yet confirmed as Cepheids.

The sample of CCs used for the PLR calibration are the 10 *bona fide* CCs that pulsate in the fundamental mode. These constitute the cluster Cepheids in which we can have the highest confidence of membership, based on our self-consistent study. For details on the analysis and the sample used (including the observing program, the new CC calibrators, etc.), we refer to our publication in preparation (R. I. Anderson et al., in prep.).

3. The PLR calibration

Since cluster membership has been thoroughly established for the Cepheids used in this calibration, the independently (from the Cepheids) determined cluster distances can be used to obtain a Galactic calibration of the PLR, in particular of its zero point. As is clear

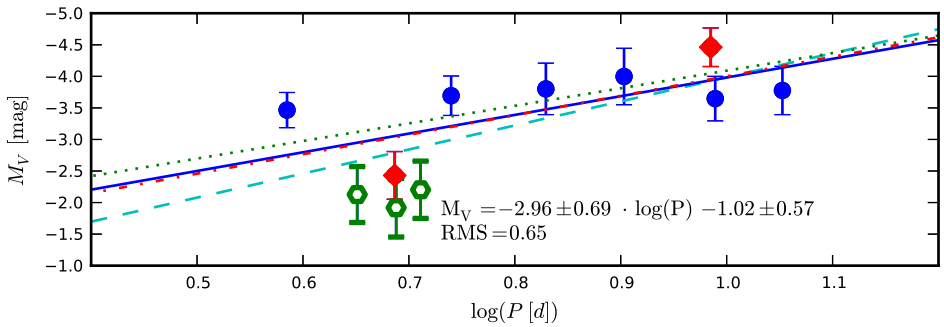

Figure 3. Solid blue line: weighted least-squares fit to the 'standard' data set (cluster data based on fewer stars, no line-of-sight dependence of reddening); red dash-dotted line: non-weighted fit; dotted green line: PLR from Benedict et al. (2007); dashed cyan line: PLR from Sandage et al. (2004).

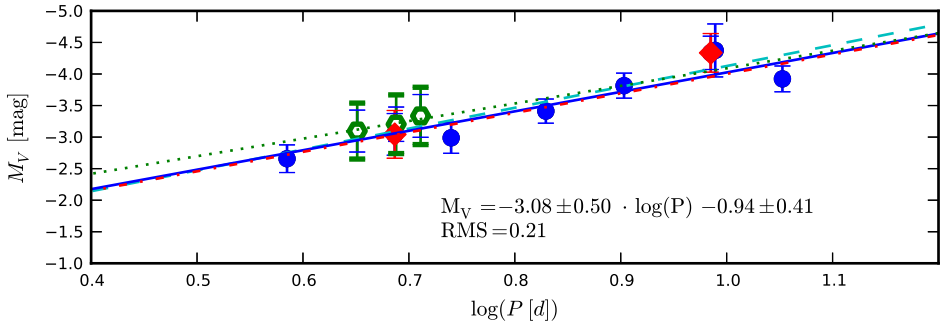

Figure 4. Solid blue line: weighted least-squares fit to the 'optimal' data set (clusters studied in detail individually, line-of-sight-dependent reddening law); red dash-dotted line: non-weighted fit; dotted green and dashed cyan lines: as in Fig. 3.

from Fig. 1, this remains an important task, and is complicated by the small number of cluster Cepheids, and the difficulties in determining accurate and precise cluster distances and space reddening values.

Obviously, the Cepheids' estimated absolute magnitudes, M_V, depend critically on the cluster distance modulus and reddening values adopted. Fig. 3 shows M_V calculated using distance moduli from catalogs containing many hundreds of clusters. Such semi-automated and often model-dependent (isochrone-based) studies do not take into account line-of-sight variations in the reddening law and typically use the canonical $R \equiv 3.1$. In addition, they are often limited in photometric depth and therefore determine distances (and ages) using relatively few stars. A great benefit of such studies, however, is self-consistency and homogeneity. We refer to these M_V magnitudes as the 'standard' set.

Fig. 4, in contrast, shows the absolute magnitudes estimated using line-of-sight-dependent reddening laws and distance moduli based on deeper photometric studies found in the literature. Unfortunately, no homogeneous detailed study could be found that provides these data for the entire sample of host clusters. However, most host clusters have been studied previously and we can therefore manually select references we deem optimal. This manual compilation of references aims to maximize homogeneity and detail (number of stars studied, treatment of reddening). No criterion to favor any existing PLR calibration was imposed. We therefore refer to this set of M_V values as the 'optimal' set, since the greatest accuracy can be assumed for these values.

The errors in M_V are estimated by taking into account uncertainties in reddening and

an *ad hoc* estimate of the distance modulus. Green open hexagons represent Cepheids in NGC 7790 studied by Gupta et al. (2000), and have slightly larger error bars to avoid excessive weight on data points that depend on a single cluster's values for reddening and distance modulus. Solid blue circles represent other CCs previously discussed in the literature. The two new cluster Cepheids (to be identified in R. I. Anderson et al., in prep.) employed in this calibration will benefit greatly from a more detailed study of their host clusters. For the time being, we employ $R = 3.1$ and the distance modulus given in the original literature. They are marked as solid red diamonds in Figs 3 and 4.

We perform weighted and non-weighted least-squares fits to both data sets (standard and optimal). The results between weighted and non-weighted fits are very similar for both data sets. As can be expected, we obtain large scatter (rms = 0.65 mag) for the standard data set. The optimal set exhibits less scatter (rms = 0.21 mag) around the relation $M_V = (-3.08 \pm 0.50) \log P + (-0.94 \pm 0.42)$ mag, with considerable uncertainty in both the zero point and the slope. We note that our result is in near exact agreement with the PLR in Sandage et al. (2004), although nearly all of the PLRs shown in Fig. 1 agree with these results to within these uncertainties. However, the discrepancy between the PLRs becomes dramatic at longer periods ($P > 10$ days) and can significantly impact the distance scale, since longer-period Cepheids are more luminous and are, therefore, seen to greater distances. The zero point of the PLR hence remains of key importance and a calibration like ours has the potential to contribute significantly. However, additional refinement is required, and can be achieved through detailed studies of Cepheid host clusters, as well as through continued efforts to discover CCs.

4. Conclusion

This work clearly shows the need for continued studies of the Cepheid PLR within our own Galaxy. Our approach aims to maximize the number of CCs that can be employed for the PLR calibration through an unprecedented eight-dimensional all-sky census that furthermore self-consistently evaluates the degree of confidence one can have in cluster membership, thereby ensuring that only the best CCs are used in the calibration. Unfortunately, the precision of our results remains limited by the small number of *bona fide* CCs and the relatively uncertain open cluster data.

A good way to improve on our results will be to carry out a homogeneous reddening and distance modulus determination for all clusters in the sample. In less than a year from now, *Gaia* will be launched. Providing homogeneous positions, astrometry, photometry and for some stars even spectroscopy, *Gaia* will provide unprecedented astrometric precision that will revolutionize membership studies such as ours. Based on *Gaia* data, it will thus be possible to significantly improve our membership analysis and enable an all-sky, and much more homogeneous study of the kind presented here.

References

An, D., Terndrup, D.M., & Pinsonneault, M.H. 2007, *ApJ*, 671, 1640
Benedict, G.F., McArthur, B.E., Feast, M.W., et al. 2007, *AJ*, 133, 1810
Feast, M.W., & Catchpole, R.M. 1997, *MNRAS*, 286, L1
Gupta, A.C., Subramaniam, A., Sagar, R., & Griffiths, W.K. 2000, *A&AS*, 145, 365
Leavitt, H.S., & Pickering, E.C. 1912, *Harvard Coll. Obs. Circ.*, 173, 1
Sandage, A., Tammann, G.A., & Reindl, B. 2004, *A&A*, 424, 43
Turner, D.G., Mandushev, G.I., & Welch, G.A. 1997, *AJ*, 113, 2104
Turner, D.G. 2010, *Ap&SS*, 326, 219

Populations of Variable Stars in Open Clusters

Richard I. Anderson, Nami Mowlavi, and Laurent Eyer

Abstract We present our work in progress that explores links between properties of variable star populations and their host open clusters. Information from WebDA and the Dias catalog [1] has been considered. We explain the context, consider open cluster red giants as tracers of a Galactic age-metallicity relationship, and outline the intended future direction and prospects of this project.

1 Context

Open clusters (OCs) can be seen as snapshots probing stellar evolution as a function of age and metallicity. The variable star content of an OC may depend on these (and further) parameters. Thus, there exists great potential for providing stringent constraints on stellar evolution theory by investigating how variable star populations differ among OCs. The following information is particularly useful in this respect: instability strip boundaries and (im-)purity; relative variable star fractions; variability properties; metallicity; memberships; multiple star fractions.

We consider published literature on variable star studies in OCs. As a first step, we take information from two sources: the WebDA OC database and Dias OC catalog [1]. While WebDA is not a variable star database, it does provide some information on certain types of stars, e.g. periodic variables or red giants (RGs). RGs can be considered (candidate) variable stars, since different kinds of variability occur during the RG phase, and many RGs exhibit solar-like oscillations (e.g. [2]). Additionally, RGs are ideal to determine abundances or binary fractions (e.g. [3] to

Richard I. Anderson and Laurent Eyer
Observatoire de Genève, Université de Genève, 51 Ch. des Maillettes, CH-1290 Sauverny, Switzerland, e-mail: richard.anderson@unige.ch

Nami Mowlavi
ISDC, Observatoire de Genève, Université de Genève, 16 Ch. d'Ecogia, CH-1290 Versoix, Switzerland

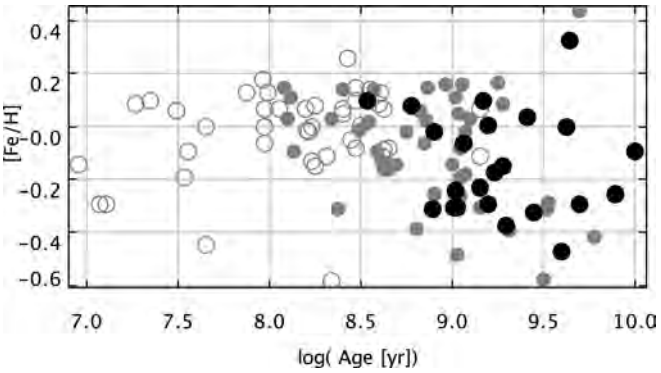

Fig. 1 [Fe/H] against age for OCs with RGs. Data from WebDA and [1]. Binned number of RGs, $N_{\rm RG}$, indicated in greyscale. Open circles: $N_{\rm RG} < 10$; grey filled circles: $10 \leq N_{\rm RG} \leq 50$; black filled circles: $N_{\rm RG} > 50$. Some entries may be erroneous: e.g. Ruprecht 97 ([Fe/H] / log(age) = $-0.59/8.34$) is actually close to solar metallicity [5].

[4]). Finally, since cluster membership can be reliably determined for RGs, chemical abundance measurements from open cluster red giants can contribute to the understanding of the age-metallicity relationship, cf. Fig. 1: older OCs harbor more RGs and show a larger spread in [Fe/H].

2 Outlook

As a next step, we will carefully check the references in WebDA and [1] (e.g. for cluster ages, since automatic age determinations are prone to errors due to presence of Blue Stragglers or contamination from non-members), and continue by considering additional sources. Supplementary data from archives or new observations, e.g. abundance determinations for individual clusters, will help to complete the picture. The inhomogeneity of the information investigated poses a major challenge, e.g. since systematic uncertainties may vary between sources. Nevertheless, we are confident that stellar evolution will benefit from combining published literature results from studies on stellar variability in OCs in such a systematic way.

Acknowledgements This research has made use of: the WEBDA database (www.univie.ac.at/webda), operated at the Institute for Astronomy of the University of Vienna; NASA's Astrophysics Data System Bibliographic Services; the SIMBAD database, operated at CDS, Strasbourg, France; the VO tool `TOPCAT` (www.starlink.ac.uk/topcat).

References

1. W.S. Dias, B.S. Alessi, A. Moitinho, J.R.D. Lépine, A&A **389**, 871 (2002)
2. S. Hekker, T. Kallinger, F. Baudin, J. De Ridder, C. Barban, F. Carrier, A.P. Hatzes, W.W. Weiss, A. Baglin, A&A **506**, 465 (2009)
3. J.C. Mermilliod, M. Mayor, A&A **219**, 125 (1989)
4. J.C. Mermilliod, J. Andersen, D.W. Latham, M. Mayor, A&A **473**, 829 (2007)
5. J.J. Clariá, A.E. Piatti, J.C. Mermilliod, T. Palma, Astronomische Nachrichten **329**, 609 (2008)

Further Acknowledgments

During my PhD, I have had the great opportunity to make use of many infrastructures, tools, and services that were provided to me free of charge and that require huge efforts to maintain.

The observational data obtained here are:

- based in part on observations collected at the ESO La Silla Observatory with the CORALIE echelle spectrograph mounted to the Swiss 1.2 m Euler telescope.
- based in part on observations made with the Mercator Telescope, operated on the island of La Palma by the Flemish Community, at the Spanish Observatorio del Roque de los Muchachos of the Instituto de Astrofísica de Canarias.
- based in part on observations obtained with the HERMES spectrograph, which is supported by the Fund for Scientific Research of Flanders (FWO), Belgium, the Research Council of K. U. Leuven, Belgium, the Fonds National Recherches Scientific (FNRS), Belgium, the Royal Observatory of Belgium, the Observatoire de Genève, Switzerland and the Thüringer Landessternwarte, Tautenburg, Germany.

The friendly and highly competent assistance of all technical and support staff was highly appreciated.

The research conducted for my dissertation has made

- extensive use of NASA's Astrophysics Data System,
- the arXiv e-print service, owned and operated by Cornell University,
- the SIMBAD database and VizieR catalogue access tool, operated at CDS, Strasbourg, France, and also of
- the WEBDA database, operated at the Department of Theoretical Physics and Astrophysics of the Masaryk University, developed and maintained by Ernst Paunzen, Christian Stütz, and Jan Janikand, and originally developed by Jean-Claude Mermilliod.

This dissertation was funded by the Swiss National Science Foundation, Geneva University, and the canton of Geneva.

Bibliography

Aerts, C., Christensen-Dalsgaard, J., & Kurtz, D. W. 2010, Asteroseismology (Springer) [ADS]

Akerlof, C., Amrose, S., Balsano, R., et al. 2000, AJ, 119, 1901 [ADS] [arXiv]

Albrow, M. D. & Cottrell, P. L. 1994, MNRAS, 267, 548 [ADS]

Alcock, C., Allsman, R. A., Alves, D. R., et al. 1999, AJ, 117, 920 [ADS] [arXiv]

Alvarez, R., Jorissen, A., Plez, B., Gillet, D., & Fokin, A. 2000, A&A, 362, 655 [ADS] [arXiv]

Alvarez, R., Jorissen, A., Plez, B., et al. 2001a, A&A, 379, 288 [ADS] [arXiv]

Alvarez, R., Jorissen, A., Plez, B., et al. 2001b, A&A, 379, 305 [ADS] [arXiv]

An, D., Terndrup, D. M., & Pinsonneault, M. H. 2007, ApJ, 671, 1640 [ADS] [arXiv]

Anderson, R. I., Eyer, L., & Mowlavi, N. 2012a, in IAU Symposium, Vol. 285, IAU Symposium, ed. E. Griffin, R. Hanisch, & R. Seaman, p. 275 [ADS]

Anderson, R. I., Eyer, L., & Mowlavi, N. 2013a, MNRAS, 434, 2238 [ADS] [arXiv]

Anderson, R. I., Mowlavi, N., & Eyer, L. 2012b, Populations of Variable Stars in Open Clusters, ed. A. Moitinho & J. Alves, Populations of Variable Stars in Open Clusters, 255 [ADS]

Anderson, R. I., Mowlavi, N., & Eyer, L. 2013b, in IAU Symposium, Vol. 289, IAU Symposium, ed. R. de Grijs, p. 153 [ADS]

Anderson, R. I., Reiners, A., & Solanki, S. K. 2010, A&A, 522, A81 [ADS] [arXiv]

Anderson, R. I., Reiners, A., & Solanki, S. K. 2011, in Astronomical Society of the Pacific Conference Series, Vol. 448, 16th Cambridge Workshop on Cool Stars, Stellar Systems, and the Sun, ed. C. Johns-Krull, M. K. Browning, & A. A. West, p. 1061 [ADS] [arXiv]

Andrievsky, S. M., Kovtyukh, V. V., Luck, R. E., et al. 2002, A&A, 381, 32 [ADS] [arXiv]

Armstrong, J. T., Nordgren, T. E., Germain, M. E., et al. 2001, AJ, 121, 476 [ADS] [arXiv]

Baade, W. 1926, Astronomische Nachrichten, 228, 359 [ADS]

Baade, W. 1956, PASP, 68, 5 [ADS]

Baker, N. & Kippenhahn, R. 1962, ZAp, 54, 114 [ADS]

Baranne, A., Queloz, D., Mayor, M., et al. 1996, A&AS, 119, 373 [ADS]

Barnes, T. G. & Evans, D. S. 1976, MNRAS, 174, 489 [ADS]

Baumgardt, H., Dettbarn, C., & Wielen, R. 2000, A&AS, 146, 251 [ADS] [arXiv]

Bayer, J. 1603, Uranometria (Augustae Vindelicorum: Excudit Christophorus Mangus.) [www]

Beaulieu, J. P., Grison, P., Tobin, W., et al. 1995, A&A, 303, 137 [ADS] [arXiv]

Becker, W. 1940, ZAp, 19, 289 [ADS]

Belopolsky, A. 1895, ApJ, 1, 160 [ADS]

Benedict, G. F., McArthur, B. E., Feast, M. W., et al. 2007, AJ, 133, 1810 [ADS] [arXiv]

Benz, W. & Mayor, M. 1982, A&A, 111, 224 [ADS]

Benz, W. & Mayor, M. 1984, A&A, 138, 183 [ADS]

Benz, W. & Stellingwerf, R. F. 1985, ApJ, 297, 686 [ADS]

Berdnikov, L. N. 2008, VizieR Online Catalog, II/285 [ADS]

Berdnikov, L. N., Pastukhova, E. N., Gorynya, N. A., Zharova, A. V., & Turner, D. G. 2007, PASP, 119, 82 [ADS]

Berdnikov, L. N., Samus, N. N., Antipin, S. V., et al. 2004, PASP, 116, 536 [ADS]

Berdnikov, L. N. & Turner, D. G. 2004, Astronomical and Astrophysical Transactions, 23, 123 [ADS]

Bersier, D. & Burki, G. 1996, A&A, 306, 417 [ADS]

Böhm-Vitense, E. & Proffitt, C. 1985, ApJ, 296, 175 [ADS]

Boisse, I., Eggenberger, A., Santos, N. C., et al. 2010, A&A, 523, A88 [ADS] [arXiv]

Bond, H. E. & Sparks, W. B. 2009, A&A, 495, 371 [ADS] [arXiv]

Bono, G., Caputo, F., & Castellani, V. 2006, Mem. Soc. Astron. Italiana, 77, 207 [ADS]

Bono, G., Castellani, V., & Marconi, M. 2000, ApJ, 529, 293 [ADS] [arXiv]

Bono, G., Marconi, M., Cassisi, S., et al. 2005, ApJ, 621, 966 [ADS] [arXiv]

Bouchy, F., Pepe, F., & Queloz, D. 2001, A&A, 374, 733 [ADS]

Brink, H., Richards, J. W., Poznanski, D., et al. 2013, MNRAS, 435, 1047 [ADS] [arXiv]

Bukowiecki, Ł., Maciejewski, G., Konorski, P., & Strobel, A. 2011, Acta Astron., 61, 231 [ADS] [arXiv]

Burki, G., Mayor, M., & Benz, W. 1982, A&A, 109, 258 [ADS]

Butler, R. P. 1993, ApJ, 415, 323 [ADS]

Campbell, L. & Jacchia, L. G. 1941, The story of variable stars, ed. H. Shapley & B. J. Bok (The Blakiston company, Philadelphia) [ADS]

Caputo, F., Bono, G., Fiorentino, G., Marconi, M., & Musella, I. 2005, ApJ, 629, 1021 [ADS] [arXiv]

Cassisi, S. & Salaris, M. 2011, ApJ, 728, L43 [ADS] [arXiv]

Castellani, V., Chieffi, A., & Straniero, O. 1992, ApJS, 78, 517 [ADS]

Chadid, M. & Gillet, D. 1996a, A&A, 308, 481 [ADS]

Chadid, M. & Gillet, D. 1996b, A&A, 315, 475 [ADS]

Chadid, M. & Gillet, D. 1997, A&A, 319, 154 [ADS]

Christiansen, J. L., Derekas, A., Kiss, L. L., et al. 2008, MNRAS, 385, 1749 [ADS] [arXiv]

Christy, R. F. 1968, QJRAS, 9, 13 [ADS]

Clementini, G. 2009, in IAU Symposium, Vol. 256, IAU Symposium, ed. J. T. Van Loon & J. M. Oliveira, p. 373 [ADS]

Cox, A. N. 1980, ARA&A, 18, 15 [ADS]

Cox, J. P. & Whitney, C. 1958, ApJ, 127, 561 [ADS]

Cox, N. L. J., Kerschbaum, F., van Marle, A.-J., et al. 2012, A&A, 537, A35 [ADS] [arXiv]

Cutri, R. M., Skrutskie, M. F., van Dyk, S., et al. 2003, 2MASS All Sky Catalog of point sources. (NASA/IPAC Infrared Science Archive) [ADS]

Dawe, J. A. 1969, MNRAS, 145, 377 [ADS]

D'Cruz, N. L., Morgan, S. M., & Böhm-Vitense, E. 2000, AJ, 120, 990 [ADS]

de Grijs, R. 2011, An Introduction to Distance Measurement in Astronomy (Wiley) [www]

de Grijs, R. 2013a, IAU Symposium, Vol. 289, Advancing the Physics of Cosmic Distances (CUP) [ADS]

de Grijs, R. 2013b, in IAU Symposium, Vol. 289, IAU Symposium, ed. R. de Grijs, p. 351 [ADS] [arXiv]

de Loore, C. & Doom, C. 1992, Structure and Evolution of Single and Binary Stars, Astrophysics and space science library (Kluwer Academic Publishers)

Dias, W. S., Alessi, B. S., Moitinho, A., & Lépine, J. R. D. 2002, A&A, 389, 871 [ADS] [arXiv]

Donati, J. & Landstreet, J. D. 2009, ARA&A, 47, 333 [ADS] [arXiv]

Doppler, C. A. 1842, Über das farbige Licht der Doppelsterne und einiger anderer Gestirne des Himmels (Verlag der Königl. Böhm. Gesellschaft der Wissenschaften)

Driebe, T., Schoenberner, D., Bloecker, T., & Herwig, F. 1998, A&A, 339, 123 [ADS] [arXiv]

Dubath, P., Rimoldini, L., Süveges, M., et al. 2011, MNRAS, 414, 2602 [ADS] [arXiv]

Dumusque, X., Pepe, F., Lovis, C., et al. 2012, Nature, 491, 207 [ADS]

Duquennoy, A. & Mayor, M. 1991, A&A, 248, 485 [ADS]

Eddington, A. S. 1917, The Observatory, 40, 290 [ADS]

Eddington, A. S. 1918a, The Observatory, 41, 379 [ADS]

Eddington, A. S. 1918b, MNRAS, 79, 2 [ADS]

Eddington, A. S. 1919a, The Observatory, 42, 338 [ADS]

Eddington, A. S. 1919b, MNRAS, 79, 177 [ADS]

Eddington, A. S. 1926a, The Internal Constitution of the Stars (CUP) [ADS]

Eddington, A. S. 1926b, The Observatory, 49, 88 [ADS]

Eddington, Sir, A. S. 1941, MNRAS, 101, 182 [ADS]

Efremov, Y. N. 1975, Classical Cepheids, ed. B. V. Kukarkin, Classical Cepheids (John Wiley & Sons, New York), 42 [ADS]

Ekström, S., Georgy, C., Eggenberger, P., et al. 2012, A&A, 537, A146 [ADS] [arXiv]

Engle, S. G. & Guinan, E. F. 2012, Journal of Astronomy and Space Sciences, 29, 181 [ADS] [arXiv]

Evans, N. R. 1991, ApJ, 372, 597 [ADS]

Evans, N. R. 1992a, ApJ, 384, 220 [ADS]

Evans, N. R. 1992b, ApJ, 389, 657 [ADS]

Evans, N. R. 1994, ApJ, 436, 273 [ADS]

Evans, N. R., Berdnikov, L., Gorynya, N., Rastorguev, A., & Eaton, J. 2011, AJ, 142, 87 [ADS]

Evans, N. R. & Bolton, C. T. 1990, ApJ, 356, 630 [ADS]

Evans, N. R., Bond, H. E., Schaefer, G. H., et al. 2013, AJ, 146, 93 [ADS] [arXiv]

Eyer, L. & Blake, C. 2002, in Astronomical Society of the Pacific Conference Series, Vol. 259, IAU Colloq. 185: Radial and Nonradial Pulsationsn as Probes of Stellar Physics, ed. C. Aerts, T. R. Bedding, & J. Christensen-Dalsgaard, p. 160 [ADS] [arXiv]

Eyer, L. & Blake, C. 2005, MNRAS, 358, 30 [ADS] [arXiv]

Eyer, L., Eggenberger, P., Greco, C., et al. 2012a, Time-Resolved Surveys of Stellar Clusters, ed. A. Moitinho & J. Alves, Time-Resolved Surveys of Stellar Clusters, 21 [ADS]

Eyer, L., Jan, A., Dubath, P., et al. 2008, in American Institute of Physics Conference Series, Vol. 1082, American Institute of Physics Conference Series, ed. C. A. L. Bailer-Jones, p. 257 [ADS] [arXiv]

Eyer, L., Palaversa, L., Mowlavi, N., et al. 2012b, Ap&SS, 341, 207 [ADS] [arXiv]

Feast, M. 1999, PASP, 111, 775 [ADS]

Feast, M. W. 1957, MNRAS, 117, 193 [ADS]

Feast, M. W. 2008, MNRAS, 387, L33 [ADS] [arXiv]

Feast, M. W. & Catchpole, R. M. 1997, MNRAS, 286, L1 [ADS]

Fernie, J. D., Evans, N. R., Beattie, B., & Seager, S. 1995, IBVS, 4148, 1 [ADS]

Figueira, P., Santos, N. C., Pepe, F., Lovis, C., & Nardetto, N. 2013, A&A, 557, A93 [ADS] [arXiv]

Fokin, A. B. 1992, MNRAS, 256, 26 [ADS]

Fokin, A. B. & Gillet, D. 1994, A&A, 290, 875 [ADS]

Fokin, A. B. & Gillet, D. 1997, A&A, 325, 1013 [ADS]

Fokin, A. B., Gillet, D., & Breitfellner, M. G. 1996, A&A, 307, 503 [ADS]

Fouqué, P., Arriagada, P., Storm, J., et al. 2007, A&A, 476, 73 [ADS] [arXiv]

Fouqué, P. & Gieren, W. P. 1997, A&A, 320, 799 [ADS]

Freedman, D. & Diaconis, P. 1981, Zeitschrift für Wahrscheinlichkeitstheorie und Verwandte Gebiete, 57, 453 [www]

Freedman, W. L. 2013, in IAU Symposium, Vol. 289, IAU Symposium, ed. R. de Grijs, p. 3 [ADS]

Freedman, W. L., Madore, B. F., Scowcroft, V., et al. 2011, AJ, 142, 192 [ADS] [arXiv]

French, L. M. 2012, Journal of the American Association of Variable Star Observers (JAAVSO), 40, 120 [ADS] [arXiv]

Frutiger, C., Solanki, S. K., & Mathys, G. 2005, A&A, 444, 549 [ADS]

Gallenne, A., Kervella, P., Mérand, A., et al. 2012, A&A, 541, A87 [ADS] [arXiv]

Gallenne, A., Merand, A., Kervella, P., et al. 2013a, ArXiv e-prints [ADS] [arXiv]

Gallenne, A., Monnier, J. D., Mérand, A., et al. 2013b, A&A, 552, A21, 1302.1817 [ADS] [arXiv]

Gautschy, A. 1997, Vistas in Astronomy, 41, 95 [ADS]

Gautschy, A. 2003, The history of radial stellar pulsation theory (Eidgenössische Technische Hochschule Zürich, ETH Bibliothek) [www]

Georgy, C., Ekström, S., Eggenberger, P., et al. 2013a, A&A, 558, A103 [ADS] [arXiv]

Georgy, C., Ekström, S., Granada, A., et al. 2013b, A&A, 553, A24 [ADS] [arXiv]

Gieren, W., Storm, J., Nardetto, N., et al. 2013, in IAU Symposium, Vol. 289, IAU Symposium, ed. R. de Grijs, p. 138 [ADS] [arXiv]

Gieren, W. P., Barnes, III, T. G., & Moffett, T. J. 1993, ApJ, 418, 135 [ADS]

Gilmore, G., Randich, S., Asplund, M., et al. 2012, The Messenger, 147, 25 [ADS]

Goodricke, J. 1783, Royal Society of London Philosophical Transactions Series I, 73, 474 [ADS]

Goodricke, J. 1786, Royal Society of London Philosophical Transactions Series I, 76, 48 [ADS]

Gorynya, N. A., Irsmambetova, T. R., Rastorgouev, A. S., & Samus, N. N. 1992, Soviet Astronomy Letters, 18, 316 [ADS]

Gorynya, N. A., Samus', N. N., Rastorguev, A. S., & Sachkov, M. E. 1996, Astronomy Letters, 22, 175 [ADS]

Gorynya, N. A., Samus', N. N., Sachkov, M. E., et al. 1998, Astronomy Letters, 24, 815 [ADS]

Gorynya, N. A., Samus, N. N., Sachkov, M. E., et al. 2002, VizieR Online Data Catalog III/229, 3229, 0 [ADS]

Granada, A., Ekström, S., Georgy, C., et al. 2013, A&A, 553, A25 [ADS] [arXiv]

Gray, D. F. 2008, The Observation and Analysis of Stellar Photospheres [ADS]

Grenfell, T. C. & Wallerstein, G. 1969, PASP, 81, 732 [ADS]

Grindlay, J., Tang, S., Los, E., & Servillat, M. 2012, in IAU Symposium, Vol. 285, IAU Symposium, ed. E. Griffin, R. Hanisch, & R. Seaman, p. 29 [ADS] [arXiv]

Groenewegen, M. A. T. 2007, A&A, 474, 975 [ADS]

Groenewegen, M. A. T. 2008, A&A, 488, 25 [ADS] [arXiv]

Groenewegen, M. A. T. 2013, A&A, 550, A70 [ADS] [arXiv]

Groh, J. H. 2011, Journal of Physics Conference Series, 328, 012020 [ADS]

Groh, J. H., Meynet, G., & Ekström, S. 2013, A&A, 550, L7 [ADS] [arXiv]

Grossmann-Doerth, U. 1994, A&A, 285, 1012 [ADS]

Guinan, E. F., Fitzpatrick, E. L., Dewarf, L. E., et al. 1998, ApJ, 509, L21 [ADS] [arXiv]

Gullberg, D. & Lindegren, L. 2002, A&A, 390, 383 [ADS]

Harris, J. & Zaritsky, D. 2004, AJ, 127, 1531 [ADS] [arXiv]

Harris, J. & Zaritsky, D. 2009, AJ, 138, 1243 [ADS] [arXiv]

Hertzsprung, E. 1912, Astronomische Nachrichten, 192, 261 [ADS]

Hertzsprung, E. 1913, Astronomische Nachrichten, 196, 201 [ADS]

Hertzsprung, E. 1926, Bull. Astron. Inst. Netherlands, 3, 115 [ADS]

Hilditch, R. W. 2001, An Introduction to Close Binary Stars (CUP) [ADS]

Hilditch, R. W., Howarth, I. D., & Harries, T. J. 2005, MNRAS, 357, 304 [ADS] [arXiv]

Hindsley, R. & Bell, R. A. 1986, PASP, 98, 881 [ADS]

Hofmeister, E., Kippenhahn, R., & Weigert, A. 1964, ZAp, 59, 242 [ADS]

Huang, W., Gies, D. R., & McSwain, M. V. 2010, ApJ, 722, 605 [ADS] [arXiv]

Hubble, E. P. 1925, ApJ, 62, 409 [ADS]

Irwin, J. B. 1955, Monthly Notes of the Astronomical Society of South Africa, 14, 38 [ADS]

Ivezić, Ž., Connolly, A., Vanderplas, J., & Gray, A. 2013, Statistics, Data Mining and Machine Learning in Astronomy (Princeton University Press)

Jaynes, E. T. 2003, Probability Theory - The Logic of Science (Cambridge University Press)

Jeans, J. H. 1925, MNRAS, 85, 797 [ADS]

Johns-Krull, C. M. & Valenti, J. A. 2000, in Astronomical Society of the Pacific Conference Series, Vol. 198, Stellar Clusters and Associations: Convection, Rotation, and Dynamos, ed. R. Pallavicini, G. Micela, & S. Sciortino, p. 371 [ADS]

Jorissen, A., Dedecker, M., Plez, B., Gillet, D., & Fokin, A. 2003, ArXiv e-prints [ADS] [arXiv]

Joy, A. H. 1939, ApJ, 89, 356 [ADS]

Keller, S. C. 2008, ApJ, 677, 483 [ADS] [arXiv]

Kervella, P., Bersier, D., Mourard, D., Nardetto, N., & Coudé du Foresto, V. 2004a, A&A, 423, 327 [ADS] [arXiv]

Kervella, P., Bersier, D., Mourard, D., et al. 2004b, A&A, 428, 587 [ADS]

Kervella, P., Bersier, D., Nardetto, N., et al. 2004c, The Messenger, 117, 53 [ADS]

Kervella, P., Coudé du Foresto, V., Perrin, G., et al. 2001, A&A, 367, 876 [ADS] [arXiv]

Kervella, P., Coudé du Foresto, V., Traub, W. A., & Lacasse, M. G. 1999, in Astronomical Society of the Pacific Conference Series, Vol. 194, Working on the Fringe: Optical and IR Interferometry from Ground and Space, ed. S. Unwin & R. Stachnik, p. 22 [ADS]

Kervella, P., Fouqué, P., Storm, J., et al. 2004d, ApJ, 604, L113 [ADS] [arXiv]

Kervella, P., Mérand, A., & Gallenne, A. 2009, A&A, 498, 425 [ADS] [arXiv]

Kervella, P., Mérand, A., Perrin, G., & Coudé du Foresto, V. 2006, A&A, 448, 623 [ADS]

Kervella, P., Mérand, A., Szabados, L., et al. 2008, A&A, 480, 167 [ADS] [arXiv]

Kervella, P., Mérand, A., Szabados, L., et al. 2012, A&A, 541, A18 [ADS] [arXiv]

Kervella, P., Nardetto, N., Bersier, D., Mourard, D., & Coudé du Foresto, V. 2004e, A&A, 416, 941 [ADS] [arXiv]

Kharchenko, N. V., Piskunov, A. E., Schilbach, E., Röser, S., & Scholz, R.-D. 2012, A&A, 543, A156, (K12) [ADS] [arXiv]

Kholopov, P. N. 1956, Peremennye Zvezdy, 11, 325 [ADS]

King, I. 1962, AJ, 67, 471 [ADS]

Kippenhahn, R., Thomas, H. C., & Weigert, A. 1965, ZAp, 61, 241 [ADS]

Kippenhahn, R. & Weigert, A. 1994, Stellar Structure and Evolution, Astronomy and Astrophysics Library (Springer) [ADS]

Kiss, L. L. & Vinkó, J. 2000, MNRAS, 314, 420 [ADS] [arXiv]

Klagyivik, P. & Szabados, L. 2009, A&A, 504, 959 [ADS] [arXiv]

Kolenberg, K. 2013, in Astrophysics and Space Science Proceedings, Vol. 31, Stellar Pulsations: Impact of New Instrumentation and New Insights, ed. J. C. Suárez, R. Garrido, L. A. Balona, & J. Christensen-Dalsgaard, p. 109 [ADS] [arXiv]

Komatsu, E., Dunkley, J., Nolta, M. R., et al. 2009, ApJS, 180, 330 [ADS] [arXiv]

Kovtyukh, V. V., Andrievsky, S. M., Luck, R. E., & Gorlova, N. I. 2003, A&A, 401, 661 [ADS] [arXiv]

Kraft, R. P. 1956, PASP, 68, 137 [ADS]

Kraft, R. P. 1967, in IAU Symposium, Vol. 28, Aerodynamic Phenomena in Stellar Atmospheres, ed. R. N. Thomas, p. 207 [ADS]

Krone-Martins, A. & Moitinho, A. 2013, ArXiv e-prints [ADS] [arXiv]

Kukarkin, B. V. 1975, Pulsating stars, IPST Astrophysics Library (John Wiley & Sons) [ADS]

Kukarkin, B. V. & Kholopov, P. N. 1982, New Catalogue of Suspected Variable Stars (Moscow: Publication Office Nauka, 1982) [ADS]

Lagarde, N., Decressin, T., Charbonnel, C., et al. 2012, A&A, 543, A108 [ADS]

Laney, C. D. & Joner, M. D. 2009, in American Institute of Physics Conference Series, Vol. 1170, American Institute of Physics Conference Series, ed. J. A. Guzik & P. A. Bradley, p. 93 [ADS]

Laney, C. D. & Stobie, R. S. 1995, MNRAS, 274, 337 [ADS]

Leavitt, H. S. 1908, Annals of Harvard College Observatory, 60, 87 [ADS]

Leavitt, H. S. & Pickering, E. C. 1912, Harvard College Observatory Circular, 173, 1 [ADS]

Lee, C.-H., Kodric, M., Seitz, S., et al. 2013, ApJ, 777, 35 [ADS] [arXiv]

Lindegren, L., Dravins, D., & Madsen, S. 1999, in Astronomical Society of the Pacific Conference Series, Vol. 185, IAU Colloq. 170: Precise Stellar Radial Velocities, ed. J. B. Hearnshaw & C. D. Scarfe, p. 73 [ADS]

Luck, R. E., Andrievsky, S. M., Korotin, S. N., & Kovtyukh, V. V. 2013, AJ, 146, 18 [ADS]

Luck, R. E. & Lambert, D. L. 2011, AJ, 142, 136 [ADS] [arXiv]

Lutz, T. E. & Kelker, D. H. 1973, PASP, 85, 573 [ADS]

Madore, B. F. 1982, ApJ, 253, 575 [ADS]

Madore, B. F. & Freedman, W. L. 1991, PASP, 103, 933 [ADS]

Maeder, A. 1985, in European Southern Observatory Conference and Workshop Proceedings, Vol. 21, European Southern Observatory Conference and Workshop Proceedings, ed. I. J. Danziger, F. Matteucci, & K. Kjar, p. 187 [ADS]

Maeder, A. 2009, Physics, Formation and Evolution of Rotating Stars, Astronomy and Astrophysics Library (Springer) [ADS]

Maeder, A. & Meynet, G. 1989, A&A, 210, 155 [ADS]

Maeder, A. & Meynet, G. 2000, ARA&A, 38, 143 [ADS] [arXiv]

Maeder, A. & Meynet, G. 2001, A&A, 373, 555 [ADS] [arXiv]

Mahabal, A. A., Drake, A. J., Djorgovski, S. G., et al. 2012, The Astronomer's Telegram, 3872, 1 [ADS]

Majaess, D., Turner, D., & Gieren, W. 2011, ApJ, 741, L36 [ADS] [arXiv]

Majaess, D., Turner, D., & Gieren, W. 2012a, ApJ, 747, 145 [ADS] [arXiv]

Majaess, D., Turner, D., Gieren, W., Balam, D., & Lane, D. 2012b, ApJ, 748, L9 [ADS] [arXiv]

Majaess, D., Turner, D. G., & Gieren, W. 2012c, MNRAS, 421, 1040 [ADS] [arXiv]

Marengo, M., Evans, N. R., Barmby, P., et al. 2010, ApJ, 725, 2392 [ADS] [arXiv]

Mathias, P. & Gillet, D. 1993, A&A, 278, 511 [ADS]

Mathias, P., Gillet, D., Fokin, A. B., et al. 2006, A&A, 457, 575 [ADS]

Matsunaga, N., Kawadu, T., Nishiyama, S., et al. 2011, Nature, 477, 188 [ADS] [arXiv]

Matthews, L. D., Marengo, M., Evans, N. R., & Bono, G. 2012, ApJ, 744, 53 [ADS] [arXiv]

McSwain, M. V. & Gies, D. R. 2005, ApJS, 161, 118 [ADS] [arXiv]

Meitner, L. & Frisch, O. R. 1939, Nature, 143, 239

Mérand, A., Aufdenberg, J. P., Kervella, P., et al. 2007, ApJ, 664, 1093 [ADS] [arXiv]

Mérand, A., Kervella, P., Coudé du Foresto, V., et al. 2006, A&A, 453, 155 [ADS]

Mérand, A., Kervella, P., Coudé du Foresto, V., et al. 2005, A&A, 438, L9 [ADS]

Merrill, P. W. & Greenstein, J. L. 1958, PASP, 70, 98 [ADS]

Miller, B., King, J. R., Chen, Y., & Boesgaard, A. M. 2013, ArXiv e-prints [ADS] [arXiv]

Monet, D. G., Levine, S. E., Canzian, B., et al. 2003, AJ, 125, 984 [ADS] [arXiv]

Monson, A. J. & Pierce, M. J. 2011, ApJS, 193, 12 [ADS]

Moskalik, P., Buchler, J. R., & Marom, A. 1992, ApJ, 385, 685 [ADS]

Mourard, D., Bonneau, D., Koechlin, L., et al. 1997, A&A, 317, 789 [ADS]

Mowlavi, N., Barblan, F., Saesen, S., & Eyer, L. 2013, A&A, 554, A108 [ADS] [arXiv]

Mowlavi, N., Eggenberger, P., Meynet, G., et al. 2012, A&A, 541, A41 [ADS] [arXiv]

Nardetto, N., Fokin, A., Fouqué, P., et al. 2011, A&A, 534, L16 [ADS] [arXiv]

Nardetto, N., Fokin, A., Mourard, D., et al. 2004, A&A, 428, 131 [ADS]

Nardetto, N., Gieren, W., Kervella, P., et al. 2009, A&A, 502, 951 [ADS] [arXiv]

Nardetto, N., Mathias, P., Fokin, A., et al. 2013, A&A, 553, A112 [ADS] [arXiv]

Nardetto, N., Mourard, D., Kervella, P., et al. 2006, A&A, 453, 309 [ADS] [arXiv]

Nardetto, N., Mourard, D., Mathias, P., Fokin, A., & Gillet, D. 2007, A&A, 471, 661 [ADS] [arXiv]

Nardetto, N., Stoekl, A., Bersier, D., & Barnes, T. G. 2008, A&A, 489, 1255 [ADS]

Neilson, H. R., Biesiada, M., Remage Evans, N., et al. 2013, ArXiv e-prints [ADS] [arXiv]

Neilson, H. R., Cantiello, M., & Langer, N. 2011, A&A, 529, L9 [ADS] [arXiv]

Neilson, H. R. & Langer, N. 2012, A&A, 537, A26 [ADS] [arXiv]

Neilson, H. R., Langer, N., Engle, S. G., Guinan, E., & Izzard, R. 2012, ApJ, 760, L18 [ADS] [arXiv]

Neilson, H. R. & Lester, J. B. 2008, ApJ, 684, 569 [ADS] [arXiv]

Ngeow, C.-C., Neilson, H. R., Nardetto, N., & Marengo, M. 2012, A&A, 543, A55 [ADS] [arXiv]

Nieva, M.-F. & Przybilla, N. 2012, A&A, 539, A143 [ADS] [arXiv]

Nordgren, T. E., Armstrong, J. T., Germain, M. E., et al. 2000, ApJ, 543, 972 [ADS] [arXiv]

O'Connell, D. J. K. 1951, Publications of the Riverview College Observatory, 2, 100 [ADS]

Oosterhoff, P. T. 1957, Bull. Astron. Inst. Netherlands, 13, 317 [ADS]

Pan, X., Shao, M., & Kulkarni, S. R. 2004, Nature, 427, 326 [ADS]

Papics, P. I. 2013, PhD thesis, Instituut voor Sterrenkunde, KU Leuven, Celestijnenlaan 200D, B-3001 Leuven, Belgium [ADS]

Parsons, S. B. 1972, ApJ, 174, 57 [ADS]

Patat, F., Cordiner, M. A., Cox, N. L. J., et al. 2013, A&A, 549, A62 [ADS] [arXiv]

Pepe, F., Mayor, M., Delabre, B., et al. 2000, in Society of Photo-Optical Instrumentation Engineers (SPIE) Conference Series, Vol. 4008, Society of Photo-Optical Instrumentation Engineers (SPIE) Conference Series, ed. M. Iye & A. F. Moorwood, p. 582 [ADS]

Pepe, F., Mayor, M., Galland, F., et al. 2002, A&A, 388, 632 [ADS] [arXiv]

Perryman, M. A. C. & ESA. 1997, ESA Special Publication, Vol. 1200, The HIPPARCOS and TYCHO catalogues. Astrometric and photometric star catalogues derived from the ESA HIPPARCOS Space Astrometry Mission [ADS]

Petersen, J. O. 1973, A&A, 27, 89 [ADS]

Petersen, J. O. & Takeuti, M. 2001, A historical sketch of the beat Cepheid studies, ed. M. Takeuti & D. D. Sasselov, A historical sketch of the beat Cepheid studies (Kluwer Academic Publishers), 1–28 [ADS]

Peterson, R. C., Carney, B. W., & Latham, D. W. 1996, ApJ, 465, L47 [ADS]

Petterson, O. K. L., Cottrell, P. L., Albrow, M. D., & Fokin, A. 2005, MNRAS, 362, 1167 [ADS]

Pickering, E. C. 1912, Annals of Harvard College Observatory, 56, 1 [ADS]

Pietrinferni, A., Cassisi, S., Salaris, M., & Castelli, F. 2006, ApJ, 642, 797 [ADS] [arXiv]

Pietrukowicz, P. 2001, Acta Astron., 51, 247 [ADS] [arXiv]

Pietrzyński, G., Graczyk, D., Gieren, W., et al. 2013, Nature, 495, 76 [ADS] [arXiv]

Pietrzyński, G., Thompson, I. B., Gieren, W., et al. 2010, Nature, 468, 542 [ADS]

Pietrzyński, G., Thompson, I. B., Graczyk, D., et al. 2011, ApJ, 742, L20 [ADS] [arXiv]

Pietrzynski, G. & Udalski, A. 1999, Acta Astron., 49, 543 [ADS] [arXiv]

Pigulski, A. 2013, ArXiv e-prints [ADS] [arXiv]

Planck Collaboration. 2013, ArXiv e-prints [ADS] [arXiv]

Pojmanski, G. 1997, Acta Astron., 47, 467 [ADS] [arXiv]

Pojmanski, G. 2002, Acta Astron., 52, 397 [ADS] [arXiv]

Pojmanski, G., Pilecki, B., & Szczygiel, D. 2005, Acta Astron., 55, 275 [ADS] [arXiv]

Popper, K. 1935, Logik der Forschung (Julius Springer, Vienna, Austria)

Pourbaix, D., Platais, I., Detournay, S., et al. 2003, A&A, 399, 1167 [ADS] [arXiv]

Prada Moroni, P. G., Gennaro, M., Bono, G., et al. 2012, ApJ, 749, 108 [ADS] [arXiv]

Preston, G. W. 2011, AJ, 141, 6 [ADS] [arXiv]

Queloz, D., Henry, G. W., Sivan, J. P., et al. 2001a, A&A, 379, 279 [ADS] [arXiv]

Queloz, D., Mayor, M., Udry, S., et al. 2001b, The Messenger, 105, 1 [ADS]

Raskin, G. & Van Winckel, H. 2013, ArXiv e-prints [ADS] [arXiv]

Raskin, G., van Winckel, H., Hensberge, H., et al. 2011, A&A, 526, A69 [ADS] [arXiv]

Reiners, A. 2011, in Astronomical Society of the Pacific Conference Series, Vol. 448, 16th Cambridge Workshop on Cool Stars, Stellar Systems, and the Sun, ed. C. Johns-Krull, M. K. Browning, & A. A. West, p. 255 [ADS] [arXiv]

Richards, J. W., Starr, D. L., Miller, A. A., et al. 2012, ApJS, 203, 32 [ADS] [arXiv]

Rimoldini, L., Dubath, P., Süveges, M., et al. 2012, MNRAS, 427, 2917 [ADS] [arXiv]

Ritter, A. 1879, Wiedemanns Annalen, VIII, 173

Robichon, N., Arenou, F., Mermilliod, J.-C., & Turon, C. 1999, A&A, 345, 471 [ADS] [arXiv]

Robichon, N., Lebreton, Y., Turon, C., & Mermilliod, J.-C. 2000, in Astronomical Society of the Pacific Conference Series, Vol. 198, Stellar Clusters and Associations: Convection, Rotation, and Dynamos, ed. R. Pallavicini, G. Micela, & S. Sciortino, p. 141 [ADS]

Roeser, S., Demleitner, M., & Schilbach, E. 2010, AJ, 139, 2440 [ADS] [arXiv]

Rosseland, S. 1949, The pulsation theory of variable stars. (Oxford, Clarendon Press) [ADS]

Rüedi, I., Solanki, S. K., Mathys, G., & Saar, S. H. 1997, A&A, 318, 429 [ADS]

Rüeger, J. M. 2002, in UNISURV Special Series, S–68, ISBN 0-7334-1866-X

Sagan, C. 1980, Cosmos (Random House and Wings Books) [ADS]

Sahlmann, J. & Fekel, F. C. 2013, A&A, 556, A145 [ADS] [arXiv]

Sahlmann, J., Ségransan, D., Queloz, D., et al. 2011, A&A, 525, A95 [ADS] [arXiv]

Saio, H. & Gautschy, A. 1998, ApJ, 498, 360 [ADS] [arXiv]

Saio, H., Georgy, C., & Meynet, G. 2013, MNRAS, 433, 1246 [ADS] [arXiv]

Samus, N., Dadsurlevich, O., Kazarovets, E. V., et al. 2012, General Catalog of Variable Stars (GCVS database, Version 2012Jan), available at the CDS as: `B/gcvs` or under `http://www.sai.msu.su/gcvs/gcvs/`

Sana, H. & Evans, C. J. 2011, in IAU Symposium, Vol. 272, IAU Symposium, ed. C. Neiner, G. Wade, G. Meynet, & G. Peters, p. 474 [ADS] [arXiv]

Sandage, A. 1958a, ApJ, 128, 150 [ADS]

Sandage, A. 1958b, ApJ, 127, 513 [ADS]

Sandage, A. & Tammann, G. A. 2006, ARA&A, 44, 93 [ADS]

Santos, N. C., Mayor, M., Naef, D., et al. 2002, A&A, 392, 215 [ADS] [arXiv]

Sasselov, D. D., Fieldus, M. S., & Lester, J. B. 1989, ApJ, 337, L29 [ADS]

Sasselov, D. D. & Lester, J. B. 1990, ApJ, 362, 333

Scargle, J. D. 1998, ApJ, 504, 405 [ADS] [arXiv]

Schaefer, B. E. 2008, AJ, 135, 112 [ADS] [arXiv]

Schaller, G., Schaerer, D., Meynet, G., & Maeder, A. 1992, A&AS, 96, 269 [ADS]

Schmidt, E. G. & Parsons, S. B. 1982, ApJS, 48, 185 [ADS]

Schmidt, E. G. & Parsons, S. B. 1984a, ApJ, 279, 215 [ADS]

Schmidt, E. G. & Parsons, S. B. 1984b, ApJ, 279, 202 [ADS]

Schmidt, E. G., Rogalla, D., & Thacker-Lynn, L. 2011, AJ, 141, 53 [ADS]

Schwarzschild, M. 1952, in Transactions of the IAU, ed. P. T. Oosterhoff, Vol. VIII (Cambridge University Press), p. 811

Ségransan, D., Udry, S., Mayor, M., et al. 2010, A&A, 511, A45 [ADS] [arXiv]

Shapley, H. 1914, ApJ, 40, 448 [ADS]

Smeyers, P. 2010, Linear Isentropic Oscillations of Stars (Springer) [ADS]

Smolec, R. & Moskalik, P. 2010, A&A, 524, A40 [ADS] [arXiv]

Soderblom, D. R., Nelan, E., Benedict, G. F., et al. 2005, AJ, 129, 1616 [ADS] [arXiv]

Soszynski, I., Poleski, R., Udalski, A., et al. 2010, Acta Astron., 60, 17 [ADS] [arXiv]

Soszynski, I., Poleski, R., Udalski, A., et al. 2008, Acta Astron., 58, 163 [ADS] [arXiv]

Stello, D. & Nissen, P. E. 2001, A&A, 374, 105 [ADS] [arXiv]

Sterken, C. 2005, in Astronomical Society of the Pacific Conference Series, Vol. 335, The Light-Time Effect in Astrophysics: Causes and cures of the O-C diagram, ed. C. Sterken, p. 3 [ADS]

Stobie, R. S. 1969a, MNRAS, 144, 461 [ADS]

Stobie, R. S. 1969b, MNRAS, 144, 485 [ADS]

Stobie, R. S. 1969c, MNRAS, 144, 511 [ADS]

Storm, J., Carney, B. W., Gieren, W. P., et al. 2004, A&A, 415, 531 [ADS] [arXiv]

Storm, J., Gieren, W., Fouqué, P., et al. 2011a, A&A, 534, A94 [ADS] [arXiv]

Storm, J., Gieren, W., Fouqué, P., et al. 2011b, A&A, 534, A95 [ADS] [arXiv]

Süveges, M., Sesar, B., Váradi, M., et al. 2012, MNRAS, 424, 2528 [ADS] [arXiv]

Suyu, S. H., Treu, T., Blandford, R. D., et al. 2012, ArXiv e-prints, 1202.4459 [ADS] [arXiv]

Szabados, L. 2003, in Astronomical Society of the Pacific Conference Series, Vol. 298, GAIA Spectroscopy: Science and Technology, ed. U. Munari, p. 237 [ADS]

Szabados, L., Anderson, R. I., Derekas, A., et al. 2013a, MNRAS, 434, 870 [ADS] [arXiv]

Szabados, L., Derekas, A., Kiss, L. L., et al. 2013b, MNRAS, 430, 2018 [ADS] [arXiv]

Szabó, R., Buchler, J. R., & Bartee, J. 2007, ApJ, 667, 1150 [ADS] [arXiv]

Takeda, Y., Kang, D.-I., Han, I., Lee, B.-C., & Kim, K.-M. 2013, MNRAS, 432, 769 [ADS] [arXiv]

Tammann, G. A., Sandage, A., & Reindl, B. 2003, A&A, 404, 423 [ADS] [arXiv]

Tang, S., Grindlay, J., Los, E., & Servillat, M. 2013, PASP, 125, 857 [ADS] [arXiv]

Testa, V., Marconi, M., Musella, I., et al. 2007, A&A, 462, 599 [ADS] [arXiv]

Thompson, R. J. 1975, MNRAS, 172, 455 [ADS]

Turner, D. G. 1976, AJ, 81, 1125 [ADS]

Turner, D. G. 2001, Odessa Astronomical Publications, 14, 166 [ADS]

Turner, D. G. 2009, in American Institute of Physics Conference Series, Vol. 1170, American Institute of Physics Conference Series, ed. J. A. Guzik & P. A. Bradley, p. 59 [ADS] [arXiv]

Turner, D. G., Abdel-Sabour Abdel-Latif, M., & Berdnikov, L. N. 2006, PASP, 118, 410 [ADS] [arXiv]

Turner, D. G., Savoy, J., Derrah, J., Abdel-Sabour Abdel-Latif, M., & Berdnikov, L. N. 2005, PASP, 117, 207 [ADS]

Udalski, A., Szymanski, M., Kubiak, M., et al. 1999, Acta Astron., 49, 201 [ADS] [arXiv]

van den Bergh, S. 1957, ApJ, 126, 323 [ADS]

van Hoof, A. 1943, Ciel et Terre, 59, 369 [ADS]

van Hoof, A. & Deurinck, R. 1952, ApJ, 115, 166 [ADS]

van Leeuwen, F. 2007, Astrophysics and Space Science Library, Vol. 350, Hipparcos, the New Reduction of the Raw Data (Springer) [ADS]

van Leeuwen, F. 2009, A&A, 497, 209 [ADS] [arXiv]

van Leeuwen, F., Feast, M. W., Whitelock, P. A., & Laney, C. D. 2007, MNRAS, 379, 723 [ADS] [arXiv]

van Paradijs, J. A. 1971, A&A, 11, 299 [ADS]

Vanderplas, J., Connolly, A., Ivezić, Ž., & Gray, A. 2012, in Conference on Intelligent Data Understanding (CIDU), p. 47

Vogt, S. S., Allen, S. L., Bigelow, B. C., et al. 1994, in Society of Photo-Optical Instrumentation Engineers (SPIE) Conference Series, Vol. 2198, Society of Photo-Optical Instrumentation Engineers (SPIE) Conference Series, ed. D. L. Crawford & E. R. Craine, p. 362 [ADS]

Walker, A. R. 2012, Ap&SS, 341, 43 [ADS] [arXiv]

Wallerstein, G. 1972, PASP, 84, 656 [ADS]

Wallerstein, G. 1983, PASP, 95, 422 [ADS]

Wallerstein, G., Jacobsen, T. S., Cottrell, P. L., Clark, M., & Albrow, M. 1992, MNRAS, 259, 474 [ADS]

Watson, C. L. 2006, Society for Astronomical Sciences Annual Symposium, 25, 47 [ADS]

Weinberg, D. H., Mortonson, M. J., Eisenstein, D. J., et al. 2013, Phys. Rep., 530, 87 [ADS] [arXiv]

Wesselink, A. J. 1946, Bull. Astron. Inst. Netherlands, 10, 91 [ADS]

Westerlund, B. 1961, PASP, 73, 72 [ADS]

Windmark, F., Lindegren, L., & Hobbs, D. 2011, A&A, 530, A76 [ADS] [arXiv]

Worthey, G. & Lee, H.-c. 2011, ApJS, 193, 1 [ADS] [arXiv]

Woźniak, P. R., Vestrand, W. T., Akerlof, C. W., et al. 2004, AJ, 127, 2436 [ADS] [arXiv]

Wyrzykowski, L., Hodgkin, S., Blogorodnova, N., Koposov, S., & Burgon, R. 2012, ArXiv e-prints [ADS] [arXiv]

Zhevakin, S. 1953, Astron. Zhurnal, 30, 161

Zhevakin, S. A. 1963, ARA&A, 1, 367 [ADS]

Zwahlen, N., North, P., Debernardi, Y., et al. 2004, A&A, 425, L45 [ADS] [arXiv]